Growth and characterization of new 2D magnetic materials

Dissertation

zur Erlangung des Grades eines
Doktor der Naturwissenschaft
(Dr. rer. nat.)

am Fachbereich Physik
der Freien Universität Berlin
vorgelegt von

Sebastien Elie Hadjadj

Berlin, 20. Juni 2024

Tag der Disputation: 03.06.2024
1. Gutachter: Prof. Dr. Wolfgang Kuch
2. Gutachter: Prof. Dr. Katharina Franke

List of Acronyms

ML	monolayer	vii
BL	bilayer	vii
TL	trilayer	vii
TMDC	transition metal di-chalcogenide	vii
TMDH	transition metal di-halide	vii
TMTH	transition metal tri-halide	vii
1D	one-dimensional	10
2D	two-dimensional	vii
3D	three-dimensional	10
GK	Goodenough-Kanamori	19
vdW	van der Waals	12
SD	spin dimensionality	10
DFT	density functional theory	12
RT	room temperature	3
DOS	density of state	53
MDOS	magnon density of state	10

CDW	charge density wave	15
CFM	Centro de Física de Materiales	22
CINN	Centro de Investigación en Nanomateriales y Nanotecnología	58
FU	Freie Universität	xi
SLS	Swiss Light Source	25
UHV	ultra high vacuum	27
ALI	atomic layer injection	59
LEED	low energy electron diffraction	xii
STM	scanning tunneling microscopy	xii
STS	scanning tunneling spectroscopy	39
AFM	atomic force microscopy	16
LT-STM	low temperature STM	58
VT-STM	variable temperature STM	62
LEEM	low energy electron microscopy	69
XPEEM	x-ray photo emission electron microscopy	69
XPS	x-ray photoelectron spectroscopy	xii
XAS	x-ray absorption spectroscopy	23
XMCD	x-ray magnetic circular dichroism	xii

XLD	x-ray linear dichroism	xii
XNLD	x-ray natural linear dichroism	49
XMLD	x-ray magnetic linear dichroism	xii
ARPES	angle resolved photoelectron spectroscopy	64
QCM	quartz crystal microbalance	53
NEXAFS	near edge x-ray absorption fine-structure	42
EXAFS	extended x-ray absorption fine-structure	42
XPD	x-ray photoelectron diffraction	64
UPS	ultraviolet photoelectron spectroscopy	57
TSP	titanium sublimation pump	57
TEY	total electron yield	42
HS	high spin	18
CR	circular right	43
CL	circular left	43
LH	linear horizontal	50
LV	linear vertical	50
NI	normal incidence	43
GI	grazing incidence	43

TEY	total electron yield	42
CC	constant current	52
CH	constant height	52
FFT	fast fourier transformation	78
WF	workfunction	37
FWHM	full width at half maximum	xii
CCD	charge coupled device	35
STN	signal to noise	33
HV	high voltage	26
PE	pass energy	34
GS	ground state	39
ES	excited state	39
AFM	antiferromagnet	16
UA	uniaxial anisotropy	11
MCA	magnetocrystalline anisotropy	10
SA	shape anisotropy	10
OoP	out-of-plane	9
IP	in plane	10

SOC	spin-orbit coupling	38
CEF	crystal-electric field	117
SC	semiconductor	12
TI	topological insulator	12
FCC	face center cubic	21
HCP	hexagonal close packed	21
BLG	bilayer graphene	25
PVD	physical vapor deposition	30
CVD	chemical vapor deposition	20
MBE	molecular beam epitaxy	30
PBN	pyrolytic boron nitride	25

Abstract

This thesis presents the experimental investigation of different magnetic two-dimensional (2D) materials on Au(111) and on Bi_2Se_3. For the experimental characterization, different structural (low-temperature scanning tunneling microscopy (LT-STM) and low-energy electron diffraction (LEED)), chemical (x-ray photoelectron spectroscopy (XPS) and x-ray absorption spectroscopy (XAS)) and magnetic techniques (x-ray magnetic circular dichroism (XMCD) and magnetization curve measurements) have been used to investigate the material properties.

The scope of this thesis was to investigate the properties of monolayer (ML) and multilayer samples of new two-dimensional (2D) transition metal di-halides (TMDH) magnetic materials. In 2017 the first 2D magnets were found and characterized and since then, the main focus in the area of new 2D magnetic materials has been on transition metal di-chalcogenide (TMDC) and transition metal tri-halide (TMTH). Only recently also TMDH has been added in the research field. The focus of this work is the characterization of different transition metal di-halide (TMDH) on Au(111) and Bi_2Se_3. The work in this thesis builds the needed fundamental background for later possible spintronic device applications.

In the first and second part of the thesis, $FeBr_2$ was grown on Au(111) and Bi_2Se_3 to investigate the material properties as a function of thickness and growth temperature. On Au(111), the $FeBr_2$ ML sample shows clear differences in the magnetic properties compared to the bilayer (BL) or trilayer (TL) sample. Additionally to the change in the magnetic properties, the structural properties are changing during the transition from ML to BL. The observed hexagonal superstructure of the first layer of $FeBr_2$ on Au(111) with a periodicity of $\approx 1\,\mathrm{nm}$ disappears after the second layer is grown. The origin of the superstructure is related to the strong interaction with the Au(111) surface. These kind of structural changes between the first and second layer of $FeBr_2$ are not observed on Bi_2Se_3, where a long-range moiré pattern was observed. Here the magnetic properties are unaffected from ML to multilayer coverages. Only for high coverages a possible bulk transition was investigated. Therefore, during the experimental investigation we were able to determine that the strong interaction with the Au(111) substrate leads to a change in the magnetic properties of the first ML of $FeBr_2$. This change is not observed by growing them on Bi_2Se_3.

In the third and last part of the thesis, $MnBr_2$ and $MnCl_2$ have been grown on Au(111) to compare how the different halides affect the magnetic properties for different coverages on Au(111). During the characterization, a temperature-related structural change was investigated for both materials which resulted in specific rotational orientations on Au(111). Nevertheless, this temperature effect does not affect the chemical composition and oxidation state on Au(111). By comparing the magnetic properties of $MnBr_2$ and $MnCl_2$ on Au(111), a difference in the magnetic saturation behavior on Au(111) is observed, which could be related to the weaker interaction of Cl with Au, compared to Br with Au.

Kurzfassung

Diese Dissertation fasst die Ergebnisse der experimentellen Charakterisierung verschiedener magnetischer zweidimensionaler (2D) Materialien auf Au(111) und Bi_2Se_3 zusammen. Die Materialien wurden mit Hilfe von Tieftemperatur-Rastertunnelmikroskopie (LT-STM) und niederenergetischer Elektronenbeugung (LEED) strukturell charakterisiert. Die chemische und magnetische Charakterisierung erfolgte mit Hilfe von Röntgen-Photoelektronenspektroskopie (XPS) sowie Röntgenabsorptionsspektroskopie (XAS) und magnetischem Röntgen-Zirkulardichroismus (XMCD). Das Ziel dieser Arbeit war es, die Eigenschaften von Monolagen (ML) und mehrschichtigen Proben neuer magnetischer 2D Übergangsmetall-Dihaliden (TMDH) zu untersuchen.

2017 wurden die ersten 2D-Magnete entdeckt und charakterisiert. Seitdem liegt das Hauptaugenmerk im Bereich der neuen 2D magnetischen Materialien auf Übergangsmetall-Dichalcogeniden (TMDC) und Übergangsmetall-Trihaliden (TMTH). Erst seit kurzem sind auch TMDH stärker in den Fokus der Forschung gerückt. In dieser Arbeit werden verschiedene TMDH auf Au(111) und Bi_2Se_3 charakterisiert. Die durchgeführten Experimente im Rahmen dieser Dissertation liefern die notwendigen grundlegenden Hintergrundinformationen für spätere Anwendungen im Bereich von spinelektronischen Anwendungen. Im ersten und zweiten Abschnitt dieser Dissertation wird das Wachstum von $FeBr_2$ auf Au(111) und Bi_2Se_3 beschrieben und die materialspezifischen Eigenschaften als Funktion der Materialdicke und Wachstumstemperatur untersucht. Im Vergleich zu dickeren Proben sind die magnetischen Eigenschaften von einer ML $FeBr_2$ auf Au(111) stark abgeschwächt. Ein weiterer Unterschied von ML und Mehrschichtproben von $FeBr_2$ auf Au(111) ist die Oberflächenstruktur. Im Falle der ersten ML entsteht eine dominante hexagonale Überstruktur der ersten ML von $FeBr_2$ mit einer Periodizität von $\approx 1\,\mathrm{nm}$ auf Au(111), welche nach dem vollständigen Wachstum der zweiten ML verschwindet. Die Ursache dieser Überstruktur ist die starke Wechselwirkung des Au(111)-Substrats mit den Br-Atomen des $FeBr_2$.

Solche dickenabhängigen Änderungen der Struktur sowie der magnetischen Eigenschaften konnten auf Bi_2Se_3 nicht beobachtet werden, jedoch kommt es zu einer dominanten langreichweitigen Moiré-Struktur. Auf beiden Substraten konnten keine Änderungen der chemischen Zusammensetzung und des Oxidationszustandes festgestellt werden. Ebenfalls konnte keine Beeinflussung der magnetischen Eigenschaften im ML-Bereich auf Bi_2Se_3 festgestellt werden. Die einzige beobachtbare Änderung der magnetischen Eigenschaften tritt in Mehrschicht-Systemen auf, wo es zu einem möglichen Übergang der Materialeigenschaften von ML zu Volumeneigenschaften kommt. Im Laufe der Charakterisierungsprozesse konnte festgestellt werden, dass es zwischen Au(111) und dem jeweiligen 2D-Material aufgrund der starken Wechselwirkung mit dem Substrat zu Änderungen der Eigenschaften der ersten ML kommt, welche im Falle von Bi_2Se_3 als Substrat nicht auftritt. Im letzten Teil der Dissertation werden $MnBr_2$ und $MnCl_2$ auf Au(111) charakterisiert. Es konnte eine temperaturabhängige Änderung des LEED-Bildes beobachtet werden, welche darauf hindeutet, dass das Material bei höheren Temperaturen präferiert unter bestimmten Winkeln auf dem Substrat wächst. Die chemischen Eigenschaften änderten sich jedoch nicht für die verschiedenen Wachstumstemperaturen. Die magnetischen Eigenschaften unterscheiden sich zwischen $MnBr_2$ und $MnCl_2$ auf Au(111). Dies kann eine Folge der unterschiedlichen Wechselwirkung von Cl oder Br mit Au sein.

Contents

1 Motivation/Introduction

In 1965, Gordon Moore postulated his famous Moore's Law. This "law" states that there is a continuous doubling of the number of transistors in integrated circuits in a regular period of 2 years [1]. If we look at the development over time, the number of transistors in 1971 was 2300 in Intel's first microprocessor, the Intel 4004 [2], [3]. Within the next 10 years, as predicted by Moore's Law, the number reliably doubled every two years, so that in 1982 a value of 55000 implemented transistors (Intel 80186) was reached by Intel [4], [5]. Nowadays the number of integrated transistors is in the region of billions, for example in the newest NVIDIA GPU, the H100, 80 billion transistors have been implemented [6]. If we follow this trend, then we will reach a value of 1.0 trillion implemented transistors in 2030 [7]. In a very simplistic image a transistor can be described as a switch, with the current flowing from source to drain controlled by the gate [8]. Since transistors are the base for all computational calculations a constant increase in the number of transistor counts needs to be achieved for increasing the computational speed.

In Fig. 1.1 the systematic increase of the installed transistors in Intel's microprocessors in the time frame from 1970 to 2023 is displayed.

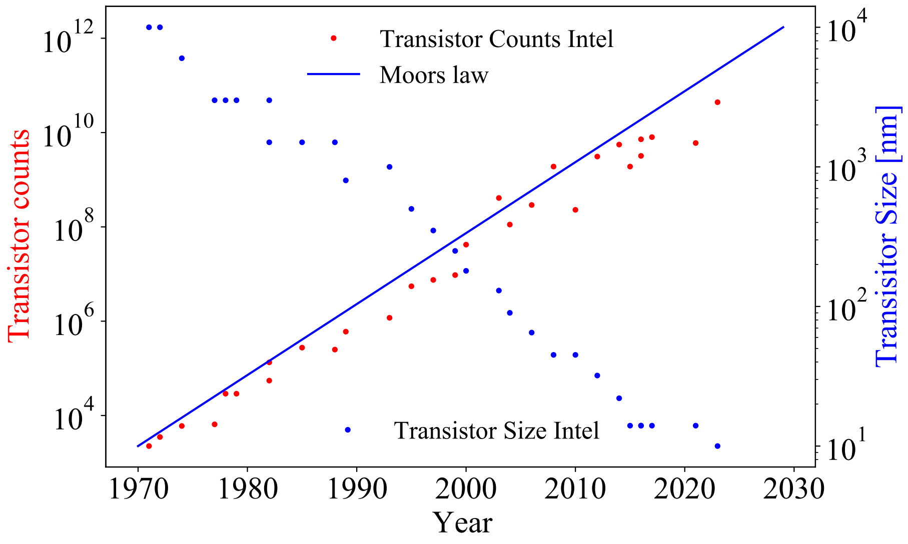

Figure 1.1: In red the amount of installed transistors in Intels microprocessors is displayed as a function of time. The continuous increase is matching with the behaviour predicted by Moors law (blue line). The used function for this continuous increase is $N = N_0 \cdot 2^{(t_2 - t_1/x)}$ [9], with $x = 2$ a, N the number of transistor counts, $t_2 - t_1 = \Delta t$ the timespan in years and $N_0 =$ 2300 the number of transistor counts of Intels 4004 microprocessor. For the used fit in this figure an offset of 1970 is used for the starting year. Corresponding to the red curve, the blue curve (dotted) shows the continuous miniaturization of the microprocessor size as a function of time. A detailed list of the microprocessors used for this plot is given in the appendix.

This rapid increase causes the new problem of the transistor size, since an increasing amount of transistors would cause problems due to the space limitation on a chip. Therefore, a miniaturization of the transistor size is needed for the increasing amount of transistors. In Fig. 1.1 the transistor size is displayed as a function of time and is plotted against the increasing amount of transistor counts.

This systematic decrease of the transistor size leads to transistor sizes of 1 nm and below for future technologies. The smallest transistor size currently achieved is 2 nm by IBM [10].

This continuous miniaturization leads to a new problem. The transistors are based on silicon (Si), a material that is very common on earth. However, we are slowly reaching the limits for conventional transistor designs and also for the usability of Si [11]. The key criteria for the conventional transistor size is the length of the gate (Fig. 1.2 a)).

Nowadays we are reaching the theoretical limit of the gate size. In the case of Si this critical point is at around 4 nm [11], [12]. By undergoing this size, the current can not anymore be controlled by the gate, since the tunneling process will become dominant [11] (Fig. 1.2 b)). Therefore, there is increasing interest in replacing Si with 2D materials (Fig. 1.2 c)). To achieve this goal, we need to understand the physical properties of a new generation of materials on a macroscopic and microscopic level. These new 2D materials show during the transition from bulk to the 2D limit new physical properties as observed for example for MoS_2 [13], [14]. Therefore, these new materials can either be used as single layers or in heterostructures for new generation of devices. The first breakthrough came in 2004 when Novoselev and Geim managed to isolate a ML of graphene. Since then, interest in new 2D materials has continued to grow. In 2016, the first transistor with a gate length of only 1 nm [15] was demonstrated by using carbon nanotubes and in 2022 this record was even broken by a transistor with a gate length of 0.34 nm [11], which is based on graphene and MoS_2 (Fig. 1.2 d)). Therefore the first steps to replace conventional transistors with transistors based on regular 2D materials have been done. Since the interest in novel nonmagnetic 2D materials was increasing, there was still one specific area of physical properties which only received little attention until 2017.

For a long time the prevailing opinion was that 2D magnetism cannot exist. This was postulated by Mermin and Wagner in 1966. The theorem says that above 0 K no magnetic order can exist in an isotropic therodynamic system [16]. This restriction can be circumvented if the systems exhibits anisotropy and thus has a strong spin-orbit coupling. In 2017, the breakthrough came with the first discovery of 2D magnets (CrI_3 [17], $Cr_2Ge_2Te_6$ [18] and Fe_3GeTe_2 in 2018 [19], [20]). Nowadays, there is a constantly increasing interest in 2D magnets, but this has been mainly focused on magnetic TMDC, since these materials have a crystalline structure and can be synthesized in different ways (from exfoliation to epitaxial growth). In recent years, some magnetic TMDC ($MnSe_2$ [24], VSe_2 [25]) and TMTH (CrI_3 [26], $CrCl_3$ [27]) have been studied intensively. However, the material family of TMDH was not in the focus until now. TMDH are showing, like some TMDC and TMTH, magnetic order up to the ML limit. However, this material class has one major advantage compared to TMDC and TMTH, the low growth temperature. For future device applications, a variety of different 2D materials need be combined in van-der-Waals heterostructures. Due to the weak interlayer coupling of the 2D materials different ways of growing and combining can be used. The most common way to obtain a ML of a existing 2D material is via mechanical or liquid exfoliation like for graphene [28]. However, since the exfoliation process cannot achieve a reproducible thickness for high quantity production as well as low defect amounts it is not suitable for this application. A solution for high reproducibility and lower defect amounts is the epitaxial growth of a 2D material. Therefore, it is mandatory to optimize and calibrate the growth parameters for different substrates to be able to achieve a large-scale device production. For many TMDC, the growth procedures have been mastered over the last couple of years [29],

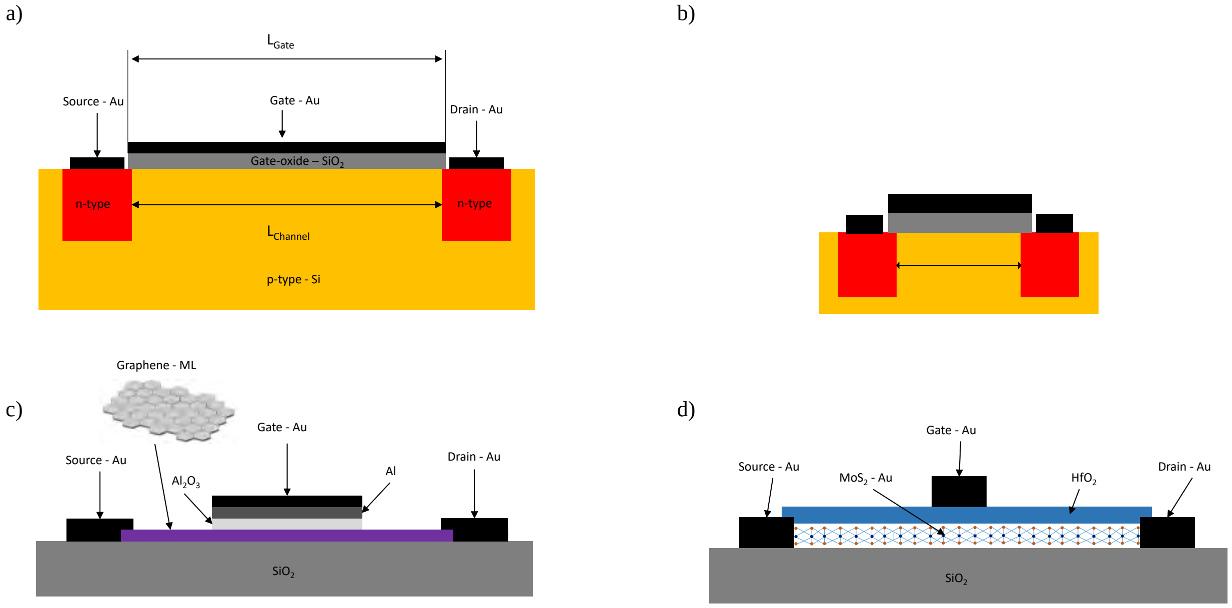

Figure 1.2: In a) the schematic design of a top-gate transistor is shown. The channel length L_{Channel} between the two n-type regions is marked by the double-sided arrow. The materials used are SiO_2 for the metal oxide gate, Si for the transistor material and Au for the contacts. In b) the same transistor design as in a) is demonstrated. The difference is the decreased channel length, which brings source and drain closer together and therefore increases the tunneling probability. c) shows one of the first 2D material transistors. Here the 2D material was grown on SiO_2 (an insulator) and the gate contact is isolated via Al_2O_3. In the top of part c) a schematic representation of the graphene surface is included. d) shows a transistor design which uses novel 2D materials like MoS_2. The design between c) and d) is nearly identical except for the exchange of the separation layer for the gate contact. The figures a), b), c), and d) were recreated from the papers [8], [21], [22], and [23].

[30], however these growth procedures are using high temperatures, e.g., WSe_2 with 850 °C [31]. This high temperature growth causes new problems, since the used substrate for these new device generations are not sustaining very high temperatures. However, this substrate-temperature sensitivity can be neglected by using TMDH, which are growing in a substrate-temperature range from room temperature (RT) to at most 423 K [32], [33].

This thesis is based and focused on three main areas. The first part is related to the calibration and the epitaxial growth of selected 2D materials ($FeBr_2$, $MnCl_2$, and $MnBr_2$). The second and third part of the work are based on the structural, chemical and magnetic characterization of different 2D materials. Here $FeBr_2$, $MnBr_2$, and $MnCl_2$ have been characterized on Au(111) and $FeBr_2$ also on Bi_2Se_3. The study of TMDH materials is completed with a detailed comparison of the magnetic properties of Fe-halides and Mn-halides. All investigated materials were measured primarily on Au(111). This choice of substrate has several reasons, one being that Au interacts strongly with the 2D material. As a result, we can get an accurate picture of whether the material decomposes or whether its properties in contact with Au, which is used for contacting, change in subsequent device applications. Another reason for Au(111) is the hexagonal structure, which provides an ideal breeding ground for the material and, with a low lattice mismatch, also creates good prerequisites for the growth of the materials.

2 Theory

In the following sections the theoretical background of the thesis will be explained.

2.1 Classification of magnetic properties

Magnetic materials can be distinguished by their different magnetic properties. The magnetic properties can range from simple cases like paramagnetism or ferromagnetism to more complex situations like helimagnetism [34] or frustrated spin systems [35], [36]. In the following we will focus on the magnetic properties of our measured material systems. Fig. 2.1 shows a schematic overview of different magnetic orders. In a ferromagnetically ordered system all spins are perfectly aligned in the same direction at $T = 0\,\mathrm{K}$ [41, p.48], which means that the systems has long-range order (Fig. 2.2), where the spin-spin correlation function decays to a finite value [42], [43], [44], [45]. If the spins are at the same position, the result for the spin-spin correlation function would be the unity matrix [44].

$$K(1,2) = \langle\sigma(1)|\,|\sigma(2)\rangle \tag{2.1}$$

$$K(1,1) = I \tag{2.2}$$

By exceeding the critical temperature (Curie temperature) of a ferromagnetic material the long-range order can be destroyed. At this temperature the system undergoes a phase transition from an ordered state (long-range order) to a disordered paramagnetic state (short range order). In the case of a paramagnetic state (Fig. 2.1 d)) the interaction between the neighboring moments can be neglected since the thermal energy of the system is higher than the interaction energy [46, p.80]. In the case of disorder or short-range order the spin-spin correlation function decays exponentially [42], [45]. In the following the Curie-temperature equation is displayed, where C is the material specific Curie constant, n is the amount of substance, and λ is the molecular field constant [41, p.50].

$$\begin{aligned} T_C &= \frac{n \cdot \lambda \cdot \mu_0 \cdot \mu_B^2 \cdot g^2}{k_B} \cdot \frac{(J+1)}{3} \\ &= C \cdot \lambda \end{aligned} \tag{2.3}$$

The most common ferromagnetic materials are Fe, Co and Ni (first row of transition metals in the periodic table) with critical temperatures above $T_C = 900\,\mathrm{K}$ [40, p.102], [41, p.6], [47, p.16]. However, by decreasing the material thickness from bulk to a thin film or ML the magnetic properties are affected and the critical temperature starts to decrease [48]. In Eq. (2.4) the thickness dependent critical temperature equation is shown

$$\frac{T_C(N)}{T_C^{3D}} = 1 - \left(\frac{C}{N}\right)^{\lambda} \tag{2.4}$$

, where N is the number of layers, C is a non-universal constant, and $\lambda = \frac{1}{\nu}$ is the inverse critical exponent of the bulk material [48]. By placing a ferromagnetic material in a magnetic field, the

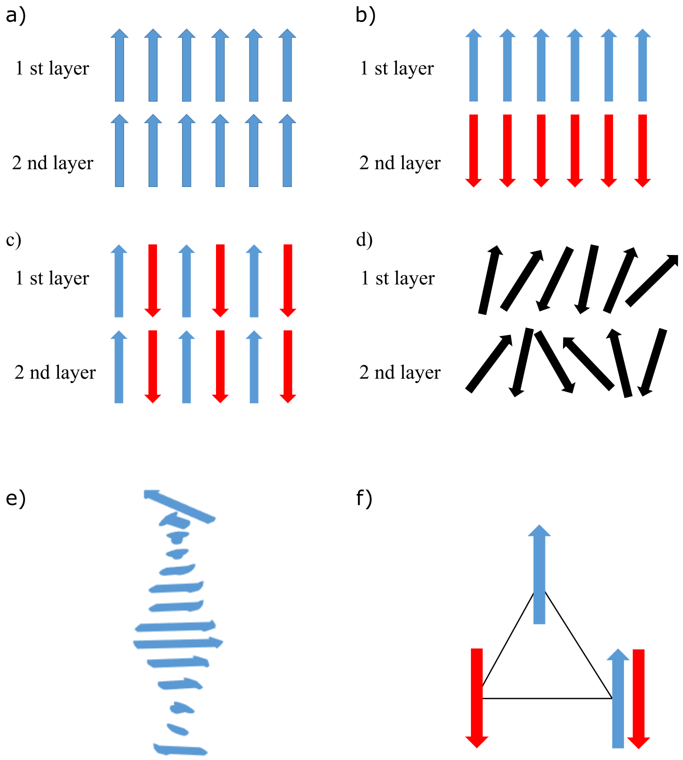

Figure 2.1: Types of magnetic order. a) Ferromagnetic interlayer and intralayer order in a BL system. In b-c) antiferromagnetically ordered systems are shown. b) shows an interlayer antiferromagnetic system with ferromagnetic order within the layer and c) shows an intralayer antiferromagnet with ferromagnetic order in between the layers. In d) a paramagnetic system is shown where the spins are not ordered relative to each other. e) shows helimagnetic order, where the neighbouring spins are rotated at angles between 0 and 180 ° [37], [38]. f) shows a triangular lattice case with spin frustration [36]. The blue arrows are spin-up and the red arrows are spin-down. The figure design is based on Ref. [39] and Ref. [40, p.102].

spins are orienting in the field direction. If the field is strong enough to completely align all spins in the same direction the ferromagnetic material is saturated [46, p.82-83]. In Fig. 2.3, a schematic hysteresis curve is visualized. The green line shows the case where the ferromagnetic material is demagnetized and the field ramping starts at $B = 0\,\mathrm{T}$ [49, p.516]. After reaching the saturation field, all spins are aligned in the direction of the external magnetic field. Changing the field direction from positive to negative will change the magnetization ($\vec{M}$) of the sample to negative values. In case $\vec{M} \neq 0$ at $B = 0\,\mathrm{T}$, the material shows remanence and is therefore ferromagnetic.

If the spins are ordered antiparallel, the system is called an antiferromagnet. Here we have to distinguish between different types of antiferromagnetism [47, p.16], [46, p.81, p.121-123]. The first two simpler types are interlayer and intralyer antiferromagnetism. In intralyer antiferromagnetism (Fig. 2.1 c)), the neighboring spins of the same layer are antiferromagnetically coupled as in the case of MnO [40, p.99-100], [41, p.44]. An interlayer antiferromagnet (Fig. 2.1 b)) has antiparallel coupling between two layers and ferromagnetic coupling within the layer, such as CrI_3 or $FeBr_2$ [17], [50]. The magnetization of an antiferromagnet is vanishing ($\vec{M}= 0$) if no or only a small external

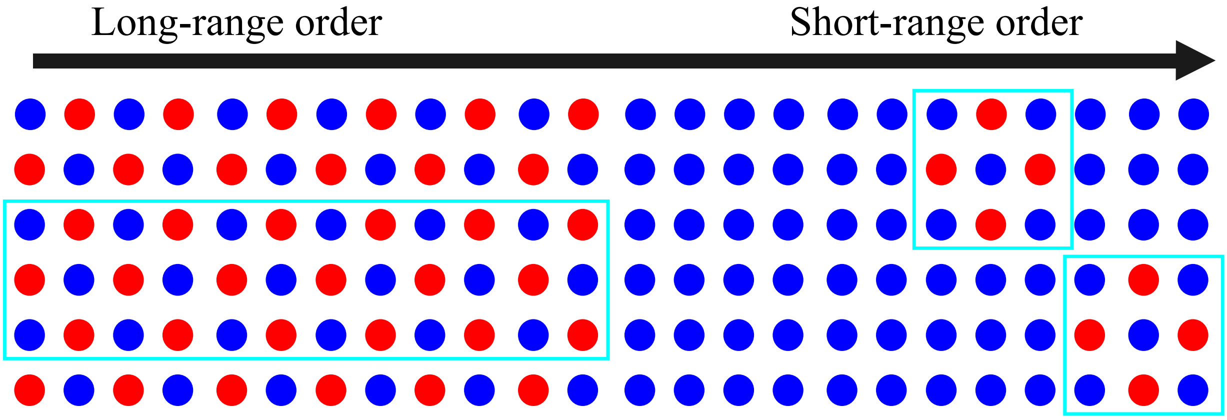

Figure 2.2: Schematic view of long- and short- range order. The cyan colored rectangles show the ordered region and the different colors (red and blue) correspond to the different spin orientations. The figure is based on the figure in Ref. [42].

magnetic field is applied [40, p.100], [46, p.81], [51, p.108]. As in the case of ferromagnetism, the magnetic order is destroyed and the system goes into a paramagnetic state when the critical temperature (Néel temperature T_N, Eq. (2.5)) is exceeded [41, p.55-56], [46, p.81].

$$\begin{aligned} T_N &= -\frac{n \cdot \lambda \cdot \mu_0 \cdot \mu_B^2 \cdot g^2}{k_B} \cdot \frac{(J+1)}{3} \\ &= -C \cdot \lambda \end{aligned} \tag{2.5}$$

Where C is the material specific Curie constant, n is the amount of substance, and λ is the molecular field constant. The negative sign is a direct consequence of the negative exchange interaction constant, therefore the sign needs to be included to calculate the critical temperature. Magnetic order is based on two types of interactions, one is exchange interaction [46, p.116] and the other one is the magnetostatic interaction. The exchange interaction is a consequence of the overlap of the wave function with a total energy described by the Heisenberg Hamiltonian (see Eq. (2.7) [41, p.48])

$$\Psi(1,2) = -\Psi(2,1) \tag{2.6}$$

$$H_{\text{exchange}} = -J_{ij} \sum_{i,j} \vec{S}_i \cdot \vec{S}_j \tag{2.7}$$

$$\Psi(r,S) = \Phi(r) \cdot \chi(S)$$

, where $\chi(S)$, $\Phi(r)$ are the spin and the spatial part of the total wave function, J_{ij} is the exchange coupling constant and $\vec{S}_{i/j}$ are the spins of the neighboring electrons. The sign of the exchange coupling constant determines whether the system is ferromagnetic ($J_{ij} > 0$) or antiferromagnetic ($J_{ij} < 0$) [41, p.62], [52]. If the energy of the system is higher than the total energy H_{ex}, then the system undergoes a phase transition and becomes disordered. As a direct consequence of the fact that the total wave function must be antisymmetric (Eq. (2.6)), a symmetric spatial wave function is associated with antiferromagnetism and ferromagnetism is associated with an antiysmmetric spatial wave function.

A more complex form of antiferromagnetism is a spin frustrated system with a non-trival spin order. Such systems have many different ground states at $T = 0\,\text{K}$ [53]. The simplest case of a spin-frustrated system is a triangular lattice, with antiferromagnetic coupling between nearest

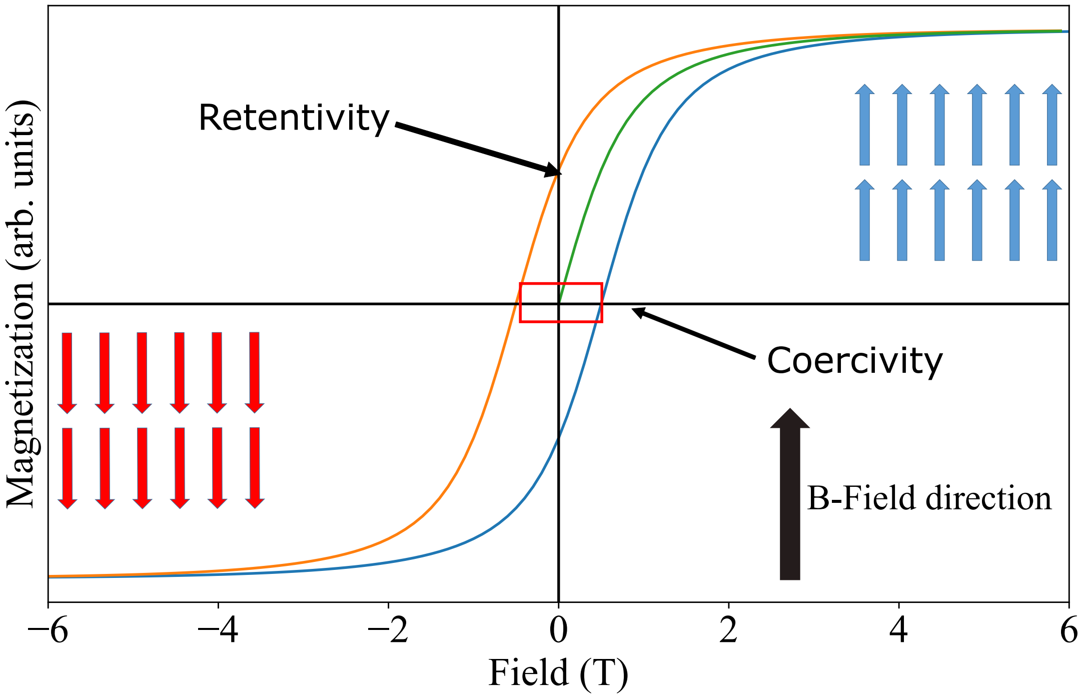

Figure 2.3: The schematic principle of hysteresis is shown. If the material is not yet magnetized, it will start from zero as the field strength increases (visualized by the green line). After the material-specific field is reached, all spins are aligned in the same direction and the ferromagnet is saturated. By reversing the field from positive to negative, the spins are starting to reorientate in the field direction as shown in the figure by the blue and red arrows for opposing field strength. In the case of a ferromagnetic material the system will have a net magnetization (remanence) at $B = 0\,\mathrm{T}$ for $T < T_C$. The splitting of the hysteresis curve for different ramping directions of the field is called coercivity and is marked by the red rectangle in the figure. The design on which this figure is based is from Ref. [49, p.516] and the image was created in python.

neighbor spins [54], [55] (Fig. 2.1 f)). To minimize the energy of the spin frustrated system an antiparallel alignment between the nearest neighboring spins would need to be achieved. However, for a triangular lattice the antiparallel alignment would lead to a frustration of the third spin, since two possible spin orders could be achieved for minimizing the energy [56] (degenerated spin configuration). Such spin frustrated systems exist not only for collinear order but also for non-collinear order [53].

Another type of magnetic order is helimagnetism. In Fig. 2.1 e), the helimagnetic order is shown, here the neighboring spins are oriented with an angle of 0-180 ° to each other, so that they form a spiral [37], [38]. Since in the case of helimagnetism the spins are not aligned in the same direction and no net magnetization exists, therefore it can be described as a special form of antiferromagnetic order.

2.2 Magnetic anisotropy

Magnetic anisotropy describes the dependence of the free energy of a system on the orientation of the magnetization [40, p.205]. It leads to a situation in which the system has a preferred direction of magnetization orientation (easy axis). When the magnetic moments are aligned along the easy axis, the anisotropy energy E_{anis} is minimized. The hard axis describes an alignment along an axis which is not in the anisotropy direction [49, p.504]. By measuring the hysteresis of an anisotropic system the effect of magnetic anisotropy can be nicely observed. In the case that the measurement is performed in the direction of the easy axis, then the magnetization is faster reaching the saturation value compared to a measurement along the hard axis (Fig. 2.4). There are several types of magnetic anisotropy such as shape and magnetocrystalline anisotropy [41, p.89-90]. The anisotropy energy density can be written in the following way [47, p-74-77], [49, p.504]:

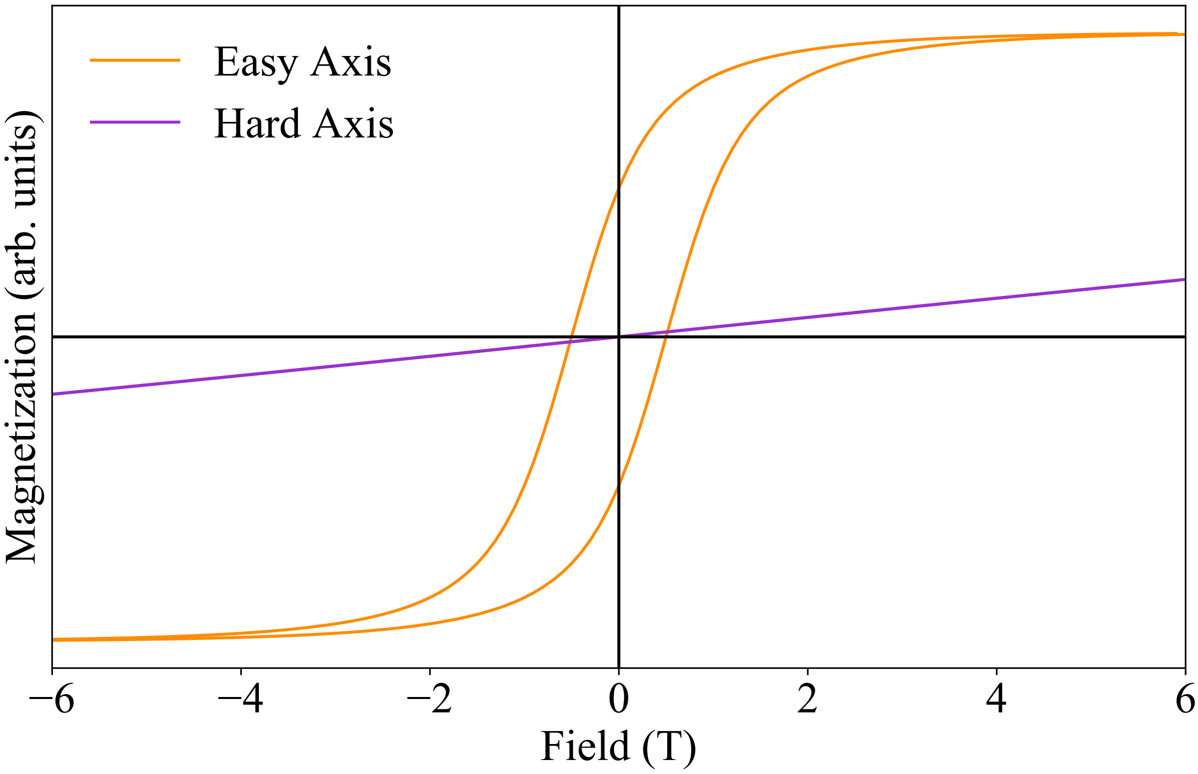

Figure 2.4: The behavior of a hysteresis curve based on the measurement geometry. The exemplary system for this plot has an out-of-plane (OoP) easy axis. Therefore, the displayed saturation of the magnetization is faster than the one of the hard axis, which is shown in purple.

$$\frac{E_{\mathrm{anis}}}{V} = K_1 \sin^2(\alpha) + K_2 \sin^4(\alpha) + K_3 \sin^6(\alpha) + \dots \tag{2.8}$$

, where E_{anis} is the anisotropy energy, V is the volume of the investigated system, K_i are the anisotropy constants and α the angle between the easy axis and the magnetization direction of the sample. The equation (2.8) can be simplified to the equation (2.9) in the case of thin films, since the K_1 term becomes dominant under these conditions.

$$\frac{E_{\text{anis}}}{V} = K_1 \sin^2(\alpha) \tag{2.9}$$

The anisotropy constant K_1 contains different components, related to the different types of anisotropy. In the case of a system consisting only of magnetocrystalline anisotropy (MCA) and shape anisotropy (SA), K_1 has the following form [49, p.505]:

$$K_1 = K_u + K_{Sha} \tag{2.10}$$

The sign of K_1 determines the direction of the anisotropy. For $K_1 > 0$ OoP and for $K_1 < 0$ in plane (IP) orientation is preferred [49, p.505-506].

In section 2.3.1 we will discuss in more detail why magnetic anisotropy is the reason for 2D magnetism.

2.3 Magnetism in two dimensions (2D)

In this section we will focus on different theoretical models of 2D magnetism as well as on the general description of the investigated material systems and the discovered 2D magnets.

2.3.1 Theoretical models

In the late 1960s, the absence of long-range order in a thermodynamic system in 2D was claimed by Mermin and Wagner [16]. The key point of the paper was that magnetism cannot occur above $T_0 = 0\,\text{K}$ for a 2D system. The basis of this theorem was the assumption of an isotropic spin system (Heisenberg model), where the spin can orient in all three-dimensional (3D) [16]. In this case, it would not be possible to stabilize the spin orientation at any elevated temperature $T > T_0$, since the thermal energy would lead to the destruction of the long-range magnetic order (due to the Bose-Einstein statistics [57]). In Fig. 2.5, the magnon density of state (MDOS) of a ML system is displayed. The MDOS represents the amount of magnon states per energy interval.

For any finite temperature ($T < T_C$) it is energetically more favorable to have a spin wave motion, rather than single spin excitation. At $T_0 = 0\,\text{K}$ all spins are aligned and therefore the system is ferromagnetic. With increasing temperature the aligned spins start to diverge from the central position (spin wave) [58, p.574-575], [59, p.701-723]. Therefore, in the model described by Mermin and Wagner, ferro- and antiferromagnetism in one-dimensional (1D) and 2D systems are not possible [16]. However, in the case of a 3D system, the magnetic order is stable until the critical temperature (T_C or T_N) is reached [48]. It should be noted that the Mermin-Wagner theorem is only valid for systems with broken continuous rotational symmetry [60]. On the right side of Fig. 2.5 a system with a lower spin dimensionality (SD) (n) is shown. This reduced number of degrees of freedom introduces anisotropy into the system and therefore 2D magnetism becomes possible. In Fig. 2.6, the different spin dimensionalities are shown. A system with a SD of $n = 1$ is described by the Ising model, which assumes only nearest-neighbor interaction and spins pointing only along one direction e.g. the z-axis [48] (only two possible orientations, either up (+1) or down (-1) along the z-axis) [61]. However, since the Ising model only assumes a 1D system, the theoretical explanation needed to be adapted to the 2D case. In 1944 the Ising model was used by Onsager to calculate an exact solution for the 2D limit of ferromagnetic order [62]. He showed that at a finite temperature $T > T_0$, a magnetic phase transition is possible by using UA. Here the excitation gap of the MDOS interrupts the direct effect of the thermal fluctuations and causes

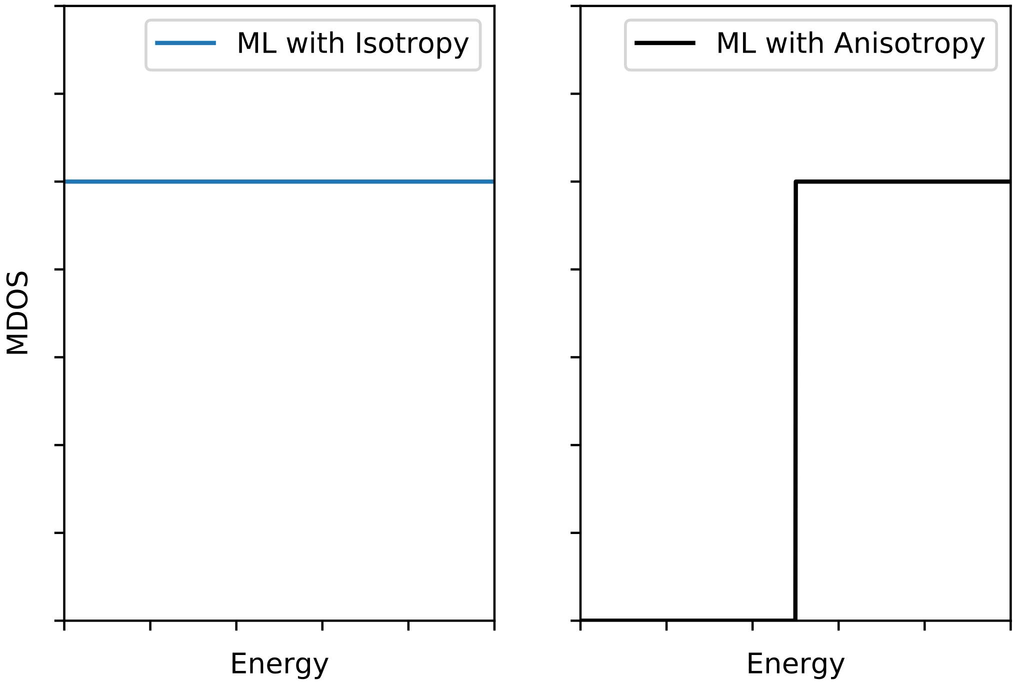

Figure 2.5: MDOS for a ML system. On the left side the system with isotropic spin order is shown. Here the MDOS has no excitation gap and starts directly at $E = 0\,\mathrm{eV}$, which leads to the case described in the Mermin-Wagner theorem [16]. On the right side the ML system with an uniaxial anisotropy (UA) is shown. UA describes the case where a system has only a single easy axis. Here an energy gap of the MDOS exists, therefore only a finite temperature above $T_0 = 0\,\mathrm{K}$ can cause the destruction of the long-range order. The figure is based on [57].

Figure 2.6: Rectangular lattice system for a single layer ordering. From left to right the different spin-dimensionalities are shown. Starting with n = 1, which represents the Ising model with a spin orientation OoP. The middle figure shows a SD of n = 2. Here the spins are aligned IP along the x-y plane. The last figure shows the isotropic case with n = 3, where the spins can be oriented in any direction of the sphere (x, y, z). The image is taken from [48].

a protection of the magnetic long-range order [48], [57]. So far we have explained the theoretical description of systems which are aligned OoP, but in reality this is not always the case. Therefore, another theoretical model has to be used, which assumes a SD of $n = 2$ and IP orientation. The theoretical model that fulfills these required parameters is the XY model, where a magnetic phase transition known as the Kosterlitz-Thouless transition can be observed [48], [63]. The model proposes that the system contains pairs of vortices that protect the topological long-range order. The vortex is a topologically protected object defined by the polarity ($p = \pm 1$) and the vortex chirality ($c = \pm 1$) of the vortex. To distinguish between a vortex and an antivortex, the winding number ($N_W = \pm 1$) is needed with $N_W = -1$ for an antivortex and $N_W = 1$ for a vortex [64].

In the XY-model a magnetic phase transition can be observed between the low- and high-temperature case. Below the critical temperature the vortices are coupled in vortex-antivortex pairs [65], but by overcoming the critical temperature the coupling of the pairs are broken and the system contains of single vortices.

2.3.2 2D materials

2D materials are defined as single-atomic layers of the corresponding bulk with a crystalline structure. They can be distinguished into two different categories, layered and non-layered materials. In the case of layered materials only a weak interlayer coupling between the first and next-layer along the stacking direction is present with strong intralayer coupling within the layer [66]. This type of coupling is based on the weak van der Waals (vdW) force [58, p.6], which allows the material to be easily exfoliated like graphene [28], [66].

The vdW force is an electrostatic force which is caused by the dipole-dipole interaction between uneven charge distributions of the atoms [58, p.11]. Nevertheless, the vdW force is for some vdW materials not as weak as for HOPG, since the crystals of MoS_2, $MoTe_2$, and Bi_2Se_3 are showing a crystalline structure with a specific diffraction pattern. In comparison to layered materials with weak interlayer coupling along the stacking direction, nonlayered materials have strong coupling via chemical, metallic or ionic bonds in all three dimensions [66], [67].

Till now already 50 different 2D nonlayered materials have been experimentally proven with interesting thickness-dependent property changes [67]. The chemical composition ranges from TMDC to metal oxides [67]. In 2004, the first 2D material (graphene) was experimentally achieved, and since then there has been an exponential increase in 2D materials, which continues to this day [67], [68].

From theory thousands of layered 2D materials should exist, but till now only a fraction of them have been discovered experimentally [69]. In a recent theory paper the authors calculated via vdW density functional theory (DFT) that there are 1825 possible 2D material candidates [69]. This number splits into 789 2D materials that are potentially easy to exfoliate according to calculations and 1036 that are easy to exfoliate [69]. However, the reason why these materials are so interesting is that the physical properties of the ML are different compared to the parent bulk material, due to quantum size effects [28], [67].

2D materials can be divided into two main categories depending on either their structural properties or their chemical composition. Since the chemical composition can include elements from nearly every group of the periodic table, the potential properties are broad [67]. They can range from a topological insulator (TI) (Bi_2Se_3) [70], insulators (hBN) [71], semiconductor (SC) ($FeBr_2$, SiC) [32], [72], [73], metals ($MoTe_2$) [74] to superconductors ($NbSe_2$) [75]. The other property which makes this material class so interesting and important for the technological future is that these materials can be stacked together, due to the vdW interaction along the z-direction [67]. By using this major advantage of the material, different vdW heterostructures can be created, without problems at the interface [67], [76].

In this work we will only discuss layered materials. Before focusing on the investigated chemical composition class we will give a brief overview of the different types of 2D materials. The first class of 2D materials are elemental 2D materials. This class contains materials from different main groups of the periodic table (III-V). In the III group, only borophene exists as a 2D material. This material has possible applications in the field of electric catalysis or energy storage and was first predicted in 1997 [77]. In 2015-2016, borophene was experimentally realized by epitaxial growth on Ag(111). A metal substrate is used, since the metal passivation is stabilizing the sp^2 hybridization [78]. It was shown that the material is sensitive to oxidation and needed an additional Si capping layer. This capping prevented the sample from oxidation for a time period of several days [79]. This breakthrough could lead to a new type of devices (boron electronics) [67], [78].

The most prominent member of the family of 2D materials is graphene, which is a part of the IV-group of the periodic table. Since 2004, several different approaches to achieve graphene have been successfully demonstrated. The approaches are ranging from mechanical [28], [80], to SiC annealing [81], to liquid exfoliation [82], till epitaxial growth via CVD and MBE [67], [83]–[85]. Besides the many different approaches to obtain graphene although many interesting properties has been observed, ranging from high thermal conductivity to high intrinsic carrier mobility [67], [86]. However, carbon-based 2D materials are not the only ones from group IV. There are also Si-, Ge- and Sn-based 2D materials, which have been experimentally achieved on various substrates ranging from metallic to semiconducting [67].

The last class of monomer 2D materials uses group V elements. In particular, one material from this group is well known, the black phosphorous. This material showed a strong dependence of the electronic bandgap by decreasing the amount of layers, resulting in an electronic bandgap of 1.5 eV in the ML case [67]. This is very different compared to other elemental 2D materials like graphene or silicene [87]. Similar to graphene different approaches have been used to create ML black phosphorous ranging from mechanical exfoliation to epitaxial growth [67], [88].

The other classes of 2D materials are based on a mixture of different elements. An example of these hetero-2D materials which are not based on transition metals is hexagonal boron nitride, hBN. The growth of hBN has been demonstrated on different metallic substrates such as Au(111) [89], [90] or Pt(111) [91]. Since the growth process of hBN is already well known and relatively easy, it is a perfect plattform for future studies of vdW heterostructures. Due to the insulating properties of hBN with a bandgap of 5.97 eV [67], it is a good candidate for new device applications [92]. Since we have now a general overview of different 2D materials, let us focus on the classes studied in this thesis. The class of material which is used in this thesis is based on transition metals.

Transition Metal Chalcogenides

The family of transition metal chalcogenides can be distinguished into different stoichiometry groups.

The most prominent group of this family class are the transition metal di-chalcogenides, TMDC. In a ML TMDC, the transition metal (Fe, W, Mo, Mn) is sandwiched between two rows of chalcogenide atoms (S, Se, Te) with a stoichiometry of MX_2 [93], [94] (Fig. 2.7). This material class is so interesting, since they show new physical properties at the ML limit, which are different from the bulk material [93]. However, since a ML of these materials consists of several stacked layers, they are described as quasi 2D materials [95] therefore, the ML can be described as a slab. The interaction between different slabs is based on vdW interaction [76], [93], but inside the layer the interaction strength is way higher, since covalent bondings are created between the transition metal and the chalcogenide atoms [96]. The properties of these materials are ranging from semiconducting (MoS_2 [97]) to topological insulating ($MoTe_2$ [98]) and even superconducting ($NbSe_2$ [99]) [100]–[102].

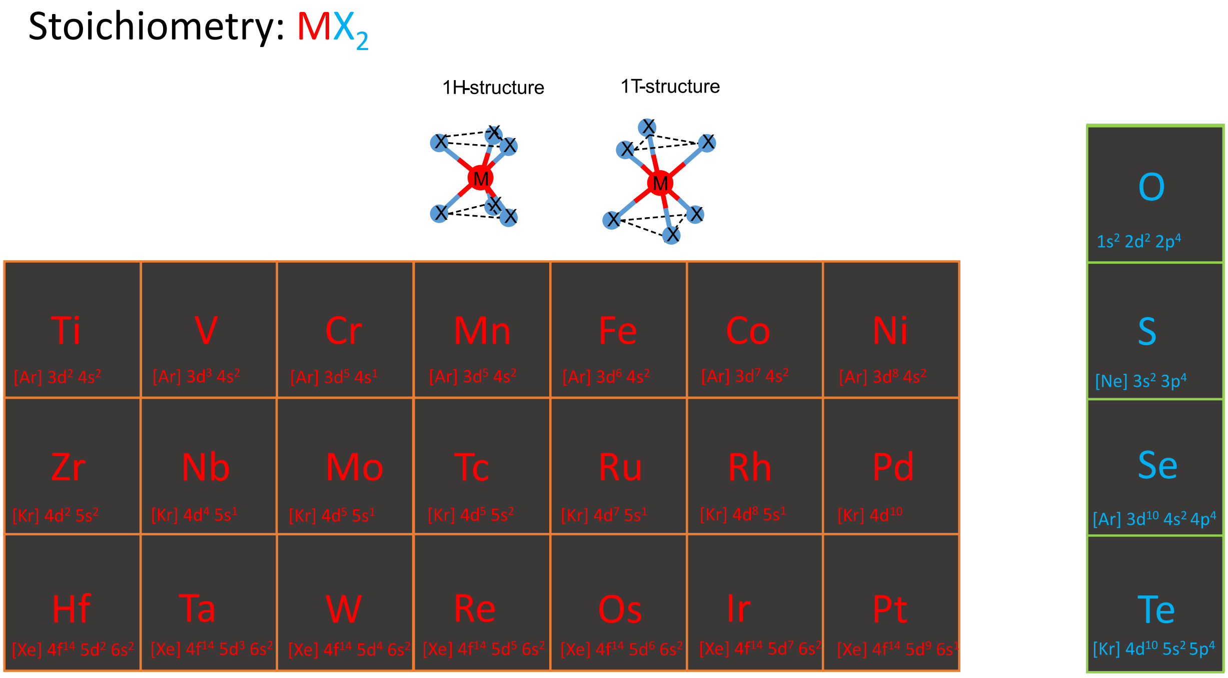

Figure 2.7: Shown is a part of the periodic table with the different transition metals in red and the most common chalcogenides in blue. The two shown structures are a three-dimensional side view of the 1H and 1T phases. The design of the 1H and 1T structure is based on [94].

The structure of TMDC's can vary depending on the growth parameters, such as for $NbSe_2$ [103]. The most common structures are octahedral (1T), trigonal prismatic (1H) [104, p.109-110] and the distorted T-phase (1T') [105]–[107], other structures are T", 3R and 2H [93]. The major difference between the last three structures and the first three is that the 1T" phase has a different distortion symmetry than 1T' and 1T structure [108]. By comparing the 1H and 2H structures with each other it can be observed, that both structures have a different stacking order, as in the case of the 3R structure [108]. The T stands for trigonal, H for hexagonal and R for rhombohedral [108], [109].

In Fig. 2.8, the different structures are presented. The main difference between the 1T and 1H phases is only the rotational orientation of the second chalcogenide row. If the first and second row are rotated by 180 ° against each other [108], then a 1T-structure is created and if no rotation between the first and second row is present it is a 1H structure. By decreasing the material thickness down to the ML limit it can be seen that the ML does not have inversion symmetry [104, p.109, 173], [114] in contrast to the bulk material.

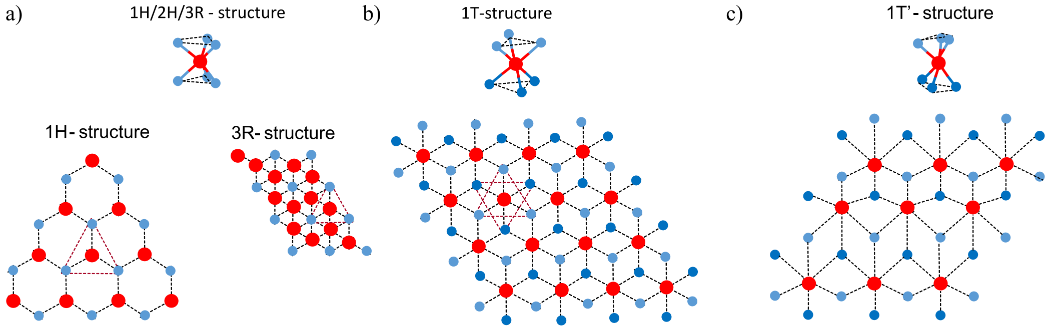

Figure 2.8: The most common structures for 2D materials displayed as a 3D side view and as a top-view. In a) the trigonal prismatic structures (1H, 2H, and 3R) are shown. In the lower part of a) the top view of the 1H and 3R structure are displayed. In b) the 1T-structure as a 3D and top view is displayed. Here the bottom and top row of chalcogenide atoms have different shades of blue. These two colors are also used in the top view of the 1T phase. In c) the distorted 1T phase (1T') is displayed from the top and as a 3D view. The design is based on [94], [108]–[113].

This material class shows interesting and new properties in the ML regime. One prominent example is the bandstructure change in MoS_2 and $MoSe_2$ from an indirect to a direct bandgap at the ML limit [115], [116], [117], which makes these materials very interesting for future device and solar-cell applications [67]. These new properties together with the possibility of downsizing the materials to the ML limit, without degrading the material properties due to surface defects [93], is a huge advantage compared to normal semiconductors [11].

Over the last couple of years, the focus was not only on normal TMDC, but since the first magnetic 2D materials were revealed, the focus switched to magnetic 2D materials. However, in the family of TMDC not many magnetic 2D materials are known. The only well-known magnetic TMDC are 2H-VSe_2 [118], $CrTe_2$ [119] and $MnSe_2$ [24], [120], [121]. In Fig. 2.9, the magnetization loops of two different ferromagnetic TMDC's are shown.

In the case of 1T-VSe_2, the previously found magnetic properties were related to the charge density wave (CDW) present in this material [25], [122]. However, by using the method of interface hybridization [123] the magnetic properties of 1T-VSe_2 can be promoted. Therefore, the authors of Ref. [123] evaporated different thicknesses of Co on 1T-VSe_2. As a consequence of the antiferromagnetically coupled Co-layers a XMCD signal of 1T-VSe_2 has been revealed (only with 3 ML of Co on top). The measured magnetic moment ($0.4\,\mu_B$) at low temperature (65 K) is good correspondence with the predicted values at $T = 0\,K$. This demonstrated that the Co-capping layer of 3 ML causes a magnetic transition from disorder to a long-range order state [123].

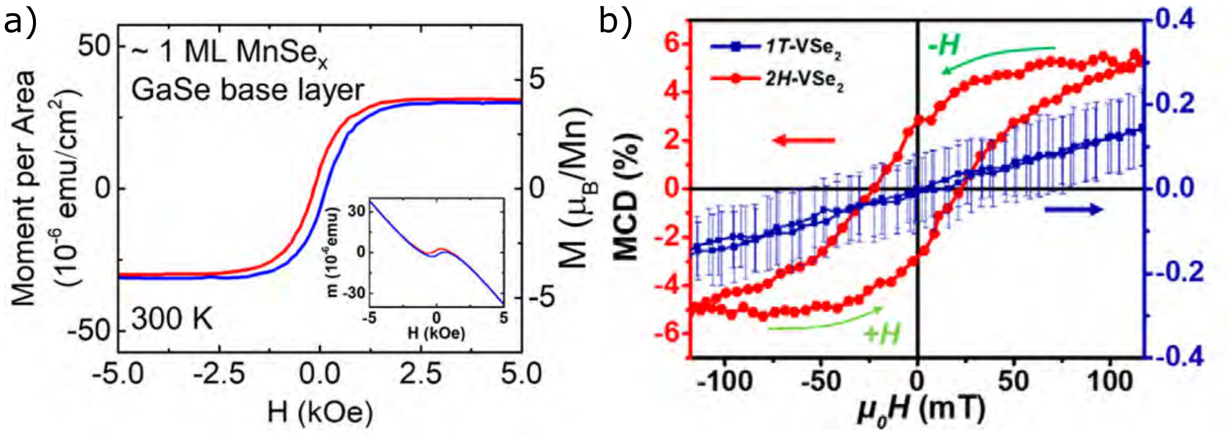

Figure 2.9: a) shows the ferromagnetic hysteresis loop of $MnSe_2$ and b) that of 2H-VSe_2. In a) the OoP hysteresis for $MnSe_x$/GaSe is shown (measured via SQUID at RT). The x refers to the unknown ratio of Se, since the sample could also be a α-MnSe. In b) the XMCD magnetization loop at RT for 2H-VSe_2 is shown. The images are taken from the papers [24] and [118], respectively.

Transition Metal Halides

The family of transition metal halides can be distinguished in TMDH and TMTH. TMDH are binary compounds of one transition metal cation together with 2 halogen anions [124]. In the following description we will focus only on the first-row transition metals from Ti to Ni (all with partially filled 3d shells) in combination with three different halogens (Cl, Br and I). All these materials are showing semiconducting to insulating properties [32], [33], [124], [125].

The here discussed TMDH have two different structure types. The materials can either appear in the 1T configuration, which is referred to as the CdI_2 structure, or in the 3R structure ($CdCl_2$) [124]. In both configurations the transition metal cations are ordered in a triangular structure with an octahedral coordination [124]. This starting configuration is causing a spin-frustrated system in the case of antiferromagnetic order [124], [126]–[129]. Figure 2.10 shows the two different structure types. In the case of the CdI_2 structure, the stacking order is repetitive (AA stacking), therefore the distance between the first and second slab (c-axis) is 1 c from the centers of the transition metal cations. The c-value is the distance between two overlaying layers, therefore the distance definition is depending on the stacking order of the material. Since the $CdCl_2$ structure consists of an ABC stacking, the distance between two slabs is $\frac{c}{3}$. For both structural configurations the distance between the transition metal cations is identical to the distance between the halogen anions ($a_{M-M} = a_{X-X}$), as shown in Fig. 2.10.

These compounds are known to form low-dimensional structures, such as 1D chains [124], [131], 2D layers [32], [33], [132] or even just molecular units [124].

In the case of TMTH, a different lattice structure can be observed (Fig. 2.10 d)-f)). For these compounds an easier spin configuration can be observed, since the lattice forms a hexagonal pattern, where no spin frustration can exist, therefore a normal antiferromagnet (AFM) order can exist [124], [130]. In the case of CrI_3, it was observed that the ML is ordered ferromagnetically with AFM coupling between the layers [17], [26]. A similar behaviour has been observed for $CrBr_3$ [133], [134] and $CrCl_3$ [27], [134], [135]. As previously mentioned, the focus of this thesis will only be on transition-metal cations of the first transition metal row and Cl and Br as the halogen anions. For all TMTH, two different layer configurations can be observed. The first one is the BiI_3

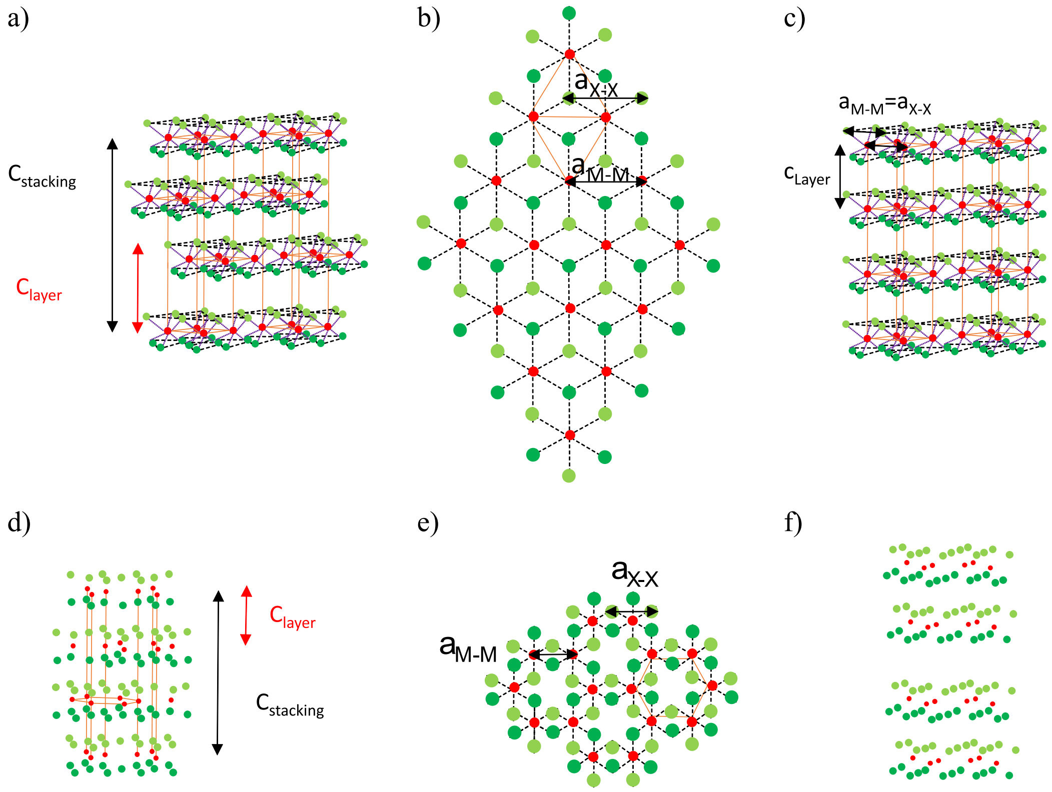

Figure 2.10: The different TMDH and TMTH structures. From a)-c) the TMDH structures are shown. a) displays the $CdCl_2$ structure, which shows an ABC stacking order and c) shows the CdI_2 structure with an AA stacking order. In b) the top-view for both structures is shown. In b) and c) the a-axis lattice constant is indicated for the distance between the transition metal cations and for the distance between the halogen anions. The different slab distances are indicated in a) and c) by the c-values. In c) the value of c is identical for the layer and stacking distance, for a) the layer distance is $\frac{1}{3}$ of the stacking distance due to the ABC stacking. The subfigures d)-f) show the two different structure types of the TMTH materials. In e) the top view with the hexagonal transition metal ordering is shown. In d) and f) the different structure types (BiI_3 and $AlCl_3$), which are all showing a form of ABC stacking are displayed. For f) the ABC stacking is irregular, since the layer distance is changing only along the c-axis [124]. The figure is a modified version of the one shown in [130], [124].

structure with a with an ABC stacking like for the $CdCl_2$ structure and the second structure type is the $AlCl_3$ structure, which also shows a form of ABC stacking [124]. The magnetic properties of these materials are related to the partially filled d orbitals of the transition metal cations. In the case of TMDH, both structures (CdI_2 and $CdCl_2$) result in an octahedral coordination of the metal cation, therefore the energy levels are split in e_g (higher energy) and t_{2g} (lower energy) orbitals. In Fig. 2.11, the general energy-level splitting including the electron distribution for some transition metals is shown.

In the case of TMDH and TMTH materials, the magnetic nearest-neighbor interaction is caused by superexchange via the halogen anions [124]. Superexchange means that a magnetic coupling between two neighboring magnetic centers is appearing through a non-magnetic atom

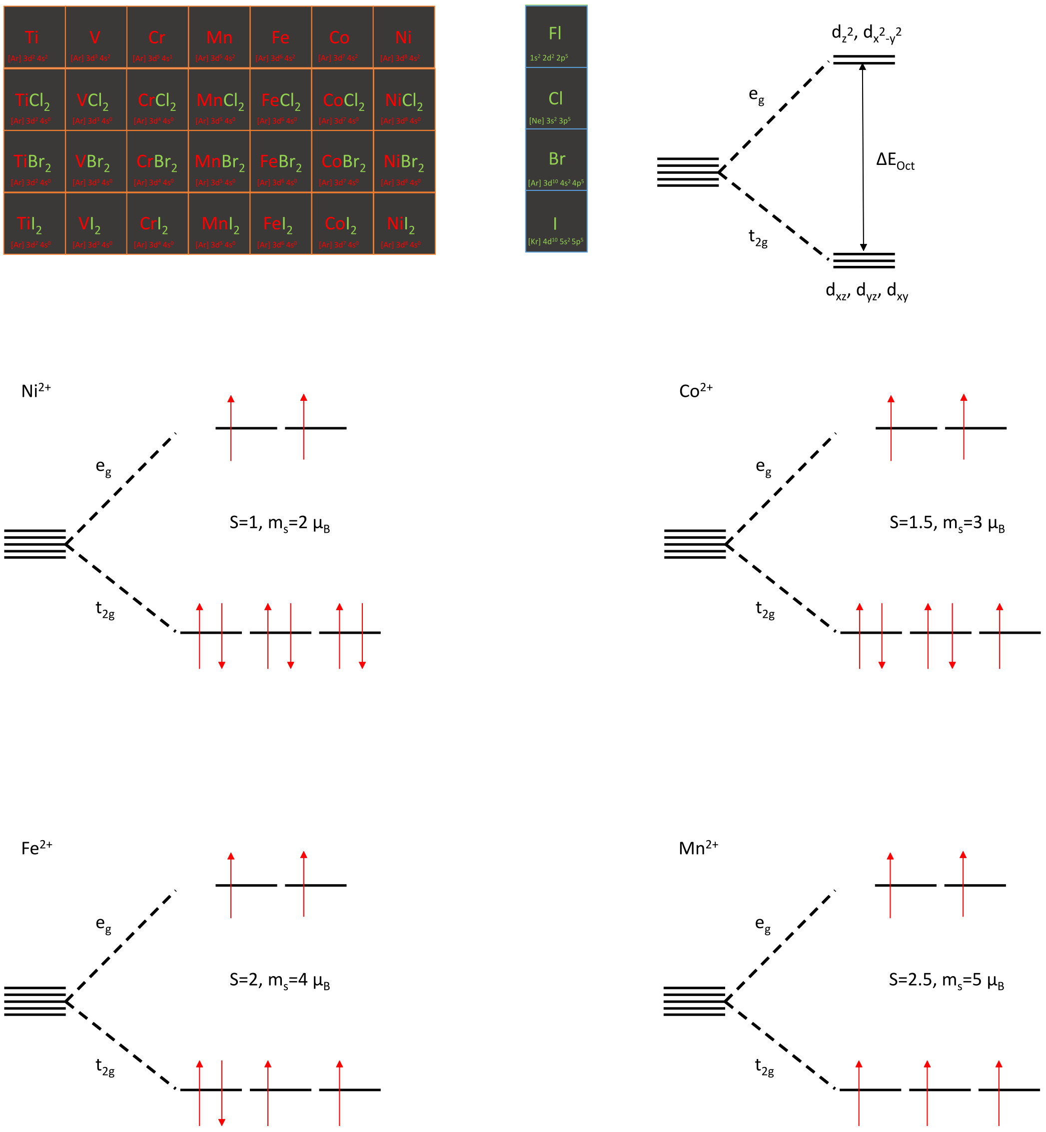

Figure 2.11: A small part of the periodic table with only the first row of transition metals and the halogen row down to I. Below the transition metals the different TMDH compound configurations are shown. On the left a schematic energy level scheme for a system with octahedral coordination is displayed [136]. In the center and the bottom of the Figure the energy levels schemes for the different TMDH compounds from Mn to Ni in a 2+ oxidation state with high spin (HS) configurations are shown. The d-orbital energy levels are filled according to Hund's rule, by first filling all levels with parallel spins and then filling the levels with spins with an opposing sign. If each t_{2g} orbital includes either only one or two spins, the system is quenched. In each element energy scheme the total spin as well as the corresponding magnetic moment are shown. The schematic energy level diagram for 3d orbitals with octahedral symmetry is based on Ref. [124], [137].

[138]. In the case of TMDH these non-magnetic atoms are the halide atoms. Therefore, no wave function overlap exists and in general, the superexchange is antiferromagnetic, however, by using

the Goodenough-Kanamori (GK)-rules [139], we can define certain circumstances in which the superexchange can be ferromagnetic. The predominant antiferromagnetic superexchange case is based on the Pauli principle [139]. This is valid when the two magnetic atoms have half-filled shells, like it is the case for Mn. This is the reason why MnO [138] as well as $MnBr_2$ and $MnCl_2$ are showing antiferromagnetic properties [140]. If the material contains different magnetic atoms, which have fully filled shells or a mixture like Fe compounds, then the system is ferromagnetically ordered [139]. In systems with only one atom type but nearly filled shells, the interaction is more favorable to be ferromagnetic like for $FeBr_2$ and $FeCl_2$, since the antiferromagnetic interaction is weakened [139]. The GK-rules are also predicting that for a 90 ° bonding angle between the two magnetic atoms, the interaction is ferromagnetic [140].

It can be observed that both material classes (TMDH and TMTH) are not "air" stable, since they are strongly hygroscopic, but in the case of heavier transition metal TMDH, the process of hydratization was reversible by degassing (more detailed information in the experimental chapters).

Another important feature of TMTH is that during the evaporation, the tri-halide compounds are growing in two different phases, related to the decomposition of the material [141], [142]. The phases are the wanted TMTH phase and the decomposed more stable TMDH phase (for evaporation from powder more stable). Sometimes even decomposes immediately to only the TMDH compound. In the later chapters it will be shown that also a full decomposition from TMTH to TMDH can appear. This is also the reason, why companies are using TMTH for creating stoichiometric TMDH powder and materials [141].

A more detailed explanation of the physical properties of the used materials in this thesis is written in each material-dependent evaluation chapter. Over the last couple of years the research was mainly focused on ML TMTH and their magnetic properties. Only recently, the investigation of ML TMDH has started with the structural and magnetic characterization of $NiBr_2$ [33], $FeBr_2$ [32], $FeCl_2$ [132], FeI_2 [143] and NiI_2 [144]. The materials investigated in this thesis are $FeBr_2$, $FeBr_3$, $MnBr_2$, and $MnCl_2$ on Au(111) and $FeBr_2$ on Bi_2Se_3. Besides the $NiBr_2$ compound all other Br-based TMDH are growing in the CdI_2 structure and are all showing AFM order with either ferromagnetic (FM), helimagnetic (HM), or stripe antiferromagnetic order in the layer. In the case of Cl-based compounds, this structure is identical to the one of $CdCl_2$, except for $TiCl_2$ and VCl_2, which have a CdI_2 structure.

Van der Waals Heterostructures

In the case of a bulk layered material a vdW homostructure exists, with each 2D layer coupled to the same material via vdW interaction. A vdW heterostructure, on the other hand, has weakly coupled layers of different 2D materials. This stacking is often described as a "lego"-style stacking [76], [145]. These material combinations can open new physical properties. Nevertheless, the creation of those heterostructures is not straightforward, since the stamping of different 2D materials on top of each other would require that they survive ambient conditions, which is in general only the case if they are passivated [76], [146], [147].

The epitaxial growth of other 2D materials on top of each other is limited, since the needed growth temperatures can already affect the layer underneath. In the following different methods for the creation of vdW heterostructures will be described. A commonly used technique to create vdW heterostructures is the mechanical assembly [145], [148]. One way of the mechanical assembly is the pick-and-lift technique [145], [149]. Here a 2D material is stored on a stationary membrane and another 2D material with a bigger size is connected to a movable membrane . By pushing the two membranes together, both 2D materials get in contact, so that during the removable of the topmost membrane also the 2D material, which was previously mounted on the stationary membrane is removed [145], [149]. This process can be repeated several times with different 2D materials, until the wanted heterostructure is created. Afterwards, the heterostructure will be combined with the substrate. The membrane, which was used for the assembly of the heterostructure, is removed by dissolving it [149]. This method is the repetitive way of the wet transfer method [145], [150].

Other growth methods such as chemical vapor deposition (CVD) or vdW epitaxy are depending on the robustness of the 2D materials [145]. During the CVD growth, the new 2D material layer is evaporated on top of either an already grown layer or a mechanically assembled layer like hBN/Graphene/hBN [145], [149], [150]. In the case of vdW epitaxy, the desired material is evaporated directly on top of the other 2D material [150], where the vdW interaction defines the preferential growth on top of the substrate or on another 2D layer [145]. However, there are more methods to create vdW heterostructures, such as heated assembly [151] or dry pick-up assembly [150], [152]. By opening this path in the creation of novel vdW heterostructures, new devices and applications can be created such as new transistors [147], [150], tunneling devices [145], and many more.

3 Experimental techniques and experimental setups

3.1 Experimental section

3.1.1 Substrate

In the follwoing sections, we will discuss the physical properties of different substrates like Au(111), Bi_2Se_3 and SiC.

Au(111)

The primary substrate material used in this work is Au(111). Au is the 79^{th} element of the periodic table and has an electron configuration ([Xe] $4f^{14}$ $5d^{10}$ $6s^1$) that causes a low reactivity with materials such as oxygen and carbon. Since the impurities are only adsorbed at the surface, the cleaning processes described later are relatively quick and easy. The single crystal material is arranged in a 3D lattice. In the case of materials such as Cu, Ag and Au, the lattice is a face center cubic (FCC) (Fig. 3.1 a)) [153]. The FCC structure has an ABC stacking sequence in the (111) direction [153], [154] and in the case of an hexagonal close packed (HCP) the stacking sequence is ABAB [155]. The naming Au(111) is referring to the crystal plane and therefore are described by the Miller indices. In the (111) case, a hexagonal surface structure is appearing with an at RT stable surface reconstruction, the so-called herringbone reconstruction (Fig. 3.1 b)) [154].

The energetically most favorable state is achieved on the material surface by creating this surface reconstruction [154]. In Fig. 3.1 b), the herringbone reconstruction is shown, which can be distinguished in FCC and HCP stacking of the topmost atomic layer. The distance between the narrow regions, which are a result of the HCP stacking, is 2.5 nm and between the broad regions, which are related to the FCC stacking, is 3.8 nm, [156] (Fig. 3.1 d) and e)). The periodicity for the narrow and broad structures is around 6 nm. In the case of transition metals the coordination number of atoms, which are located at the surface is lower than in the bulk, therefore a tensile stress is caused [157]. In the case of Au(111), there are two reasons for the herringbone reconstruction. One part for the creation is based on the stress release of Au(111). Since the stress is only released along the <110> direction, a surface instability is introduced, which causes the herringbone reconstruction pattern [157]. Another reason for the creation of the herringbone reconstruction is the high density of the surface, which creates the characteristic $22 \times \sqrt{3}$ superstructure [156], [158], where an extra Au-atom is implemented every 22 lattice constants along the <110> direction [157].

This substrate is an ideal platform for testing the growth of new 2D materials, since they are growing vdW coupled between the layers and have stronger interaction between vdW materials and the substrate surface. Therefore, the comparison between the first ML and the TL case reveals important information about the material substrate interaction. The hexagonal surface is also an ideal symmetry for the material growth. Another reason for using Au as a substrate is that the interface with Au needs to be investigated since it is used for the electronic connections in devices [156], [159].

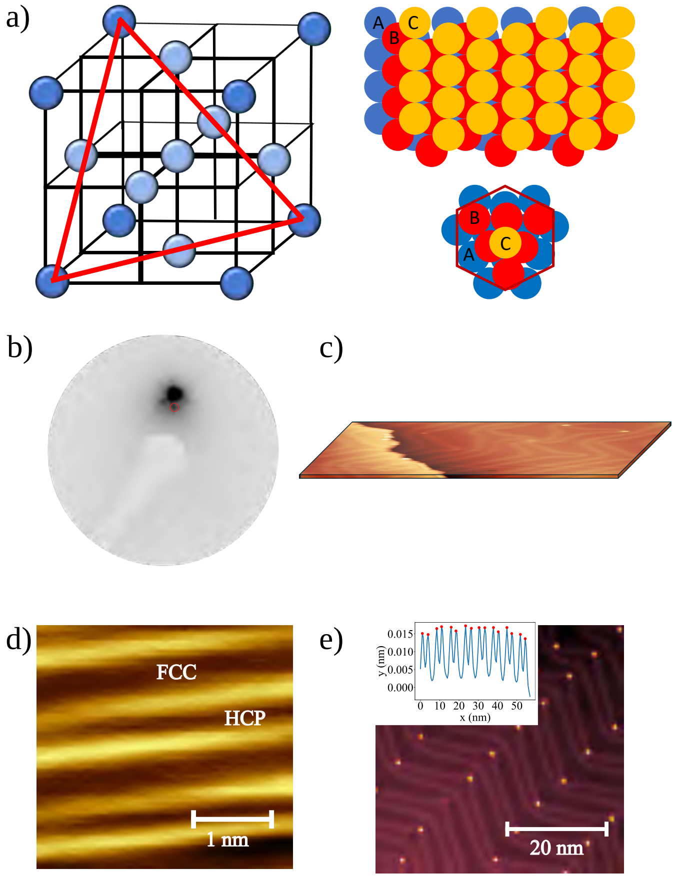

Figure 3.1: a) 3D - view of the FCC lattice, with the red triangle representing the (111) plane. On the right side of a) the stacking order (ABC) of the FCC lattice along the (111) direction is displayed. In b) the observed LEED pattern of Au(111) at 25 eV is displayed. The (1,0)-Au spot is surrounded by the spots caused by the herringbone reconstruction. In c) a 3D view of the Au(111) surface with a terrace edge and the herringbone reconstruction is displayed. d) and e) show STM images of the herringbone reconstruction of a clean Au(111) sample, d) including atomic resolution. This sample was measured at 77 K. As an insert, the FCC and HCP areas are indicated. e) shows the herringbone reconstruction of clean Au(111) areas of a sub-ML $FeBr_2$ sample measured at 4.3 K. The insert is showing the measured distances over 8 herringbone rows. The FCC structure showed a lattice constant of 4.56 ± 0.31 nm and for the HCP region a lattice constant 2.68 ± 0.24 nm. The values are in good correspondence with the measured values for clean Au(111) [156]. Part a) is based on the design of [154], [160], [161]. The LEED measurement was performed at Centro de Física de Materiales (CFM) in 2022 and the STM measurements were performed in 2020 (e)) and 2023 (d)).

Bi_2Se_3

Bi_2Se_3 is a 3D topological insulator (TI) [162], which belongs to the family of layered vdW materials. Therefore, the material does not fit in any of the conventional categories for solid materials (conductor, semiconductor and insulator). A TI behaves in the bulk state like a normal insulator with an energy band gap, but has gapless conducting surface states [163]. The material composition ratio is Bi 40.02 ± 0.02 to Se 59.98 ± 0.02 [163], [164]. x-ray absorption spectroscopy (XAS) measurements on Bi_2Se_3 revealed, that the Se atoms in this material are present in two different species, which are specified as Se^I and Se^{II} [165]. The different species of Se atoms are related to the position within the Bi_2Se_3 quintuple layer (Se-Bi-Se-Bi-Se) [166].

In Fig. 3.2 a), the structure of two layers of Bi_2Se_3 separated by the vdW gap is display. In the case of a Se^I atom the Se layer has only one Bi layer above or below it with a layer spacing of 2.97 Å [163]. This results in a strong Bi, Se coupling, where the Se atom is coupled to three metal atoms and weakly coupled to the other three Se atoms. In the case of Se^{II} a nearly perfect octahedral symmetry is present with the Se coupled to six Bi atoms with an interlayer spacing of 3.04 Å [163]. Along the c-axis every third layer is aligned to each other (as indicated by the dashed black lines in Fig. 3.2 a)) [163].

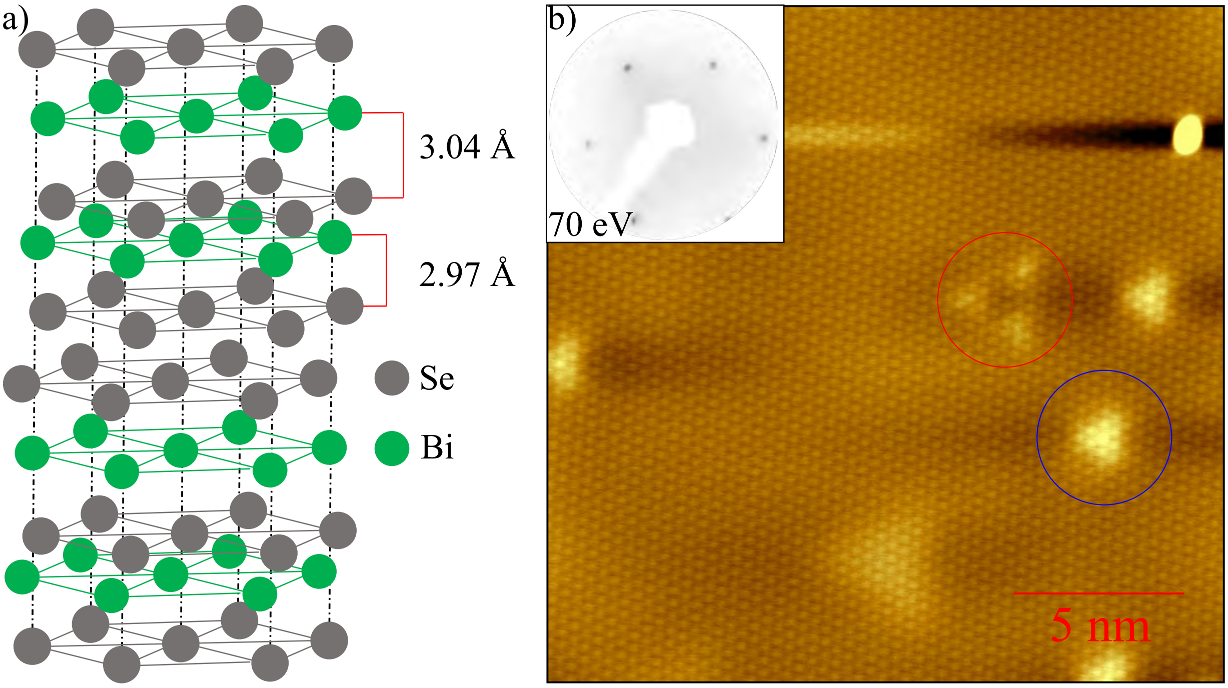

Figure 3.2: a) Schematic structure of two quintuple layers of Bi_2Se_3 separated by the vdW gap. b) STM image of a freshly cleaved Bi_2Se_3 single crystal. The calculated lattice constant is 4.1 ± 0.29 Å. Indicated in red and blue are the two different defect types, which are related either too only one missing Se atom at the surface or several. As in insert the measured LEED image at 70 eV is displayed, which shows a hexagonal pattern. The STM parameter are U_{Bias} = -2 V and I_{TC} = 100 pA. The measurements were performed at the PEARL beamline at SLS in 2023. The lattice structure of Bi_2Se_3 was redesigned after Ref. [163], [166], and [167].

In b) the measured STM and LEED image of a freshly cleaved Bi_2Se_3 crystal is shown. The measured lattice constant is 4.1 ± 0.29 Å, which matches perfectly with the literature value of 4.143 Å [163], [166]. The appropriate LEED image in b) was measured at 70 eV and shows the expected hexagonal structure. The STM image shows also different defect types of Bi_2Se_3. In Fig. 3.2 b), two different types of defects can be observed. The first one, which is marked with a red circle is related to a single atomic Se vacancy [168]. The second observed defect type, which is marked in blue is related to several missing Se atoms [168].

Graphene on SiC

SiC crystals exist in different structural phases with a Si:C ratio of 1:1 [169]. The different polytropes of SiC can be distinguished by the crystallographic order from hexagonal (H) to cubic (C) to rhombohedral (R) [169]. The substrate used in this thesis to grow graphene is 6H-SiC(0001) bought from *SITUS Technicals GmbH*. The numbering in front of the crystallographic phase is related to the amount of layers needed to repeat the lattice stacking [169]. In the case of a 6H-SiC(0001) a lattice stacking order of ABCACB is present [169], [170].

In Fig. 3.3, the 6H-SiC structure is shown.

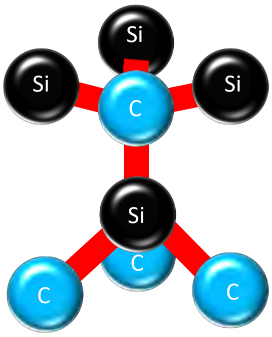

Figure 3.3: Material structure of 6H-SiC(0001). The blue spheres represent the carbon atoms and the black ones the Si. With this structure, a stacking periodicity of 6 is achieved. The figure is based on Ref. [169].

Since graphene was exfoliated in 2004, a way to create large-scale graphene films was in the focus of research, since it can be used as a base for new transistor generations [171], [172]. To achieve the large-scale production, it is very important to grow epitaxial graphene layers with reproducable thickness.

In 2007, the epitaxial growth of graphene layers on 6H-SiC(0001) has been published in Ref. [173]. By heating the substrate, different new phases of SiC can be achieved, until the desired epitaxial graphene phase can be created. This process is possible because the substrate starts to decompose and evaporates pure Si from the surface [174] until a carbon-rich surface is achieved, which creates the graphene layers [172]–[174]. During the annealing process, the graphene formation is not uniform and in different areas different amount of graphene is achieved from ML to multilayer [174]. In Fig. 3.4, the LEED patterns of SiC are seen to be different at different temperatures. The surface evolution of SiC is driven by the applied temperature. At low temperatures around 600 °C, a clean surface can be achieved (Fig. 3.4 a)) and with increasing temperature the growth of graphene is driven. At an intermediate temperature (around 950 °C), the LEED pattern shows the first indication of the starting growth process. Now a structure of $\sqrt{3} \times \sqrt{3}R30\,^\circ$ [172] is appearing with a 30 ° rotation to the SiC (Fig. 3.4 b)). By increasing the substrate temperature even higher via flashing or direct current heating, the buffer layer [173] and later the bilayer graphene (BLG) layer can be created. In Fig. 3.4 c) and d), both different layer types are displayed. If the temperature is either increased even higher or the annealing process is running for too long, multilayer graphene can be achieved [172]. In Fig. 3.4 c), the BLG structure is visible. Here the main intensity is located at the graphene spots, which are rotated by 30 ° with respect to the clean SiC (Fig. 3.3 a)). The measured pattern has a $(6\sqrt{3} \times 6\sqrt{3})R30\,^\circ$ structure [172], [175], [176]. In Fig. 3.3 c), the SiC and graphene spots are indicated with blue and green circles, respectively. In d) the pattern of the buffer layer/nanomesh is displayed [175], [177], [178]. Both patterns were measured on the same sample. This is due to a non uniform growth of the BLG. Another point is that the pattern displayed in d) was measured at a higher energy, which makes it less surface sensitive. The displayed LEED images in Fig. 3.4 c) and d) were measured after flashing the sample via direct current heating at 85-90 % of the needed temperature. A temperature of around ≈ 1100 °C was reached.

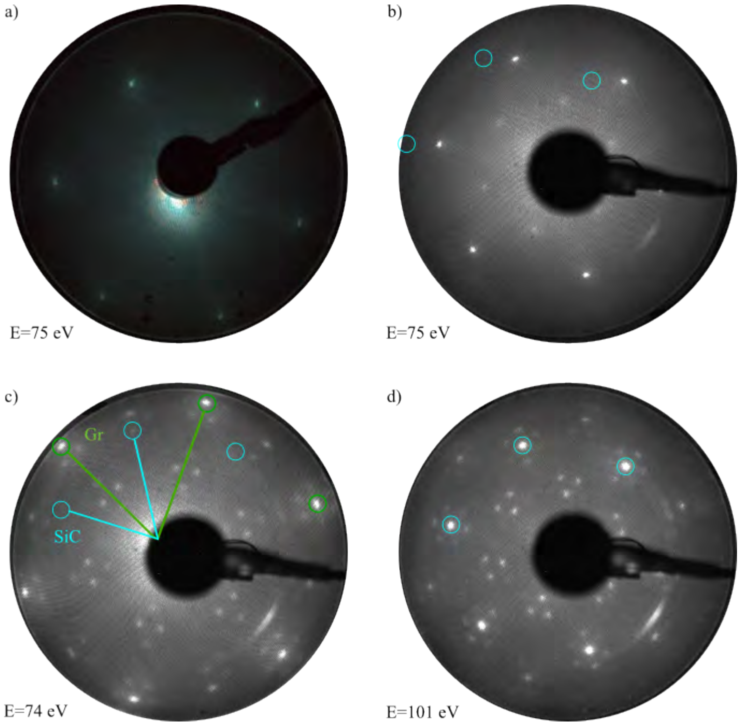

Figure 3.4: LEED images of SiC were measured in different laboratories. a) Clean SiC. The crystal was annealed to around 650 K at the XPS lab in Berlin in 2023. The surface was heated by using the resistive heating (pyrolytic boron nitride (PBN)). In b-d) the structural evolution of the LEED pattern of SiC for increasing flashing temperatures is shown. In c) and d) the moiré pattern of the BLG film is observed. This sample was heated by direct current heating at the PEARL beamline at Swiss Light Source (SLS) in 2023. The direct current heating was used as a flashing process, so only for short times the current was applied directly to the crystal. The blue circles are representing the SiC LEED spots and the green circles the spots of the grown BLG pattern.

3.1.2 Cleaning of Au(111) via sputtering and annealing

The cleaning procedure for most single crystal substrates can be divided into two steps. The first step is to remove the surface layers that contain the evaporants and adsorbed materials such as C and O. This first cleaning step is called sputtering and requires that the sample is close enough to the sputter gun under an angle of $\theta \approx 50 - 75\,°$ (Fig. 3.5) [179].

Sputtering parameter				
Lab	HV [kV]	Em. [mA]	I_{Sample} [μA]	p [mbar]
CFM XPS	1.0-1.2	6.0	9.6	$1.0 - 2.0 \cdot 10^{-5}$
CFM Prep	1.0-1.2	6.0	9.6	$1.0 - 2.0 \cdot 10^{-5}$
APOLLO STM	1.5	10	2.5	$2.0 \cdot 10^{-5}$
FU XPS	1.5-1.9	20-25	2-4	$6.5 - 9.0 \cdot 10^{-5}$
VEKMAG	1.0	6	8	$9.0 \cdot 10^{-6}$
BOREAS	1.0	10	20	$4.0 - 5.0 \cdot 10^{-6}$
DEIMOS	1.5	9	5	$3.1 \cdot 10^{-6}$
PEARL	1.5	4.5	/	$1.7 - 1.9 \cdot 10^{-5}$

Table 3.1: Sputtering parameters for Au(111) in different labs and chambers, where the samples were grown. The high sputtering parameter at the FU-lab are related to a problem with the sputter gun. However, after sputtering XPS measurements where performed to check the surface cleanliness.

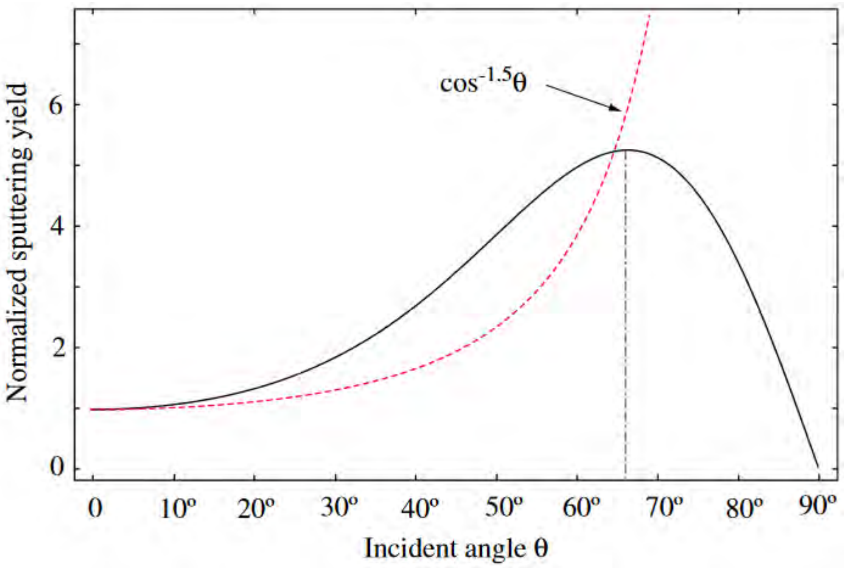

Figure 3.5: Angle dependence of the normalized sputtering yield with a maximum value at $\approx 67\,°$. The red line is representing Sigmund's theory [180]. The figure was taken from Ref. [179].

During the sputtering the chamber is filled with Ar gas at a nominal base pressure of $1.0 - 5.0 \cdot 10^{-5}$ mbar. The sputter gun contains a filament which is emitting electrons. By applying a high voltage (HV) of 1-2 kV, the Ar atoms are getting ionized and guided to the sample surface. For this whole process it is very important that the sample is grounded. In Tab. 3.1, the sputtering parameters used in the different chambers are displayed. The sample, which is close to the sputter gun, needs to be in the optimal position, such that the guided ion beam is covering the sample surface completely. The optimization of the sputtering process is based on many different factors like energy of the ions, angle between substrate and sputter gun, as well as on the mass of the materials atoms. Depending on the material, which needs to be sputtered different gas needs to be used to achieve optimal results. The sputtering time and parameters must be adjusted for different film materials and film thicknesses. In general the sputtering time for some ML to multilayer thick samples is in the range of 30 min to some hours (depending also on the material). After sputtering, the base pressure drops rapidly to the low 10^{-9} mbar if the Ar line was not contaminated with water. At this low pressure, the ion getter pump of the ultra high vacuum (UHV) chamber can be opened again. Before starting the next cleaning step, it is sometimes important to check if the sample surface is clean, by XPS. This step is important if the sample was covered with materials, which can diffuse inside the substrate material or if the sputtering procedure is not calibrated well. The structural measurements such as LEED cannot reveal during that stage the cleanliness of the surface, since during the sputtering the sample surface becomes rough, so that no sharp LEED image can be taken. The second cleaning step is annealing. This process can be done in many different ways by either a regular resistance heating system like PBN (Fig. 3.6 a)), a filament heating system (Fig. 3.6 b)) or even by direct current heating (Fig. 3.6 c)). The filament heating system can be used in different ways. Either the filament is used as a resistance heater, by just applying a current or a HV is applied, so that the electrons are directly guided to the sample.

The HV supported heating is a more efficient way of heating, than only using the filament. In contrast to the filament heating without HV the PBN system has the advantage of a fast and uniform heating. If very high temperatures are required to flash the substrate, then the same working principle as for HV supported filament heating is used, but with two differences. The first one is that the sample plate has a hole in the back, so that the guided electrons are directly hitting the substrate and the second part is that the flashing is only done for a short specific amount of time depending on the substrate. In the case of a direct heating system, the current is directly guided through the sample to reach very high temperatures, but without heating up the sample plate. The annealing parameters and systems used are shown in Tab. 3.2. The annealing procedures, except for flashing, are all performed in a time frame from 10-15 min (fast annealing) to 1 h (slow annealing). The maximum temperature used should always be lower than $\frac{2}{3}$ of the melting point, which for Au means to be in the range of 450-650 °C [182], [183], [184] (Au(111)

Annealing parameter			
Chamber	Current [A]	High Voltage [kV]	Temperature [°C]
CFM XPS	2.5	0.22	267/480
CFM Prep	7	-	262/414
APOLLO STM	3.67-4.32	/	495-550
FU XPS	1.83 A	-	475
FU Prep	2.2	-	525
VEKMAG	2.06	/	427
BOREAS	2.3	0.5	500
DEIMOS	1.7	0.45	500
PEARL	-	-	530

Table 3.2: Annealing parameters for Au(111) in different labs and chambers. The temperatures, which are displayed in red are the ones, which are displayed by the thermocouple readout. The black temperatures behind are the real temperatures due to the calibration measurements. The annealing at the PEARL beamline is computer controlled. The parameters, which can be set are the total power, as well as chamber pressures and ramp/hold time. For Au(111) a power of 30 W is used.

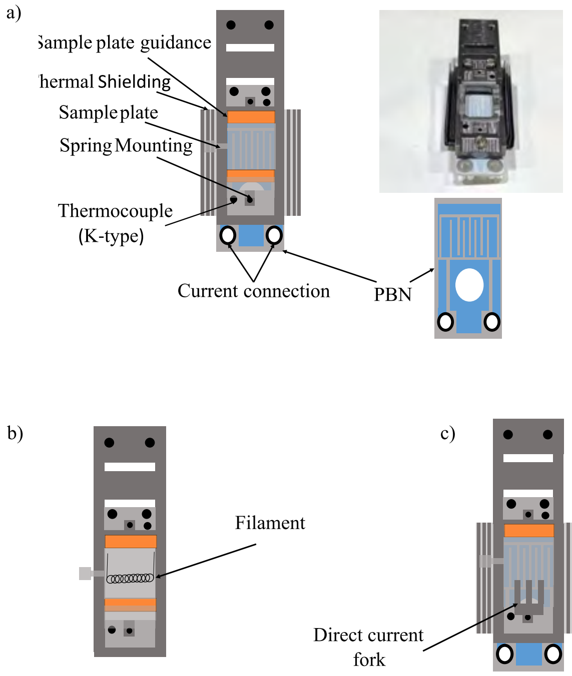

Figure 3.6: Displayed are different types of sample heater designs. a) Resistive PBN heating system. The PBN is directly contacted by the two connections in the bottom. By increasing the current, the PBN heats the sample uniformly, since it covers the whole back of the plate. On the left side a detailed schematic view of the sample holder including the mounted PBN heater is displayed. On the right side the assembled design and a schematic sketch of the PBN is shown. The PBN which is used inside the preparation chamber at the university is from *Scienta Omicron* and can reach a maximum power of 100 W. In b) a filament-heating sample holder is displayed. The shields in the back of the sample holder are used to reduce the heating of the whole chamber environment. Here the current is applied to the filament and an applied HV is guiding the emitted electrons to the sample. In c) a combined design of resistive (PBN) and direct current heating is shown. The direct current heating fork, which is also used to hold the sample in place, is used to apply a current directly to the sample plate. This heating method quickly heats the sample to high temperatures without strongly affecting the temperature of the surrounding environment. Since this heating method requires better sample isolation, the sample cooling takes more time. This design is also sold by *Scienta Omicron* and was used at the PEARL beamline at SLS. In a) the sketches are based on the used lab equipment. The direct current heating system is based on the used system at the PEARL beamline at SLS and is sold by Scienta Omicron [181].

1064 °C [185]). By overcoming this $\frac{2}{3}$, the sample surface starts to become rougher, since the flat surface is an energetically meta-stable state. Therefore the sample temperature must always be tracked via thermocouples (for regular single crystals K-type is sufficient) or even by using a pyrometer with the correct emissivity and the correct window materials. For flashing, the sample temperature is increased fast and stays at this value only for some seconds. This cleaning method also requires a different type of sample holder (hole in the backside).

This cleaning procedure is performed 1-2 times to clean an already used crystal prior to evaporation. In the case of a fresh crystal that has never been used, this procedure must be adapted and repeated several times. Therefore, the annealing must be done slowly in two steps (low temperature annealing followed by target temperature annealing) with an additional sputtering step in between.

3.1.3 Growth techniques

The production of 2D materials can be divided into two main principles. The first is the top-down method and the second is the bottom-up method. A brief introduction to both methods is given below. Figure 3.7 gives a general overview of the different bottom-up and top-down methods [80].

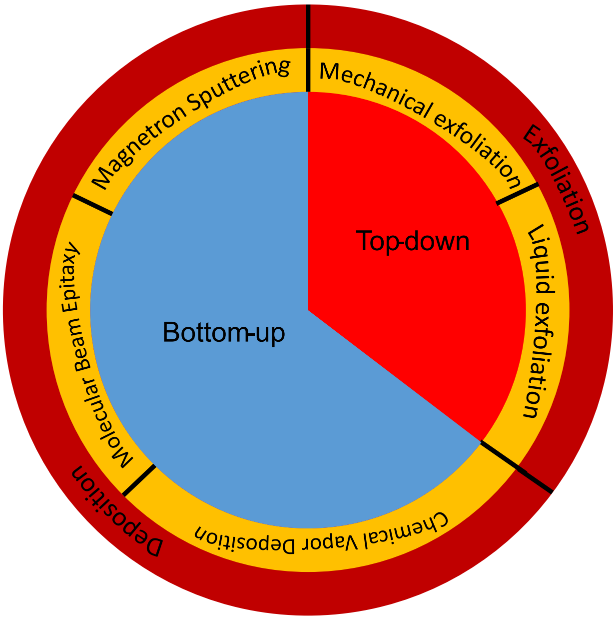

Figure 3.7: The circular diagram shows the different growth/preparation methods, with the most common methods related to the bottom-up growth and top-down assembly mechanisms. The figure is based on [186], [187], and [188] and is an adapted version of Figure 3 in Ref. [187].

The mechanical exfoliation was first achieved in 2004 by Novoselev and Geim [80], [28]. This method is using scotch tape or other types of tape such as Cu tape to remove layers from the bulk material. In Fig. 3.8 a), the general principle of mechanical exfoliation is displayed. One of the main disadvantages of mechanical exfoliation is that it is not controllable, so that the island sizes are different and the surface is not perfectly flat everywhere [189]. The exfoliated layers can be pressed on top of another substrate and by removing again the tape, some flakes of multilayer thickness are staying on the new surface without major contamination [189]. The same method is not only used to exfoliate layers from a bulk crystal to investigate the ML properties, but also to remove the contaminated surface layers of a bulk crystal for experiments. In this thesis we only used mechanical exfoliation for the second purpose, so that the substrate is clean [189]. Depending on the used exfoliation method, the island size can be increased [190].

Recently the Au-assisted exfoliation was presented, where a layer of Au is deposited on a substrate. On top of this layer a Ti or Cr layer is deposited before the 2D material is put in contact with the surface [190]. The last step is to put the tape on the back of the 2D material and exfoliate it. This method has already been tested on several 2D materials and the results were promising [190]. Another exfoliation technique, which is not only removing layers but is also creating fragments with different thickness is the liquid exfoliation (Fig. 3.8 b)) [191]. For this method the material is stored in a solution and by using an ultrasonic bath, the layers start to be removed in different sizes and thicknesses [191]. The liquid exfoliation can be distinguished into ion exchange and regular solution-based exfoliation via an ultrasonic bath [192]. In the case of exchanging ions, the layer distance is increased, therefore the ultrasonic bath can remove easily the layers [192]. In some cases the materials are already containing ions and by exchanging them, the previously described scenario is recreated. For some materials the regular exfoliation inside a solution is enough, here it can be distinguished between good and poor solutions. In a poor solution the layers can be rearranging themself, so that the exfoliation did not work [192].

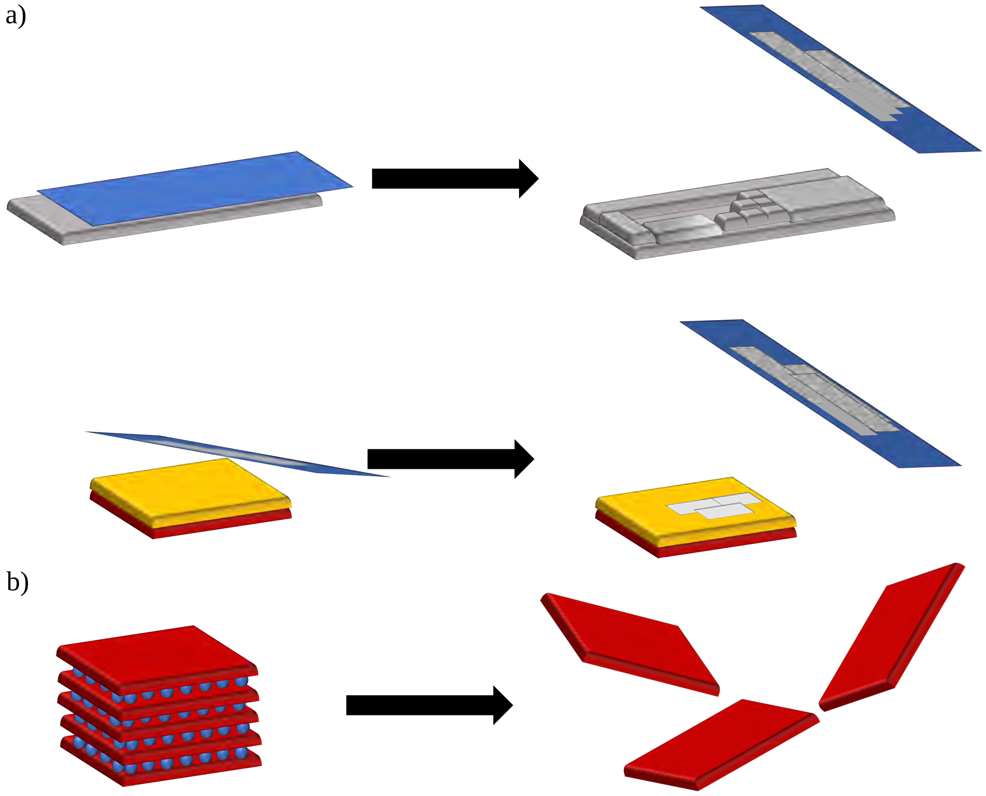

Figure 3.8: a) Mechanical exfoliation. Shown is the stepwise exfoliation and implementation of a ML to multilayer vdW material on top of another surface. b) The liquid exfoliation method by using ion exchange is shown. The designs are based on [189], [192].

These two techniques do not solve the ongoing problem of scalability and creating flat surfaces over large areas with reproducible thickness. The next methods (bottom-up) are showing ways to create relatively flat surfaces with the advantage of reproducible thickness. These deposition techniques can be divided into physical vapor deposition (PVD) and CVD. In both processes, the substrate is exposed to the vaporized material, resulting in the formation of a coating on the surface [193]. In the case of PVD, the material source is in the same chamber as the substrate [193]. Inside the evaporator, the material will be heated to its evaporation temperature. Now the material can react with the surface and create the surface coating. This would be the process of molecular beam epitaxy (MBE) [194]. In an MBE setup, several different materials are stored in either one or more evaporators to create either a layer-by-layer growth of different materials, or two evaporators work in parallel to create the wanted stoichiometry during co-deposition. This process requires, depending on the material, a heated substrate. A similar way to grow a thin film is the sublimation process. This process also requires an evaporator, but for the most cases a lower power is needed. Here the material is evaporated in a stoichiometric form onto the surface to create the thin film. This method has the advantage of low substrate temperatures and that the desired stoichiometry is already created. Another PVD process is magnetron sputtering, here a target is sputtered by the constant bombardment of an ionized gas. By this process the material is removed from the surface and guided to the substrate to create the thin film [195], [196]. In Fig. 3.9, the different PVD methods are displayed.

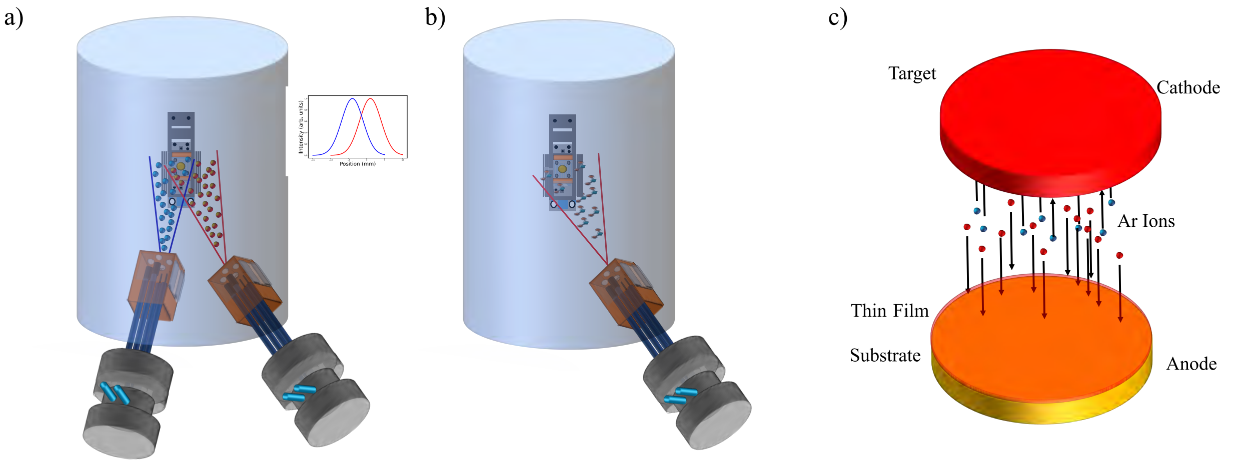

Figure 3.9: Different PVD techniques are shown. In a) the MBE method in the setup of co-deposition is displayed. Two evaporators are operated in parallel with the sample in a central position. The evaporation has a Gaussian distribution, which is shown as a insert in a). Here the overlap of the two Gaussian functions is shown. The sample is placed at the spatial intersection point of the two Gaussian distributions. b) shows the sublimation process of a stoichiometric powder. c) Magnetron sputtering process. The Ar ions are accelerated onto the target surface and remove the target material. The material is then directed onto the substrate surface to grow a thin film. The magnetron sputtering design is based on [197].

In CVD, the vacuum chamber is filled with an atmosphere of precursors [198]. This process is done stepwise, depending on the material that should be grown. In the case of a more complex growth, the reaction chamber is separated into different areas [198]. A constant gas flow is injected either with only a reacting gas or also with the material phase. In Fig. 3.10, a schematic principle is displayed. The different substrates are heated either for creating an evaporation or for helping the surface reaction process [198], [199]. This technique is also used to grow specific ceramics such as crucibles, since the seeding substrate can be removed after the coating layers are thick enough [200], [201].

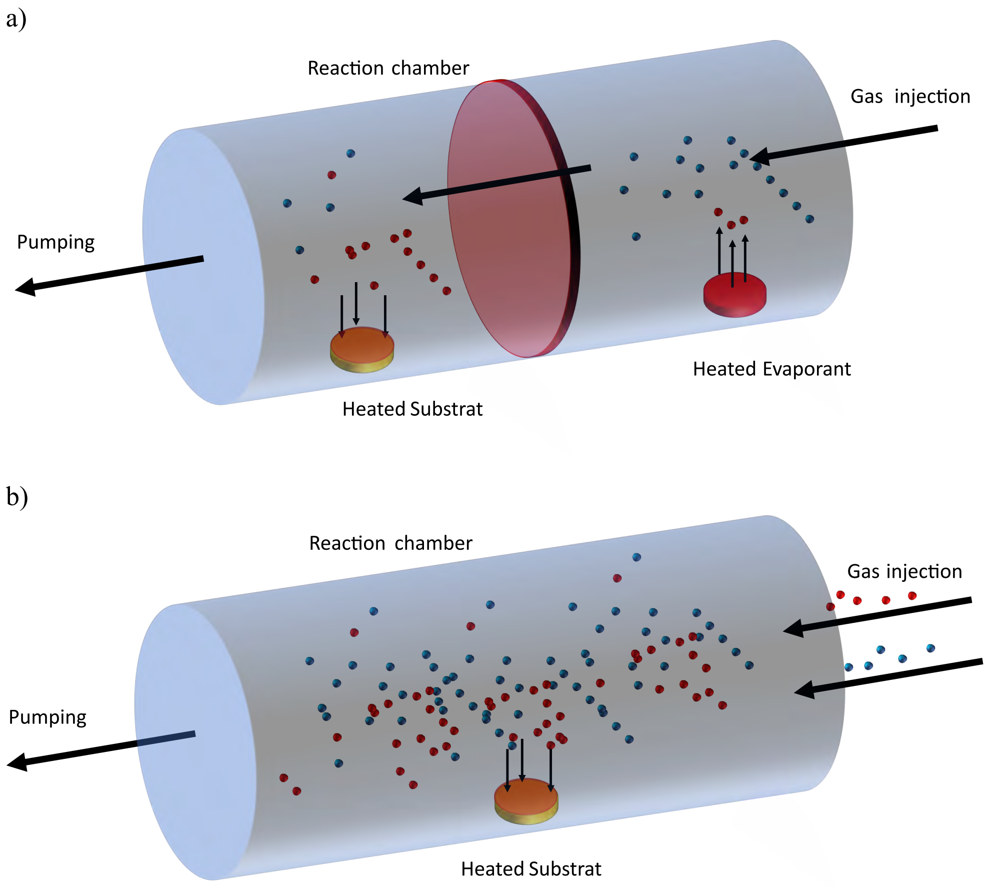

Figure 3.10: During the CVD process a constant flow of a reactive gas is introduced into the reaction chamber. Since the chamber is pumped, always fresh gas is entering and the waste products are removed. The design is based on [198], [199]. a) shows the stepwise CVD. Here also some evaporants are heated and the material is transported via the injected gas into the chamber part with the substrate. b) shows the CVD mechanism with two gases injected into the chamber. A reaction appears between gas one and two, so that the first gas is decomposed and the wanted material is deposited onto the substrate. The new reacted atmosphere is constantly pumped away.

Both techniques have advantages and disadvantages, as the CVD method allows large constant surfaces to be grown. The advantage of PVD, and sublimation in particular, is that the substrate surface does not need to be strongly heated [198]. This makes the technique very attractive for future device growth applications.

3.1.4 Experimental techniques

The experimental techniques used are explained in the following subchapters.

X-ray Photoelectron Spectroscopy

XPS is a non-destructive and element-sensitive measurement technique, which is used to investigate the chemical composition and state of the investigated material [202]. The high resolution spectrometer setup, which allowed for the first time the precise measurement of the element-dependent binding energy E_B, was developed and constantly further developed by K. Siegbahn and his colleagues [203], [204]. This major contribution lead finally in 1981 to a Nobel Prize for K. Siegbahn [203], [204]. This technique can be used for nearly all elements of the periodic table, besides H and He, this is caused by their low number of electrons [205]. In general a XPS setup only consists of three main components. The first one is the X-ray source, which usually consists of two different anode materials Mg ($E_{Photon} = 1253.6\,\text{eV}$) and Al ($E_{Photon} = 1486.6\,\text{eV}$) [205], [206]. In Fig. 3.11, the structure of a typical X-ray tube is displayed.

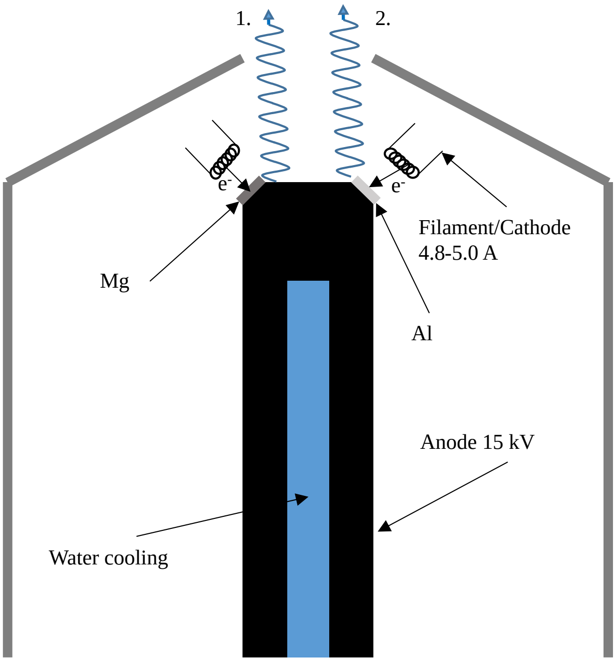

Figure 3.11: Displayed is the working principle of an x-ray tube. The dual anode x-ray gun consists of two filaments, which can sustain a current of max. 5.0 A. The emitted electrons are guided to the anode, which is water-cooled and where a HV of 15 kV is applied. The numbers 1. and 2. are describing the two possible emission cases depending on the anode material. The design is based on [207], [208].

For the dual anode design, two filaments are mounted inside the x-ray gun head [209]. The filament is emitting the electrons, which are accelerated onto the anode material (Mg or Al). This is causing a core-level electron excitation, which emits x rays during the relaxation process. However, the here described and used X-ray tube is not emitting monochromatic radiation. In the case of an Al anode the FWHM is 0.9 eV and for a Mg-anode 0.7 eV [209], [210]. To achieve fully monochromatic X rays, a monochromator (quartz crystal) must be used, which increases the signal to noise (STN) ratio and decreases the FWHM [204] [209]. The reason that two different anode materials are used is that during the XPS measurements not only the wanted XPS peaks are observed, but also Auger peaks resulting from secondary electron processes. By switching the anode material from Mg to Al the XPS core-level peaks are stable in binding energy and are not shifting. However, the Auger peaks do depend on the excitation energy, such that the photoemission peaks change their energy position in a binding energy spectrum. The second and third part are the analyzer and the detection systems (Fig. 3.12).

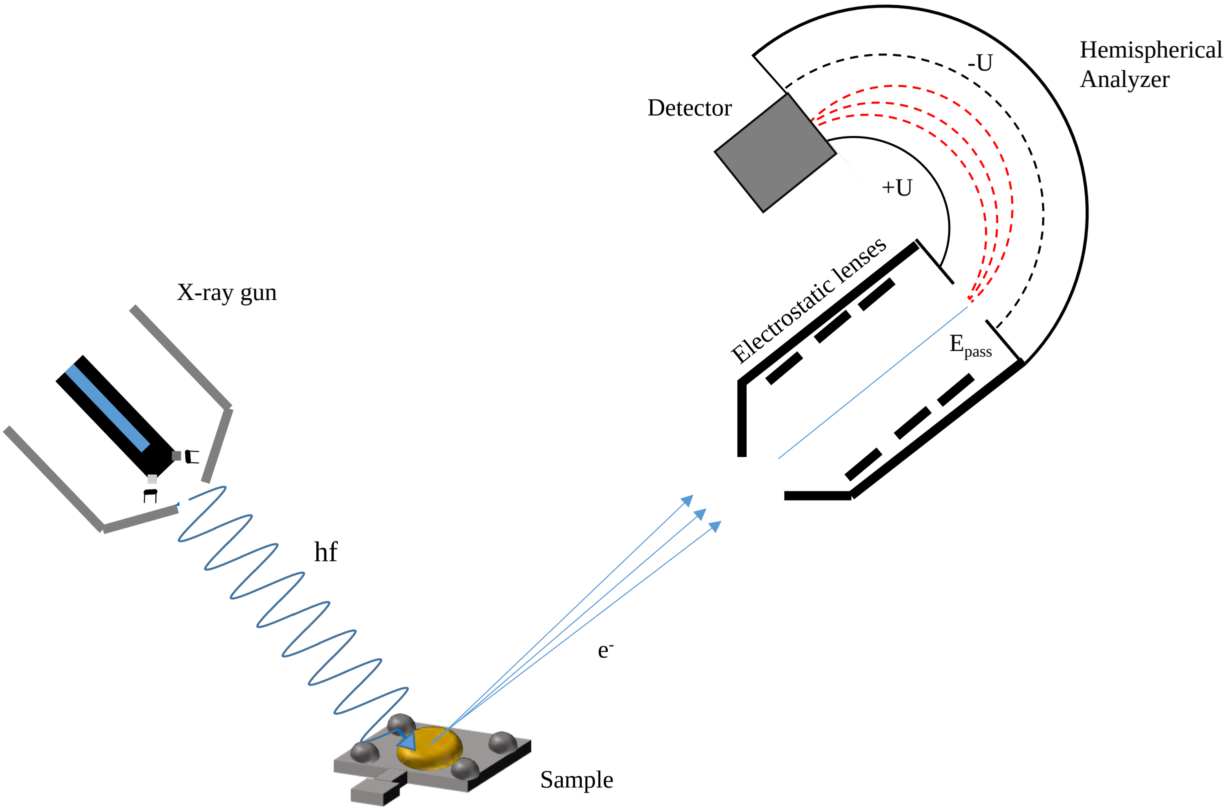

Figure 3.12: A general XPS setup design. The x rays emitted from the x-ray gun onto the sample release core-level electrons from the sample surface. These electrons are entering the hemispherical analyzer and are focused by electrostatic lenses inside the analyzer nose. The applied voltages allow only such electrons which are fulfilling the energy restrictions to be refocused and to enter the detector system. The figure is based on the design from [211] and [212].

Over the last decades, different analyzer designs have been developed and used. However, the nowadays primarily used analyzer type is the hemispherical analyzer, which has the highest resolution from all analyzer designs [209]. The emitted electrons from the sample surface reach the entrance of the analyzer system, where they are either accelerated or decelerated and focused by the electrostatic lenses. Inside the analyzer, an electric voltage is applied to the outer and inner hemispheres (opposing signs). The applied voltage is used as a selection mechanism, so that only electrons with the wanted pass energy (PE) (E_{pass}) are refocused and reach the detector [209]. The PE is set constant during the measurements, so that even for different kinetic energies the analyzer resolution is independent of energy. The selection of the correct PE is important, since for low pass energy the amount of counts is dropping and therefore the STN is getting worse.

However, the decreased STN ratio can be fixed by increasing the measurement time (more scans and higher dwell time), but the main advantage is the higher resolution [209], since the resolution $\Delta E \propto E_{\text{pass}}$. As a detection system either channeltron or charge coupled device (CCD) detector systems are used. Since this technique can resolve also low material amounts, it is very important to keep the investigated sample in a clean environment, otherwise some materials like O and C can contaminate the sample surface. This would cause wrong thickness estimation and the material could also react with O, so that the properties could change. Therefore it is very important that the measurements are performed at low pressures in the range from low $10^9 - 10^{11}$ mbar, otherwise the ML formation of the contaminant material is very fast (Fig. 3.13) [209].

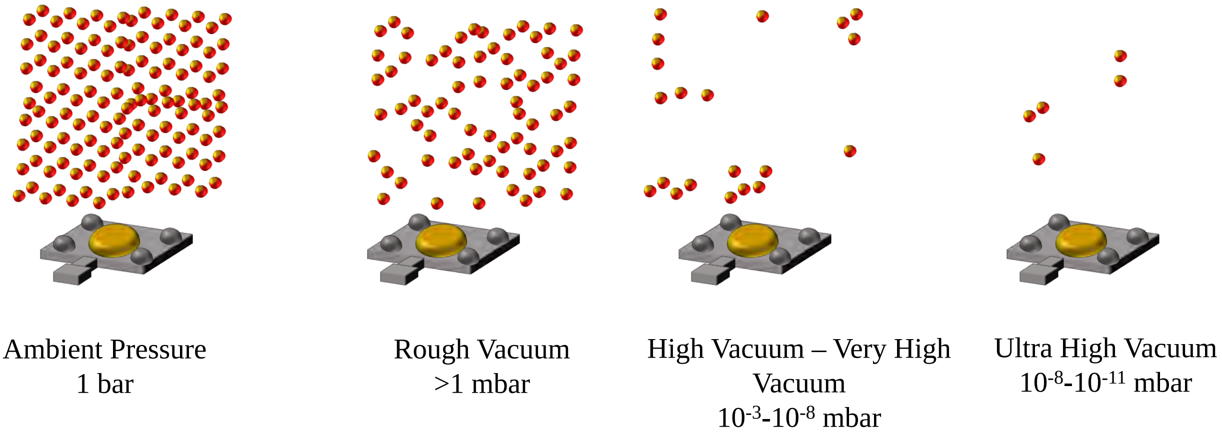

Figure 3.13: Schematic representation of the amount of atoms depending on the vacuum condition. With decreasing amount of atoms inside the vacuum atmosphere, the formation time of an adsorbed ML is increasing. The time for the formation of 1 ML with a sticking coefficient of 1 to form 1 L (Langmuir) is 1 s at 10^{-6} mbar [213], [214]. The figure is based on Ref. [215].

Not only that the sample surface would be contaminated at higher pressures, also the increased amount of atoms inside the chamber atmosphere would interfere the traveling process, due to scattering processes [209], [214]. In Fig. 3.14, the theoretical concept of XPS is shown.

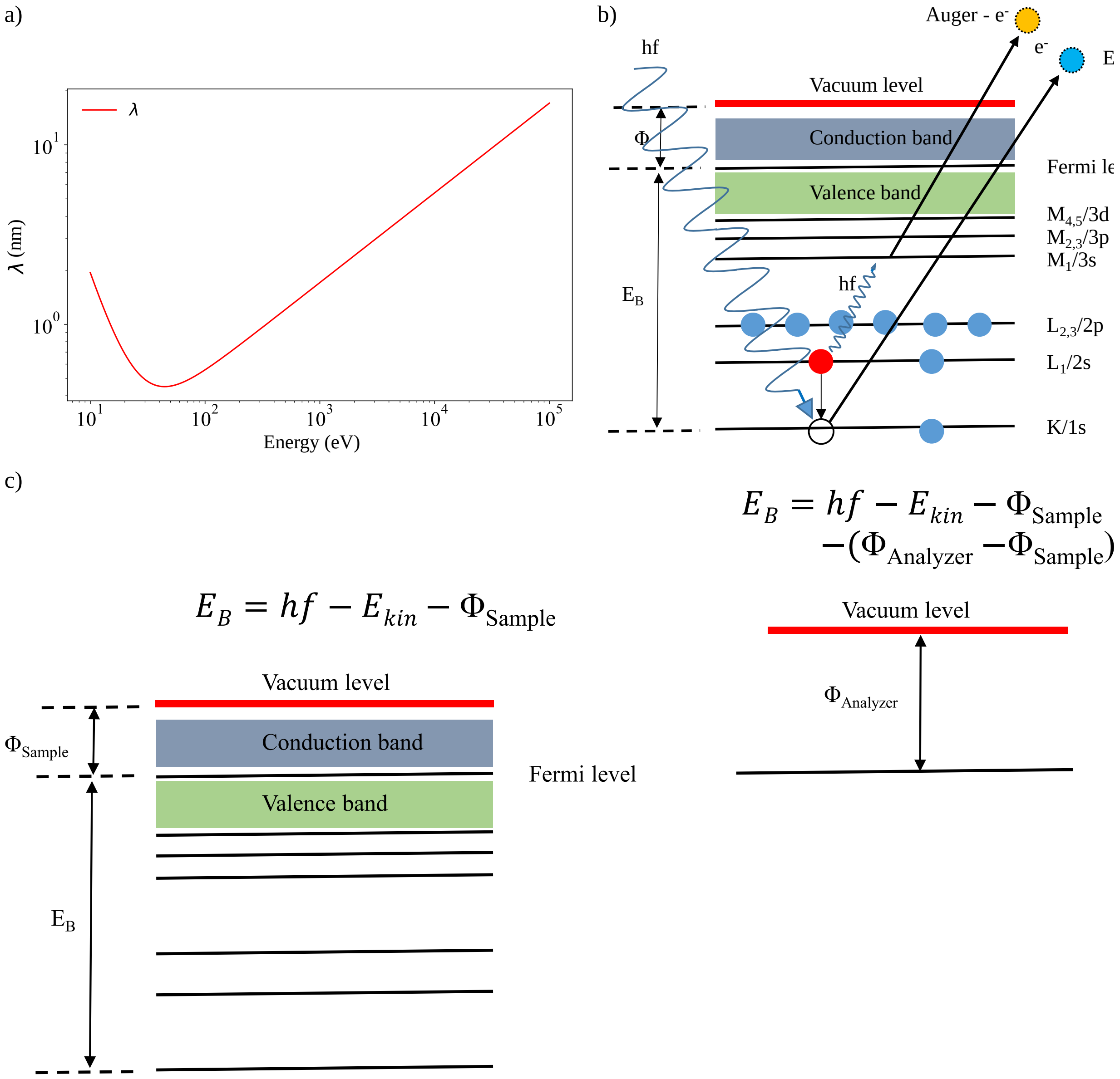

Figure 3.14: a) Inelastic mean free path λ of electrons in solids in nm as a function of the kinetic energy. The displayed universal curve is based on the parameters for Au. However, the shape and behavior is the same for other elements. b) Excitation process during the illumination with Al K_α radiation. The x rays are exciting an electron from the core-level so that it overcomes the vacuum level and leaves the atom (primary electron). As a result, the secondary electron processes start. An electron from a higher energy level is jumping to an energetically more favorable state and by this process it is emitting radiation with a discrete energy, which is exciting another electron from a higher energy level, which then leaves the atom as an Auger electron. c) Energy level scheme as a base understanding for the binding energy equation. The Fermi level of the sample and the spectrometer are equal, since the system is grounded. The figure is based on designs from [204], [209], [216]–[218].

The emitted X-rays can penetrate deep into the sample, however not all excited electrons are reaching the sample surface and can be measured [209]. This is a direct consequence of the energy-dependent inelastic mean free path λ, which is an average value for the expected decay length before getting absorbed. In Fig. 3.14 a), the universal curve is displayed, which is based on the following equation [219]:

$$\begin{aligned} \lambda &= \frac{A}{E^2} + B \cdot \sqrt{E} && (3.1) \\ &= \frac{177}{E^2} + 0.054 \cdot \sqrt{E} && (3.2) \end{aligned}$$

Here the values for A and B are related to Au, but they are not much different for other elements, where A is 143 [219]. In the case of XPS measurements, the important energy region is in the range from 200 eV-1476 eV (Al anode). This equation of the inelastic mean free path has to be adapted in the case of a different emission angle θ.

$$\lambda(\theta) = \lambda \cdot \cos(\theta) \tag{3.3}$$

Therefore only the topmost 5-10 nm ($3 \cdot \lambda \cdot \cos(\theta = 0)$) are contributing to the XPS spectra [209], [220], [221]. In Fig. 3.14 b), the excitation and ejection process is displayed including the secondary electron/Auger process. The emitted X-rays are exciting the core-level electrons, so that they can leave the atom by overcoming the vacuum level. The binding energy E_B of the photoelectron can be calculated in the following way [206, p.10], [209]:

$$\begin{aligned} E_B &= E_{\text{Photon}} - E_{\text{kin}} - \Phi_{\text{Sample}} - (\Phi_{\text{Analyzer}} - \Phi_{\text{Sample}}) && (3.4) \\ E_B &= E_{\text{Photon}} - E_{\text{kin}} - \Phi_{\text{Analyzer}} && (3.5) \end{aligned}$$

Here E_{kin} is the kinetic energy of the excited electron and Φ is the workfunction (WF) of the detector and sample. In Fig. 3.14 c), the origin of the binding energy equation is schematically displayed. Since the general working principle of XPS measurements is now explained, we can start with the explanation of the information, which is embedded in the spectra. Within the full spectral range of the measurement, different peaks can be observed, which have different origin. In Fig. 3.15, a survey scan of Au(111) is displayed.

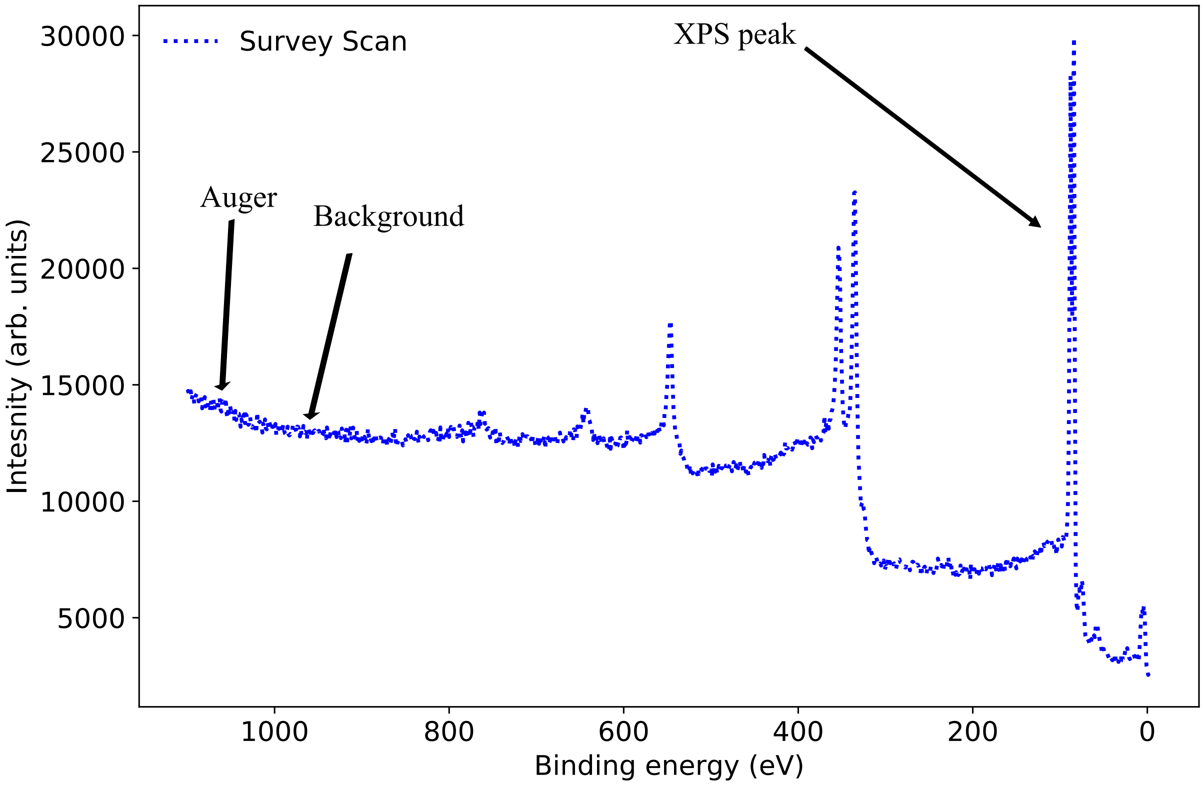

Figure 3.15: Displayed is a survey spectra of Au(111), measured at CFM with a non-monochromatic Al anode ($K_{\alpha_{1,2}}$ radiation). Indicated are an exemplary Auger and XPS peak of Au as well as the background.

The background, which is indicated in Fig. 3.15, originates from inelastic scattering processes of the excited/ejected electrons [217]. For later evaluation of the data, the background needs to be subtracted from the measured spectral peaks. Several different background approaches can be used, however, the physically most correct background subtraction is by using either a Shirley [222] or a Tougaard-type background [223]–[226]. The first peak type is the XPS peak (Fig. 3.15) from the first-order excitation. The peak shape is an convolution of Lorentzian and Gaussian curve (the latter caused by the analyzer and the x-ray gun) [227], which results in the typical Voigt profile. Depending on the measured material, the line shape and FWHM is changing, however, the measured line width is always based on the system energy resolution and therefore it is a convolution of several factors. The following equation is an approximation for a convolution of Gaussian profiles [227].

$$\Delta E = \sqrt{(\Delta E_r^2 + \Delta E_{\mathrm{X}}^2 + \Delta E_{\mathrm{A}}^2)} \tag{3.6}$$

Here ΔE_r is the natural FWHM of the elemental peak, ΔE_{X} is the FWHM of the x-ray tube and ΔE_{A} is the energy resolution of the analyzer [206], [227].

Except peaks, resulting from s orbitals, all other orbitals result in two peaks (doublet configurations) with the same FWHM, this is caused by the spin-orbit coupling (SOC). In Tab. 3.3, the orbital configurations for each orbital are displayed as well as the area ratio between the corresponding XPS peaks. If the XPS peaks are shifted compared to literature values, this can have several reasons. The first could be that the sample is not grounded or an insulator, which

Orbital	Configurations l^j	Area Ratio $\frac{A_{LB}}{A_{HB}}$
s-Orbital	$\mathrm{s}^{\frac{1}{2}}$	/
p-Orbital Prep	$\mathrm{p}^{\frac{1}{2}}$, $\mathrm{p}^{\frac{3}{2}}$	$\frac{2}{1}$
d-orbital	$\mathrm{d}^{\frac{3}{2}}$, $\mathrm{d}^{\frac{5}{2}}$	$\frac{3}{2}$
f-orbital	$\mathrm{f}^{\frac{5}{2}}$, $\mathrm{f}^{\frac{7}{2}}$	$\frac{4}{3}$

Table 3.3: Orbitals and their configurations, which are measured in XPS, as well as the area ratio between the two XPS peaks [210, p.4]. The area of the peaks are indicated by A_{LB} and A_{HB}, where LB and HB are standing for lower and higher binding energy. l is the orbital quantum number and j is the total angular momentum ($j = \mid l \pm s \mid$) with s as the spin quantum number [206, p.10]. The table is a modified version of the one in Ref. [204].

causes therefore a charging shift. This can be easily checked by comparing the substrate peak position of the main transition to literature values, since charging would affect all peaks equally. Charging of a sample can also be identified by peak broadening [206], [209]. Another possibility for a peak shift is a chemical shift [206], [209], which is caused if the material is reacting and creating a different oxidation state. A positive oxidation state like Fe^{2+} is causing a shift to higher binding energies compared to the Fe^{0} state. If the peak positions are starting to shift with increasing sample thickness, it can be caused by a quasi WF change. This phenomenon has been observed in the Ref. [32], [228], [229]. Here the shift has been observed due to the interaction with the substrate material. Another possible reason is thickness dependent shift to higher binding energies, due to the vdW behavior of multilayer materials. This shift can also be observed in scanning tunneling spectroscopy (STS) measurements for different thicknesses. It has been observed that the conduction band shifts with increasing thickness [33], [230].

The other peak type which is displayed in Fig. 3.15 are Auger peaks, which are a result of the secondary electron process as described before. By changing the anode material, the XPS peaks are staying at the same binding energy and the Auger peaks are moving to a new energy position depending on the new photon energy. Satellite peaks can be distinguished into artificial peaks (x-ray tube related) and process peaks (Shake up) [206]. By using a non-monochromatic X-ray tube, not only the characteristic peak but also peaks from higher photon energies are visible. Depending on the anode material also different minor intensity peaks are visible, which have all very low intensity. In the case of an Al-anode, the second-most intense peak is shifted by 9.8 eV to lower binding energies with an intensity of only 6.4 % of the main peak [206, p.17-18], [209]. The other type of satellite peaks are called shake-up peaks. In the case of an shake-up peak, the created ion is staying in an excited state (ES) [206]. This ES is energetically some eV above the ground state (GS), which causes a shift to higher binding energies [206, p.18-19]. These peak types are normally nicely visible in lab XPS setups, however there are peaks (multiplet peaks), which can only be observed in setups with very high resolution, since they are energetically very close and have a small FWHM. The multiplet peaks are occurring in systems with partially filled shells (unpaired valence electrons [231]). Here the unpaired electrons can couple to the unpaired electrons in the core-level and therefore create different final states, which are broadening the peak structure [232]. This is the reason why the XPS and XAS spectra of metallic Fe (Fe^{0}) show no multiplet peaks, but Fe^{2+} and Fe^{3+} does [233], [234]. These peaks can be resolved by using synchrotron radiation, where the photon energy can tuned and the energy resolution is high enough.

Synchrotron radiation

In Fig. 3.16, the general structure of a synchrotron is displayed.

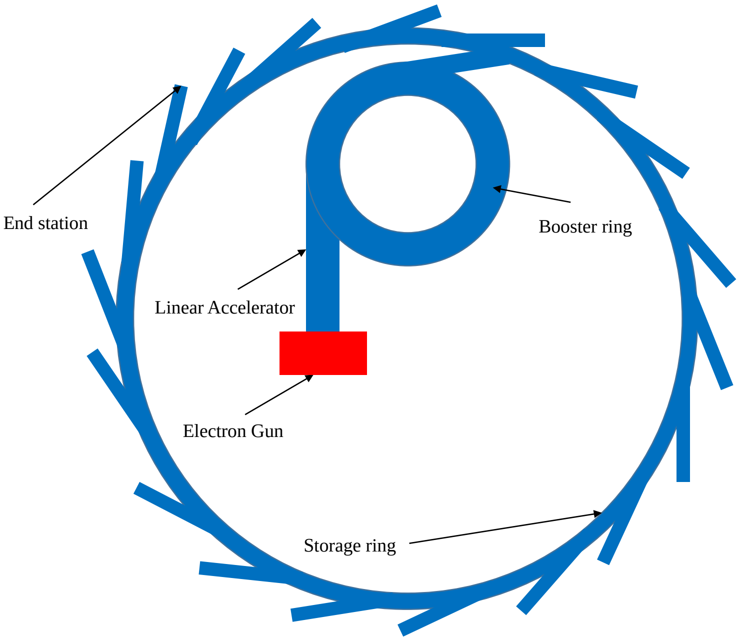

Figure 3.16: General structure of a synchrotron. It contains the electron gun, which is connected to the Linear accelerator. From the linear accelerator the electrons are entering the booster ring. From the booster the electrons are entering the final stage, the storage ring. The endstations are directly connected to the storage ring and are containing the measurement setups. Before each end station either an undulator or bending magnet is mounted. The design is based on [235], [236].

The electrons are created by an electron gun, which is directly connected to the linear accelerator, where the electrons are accelerated until they have the injection energy of around 100 MeV [237], [238]. Now they are entering the booster ring, which is a circular accelerator, which is increasing the electron energy by using an array of bending magnets, which are keeping the electrons on the circular orbit [238], [239]. To reach the extraction energy, which is in the range of some thousand MeV [239], [240], the magnetic field is constantly adapted. The electrons which are entering the storage ring have relativistic energies E_{rel} [237]. After the electrons have reached the maximum energy they are extracted and entering the storage ring. The storage ring consists of different magnet setups (undulator, wiggler and bending/dipole magnets), which are used to emit the X-ray radiation by deflecting the electrons in the magnetic field. Each of these have own advantages and disadvantages. Since the electrons have relativistic energies, the radiation cone is narrow and is only emitted along the trajectory [237]. The performed synchrotron experiments always require a high flux and a high degree of circular polarization (σ) as well as the possibility of switching the polarization of the light depending on the performed experiment [237]. However, depending on the magnet setup it is not always possible to have a high flux and high degree of polarization [237]. In the following we will compare bending magnet setups with undulator and wiggler setups.

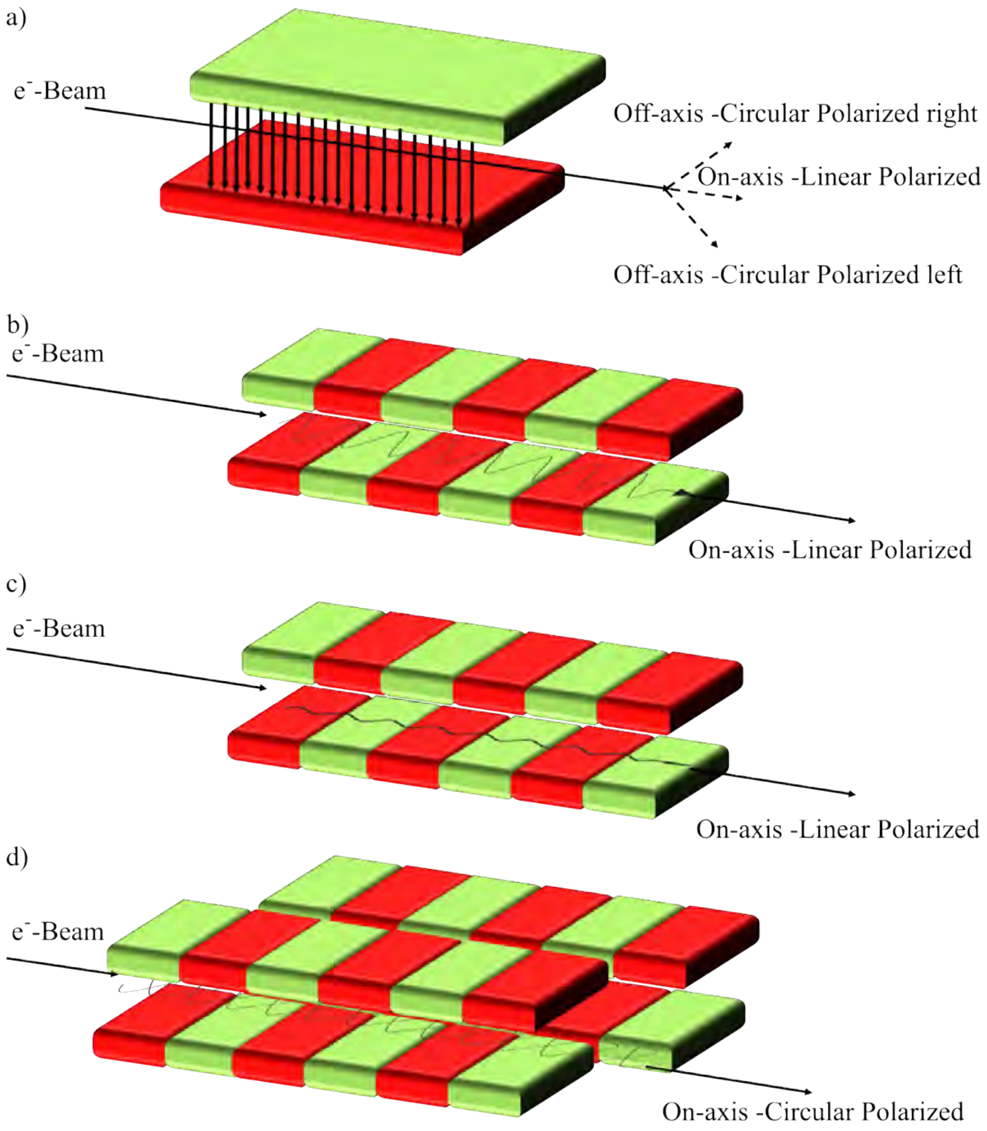

Figure 3.17: a) Bending magnet setup. The electron beam is entering the bending magnet. The deflection inside the magnetic field is causing the emission of X-ray radiation. On the plane of the electron trajectory, the emitted X-ray radiation is linearly polarized and above and below the plane the X rays are circular left and right polarized. b) Wiggler setup. The electron beam is entering an array of bending magnets with opposing signs. Due to the magnet array, an oscillation of the electron beam is achieved, which is emitting at each bend X-ray radiation. Therefore the X-ray flux is higher than for a single bending magnet. The radiation is summing up incoherently. Here only linear polarized light is emitted. c) Undulator magnet setup. The structure of the undulator setup is identical to the wiggler setup. The major difference is the strength of the applied magnetic field. In the undulator the oscillation has a smaller amplitude, so that the emitted X-ray radiation is adding coherently. Here horizontal linear polarized light is emitted. d) Helical undulator. The helical undulator setup is used to create circular polarized light, therefore two regular undulator setups are shifted with respect to each other, so that a helical electron beam trajectory is created. To create vertical linear polarized light a similar setup type is used, only with a different shift between the two undulator arrays. The designs are based on [236], [237], [241]–[244].

In Fig. 3.17 a), the structure of a bending/dipole magnet is displayed. The electrons which are entering the bending magnet are emitting X rays (Bremsstrahlung) [243]. For a bending magnet setup, the X-ray polarization needs to be distinguished in on-axis and off-axis [237]. The polarization on-axis is linearly and off-axis is circular left or right. Therefore, in experiments where circular polarization is needed and a bending magnet setup is mounted the X-ray flux is strongly reduced [237] by nearly a magnitude. Also the fact, that the two different degrees of circular polarization are located at different off-axis positions is causing some problems, because the needed movement of the measurement setup for switching the polarization can cause spectral shifts due to a different incident angle on the monochromator [237], [245]. In Fig. 3.17 b), the structure of a wiggler magnet setup is displayed. This setup consist of periodically ordered magnet arrays [241], which are used to create an oscillation of the electron beam. The X-ray radiation which is obtained by such a setup has a higher flux compared to the previously discussed setup. The structural scheme of a wiggler setup is identical to the one of an undulator. These two magnet setups can be distinguished by the oscillation amplitude and period. If the radiation from each separate magnet system is adding up coherently the setup is called undulator ($I_{\mathrm{Flux}} \propto N_{\mathrm{electron}} \cdot N_{\mathrm{Poles}}^2$), if not, it is a wiggler ($I_{\mathrm{Flux}} \propto N_{\mathrm{electron}} \cdot N_{\mathrm{Poles}}$) [237], [243]. The primarily used magnet setups in this thesis are undulator setups. The setups described in Fig. 3.17 b) and c) are producing only linear polarized light along the beam axis, since an equal amount of oscillation minima and maxima is existing. To create circular polarized light with an undulator setup a helical path needs to be created (Fig. 3.17 d)) [237]. This can be either achieved by using an alternating array of permanent magnets, which has the disadvantage of slower polarization changes due to a mechanical movement of the magnet arrays, or by two arrays of electromagnet setups, which are shifted with respect to each other [237], [246], [247] [248]. This permanent magnet setup is found at many beamlines. The majority of experiments in this thesis were performed at beamlines with an APPLE II undulator (permanent magnet setup) [246]. At the DEIMOS beamline a setup exists to achieve fast switching between the two polarization directions with a frequency around 10 Hz [249], [250].

X-ray Absorption Spectroscopy and X-ray Magnetic Circular Dichroism

XAS measurements are element-specific, due to the unique binding energy of each element. During the measurements, x-ray radiation is absorbed by the atoms of the material, which results in an excitation of a core electron into the unoccupied part of the valence band [251]. The excitation of the core electron causes a strong increase of the absorption, which is called edge [251]. At the core-level position a hole is created [252], which causes subsequent electron processes (Auger). The XAS measurements are performed in total electron yield (TEY), which is proportional to the absorption coefficient [252]. Since TEY measurements are dominated by scattered low energy secondary electrons from the Auger process [253], this measurement technique is very surface sensitive (range of some nm) [252], [254]. Depending on the measured energy range, two experimental classes can be distinguished, the near edge x-ray absorption fine-structure (NEXAFS) [255] and the extended x-ray absorption fine-structure (EXAFS) [256]. During the NEXAFS measurements, the large post-edge energy range > 50 eV will be measured [257]. The XAS spectra, which are presented in this thesis are all measured in NEXAFS mode, which is used to determine the chemical oxidation state of the investigated material [258] as well as the coordination. Since the XAS measurements were performed by using soft X-ray radiation, it is mandatory to have a low pressure (max. 10^{-8} mbar). This restriction is related to the relatively low observable thickness, therefore if the surface is contaminated (at higher pressures) it would not be possible to characterize the sample properly. In Fig. 3.18, the working principle of XAS is displayed.

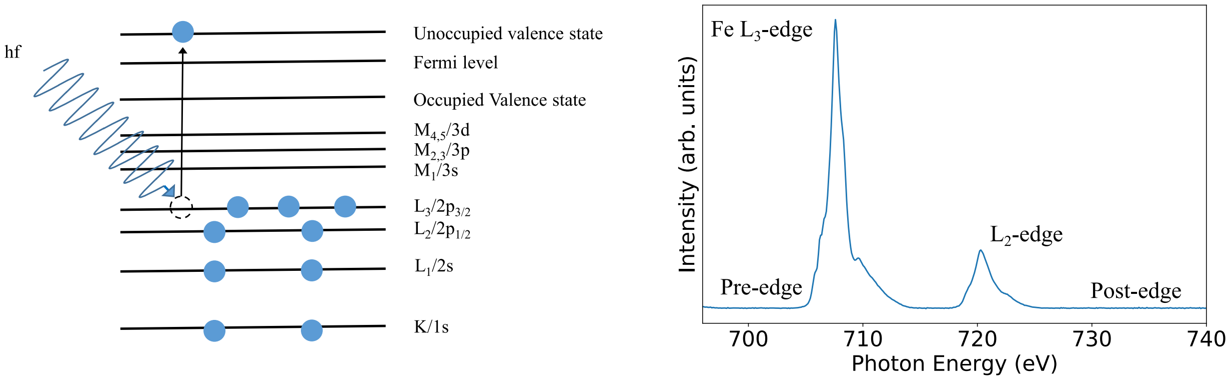

Figure 3.18: Working principle of XAS measurements. On the left side the excitation process is shown. A core-level electron (here $2p_{\frac{3}{2}}$) is absorbing the X-ray radiation and the excitation process is moving it to an unoccupied state in the valence band. By driving the photon energy from a pre-edge value (10 eV before the edge) to a post-edge value (10-15 eV after the edge), the XAS spectra is measured. On the right side an exemplary XAS image of $FeBr_2$ on Au(111) is shown. Inside the figure the different edge positions for Fe as well as the pre- and post-edge are indicated. The design is based on [237], [244], [253], [257].

Depending on the oxidation state, the multiplet splitting, which is a consequence of the SOC as well as exchange effects, can be observed. On the right side of Fig. 3.18, a XAS of $FeBr_2$ is displayed. It can be observed that inside the main Fe L_3 edge additional peaks are visible, which are caused by the multiplet splitting. Depending on the measurement setup, there are two different ways of characterizing the magnetic properties of a sample via XMCD. If the beamline has a bending magnet setup in front, then XMCD measurements are performed by switching the magnetic field, which is applied to the sample from +B to -B and keeping the polarization of the x rays constant. If an undulator setup is in front of the measurement beamline, then the polarization of the x-rays can just be changed and the field kept constant at a needed maximum level. The data which are shown in this thesis were measured at different beamlines, but a majority of the performed measurements were done by using an undulator setup. The energy range for XMCD is always in the energy range of NEXAFS measurements. The XAS and XMCD measurements can be performed at different geometries. If the x-ray beam is reaching the sample perpendicular to the surface, then it is called normal incidence measurements (normal incidence (NI)=0/90 °). The other possibility is to measure under an angle of 20/70 °, this is called grazing incidence (grazing incidence (GI)). The importance of these two angles is that by measuring under both angles it can be distinguished if the magnetic moments are aligned IP or OoP and therefore the anisotropy of the sample can be probed. In Fig. 3.19, the working principle of XMCD is displayed as well as an exemplary spectrum. XMCD measurements can be performed in different repetition ways either in the zig-zag mode (circular right (CR)-circular left (CL)-CR-CL) or in the step-function way (CR-CL-CL-CR).

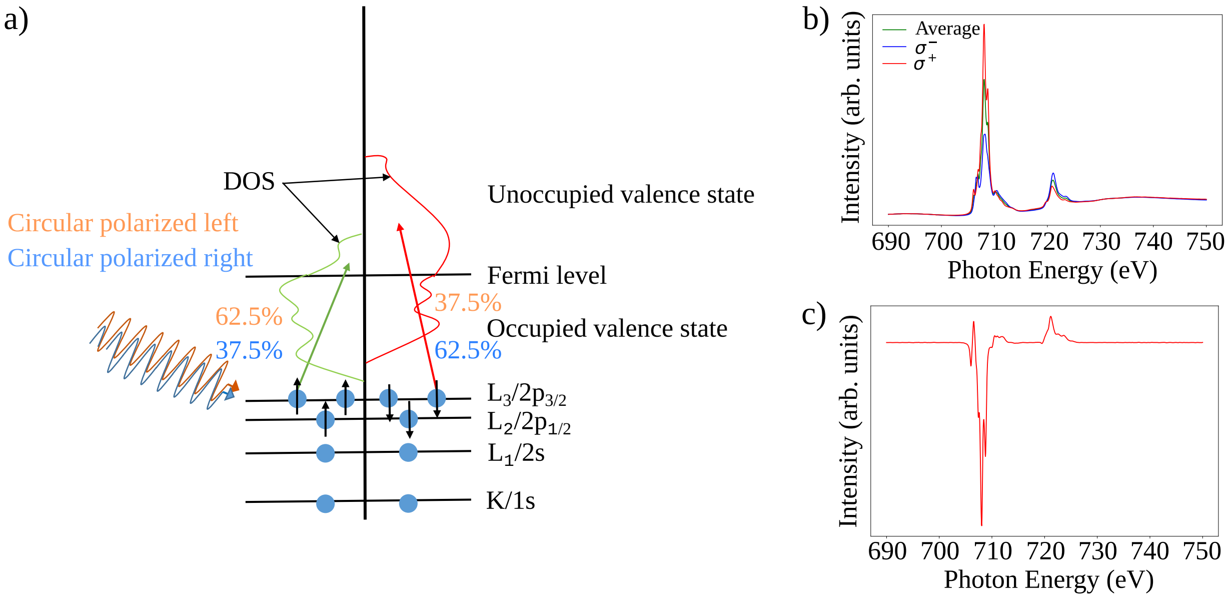

Figure 3.19: a) Working principle of XAS and XMCD measurements. Light with circular left and right polarization is irradiated onto the sample and is causing an excitation with different probabilities depending on the spin orientation. In b) the resulting XAS spectra for σ^+ and σ^- are displayed. The green spectrum is representing the average of the two polarization directions (isotropic XAS). In c) the resulting XMCD spectrum, which is the subtraction of both polarization directions, is displayed. The measurements for this sample were performed at the BOREAS beamline at ALBA synchrotron on an $FeBr_2$ on Au(111) sample. The design in a) is based on [253], [257], [259], [260].

The XMCD signal strength depends on several internal and external parameters. The internal ones are related to the properties of the investigated material (magnetic properties and amount of material). The external ones are UHV conditions for soft X-ray measurements, degree of circular polarization of the light, and relative magnetic saturation of the material. By using different circular polarization (σ^+ or σ^-), different transition probabilities exist for the two specific spin orientations. To calculate the transition probabilities, Fermi's golden rule is used. However, not all transitions are allowed and this can be checked by applying the dipole selection rules and the conservation of the spin and the angular momentum [237].

$$\Delta m_l = 0, \pm 1 \tag{3.7}$$

$$\Delta m_s = 0 \tag{3.8}$$

$$\Delta l = \pm 1 \tag{3.9}$$

For linear polarized light the case of $\Delta m_l = 0$ is valid [237]. The quantitative analysis of the XMCD spectra is not only revealing preferential spin orientations in a sample, but also the expectation value of the spin S_Z and orbital moment L_Z as well as the spin magnetic dipole T_Z along the z-direction. The dipole term includes charge transfer effects, crystal field strength, and many more effects [261], however in the case of a system which does not contain strong anisotropy the dipole term can be ignored, since it is very weak [237]. The magnetic moment information can be extracted from the sum-rules [262], [263]. In the following the equation of the spin and orbital magnetic moments for the $L_{2,3}$ edge are displayed [244], [253], [257], [264], [265].

$$m_{Sz,Eff} = 3 \cdot \frac{\int_{L_3} XMCD \cdot dE - 2 \cdot \int_{L_2} XMCD \cdot dE}{\int_{L_3+L_2} XAS \cdot dE} \cdot N_H \tag{3.10}$$

$$\mu_{Sz,Eff} = -\frac{A_{L_3} - 2 \cdot A_{L_2}}{A_{XAS}} \cdot N_H \cdot \mu_B \tag{3.11}$$

$$m_l = \frac{4}{3} \cdot \frac{\int_{L_3+L_2} XMCD \cdot dE}{\int_{L_3+L_2} XAS \cdot dE} \cdot N_H \tag{3.12}$$

$$\mu_l = -\frac{2}{3} \cdot \frac{A_{L_3} + \cdot A_{L_2}}{A_{XAS}} \cdot N_H \cdot \mu_B \tag{3.13}$$

Here N_H is the element-specific number of holes in the d-shell. In the case of a HS Fe^{2+} state, $N_H = 4$. The terms A_{L_3}, A_{L_2}, and A_{XAS} are representing the calculated area of the L_3 and L_2 edge of the XMCD spectrum and the total area of the normalized and background subtracted XAS spectrum. Depending on the evaluation routine the equation can look slightly different. The simplified version of Eq. (3.11) is displayed in the following and only using the values of the integrated spectra [266].

$$m_{Sz,Eff} = m_{Sz} + \frac{7}{2} \cdot T_z \tag{3.14}$$

$$= \frac{3 \cdot p - 2 \cdot q}{r} \cdot N_H \tag{3.15}$$

$$m_L = \frac{4 \cdot q}{3 \cdot r} \cdot N_H \tag{3.16}$$

Here r is the maximum value of the integrated XAS spectra and p, q are the distance of the integrated XMCD L_2 pre-edge and post edge to zero. In Fig. 3.20, the XAS and XMCD spectra for applying the sum rules are displayed.

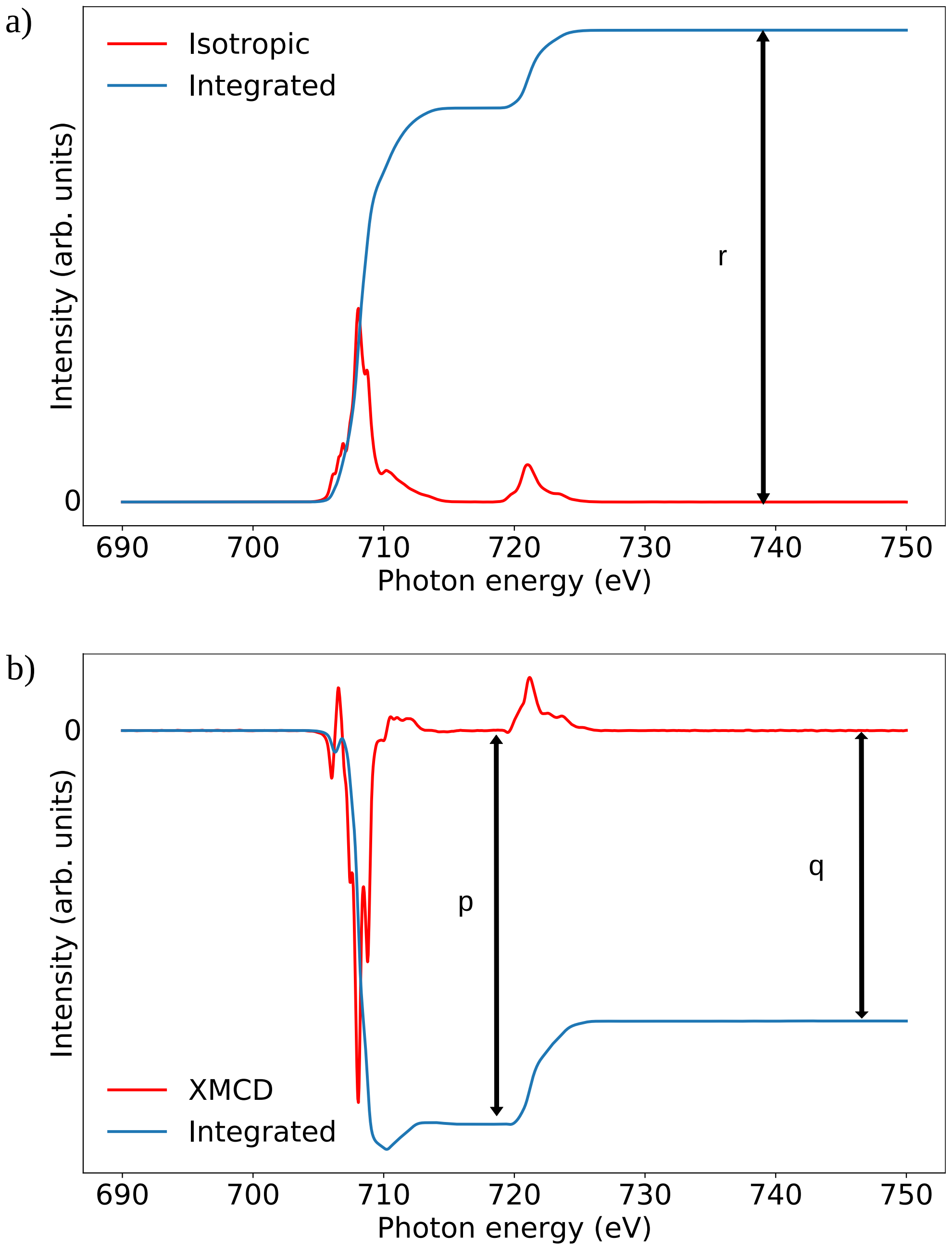

Figure 3.20: a) Isotropic XAS together with its integrate. The arrow indicates the r value, which can be extracted from the integrated spectrum. The isotropic XAS spectra was background subtracted before integrating it. In b) the p and q values of the integrated XMCD are explained. The displayed spectra were measured at the BOREAS beamline at ALBA synchrotron on BL $FeBr_2$ on Au(111).

However, sum-rule analysis is not giving for every material system the correct values. With decreasing energetic separation between the L_3 and L_2 edge, the calculated values are getting less precise. This is the case for lighter transition metals like Cr and V, but also for Mn [261]. Depending on the amount of material, also the substrate background needs to be taken into account. In the case of a bulk or nm thick material, the substrate background can be neglected, however, with decreasing material amount down to the ML and sub-ML limit, the background plays a more important role [237]. This is visible in the case of Au(111), which has a very dominant curvature in the regions of the transition metals (Fig. 3.21).

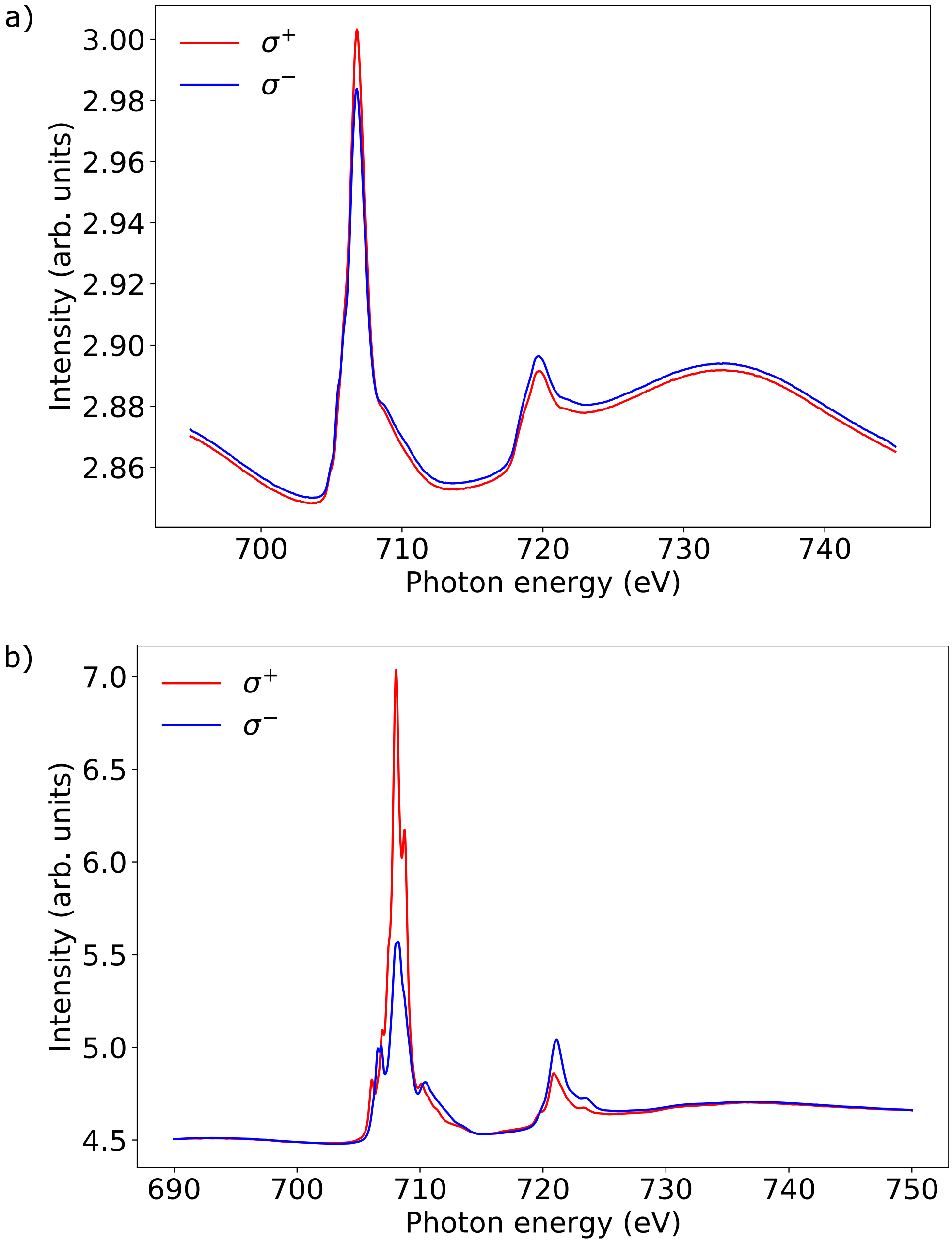

Figure 3.21: In a) the XAS measurements of a sub-ML $FeBr_2$/Au(111) and in b) BL $FeBr_2$ on Au(111) are displayed. Both measurements were performed at 2 K with an applied field of 6 T at the BOREAS beamline at ALBA synchrotron. By comparing the backgrounds it is visible, which strong influence the substrate has for low coverages.

At the beamlines not only static XMCD measurements can be performed, but also dynamic and static magnetization curve measurements. For performing magnetization curve measurements, it is important to measure the XMCD at least at two different energies. One needs to be located at the pre-edge and the other at the region of maximum intensity of the XMCD signal. In Fig. 3.22, a schematic magnetization loop measurement is displayed. After the two energies are fixed, the magnetic field is moved from $+B \rightarrow -B \rightarrow +B$. By measuring in TEY mode, a measurement-specific artifact peak at around 0 T is appearing. This artifact at around 0 T is related to the reduced electron guidance at low fields.

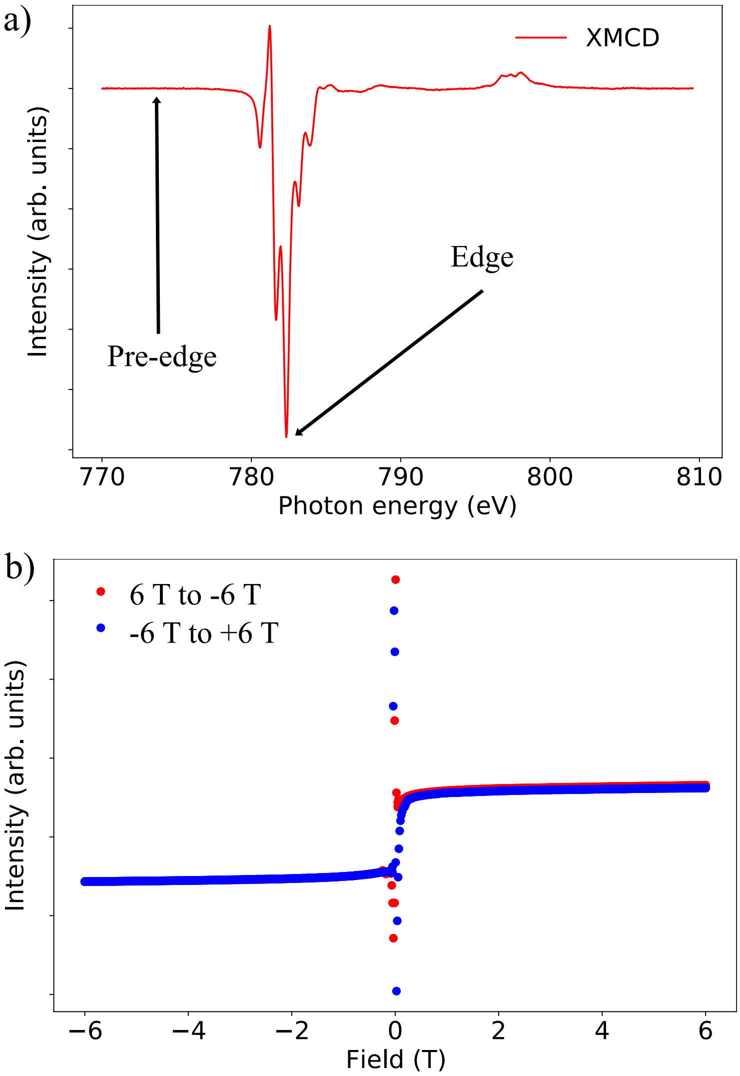

Figure 3.22: XMCD spectra of a BL $CoCl_2/Au(111)$ measured at 2 K at the DEIMOS beamline (SOLEIL synchrotron). The arrows are indicating the measurement position for the magnetization loop. In b) the corresponding magnetization loop is displayed including the TEY artifact peak. The $CoCl_2$ spectra were measured together with the Ph.D. student Samuel Kerschbaumer at SOLEIL. He will use the data inside his thesis, therefore this figure is just an exemplary one to explain the principle of TEY magnetization loop measurements and was used with the permission of his supervisor Dr. Maxim Ilyn.

X-ray Linear Dichroism and X-ray Magnetic Linear Dichroism

Equivalent to XAS and XMCD measurement, which are based on circular polarized light, there exist also measurements based on linear polarized light. If the measurements using linear polarized light are performed without applying an external field, they are called XLD [267] or x-ray natural linear dichroism (XNLD) and with an external field XMLD [244]. In Fig. 3.23, the working principle of XLD and XMLD is displayed.

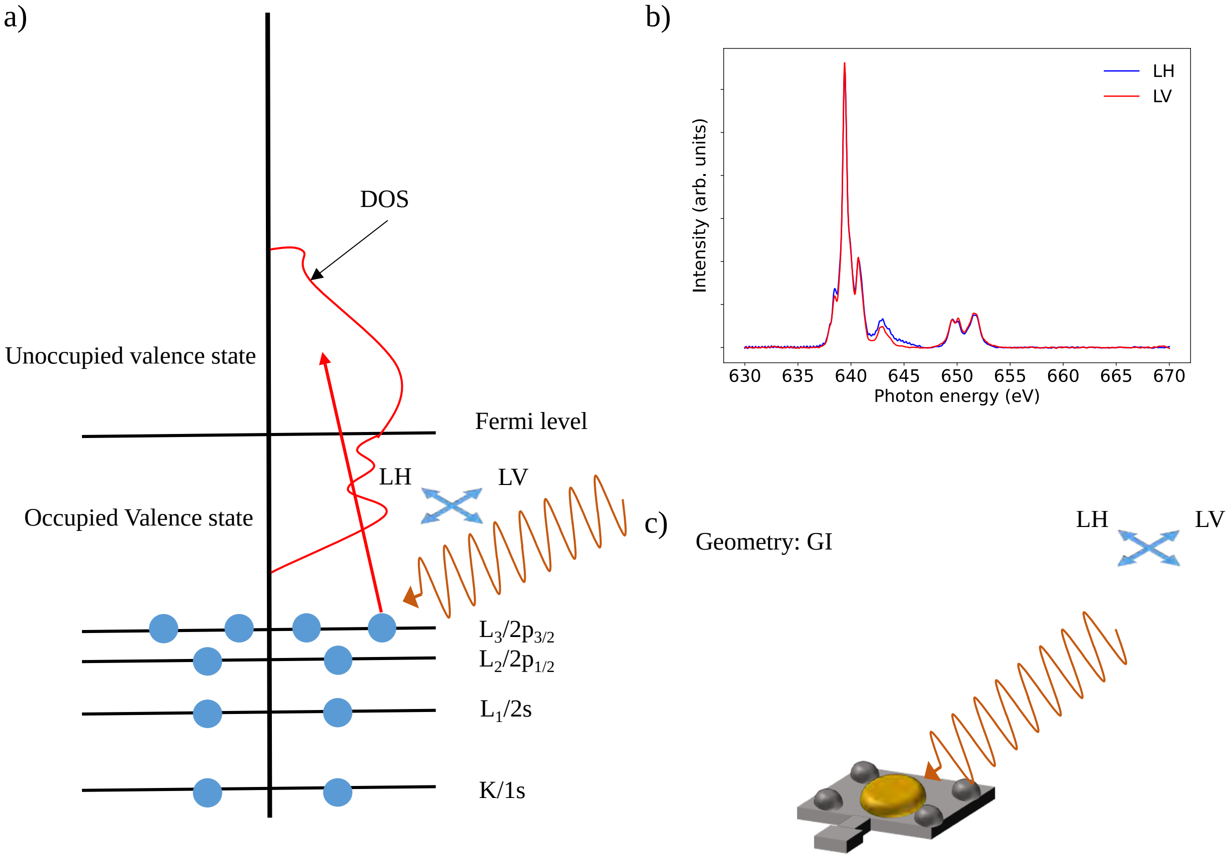

Figure 3.23: a) Working principle of XLD and XMLD measurements. b) Exemplary spectra of an XLD measurement performed at the BOREAS beamline in ALBA at 2 K of $MnCl_2$ (around 1.0 ML). The exemplary measurement geometry is displayed in c). Here the sample is aligned in GI. The figure a) is based on [268], [269].

By radiating linear polarized light onto the material, the X rays are interacting with the non-spherical charge distribution [267], this interaction acts as a probing mechanism for the unoccupied states along the direction of the electric field (orientation of molecular orbitals [269]), which is the reason to perform the measurements with vertical and horizontal linear polarized light. The XLD effect, commonly also called search-light effect [269], is based on the different transition probabilities for different electric field vectors [244]. In the case of XMLD measurements, the sample magnetization is either IP or OoP. Therefore by irradiating the linear polarized light, the magnetic anisotropy can be probed. A prominent example of using XMLD as a probe for anisotropy and antiferromagnetic order is NiO [269], [270], and [271]. In NiO a cubic symmetry exists, which is causing that no XLD effect can be measured [269], but since NiO is antiferromagnetic, the cubic symmetry is broken and a small anisotropy is existing [269]. This anisotropy is causing that the material can be observed by the searchlight effect under the presence of a magnetic field [269]. With both methods, XMCD and XMLD, the material can be investigated and antiferromagnetism can be detected [270]. The XLD and XMLD measurements, which will be shown in the later evaluation chapters were performed by measuring the sample at GI with linear horizontal (LH) and linear vertical (LV) polarized light with and without applying an external field.

Low-Energy Electron Diffraction

LEED is a technique for the structural analysis of the surface of single-crystalline samples. The technique is based on the diffraction of electrons with a constant energy from surfaces in an energy range of 10 eV to 1000 eV [272, p.72]. Since we want to observe the atomic structure, it is necessary that the used wavelength is in the same regime as atomic lattice distances. By using the de-Broglie wavelength equation [273] for an electron with 100 eV, a wavelength of 1.2 Å can be calculated [274, p.92].

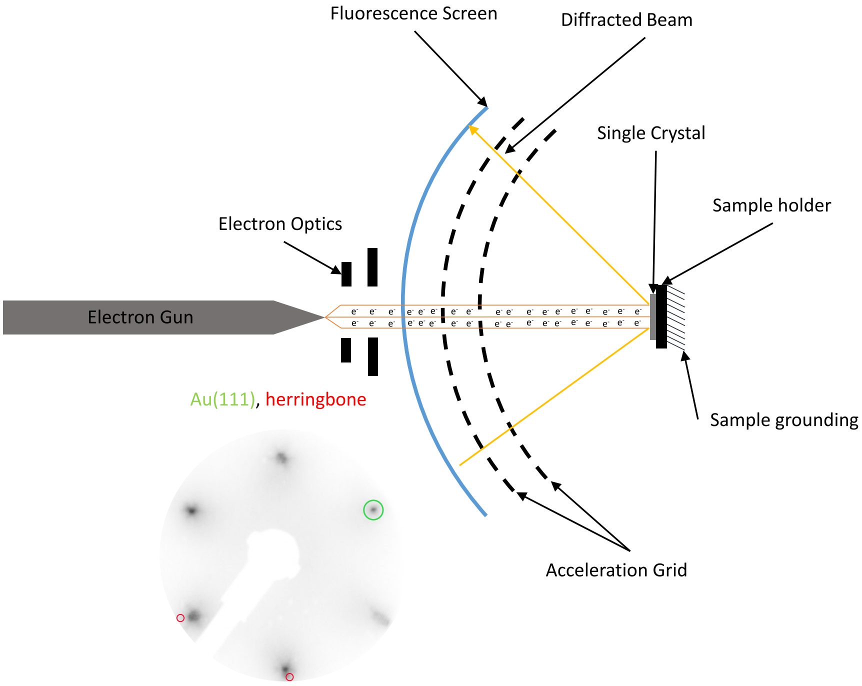

Figure 3.24: Schematic LEED setup. The central part shows the electron gun including the electron optics. The sample is hit by the electrons and the diffracted electron beam is reaching the fluorescent screen, where the diffracted image is displayed. In the lower part, a Au(111) LEED pattern (green) including the herringbone reconstruction (red) is displayed (measured at CFM). Design based on [272, p.72], [275].

$$\lambda_D = \frac{h}{p} = \frac{h}{\sqrt{2 \cdot m \cdot E_{\text{kin}}}} \tag{3.17}$$

In Fig. 3.24, a schematic LEED setup is displayed, which consists of a fluorescence screen, acceleration grids, electron optics (L_2 and $L_{1,3}$) and the electron gun. All these parts are inside the vacuum at UHV conditions. The reason that these experiments are performed under UHV conditions are manifold. One reason is related to the electron gun system and the used filament. Another reason is the surface contamination at higher pressures or ambient conditions [272, p.72]. The LEED image is captured by a CCD camera, which is mounted outside the vacuum. It is important that no light can enter the chamber, otherwise artifacts are also displayed on the LEED image. The electron gun (cathode) is emitting electrons from the filament, which are focused via the electron optics onto the sample surface under an angle of 90 ° (perpendicular to the sample surface). Before reaching the fluorescent screen, the diffracted electrons from the sample surface are filtered by the acceleration grids. In Fig. 3.24, the LEED pattern (reciprocal lattice structure) of Au(111) is displayed. The LEED pattern of Au(111) behaves special compared to other single crystals. In general, the LEED pattern consists of very sharp spots, however since Au(111) shows the herringbone reconstruction, the main spots are bigger and more blurry compared to other materials with identical surface flatness. To identify the (0,0)-spot the electron energy needs to varied. With varying energy, all diffraction spots besides the (0,0)-spot are moving.

Scanning Tunneling Microscopy

Scanning tunneling microscopy (STM) was invented in 1982 [276] and was rewarded later by a Nobel price in 1986 [277]. This technique allows to characterize in real space the sample surface (surface topology and atomic resolution) [276]. To achieve the needed resolution different external factors (system noise, surface cleanness and measurement temperature) are playing an important role [276]. However, one of the most important parts is to have a sharp tip [278], [279], [280]. Since the tip is attached to a piezo motor, it can be moved precisely in all three degrees of freedom with a lateral resolution of a few Å [276]. In Fig. 3.25, the tunneling process is illustrated from a classical and quantum mechanical point of view. In a) the classical view is shown, where the particle cannot overcome the one-dimensional potential well because the energy of the particle is lower than the potential energy ($E < U_0$).

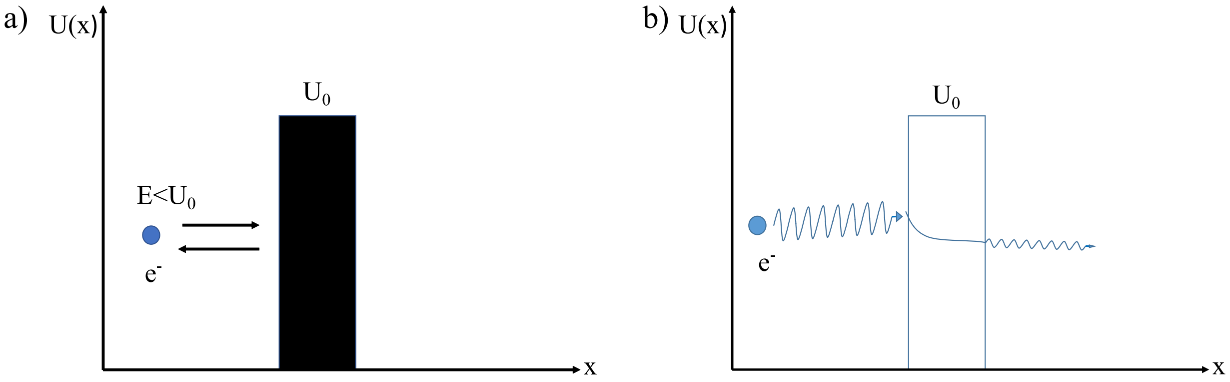

Figure 3.25: a) Classical description of an electron in a potential well system. In the case that the electron energy is not higher than U_0 (height of the potential well), it can not reach the area behind the well. In b) the quantum-mechanical description is displayed. Here the electron wave function can penetrate the potential well by a certain probability and therefore reach the area behind. Design is based on [281].

In b) the electron is not described as a classical particle but as a wave function. Therefore, the electron can to travel through the potential well, because it has a non-zero solution in the classical forbidden region (inside and behind the potential well). The illustration in b) shows three regions of interest, the first and third regions are related to the tip/sample surface and the second is the vacuum barrier between the sample and the tip. Since the tunneling current depends exponentially on the distance between tip and sample only a few Å separate them in the tunneling regime (overlap of tip and surface wave functions). Figure 3.26 shows the STM tunneling process with Φ as the WF of the surface. In the case that no bias voltage is applied between the tip and sample the net tunneling current vanishes (bidirectional tunneling) [282]. By applying a bias voltage, the Fermi level of the tip is lowered or raised and the tunneling process is going into the direction of the tip or the sample. The electron can tunnel either elastically or inelastically [283], [284]. The inelastic tunneling process requires that the electron excites a quasiparticle (phonon excitation) [284]. This process only occurs if the initial energy is larger than the excitation energy [285]. In the elastic tunneling process there is no energy loss due to quasiparticle excitation [286].

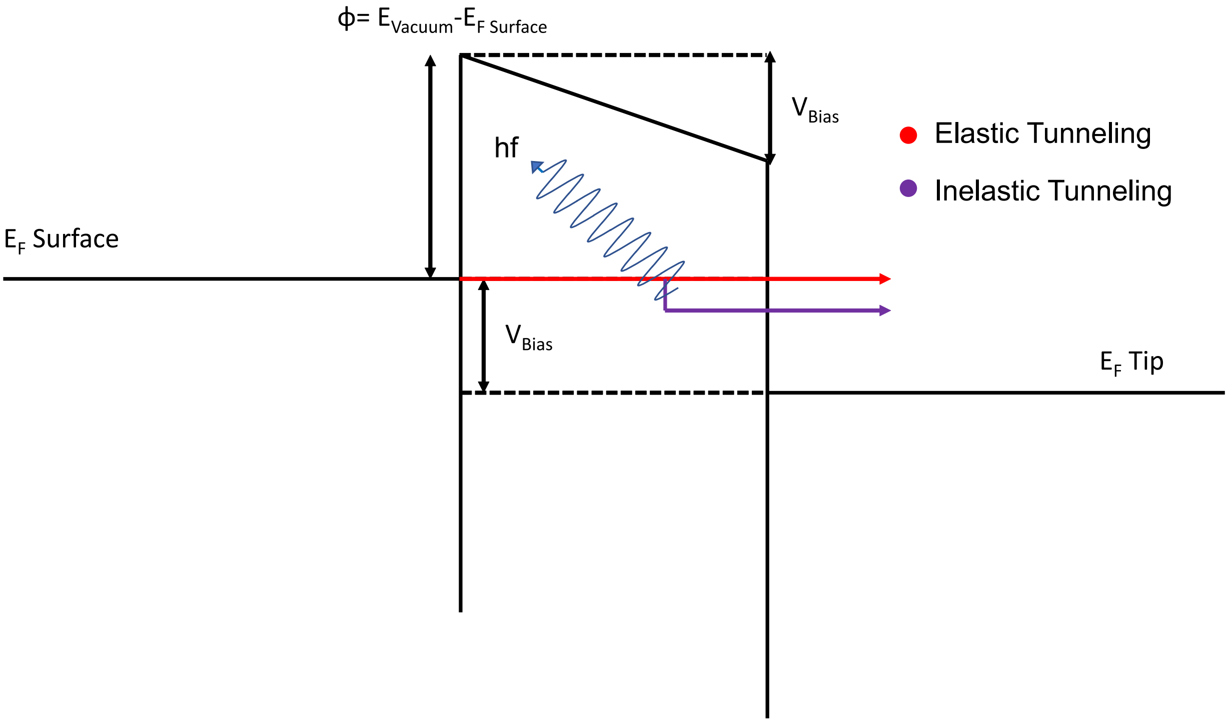

Figure 3.26: Potential between the sample surface and the STM tip (both metallic materials). Without applying a bias voltage (V_{Bias}), the Fermi levels of surface and tip are aligned. This would result in a tunneling process in both directions, with no net tunneling current. To achieve the wanted tunneling process, the Fermi energy of the tip is getting lowered or raised by applying V_{Bias}. The different colors are representing the processes of elastic (red) and inelastic (purple) tunneling. Design is based on [282], [287], [283].

The STM measurements can be performed in two different modes, either in constant current (CC) or at constant height (CH). In the CH mode the tip does not approach the sample surface and only the tunneling current is measured, therefore the measurements can only be performed on relatively flat samples, since otherwise the tip would crash into the sample surface. In the CC mode the z-piezo regulates the height of the tip, so that the tunneling current is kept constant, therefore this mode is preferable for non-flat surfaces [276], [282], [284], [288]. In the case that the substrate is a semiconductor or an insulator, the measured height between the material and surface is wrong. The reason for the height problem is that the relation between substrate surface (metal) and tip are not identical to sample surface (semiconductor or insulator) and tip. However, with increasing thickness of an insulator the STM measurements will get more difficult, until they are impossible. Another measurement method, which can be performed at low temperatures inside the same STM setup is STS. STS measurements are used to probe the local density of state (DOS) of the investigated material [284], [289] and are used to obtain information about the electronic properties. The STM measurements performed in this thesis were all measured at low temperatures (4.3-77 K). In the temperature regime of 4.3 K the measurements have reduced thermal noise and sample drift is suppressed.

Quartz Crystal Microbalance

A quartz crystal microbalance (QCM) is used to monitor and calibrate the amount of evaporated material. It measures the eigenfrequency change (Δf) due to the mass change (Δm) during the evaporation. The measured rate is displayed in units of $\frac{\text{Å}}{\text{s}}$ or $\frac{\text{Å}}{\text{min}}$. This calibration procedure needs to be redone before every evaporation, so that the evaporation conditions are reproducible. The critical parameters to monitor the correct rate are the density of the material, the tooling factor and the measured frequency change Δf. The tooling factor needs to be determined before the evaporation. If the value is 100 %, it means that the QCM is at the same position as the sample holder during the evaporation. During the evaporation the eigenfrequency (f_0) of the quartz crystal is changing. In the following equation the relation between the frequency change Δf and the increasing mass (Δm) is displayed [290]. The used quartz crystals inside the vacuum chambers are protected by a Au coating layer. In the case of a QCM, which is implemented in the evaporator setup (Fig. 3.28), a regular battery watch quartz crystal is used with $f_0 = 6$ MHz.

$$\Delta f = -\frac{\Delta m \cdot f_0}{A \cdot \rho \cdot d} \tag{3.18}$$

Here ρ is the density of the material, A is the total area and d is the thickness of the crystal [290]. In Fig. 3.27, the working principle and structure of the QCM is displayed. After the material is degassed and the temperature of the crucible and powder is equilibrated, the total rate (R) will increase linearly with time and the eigenfrequency (f_0) will drop constantly. To have an accurate reading, the QCM needs to be cooled with water or air.

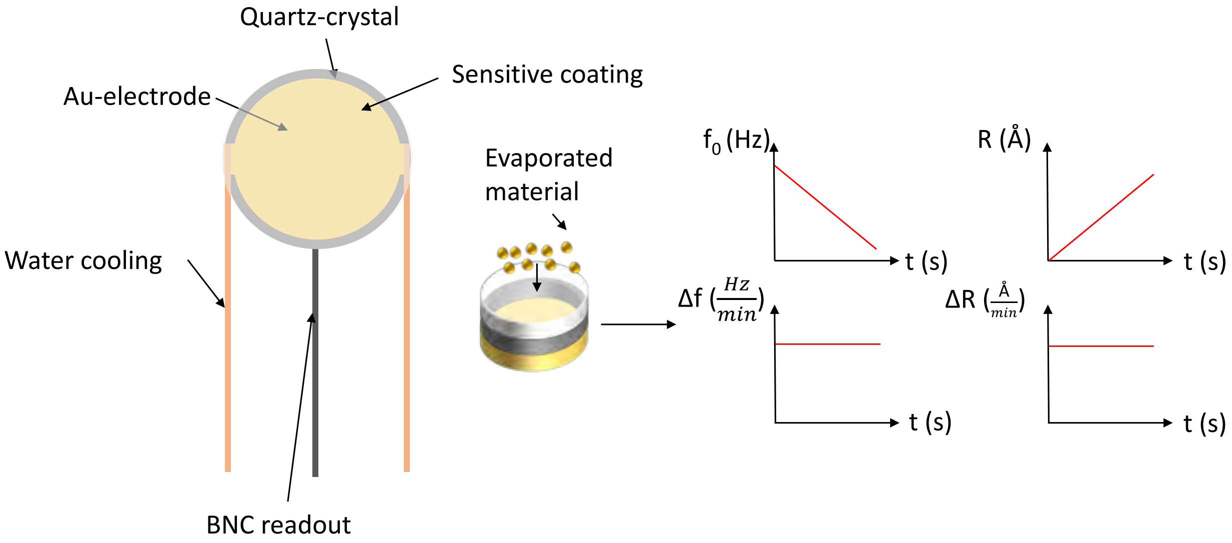

Figure 3.27: Left: Top view of the QCM design inside the vacuum chamber. Middle: The upper image shows the layers of the measuring unit divided in Au electrode, quartz crystal and sensitive coating layer. The bottom image shows the evaporation of material on top of the crystal. Right: Time evolution of the eigenfrequency (f_0), the frequency change (Δf), the evaporation rate (ΔR) and the total rate (R). The design of the QCM is based on the PREVAC design [291] and the image is a modified version of the figure from my master thesis.

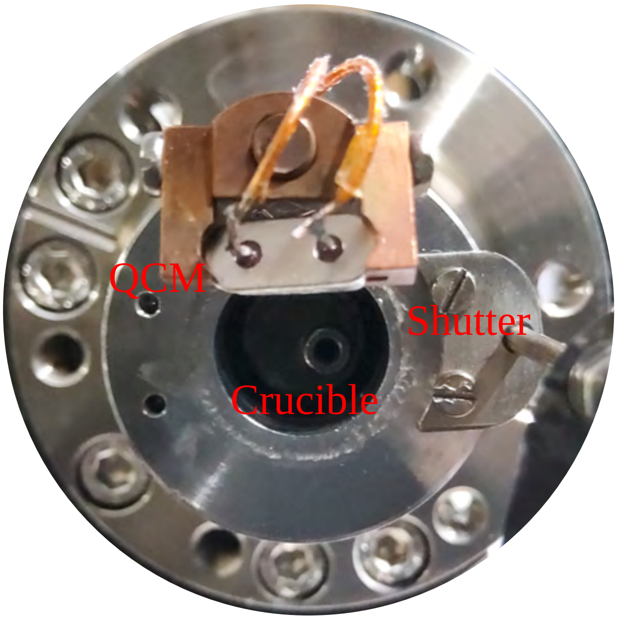

Figure 3.28: Home made single pocket evaporator. The evaporator is used for the evaporation of stoichiometric powders. In the front a QCM with an eigenfrequncy of 6 MHz is mounted. The Cu-block is used as a holding mechanism of QCM.

3.2 Measurement setups

In the following sub-chapters the different laboratories and measurement chambers are described in detail. Here only the setups where the majority of data was acquired will be described. In all systems the preparation and measurement chambers were separated, since the analyzing equipment can be damaged by the evaporated materials. The used measurement equipment, besides the equipment and parts from synchrotron radiation sources, are listed in the Appendix in Tab. 7.2. In the following the chamber designs are redesigned on the experience gained during the beamtimes and laboratory measurements.

3.2.1 List of Laboratories

In Tab. 3.4 a location list of the different laboratories and synchrotron radiation sources where the measurements were performed is given.

Measurement Labs			
Country	Facility	Beamline/Lab	Used Techniques
France	SOLEIL	DEIMOS	Prep, LEED, XAS and XMCD
Germany	FU-Berlin	BESSY Lab	Prep, LEED and XPS
Germany	FU-Berlin	Supra Fab Lab	STM and STS
Germany	BESSY II	VEKMAG	Prep, LEED, XAS, XMCD
Spain	CFM	XPS-Lab	Prep, LEED, XPS
Spain	CFM/CINN	APOLLO	Prep, LEED, STS and STM
Spain	ALBA	BOREAS	Prep, LEED, XAS, XMCD, XMLD
Swiss	SLS	PEARL	Prep, LEED, XPS and STM

Table 3.4: Displayed are the measurement locations, including the beamlines and labs, where the measurements were performed. The abbreviation Prep stands for preparation. The list is ordered alphabetically with the state name.

3.2.2 Preparation and measurement chamber FU-Berlin

The chamber setup at FU-Berlin contains a preparation and measurement chamber (XPS chamber). Figure 3.29 shows the general overview as a 2D representation.

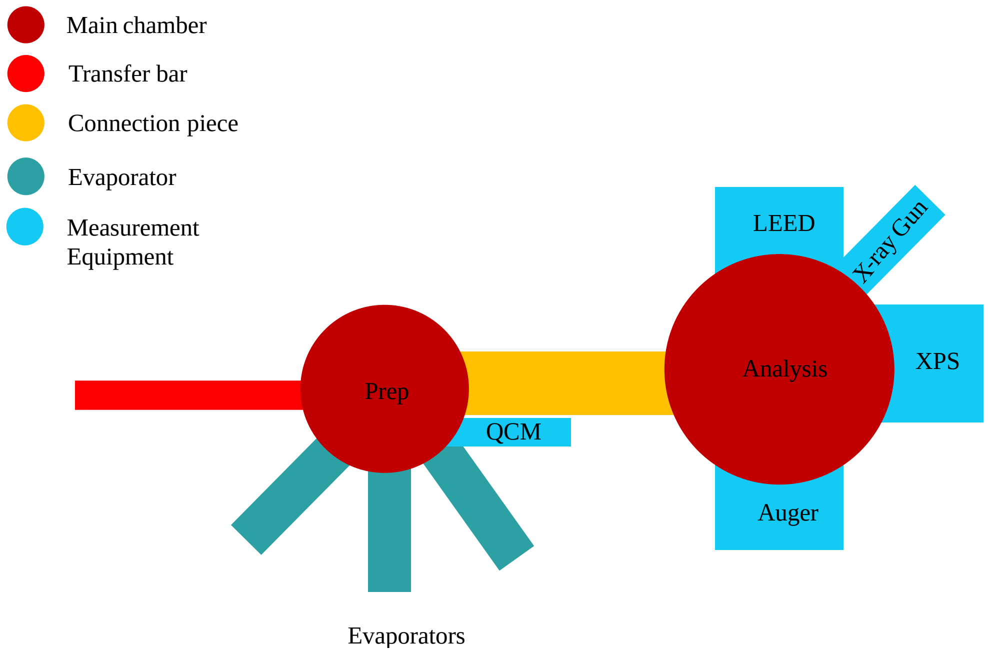

Figure 3.29: Top view of the preparation and XPS chamber setup at FU-Berlin. Shown are the two connected chambers with the different equipment parts.

Figure 7.1 a) shows the preparation chamber in more detail. The chamber contains of two pumping systems, one permanently running (turbo pumps) and one which is started after the evaporation (Cryopump). The permanently running system consists of three stages to reach UHV conditions. The first two stages are the pre-pump system, which consists of a HiScroll6 pump (10^{-2} mbar), which is connected to a 50 l barrel as a buffer volume and a HiPace80 turbo pump (10^{-8} mbar). The main pump is a HiPace700, which is used to reach an end pressure of low 10^{-10} mbar. In general the second pre-pump system is not mandatory, however due to some of the evaporated materials (Se) it is necessary, to reach faster low pressures. The second pumping system is a cryopump (Fig. 7.1 c)). This system is only started after the evaporation is finished to reach faster a lower pressure, so that the sample can be transferred to the XPS chamber (Fig. 7.1 b)). The chamber has three evaporation ports which are all aligned to the same focus point. This allows a controllable co-evaporation of materials. The main evaporators of this chamber are a four pocket metal evaporator (EBE-4), a Knudsen cell evaporator for the evaporation of Se and a non-commercial Knudsen cell evaporator with a QCM system mounted in the front for reproducible evaporation rates. The non-commercial evaporator is used to sublimate powders for stoichiometric growth. The chamber also contains a QCM, which is aligned with the evaporation position (tooling factor 100 %) and a PBN heating system which is mounted on the sample holder of the manipulator. To transfer the sample between the chambers a 1 m transfer bar is used, which has pincer grabbing system. The bar has two degrees of freedom, moving along the x-axis and rotating around the x-axis. The XPS chamber consists of different characterization tools. For chemical characterization an Auger and an XPS system are mounted and for the structural investigation a spherical LEED setup is on the opposing side of the Auger system. The LEED setup is using a hemispherical screen, which is mainly used to measure metallic surfaces. This setup cannot be used for insulating substrates, since they would charge. The XPS chamber also consists of the equipment for sample cleaning (sputter gun and PBN heater). The manipulator can be cooled with liquid He down to low temperatures. The pumping system of the XPS chamber only consists of an Edwards scroll pump, which is connected to a 50 l barrel buffer volume and a HiPace300 turbo pump. After the chamber is at UHV conditions, the ion getter pump together with the implemented titanium sublimation pump (TSP) is used to keep the chamber at low pressures ($2.0 - 5.0 \cdot 10^{-10}$ mbar).

3.2.3 CFM preparation and measurement chamber

Figure 3.30 shows a general overview of the measurement setup at CFM in Donostia.

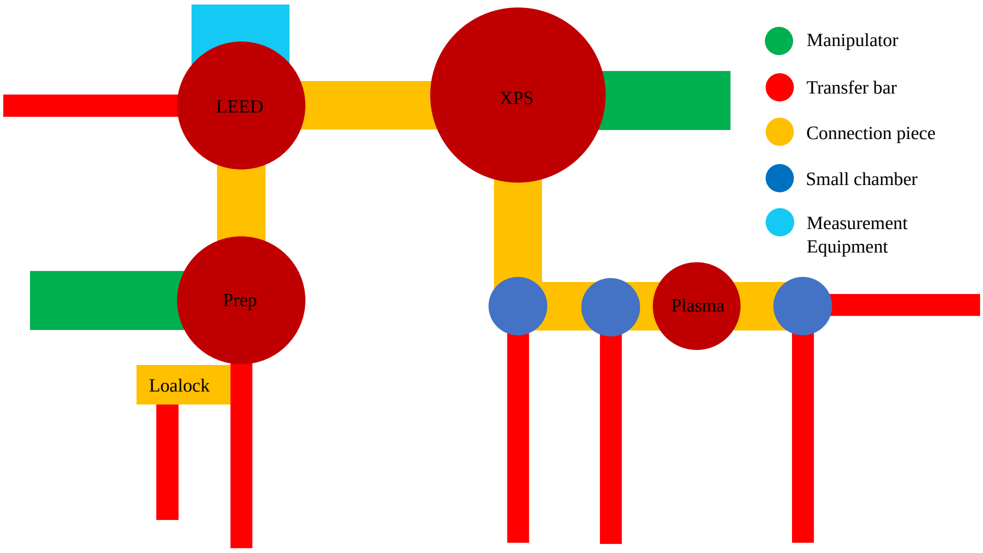

Figure 3.30: Top view of the whole measurement setup at CFM. On the right side the color code explains the main parts.

The single-crystal samples are transferred from the load lock chamber transfer bar to the prep chamber, via a transfer bar with bayonet grabber. The prep chamber ($2.0 \cdot 10^{-9}$ mbar) contains a sputter gun with integrated Ar line and a filament heater for annealing the substrates during the cleaning procedure. The air cooling system of the manipulator can also be used for cold deposition by connecting it to the cold gas of liquid nitrogen. The sample holder of the manipulator has two slots, one for storing the single crystal during evaporation and the other for inserting shadow masks for device contact deposition. The calibration of the evaporation amount is performed by a QCM, which can be moved to the same position as the sample will have during evaporation (tooling factor 100 %). The chamber has in total four ports for mounting evaporators, however one of the three lower ports, where the stoichiometric powder evaporators can mounted, is blocked due to the surrounding. The last evaporator port is on top of the prep chamber and is used for E-beam evaporators, where the material is a metallic rod like Co. This port is also used for mounting the QMS when needed. After the sample is grown it is transferred via the bayonet transfer arm to the transfer bar of the LEED chamber ($5.0 \cdot 10^{-10}$ mbar), where the sample garage is also mounted. The used LEED system is a MCP LEED, which can be used also for insulators. The LEED chamber consists a transfer bar, which is used as manipulator for the LEED measurements. Therefore, the LEED image can be rotated along the z-axis. After the structural characterization is finished the sample is transferred into the XPS chamber ($2.0 - 9.0 \cdot 10^{-10}$ mbar), where the sample can be chemically characterized by using XPS and ultraviolet photoelectron spectroscopy (UPS). The electron analyzer has a channelplate detector, which is exchanged every

2-3 years, since it degrades. Inside the XPS chamber another sputter gun and filament heater is mounted for cleaning the substrates. Connected to the XPS chamber are several small preparation chambers and load locks for preparing molecule samples. In between the small chambers a plasma chamber with a dry oxygen source is mounted. The majority of the mentioned parts are shown also in the 3D view of the Nanophysics lab chamber in Fig. 7.3.

3.2.4 LT-STM setup at CFM and CINN

In Fig. 3.31 a), a schematic overview of the used low-temperature scanning tunneling microscope (LT-STM) setup is displayed.

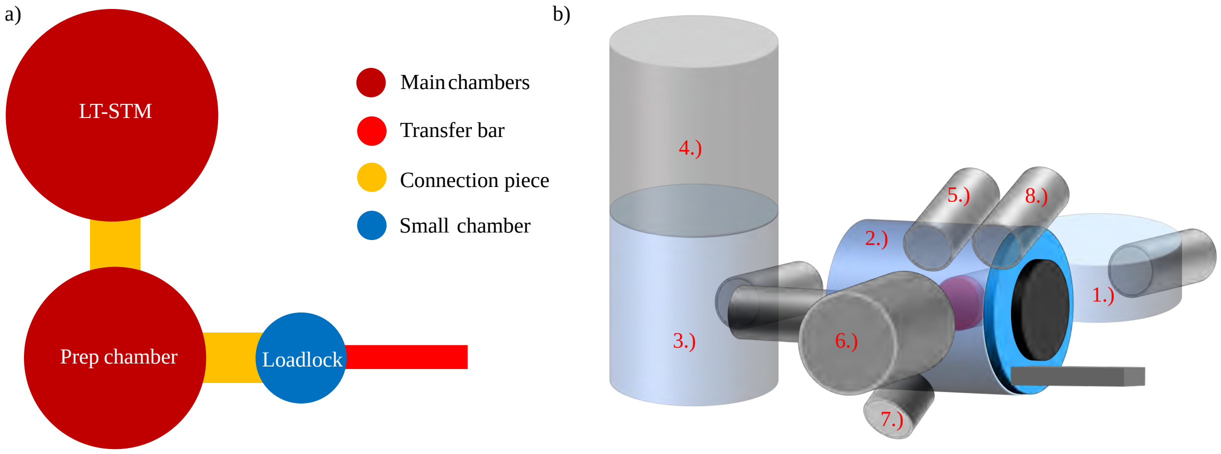

Figure 3.31: a) Schematic top view of the APOLLO setup, which was until October 2022 at CFM in San Sebastian and is now located at CINN in Oviedo. b) 3D view of the used low temperature STM (LT-STM) setup. The numbers are indicating the main equipment positions, which are listed in Tab. 3.5.

The setup consist of a preparation chamber and a LT-STM. The majority of the STM and STS data which are shown in this thesis were measured at this setup either at 4.3 K or at 77 K. Inside the preparation chamber the sample cleaning as well as growth take place. To calibrate the evaporation rate, a QCM system is mounted and to characterize the surface, LEED measurements can be performed before transferring the sample to the STM. In Fig. 3.31 b), a 3D view of the LT-STM is displayed.

Equipment Part	Equipment	Equipment Part	Equipment
1.)	LL	5.)	QCM
2.)	PC	6.)	LEED
3.)	LT-STM	7.)	Evaporator
4.)	Cryostat	8.)	Sputter Gun

Table 3.5: List of chamber parts of the APOLLO lab previously at CFM in Donostia and now at Centro de Investigación en Nanomateriales y Nanotecnología (CINN) in Asturias. The numbers are referring to the numbers in Fig. 3.31. The abbreviation LL stands for Load Lock, and PC for prep chamber.

3.2.5 Synchrotron light source setups

In the following sub-chapters the measurement setups at different synchrotron light sources will be explained. All used measurements were performed at third generation synchrotron light sources. The main difference between new and older synchrotron light sources is the brilliance, which is describing by the brightness of the beam and how coherent the photon beam is. In Fig. 7.6, the sample plate shuttles, which are used at different XMCD beamlines are displayed.

VEKMAG preparation and measurement chamber

In Fig. 3.32, a top view of the VEKMAG endstation at BESSY II synchrotron is shown.

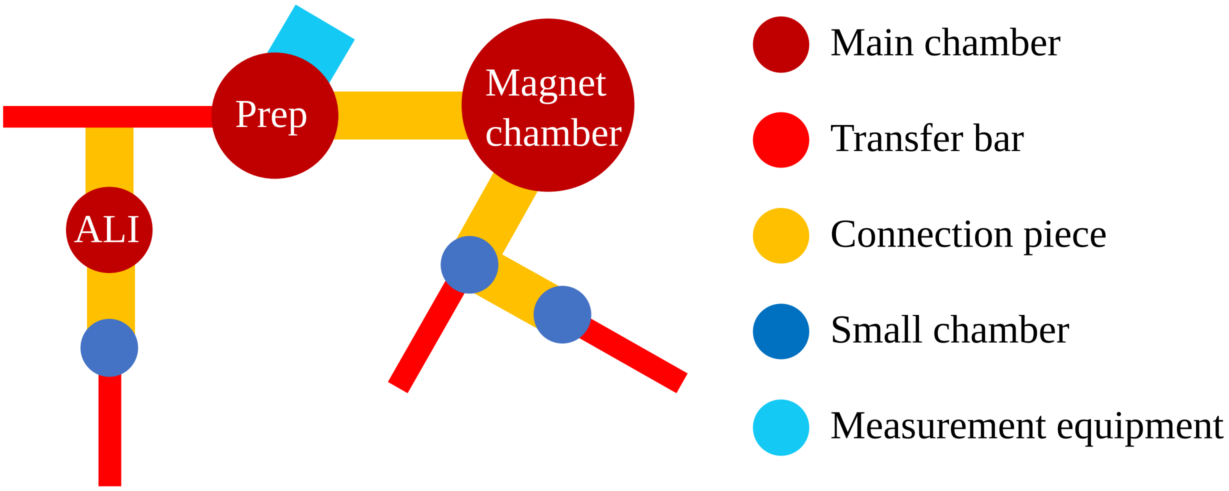

Figure 3.32: Top view of the VEKMAG setup including the different preparation chambers and the magnet chamber. The color coding is listed on the right side. The displayed measurement equipment in the main preparation chamber is an MCP-LEED.

This setup consists of a small and a main preparation chamber. The small chamber is used for liquid depositions (atomic layer injection (ALI) [292]). In the main preparation chamber, the stoichiometric powder is evaporated from a single-pocket evaporator with a QCM system mounted in the front for reproducible evaporation. The main preparation chamber includes an MCP-LEED setup for characterizing the metallic and insulating surfaces. To pre-characterize the evaporated material, the x-ray beam can be guided directly to the preparation chamber. A detailed 3D view is displayed in Fig. 7.7. The beam connection between the VEKMAG and the main preparation chamber can be removed and replaced by a CCD camera, depending on the measurements which need to be performed. After the samples are pre-characterized, they are mounted on the shuttle system (Fig. 7.6 b)) and transferred via the transfer bar from the preparation chamber to the transfer chamber below the magnet chamber [293]. The sample plate needs to sit tight inside the shuttle for the optimal thermal conductance, otherwise the displayed temperature is not the real sample temperature. Another reason that the shuttle needs to be tight is that vibration could introduce additional noise to the measurements. Depending on the inserted variable temperature insert (VTI), different base temperatures can be reached. In total three different VTI setups exist at VEKMAG with temperature ranges from 2.5 K up to 10 K [294] as lowest temperature. For the very low temperature VTIs it is important that every window and gate valve is closed and Cu shields are inserted. In the future also a VTI system to reach 300 mK ^{3}He with will be used (information via internal communication).

The VEKMAG setup has a vector magnet setup, which allows to apply different field strength in all three dimensions. The strongest field of ±9 T [293], [294] can be applied along the beam direction. However, for nearly all measurements a maximal field of ±6 T was used. Along the x and y-direction a maximum field of ±2 T and ±1 T can be applied [293]. In front of the VEKMAG endstation a bending magnet is mounted, therefore the degree of circular polarized light is reduced (77 % [294]) compared to regular undulator lines. The reason is that a maximum photon flux needs to be reached and since the bending magnet is only producing off-axis circular polarized light, the setup needs to be moved up or down. Due to the position change along the z-axis, the photon flux reduces, therefore an intermediate position is used with high degree of circular polarized light and high photon flux. At this beamline different measurements can be performed, however all measurements in this thesis, which were performed at VEKMAG, are XAS and XMCD in TEY mode. The performed XAS measurements were performed in NI and GI as well as at the magic angle (55 °) for linear polarized light. The beam spot size on the sample can be varied in the range from $120 \times 50\,\mu\mathrm{m}^2$ (small spot) and $0.8 - 1 \times 0.8 - 1\,\mathrm{mm}^2$ (large spot) and can be reduced down to $20 \times 60\,\mu\mathrm{m}^2$ if the smallest exist slit is used (information via internal communication). The beamline at the VEKMAG chamber offers an energy range from 20-1600 eV with a photon flux of around $5 \cdot 10^9\,\frac{\mathrm{Photons}}{\mathrm{s \cdot mm^2}}$ at 700 eV [295], [296].

BOREAS preparation and measurement chamber

The majority of XAS and XMCD measurements in this thesis were performed at the BOREAS beamline at ALBA. In Fig. 3.33, a top view of the BOREAS beamline is displayed.

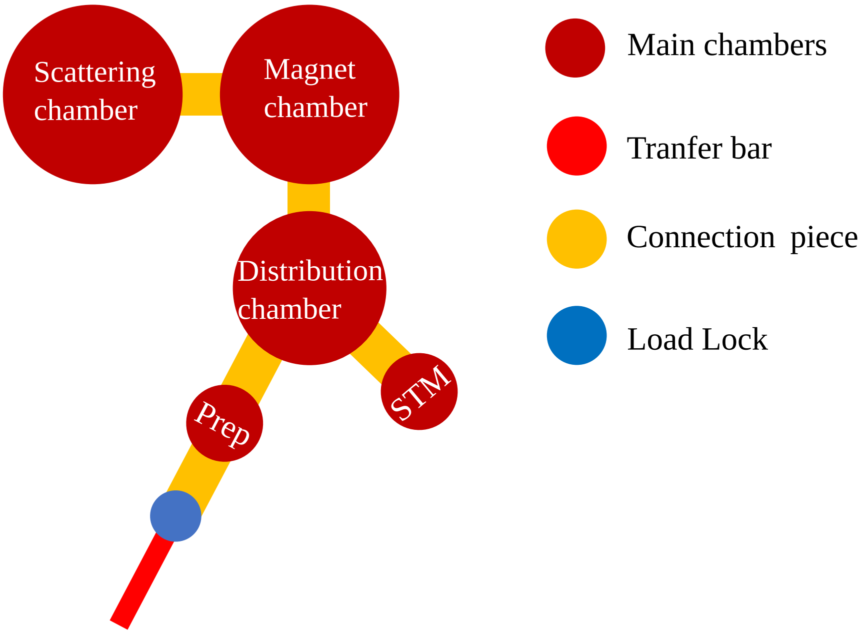

Figure 3.33: Top view of the BOREAS measurement setup. For completeness also the second endstation (scattering chamber) is displayed. However, no data in this thesis was acquired in this endstation chamber (scattering chamber).

The BOREAS beamline consists of two endstations with a shared beam, the magnet chamber (HECTOR chamber) and the scattering chamber. Connected to the beamline are two preparation chambers. The first one is the main preparation chamber, which was used to grow the 2D materials. The chamber consists of a sputtering and annealing system to clean the sample as well as evaporator ports on the lower part of the chamber. The QCM is mounted on a linear motion and can be moved to the sample holder position during evaporation (tooling factor 100 %). The exfoliation of vdW substrates is performed inside the load lock chamber. After the sample is grown, it can be pre-characterized by using a LEED with a hemispherical screen. The chamber is connected to a half-automatized distribution chamber (UFO chamber). The transfer arm has place for two sample plates. In general the samples can either be transferred from the distribution chamber to the STM chamber or to the magnet chamber. However, in 2023 the STM setup was not available, so the only measurements in this thesis which were performed at the STM are from 2021. Behind the STM chamber, another prep-chamber is mounted, which also consists of a sputtering and annealing system, as well as a LEED setup. From the distribution chamber, the samples are transferred to the transfer chamber below the magnet chamber and mounted to the shuttle system (Fig. 7.6 c)). After the samples are mounted to the shuttle, they are transferred to the manipulator of the magnet chamber. At the front end of the magnet chamber, an APPLE II undulator is mounted, which allows to have a degree of circular polarized light of nearly 100 % [297]. The APPLE II undulator allows a fast switching between the different polarization's. Inside the magnet chamber a maximum field of ± 6 T can be applied along the beam direction with a sweep rate of $2\,\frac{\mathrm{T}}{\mathrm{min}}$ and a maximum field of ± 2 T (sweep rate $0.6\,\frac{\mathrm{T}}{\mathrm{min}}$) perpendicular to the beam [298]. The pressure inside the magnet chamber is at low 10^{-10} mbar [298] . The sample temperature can be varied between 1.8 K and 350 K [299], [298]. The lowest temperature can only be reached by inserting a cryo shield at the beam port, therefore only a small aperture is left where the x-ray radiation goes through. The photon energy at this beamline can be changed from 80-4000 eV, however, in the case of our measurements the photon energy was mainly varied in the region of 500-1000 eV, and only changed to 1300-1700 eV for the Br-edge measurement. The low-photon-energy measurements were performed by using the SM1 and MEG (grating and mirror combination) with a photon flux of $10^{12}\,\frac{\mathrm{Photons}}{\mathrm{s}}$ at a resolving power of > 7000 for this energy range [298] (maximum resolving power >10000 in the energy range 80-1500 eV). The measurements can be performed with a variable spot size on the sample, ranging from $100 \times 100\,\mu\mathrm{m}^2$ to $1 \times 1\,\mathrm{mm}^2$ [298]. This is important, since some investigated materials are sensitive to x-ray radiation and can easily be damaged.

DEIMOS preparation and measurement chamber

The DEIMOS beamline at SOLEIL synchrotron consists of six different chambers, one preparation chamber, one loadlock chamber, one transfer/storage chamber, and three measurement chambers. In Fig. 3.34, a top view of the whole setup is displayed [300].

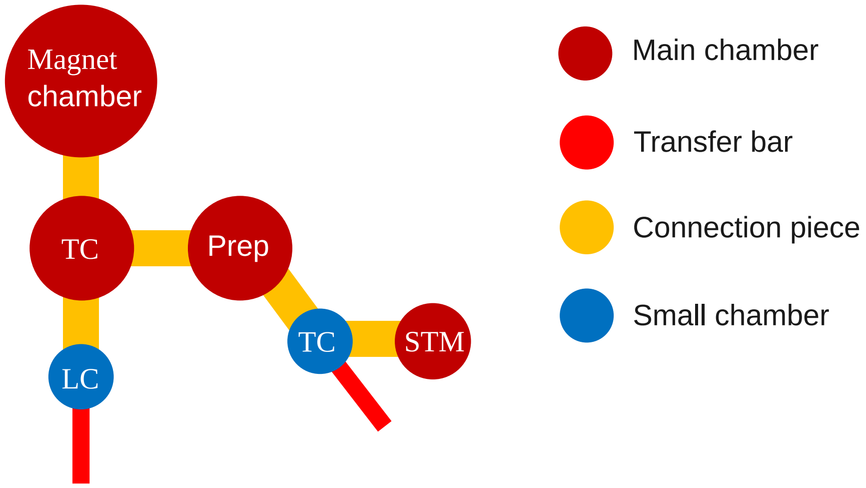

Figure 3.34: Top view of the DEIMOS beamline. This figure is an overview sketch to identify the different chambers and their connections. The abbreviation TC and LC are staying for transfer and loadlock chamber.

The loadlock chamber has space for four samples, which can also be exfoliated insitu by connecting the tape to the chamber walls. During the transfer arm movement, the tape exfoliates the top layer of the vdW material. After the substrates are loaded, they are transferred to the storage chamber. Here the manipulator has space for several samples and the mounting system for the shuttle exchange. The chamber is always in good vacuum (10^{-9} mbar). From this chamber, the samples can either be transferred to the preparation chamber or to the magnet chamber. In our case the samples are always transferred to the preparation chamber to either clean the metallic surfaces by sputtering and annealing or by directly evaporating the material on top of the vdW material. This preparation chamber is only used for inorganic materials. Inside the chamber, the evaporation rate can be calibrated by using a QCM. The QCM is mounted in a way that the manipulator is reaching the same position as the QCM (tooling factor 100 %). Before and after the sample preparation, the surface can be checked by using LEED with a hemispherical screen. In case a wedged sample or different thicknesses are needed to be evaporated, a shutter can be moved in front of the sample plate. After the pre-characterization is finished, the sample can either be transferred to the variable temperature STM (VT-STM) chamber, which has the possibility of measuring at temperatures from 50-500 K [300]. In Fig. 7.8, a detailed 3D view of the DEIMOS setup is shown.

The spectroscopic characterization is afterwards performed inside the magnet chamber with a maximal field of $\pm$ 7 T along the beam direction and $\pm$ 2 T perpendicular to the beam [300], [301], [302]. The advantage of the DEIMOS beamline compared to other beamlines is the possibility of changing the used undulator from an APPLE II undulator [300], [303] with a permanent magnet setup to an electromagnet undulator with a switching rate of 10 Hz (EMPHU-65) [300]. Therefore the magnetization loop measurements can be performed in a static and dynamic sense. At this beamline XAS, XMCD, XLD, XMLD, and magnetization loop measurements can be performed. Depending on the inserted VTI setup a temperature range of 1.8-350 K or 0.2-350 K (dilution manipulator) can be reached [300], [302]. The energy at the DEIMOS beamline can be varied in a range from 350-2500 eV with an energy resolution of 6000-10000 over the whole energy range. The sample spot size can be varied between $80 \times 80\,\mu\text{m}^2$ and $0.8 \times 0.8\,\text{mm}^2$ with a photon flux of $6 \cdot 10^{12}\,\frac{\text{Photons}}{\text{s}}$ at 750 eV [300].

PEARL preparation and measurement chamber

In Fig. 3.35, a top view of the whole PEARL endstation at SLS synchrotron is displayed. The setup is separated in two growth chambers, one load lock chamber, one distribution chamber and two measurement chambers for the structural and chemical characterization of the samples [304].

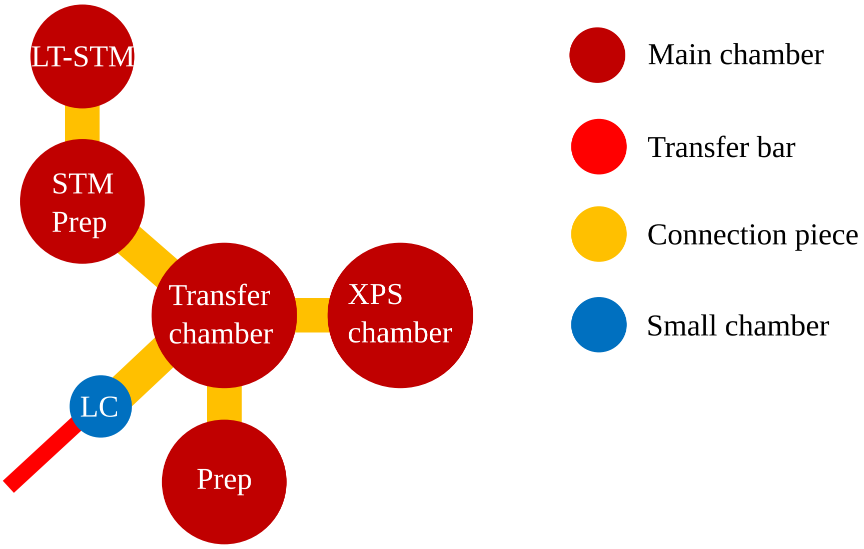

Figure 3.35: Schematic top view of the PEARL beamline at the SLS synchrotron light source. The abbreviation LC stands for loadlock chamber.

Inside the loadlock chamber, four substrates can be stored simultaneously. Additionally the exfoliation of vdW substrates is performed inside. After the loadlock chamber has reached a pressure of 10^{-8} mbar, the valve to the distribution chamber ($1.8 \cdot 10^{-10}$ mbar) can be opened. This chamber has space for four samples on the transfer stage. From the distribution chamber, the sample can be either transferred to one of the two prep chambers ($5.0 - 9.8 \cdot 10^{-10}$ mbar) or to the XPS chamber (10^{-11} mbar). The main preparation chamber consists of a manipulator with the possibility of resistive heating and direct current heating. In Fig. 3.6 c), the heating system is displayed and in Fig. 3.36 the needed sample holder for direct current heating.

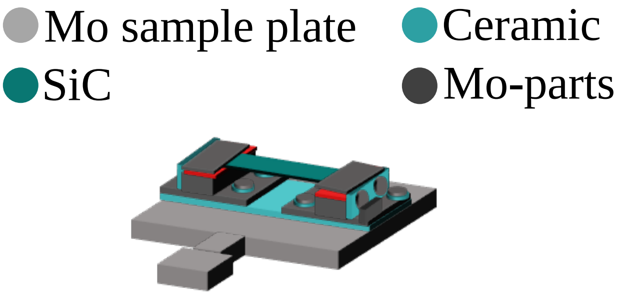

Figure 3.36: Sample plate design for the direct current heating system. The screws, which have a connection to the sample plate, need to be isolated by ceramic spacers. The substrate is mounted between the two clamps and has the electric contact only via the spring mounting. The fin on the right side is the connection point to the fork on the direct current sample holder. This figure is based on the sample plate for direct current heating used at the PEARL beamline at SLS.

After the sample surface is clean, it can be checked by using a LEED setup with hemispherical screen. The pressure for the LEED measurements needs to be good (low 10^{-9} mbar), since otherwise the La-filament needs to be reformed. On the lower part of the chamber the evaporator can be mounted. The chamber also consists of a thermal evaporator, which is located at the bottom of the chamber and a QCM, which can be moved into the sample position for checking the evaporation rate. The STM preparation chamber only consists of a sputtering and annealing system as well as a QCM and evaporator port. After the samples were grown, they are transferred to the LT-STM chamber (with a minimal temperature of 4.3 K) to characterize the sample surface and investigate the structural properties of the material [304], [305]. Afterwards, the sample is transferred to the XPS chamber, where XPS, angle resolved photoelectron spectroscopy (ARPES), XAS, and x-ray photoelectron diffraction (XPD) [305]–[307] measurements can be performed. At this beamline, the photon energy can be changed from 60-2000 eV with a maximum photon flux of $2 \cdot 10^{11}\ \frac{\text{Photon}}{\text{s}}$ at 1000 eV [306].

4 Epitaxial growth and structural, chemical, and magnetic characterization of $FeBr_2$

4.1 Epitaxially grown monolayers of $FeBr_2$ on Au(111) and Bi_2Se_3

In the following sections the structural, chemical, and magnetic characterization of $FeBr_2$ on Au(111) as well as on Bi_2Se_3 will be explained. In Tab. 7.19 the measurements that were performed entirely by collaborators are listed. These were done in 2020, 2021, and 2023, in the beginning of the collaboration and as additional part for the publication in 2023. For all the data that was measured by collaborators I have the permission of the collaborators to evaluate and use them in my thesis. All data in this thesis was evaluated by me. Part of the data of $FeBr_2$ on Au(111) has already been published in Ref. [32]. In the following chapter and the appendix some figures and content is taken literally from Ref. [32]. A majority of the measurements in the paper were done by the collaborators. My contribution to that paper was the full evaluation and explanation of the XPS and XMCD data and the partial evaluation of the STM and LEED data. In addition, I have written the paper drafts.

4.1.1 Material introduction

Over the last decades, $FeBr_2$ has been a subject of many theoretical and experimental investigations [308], [309], [310]. The bulk properties of $FeBr_2$ show a 1T structure (CdI_2) with a P3m1 point group [124], [311]. For this 1T structure, the transition metal is sandwiched between two planes of bromine atoms (MX_2), where each Fe atom is coupled to six Br atoms [124]. This triangular structure is rotated by 180 ° with respect to the bottom plane.

In Fig. 4.1, the structure of $FeBr_2$ is shown, including a top and a side view of the material. This material consists of equally spaced Br-Br and Fe-Fe bonds, with a lattice constant of $a = b = 3.776$ Å and a c-axis lattice spacing including the vdW-gap of 6.227 Å [314], [315]. The height of a single slab is about 3 Å [316]. The atomic coordinates for the $FeBr_2$ structure are Fe (0,0,0) and for the two Br atoms $\pm(\frac{2}{3},\frac{1}{3},0.24)$ [309], [315] (Fig. 4.2). The material shows semiconducting [32] properties for the ML and insulating properties for bulk [130] together with a metamagnetic phase transition [124], [130] with an external field of 3.15 T [317]. The bulk material consists of ferromagnetic layers which are coupled antiferromagnetically along the c-axis [318]. Each Fe atom is bonded to six surrounding Br atoms [317] by strong covalent bonds (intralayer coupling). The coupling between the slabs is weaker than the intralayer coupling and is based on vdW interactions [124]. The magnetic properties of the bulk material have been well studied and it was found that the sample is fully saturated at about 3.15 T with a $T_N = 14.2\,\mathrm{K}$ [311], [317], [319], [320]. The material shows an Ising-type spin ordering with an easy axis along the c-axis [316], [318]. In Fig. 4.3, the spin and magnetic structure of bulk $FeBr_2$ is displayed. Inside the slab two different types of interactions have been revealed.

The material exhibits ferromagnetic nearest-neighbor coupling with antiferromagnetic next nearest- neighbor coupling [318]. It has been shown that the bulk material has a large magnetic moment of 4.4 μ_B [309], which exceeds even the value of 4.0 μ_B predicted by Hund's rule.

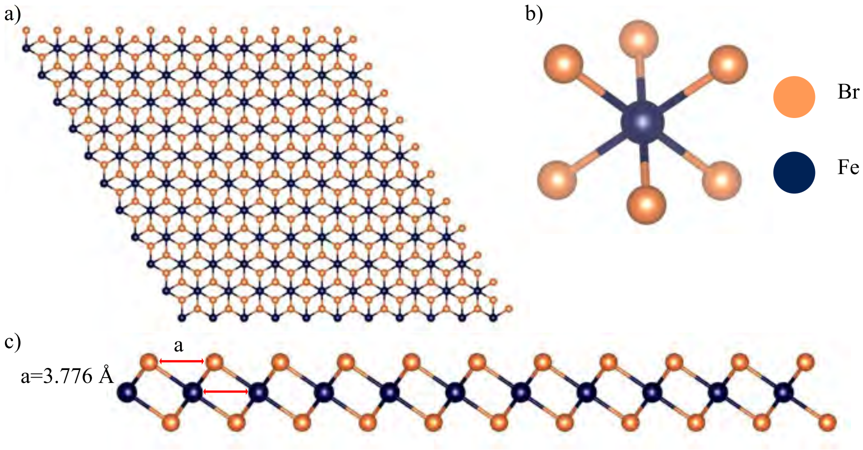

Figure 4.1: a) Top view of the $FeBr_2$ 1T structure, b) 1T-structure of $FeBr_2$, here the Br atoms in the back plane are displayed in a less bright orange color. In c) the side view is displayed including the red arrows between the Fe-Fe and Br-Br distance with a lattice distance value of 3.776 Å for the bulk material. The image was created via Vesta [312] and is based on the informations of Ref. [313].

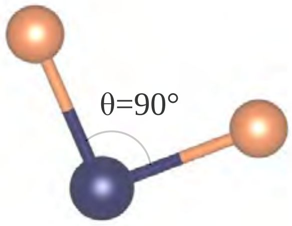

Figure 4.2: Molecular structure of $FeBr_2$. The angle between the two Br atoms is displayed with a value of 90 °. The image was created via Vesta [312] and is based on the informations of Ref. [313].

It was theoretically predicted that the orbital contribution to the total magnetic moment is substantial with around 0.74 μ_B [317]. The moment and magnetic calculations for this material were performed in different ways. Previously an effective spin of $S_{\text{eff}} = \frac{1}{2}$ or $S_{\text{eff}} = 1$ was used for the effective anisotropic Heisenberg Hamiltonian [318], however, this neglects the contribution of the orbital moment, which exists for this material [317], since it is not fully quenched [124]. The newer calculations are including the contribution of the orbital moment, therefore an effective spin of $S_{\text{eff}} = 2$ together with $L = 2$ is used, which are representing the orbital configuration of the Fe^{2+} $3d^6$ system. In the paper by Ropka et al. [317] this situation was calculated, as well as the influence of different distortions on the effective magnetic moment. For the undistorted case they calculated a total magnetic moment of 4.26 μ_B with a large orbital contribution of 18 % (m_l=0.78 μ_B) [317]. Till now the properties at the ML limit are mainly investigated via DFT. The DFT calculations were predicting that the magnetic properties of these materials are stable down to the ML-limit with a layerwise antiferromagnetic order [131], [140] and a magnetic moment of 4 μ_B including an orbital contribution of $0.1 - 0.2$ μ_B [131]. From the DFT calculations a lattice constant of 3.69 Å was extracted [131].

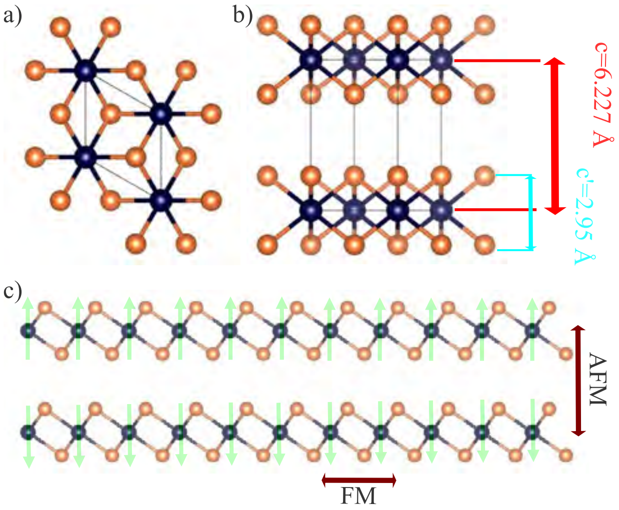

Figure 4.3: a) and b) unit cell of $FeBr_2$ in the BL case, displayed from the top and from the side respectively. In b) the complete lattice distance c including the vdW gap and the slab height c' are indicated. In c) a side view of the BL structure is displayed including the spin structure (green arrows). Inside each slab ferromagnetic (FM) interaction is present with antiferromagnetic (AFM) interaction between the layers. The image was created via Vesta [312] and additional modifications were performed on it. The figure is based on the information of Ref. [313].

4.1.2 Experiments and Methods

Different coverages from sub-ML to multilayer of $FeBr_2$ on Au(111) were grown by evaporating stoichiometric powder and anhydrous beads from Sigma Aldrich with a purity of 98 % (powder) [321] and 99.9 % (anhydrous beads) [322] from a Knudsen cell evaporator. The used evaporator was a four pocket evaporator from Dodecon with quartz crucibles. The material was loaded into the crucibles after they were cleaned twice by using ethanol and acetone in an ultrasonic bath and dried. The loaded powder had an orange color, since the material is highly hygroscopic, however, after a bakeout of the evaporator the material changed back to the wanted dry color (yellow) [317], [323], which shows that the process of hydration is reversible. The anhydrous beads have a orange to brown color, which changes also to yellowish during the degassing/evaporation. The color is related to the hydrate shell of the beads [324], since the anhydrous beads only mean less surface area, which can be hydratized. The different colors are displayed in Fig. 7.11.

The material was stepwise degassed until we reached the sublimation temperature ranging from 390-430 °C depending on the growth rate, which is in good relation to the expected values [325], [326]. The evaporation was performed under UHV conditions with an evaporation pressure ranging from $10^{-8} - 10^{-9}$ mbar. In Fig. 4.4, a schematic growth process of $FeBr_2$ on Au(111) is displayed. All samples of $FeBr_2$ on Au(111) were grown at RT, besides the samples for which another temperature is explicitly mentioned. The RT growth is an approximation, since after annealing the temperature can still be higher at the substrate, even if the thermocouple shows already RT (between RT and 50 °C).

The rate was mainly checked via a thickness monitor (QCM) from Tectra. To have a more accurate rate, monitoring the density was set to the minimum value 0.5 $\frac{g}{cm^3}$, which is around 10 % of the $FeBr_2$ density (4.63 $\frac{g}{cm^3}$) [321]. This was done, since the monitor only displays nm and the needed thickness for ML samples was in the Å regime. In the case of beamline samples a similar

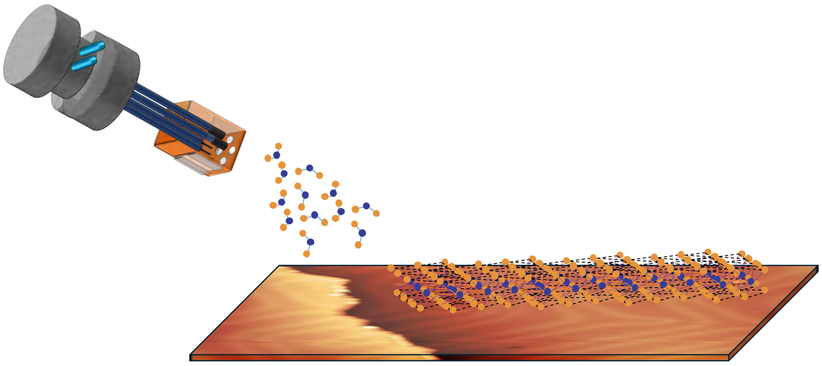

Figure 4.4: Schematic growth process of $FeBr_2$ on Au(111). On the top a schematic representation of the Dodecon evaporator is displayed.

procedure was performed, besides that here the cleaning chamber was the same as the growth chamber. The rate calibration was performed for longer times, than at CFM, since the manipulator at the BOREAS beamline has no air cooling system. Therefore, the sample temperature decreases more slowly and the substrate could still be at slightly elevated temperature. The Au(111) samples were cleaned by sputtering with Ar^+ and subsequent annealing. This procedure was performed depending on the sample conditions in cycles. Afterwards the LEED pattern before and after the evaporation was checked. In the case of growing $FeBr_2$ on Bi_2Se_3, the substrate was cleaved in situ, so that the surface for growing $FeBr_2$ was clean. Afterwards the sample was grown in two different ways either by keeping the substrate at RT or by warming it to 100 °C. In most of the cases the substrate (Bi_2Se_3) was heated, if some samples were grown at RT, this is explicitly mentioned in the figure captions.

After the samples were grown, they were structurally, chemically, and magnetically characterized. The structural characterization was performed via different LEED setups with and without an MCP system. The LEED measurements were performed to track the thickness-dependent structural changes. To have a detailed understanding of the sample surface, LT-STM measurements at 4.3 K and 77 K were performed. These measurements were performed at CFM, CINN and at the BOREAS beamline at ALBA. To chemically characterize the samples XPS and XAS measurements were performed. All characterization measurements were performed at a base pressure $\approx 10^{-10}$ mbar.

The magnetic characterizations were performed either at the VEKMAG beamline [293] or at the BOREAS beamline [297]. The measurements at VEKMAG were performed with a lowest temperature of 10 ± 2.5 K and a bending magnet setup, which decreases the degree of circular polarized light down to 77 % [294]. Since a bending magnet setup was used, the helicity was kept constant and only the field was ramped ± 6 T. At the BOREAS beamline, an undulator setup (APPLE II) is used, which has permanent magnets mounted, therefore the field was kept constant and the polarization of the light was switched between left and right (degree of circular polarized light ≈ 100 %). The lowest reachable temperature is around 1.7 ± 0.5 K, this can be achieved by inserting the last cryo-shield, which only allows the beam to enter the magnet chamber. The XMCD spectra were measured at NI (0 °, out of plane) and GI (70 °, in plane). To measure the XMCD magnetization curve, two energies were chosen (pre-edge and edge) and the field was ramped in the range $\pm$ 6 T.

4.1.3 Structural characterization

The epitaxial growth of $FeBr_2$ thin films on Au(111) was characterized by using microscopic and macroscopic surface sensitive techniques like LEED, LT-STM, low energy electron microscopy (LEEM) and x-ray photo emission electron microscopy (XPEEM). Depending on the coverage of $FeBr_2$ on Au(111) the LEED pattern starts changing. In Fig. 4.5 (a-c), the LEED pattern evolution for different thicknesses is displayed. All three images were measured at an energy of 137 eV. In Fig. 4.5 a), the LEED pattern of clean Au(111) is displayed, here the herringbone reconstruction is still slightly visible around the main diffraction spots. However, the weak visibility of the herringbone reconstruction is a direct consequence of the higher measurement energy, since at this energy a lower surface sensitivity is present. In b), the sub-ML pattern, spots around the main diffraction spots of Au(111) are visible. It seems that the diffraction spots are not equally distributed around the Au(111) spot, but this is only a consequence of the sensitivity of the camera. In Fig. 4.6, the low energy pattern is displayed and all spots exhibit a symmetrical distribution.

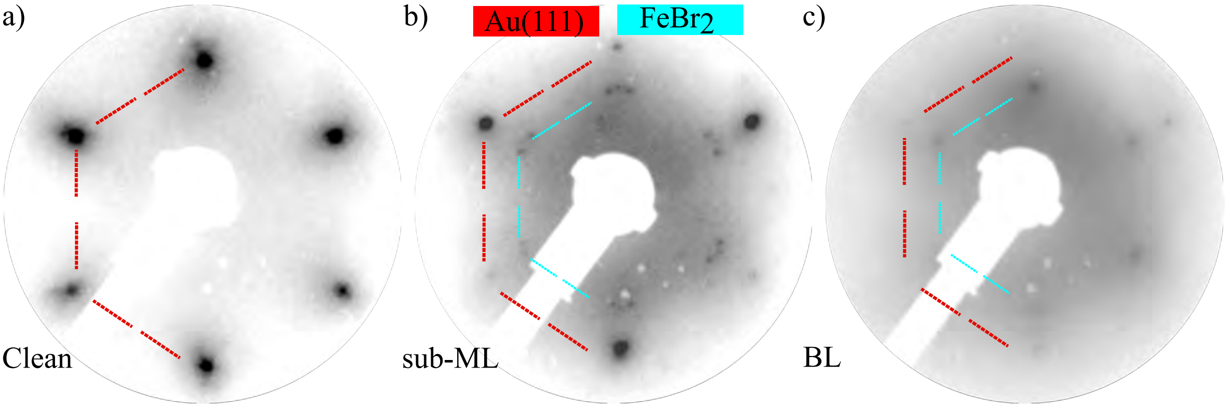

Figure 4.5: LEED pattern measured at an energy of 137 eV. In a) the LEED patterns of clean Au(111), in b) of a sub-ML (0.6 ML) and in c) of a BL of $FeBr_2$ are displayed. In red a half hexagon is indicating the hexagonal structure of Au(111) in all sub-figures and a b) and c) a light blue hexagon is indicating the structure of $FeBr_2$. The LEED images were measured at CFM in 2022.

In Fig. 4.5 c), the BL pattern is displayed with a hexagonal structure, which is closer to the (0,0)-spot. This is expected, since $FeBr_2$ has a bigger lattice constant than Au(111) and therefore the spots will be closer to the (0,0)-spot in reciprocal space. The orientation of the BL pattern shows that the material grows along the main symmetry direction of the substrate. No additional superstructure spots are visible anymore and no second rotational domain. This could indicate that either the first layer structure changes when enough material is deposited on top of it or that the additional material causes a push together and therefore the domains disappear and the material is realigned to the substrate high-symmetry direction. At this coverage, the Au spots are still slightly visible. The reason for using this high energy for the LEED measurements was that an easy comparison between the pattern and distances is possible. However, for higher surface sensitivity, LEED measurements were also performed at different low energies to characterize the surface structure (Fig. 4.6). The samples were rotated in front of the LEED screen to compare the Au(111) spots with the material diffraction spots. A structural transition appears from ML to BL.

In the lower sub-ML case (Fig. 4.6 b)), the hexagonal main diffraction pattern is surrounded

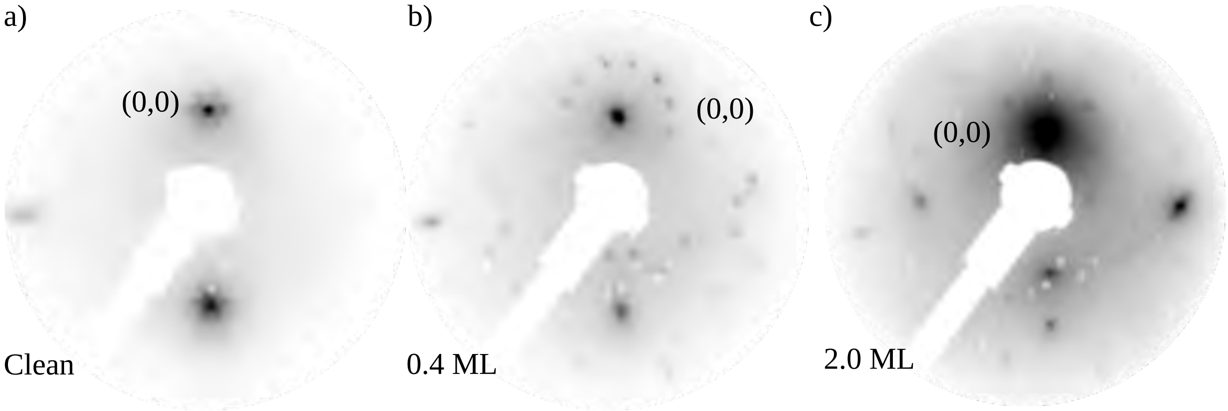

Figure 4.6: LEED patterns measured at an energy of 62 eV. In a) the clean Au(111) pattern including the herringbone reconstruction is displayed. The sample was rotated in front of the LEED screen to have at this low energy the possibility to observe the material diffraction spots as well as the herringbone reconstruction. In the figures b) and c) the diffraction patterns for the sub-ML and BL case are displayed. For orientation the (0,0)-spot is marked in every image due to the sample rotation. The samples were all measured in the XPS lab at CFM in 2022.

by many spots, which are creating a circular structure, consisting of 12 spots around each main diffraction spot. In between, parallel lines of each 2 spots are visible between the (0,0) spot and the other first-order diffraction spots (Fig. 7.29 c)). By increasing the amount of material the structure starts changing and a mixed phase appears, which ends in the new structure of the BL sample. This new phase is only dominant in the case that the second layer is completely grown. In Fig. 7.12 and 7.13, the mixed phase between first and second layer is displayed in detail. For the BL case, the Au(111) diffraction spots are still visible, however with increasing coverage and thickness they disappear. The inner hexagon in Fig. 4.6 is related to a moiré reconstruction. It can be reported that in this coverage regime a moiré pattern can be observed at low coverages. By increasing afterwards the coverage the multilayer structure appears with only one dominant hexagon of the $FeBr_2$ and no contribution of the Au diffraction spots anymore.

The coverage estimation was performed by using the isotropic XAS spectra. The complete thickness calculation is displayed in subsection 4.1.5.

In Fig. 4.7, the moiré reconstruction of the second layer is displayed and compared to higher-coverage LEED images. It can be observed that this moiré pattern is long range with a lattice constant of around 1.3 nm (3.5 times the lattice constant of $FeBr_2$). This pattern is even visible for higher coverages, which is probably caused by a next-layer growth before finishing the layer below. However, it is clearly visible that the Au spots disappear in the 3-ML sample and that the moiré pattern is only slightly visible, which is caused by the previously discussed effect of initiated next-layer growth. In Fig. 4.7, the $FeBr_2$ and Au spots are indicated in the same color coding as in Fig. 4.5. The purple spots indicate the spots of the moiré pattern. This pattern shows strong and bright spots around the main diffraction spots of $FeBr_2$, but weak intensity in between the main diffraction spots. This indicates that the pattern is not continuous and uniform over the whole sample surface. In the STM analysis discussed later we will see that for the BL sample the moiré pattern is not observed. However, this could be related to the effect that STM is a local technique and therefore this pattern could have been missed during the measurements. Also only a small amount of BL samples were measured. A possible explanation for the absence of the moiré pattern in the STM measurements could be that the material grows in two different phases. One phase which shows the moiré pattern and one without. This possibility is supported by the fact that during the extensive STM measurements of $CoBr_2$ on Au(111) performed by our collaboration this moiré was not observed (internal communication). Therefore, the probability of measuring the moiré pattern on the surface is small, but since the pattern is visible in LEED, it is probably covering around 10-20 % of the surface. The observed structural phase from the BL sample is different compared to the superstructure observed for the ML. In Fig. 4.8, the superstructure at different low energies is displayed. The sample has a coverage of 0.3 ML and the structure only shows the 12-spot rings around the diffraction spots. With increasing energy

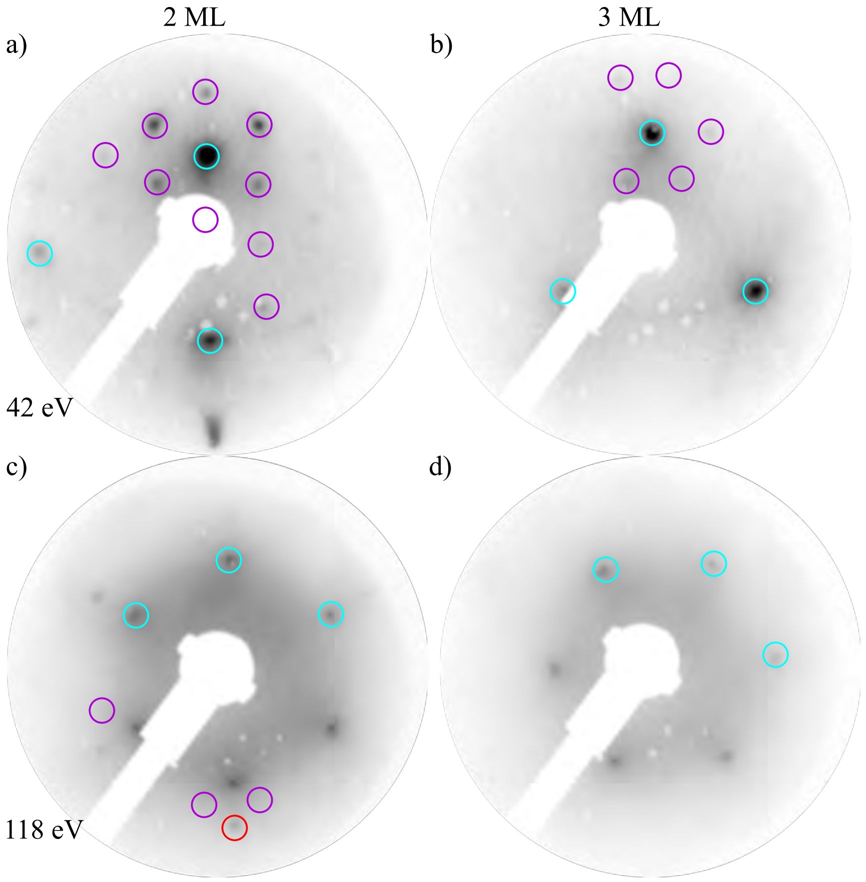

Figure 4.7: In a) and b) the LEED patterns of a BL and TL $FeBr_2$ on Au(111) at 42-43 eV are displayed. Here the moiré pattern is indicated by the purple circles around the spots. In c) and d) the same samples as in a) and b) are displayed, but measured at 118 eV. In the case of the BL sample the moiré pattern is still visible around the main diffraction spots. The light blue circles indicate the position of the $FeBr_2$ and the red circles the one of the Au(111) spots. The two different thicknesses were not grown on the same Au(111) crystals. Both substrates were cleaned by sputtering and annealing cycles and checked via LEED before the evaporation. The different rotation of the Au(111) crystal diffraction spots in a) and b) is caused by the fact, that two different Au(111) crystals were used for the different samples. The same Au(111) crystal was used for a) and c) and another Au(111) crystal for b) and d). The LEED images were measured at CFM in 2022.

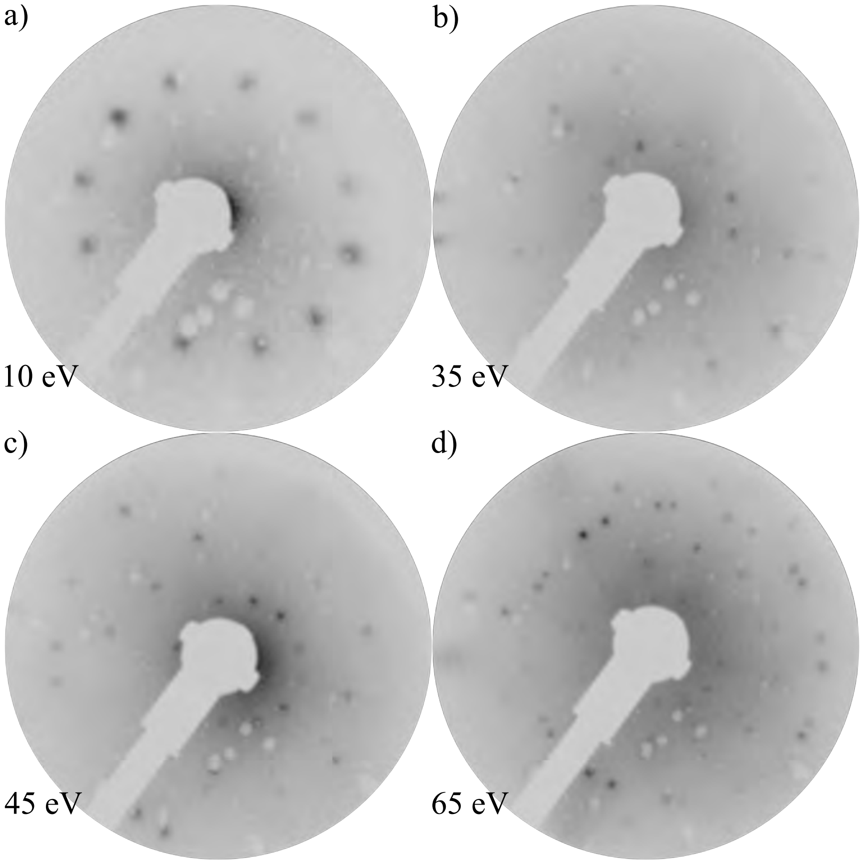

Figure 4.8: LEED patterns of a 0.3-ML sample of $FeBr_2$ on Au(111) at different energies. At low energy the 12-spot ring structure can be observed around the (0,0)-spot. From a)-d) the patterns at different energies form 10-65 eV are displayed. The LEED images were measured at CFM in 2023.

the full superstructure pattern can be observed with 12-spot ring structures around every main diffraction spot. For this low coverage no additional spots were observed.

However, by increasing the coverage, the previously discussed third spot is appearing, which is related to the second layer. Therefore, the measured LEED patterns, that are showing the third spot are a mixture of the first layer and the second layer diffraction patterns. In Fig. 7.12 and Fig. 7.13, the coverage-dependent evolution of the LEED pattern, as well as the energy dependent pattern of a 1.1 ML sample are shown. Since with increasing coverage the second layer becomes more dominant, the third spot becomes more intense and the superstructure of the first layer starts to disappear.

The epitaxial growth of $FeBr_2$ on Bi_2Se_3 is creating a completely new pattern. In Fig. 4.9 the coverage-dependent LEED pattern is displayed. The exfoliated Bi_2Se_3 crystal shows a hexagonal pattern, which is expected for this material. In b) and c) $FeBr_2$ was grown on a heated substrate and in d) the substrate was kept at RT. With increasing coverage a moiré pattern can be observed. For the heated substrates, a lower amount of material was evaporated compared to the RT sample in Fig. 4.9 d). The lower coverage, together with the increased mobility of $FeBr_2$ on the heated Bi_2Se_3 surface causes the weaker visibility of the moiré pattern in LEED. The $FeBr_2$ grows epitaxially on the vdW substrate with a moiré lattice constant of around 4 nm (extracted from the LEED measurements). During the heating process less material sticks to the surface, which

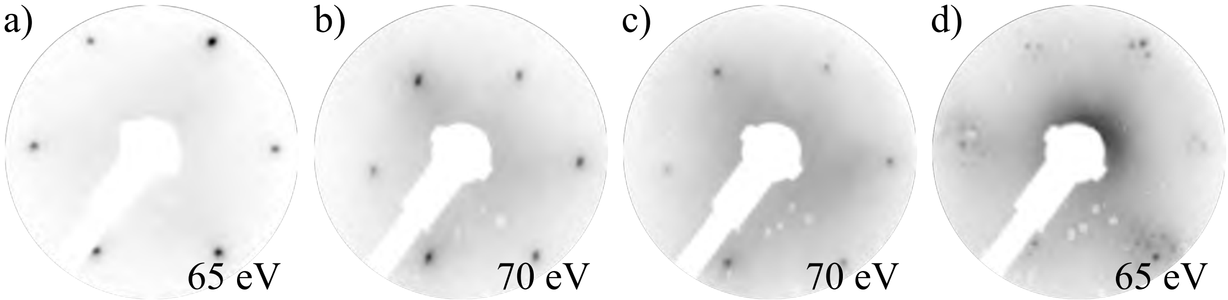

Figure 4.9: a) clean Bi_2Se_3, b)-d) epitaxial growth of $FeBr_2$ on Bi_2Se_3. The substrate in b) and c) was heated to 100 °C and in d) it was kept at RT. b) 0.5-1 ML, c) 1-1.5 ML and d) 1.5-2.0 ML. The LEED images were measured at CFM in 2023.

means that the coverage is probably lower than the one estimated via QCM of around 1 ML, possibly in the region of 0.5 ML. The observed moiré LEED pattern can be simulated in real space by overlaying the $FeBr_2$ lattice with a lattice constant of 3.776 Å with the Bi_2Se_3 lattice (lattice constant of 4.14 Å). Therefore, a moiré pattern with a periodicity of around 4.1-4.2 nm can be extracted.

By comparing the orientation of the main LEED spots of $FeBr_2$ with the ones of Bi_2Se_3, it can be observed that they are aligned, which means that the atomic structure of $FeBr_2$ has no rotation to the one of Bi_2Se_3. The observed LEED pattern shows the same reconstruction as observed for $FeBr_2$ on Bi(111) [316], where a lattice coincidence of $13 \times a_{\mathrm{FeBr_2}}$ to $11 \times a_{Bi(111)}$ was observed.

In Fig. 4.10, the simulated moiré pattern for $FeBr_2$ on Bi_2Se_3 is displayed. Here, the simulation contains that both lattices are without rotation on top of each other. This overlay of both lattices causes a moiré pattern with a periodicity of $12 \times a_{\mathrm{FeBr_2}}$ and $11 \times a_{\mathrm{Bi_2Se_3}}$. This change in the periodicity compared to the lattice overlay in Ref. [316] can be explained by the difference of the substrate lattice constants. In comparison to Bi_2Se_3, Bi(111) has a bigger lattice constant of 4.48 Å, therefore, if a lattice of 13 Br atoms would like to align on the surface, it would need 11.85 Se atoms in Bi_2Se_3. This would not create a commensurate overlay of the $FeBr_2$ and Bi_2Se_3 lattices. Therefore, a smaller periodicity of the $FeBr_2$ is needed with a repetition of 12 Br atoms on 11 Se atoms. The observed structure is nearly identical to the one observed on Bi(111). However, since the lattice constant of Bi_2Se_3 is smaller by nearly 10 % compared to Bi(111), a smaller unit cell for the moiré pattern is observed.

In Fig. 4.11, the moiré pattern as observed in STM together with an atomic-resolution image is displayed. From the atomic-resolution image, a maximum distance of the moiré pattern of $12 \times a_{\mathrm{FeBr_2}}$ can be extracted (13 Br atoms). This would be a lattice constant of 4.53 nm. The measured average lattice constant of $FeBr_2$ is 3.71 ± 0.06 Å, which is in good agreement with the literature value. The lattice constant error only includes the standard deviation error. By including the other error sources for the atomic resolution, an additional lattice constant error of 7 % is introduced. The atomic lattice constant is therefore 3.71 ± 0.32 Å. In a) an island of $FeBr_2$, with the long range moiré pattern is displayed, together with the start of the second layer growth. Therefore, the second-layer growth starts immediately after the first-layer island size is big enough. As observed, the second layer does not show any reconstruction pattern, therefore the lattice constants are nearly identical, which means, that the first layer has no strain effects. The lattice constant of the moiré pattern is around 4.19 ± 0.13 nm, which matches the extracted value from the LEED measurements. Since the periodic distance error for the moiré pattern is

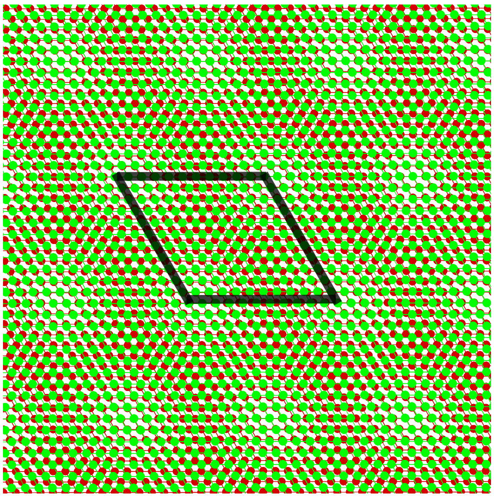

Figure 4.10: Simulated moiré pattern of FeBr$_2$ (red) on Bi$_2$Se$_3$ (green). For the simulation, the literature lattice constants of FeBr$_2$ and Bi$_2$Se$_3$ were used. In black the unit cell of the moiré pattern is shown. By aligning the atomic lattice of FeBr$_2$ with the one of Bi$_2$Se$_3$ a commensurate structure of (12 × 12) FeBr$_2$= (11 × 11) Bi$_2$Se$_3$ can be observed.

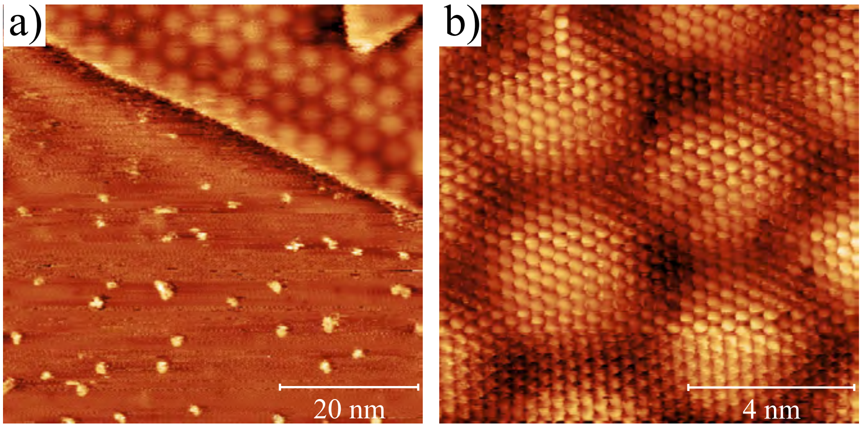

Figure 4.11: a) Island of FeBr$_2$ on Bi$_2$Se$_3$, which shows a long-range moiré pattern. b) Atomic-resolution image of FeBr$_2$. a) U_{Bias} = 1.2 V and I_{TC} = 20 pA and b) U_{Bias} = -900 mV and I_{TC} = 150 pA. The STM images were measured at the PEARL beamline at SLS in 2023.

in the nm regime, the other error sources are smaller and can be neglected. The periodicity of the moiré pattern was extracted from an average of 16 different profiles. The extracted lattice constant matches roughly the simulated distance of ≈ 4.5 nm. By using the atomic-resolution STM image, 12 Br atoms can be counted between the centerrs of the moiré pattern, which would be ≈ 4.53 nm with a FeBr$_2$ lattice constant of 3.776 Å. From the STM image, we only measured 3.71 ± 0.32 Å for FeBr$_2$, which results in a moiré lattice constant of 4.45 nm. This offset could also indicate a possible rotation of the FeBr$_2$ lattice on top of the Bi$_2$Se$_3$. By using the atomic resolution image in Fig. 4.11 b) and measuring the distance between the moiré pattern maxima in numbers of Br atoms, a value of 4.4 – 4.5 nm can be extracted. In addition to the main phase, a second type of moiré pattern with a smaller periodicity has been observed (Fig. 4.12). Here

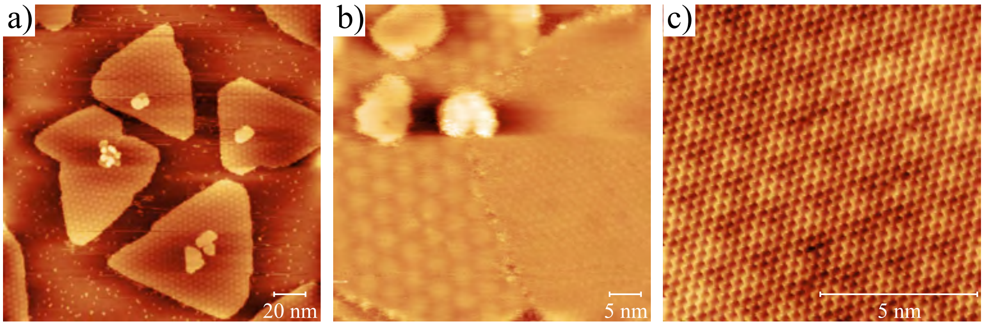

Figure 4.12: a) Topographic image, with several $FeBr_2$ islands, which are showing the big-periodicity moiré pattern. In the top left corner the second moiré pattern type is visible. b) Domain boundary between big- and small-periodicity moiré patterns. c) Atomic resolution of $FeBr_2$ on the small periodicity moiré pattern. a) U_{Bias} = -900 mV and I_{TC} = 10 pA, b) U_{Bias} = -900 mV and I_{TC} = 60 pA, and c) U_{Bias} = -300 mV and I_{TC} = 100 pA. The STM images were measured at the PEARL beamline at SLS in 2023.

the second type of pattern grows at a boundary of the main pattern. The smaller moiré pattern has a periodicity of 1.60 ± 0.18 nm. The periodic lattice distance of the moiré pattern has been averaged over 10 moiré spot distances. From the observed LEED pattern no structure which would correspond to the second pattern type can be extracted, therefore it is most likely that the small periodicity moiré pattern does not occur often. The atomic resolution in Fig. 4.12 reveals an average lattice constant of 3.72 ± 0.07 Å (error from standard deviation) or 3.72 ± 0.33 Å (including the 7 % due to other error sources), which is still in good agreement with the literature value and the one observed for the big moiré pattern. The reason for the reduced periodicity is a rotation of the $FeBr_2$ on top of Bi_2Se_3. From a simulation of the second moiré pattern in Fig. 4.13 a rotation of around 30 ° can be extracted. In the following, the simulation of the superstructure

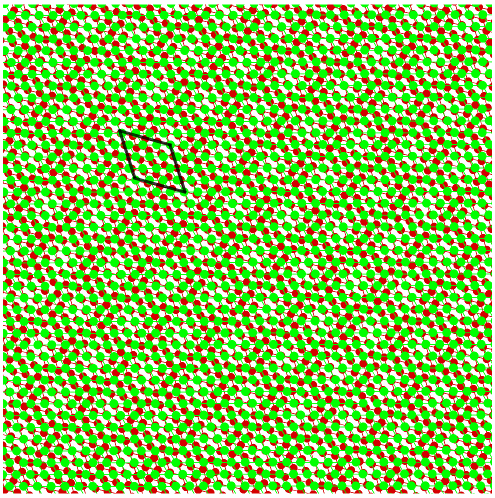

Figure 4.13: Simulated moiré pattern for a 30 ° rotated $FeBr_2$ (red) layer on top of Bi_2Se_3 (green). In black the unit cell of the moiré pattern is indicated.

pattern on Au(111) as well as the third spot pattern will be stepwise explained including the corresponding vector calculations. To fully understand the origin of the sub-ML LEED pattern, LT-STM measurements were performed at a temperature of 4.3 K. In Fig. 4.14, the different LT-STM measurements are displayed. In Fig. 4.14 a) the clean Au(111) substrate including the herringbone reconstruction is shown. This sample was measured at 77 K. In b) and d) different sub-ML samples are shown which were measured at 4.3 K. In b) the clean Au(111) surface between two islands of $FeBr_2$ shows mostly the regular herringbone reconstruction. However, close to the $FeBr_2$ island, the herringbone pattern starts to distort. As a possible part of the growth mechanism it can be observed that at the elbow sides of the herringbone material is concentrated (Fig. 4.14 b)). Therefore, these areas can be seeding points or growth centers. Another possible explanation can be, that the elbows are the energetically favorable nucleation sites for free Br atoms. The possibility of free Br atoms becomes more likely, since the nearly full ML sample shows areas with Br meshes (Fig. 4.15), as observed for pure Br on Au(111) [327].

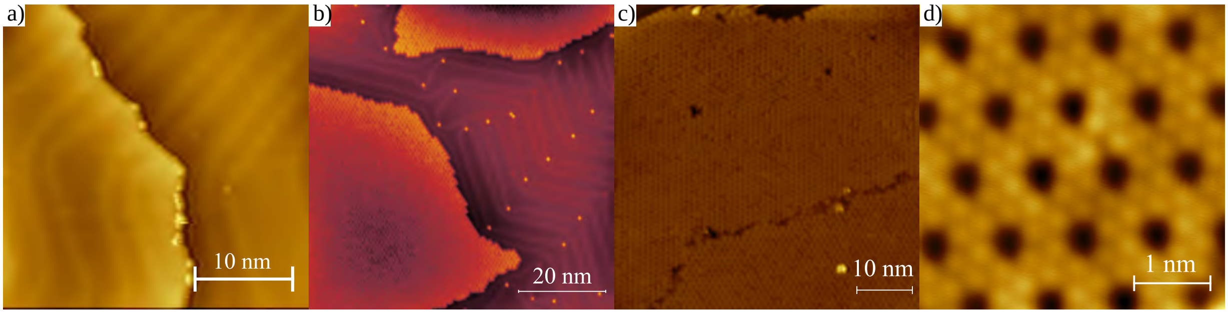

Figure 4.14: LT-STM measurements performed on Au(111) and the sub-ML $FeBr_2$ sample on Au(111). a) Clean Au(111) surface together with the herringbone reconstruction and two terraces. b) Sub-ML sample with two $FeBr_2$ islands and the clean Au(111) surface in between. The clean Au surface still displays the herringbone reconstruction with distortion regions close to the material islands. c) Sub-ML $FeBr_2$ on Au(111) sample with a domain boundary between the two $FeBr_2$ orientations. d) Atomic resolution of $FeBr_2$ on Au(111) together with the superstructure pattern (dark spots). The panels a) and c) were measured at 77 K and b) and d) at 4.3 K. The STM parameters are the following: a) U_{Bias} = -500 mV and I_{TC} = 0.5 nA, b) U_{Bias} = 1000 mV and I_{TC} = 0.1 nA, c) U_{Bias} = 1200 mV and I_{TC} = 0.02 nA and d) U_{Bias} = 10 mV and I_{TC} = 1 nA. The STM measurements at 77 K and 4.3 K were all performed in the same machine (APOLLO) STM but at different locations. The 77 K were measured in 2023 at CINN and the 4.3 K in 2020 at CFM.

In Fig. 4.15 a), b) and c), STM images of 0.9 ML $FeBr_2$ on Au(111) are displayed. Besides the regular superstructure pattern, also free Br on the Au(111) surface can be observed. The Br forms the characteristic meshes (Fig. 4.15 b)) [328], [329], [330] if the amount is high enough. This can have different reasons, either this is related to the evaporation, the sample temperature, or to the amount of material. The first parameter, the evaporation temperature, was kept the same as in the other samples, the only difference is that another type of evaporator was used (higher temperature effusion cell [331]). The second possibility is the sample temperature. The sample was kept at RT, however, since the manipulator is connected to a liquid nitrogen dewar, this could have affected the substrate temperature to be in the range of perhaps below 0 °C even if no active liquid nitrogen flow was present. The more plausible explanation is that the previously discussed elbow nucleation sides are free Br centers. Therefore, with increasing amount of deposited material the Br atoms are pushed together and are creating the meshes. The case that this was not observed previously can be based on the fact that the Br is very mobile and

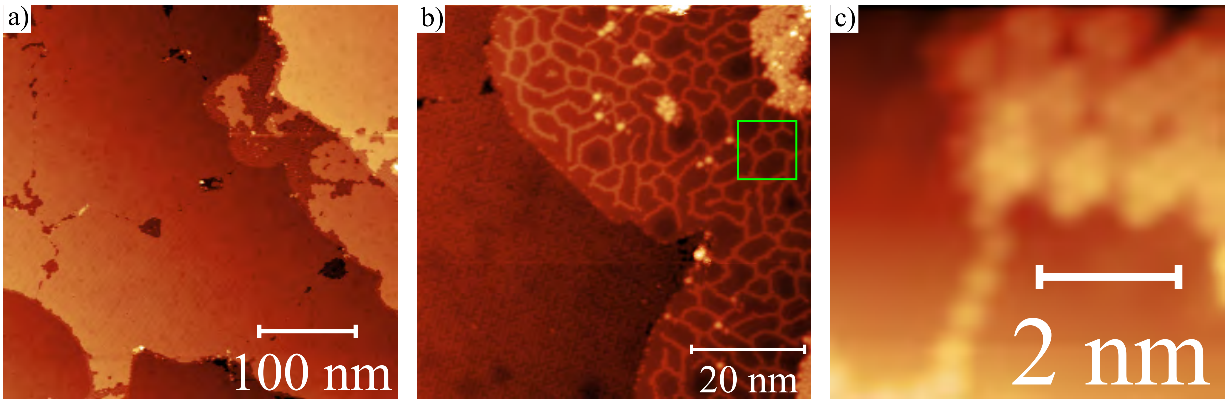

Figure 4.15: STM images of 0.9 ML $FeBr_2$ on Au(111). In a) a topographic overview of a larger area is shown. In b) a zoomed-in view of a) is shown, where the superstructure pattern can be observed as well as the Br mesh, which is indicated by the green rectangle. In c) a closer view of free Br and part of the superstructure pattern is displayed. The measurements were performed at SLS at the PEARL beamline in 2023. The STM parameters are: a) and b) $U_{\mathrm{Bias}} = 1.3\,\mathrm{V}$ and $I_{\mathrm{TC}} = 0.05\,\mathrm{nA}$, and c) $U_{\mathrm{Bias}} = 1.5\,\mathrm{V}$ and $I_{\mathrm{TC}} = 0.2\,\mathrm{nA}$. The sample was grown at 2 °C and the measurements were performed at 4.3 K.

therefore distributes better over the whole free Au surface for lower coverages. In Fig. 4.14 c) a domain boundary inside the $FeBr_2$ island is displayed. The boundary is part of the explanation of the LEED pattern. Fig. 4.14 d) shows the atomic resolution of the $FeBr_2$ sample on Au(111). Here two different dominant structures can be observed. The first is the pure $FeBr_2$ structure and the second is the superstructure (dark spots). The measured lattice constant for the $FeBr_2$ structure is $3.66 \pm 0.3\,\text{Å}$ and for the superstructure $9.7 \pm 0.72\,\text{Å}$ (Fig. 7.14). The error of these measurements includes the error from standard deviation and the measurement related STM error. By using Fig. 4.14 d), the angles and the structural matrix can be extracted. Between the black superstructure spots the vectors $\vec{C_1}$ and $\vec{C_2}$ can be drawn, which can be used together with the unit vectors $\vec{b_1}$ and $\vec{b_2}$ of the Br plane to calculate one structural matrix of the system. The top and bottom Br plane have the same orientation of the high-symmetry directions but due to the 1T-symmetry of $FeBr_2$, the lateral position is shifted along the b_1-b_2 direction.

$$\begin{pmatrix} C_1 \\ C_2 \end{pmatrix} = \begin{pmatrix} 2 & -1 \\ 1 & 3 \end{pmatrix} \cdot \begin{pmatrix} b_1 \\ b_2 \end{pmatrix}, \tag{4.1}$$

To calculate the structural matrix for the relation between the superstructure pattern and the Au surface, the same procedure as previously for the relation between the Br layer and the superstructure is used.

$$\begin{pmatrix} C_1 \\ C_2 \end{pmatrix} = \begin{pmatrix} 3 & -1 \\ 1 & 4 \end{pmatrix} \cdot \begin{pmatrix} a_1 \\ a_2 \end{pmatrix}. \tag{4.2}$$

Due to the symmetry of the system, a rotational domain exists. Therefore, the $FeBr_2$ can have two different orientations with respect to Au.

$$\begin{pmatrix} \tilde{C}_1 \\ \tilde{C}_2 \end{pmatrix} = \begin{pmatrix} 3 & 1 \\ -1 & 2 \end{pmatrix} \cdot \begin{pmatrix} \tilde{b}_1 \\ \tilde{b}_2 \end{pmatrix} = \begin{pmatrix} 4 & 1 \\ -1 & 3 \end{pmatrix} \cdot \begin{pmatrix} a_1 \\ a_2 \end{pmatrix}. \tag{4.3}$$

These matrices can be used to simulate the LEED pattern via LEEDpat [332] and are giving an indication about the angles between the structures and the substrate.

In Fig. 4.16 b), the Fourier-transformation of the atomic-resolution STM image is displayed (Fig. 4.16 a)). As an insert, the matrix for the relation between the superstructure and the Br plane is displayed. The matrix was used to simulate the pattern, which is used as an overlay of a 2D-fast fourier transformation (FFT) image.

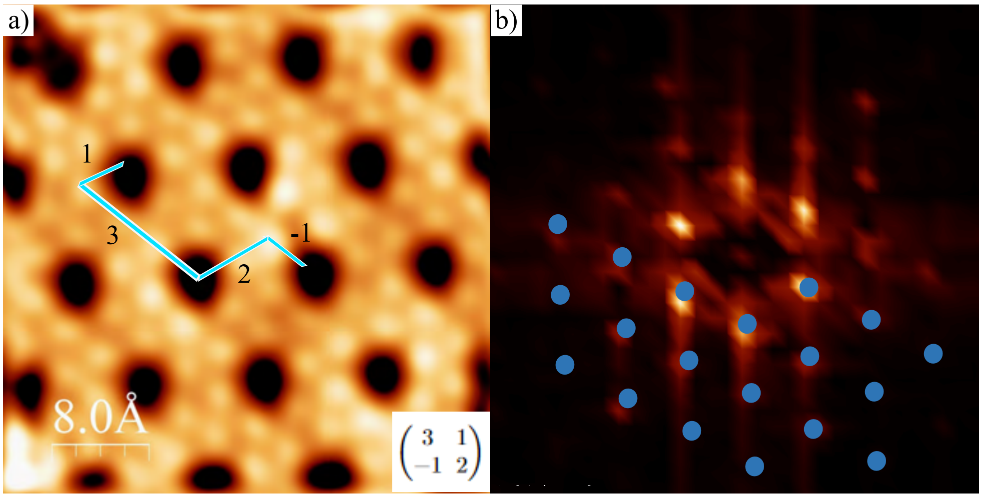

$\begin{pmatrix} 3 & 1 \\ -1 & 2 \end{pmatrix}$

Figure 4.16: a) Atomic-resolution STM image of the 0.6-ML FeBr$_2$ on Au(111) sample. As an insert, the structural matrix is included and the blue lines represent the path of extracting the structural matrix. b) 2D-FFT of the STM image from a). The FFT image is overlayed by the simulated LEED pattern (only one domain). The STM image was measured with $U_{\text{Bias}} = 10\,\text{mV}$ and $I_{\text{TC}} = 1.0\,\text{nA}$. The STM measurements were performed in 2020 at CFM.

In Fig. 4.17 a), the atomic-resolution image of the first layer of FeBr$_2$ on Au(111) is displayed, together with the material lattice vectors of Au(111), FeBr$_2$, and the superstructure. By using the information extracted from this STM image, together with the measured LEED patterns, the origin of the observed pattern can by simulated and recreated. The black arrows indicate the closed-packed Au[1$\bar{1}$0] direction. From the displayed STM image, the angles between the material and superstructure, as well as between material and substrate, can be extracted. The angle between the Br and Au(111) symmetry directions is $\approx 5 \pm 0.5\,°$ and between the Br and the superstructure $\approx 19 \pm 0.5\,°$. The simulation in b) is used to calculate the accurate angle between the structures as well as the vectors and the corresponding vector length. The displayed structure is adapted to the correct lattice constant ratio between the Au(111) surface lattice constant and the one of FeBr$_2$. The magenta-colored structure represents the top most Br layer of FeBr$_2$ and the orange structure represents the Au(111). In black the superstructure is indicated, which forms a hexagon at the coincidence points of the Br layer and the Au(111). Now we will discuss step by step how to extract the angle between the different lattices and the vector length. The vector $\vec{a}$

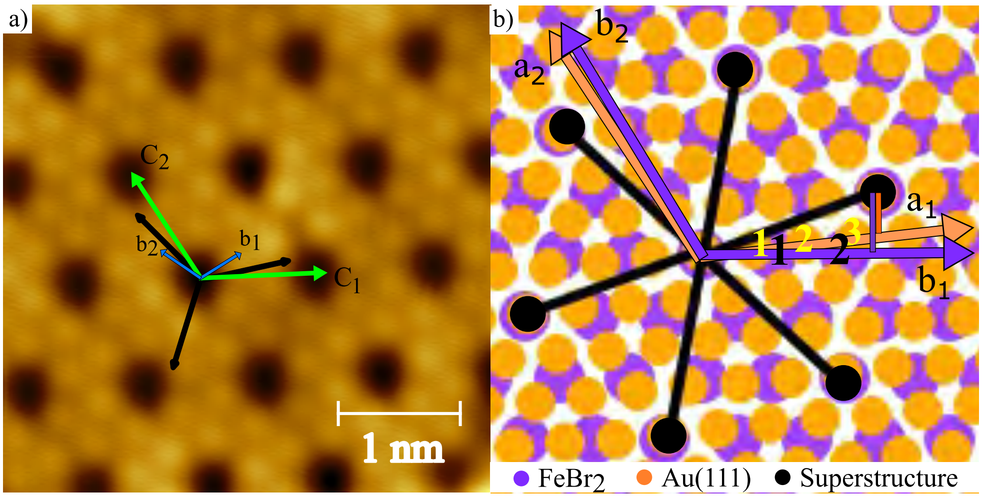

Figure 4.17: a) Atomic-resolution STM image of the 0.6-ML $FeBr_2$ on Au(111) sample. The black arrows indicate the close-packed Au$[1\bar{1}0]$ and equivalent directions. The arrows which are marked in green and blue are representing the superstructure unit cell and the hexagonal Br lattice unit cell respectively. b) Structural overlay of $FeBr_2$ (magenta) and Au(111) (orange). In black the hexagon of the superstructure is displayed. The numbers inside the figure (yellow and black) are referring to the Au atom and Br atom steps to reach a point of the superstructure. Part b) is an adapted version of [32]. The STM parameters are $U_{\text{Bias}} = 10\,\text{mV}$ and $I_{\text{TC}} = 1\,\text{nA}$. The STM measurements were performed in 2020 at CFM. The image is a modified version of the one in Ref. [32].

represents the orientation of the superstructure to the substrate.

$$\vec{a} = \begin{pmatrix} \frac{7}{2} \\ \frac{\sqrt{3}}{2} \end{pmatrix} \tag{4.4}$$

$$|\vec{a}| = \sqrt{a_x^2 + a_y^2} = \sqrt{\frac{49}{4} + \frac{3}{4}} = \sqrt{13} \tag{4.5}$$

$$\alpha = \arctan\left(\frac{\sqrt{3}}{7}\right) \approx 13.9^\circ \tag{4.6}$$

The value of a_x corresponds to the 3.5 steps along the x-direction. Theses steps are indicated as yellow numbers in b). The a_y value is just corresponding to the regular triangle height. From this vector the length of $|\vec{a}|$ can be calculated, which is later used to determine the strain of the structure. From $\vec{a}$ the angle α can be extracted, which has a value of $\approx 13.9 \pm 0.5\,^\circ$, which is good agreement with the extracted value from the STM measurement. The next vector is representing the relation between the superstructure and the $FeBr_2$.

$$\vec{b} = \begin{pmatrix} \frac{5}{2} \\ \frac{\sqrt{3}}{2} \end{pmatrix} \tag{4.7}$$

$$|\vec{b}| = \sqrt{b_x^2 + b_y^2} = \sqrt{\frac{25}{4} + \frac{3}{4}} = \sqrt{7} \tag{4.8}$$

$$\beta = \arctan\left(\frac{\sqrt{3}}{5}\right) \approx 19.1^\circ \tag{4.9}$$

Here only 2.5 steps along the x-axis need to be done to reach the position of the superstructure spot. Here an angle of $\approx 19.1 \pm 0.5$ ° can be extracted between the FeBr$_2$ and the superstructure. To now finally extract the vector between the FeBr$_2$ and the substrate, we can either subtract the angle α from β or calculate the scalar product between $\vec{a}$ and $\vec{b}$.

$$\vec{a} \cdot \vec{b} = \begin{pmatrix} \frac{7}{2} \\ \frac{\sqrt{3}}{2} \end{pmatrix} \cdot \begin{pmatrix} \frac{5}{2} \\ \frac{\sqrt{3}}{2} \end{pmatrix} = \frac{14}{2} \tag{4.10}$$

$$\vec{a} \cdot \vec{b} = |\vec{a}| \cdot |\vec{b}| \cdot \cos(\gamma) = \sqrt{13} \cdot \sqrt{7} \cdot \cos(\gamma) \tag{4.11}$$

$$\gamma = \arccos\left(\frac{19}{2\sqrt{91}}\right) \approx 5.21^\circ \tag{4.12}$$

The calculated angle γ fits with the extracted angle from the STM measurements. To identify now the strain of the FeBr$_2$ lattice caused by the lattice mismatch, the ratio of $|\vec{a}|$ and $|\vec{b}|$ needs to be calculated. As a result a value of 1.36 is obtained, which is 3 % higher than the ratio expected from the theoretical values and 6 % higher than the one extracted from the STM measurements using a surface lattice constant of Au(111) of 2.86 Å. As previously already mentioned, the rotation of ≈ 5 ° needs to be symmetric in both directions. Therefore, the observed 12-spot LEED pattern can be explained by two different rotational domains of $\approx \pm 5$ ° with respect to the Au direction. These domain structures are visible in Fig. 4.14 c). By knowing the angles between the different structures, the LEED pattern can be simulated by using the software LEEDpat [332]. For the beginning of the LEED pattern simulation we need to introduce the substrate. In Fig. 4.18 and Fig. 7.16, the simulation steps are displayed. The Au(111) substrate is constructed by using a P3m1 point group and a hexagonal lattice with a lattice constant (a) of 2.86 Å. Now the material needs to be introduced by using the theoretical lattice constant of a_{FeBr_2} =3.776 Å. This value will be used for r_1 and r_2, since it is identical for both distances. By using the strained value, the superstructure pattern can be simulated. However, the unstrained version shows that the domain structure is appearing. The simulation which includes strain is displayed in Fig. 4.20. From the LEED calculation and the STM evaluation the angle between material and substrate was extracted. By using now for $\alpha_1 = 5$ ° and for $\alpha_2 = 125$ °, the FeBr$_2$ lattice is rotated on top of the Au substrate. The LEED pattern displayed in Fig. 4.18, which is based on the literature lattice constants, represents the high-energy LEED images. Here no superstructure can be observed, since the lattice constant is too small for the corresponding pattern around the (0,0) spot. By

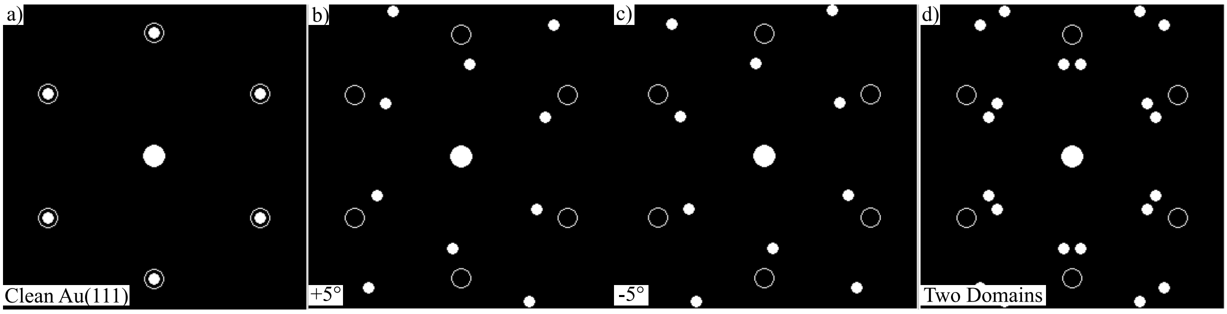

Figure 4.18: a) Simulated LEED pattern of Au(111). b)-c) Combination of the FeBr$_2$ structure at $\approx \pm 5$ ° on top of Au(111). Here the Au spots are represented as hollow circles and the FeBr$_2$ is represented with white circles. d) High-energy pattern of FeBr$_2$ on Au(111) including both rotational domains. The simulation of the pattern was performed by using LEEDpat [332].

using now the two domains with ±5 ° and overlaying the simulated patterns on top of each other, the measured high-energy LEED pattern can be reproduced.

Another way to simulate the superstructure pattern at low energies is to use the periodic distance between the dark spots (Fig. 4.17 a)). Therefore, the extracted periodic distance of the dark spots in STM (9.7 Å) is used for r_1 and r_2. The angle used for the simulation is the one extracted previously, therefore we use $\alpha_1 = 13.9\,°$ and $\alpha_2 = 133.9\,°$. By rotating both domains with respect to each other, the low-energy LEED pattern is visible (Fig. 4.19 d)). The appearance of the third outer spot (Fig. 7.13) is related to the growth of the second layer and can be observed by overlaying the LEED pattern of the first and second layer. The corresponding step by step simulation for the real-space image is displayed in Fig. 7.16. The simulated pattern of one ML of $FeBr_2$ on top of Au(111) in Fig. 4.20 was simulated simultaneously in VESTA [312], [313]. Both Br layers are still visible and are indicated in red (bottom layer) and green (top layer). The coincidence points can be visualized by following the structural matrix and including a lattice strain as discussed before. For this simulation, the Br-bottom and top layer atoms are displayed with different sizes. The different colors of the Br atoms (top- and bottom-layer) are just for a better visualization of the pattern, since a Br atom from the top-layer was removed to demonstrate the coincidence pattern, where the Br atom is sitting directly on top of a Au atom.

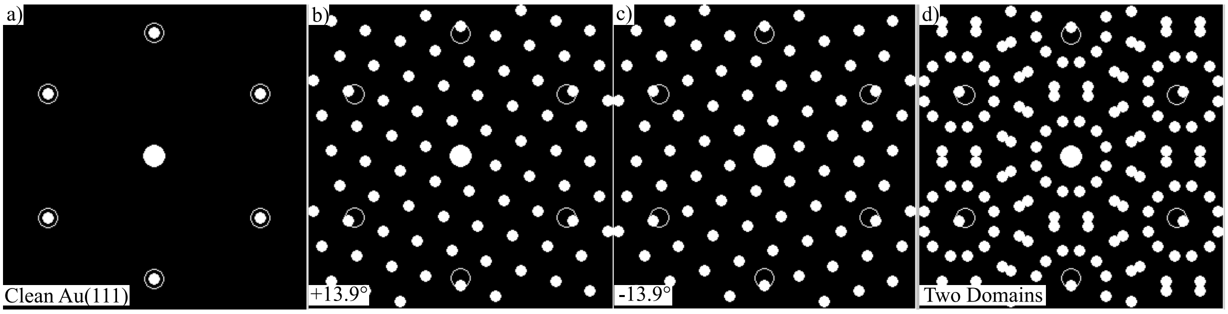

Figure 4.19: a) Simulated LEED pattern of Au(111). b)-c) Combination of the superstructure at ±13.9 ° on top of Au(111). d) Simulated pattern for both rotational domains. The simulation of the pattern was done by using LEEDpat [332].

The superstructure of the first layer was measured with different bias voltages to investigate if the structure is a purely electronic effect or if it is a real structural effect. In Fig. 4.21, the first-layer superstructure is displayed for different bias voltages. It can be observed that the superstructure is not changing for the displayed bias voltages except for -3 V. However, the change for the high negative bias voltage can also be tip-related. The only real difference for different bias voltages is that the triangular defects are changing in the linking area, but not the position or visualization of the dark spots. Therefore, the dark spots are most likely a structural feature rather than purely electronic. This could be an indication that the first layer shows some Br vacancies. Another possible explanation is based on the Ullmann-coupling between the halide and the noble metal Au. However, it is not clear how the coupling of the bottom layer and the surface can create this kind of structure.

In addition to the already discussed superstructure, the first layer shows also two different kinds of defects, the dark triangular defects and the circular bright defects. In Fig. 4.22 an overview, together with a zoomed in image are displayed. In the case of the dark triangular defects, around the central dark spots Br atoms are centered (Fig. 4.22 b)). The triangular defects are probably related to a missing Br atom in the bottom plane, since the top layer seems unaffected in between the dark spots. As observed from the LEED measurements (Fig. 4.5 c)), the structure of the

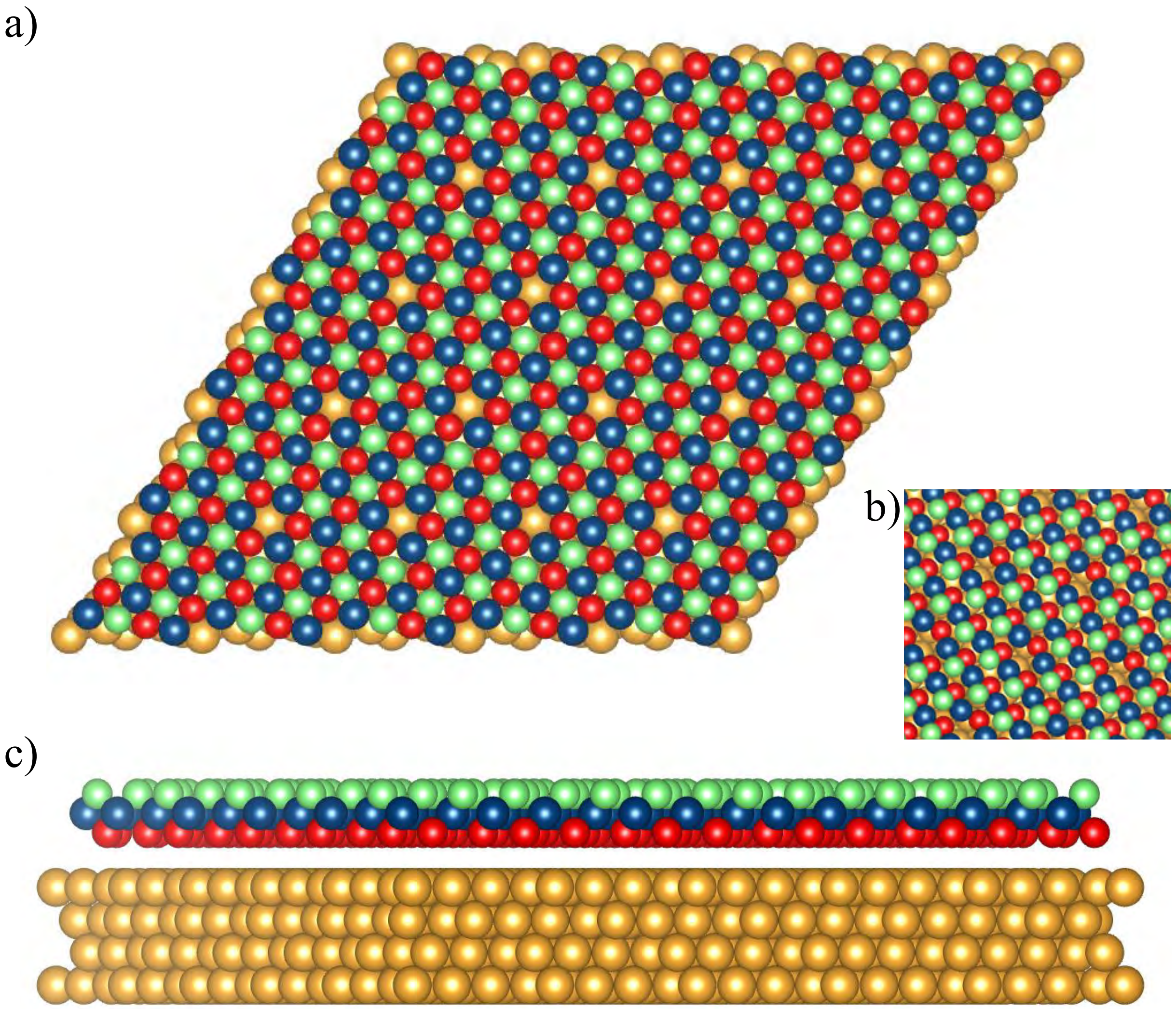

Figure 4.20: The upper part of the image shows the top view of $FeBr_2$ on the Au(111) surface. Following the $FeBr_2$ superstructure with respect to the Au(111) matrix, the top-layer Br atoms (in green) were removed to show the position of the Au atoms underneath. Therefore, the observed superstructure is appearing. However, it is not 100 % clear, if the superstructure is related to missing top-layer Br atoms or only stronger attracted Br atoms, which causes this periodic pattern. The lower image is showing the side view of $FeBr_2$ on the Au(111) surface. The $FeBr_2$ lattice is strained to match the LEED simulation. The simulation was done by using VESTA [312]. The parameter are from Ref. [333] and [313].

second layer is different and the superstructure as well as the rotational domains are disappearing. In Fig. 4.23, the BL sample including atomic-resolution measurements of the second and third layer are displayed. For the second layer, a lattice constant of 3.68 ± 0.11 Å (error from standard deviation) can be extracted and by including the other error sources from STM (systematic error of 7 %), a lattice constant of 3.68 ± 0.37 Å is obtained. For the third layer, a lattice constant of 3.69 ± 0.08 Å (error from standard deviation) can be extracted and by including the other

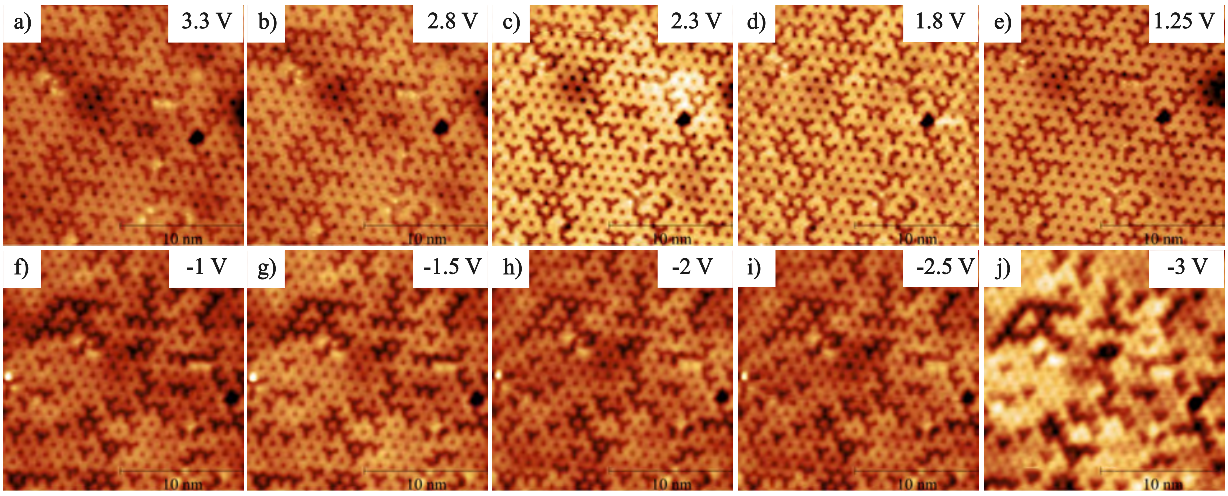

Figure 4.21: Bias dependence of STM images of the first layer of FeBr$_2$ on Au(111), with bias voltages ranging from 3.3 V down to -3 V. All images were taken at nearly the same sample position except j). The tunneling current for all images is $I_{TC}=0.1 \cdot 10^{-9}$ A. The measurements were performed at 4.3 K. The STM measurements were performed in 2023 at the PEARL beamline of the SLS synchrotron radiation source. Image has been taken out of Ref. [32].

error sources a lattice constant of 3.69 ± 0.34 Å is obtained. These values are very close to the theoretical bulk value from DFT [131]. By comparing the first and second layer structure it is visible that the Au(111) surface has a big influence on the structure of the material, since the first layer shows a superstructure pattern, which disappears for the second and all following layers. This indicates a different growth mechanism, due to the different surface underneath the material. The observed corrugation of the second layer can be caused by strain effects on top of the underneath-lying material, since the first layer shows strain on top of the Au(111) surface. In Fig. 4.24, STM images of a 1.8 ML sample are displayed. On this sample different local coverages can be observed, ranging from the first layer in b) till second and third layer (c) and d)). In b) the two different rotational domains can be observed. The domain boundary is indicated by a red rectangle in the upper right corner of the figure. It can be observed that the first and second layer are co-existing in the same topographic area, but they are never measured on top of the same terrace.

After the second layer is grown, the third and following layers are growing on top after the needed critical area of the layer underneath is big enough. In c) the corrugation phase can be observed, which is characteristic for Br-based TMDH (maze structures). This corrugation phase looks different in the case of Cl-based TMDH, as observed for FeCl$_2$ on Au(111) [132] and in our own measurements for CoCl$_2$ on Au(111) (internal communication). However, as later shown, those corrugations were not observed for MnBr$_2$ and MnCl$_2$, which indicates a specific reason for the corrugation phases like a possible lattice constant mismatch. An important parameter for the growth of FeBr$_2$ is the substrate temperature. In Fig. 7.17, STM images for different coverages of FeBr$_2$ on Au(111) are displayed. All samples are grown without heating the substrate, however, c) was grown on a manipulator which was still connected to the liquid nitrogen cooling. The cooling itself was off, however the manipulator was still around 270-273 K (thermocouple). Therefore, the growth of FeBr$_2$ on Au(111) can be affected by low temperatures. By comparing the different coverages and the two different growth temperatures, it can be observed that the material is

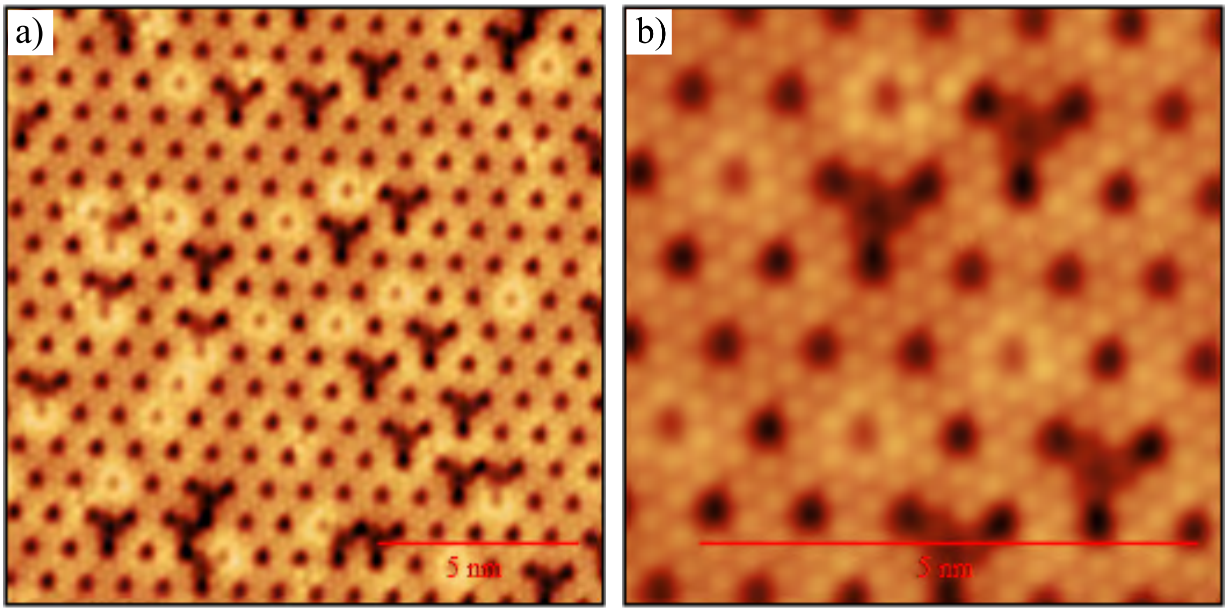

Figure 4.22: a) Large-area scan with atomic-resolution of 0.6 ML FeBr$_2$ on Au(111). Here the two different defect types are visible together with the regular material structure. b) Atomic-resolution image of the first layer together with the triangular dark defects. It can be observed that around the central dark spot three Br atoms are ordered. a) was measured with $U_{\mathrm{Bias}} = 0.01\,\mathrm{V}$ and $I_{\mathrm{TC}} = 0.5\,\mathrm{nA}$, and b) with $U_{\mathrm{Bias}} = 0.002\,\mathrm{V}$ and $I_{\mathrm{TC}} = 0.38\,\mathrm{nA}$. The STM measurements were performed in 2020 at CFM.

still growing with the same reconstruction, therefore the reduced mobility of the material on the surface is not strongly affecting the growth. However, in the case of the colder growth defect areas can be found, where the superstructure is not appearing. These defect areas can also be found on the RT-grown sample, but they are in general less often appearing and smaller. This observation implies that even if the growth works at RT and lower temperatures more optimal results can be achieved by growing at slightly elevated temperatures so that bigger and potentially defect area free islands/terraces are grown.

Another important information which can be extracted from the displayed STM images is the coverage behavior. The samples displayed in Fig. 7.17 a), b), and d) were calibrated and evaporated under the same conditions. This reveals that even if the growth is uniform all over the substrate, locally the coverage is varying. Due to a high surface mobility, the local coverage is changing, since the material seems only to stop at terrace edges or at the elbow sites of the Au(111) herringbone structure. However, with increasing coverage the lateral island size is increasing. In the range of around 0.6 ML the lateral island size is $\approx 70\,\mathrm{nm}$. Since the LEED and STM measurements are representing a more global and local view of the sample surface, other techniques were used to observe if the material grows uniform on the substrate. By using LEEM and XPEEM measurements, the uniform epitaxial growth was characterized on a mesoscopic scale. In Ref. [32] the performed LEEM and XPEEM measurements are shown. The measurements revealed a uniform growth on a μ-scale with first and second layer areas, which correspond to the observed 1.5 ML μ-LEED image. The different coverage regions were also proven by the performed XAS spectra, which showed a higher Fe L$_3$ edge peak intensity in the BL region.

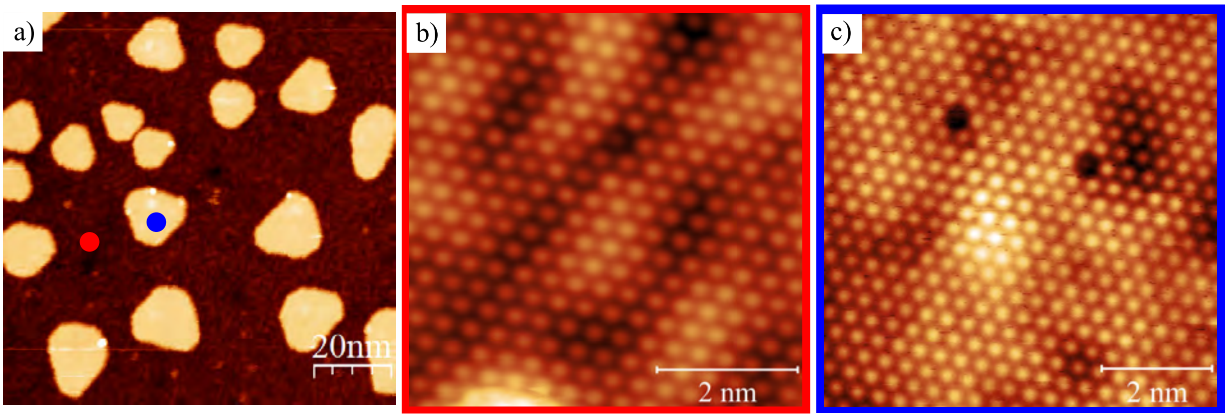

Figure 4.23: STM measurements of a BL $FeBr_2$/Au(111). a) Topographic overview of the BL $FeBr_2$ on Au(111) sample. On top of the second layer, the third layer shows the previously observed corrugation (weaker than for the second layer) of the second layer, as well as triangular islands of the third layer. b) and c) Atomic-resolution images of the second and third layer. The measurements were performed at 4.3 K. a) was measured at U_{Bias}= 1.7 V and $I_{TC} = 0.04 \cdot 10^{-9}$ A, b) at U_{Bias}= -0.2 V and $I_{TC} = 0.4 \cdot 10^{-9}$ A, and c) at U_{Bias}= 1.6 V and $I_{TC} = 0.1 \cdot 10^{-9}$ A. The second and third layer are indicated by red and blue dots in a). The corresponding atomic-resolution images have a red and blue frame for the second and third layer. The STM measurements were performed in 2023 at the PEARL beamline of the SLS synchrotron. Image has been taken out of Ref. [32].

4.1.4 Chemical characterization

The chemical characterization of $FeBr_2$ on Au(111) and Bi_2Se_3 was performed by using XPS and XAS measurements. For the XPS fitting routine a Shirley-background-correction is performed. Afterwards, for the investigated element core-level a specific amount of Voigt profiles is used in addition to a linear fit. The XPS measurements of $FeBr_2$ on Au(111) and Bi_2Se_3 were performed in the Nanophysics XPS lab at CFM in 2020, 2022, and 2023. Additionally some measurements were performed at the PEARL beamline, which will be indicated in the figure caption.

XPS measurements

The majority of XPS measurements was performed by using the Al anode of a non-monochromatic x-ray gun at CFM. The other measurements were performed by using either a high resolution synchrotron-radiation XPS (PEARL beamline at SLS synchrotron) or the Mg anode of the non-monochromatic gun at CFM. Before evaporating $FeBr_2$ on Au(111) the substrate surface was investigated always by measuring LEED and sometimes XPS on clean Au(111) and Bi_2Se_3. In Fig. 4.25 a) and b), the survey spectra of a clean Au(111) and of 0.95 ML $FeBr_2$ on Au(111) are shown. The measurement of the clean Au(111) crystal was performed at CFM by using a non-monochromatic x-ray source (Al anode) and the survey scan of the 0.95 ML $FeBr_2$ was performed with a photon energy of 950 eV at RT at the PEARL beamline. All important core-level peaks for our material are indicated by the vertical lines. The small C and O peak in the survey spectrum (Fig. 4.25 b)) are related to the long exposure time of the sample inside the XPS chamber. Therefore, C and O was physisorbed on the surface. The only visible core-level peaks in Fig. 4.25 a) are the ones of the Au(111) substrate, therefore the sample surface is completely

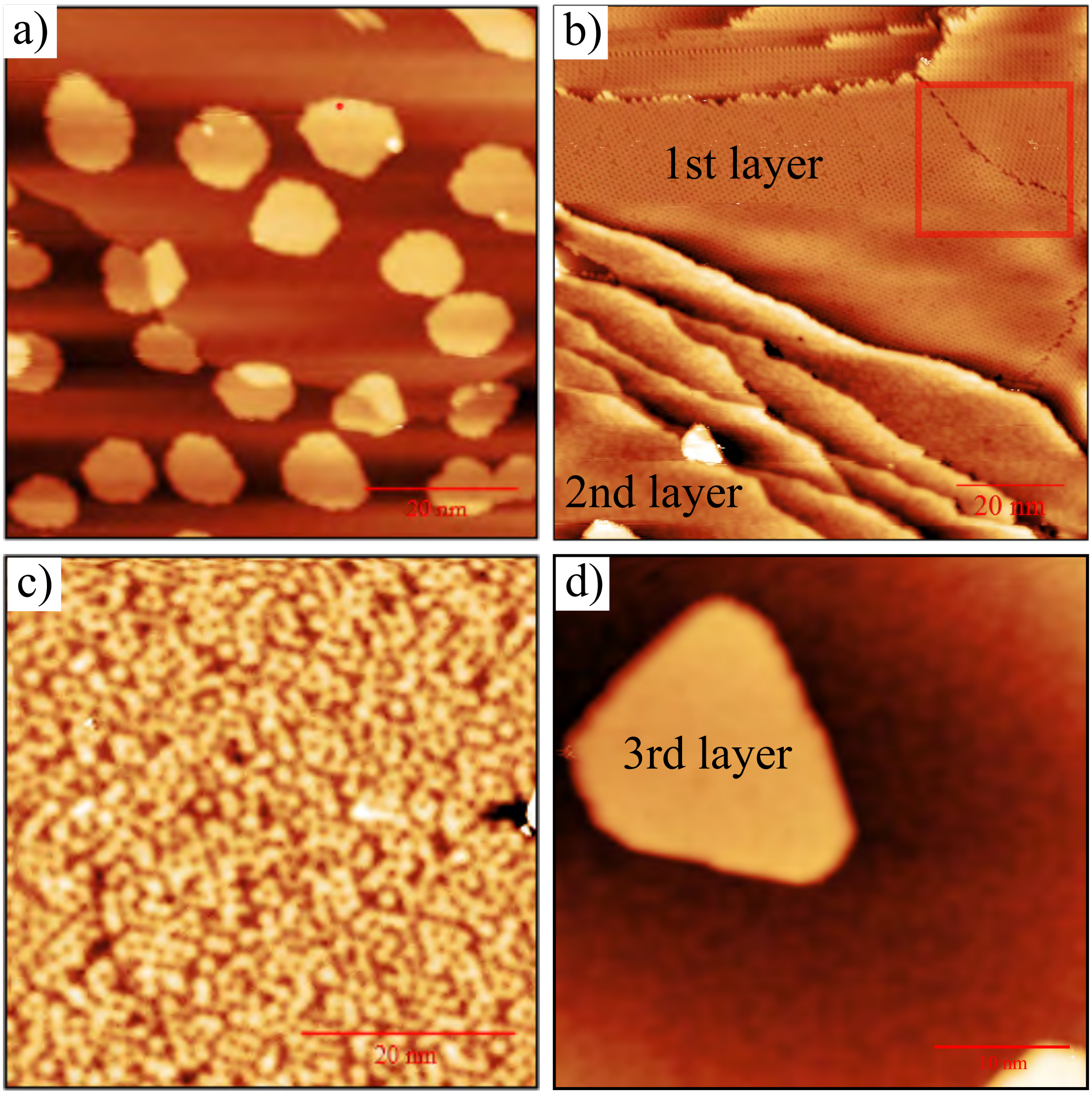

Figure 4.24: a) Topographic overview STM image of the a 1.8-ML sample. The second layer grows over the terraces of the Au(111) substrate and the third layer grows as islands on top of the second layer. b) Topographic image of different coverages ranging from sub-ML to TL on different terraces. Here the first layer and second layer are growing side by side, but not on the same terrace. In the upper right corner the two different (±5 °) domains are visible with the domain boundary (red rectangle). In c) a closer look on the second layer is displayed, which shows strong corrugation and in d) a closer look on the 3rd layer is displayed. The STM measurements were performed at 77 K. The STM parameter are $U_{\mathrm{Bias}} = 1.3$ V and $I_{\mathrm{TC}} = 0.01$ nA for a), for b) $U_{\mathrm{Bias}} = 1.2$ V and $I_{\mathrm{TC}} = 0.1$ nA, for c) $U_{\mathrm{Bias}} = 1$ V and $I_{\mathrm{TC}} = 0.03$ nA, and for d) U_{Bias} =1 V and $I_{\mathrm{TC}} = 0.04$ nA. The STM measurements were performed in 2023 at CINN.

clean from any contamination. The survey scan was measured in a binding energy range from -4-1100 eV. In b) the Fe 2p (blue lines), Br 3p and Br 3d (orange lines) core-level peaks are visible as well as the core-level peaks related to the Au(111) substrate.

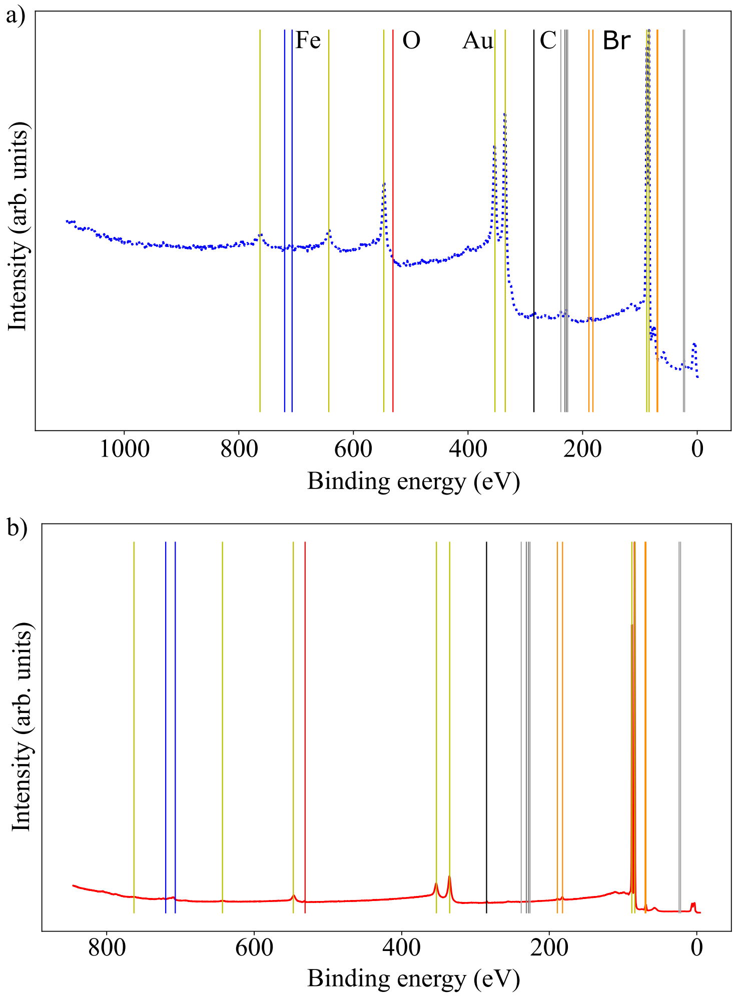

Figure 4.25: a) XPS survey spectrum of clean Au(111) measured at CFM by using a non-monochromatic x-ray source (Al anode). b) Survey spectrum of 0.95 ML FeBr$_2$ on Au(111). The yellow, blue, red, black, orange, and grey lines are indicating the core-level peaks of Au, Fe, O, C, Br, and Mo/Ta, respectively. The measurement was performed at the PEARL beamline at SLS in August 2023.

The physisorbed material is not affecting the FeBr$_2$ on Au(111) as later shown (Fig. 4.29). In Tab. 7.7 the binding energies for the different core-level peaks are listed. To compare the FWHM and the spectral shape of the Au 4d peaks after the material is evaporated on top of Au(111), the clean Au 4d spectrum was measured and fitted (Fig. 4.26). In a) the clean Au 4d spectrum is shown, together with the Shirley background, which needs to be removed for further evaluation. In b) the fitted spectra is shown, therefore four Voigt profiles were used. Two fits for the main core-level peaks and two fits for the satellite peaks caused by the non-monochromatic Al anode (shifted by about 9.8 eV). In Tab. 4.1 the fitting parameter for Fig. 4.26 b) are shown.

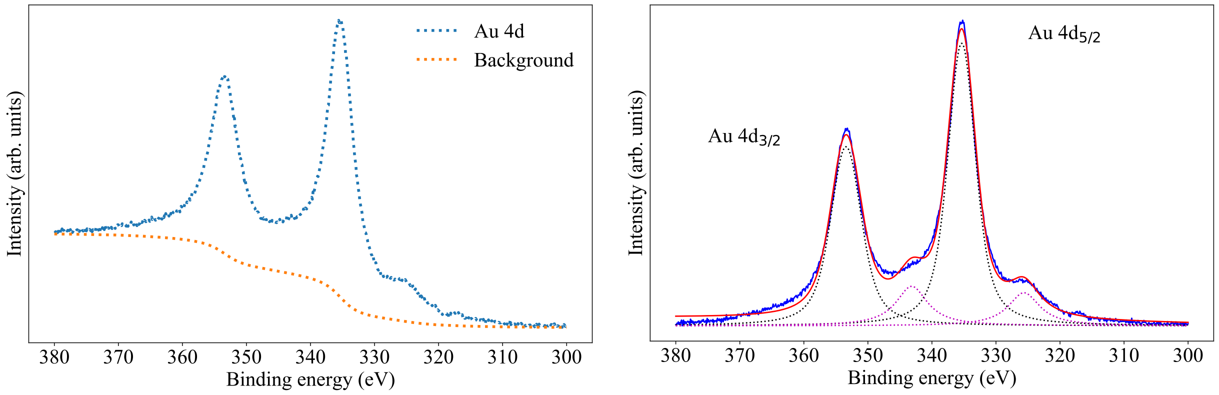

Figure 4.26: Au 4d XPS spectrum. a) Raw data in blue together with the calculated Shirley background. b) Fitted background-subtracted spectrum. The full fit is displayed in red and the single peak fits are displayed in black and magenta.

Element	Core-level	Peak position (eV)	FWHM (eV)
Au	4d$_{\frac{3}{2}}$	353.14	5.72
Au	4d$_{\frac{5}{2}}$	335.18	5.35
Au Al Anode	4d$_{\frac{3}{2}}$	343.34	6.00
Au Al Anode	4d$_{\frac{5}{2}}$	325.25	6.00

Table 4.1: Fitting parameters for the core-level peaks of Au 4d together with the satellite peaks caused by the Al anode of the non-monochromatic x-ray gun.

By comparing the fit parameter with the theoretically expected peak positions, we observe that the measured peaks are exactly at the expected positions for the Au 4d core-levels. The area of the fitted core-level peaks is afterwards used to calculate the peak ratio and to check if the expected value for d-orbital splitting is reached.

$$R = \frac{A_{4d5/2}}{A_{4d3/2}} = 1.48 \tag{4.13}$$

The extracted ratio is matching with the expected value of 1.5 and has only an offset of 1.3 %. Since the substrate surface cleanliness was checked via LEED and XPS, the material evaporation was started.

In Fig. 4.27, the XPS spectra for the sub-ML and BL sample are displayed. The measurements at different thicknesses were performed to observe that the chemical composition remains constant and to discard the presence of different phases besides the proper FeBr$_2$ phase. Both samples were grown inside the same chamber at CFM under the same conditions. After the sub-ML sample was prepared and characterized, the substrate was sputtered and annealed and the BL sample was prepared. In between each step (after annealing and after growth) LEED measurements of the clean Au(111) and of the sample were performed. The XPS measurements were performed with a pass energy (E_{pass}) of 30 eV, a lens mode of medium area (MA), an applied HV of 1.5 kV and an analyzer work function of 4.309 eV. The same amount of scans was used for each energy region at the two different thicknesses. A Shirley background was subtracted before fitting the data via Voigt profiles using the python lmfit routine [334]. In total four Voigt fits were used to fit the Fe 2p spectra (two for the Fe^{2+} peaks and two for the satellite peaks). The measured spin-orbit

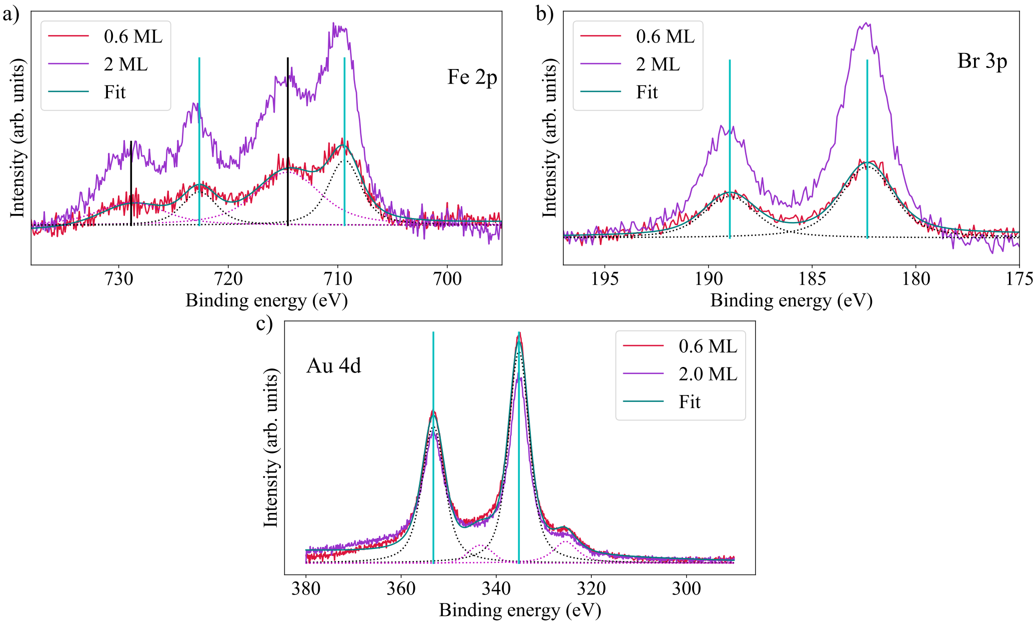

Figure 4.27: Fe 2p, Br 3p, and Au 4d spectra for a sub-ML (0.6 ML) and BL (2.0 ML) sample of $FeBr_2$ on Au(111), including the spectra fit. In a) the Fe 2p, in b) the Br 3p and in c) the Au 4d core-level spectra are shown. The Fe 2p spectra are confirming a Fe^{2+} oxidation state. The cyan- colored vertical lines are used as a guide to the eye and are indicating the core-level peaks for the different elements. For the Fe 2p spectrum black lines are included, which indicate the satellite peak positions. For all spectra of the sub-ML sample, the single-peak fits are shown by black dotted lines and the full fit is displayed in red. The shown data are published in Ref. [32]. The Fe and Br spectra are normalized to the Au $4d_{\frac{5}{2}}$ peak intensity.

(SO) splitting of around 13 eV for the Fe 2p spectra are matching the literature values [335]. The spectra also includes the contribution of the shifted Fe peaks due to the non-monochromatic Al anode. However, due to the low signal intensity for the ML and BL samples it has been ignored for the fit. Since no additional peaks are needed to fit the data, the sample has no other oxidation state. By comparing the fitting parameters of the element-specific spectra (Tab. 4.2), it can be observed that the peak structure matches with the literature structure as well as with the literature values of the peak positions for an Fe^{2+} state. The peaks for $FeBr_2$ are shifted to higher binding energies with respect to the reported values for bulk $FeBr_2$ ($2p_{3/2}$ 708 eV), coinciding with the Fe^{2+} oxidation state for FeO (709.7 eV) [335], [336]. In Fig. 4.27, the BL Fe 2p and Br 3p spectra are shifted for the evaluation by 0.2 eV to lower binding energies, therefore the peak maxima are matching again. The fact that for the thicker sample the peak position is shifted to higher binding energies is not related to any chemical shifts like in the case by comparing C-O and C-C bonding system, but due to shifts to the reference work function [228], [229]. In the case of a chemical shift both contributions should still be visible. Also the shift is not related to charging, since the Au 4d and 4f spectra are not shifted for different sample thicknesses (Fig. 4.27 c) and Fig. 4.28 c)). The full width at half maximum (FWHM) used for the fit of the Fe^{2+} peaks is 3.7 eV, as reported in Ref. [335], [337] for FeO.

However, due to the resolution of the lab XPS caused by the non-monochromatic gun, we could not resolve the multiplet splitting peaks (result of the high-spin state, HS, of the Fe) for the

Coverage	Element Peaks	FWHM (eV)	Peak position (eV)	Amplitude (arb. units)
sub-ML	Br 3p 3/2	3.00±0.05	182.35±0.03	1602.16±39.35
	3p 1/2	2.89±0.09	188.97±0.05	800.00± 33.59
sub-ML	Au 4d 3/2	5.73±0.18	353.16±0.03	53228.12±704.15
	4d 5/2	5.66±0.03	335.25±0.02	80988.04±653.07
sub-ML	Fe 2p 3/2	3.59±0.11	709.38±0.06	2121.41±173.07
	Fe 2p 1/2	3.78± 0.21	722.64±0.11	1147.94±104.84
	Fe Sat. 2p 3/2	7.10±0.31	714.57±0.16	3435.25±261.87
	Fe Sat. 2p 1/2	7.20± 0.40	728.87±0.26	1503.78±97.71
BL	Br 3p 3/2	2.78±0.02	182.69±0.01	3682.57±42.09
	3p 1/2	2.81±0.04	189.30±0.02	1800.00±40.48
BL	Au 4d 3/2	5.510±0.004	353.18±0.03	43264.20±570.11
	4d 5/2	5.48±0.03	335.27±0.02	63097±532.28
BL	Fe 2p 3/2	3.60±0.09	709.87±0.03	4651.17±159.05
	Fe 2p 1/2	3.82±0.09	723.18±0.05	2754.43±119.41
	Fe Sat. 2p 3/2	6.92±0.13	715.13±0.07	7149.08±242.87
	Fe Sat. 2p 1/2	6.61±0.18	729.38±0.08	3701.90±181.61

Table 4.2: Fit parameters for the different elemental lines and coverages. Shown are the fitted FWHM and the peak position. The data was fitted by using the fitting routine lmfit [334]. The more detailed version of this table is shown in Tab. 7.8.

fitting. This causes a multiplet broadening of the FWHM. The observed strong peak intensity of the Fe 2p satellite peaks arises due to the decreased electronegativity of the ligand (Br) compared to, for example, oxygen [338]. These satellite peaks are related to the shake-up process, due to the electron transfer from a 3d orbital to the empty 4s orbital during ejection of the core 2p photoelectron [336], [232]. The satellite FWHM is around 1.8 times bigger than the core-level FWHM and is in good correspondence to [335]. The Au 4d and Br 3p core-level peaks are not shifted with respect to the literature values for Br (E_B =182 eV for 3p$_{\frac{3}{2}}$ and E_B =189 eV for 3p$_{\frac{1}{2}}$) and Au (E_B =335 eV for 4d$_{\frac{5}{2}}$ and E_B =353 eV for 4d$_{\frac{3}{2}}$) [206]. The extracted area ratios for the Au 4d, Br 3p and Fe 2p peaks are mostly matching with the expected results (Tab. 4.3). In the case of the BL Fe 2p peak, the strong difference is caused by the fitting routine. The fit was optimized for matching FWHM for the two p-orbital peaks.

Element	Area 1/Area 2	Ratio	Literature
Sub-ML Br 3p	1536.77/769.33	1.99	2.0
BL Br 3p	3545.55/1730.90	2.05	2.0
Sub-ML Au 4d	79185.13/51795.23	1.53	1.5
BL Au 4d	67326.69/46789.91	1.44	1.5
Sub-ML Fe 2p	2064.69/1114.03	1.85	2.0
BL Fe 2p	4527.35/2670.97	1.69	2.0

Table 4.3: Measured area ratios for the different core-levels. The sometimes strong variation from the expected value is based on the fit. Here the fit was optimized to have nearly equal FWHM.

The peak height ratio of the core-level to the corresponding satellite peaks of Fe 2p is nearly constant. The ratio for the Fe $2p_{\frac{3}{2}}$ and the corresponding satellite peak is for the sub-ML sample 1.95 and for the BL 1.79. The two ratios are off by around 8 %, therefore they can be considered as nearly identical. The ratio between the $2p_{\frac{1}{2}}$ and the corresponding satellite peak is not constant, since the sub-ML sample has more noise and a weaker signal for this peak. However, by using the background-corrected spectra and not the single fits, a ratio offset of 1.5 % $\left(\frac{1.447}{1.425}\right)$ can be achieved for the Fe $2p_{\frac{3}{2}}$ and the corresponding satellite peak for both coverages. By using the element-specific sensitivity factors, the ratio between Br and Fe can be roughly calculated. From the stoichiometry of the material, a ratio of 1 : 2 is expected for Fe:Br. Shown is the used ratio equation

$$R = \frac{A_{Fe2p}/S_{Fe2p}}{A_{Br3p}/S_{Br3p}} \tag{4.14}$$

, where R is the ratio between Fe and Br and S is the element specific sensitivity factor (atomic sensitivity factor) for an angle of 55 ° ($S_{Fe2p} = 2.957$ and $S_{Br3p} = 1.279$) [32], [206], [339]. For the sub-ML sample a ratio of 0.60 and for the BL sample a ratio of 0.59 was obtained. By using the bulk ($S = 1.14$) and surface ($S = 0.79$) Br values Ref. [340], [341] we obtain $R = 0.53$ and $R = 0.37$ for the sub-ML sample. In the case of the BL sample, values of $R = 0.53$ and $R = 0.36$ were obtained. Another sensitivity factor list is provided in Ref. [342], here the sensitivity factor of Fe 2p and Br 3p are $S = 11.33$ and $S = 5.38$ respectively (combination of the core-level sensitivity factors), with an error of 10 %. By using these values a ratio for the sub-ML and the BL sample of $R = 0.65$ is obtained. Besides the surface approximation in the Wagner paper, all ratios are in good agreement with the expected value of 0.5. A reason for the imperfection is the use of a non-monochromatic x-ray gun, which results in doublet peaks where the extra peaks are displaced towards lower binding energies by 9.8 eV with an intensity percentage of 6.4 % of the real peaks [206].

In Fig. 7.18, the survey spectra for the two different samples are displayed. From these spectra it is clear that the samples have no oxygen or carbon contamination. The shown survey spectra confirm that only the wanted material ($FeBr_2$) is on top of the Au(111) substrate. This is why an increase of intensity can be observed in the Br 3p and Fe 2p region. In the case of the BL sample, an additional peak structure can be observed between 800-900 eV. These peaks are related to the Auger peaks of Fe. In the following an overview of the performed XPS measurements for different sample thicknesses on Au(111) is shown. In Fig. 4.28, the thickness-dependent shift of the photoemission lines of $FeBr_2$ on Au(111) is displayed. Since the XPS measurements are not all taken in the same year, a normalization to the maximum of the Au $4d_{\frac{5}{2}}$ peak was performed. Therefore, the maximum intensity of the Fe 2p and Br 3p spectra are normalized to the maximum intensity of the Au 4d peak. This normalization allows the direct comparison of the different coverages of $FeBr_2$ on Au(111), which were measured at different times (necessary because the XPS used at CFM has a channeltron detector, which degrades over time). Also a different lens setting was used for the newer measurements. In Fig. 4.28 b), the Br 3p spectra for various different coverages are displayed. The coverages presented in a) for the Fe 2p spectra are lower, since the background affects the spectra more strongly for lower coverages and therefore the Shirley background subtraction of the Fe 2p did not work. In Fig. 4.28, the thickness-dependent Fe and Br intensities are displayed. The spectra are all averaged spectra of multiple iterations and normalized by the Au $4d_{\frac{5}{2}}$ peak intensity. With increasing amount of $FeBr_2$, the intensity of the Au 4d peaks is decreasing. As previously discussed, no shift of the Au 4d spectra is observed, but for the Fe 2p and Br 3p above the ML coverage (Fig. 4.28 d)). The displayed Au position is also moving (only minor shifts), but not as much as for Br and Fe. The reason for the Au shift

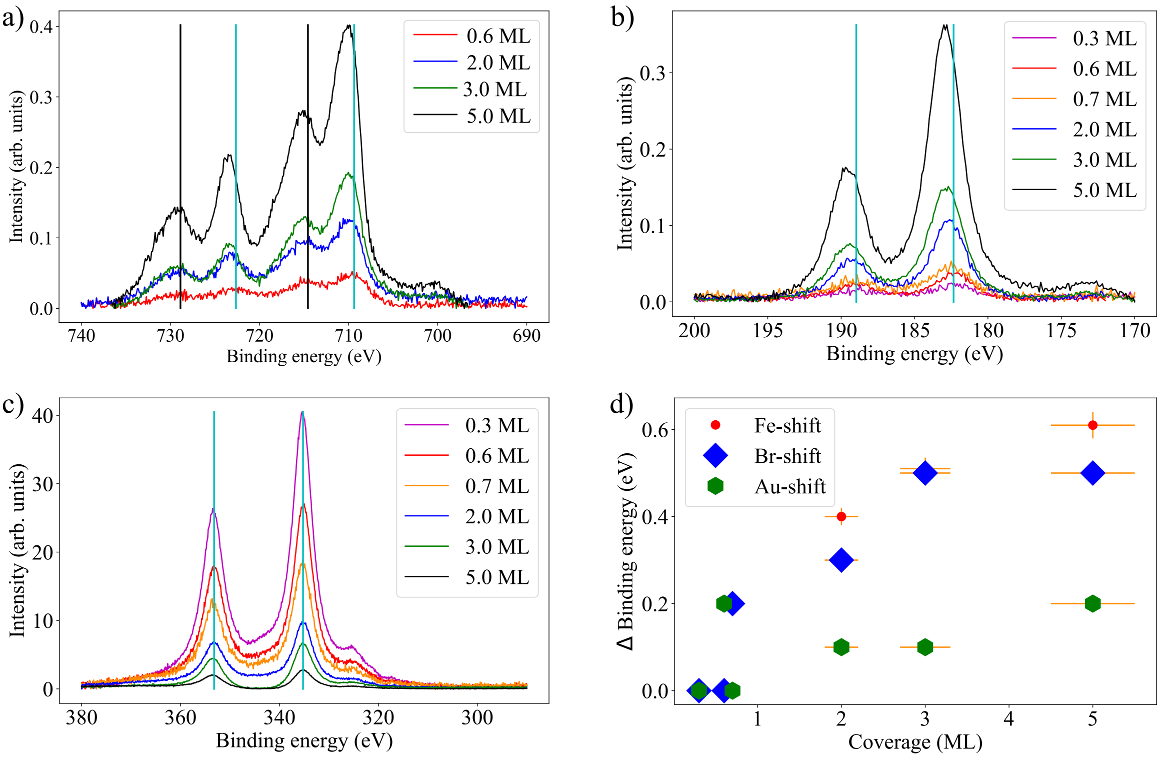

Figure 4.28: a) Fe 2p , b) Br 3p, and c) Au 4d core-level peaks of FeBr$_2$ on Au(111). The cyan-colored lines are indicating the core-level peaks and the black lines the satellite peak position. The vertical lines are used as a guide to the eye and are based on Ref. [206], together with the sub-ML (0.6 ML) measurements. In the case of the Au 4d peaks no shift is observed, but the thicker the sample is, the stronger are the shifts of the Fe 2p and Br 3p lines to higher binding energies. d) shows the relative shift for the different coverages with respect to the lowest coverage position. The displayed shifts are calculated for Au 4d$_{\frac{5}{2}}$, Fe 2p$_{\frac{3}{2}}$, and Br 3p$_{\frac{3}{2}}$. The coverage error in d) is 10 % and the binding energy shift error is 5 %.

could be the noise of the scan as well as the background subtraction.

In Tab. 7.8, the fitting parameters for the spectra of Br, Fe and Au are listed. In the case of the higher coverages (3.0 and 5.0 ML), the fit of the Au 4d spectra did not work perfectly due to a small background correction problem. Therefore, the FWHM values are affected, also the Au 4d spectra is only fitted with the two main peaks and not with the two additional x-ray gun related peaks. This can also cause a different FWHM value for the higher coverage values. In Tab. 7.8 it can be observed that with increasing thickness, the FWHM of the Br 3p core-level peaks are decreasing. This decrease in FWHM can be related to the reduced interaction between FeBr$_2$ and the substrate (Au(111)), since the second layer has a bigger distance to the substrate.

In Fig. 7.19, the ≈1.5 ML FeBr$_2$ on Au(111) is shown. It can be observed that with increasing temperature the peak intensity starts to reduce instantly at around 200 °C. At this temperature, the material reevaporates from the surface. The measurements were performed by using the filament heater of the CFM XPS chamber, without applying HV. The temperature was increased every 18 min by 8 K. In Fig. 7.19 d), the temperature calibration curve of the filament heater is displayed. In Fig. 7.21, the oxidation behavior for a ≈ 0.7 ML FeBr$_2$ film on Au(111) has been investigated by XPS. Here, no different Fe oxidation state has been observed for different amounts of oxygen. However, by keeping a high pressure (10^{-3} mbar) inside the plasma chamber and running the plasma source, the $FeBr_2$ film was completely covered with oxygen and oxidized through. Therefore, it seems like that the $FeBr_2$ film is protective against oxygen (without starting the plasma source) and does not allow the oxygen to physisorb in big amounts on the surface. This was expected, since the oxidation state is very stable for the heavier transition metals like Fe, Co and Ni. However, by running the plasma source at high oxygen pressures the Br is substituted with O and the $FeBr_2$ changes.

The XPS coverage calibration was performed by cross checking the STM images with high-resolution XPS at the PEARL beamline at SLS. The XPS measurements were performed on the 0.95 ML $FeBr_2$ on Au(111) sample. Since the Br 3d peak can not be perfectly resolved on Au(111) with the lab XPS the measurement was performed with the high-resolution XPS at the PEARL beamline. Therefore, not only the main core-level transition of Br in $FeBr_2$ was measured but also the correlation of peak intensity to material coverage was achieved. In Fig. 4.29, the high-resolution spectra of Fe 2p, Br 3p and 3d as well as the Au 4d spectra are displayed. It can be observed that the peak structure as well as the fits are nearly identical to the one performed at CFM. The used photon energy is 950 eV with a work function of 4.5 eV. All scans where recorded with a pass energy of 50 eV and the lens setting $DSF14_08_1$. The measured FWHM for the sample are nearly identical to the ones measured at CFM, however, in the case of the Fe 2p spectra (Fig. 4.29 a)), a second peak was needed to fit the Fe $2p_{\frac{3}{2}}$ signal, since it shows a shoulder. This extra peak indicated the presence of the second layer, which energetically shifts to higher binding energies. Therefore the 0.95 ML (STM calibration) delivers also information about the second layer, which already exists in parallel on the sample even if some parts are still first layer. These are the same results as observed via STM for the 1.75 ML sample.

The core-level ratios are matching the theoretical prediction for the p- and d-orbitals. To calculate the material ratio Fe:Br, a single fit function for each peak is used. Here we only assume the pure Fe $2p_{\frac{1}{2}}$ single peak for the calculation and not a mixed state. By using these values we receive a Fe:Br ratio of 0.66 for Fe 2p to Br 3p ($S_{Br3p} = 1.279$ and $S_{Fe2p} = 2.957$) and 0.62 for Fe 2p to Br 3d ($S_{Br3d} = 1.053$ and $S_{Fe2p} = 2.957$). The ratio is still in good correspondance with the expected value of 0.5. The reason for the different ratios could be in the low growth temperature (around 0-2 °C).

However, the material still shows a stoichiometric growth. A good fit of ML to BL $FeBr_2$ on Au(111) requires five Voigt profiles, which indicates that the second layer is already growing. By only using the main peaks of the first layer without satellite peaks, a Fe:Br ratio of 0.56 for Fe 2p to Br 3p ($S_{Br3p} = 1.279$ and $S_{Fe2p} = 2.957$) and 0.53 for Fe 2p to Br 3d ($S_{Br3d} = 1.053$ and $S_{Fe2p} = 2.957$) can be calculated. However, all these calculations are still within the error range of the expected stoichiometry, since the fits are not perfect and include, for the case of Br 3p and 3d, only two Voigt profiles, which corresponds only to the first layer.

In the case of the XPS measurements with a non-monochromatic x-ray gun, the different layers can not be distinguished. However, the fluctuation in the Fe:Br ratio is a direct consequence of the different layers, but not related to the stoichiometry of $FeBr_2$ on Au(111). In the case of a different stoichiometry, the oxidation states of $FeBr_2$ on Au(111) would be different and this would be recognized by XAS measurements. The only possible Fe and Br compound which has the calculated ratio and is not $FeBr_2$ would be Fe_2Br_3, which has a Br^{1-} state and Fe^{2+} and Fe^{3+} oxidation states. Also the lattice constant measured via STM and LEED would be different as well as the areal density. Therefore, this proves that the material has only one single stoichiometric phase (the one of $FeBr_2$ with Fe^{2+}). Tab. 4.4 the Br 3p:Au 4d and Fe 2p:Au 4d ratios for the

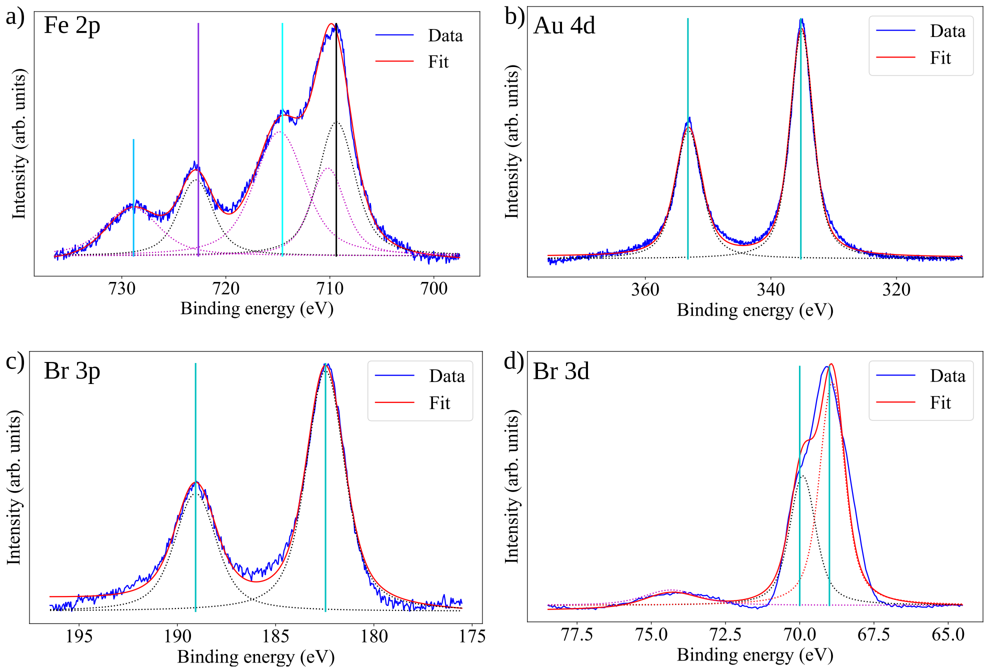

Figure 4.29: a) Fe 2p, b) Au 4d, c) Br 3p, and d) Br 3d core-level peaks of FeBr$_2$ on Au(111). The sample was measured with a photon energy of 950 eV at the PEARL beamline. The final signal at PEARL is not automatically averaged, only added. Therefore, the intensity is afterwards normalized by the number of scans. The vertical lines are guides to the eye and indicate the core-level peak positions of FeBr$_2$ on Au(111).

different coverages.

Coverage	Br 3p : Au 4d	Fe 2p : Au 4d
0.4-0.6 ML	0.025	-
0.7-0.9 ML	0.037	0.049
0.9-1.2 ML	0.053	-
0.95 ML-1.6	0.111	0.132
1.3-2.0 ML	0.101	0.115
2.0-2.3 ML	0.150	0.188
4.0-5.0 ML	0.360	0.397

Table 4.4: Calculated coverage-dependent intensity ratios between the material core-levels and the substrate core-level. As the substrate core-level the Au 4d peaks and for the material the Br 3p and Fe 2p peaks are used. To calculate the ratio, the maximum intensity at the lowest binding energy peak was used.

In Fig. 4.30, the survey spectra of Bi$_2$Se$_3$ measured with an Al and a Mg anode are displayed. For the measurement with either the Al or the Mg anode it can be observed that the substrate peaks of Bi$_2$Se$_3$ are interfering with the Br peaks of FeBr$_2$. In Fig. 4.30, the substrate-related core-level peaks as well as the core-level peaks related to FeBr$_2$ are displayed by the vertical lines. As a result of the measurements with both anodes, it can be observed that a strong C 1s core-level peak is visible as well as a small O 1s peak. The reason for the strong carbon signal is related to

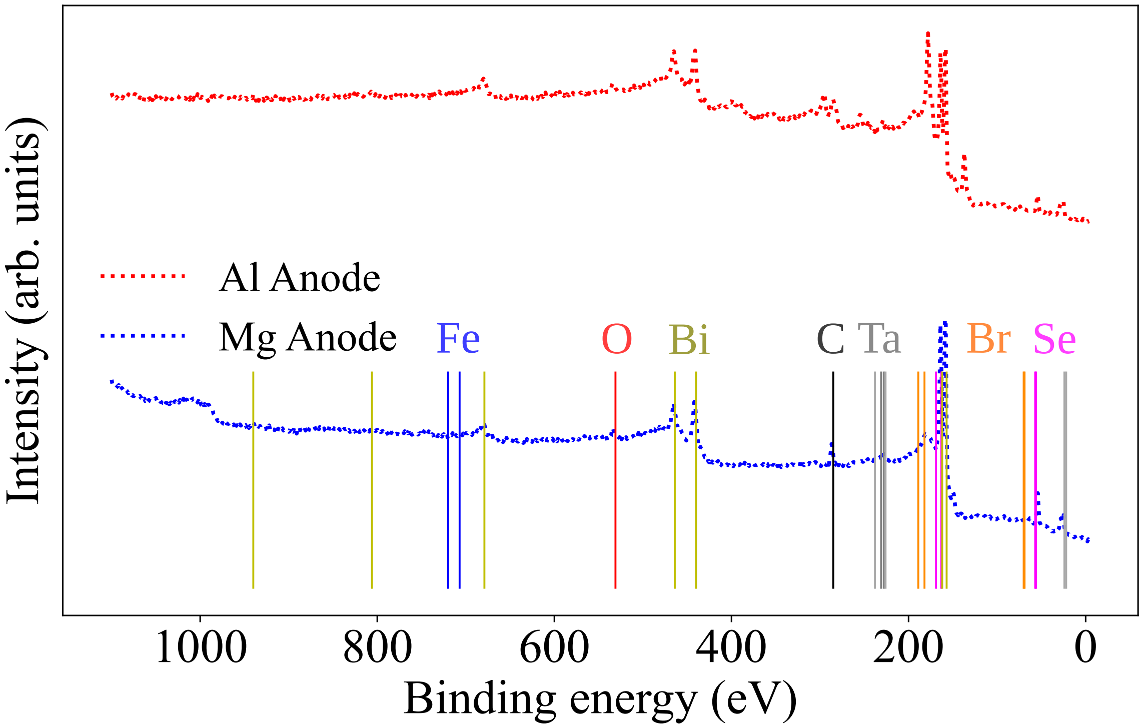

Figure 4.30: Survey spectra for in-situ-cleaved Bi_2Se_3 crystals measured with two different anodes. The vertical lines are guides to the eye and indicate the main core-level positions. Each element has a specific color, which is represented in the fontcolor of the element.

the exfoliation method. Since the exfoliation process can never be perfect, small areas at the edge of the sample are not well cleaved. Therefore, the carbon peaks are only related to the edges of the Bi_2Se_3 crystal and not a surface contamination. Additionally, Ta 4d and Mo 3d peaks can be observed in the spectra, which also contribute to the C 1s and O 1s core-level peaks since the sample plate is never 100 % clean from carbon for an exfoliated sample. On the other hand, a time-dependent oxidation of the Bi_2Se_3 surface has already been studied.

In Ref. [343], it was observed that with increasing time the surface of Bi_2Se_3 starts to oxidize. With increasing oxidation also the top Se layer starts to change and SeO_2 can be observed. In Fig. 4.31, the element-specific measurements of 2 ML $FeBr_2$ on Bi_2Se_3 are shown. In the specific energy range of SeO_2 (Se 3d 58-60 eV), no peak is observed, therefore the measured oxygen peak is not a result of surface contamination, but of either a not perfectly cleaved Bi_2Se_3 crystal (in the crystal corners) or related to the sample plate (including the Ta mounting). In a) and b) the Fe 2p and Br 3d peaks of a 1.5 ML $FeBr_2$ on Bi_2Se_3 sample are displayed. The Fe 2p peaks show the same strength of the satellite peaks for the $2p_{\frac{3}{2}}$ and $2p_{\frac{1}{2}}$ core-level peaks as on Au(111). All spectra are fitted by using Voigt profiles with a previously subtracted Shirley background. In the case of the Fe 2p spectra, four Voigt profiles were needed to fit the data, as already previously observed for $FeBr_2$ on Au(111). In b) the Br 3d region is displayed, which consists of an additional peak, which is substrate-related, at higher binding energies. In c) and d) the substrate-related main core-level peaks (Bi 4d and Se 3d) are displayed. As previously discussed, no additional peaks in the energy range of the Se 3d peaks can be observed, which confirms the surface cleanliness. The positions of the Bi 4d and Se 3d core-level peaks are matching with the literature values for Bi_2Se_3 [343], [344]. In Tab. 4.5, the fitting parameters for $FeBr_2$ on Bi_2Se_3 are displayed. It can

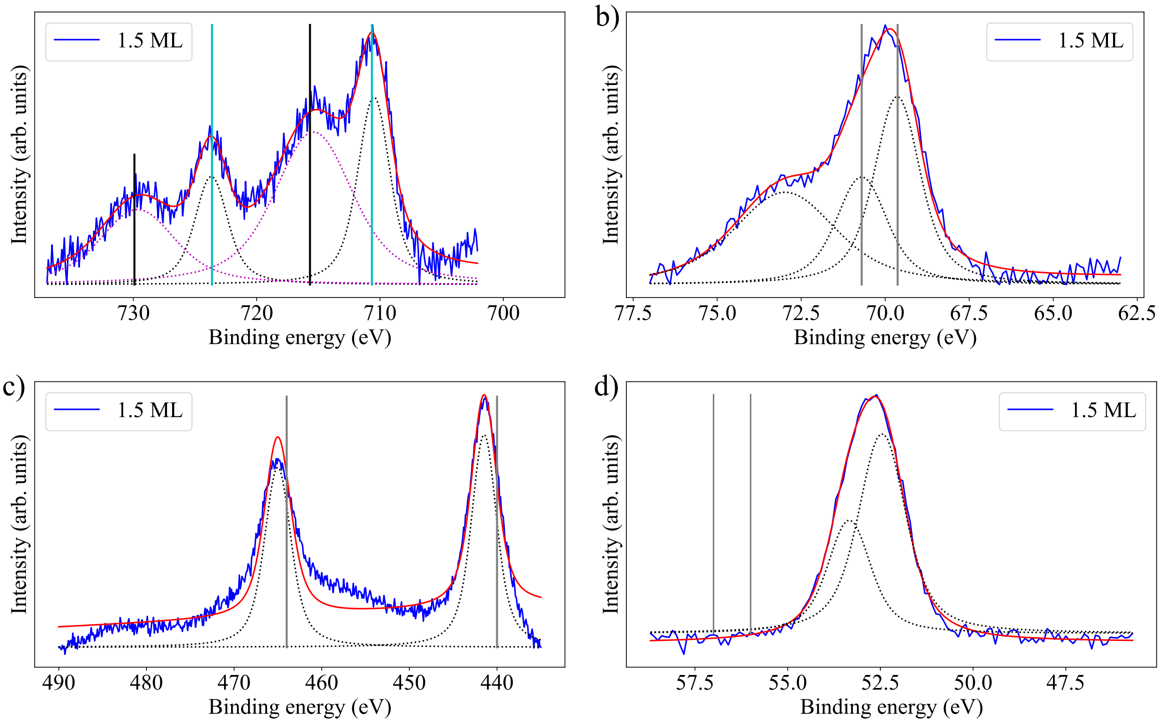

Figure 4.31: a)-d) XPS core-level peaks of 1.5 ML FeBr$_2$ on Bi$_2$Se$_3$. a) Fe 2p, b) Br 3d, c) Bi 4d and d) Se 3d. All spectra were measured with the Al-anode of a non-monochromatic x-ray gun. The vertical lines are guides to the eye and indicate the core-level positions. The mentioned coverage is the estimated maximum value of FeBr$_2$ on Bi$_2$Se$_3$. The real coverage can vary by around ±0.5 ML.

be observed that the values are nearly identical to the ones observed for FeBr$_2$ on Au(111). By comparing the fitting parameters with the ones calculated on Au(111), it can be observed that the energy position as well as the FWHM are matching the values observed for high coverages on Au(111). By comparing different coverages of FeBr$_2$ on Bi$_2$Se$_3$, no thickness-related shift or change of FWHM in the Fe 2p peaks can be observed. In Fig. 4.32, the different coverages of FeBr$_2$ are compared. To compare the intensities, the material peaks were normalized to the Bi 4d peak of the substrate. The Fe 2p peaks are continuously rising in intensity with increasing FeBr$_2$ thickness for different growth conditions. The ML and 1.5 ML sample are grown at 100 °C substrate temperature and the 2 ML was grown at RT. Therefore, the substrate temperature is not affecting the chemical properties like composition of the material. The coverages are an estimation from the observed LEED patterns. However, for these coverages an error of ± 0.5 ML can be assumed. The growth temperature of 100 °C allows an island growth with bigger island sizes, without decomposing the material. This non-destructive effect of the growth temperature was also observed on Au(111), where during the post-annealing the material does not decompose or reevaporate from the surface until reaching around 200 °C (Fig. 7.19). However, the major difference between the substrates can be observed in the peak position as well as in the FWHM of the Fe 2p satellite peaks. On the Au(111) substrate, a constant shift to higher binding energies was observed as a function of coverage until a critical coverage was reached, which was in the multilayer regime. Additionally to the shift to higher binding energies, the FWHM of the Fe 2p satellite peaks are narrowing down by around 1.5 eV. All these effects are not observed on Bi$_2$Se$_3$,

Element	Core-level	Peak position (eV)	FWHM (eV)	Amplitude (arb. units)
Bi	$4d_{\frac{5}{2}}$	441.47±0.03	3.43±0.06	2669.53±74.75
Bi	$4d_{\frac{3}{2}}$	465.02±0.04	3.60±0.12	2367.62±60.95
Fe	$2p_{\frac{3}{2}}$	710.49±0.04	3.12±0.08	317.77±20.77
Fe	$2p_{\frac{1}{2}}$	723.68±0.06	3.17±0.23	185.68±13.06
Fe	$2p_{\frac{3}{2}}$ satellite	715.38±0.13	7.57±0.24	626.25±38.56
Fe	$2p_{\frac{1}{2}}$ satellite	729.66±0.16	7.27±0.44	296.04±41.15
Br	$3d_{\frac{5}{2}}$	69.64	1.62	157.14
Br	$3d_{\frac{3}{2}}$	70.70	1.80	100.00
Substrate peak	-	72.98	3.60	171.39
Se	$3d_{\frac{5}{2}}$	53.75±0.08	1.51±0.05	505.32±85.09
Se	$3d_{\frac{3}{2}}$	54.64±0.11	1.37±0.08	259.99±399.86

Table 4.5: Fitting parameters for the main core-level peaks of Bi, Se, Fe, and Br of the 1.5 ML $FeBr_2$ on Bi_2Se_3 sample. The mentioned coverage is the estimated maximum value of $FeBr_2$ on Bi_2Se_3. The real coverage can vary by around ±0.5 ML. The fitting for the Br 3d spectrum was not giving a error bar, since the peaks are very close and the additional substrate peak is also interfering. The origin of the substrate peak is unknown.

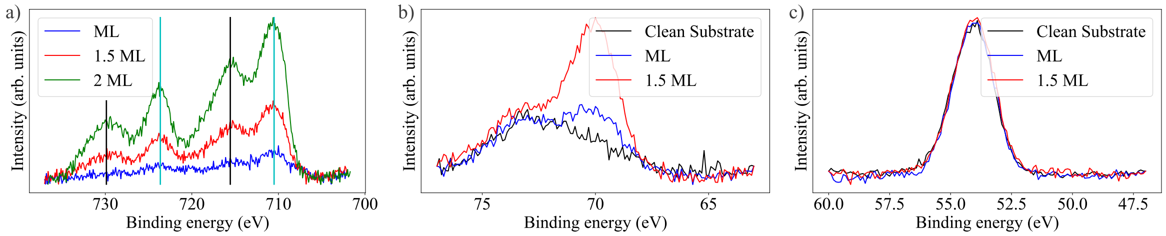

Figure 4.32: a)-c) Coverage-dependent core-level peaks of Fe 2p, Br 3d, and Se 3d of $FeBr_2$ on Bi_2Se_3. In b) and c) the ML and 1.5 ML coverage are compared to the clean substrate. All spectra are normalized to the maximum peak intensity of the Bi $4d_{\frac{5}{2}}$ peak. The ML and 1.5-ML samples were grown at elevated temperatures of ≈ 100 °C, and the 2-ML sample at RT. The vertical lines in a) are a guide to the eye and indicate the core-level binding energy positions. For all coverages the peak maxima do not shift to higher binding energies. The mentioned coverages are the estimated maximum value of $FeBr_2$ on Bi_2Se_3. The real coverage can vary by around ±0.5 ML.

which means that the material grows identical in electronic properties for all coverages from sub-ML to multilayer samples. As a direct consequence of the observation on a vdW substrate, the Au(111) substrate causes changes of the material properties as also visible in the first-layer LEED and STM images. Therefore, the observed shift is not only the indication of the work function change, since the sample is behaving more insulating, but also shows that the electronic properties of the first layer are strongly affected by the Au(111) substrate.

4.1.5 Magnetic characterization

In the following sections, the performed magnetic measurements as well as the XAS cross check of the material coverage will be explained. The majority of samples were measured at the BOREAS beamline at ALBA.

Thickness calibration via XAS

For the sample thickness determination, different structural techniques (LEED and STM) were used. To calibrate the thickness from spectroscopic techniques, we cross-correlated the coverage information measured at the beamlines with the XAS whiteline height or the normalized peak intensity in XPS. The XAS calibration is based on the comparison with another Fe^{2+} molecule on Au(111) (Ref. [345]). The first step to calculate the sample coverage is to calculate the areal density of Fe in $FeBr_2$. Therefore, an equilateral triangle with a length of 3.776 Å is used, since the Br-Br or Fe-Fe distances are equal [124], no difference between the different part of the slab needs to be considered.

Each triangle contains 0.5 Fe atoms. Therefore, the geometrically calculated areal density of 8.344 $\frac{\text{Atoms}}{\text{nm}^2}$ by using the literature lattice constant of $a = 3.776$ Å for $FeBr_2$. When using the measured lattice constant of a =3.66 Å, an areal density of 8.098 $\frac{\text{Atoms}}{\text{nm}^2}$ is calculated. For the following calibrations, we used the areal density based on the measured lattice constant. To calibrate the thickness, the areal density in Ref. [345] is used to calculate the conversion factor (9.87 ($\frac{\text{FeBr}_2\ 8.10}{\text{Fe molecule } 0.82}$)). Since the measurements in Ref. [345] were performed with linear polarized light under an angle of $54.7 \approx 55$ ° (magic angle for linear polarized light), the same conditions were reproduced for our measurements.

The calibration measurement was performed at both beamlines to check the method, since the needed measurement at the VEKMAG beamline was performed inside the preparation chamber. The sub-ML $FeBr_2$ sample was measured by using linear polarized light under an angle of 55 ° (magic angle) at RT and without applying an external field. Therefore, no contribution of different polarization's on the different d-orbitals is contributing to the spectrum, since they are all equal at this angle. In Fig. 4.33, the magic-angle measurement performed at the VEKMAG beamline is shown. The calculated coverage of the sub-ML sample is in good agreement with the expected coverage from LEED.

The VEKMAG sample showed a peak intensity of around 11 % for the pre-edge normalized Fe L_3 peak. In the case of the $Fe(bpz)_2(phen)$ molecule measured in Ref. [345], an edge jump of 1.2 % was determined for a 0.8-ML sample. Therefore, the approximated peak height for the sample measured at BESSY is 0.7 ML. However, this does not mean that the sample has exactly this thickness, since the second-layer growth can already have started in some regions of the sample (since the third set of LEED spots was observed). This is based on the fact that the material likes to grow in compact islands and not perfectly uniform all over the sample. In Fig. 7.27, the angle dependence of the isotropic XAS spectra with linear polarized light is shown. It reveals, that the peak intensity does not strongly depend on the angle for Fe^{2+}. The assumed θ angle error is 1 °, since the angle calibration at NI is based on the sample alignment by eye. For the intensity error, 10 % is assumed, since for low coverage the background correction can affect the signal intensity in this range. The calculated coverages for all $FeBr_2$ samples on Au(111) mentioned in this thesis which were measured via XAS are displayed in Tab. 4.6, together with the corresponding peak height of the isotropic XAS spectra. The performed coverage calibration at 55 ° is afterwards adjusted to the low-temperature spectra of the sample. Therefore, the 0.7-ML sample which was measured at VEKMAG has a peak height of 14 %. Since the coverage error for the material is

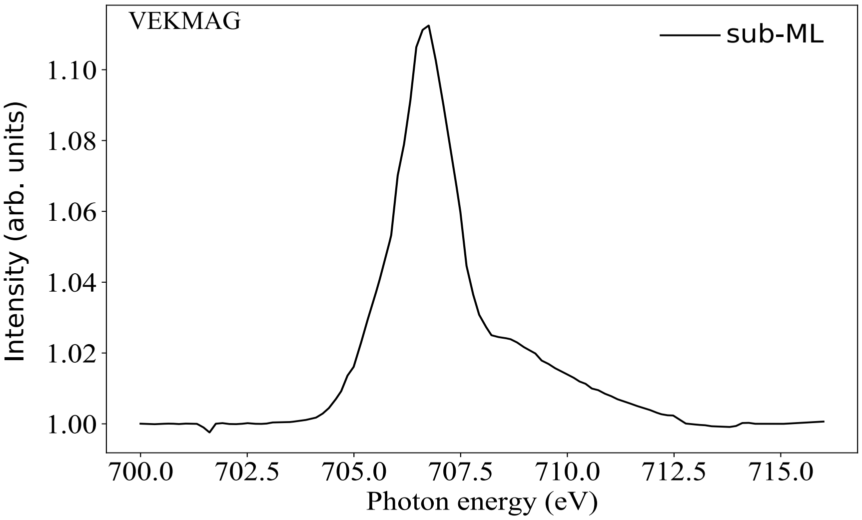

Figure 4.33: Sub-ML $FeBr_2$ on Au(111) XAS spectrum measured with linear polarized light at RT without applying an external field under an angle of 55 ° at the VEKMAG beamline in 2021. The figure is adapted from Ref. [32].

composed of different errors, like the background subtraction and the resulting XAS height as well as the used lattice constant, a relative error of around 20-25 % is assumed.

Beamline	Year	C (ML)	PH
BOREAS	October 2020	0.6	0.12
BOREAS	May 2021	0.15	0.029
BOREAS	May 2021	1.5	0.30
BOREAS	May 2021	2.0	0.4
VEKMAG	April 2021	0.7	0.14
VEKMAG	April 2021	2.9	0.58
BOREAS	March 2023	0.3	0.058
BOREAS	March 2023	0.5	0.105
BOREAS	March 2023	0.3	0.051
BOREAS	March 2023	2.9	0.57
BOREAS	July 2023	0.8	0.156
BOREAS	July 2023	0.7	0.1311

Table 4.6: Coverages of the different samples of $FeBr_2$ on Au(111) measured at the BOREAS and VEKMAG beamlines. The abbreviation C stands for coverage and PH for peak height. The peak height is measured relative to the normalized pre-edge intensity of the average XAS spectrum for each sample measured at NI and lowest temperature. In the case of the BOREAS and VEKMAG samples the lowest temperature is nominally 2 K and 10 K, respectively.

Magnetic properties of $FeBr_2$ on Au(111)

The magnetic properties for different coverages of $FeBr_2$ on Au(111) were investigated via XAS and XMCD. In Fig. 4.34 a), the average/isotropic XAS spectra for different coverages are shown.

In the following parts the helicity-averaged XAS spectra are named "isotropic". In general this naming would not be correct, since the XAS spectra at NI and GI are changing as for Fe OEP on Cu(001) [346] or FePc on Au(111) [347]. However, in the case of $FeBr_2$ on Au(111) as well as on Bi_2Se_3, no difference between the two geometries can be observed. A similar phenomenon has been observed for molecules with an octahedral symmetry. The isotropic XAS spectrum is the average of the two different circular polarization's at 6 T $\left(\frac{\sigma^+ + \sigma^-}{2}\right)$, which corresponds to the XAS spectra, without magnetic contributions. Since the samples were measured in different years, the edge position needed to be aligned, due to minor energy shifts in the beamlines. The samples with a coverage of 0.6 ML, 1.5 ML and 2.0 ML were measured in the years 2020 and 2021. These samples needed to be aligned the strongest with an energy shift ranging from -0.75 eV to 0.5 eV. The samples are all aligned to the 0.6-ML sample like in Ref. [32]. The mentioned coverages are based on the VEKMAG calibration. In b) and c) only the Fe L_3 and L_2 edges for the different

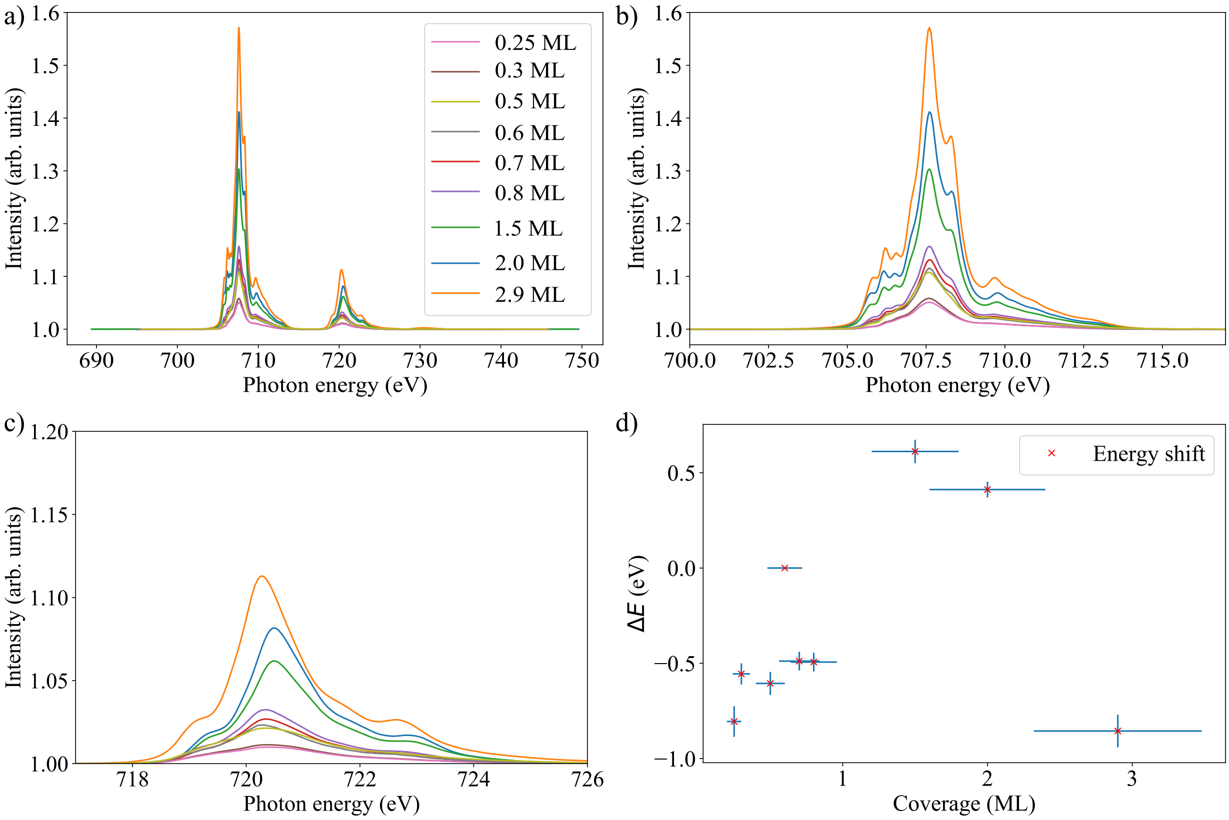

Figure 4.34: a) Isotropic XAS spectra of the Fe $L_{2,3}$ edges of $FeBr_2$ on Au(111) for different coverages ranging from 0.25 ML to 2.9 ML. b) and c) Zoomed-in region of the Fe L_3 and L_2 edge, respectively. d) Applied shift corrections for all spectra. All displayed spectra were measured at NI and at 2 K, with an applied external field of 6 T. The energy shift has a relative error of 10 % and the coverage of 20 %. The measurements were all performed at the BOREAS beamline at ALBA. All spectra are corrected to the position of the Fe L_3 edge for the 0.6 ML coverage as in Ref [32]. The sample with a coverage of 0.6 ML was measured in 2020, the ones with 1.5, and 2.0 ML were measured in 2021, and the other samples were all measured in 2023 during two beamtimes in March and July.

sample coverages are shown. Here it can be observed that the peak/multiplet structure as well as the peak ratios are not changing for the different coverages, only the intensity due to the different amount of material.

In Ref. [348] the identical peak structure was observed for $FeCl_2$ which has a Fe^{2+} oxidation state [349], [350]. Since the peak structure does not vary for different thicknesses or as a function of temperature, this confirms the observation of the XPS analysis. Therefore, the films are growing uniformly with Fe^{2+} ions in a octahedral coordination and with only one composition [32]. In Fig. 4.35 a), the XAS spectra of a sub-ML, BL, and TL sample are displayed together with the nominal energy position of the Fe L_3 and L_2 edges for an Fe^{2+} oxidation state with octahedral symmetry. The spectra in this figure are aligned to the 2.0 ML sample, since the peak structure is better resolved for a higher coverage and the material is still less insulating than the 2.9-ML sample. However, the energy position is less indicative, since the shift correction is performed in relation to one spectra and since the shifts can have multiple reasons. Nevertheless, the peak structure is giving an indication about the oxidation state with octahedral symmetry. This information together with the fact that the peak structure does not change for first and second-layer and that no different phases within each layer have been observed, are leading to the conclusion that the material is present in an Fe^{2+} oxidation state. In b) the simulated XAS spectra for an Fe^{2+} and Fe^{3+} state with octahedral symmetry are displayed. The simulation was performed by using the software Crispy [351]. It is visible that in the case of an Fe^{3+} state, the L_2 edge shows a completely different peak structure than for the Fe^{2+} state. By comparing the main peak features and the energy distances for the measured spectra with the simulated Fe^{2+} state, a similarity can be observed, which leads to the interpretation of a Fe^{2+} state with octahedral symmetry. However, a main difference between the simulation and the measured spectra are the intensities of the multiplet side peaks. Nevertheless, the simulation can not exactly

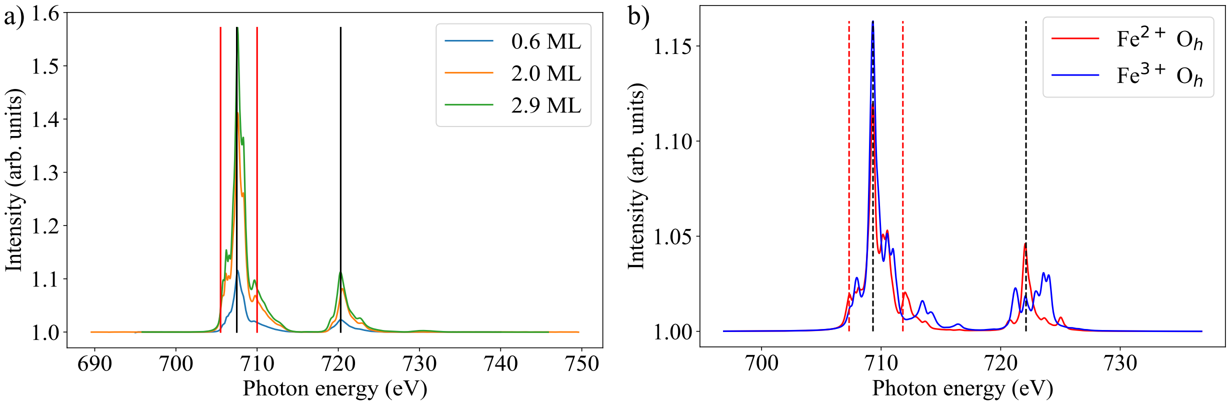

Figure 4.35: a) Isotropic XAS spectra for different coverages. The spectra were measured at 2 K and 6 T at NI. The vertical red and black lines correspond to the multiplet and edge peaks of Fe^{2+}. All samples were measured at the BOREAS beamline at ALBA. b) Simulated XAS spectra for Fe^{2+} and Fe^{3+} states with octahedral symmetry. The red and black lines are corresponding to the ones in a). The simulations were performed by using a crystal electric field (10 Dq) of 1 eV. As environmental parameter, an external field of 6 T OoP and a temperature of 2 K is used. The used scale factors for Fe are $F_k = 0.8$ (Slater radial direct integral), $G_k = 0.8$ (Slater radial exchange integral), and $\chi = 1.0$ (Spin-orbit coupling integrals). The final parameters are $F_2(3d, 3d) = 11.780$, $F_4(3d, 3d) = 7.328$, $\Gamma(3d) = 0.067$, and $\Gamma(2p) = 8.201$.

identify the symmetry of the material, therefore, the octahedral symmetry (same as for the bulk material) is used as default. The red and black lines in Fig. 4.35 a) and b) are representing the side peaks which are known for an Fe^{2+} state with octahedral symmetry [345], [352]–[355]. Another important information which can be extracted from the XAS spectra is the spin state of the material, which is necessary to pre-evaluate the possible magnetic moment of the material. In the case of FeBr$_2$, the XAS spectra are showing the peak structure for an Fe^{2+} HS state [356]. Therefore, a magnetic moment of $\mu_s = 4\,\mu_\mathrm{B}$ can be expected as a result from Hund's rule.

In Fig. 4.34 d), the beamline-dependent energy shifts are displayed. Since the spectra were measured at different beamtimes ranging from 2020-2023, the beamline energy calibration may have changed during this time. In Tab. 4.6, the beamtime-related measured coverages are listed. Another possible reason for the observed shifts can be that the work function changed. These possible reasons, together with the constant monochromator movement during XAS and magnetization curve measurements, are the most probable reasons for the shift. The background subtraction, which was performed for the isotropic XAS spectra, is based on an asymmetrically reweighted penalized least-squares smoothing [357].

In Fig. 4.36, the temperature-dependent XMCD spectra of the 2.0-ML sample are displayed together with the corresponding isotropic XAS spectrum. It can be observed that the XMCD spectra in the low-temperature range between 2-7 K (shown are the spectra for 2-4 K) are stable. In Fig. 4.36 b), this stability of the XMCD signal is displayed for 2 K and 4 K. However, by exceeding the antiferromagnetic ordering temperature around 10 K, the intensity of the XMCD spectra is continuously dropping, as displayed for the temperatures of 25 and 40 K. To confirm that the intensity decrease is purely temperature-related and not related to any x-ray damage or to a different sample position, the isotropic XAS spectra for the same temperatures are displayed. Here it is visible that the peak structure as well as the peak intensity are not changing for the different temperatures. In Fig. 4.37 a), the XMCD spectra for different coverages are shown. It can be observed that with increasing coverage the XMCD intensity is also increasing, which is expected due to the increased amount of Fe. In b) and c) the signal strength of the Fe XMCD at the L$_3$ and L$_2$ edges is displayed as a function of coverage. It can be observed that the behavior is linear for both edges as well as for the corresponding area in d). All displayed spectra where measured at 6 T and NI. By using the sum rules, we can calculate the magnetic moment at 6 T.

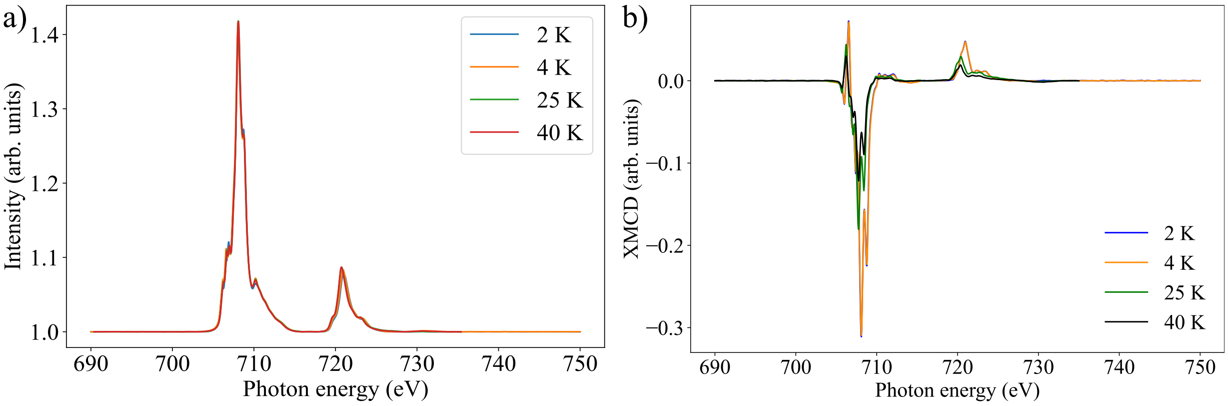

Figure 4.36: a) Isotropic XAS spectra for the different temperature ranging from 2 K to 40 K. b) XMCD spectra of the 2.0-ML sample at different temperatures. The spectra were all measured at NI and 6 T. All measurements displayed in a) and b) were performed at the BOREAS beamline in 2021.

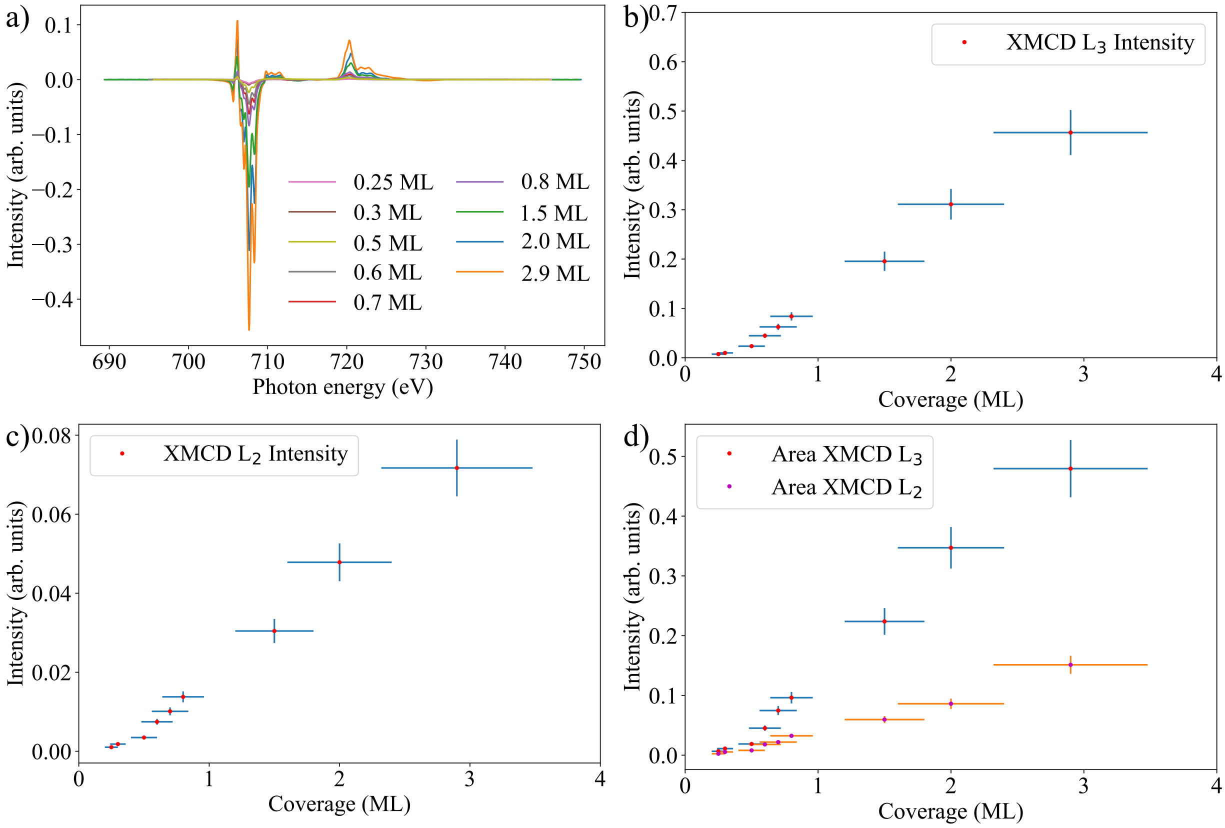

Figure 4.37: a) XMCD spectra for different coverages of $FeBr_2$ on Au(111). The XMCD spectra are all aligned with respect to the 0.6-ML sample and the coverages are based on the VEKMAG calibration. The coverages in this figure are ranging from 0.25 ML to 2.9 ML. In b), c), and d) the XMCD intensity at the L_3 and L_2 edges as well as the respective areas at the two edges are displayed as a function of coverage. All XMCD spectra are normalized to the XAS peak height. The coverage error is 20 % and for the intensity of the XMCD, a 10 % error is used due the spectral background.

In Fig. 4.38, the effective spin, orbital, and total moment for all different coverages at lowest temperature and 6 T are displayed. By comparing the behavior of the calculated moment values with the behavior of the XMCD intensity (Fig. 4.37), it is visible that they are different. In the case of the XMCD intensity, a linear trend can be observed, which is a direct consequence of the increased amount of material. Here, the XMCD spectra are normalized to the maximum peak height of the XAS signal. For the calculated moments, two trends are visible. The first trend is related to low coverages, here the calculated moments are very weak, which can be a combination of several factors. For coverages of around 0.25 ML, superparamagnetism can play a role in the moment reduction, however, with increasing amount, this can not be the case anymore. For higher coverages starting from 0.4-0.5 ML, the island size is big enough to neglect the contribution of superparamagnetism. Therefore, the behavior is probably more related to spin frustrations. If the coverage overcomes the ML regime and is closer to the BL case, the moment saturates to a value around $m_{s_{eff}} = 2.2\,\mu_B$, which is only around 50 % of the expected value by Hund's rule for a HS Fe^{2+} state with octahedral symmetry for a magnetically saturated system. Nevertheless, in a purely octahedral system, the orbital magnetic moment contribution should be zero, which is not the case for this material at any coverage. In Fig. 4.39, the total magnetic moment of the

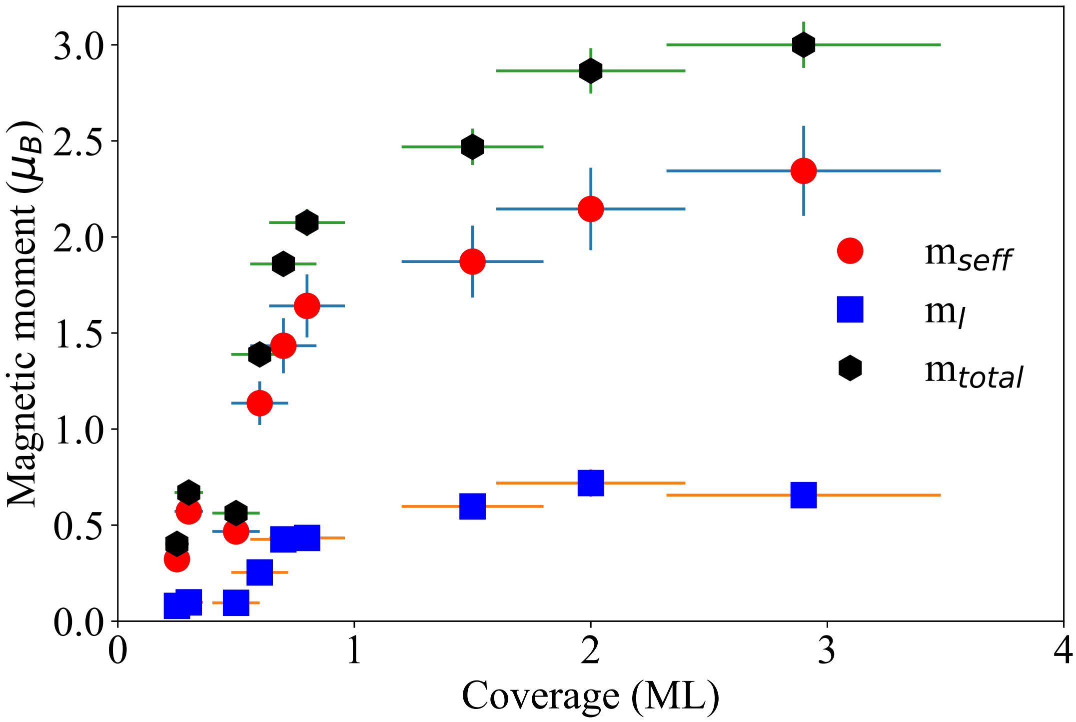

Figure 4.38: Coverage-dependent effective spin, orbital and total magnetic moment at 6 T, 2 K and NI. All moments were calculated from measurements performed at the BOREAS beamline at ALBA. The error for the effective spin and orbital moment is 10 % and for the total moment the error was calculated via Gauss error calculation. The x-axis error is around 20 %.

2.0 ML FeBr$_2$ on Au(111) sample as function of temperature is shown. Since the 2.0 ML sample contains magnetic information of the first and second layer, the analysis of this heterogeneous magnetic system is not straightforward. However, some information about the magnetic order can be already extracted from the temperature dependence of the magnetic properties. In Fig. 4.39 a) and b), the expectation value of the total magnetic moment of the 2.0 ML sample and the corresponding inverse total magnetic moment as a function of temperature are displayed. The calculated values where extracted via sum rules under the assumption of an calculation error of 10 % [358] in the case of the Fe L edge. In the case of the paramagnetic state, $1/m_{total}$ is proportional to the susceptibility measured in the field 6 T [32]. This is the case if the temperature is high enough, so that the magnetization curve behaves linear as a function of the field, as shown in Fig. 4.40 b) for $J = 2$ at T $\geq$ 17 K. The linear fit of the inverse total magnetic moment (4.39 b)) in the high-temperature regime above 17 K leads via extrapolation to an ordering temperature of ~ -10 K, well below the reported value for the bulk material of 3.5 K [32], [124]. Therefore, the negative sign could be an indication of an antiferromagnetic behaviour of the material. In Fig. 4.39, the total magnetic moment of the 2.0 ML FeBr$_2$ on Au(111) sample is compared to the Brillouin function. In a) the total magnetic moment data were fitted by the Brillouin function for two different starting temperatures. By only using the expectation value of the magnetic moment above the ordering temperature the Brillouin function fits to the experimental results in

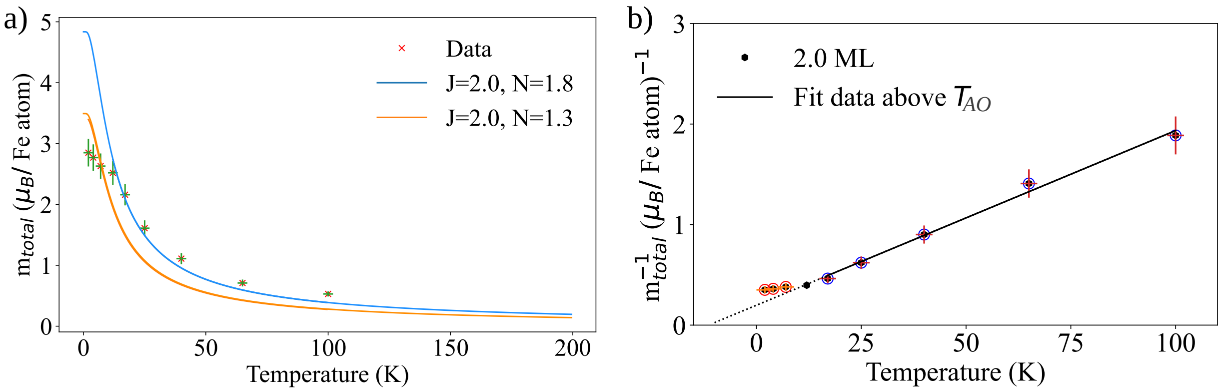

Figure 4.39: a) Total magnetic moment values extracted from the XMCD and isotropic XAS spectra of the 2.0-ML sample at NI and 6 T. The moments were calculated by using the sum-rule equations Eq. (4.17). The blue and orange lines show Brillouin function fits for different N values with $J = 2$. The blue fit is using the data starting at 12 K and the orange one includes the measurements at lower temperatures (down to 2 K). b) Inverse total magnetic moment values as a function of temperature. The hollow blue circles represent the data which were used for the linear fit of the high-temperature regime (17-100 K > T$_{\mathrm{AO}}$). The excluded data points are displayed in red. A slope of $0.017 \pm 0.001 \left(\frac{\mathrm{K}\cdot\mu_\mathrm{B}}{\mathrm{Fe\ atom}}\right)^{-1}$ and a linear intercept of $-0.198 \pm 0.049\, (\frac{\mu_\mathrm{B}}{\mathrm{Fe\ atom}})^{-1}$ ($\chi^2 = 0.01$) give the estimation of an antiferromagnetic ordering temperature of -10 ± 1 K [32]. The chosen temperature range for the performed fit was based on the fact that the lowest used temperature is far away from saturation of a Brillouin function in a $J = 2$ system. At 17 K, x would be 1.9 (not in saturation, see Fig. 4.40 b)). The figure is taken from Ref. [32] and was slightly modified. The displayed coverage error is 20 % together with 10 % error for the effective spin magnetic moment and the orbital moment. The error for the total moment is calculated via Gaussian error propagation.

the temperature regime from 12-100 K (Fig. 4.39 a) blue curve). We observe a slope change of the m_{total} vs. T curve at $\sim 7-8$ K, in contrast to the behavior expected from a paramagnetic system with $S = 2$, supporting the presence of magnetic correlations in the 2.0 ML sample [32]. By assuming a simple antiferromagnetic model, where $\frac{1}{\chi}$ (χ is the susceptibility) is proportional to $T + T_C$, an antiferromagnetic ordering temperature T_C can be extracted as 10 K (Fig. 4.39 b)). This is in good agreement with the measured data, since the slope change of $\frac{1}{m_{\mathrm{total}}}$ is appearing in this temperature regime. In Fig. 4.40 a), the Brillouin functions for four different J values ranging from 1 to 4 at temperatures of 17 and 25 K as a function of field are displayed. Besides for $J = 4$, all Brillouin function curves show at these temperatures a linear behavior in the field range up to 6 T. The N value is the scaling factor, which is reduced for $J = 4$ to have an easier comparison for the different J values. In b) an exemplary Brillouin function for $J = 2$ and a maximal field strength of 6 T is displayed. The vertical lines in b) and c) indicate the x values for a field of 6 T at different temperatures. The previously discussed temperature of 17 K is far from saturation, as shown in b). In c) the Brillouin function for different J values is plotted and the vertical lines, which are corresponding to the calculated x values, are inserted. It is visible that the x value for 17 K at $J = 1$ is closer to saturation. However, since the value of $J = 1$ is physically unreasonable,

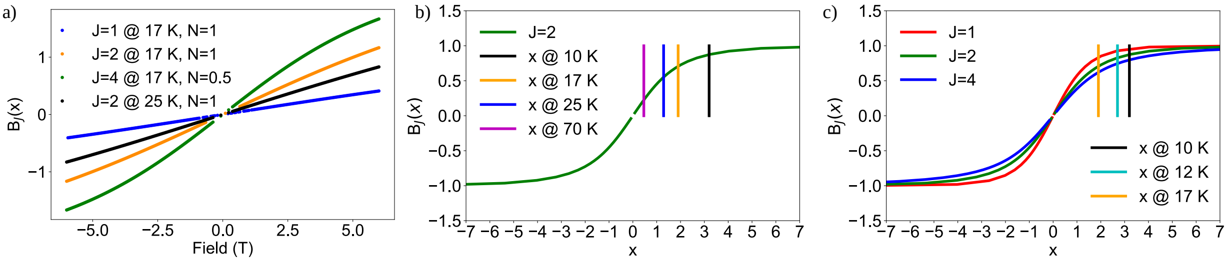

Figure 4.40: a) Brillouin functions for $J = 1$, $J = 2$, and $J = 4$ for a temperature of 17 K as well as for $J = 2$ and 25 K as a function of magnetic field. b) Brillouin function for $J = 2$ as a function of x. The vertical lines represent the values of x for a field of 6 T and temperatures of 10 K, 17 K, 25 K, and 70 K. c) Brillouin functions for different J-values. The vertical lines mark the x values for the field of 6 T at temperatures of 10 K, 12 K, and 17 K. It is clearly seen that at 17 K the field of 6 T is not enough to come close to saturation. The figure is taken from Ref. [32].

this system can be ignored. The x values are calculated via equation (4.15).

$$x = \frac{J \cdot g \cdot B \cdot \mu_B}{k_B \cdot T} \tag{4.15}$$

, where J is the total angular momentum quantum number, g is the g-factor, B the magnetic field, T the temperature, k_B the Boltzmann constant, and μ_B the Bohr magneton. In Fig. 4.39 a), the calculated total magnetic moment values at 6 T for the 2.0-ML sample as a function of temperature are fitted with the Brillouin function for two different temperature ranges (Eq. (4.16)).

$$M = N \cdot g \cdot J \cdot \left(\frac{2 \cdot J + 1}{2 \cdot J} \cdot \coth\left(\frac{2 \cdot J + 1}{2 \cdot J} \cdot x\right) - \frac{1}{2 \cdot J} \cdot \coth\left(\frac{1}{2 \cdot J} \cdot x\right)\right) \tag{4.16}$$

, where M is the magnetization and N is the scaling factor. The orange curve uses a temperature range starting from 2 K and the blue from 12 K for the fit. It can be observed that the decrease of the magnetization as a function of temperature is always steeper for the Brillouin function than for the experimental data, which points towards antiferromagnetic interactions in the experimental data. In Tab. 7.9 the calculated expectation values at 6 T at different coverages and temperatures of the effective spin, orbital, and total magnetic moment are listed. The expectation values for the effective spin ($m_{\mathrm{s\ eff}}$), orbital magnetic (m_l), and total magnetic moment (m_{total}) were obtained by using the sum-rule calculation based on the area of the isotropic XAS spectra ($A_{\mathrm{Isotropic}}$) and the L$_3$ and L$_2$ -edge of the XMCD spectra (A_{L_3} and A_{L_2}). In equation (4.17) and equation (4.18) the sum rule equations for the magnetic moments are shown [262]–[264], [266].

$$m_{\mathrm{s,eff}} = -\frac{A_{L_3} - 2 \cdot A_{L_2}}{A_{\mathrm{Isotropic}}} \cdot N_H \cdot \frac{1}{\sigma} \tag{4.17}$$

$$m_l = \frac{-2}{3} \cdot \frac{A_{L_3} + A_{L_2}}{A_{\mathrm{Isotropic}}} \cdot N_H \cdot \frac{1}{\sigma} \tag{4.18}$$

The term N_H stands for the number of holes (= 4 for Fe^{2+} in FeBr$_2$) and σ stands for the degree of circular polarization, which is beamline-dependent (VEKMAG 77 % [294] and BOREAS 99.9 % [297]). The used equation for the expectation value of the spin magnetic moment at 6 T does not include the dipole term $\frac{7}{2} \cdot T_z$, that is why the calculated values are called effective spin magnetic moment. The calculated moments for different coverages and temperatures show a trend. The moment for samples with an increased coverage (above one ML or mixture of first and second layer) show a stabilization of the total magnetic moment of around 3 μ_B and the effective spin magnetic moment of around 2 μ_B. The obtained antiferromagnetic ordering temperature, which can be extracted from Tab. 7.9, is around 10 K, which was also visually observed in Fig. 4.39.

In Fig. 7.31, the field-dependent XMCD measurements at a temperature of 10 K are displayed. Here, it can be observed that above the antiferromagnetic ordering temperature of 10 K the material becomes paramagnetic. Between the lowest temperature and the temperature around 8 K, the calculated moments are relatively stable within the error. In Fig. 7.33 b), the magnetization curve of the 2.0-ML sample shows also a stable magnetic behavior for the measured temperature range up to 7 K. In the case of lower coverages (0.6-1.5 ML), the magnetic moment is a mixture of the moments obtained for the first and the second layer. This is a direct consequence of the fact that XMCD measurements are probing the information of a big surface area, which only yields to an averaged value. Even if the listed coverage values are indicating no second layer growth, it needs to be taken into account that the material coverage is not perfectly uniform and the next-layer growth can already start in some places. The mentioned coverage values are related to the STM and LEED calibration, but are also taking the VEKMAG and BOREAS measurements into account. Therefore, these values have, like previously mentioned, an error of 20 % for the high-coverage samples, but a higher error of 0.4 ML is assumed for lower coverages. This is also confirmed by the LEED measurements performed on these samples, where the third set of spots of the (1,0)-spot as well as the start of the moiré pattern can be observed. The samples with an even lower coverage are only showing the properties of the first layer, which is affected by the substrate interaction. For lower coverages the moments are way lower and are even not completely stable in similar coverage regimes. However, the difference in the strength can have different reasons, starting with superparamagnetic properties for very low coverages, which cause a strong reduction of the expectation value of the magnetic moment at 6 T. Another possible reason for this strong reduction is the substrate interaction. Here the electrons of the first layer can be strongly delocalized due to the Br-Au interaction.

In addition the metallic substrate can also cause shielding effects, which are reducing the observed moments. In the case of TMDH with Br as halide material, this Br-Au interaction cannot be neglected, since the Ullmann coupling between Au and Br was well investigated over the last decades [33], [327], [359], [360]. A reason for the moment fluctuation is the low peak intensity and the strong background, which can cause errors bigger than the typical 10 %, which are always valid for the moment calculation of Fe. By comparing the strongly reduced moments with the multiplet peak structure of $FeBr_2$ for different coverages, it can be observed that for the low-coverage samples below 0.7 ML one of the multiplet peaks at higher photon energies compared to the L_3 main peak is not visible. This peak starts to appear clearly for samples with a larger second-layer coverage (1.5 ML), which is an $FeBr_2$ layer with less or no substrate interaction.

However, this peak has been observed for other samples with an Fe^{2+} oxidation state and octahedral symmetry on HOPG [295], even for samples with less coverage and even less Fe. Therefore, the weak intensity of this peak is not related to the measurement technique nor the material amount. The reason for the peak intensity reduction is related to the Au(111) substrate. Either the interaction of Au(111) with the material is changing the electronic properties or the suppression of the peak intensity is background-related. From the fact that the Au(111) background in this energy range is nearly linear, the background should not be the reason for this change. Since the same peak is suppressed for some Fe spin-crossover molecules on Au(111) (Ref. [345]), the substrate interaction is the probable reason.

In Fig. 4.34 b), the coverage-dependent peak evolution for different $FeBr_2$ coverages can be observed. The calculated moment for the different sub-ML samples are all in the same range and are not affected by a longer storage time (0.6 ML transferred via vacuum suitcase to the beamline at $\approx 1.5 \cdot 10^{-9}$ mbar). This was tested by comparing samples which where grown in situ directly at the BOREAS beamline with a sub-ML that was transferred from a suitcase (prepared at CFM). Since the properties were identical, we can exclude that the reduced moments or magnetization is the result of any surface contamination, since oxygen would create a mixture of different oxidation states and as previous shown only substitutes Br in plasma environment.

The expected spin magnetic moment values based on Hund's rule are larger by a factor of around 2 compared to the BL sample. Since the magnetic moment of the first layer is affecting the moment results, the pure moment of the second layer can be calculated. This calculation is only valid in the case that the first and second layer are treated as the material with the same structure and that the reduction of the moment is a pure interaction effect. For the case of the 1.5 ML sample, the calculation reveals under the assumption of identical first and second layer a moment of 3.3 μ_B (Eq. (4.19)).

$$m_{seff,1.5ML} = \frac{2}{3} \cdot m_{seff,0.6ML} + \frac{1}{3} \cdot x \tag{4.19}$$

, where x is the effective spin magnetic moment at 6 T for the second layer. By inserting the calculated moment values for the 1.5 ML sample as well as for the 0.6 ML sample, a magnetic moment of 3.3 μ_B can be calculated for the second layer. This value is already very close to the expectation from Hund's rule. In the case of the pure BL sample, a magnetic moment of 3.2 μ_B can be extracted for the second-layer. However, this assumption is properly not valid, since the material structure visibly changes from the first to the second-layer. Also it can be observed that even for higher coverage the magnetic moment is not rising strongly. Therefore, the more probable explanation is that the effective spin moment for the material is around 2 μ_B, which is until now not fully explained. The calculation of 4 μ_B would also only be valid in a system with pure octahedral symmetry, which would mean that no orbital moment could exist, since it would be fully quenched [124]. The theoretical calculation by Ropka et al. (Ref. [317]) was already predicting a reduced moment (2.7 μ_B) for a system where the structure is distorted. In the previous STM and LEED analysis, a strain of the material on Au(111) was observed for the first layer. This could still affect the second and third layer of the material.

The different magnetic properties of the first layer on Au(111) compared to the second or third layer can also be observed via the XMCD magnetization curve measurements. In Fig. 4.41, the magnetization curves for a sub-ML and a BL sample measured at NI and GI are shown. The magnetization curves for both coverages are behaving equal. For both coverages no preference between NI or GI can be extracted. This is also visible in the measured XMCD spectra, where the peak structure as well as the intensity are equal. By comparing the sub-ML measurements with the BL, it can be observed that the curvature is way more shallow for the sub-ML sample. For both coverages the magnetization still shows a linear slope even at high fields. In Fig. 4.42, the magnetization-curve measurements for different sample coverages are displayed. The magnetic behavior of the ML $FeBr_2$ films on Au(111) is strongly different from the ones with higher coverage. Not only that the magnetic moments are decreased by 50-75 % (75 % for sub-ML) from the bulk value (Tab. 7.9), but also the magnetization curves are more shallow for both measured geometries (NI and GI at sub-ML coverage) compared to the ones at higher thickness (Fig. 4.42). Starting from a nominal coverage of 0.7 ML, the magnetization curves are showing a kind of saturating behavior. This behavior is most likely related to the onset of the second-layer growth in some areas of the sample (as observed by the third set of spots in the LEED measurements). Figure 4.43 a) demonstrates that fitting of the NI 0.6-ML sample loop to the Brillouin function does not yield

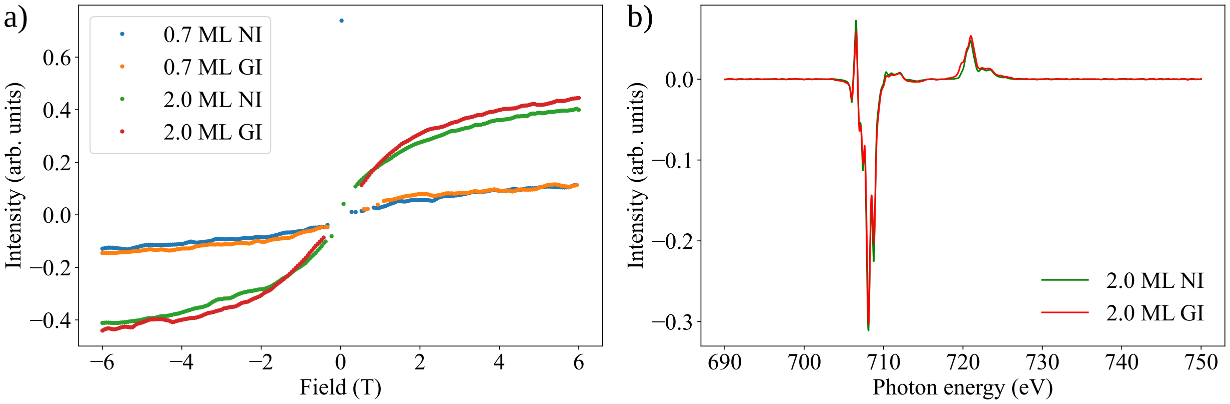

Figure 4.41: a) Magnetization curves of the sub-ML (0.7 ML) and the 2.0-ML $FeBr_2$ on Au(111) sample. Both coverages are measured at NI and GI. The magnetization curves are scalled to the peak height of the isotropic XAS signal. b) NI and GI XMCD spectra of the 2.0 ML sample. The displayed measurements were all performed at 2 K and the XMCD spectra are measured at 6 T. The magnetization curves a) and XMCD spectra were measured in 2021 (2.0 ML) and 2023 (0.7 ML) at the BOREAS beamline.

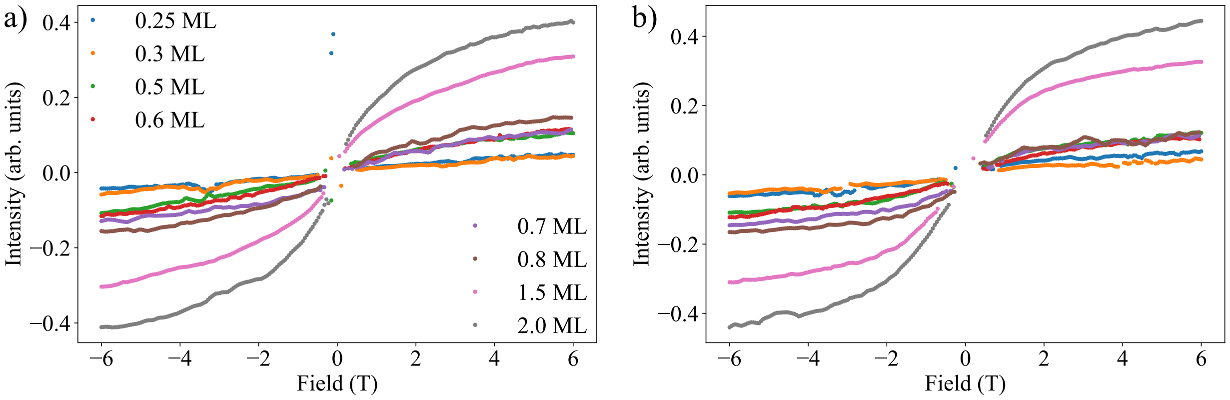

Figure 4.42: a) and b) Magnetization curves for different coverages of $FeBr_2$ on Au(111) measured at 2 K at NI and GI. The magnetization curves in a) and b) are scaled by the peak height of the isotropic XAS signal. In a) and b) the magnetization curves were measured in 2021 (0.6, 1.5, 2.0 ML) and 2023 (0.25, 0.3, 0.5, 0.7, 0.8 ML) at the BOREAS beamline.

a satisfactory result. The 0.6-ML sample was transferred via vacuum suitcase ($p=1.5 \cdot 10^{-9}$ mbar) to the BOREAS beamline. However, for excluding effects of the transfer, a sample with similar coverage was directly grown at the beamline (0.5 to 0.8 ML coverage, shown in Fig. 4.42).

These coverages show a similar behavior of the magnetization curves as the 0.6-ML sample. The difference in the values of the magnetic moment is a result of the different coverages and the third set of spot LEED pattern. This together with the shallow shape of the magnetization curve implies a magnetic behavior that is neither paramagnetic nor ferromagnetic. The sub-ML magnetization curve was fitted by using different boundaries for the values of J and N (0 to 2 and 1 - 10) by using a temperature of 2 K and $g = 2$. In b) the three different main coverages (0.6 ML, 1.5 ML and BL) are compared to the pure Brillouin function without adapting the scaling factor. This was calculated for a system which reaches a total magnetic moment of 4 μ_B like expected from Hund's rule. By comparing the paramagnetic curve without assuming OoP anisotropy with the measured magnetization curve, a steeper increase can be observed, which would be even stronger if anisotropy would be considered for FeBr$_2$. As a consequence of this, the magnetic behavior cannot be explained by nonexisting long-range magnetic order of the first layer. The performed STM and LEED measurements reveal, that the grown islands for 0.5 ML and larger coverages are large enough with a value of around 100 nm (Fig. 7.17) to neglect size effects like superparamagnetic behaviour. The published neutron diffraction data give also no hint, since antiferromagnetism inside the layers of FeBr$_2$ was never observed [309], [311], [314]. As a result of the neutron diffraction measurements a nearest-neighbour coupling J_1 with equal signs, which indicates ferromagnetic order, and a next-nearest-neigbor coupling J_2 with opposing sign (antiferromagnetic order) was extracted. These two competing interactions lead to a frustrated behavior, which can cause a complex magnetic structure [32], [361]. In Ref. [361], the phase diagram for FeBr$_2$ shows that the magnetic structure changes depending on the J_1/J_2 ratio, but also depending on the anisotropy of the system, which can be affected by different coverages and island sizes [32]. As previously discussed, the first layer of FeBr$_2$ on Au(111) shows a strain of 3 %, which leads to the different lattice constant observed in LEED. Therefore, the superexchange interaction will be affected, since it strongly depends on the angle between the Fe-Br-Fe bonds [32].

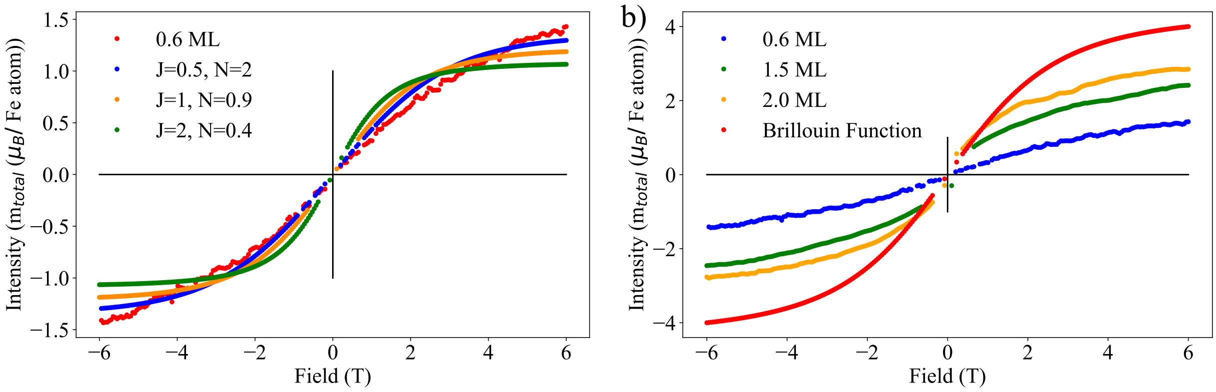

Figure 4.43: a) Overlay of the sub-ML magnetization curve (red) with fitted Brillouin functions for different J values (J = 0.5-2). b) Magnetization curves for different coverages of FeBr$_2$ on Au(111) overlayed with an unscaled Brillouin function for J = 2. All measurements were performed at 2 K and NI. The figure is taken from Ref. [32]. The magnetization curves a) and b) were measured in 2021 at the BOREAS beamline.

The origin of the complex magnetic behavior, which is different compared to the second layer, can be caused by either a spin-glass phase but also by a non-collinear magnetic texture due to frustration. However, the magnetic behavior is purely related to the transition metal and not to the halide (Fig. 7.32). Here the XMCD measurements only revealed a very weak signal for Br. In Fig. 4.44, the magnetization curves for the 1.5-ML and BL samples are displayed after the contribution of the first layer was removed. This procedure was done since the structural phase and magnetic behavior for the first and second layer are different. Especially in the case of the 1.5 ML sample, both, first and second layer, are still present on the surface, which leads to a mixed magnetic behavior. Also in the BL case the magnetic properties are still affected by the layer underneath or affected by the existence of only the first layer in some regions of the samples. As a result of the removal, it can be observed that the magnetization curves look more flat and seem to saturate for higher fields. The subtraction of the sub-ML magnetic contribution can to be performed, since the magnetic response measured via XMCD is an average of both layers.

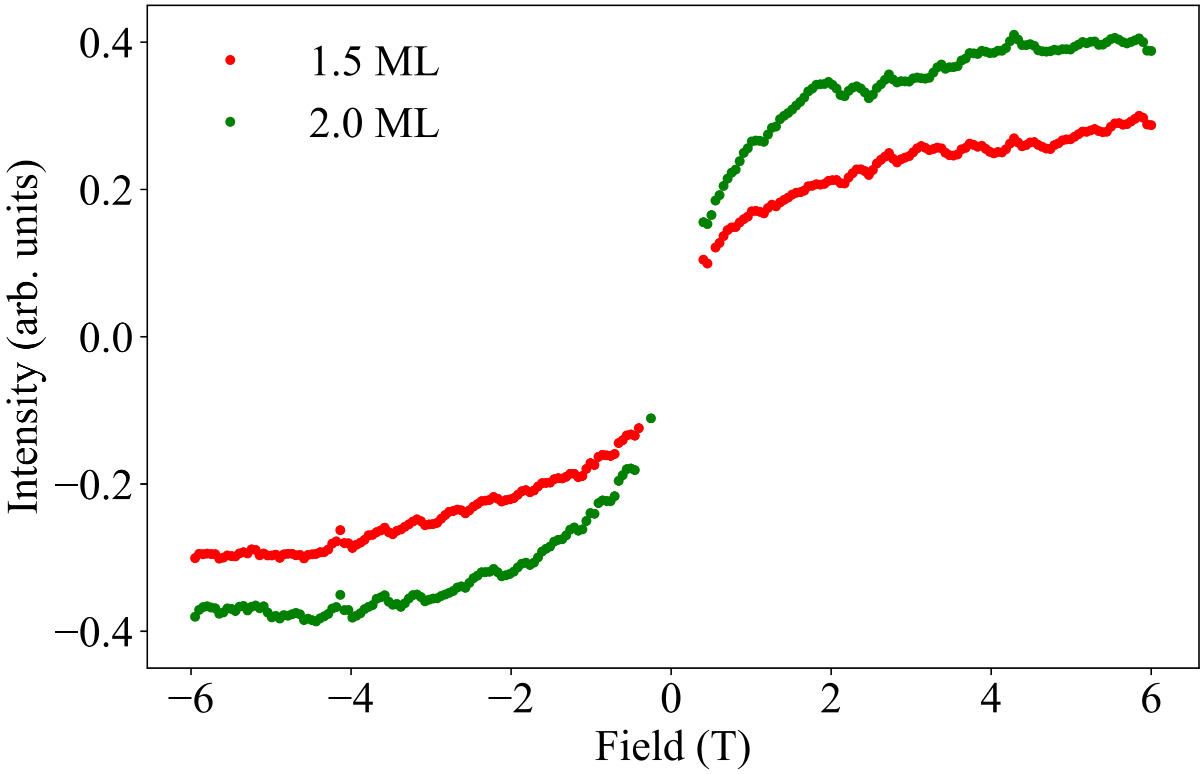

Figure 4.44: 1.5 ML and BL magnetization curves, from which the first-layer curve has been subtracted. The resulting magnetization curves are scaled to the peak height of the corresponding isotropic XAS spectra. The displayed measurements were performed at 2 K and NI. The magnetization curves a) and b) were measured in 2021 at the BOREAS beamline.

Magnetic properties of $FeBr_2$ on Bi_2Se_3

In the following section the magnetic properties of $FeBr_2$ on Bi_2Se_3 are characterized by using XAS and XMCD. Before growing the sample on Bi_2Se_3, 0.7 ML $FeBr_2$ was grown on Au(111) and characterized by LEED and spectroscopic techniques (XAS, XMLD and XMCD). Afterwards all growth parameters were kept constant and the material was evaporated on a freshly cleaved Bi_2Se_3 surface, which was kept at RT. The isotropic XAS peak height was then used for the coverage estimation of all other samples. In the case of 0.7 ML $FeBr_2$, the peak height of the isotropic XAS is around 13 % on Au(111) and 32 % on Bi_2Se_3, which means the scaling factor is around 2.5 . In Fig. 4.45, the coverage-dependent XAS and XMCD spectra as well as the resulting expectation values of the magnetic moment at 6 T are displayed. It can be observed that with increasing coverage the multiplet peak structure of the isotropic XAS (a)) at NI and 2 K is not changing, and therefore also the corresponding XMCD (b)) does not change in shape. In c) the calculated expectation values of the magnetic moments at 6 T are displayed. The values change only slightly for the different coverages and are starting even for lower coverages at the same value as the ones calculated for higher coverages on Au(111).

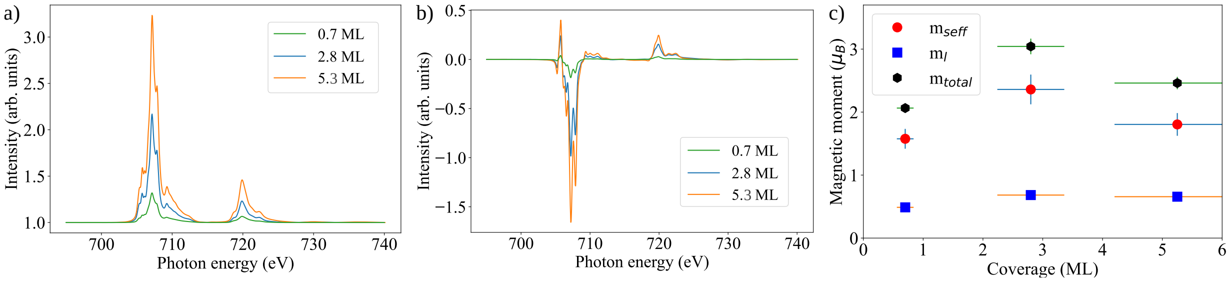

Figure 4.45: a) Isotropic XAS spectra for different coverages ranging from sub-ML to multilayer of FeBr$_2$ on Bi$_2$Se$_3$. b) XMCD spectra scaled to the peak height of the isotropic XAS spectra. c) Calculated expectation values of the magnetic moment at 6 T. All displayed spectra were measured at NI and 2 K, with an applied external field of 6 T and were grown at RT. The measurements were performed at the BOREAS beamline in 2023.

In Fig. 7.41 and Fig. 7.42, the corresponding LEED images for the different samples measured at the BOREAS beamline are displayed. Since the LEED pattern were not very sharp and showed more smeared-out structures after the evaporation at RT, the temperature during the growth was increased to 100-150 °C. By increasing the growth temperature, the island size will increase and form less but bigger islands on the substrate surface, which are contributing to a sharper LEED pattern. To identify how strong the sticking coefficient is affected by the growth on a heated substrate, the peak height for a RT sample of one ML can be compared to the one of a sample grown at 100-150 °C. For a not heated sample, the peak height would reach around 47 %, but by heating the substrate only a peak height of 41 % can be extracted. Therefore, it indicates that with increased temperature around 13 % of the material does not stay on the crystal surface. However, this is not related to a reevaporation process like on Au(111) at around 200 °C, since the FeBr$_2$ is not coupled to the substrate material. In Fig 4.46, the isotropic XAS spectra for the different coverages of FeBr$_2$ on Bi$_2$Se$_3$ as well as the XMCD spectra, and the magnetic moments at 6 T are displayed. By comparing the calculated values with the ones measured at RT it is visible that no change appears and that for all coverages, independent of the growth temperature, the moment stays stable. This proves the assumption, which was already previously mentioned in the chemical characterization section, that the first layer on Au(111)

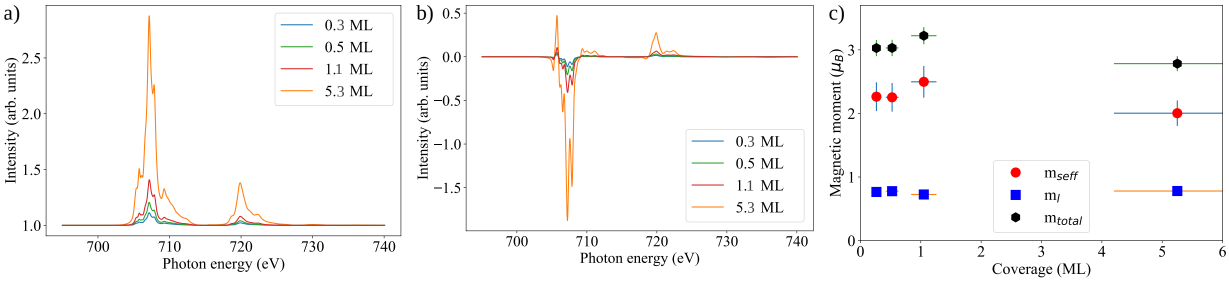

Figure 4.46: a) Isotropic XAS spectra for different coverages ranging from sub-ML to multilayer of FeBr$_2$ on Bi$_2$Se$_3$. b) XMCD spectra scaled to the peak height of the isotropic XAS spectra. c) Calculated expectation values of the magnetic moment at 6 T. All the samples were grown at 100-150 °C. The measurements were performed at the BOREAS beamline in 2023.

behaves completely different in the electronic and magnetic properties. By measuring the sample under different incidence angles, no strong difference of the L_3 edge nor the structure of the XMCD can be observed. In Fig. 4.47, the isotropic XAS and the corresponding XMCD spectra of the 1.1-ML sample at 2 K are displayed. The intensity difference of the L_2 edge is related to the applied background subtraction. The only relevant change between NI and GI is visible in the multiplet peak structure of the L_3 edge. Since the peak structure besides the one multiplet peak at lower photon energies next to the main Fe L_3 edge is identical between NI and GI, no strong anisotropy can be present in the film, which is also visible in the not changing calculated magnetic moment values at 6 T (Tab. 7.10 and Tab. 7.11). To identify if the ordering temperature of $FeBr_2$ changes with the substrate, temperature-dependent spectra of the 0.3- and 2.8-ML samples were acquired (Fig. 4.48). As observed in Fig. 4.48, the XAS spectra are not changing in intensity for the different temperatures and over time, therefore, the sample does not show any indications of x-ray damage. The XMCD spectra at 6 T show a stable intensity in the range from 2-10 K and start to decrease in intensity at 15 K, which matches with the literature critical temperature of 14.2 K [124]. This behavior can also be observed in c), where all the magnetic moment values are nearly stable up to a temperature of 15 K. Therefore, the ordering temperature of $FeBr_2$ on Bi_2Se_3 reaches the literature value. Since the same magnetic behavior is also observed for 0.3 ML, which was grown at 100-150 °C, we can assume that no structural difference exists between the first and second layer. The difference of the extracted ordering temperature compared to the 2.0-ML sample on Au(111) is caused by the used measurement temperatures.

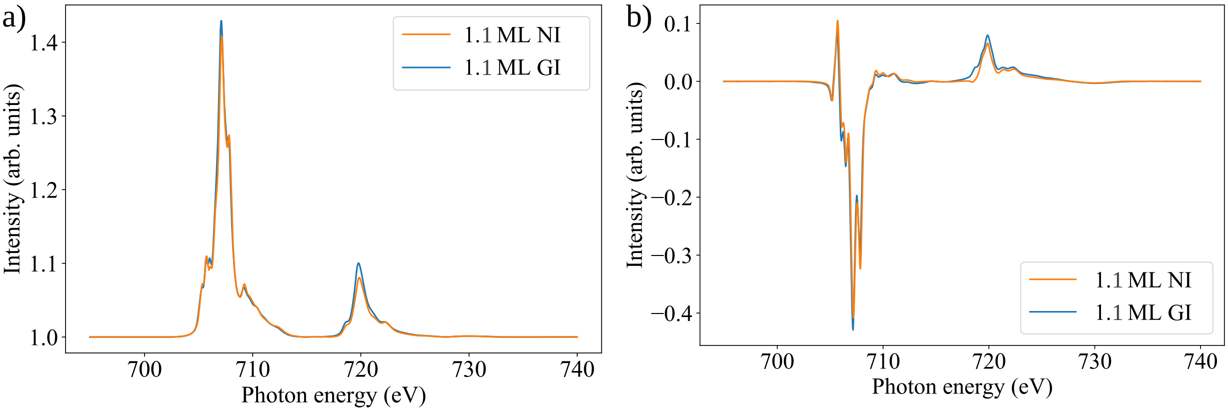

Figure 4.47: a) and b) Isotopic XAS and normalized XMCD spectra of the 1.1-ML sample for NI and GI. The sample was grown while heating the substrate to 100-150 °C. The measurements were performed at 6 T and 2 K. The measurements were performed at the BOREAS beamline in 2023.

In Fig. 4.49, the XMCD magnetization curves at NI and GI of the ML sample are shown. For both geometries, no strong difference, besides a slightly shallower curvature at GI, can be observed, but this difference can be a consequence of the measurement noise. By comparing the magnetization curves for both geometries, the saturation appears at around 2.0-3.0 T and is therefore faster than in bulk, which needed 3.5 T. Since no significant difference between the two curvatures at NI and GI is observed, no magnetic anisotropy is present. In Fig. 7.37 and 4.50, the temperature-dependent magnetization curves for different thicknesses of $FeBr_2$ on Bi_2Se_3 are displayed. From the temperature-dependent magnetization curves, a different critical temperature can be extracted. For all coverages and growth procedures, the 2 K and 4 K measurements are nearly identical, but for all 10 K measurements a way more shallow curvature and a different

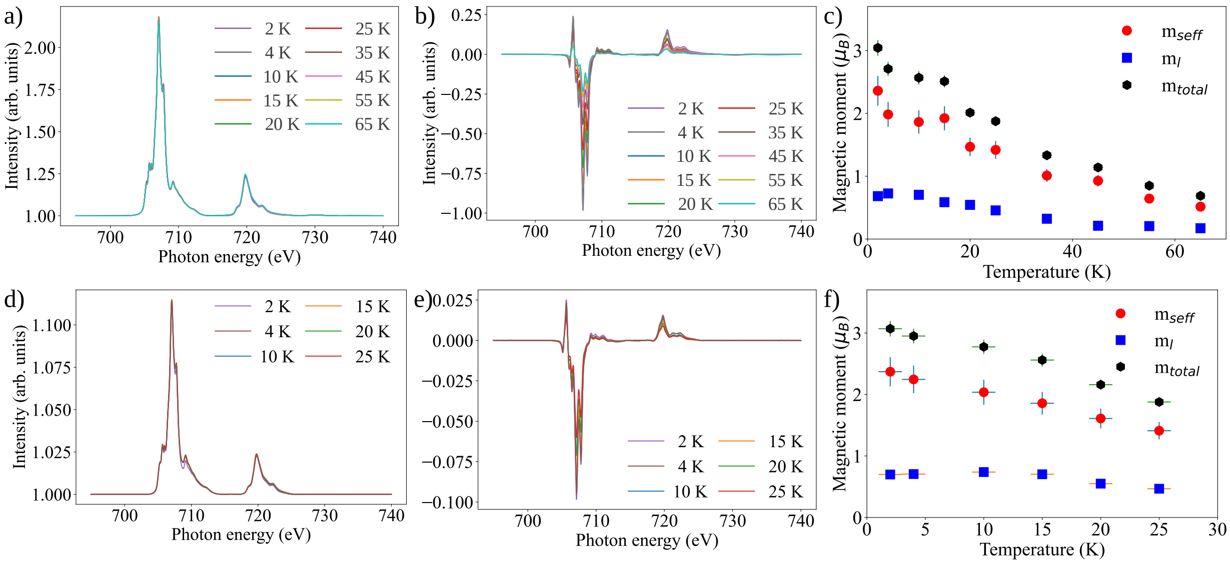

Figure 4.48: a)-c) 2.8-ML sample, d)-f) 0.3 ML sample. a) and d) Isotropic XAS spectra, b) and e) temperature-dependent XMCD spectra. c) and f) calculated magnetic moment values as a function of temperature for both coverages. The magnetic moments as well as the XMCD strength stays nearly stable until 10 K. The measurements were performed at the BOREAS beamline in 2023.

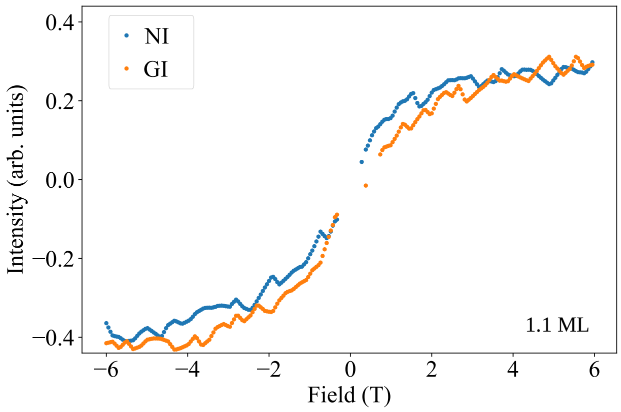

Figure 4.49: Magnetization curve of the ML $FeBr_2$ on Bi_2Se_3 measured at 2 K in NI and GI. Both magnetization curves are not showing any significant difference between the saturation values nor in the magnetization behavior. The magnetization curves are scaled by the corresponding isotropic XAS peak height. The measurements were performed at the BOREAS beamline in 2023.

saturation magnetization is present. This can either be related to a higher noise level, but most likely is that the ordering temperature is around 10 K. In 4.50 d), the multilayer magnetization curves are displayed, which are behaving different compared to all other coverages. For this sample the magnetization curves are not saturating up to 6 T. By comparing the slopes in b), a slightly steeper slope at 2 K can be observed, which indicates that the saturation will be reached faster at 2 K. No difference between the 2 K and 10 K measurements can be observed. This magnetic behavior is also independent from the growth temperature (Fig. 7.36). Therefore, it could show a

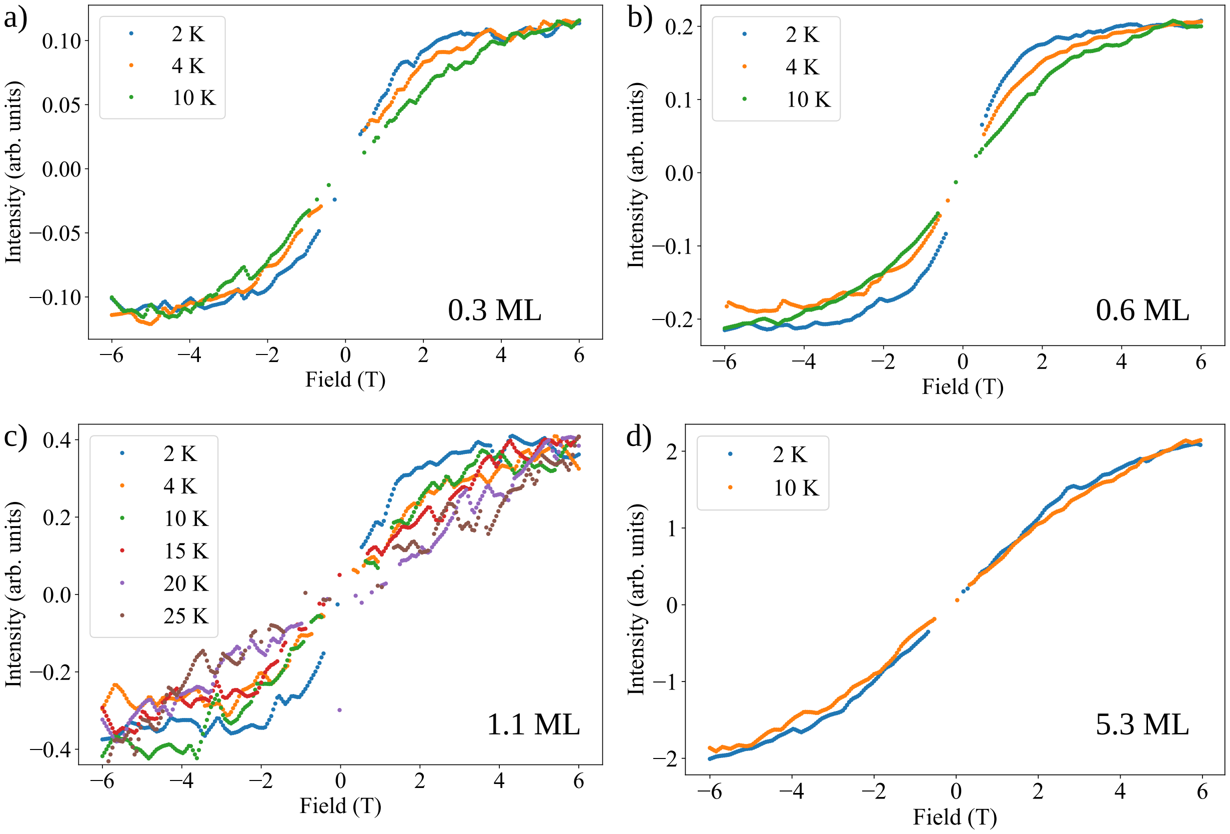

Figure 4.50: a)-d) Temperature-dependent magnetization curves for different coverages ranging from sub-ML to multilayer of $FeBr_2$ on Bi_2Se_3. All samples were grown on a heated substrate (100-150 °C) and measurements done at NI. The magnetization curves are all scaled to the peak height of the corresponding isotropic XAS. The measurements were performed at the BOREAS beamline in 2023.

transition phase from the 2D properties to the bulk properties. For all samples including this coverage the moments are identical, therefore no antiferromagnetic interlayer coupling is observed. The most probable answer for the change in saturation behavior is a change of structure, which causes the transition to bulk behavior. A possibility of the structural change can be that the material changes from 1H to the bulk 1T phase. This hypothesis is also supported by the fact that for all different coverages on Bi_2Se_3, the magnetic moment values are nearly identical at each temperature (Tab. 7.10 and Tab. 7.11).

In Fig. 4.51, the magnetization curves at 2 K for different coverages normalized to the maximum peak height of the isotropic XAS and the expectation value of the effective spin magnetic moment at 6 T are displayed. By comparing the different magnetization curves at 2 K normalized either to the peak height (a) and b)) or to the moment (c) and d)), it is visible that all coverages are saturating at the same field value and are behaving similar (differences are caused by the noise). Only for high coverages, where the structural phase transition is supposed to be, the difference is obvious.

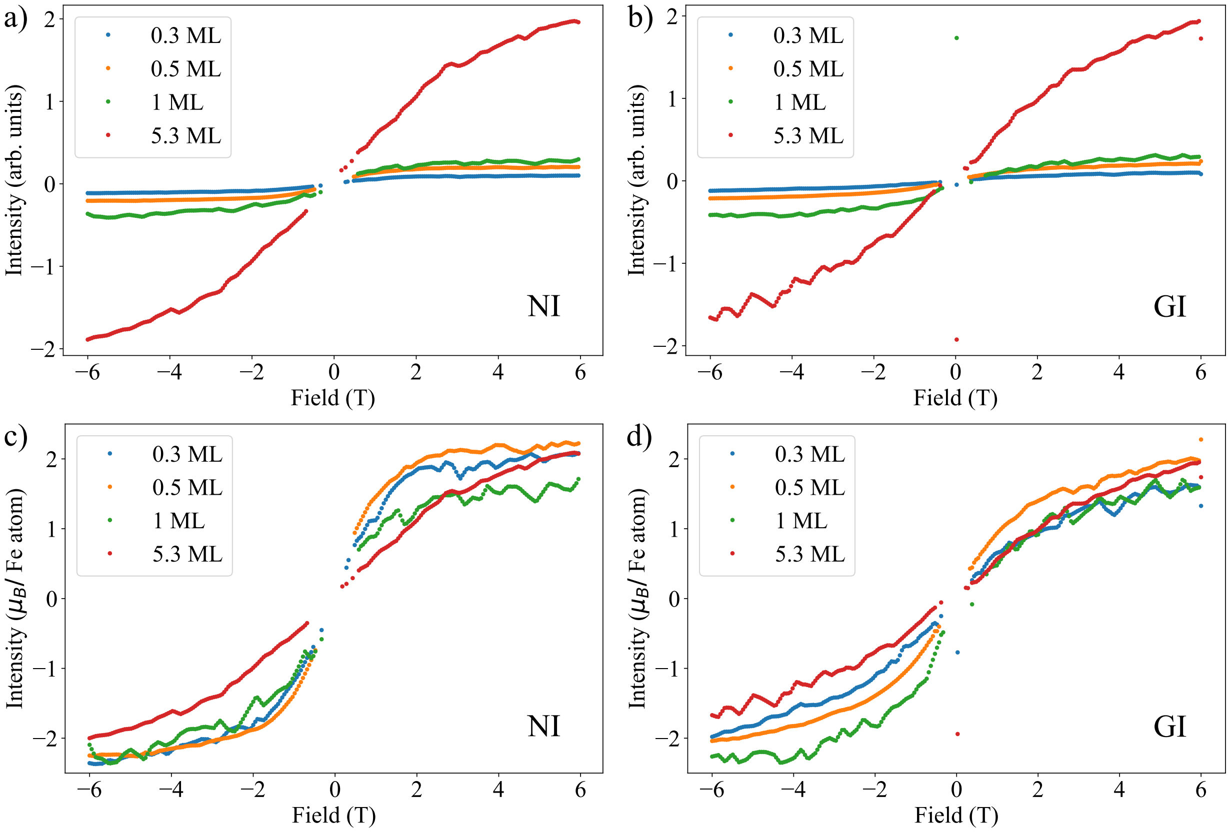

Figure 4.51: a) and b) Coverage-dependent magnetization curves scaled to the maximum peak height of the isotropic XAS measured at NI and GI. c) and d) Coverage-dependent magnetization curves scaled to the expectation value of the spin effective magnetic moment at 6 T. All measurements were performed at the BOREAS beamline at ALBA at a temperature of 2 K in 2023.

4.1.6 Summary

In the last sections, the structural, chemical, and magnetic properties of $FeBr_2$ on Au(111) and Bi_2Se_3 have been analyzed and discussed. By comparing the sub-ML behavior on Au(111) with Bi_2Se_3, it is visible that the material grows in a different structural phase in the first ML on Au(111), which changes for higher coverages. During the phase change the two rotational domains of a moiré superstructure disappear and only one domain is left, which is oriented along the main symmetry direction of Au(111). Additionally, the lattice constant is changing to literature values, which indicates that the first layer on Au(111) is strained, which causes the superstructure pattern of the first layer. By growing $FeBr_2$ in different coverages on Bi_2Se_3, no structural changes can be observed between the layers in STM and LEED for the first- to second-layer. Here, the lattice constant matches the literature value starting from the first layer.

The LEED pattern only shows contributions of the main moiré pattern, which indicates that on Bi_2Se_3 the second moiré with the smaller periodicity is less probable on the surface. The long-range moiré, which causes the LEED pattern, shows that the $FeBr_2$ grows from the start along the main symmetry direction of Bi_2Se_3.

By comparing the chemical properties of $FeBr_2$ on Au(111) and Bi_2Se_3, no dominant peak-shape changes in XPS or XAS can be observed for the main transitions. However, in the case of Au(111), the FWHM of the main core-level peaks in XPS do not change. Nevertheless, the satellite peaks which are related to the low electronegativity of Br are decreasing in FWHM for higher coverages on Au(111). Additionally, the XAS spectra change in the multiplet peaks at higher photon energies as observed on Au(111) for the transition from ML to BL systems. In comparison, all these changes are not happening on Bi_2Se_3. Therefore, the changes of the FWHM, peak shift for higher coverages in XPS, and multiplet peak structure are related only to the different properties of the first layer on Au(111), since the higher coverages on Au(111) are behaving identical to all coverages on Bi_2Se_3 (Fig. 7.47 shows the comparison of the XAS, XMCD, and XLD spectra).

The magnetic properties of $FeBr_2$ on the two different substrates are identical in the case of higher coverages on Au(111). However, for low coverages, the superstructure has different magnetic properties, which can indicate a spinglass behavior or a frustrated AFM system within the layer. Nevertheless, the reduced moments of the first layer as well as the structural change between first and second layer on Au(111) could either be caused by the alignment of $FeBr_2$ on the substrate, which causes a strong strain, or by a different growth mechanism. In Fig. 4.20, the superstructure appearance is visible by applying a strain of 3 % to the material lattice. It could be that the top-layer Br atoms are sitting directly on top of Au atoms, which would cause -due to strong interactions- a higher attraction of the Br atoms. Nevertheless, also other origins of the superstructure cannot be neglected, like that the Br atoms are sitting in a 3-fold hollow site. These two possibilities would mean that the superstructure is not defect based but a periodic pattern due to stronger interaction zones. By overlaying the $FeBr_2$ structure with the measured STM image, the origin of the triangular defects can also possibly be identified. Here it seems, that the center of the triangular defects is caused by a missing transition metal atom (Fig. 7.15). Nevertheless, even if the superstructure pattern is caused by missing Br, this would create a ratio of 7 Fe atoms to 13 Br atoms, which is still 1.86 and could be hardly visible in the XPS element ratio. The performed bias-dependent measurements of the first-layer of $FeBr_2$ on Au(111) clarifies, that the superstructure pattern is no electronic effect. However, the vacancy theory would include a different oxidation state, which should be easily detectable via XAS. Therefore, the most likely possibility for the first growth mechanism is the stronger attraction case with an unchanged configuration. Since the Br and Au are interacting via Ullmann coupling, a charge transfer could already decrease the observed magnetic moment.

In the case of bulk $FeBr_2$, a literature value of $4\,\mu_\mathrm{B}$ is expected for the Fe magnetic moment for an octahedral symmetry with S = 2. However, the ML to multilayer samples are not behaving as the bulk, since already a strong orbital moment exists for both substrates. Therefore, a purely octahedral symmetry can not exist for the thin layers, since the system should be quenched and therefore the orbital moment should be zero. Since the orbital moment is not negligible and for sub-ML coverages is in the region of 10-35 % of the effective spin moment, an unquenched orbital moment is the reason. This can be caused by SOC or a weak crystal-electric field (CEF) [362]. The low values in the case of the sub-ML (0.25 ML) $FeBr_2$ on Au(111) (Tab. 7.9) are caused by the low intensity of the spectra, which increases the error for the moment calculation. However, for all samples with higher coverages around or above one ML, the orbital moment is not small anymore and is in the range of 30 % of the effective spin magnetic moment. It seems that the saturation moment for $FeBr_2$ in the 2D limit is around $2\,\mu_\mathrm{B}$ for the effective spin moment. On the other hand, the T_z term is ignored for the calculation of the spin moment, nevertheless, since nearly no difference for the calculated moments at 6 T for NI and GI has been observed, the contribution of the dipole term can be neglected. The fact that the second layer on Au(111) grows identical to the first and next layers on vdW substrates is also confirmed by the XLD and XMLD measurements (Fig. 7.34, 7.38, and 7.39). The reduced moment of the first layer on Au(111) can have similar reason as for FePc on Au(111), where the magnetic moment is decreased to $1\,\mu_\mathrm{B}$

on the Au(111) surface and reaches 2 μ_B if it is not interacting with Au(111) [363], [347]. For both substrates (for the second layer on Au(111) and first layer on Bi_2Se_3) a critical temperature of around 8-10 K was extracted, since at higher temperatures the expectation value of the total magnetic moment at 6 T follows the Brillouin function (Fig. 4.39 and Fig. 7.43)

The strong reduction can result from the interaction Br-Au, which causes a charge transfer. On the other hand also the Fe could interact with the Au atoms and therefore causes an additional effect, also reducing the moment. This interaction could be perhaps visible in the XAS spectra for low coverages, where the multiplet peak at lower photon energies close to the L_3 edge is not visible. This has been also observed for other Fe molecules with an Fe^{2+} octahedral environment on Au(111) [364]–[366]. However, the multiplet peaks are visible on Bi_2Se_3 for all coverages, even for 0.26 ML.

5 Characterization of epitaxially grown $MnBr_2$ and $MnCl_2$ on Au(111)

5.1 Epitaxially grown monolayers of $MnBr_2$ and $MnCl_2$ on Au(111)

In the following sections the properties of $MnBr_2$ and $MnCl_2$ on Au(111) are characterized by using different structural, chemical, and magnetic measurement techniques.

5.1.1 Material introduction

For decades, $MnBr_2$ and $MnCl_2$ have been studied for their structural, optical and magnetic properties [367]–[378]. However, these investigations have focused exclusively on the properties of the bulk crystals. The materials are part of the TMDH family, which has recently seen a strong increase in interest. Over the past years several publication about different ML TMDH like $NiBr_2$ [33], NiI_2 [144], [379], [380], $FeBr_2$ [32], [142], [316], and $FeCl_2$ [132], [348], [381] has been published. $MnBr_2$ and $MnCl_2$ have both a 1T structure, just with different layer repetitions. $MnBr_2$ has, like $FeBr_2$, a CdI_2 structure with a symmetric layer repetition c and with a P3m1 point group [124], [374]. In the case of $MnCl_2$, a $CdCl_2$ structure is present, which has a symmetric layer repetition of $3 \cdot c$ and an R3m point group [124], [376]. For both materials, the transition metal is sandwiched between two Br or Cl planes (Fig. 5.1 a) and b)).

$MnBr_2$ and $MnCl_2$ consist of equally distanced Br-Br/Cl-Cl and Mn-Mn bonds, with a lattice constant of $a = b = 3.89$ Å ($MnBr_2$) and $a = b = 3.71$ Å ($MnCl_2$) and a layer spacing $c_{\text{Stacking}} = 6.27$ Å and $c_{\text{layer}} = 5.86$ Å, which results in $c = 17.58$ Å [124], [374], [376], [382]. For both materials, the Mn atoms have a HS $3d^5$ configuration, which leads to a total spin of $S = \frac{5}{2}$, resulting in an expected total spin magnetic moment of $5\,\mu_B$ [124], [367], [382]. From DFT calculations, a bond length of around 2.703 Å [382] was extracted for 2D $MnBr_2$, which is close to the literature values obtained from bulk measurements. Additionally, the calculation predicted that $MnBr_2$ should be thermally stable and therefore possible to be exfoliated from the bulk crystal [382].

In the case of $MnBr_2$, heat capacity measurements revealed that the material undergoes two phase transitions by increasing the temperature, until reaching the paramagnetic phase. The low-temperature phase consists of stripe domains, were the domains show parallel ferromagnetically coupled spins, with antiferromagnetic coupling inbetween (Fig. 5.1 d)). This phase exists until reaching the first-order phase transition temperature of 2.17 K, where the material changes from the low-temperature phase to the intermediate-temperature phase. The intermediate state shows the same stripe behavior as the low-temperature phase, just the moment strength varies along the stripes [368], [383]. At 2.32 K, a second-order phase transition happens for the transition from the intermediate state to the paramagnetic phase [124], [368].

A similar effect was also observed for $MnCl_2$, where two second-order phase transitions are happening. The first transition is between low temperature and an intermediate temperature at 1.81 K, where the spins reorder and change from a low-temperature antiferromagnetic state to a different antiferromagnetic state. The difference between the two states are only minor and related to the domain structure as well as changes of the magnetization direction [384]. By only increasing the temperature about 0.15 K, the second transition from the intermediate to the paramagnetic state occurs [124], [372], [384]. The two critical temperatures were obtained without external field. However, by increasing the external field, the transition temperature at 1.81 K decreases and the one for the second transition at 1.96 K increases [384]. This increase of the transition temperature was unexpected, since for other materials the paramagnetic-antiferromagnetic transition temperature does not increase with increasing external field. A possible explanation for this phenomenon is that the domain size, by increasing the external field, increases and therefore a higher temperature is needed to cause the transition [384].

The magnetic structure for both materials is very complicated and also changes between the different transition temperatures. In Fig. 5.1 c) and d), the magnetic structure of $MnBr_2$ at a temperature below 2.2 K is displayed. In the case of $MnBr_2$, the structure contains ferromagnetically aligned moments which are oriented in-plane as stripes along the easy axis. The ferromagnetic stripes are coupled antiferromagnetically to neighboring stripes. Between the material layers, also an antiferromagnetic order has been observed [124], [374]. A similar stripe structure has been investigated via neutron diffraction for $MnCl_2$ [384].

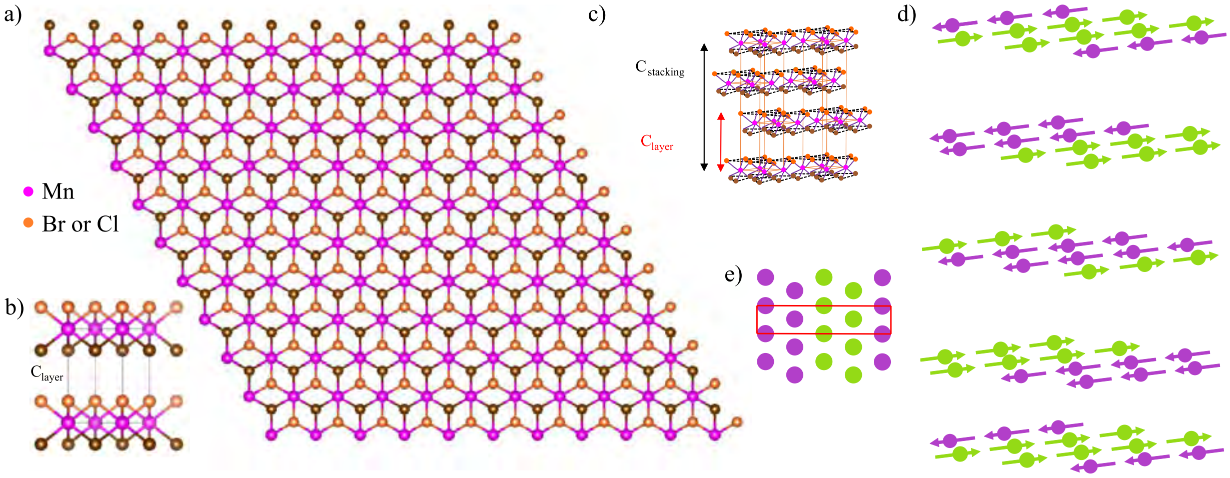

Figure 5.1: a) Top view of the $MnBr_2$ and $MnCl_2$ surface. The Mn atoms are indicated in purple and the Br/Cl atoms of the top and bottom layer in orange and brown. b) and c) Side view of a BL and multilayer system of $MnBr_2$ and $MnCl_2$. The multilayer system for $MnCl_2$ represents the lattice distance and the stacking distance. In the case of $MnBr_2$, the stacking distance and lattice distance are identical due to the CdI_2 structure. The unit cell is displayed as black and orange lines for $MnBr_2$ and $MnCl_2$. d) Magnetic structure of $MnBr_2$ for temperatures below 2.2 K. The magnetic moments are aligned IP along the easy axis. The green and purple spheres are only representing the Mn atoms, without the surrounding halide atoms. e) Top view of magnetic ML of $MnBr_2$. The stripes have an antiferromagnetic interlayer coupling and periodically changing ferromagnetic and antiferromagnetic intralayer coupling, which is shown in d). The red rectangle visualizes the repetition cell for the ferromagnetic order in one direction. The panel a) was created partly by using VESTA [312] and is based on the information of Ref. [385]. The panels in this figure are based [124].

5.1.2 Experiments and Methods

The different coverages of $MnBr_2$ and $MnCl_2$ were grown from stoichiometric powders bought at Sigma Aldrich. The used powder purity of $MnBr_2$ was 98 % [386] and for $MnCl_2$ $\geqq 99\,\%$ [387]. The powder was evaporated from quartz crucibles inside a Dodecon four pocket evaporator [388]. The crucibles were cleaned several times with ethanol and acetone in an ultrasonic bath before loading the powders. $MnBr_2$ has a white to light pinkish color, similar to $MnCl_2$ [389], [390]. During the degassing process, the powder colors did not change. The crucible temperature was slowly increased during the degassing procedure, which allowed a base pressure during the evaporation in the HV to UHV pressure regime ($10^{-8} - 10^{-9}$ mbar). The evaporation temperature for both compounds is in the regime of 450-480 °C. This temperature was measured via a K-type thermocouple, which has always an offset compared to the real temperature, since the thermocouple position is not at the same position as the powder. The samples were grown under various different substrate temperature conditions.

The structural and chemical characterization was performed for substrate temperatures ranging from RT to $\approx 130\,°C$ for both materials. The measurements performed at the different beamlines (XPS, STM, and XAS) always used $MnBr_2$ and $MnCl_2$ samples evaporated at RT on Au(111). The $MnBr_2$ sample thickness was determined by cross checking with the previous calibration of $FeBr_2$ on Au(111) and for $MnCl_2$ the calibration was based on $MnBr_2$. Additionally to the cross checking mechanism, the coverage was determined by a QCM. The powder was evaporated for 20-30 min to achieve a stable evaporation rate due to an equilibrated temperature before growing the sample on the substrate. The density of $MnBr_2$ is $4.38\,\frac{\mathrm{g}}{\mathrm{cm}^3}$ [386], which is similar to the one of $FeBr_2$. In the case of $MnCl_2$ the density is reduced to a value of $2.98\,\frac{\mathrm{g}}{\mathrm{cm}^3}$ [387].

The LEED measurements were performed at two different locations. At CFM, an MCP-LEED setup is used and at the BOREAS beamline a hemispherical LEED. The XPS measurements were performed by using the Al-anode of a non-monochromatic x-ray gun together with a Phoibos 100 hemispherical analyzer. To complete the structural characterization LT-STM measurements at 4.3 K were performed at the PEARL beamline at the SLS. At the BOREAS beamline, a full magnetic characterization was performed. The Au(111) single crystals were cleaned via sputtering and annealing procedures.

5.1.3 Structural characterization

The structural properties of $MnBr_2$ and $MnCl_2$ on Au(111) were characterized by LEED and LT-STM. Depending on the growth temperature as well as the coverage, the surface structure starts to change (Tab. 5.1 and Tab. 5.2). For both materials a temperature-dependent structure with only specific domain directions can be observed. In the case of $MnBr_2$ on Au(111), the high-temperature growth creates a superstructure pattern and in the case of $MnCl_2$, a pattern with specific rotational domains. For both materials a ring structure is observed for low growth temperatures, which means that many small islands with different rotations are grown. In the following the different coverage- and temperature-dependent structures will be explained. Nearly all shown LEED and XPS measurements on $MnBr_2$ and $MnCl_2$ on Au(111) were performed at the Nanophysics XPS lab at CFM in 2022 and 2023. The STM measurements of $MnBr_2$ and $MnCl_2$ on Au(111) were measured at the PEARL beamline in 2023 and the magnetic measurements were performed at the BOREAS beamline in 2023.

Coverage/ Temperature	0.4 ML	0.9 ML	1.1 ML	4.2 ML
RT	Ring structure with three domains	-	-	-
50 °C	Ring structure with three domains	-	-	-
93 °C	Superstructure and three domain phase	-	-	-
120 °C	Superstructure	Superstructure	Mixed phase	Hexagonal pattern

Table 5.1: LEED pattern of $MnBr_2$ on Au(111) depending on the growth temperature and coverage. The temperatures are measured via K-type thermocouple.

Coverage/ Temperature	RT	50 °C	100 °C
0.9 ML	Ring structure	-	-
1.0 ML	-	-	Ring structure
1.4 ML	Ring structure	-	-
1.5 ML	-	-	Three domains
1.7 ML	-	Ring structure	Rings structure (with domains)

Table 5.2: LEED pattern of $MnBr_2$ on Au(111) depending on the growth temperature and coverage. The temperatures are measured via K-type thermocouple.

In Fig. 5.2 and Fig. 5.4, the temperature-dependent LEED patterns of both materials on Au(111) are displayed. The estimated coverages for the LEED measurements are extracted from XPS measurements and will be explained in the chemical characterization chapter. In Fig. 5.2, the samples were grown at elevated temperatures in the range from 117-128 °C (measured at the thermocouple). It can be observed that for the first layer (a)) a kind of superstructure at 42 eV around the (0,0)-spot appears. This superstructure pattern shows similarities with the superstructure observed for 1 ML $FeBr_2$ and $CoBr_2$ on Au(111) ($CoBr_2$ internal communication). The pattern observed for $MnBr_2$ on Au(111) shows a 12-spot structure (purple circles in Fig. 5.2 a)) with another hexagonal structure closer to the (0,0)-spot (green circles in Fig. 5.2 a)), which indicates a bigger lattice constant for the $MnBr_2$ hexagonal pattern (green circles in Fig. 5.2 a)) aligned to the Au(111) surface normal. In the case of the 12-spot structure, the spots are not equally distributed.

By comparing the observed structure with the one of $FeBr_2$ on Au(111), it can be seen that the superstructure pattern has a larger angle of azimuthal rotation to the substrate lattice. This bigger rotation leads to the non-equal distribution of spots with the appearing double hexagon structure as shown in Fig. 5.2 a). By extracting the lattice constants from the LEED images, a superstructure periodicity of ≈ 11 Å can be extracted for the split structure. The lattice constant corresponding to the central $MnBr_2$ spots close to the (1,0)-diffraction spot of Au(111) is ≈ 3.91 Å,

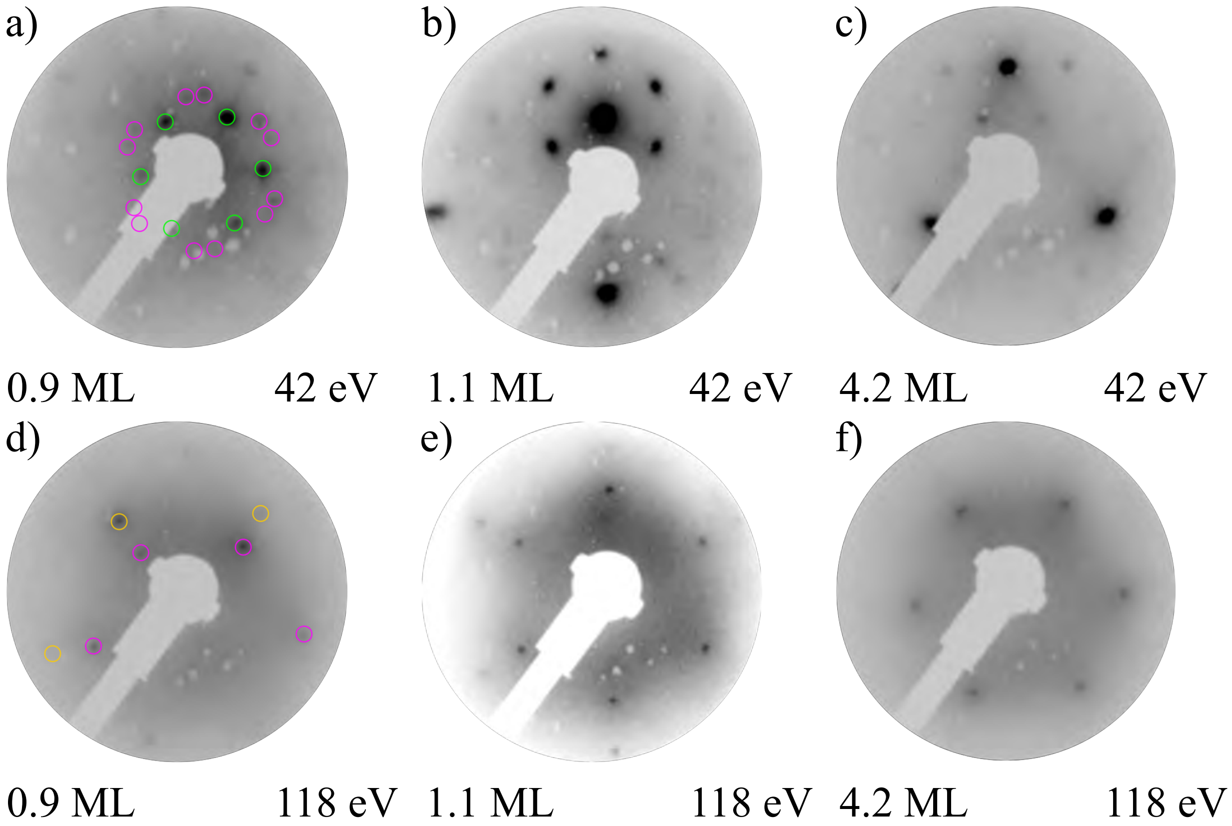

Figure 5.2: Coverage-dependent LEED patterns of MnBr$_2$ on Au(111). a)-c) shows the 0.9-, 1.1-, and 4.2-ML samples measured at 42 eV and d)-f) at 118 eV. All samples were grown at elevated temperatures between 117-128 °C (measured at the thermocouple). The green circles in a) indicate the third set of spots of the MnBr$_2$ superstructure and the purple spots indicate the superstructure. In d), the purple circles indicate the MnBr$_2$ spots and the golden circles the Au diffraction spots.

which is in good agreement with the literature value. For increasing coverage, in b) and c) the split hexagonal pattern disappears and a moiré pattern can be observed. This pattern could indicate that already for ≈ 1.1 ML bigger islands of the second layer exist.

At a coverage of ≈ 4.2 ML, the hexagonal pattern around (0,0) is still visible, but less intense. However, since the coverages are extracted by XPS, the real coverage could be significantly lower, since, as shown later, the background correction for Au was not working perfectly at higher coverages. Therefore, the error could be around -1 ML and therefore the moiré pattern would still be visible, since islands of the second layer might not yet be fully covered. For higher energies, the LEED pattern shows a structure mainly aligned to the close-packed Au[1-10] direction of Au(111), with a possible splitting of the LEED spots for the 0.9 ML sample. In Fig. 5.3, the energy-dependent LEED patterns of a sub-ML MnBr$_2$ sample on Au(111) are shown. The energy-dependent LEED pattern, are very similar to FeBr$_2$ and CoBr$_2$ for higher energies on Au(111) (CoBr$_2$ internal communication). However, the pattern around the (0,0)-spot varies strongly from the previously observed pattern, since the rotation angle is different. In Fig. 5.4 a), the LEED pattern of the clean Au(111) surface is shown. Here the typical surface reconstruction (herringbone) around the first-order diffraction spots as well as the (0,0)-spot are visible. In c)-d) the coverage of MnCl$_2$ was continuously increased by keeping the substrate temperature nearly

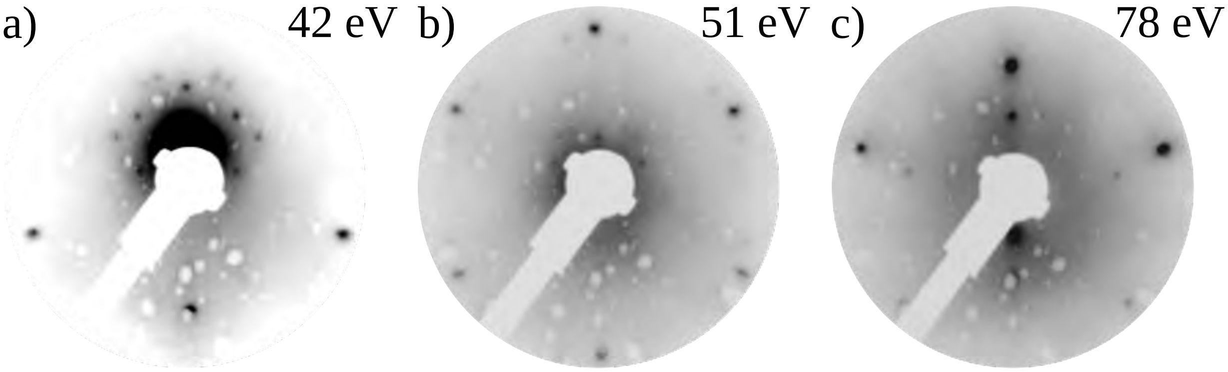

Figure 5.3: LEED patterns of a sub-ML of $MnBr_2$ on Au(111) measured at different energies. In b) a similar pattern as for $FeBr_2$ on Au(111) can be observed, where the three-spot structure close to the (1,0) diffraction spot of Au(111) appears. From c) a lattice constant of ≈ 3.91 Å for the central $MnBr_2$ spots can be extracted, by using for Au a lattice constant of 2.86 Å. The sample has a coverage of around 0.6 ML according to the XPS measurements, by using the calibration via the Mn peak.

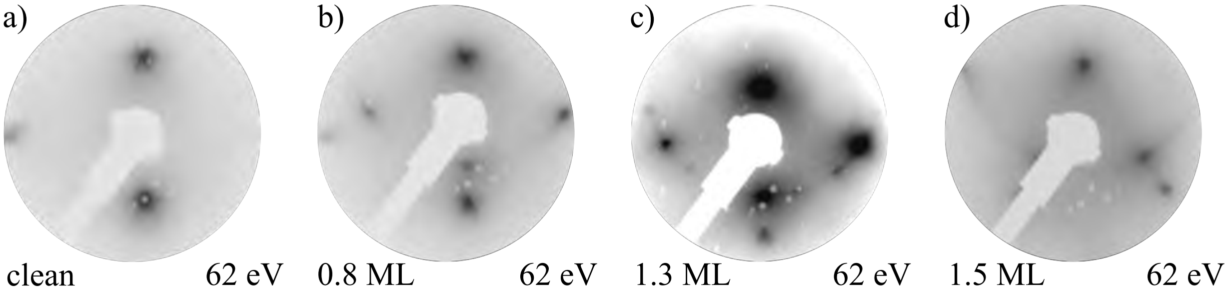

Figure 5.4: Coverage-dependent LEED pattern of $MnCl_2$ on Au(111). a) Clean Au(111) with the herringbone surface reconstruction spots. b)-d) Different coverages of $MnCl_2$ on Au(111) ranging from 1.0 to 1.7 ML. The samples were all grown at elevated surface temperatures of 101-106 °C (measured at the thermocouple).

identical for each sample. In the case of the 1.0-ML sample, the LEED pattern shows a ring structure with one predominant rotational domain, which is aligned to the close-packed Au[1-10] direction. This indicates that the material mainly grows in this direction with many additional small islands, which are growing under different angles, so that the ring appears as shown in Fig. 5.4 b). Therefore, by completing the first ML, domains should be visible by STM.

However, since the material starts very early the growth of the second layer (shown later in the STM measurements), this ring can also be caused by rotated layers on top of each other like in HOPG. Therefore, no domains would be visible in STM. For increasing coverage (c)-d)), the ring starts to loose intensity and only ring patches are visible. In c) the ring disappeared and only a structure with three spots, all with the same lattice constant, is left. This sample should have been the highest coverage with a targeted coverage of BL to TL, however, from the XPS analysis this sample has only a coverage of 1.5 ML. Nevertheless, since the coverage is estimated via XPS and based on the Shirley background subtraction of the Au $4d_{\frac{5}{2}}$ peak, the error can be estimated with ≈ 1.0 ML. This would also match the coverage estimation, which was targeted by using the QCM.

Additionally, since the samples were all grown at the same temperature, only two possible explanations for the not matching coverage but different pattern can be found. The first is that at this temperature regime the sticking coefficient is lower, so that the next layer growth for the Cl compounds does not start or that the coverage is actually higher and that for higher coverages only three rotational domains are dominant at higher temperatures. For this triple-spot structure, all three rotational domains have the same lattice constant, since they are on the same radius. To observe if this structural change in $MnCl_2$ is temperature- or coverage-related, a sub-ML and BL sample were grown at RT (Fig. 5.5). Here, it can be seen that the triple-spot structure does not appear for high coverages if they are grown at RT, therefore this transition to only three rotational domains is temperature- and not coverage-driven. A similar effect can be observed for $MnBr_2$ on Au(111), but here the three-domain structure is growing at RT with a change to the superstructure pattern for higher temperatures. In Fig. 5.6, the LEED patterns for different growth temperatures of a sub-ML are shown. For all three samples the evaporated coverage is identical and controlled by using the QCM inside the preparation chamber. After growth at 50 °C, the superstructure pattern is not visible, however a ring structure with three rotational domains is visible in Fig. 5.6 a) and d). Since the spots of the three rotational domain LEED pattern have all the same distance to the (0,0)-spot, the same lattice constant is present. Therefore, no strain effects can be observed since the extracted lattice constant for $MnBr_2$ matches the literature value. By increasing the temperature to more than ≈ 90 °C, the pattern of the three rotational domains becomes less dominant and the previously discussed superstructure pattern starts to appear (Fig. 5.6 b) and e)).

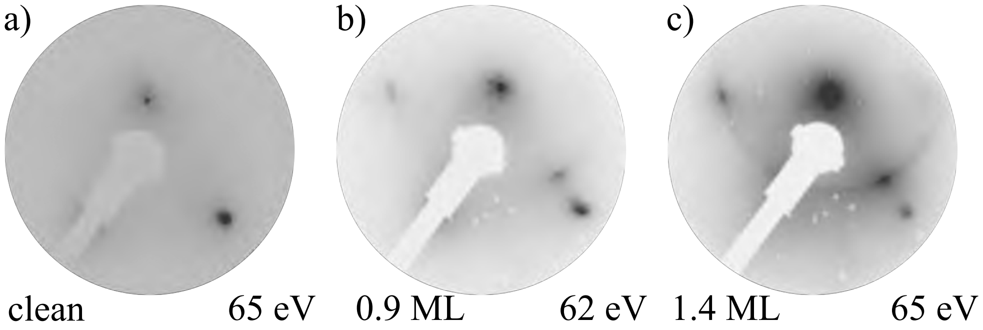

Figure 5.5: a)-c) LEED images of $MnCl_2$ on Au(111) measured at 65 eV. a) Clean Au(111) surface with the herringbone reconstruction, b) sub-ML sample with the herringbone structure still visible and the ring for sub-ML $MnCl_2$ appearing. c) BL sample with one preferred rotational domain and the ring structure. Both samples were grown at RT.

At 48 eV, the superstructure pattern points towards a strain effect for the first-layer, which is visible by the different distances of the central $MnBr_2$ spot for the first-order diffraction spots and the two rotational domains in Fig. 5.6 b). The superstructure becomes the more dominant contribution at 120 °C. In Fig. 5.7, the LEED patterns for different growth temperatures for 1.5 ML $MnCl_2$ on Au(111) are shown. The LEED pattern does not show significant changes until a growth temperature of ≈ 100 °C is reached. Then the ring pattern changes into a domain structure. However, all the coverages are extracted from XPS measurements and therefore are not necessarily correct. In the chemical characterization chapter, the detailed method to calculate the coverage and the possible source of error are explained. Both materials, $MnBr_2$ and $MnCl_2$, have a temperature-dependent growth on Au(111), but in the case of $MnBr_2$ the material forms a superstructure with a strained lattice for high growth temperatures. This superstructure could be related to the higher interaction of Br with Au compared to Cl. For both materials, the higher temperature causes a reduction of the ring-pattern intensity for low coverages, since less

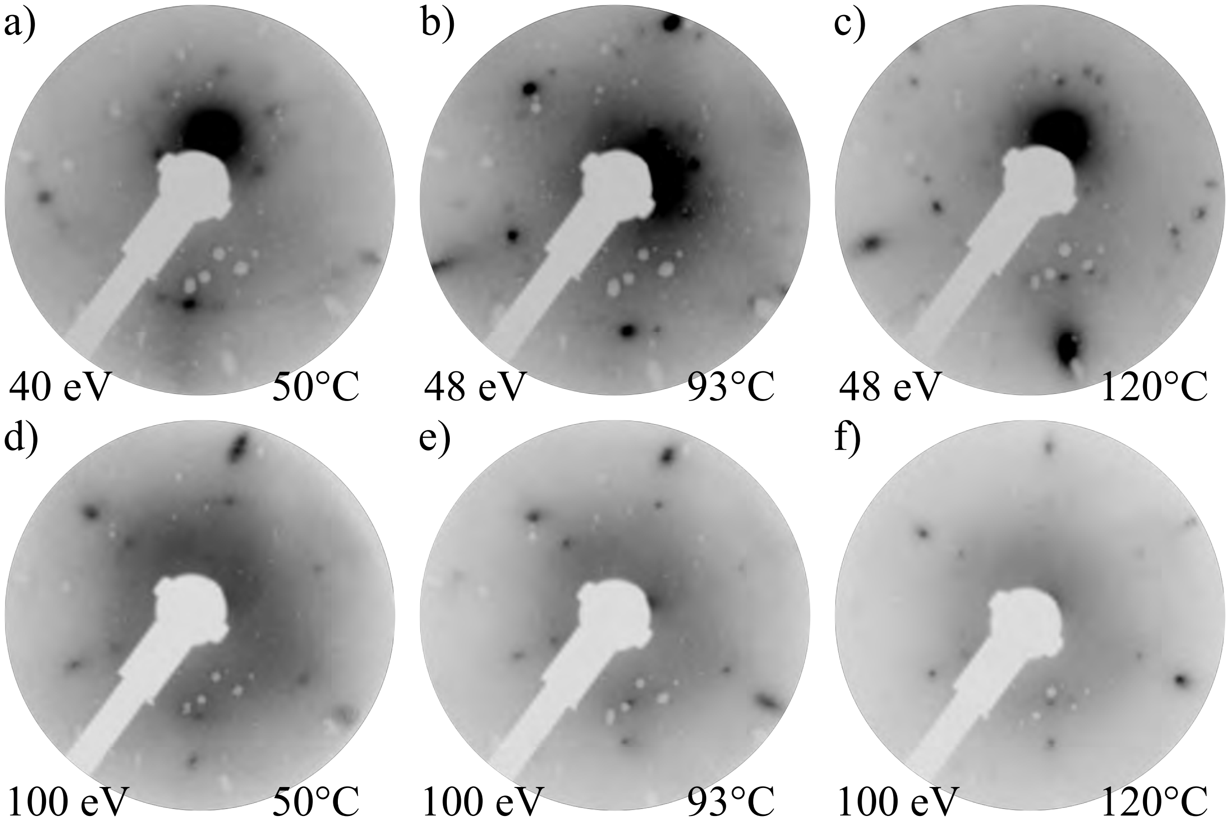

Figure 5.6: LEED patterns of $MnBr_2$ on Au(111) for different growth temperature a)-c) 40-48 eV electron energy and d)-f) 100 eV electron energy. All samples have nominally the same coverage and are in the sub-ML regime (around 0.4-0.6 ML). The growth rate was calibrated by a QCM in the preparation chamber and the coverage is estimated via XPS. The temperature between the three samples was continuously increased, to observe the transition temperature of the LEED pattern. A full transition of the ring pattern to the superstructure can be observed at 120 °C (0.4 ML). Two of the three different samples were grown on the same Au(111) single crystal, therefore the rotation of the Au(111) hexagon is identical. The third sample at 120 °C was grown on another Au(111) single crystal, with a different mounting orientation on the sample plate.

small islands are growing. In Fig. 5.8, the simulation for the LEED pattern with three rotational domains is displayed. By simulating the pattern for $MnBr_2$ on Au(111), a rotation of $\pm 10^\circ$ can be extracted. Since the LEED measurements are an average of the surface structure of $MnBr_2$ and $MnCl_2$ on Au(111), STM measurements needed to be performed to characterize the surface more locally. In the following, LT-STM measurements of $MnBr_2$ and $MnCl_2$ on Au(111) performed at the PEARL beamline at SLS are shown. All samples, except where mentioned explicitly, were grown at RT. In Fig. 5.9 and Fig. 5.10, the STM images of the first and second-layer of $MnBr_2$ on Au(111), respectively, are shown. In Fig. 5.9, a topographic image of a sub-ML $MnBr_2$ on Au(111) is shown. The different dots indicate specific coverages on the sample. The surface contains first- and second-layer islands of $MnBr_2$ on Au(111) as well as clean Au. This is indicated by the green and magenta dots in Fig. 5.9 a) and b). Since the sample was grown at RT, no superstructure is visible in STM, therefore the second layer starts to grow early on top of the first layer, which

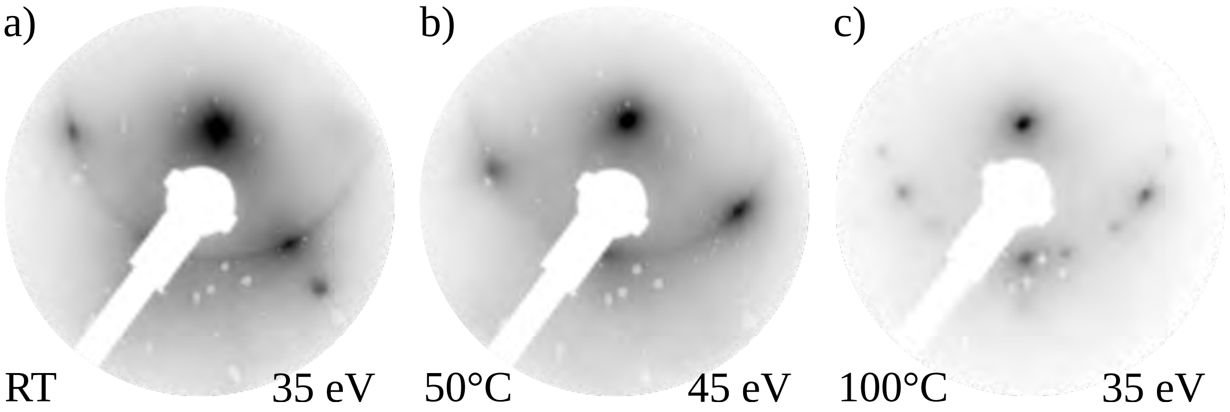

Figure 5.7: a)-c) LEED pattern of $MnCl_2$ on Au(111). The growth rate was calibrated by using a QCM in the preparation chamber and the coverage is estimated via XPS. The growth temperature between the three samples was continuously increased, to observe the transition temperature of the LEED pattern. The coverages range from 1.4 ML to 1.7 ML.

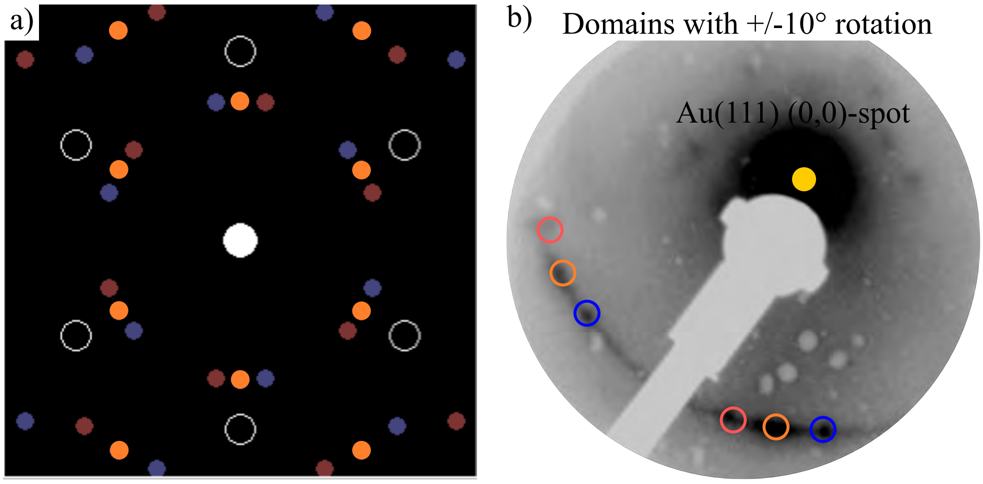

Figure 5.8: a) Simulated LEED pattern via LEEDpat [332]. Here the surface lattice constant of Au and the bulk lattice constant of $MnBr_2$ were used. The hollow circles in a) are the Au(111) diffraction spots and the blue, orange, and brown circles are spots of the three domains of $MnBr_2$ on Au(111) with a rotation of $\pm 10\,°$ and $0\,°$. In b) the overlay of a LEED pattern of $MnBr_2$ on Au(111) with the simulated pattern is shown. The LEED image was acquired at 45 eV on a sample grown at RT.

could cause the ring structure. In addition to the first and second layer of $MnBr_2$ on Au(111), still clean Au areas are visible, where the typical herringbone reconstruction with adatoms sitting in the elbow sites are still visible (a) yellow circle). For the first layer, a shining through of the herringbone reconstruction is visible, which was also seen for $MnCl_2$ (Fig. 5.12 e)) and for $FeCl_2$ on Au(111) [132]. The second layer does not show this shining through of the herringbone, but a surface with some defects, which can be related to the low growth temperature. In c) the atomic-resolution image of the first layer of $MnBr_2$ on Au(111) is shown. Here a lattice constant of 3.91 ± 0.13 Å can be extracted, which matches the literature value of 3.89 Å [124]. The error was calculated via standard deviation. In Fig. 5.10, the BL to TL sample of $MnBr_2$ is displayed.

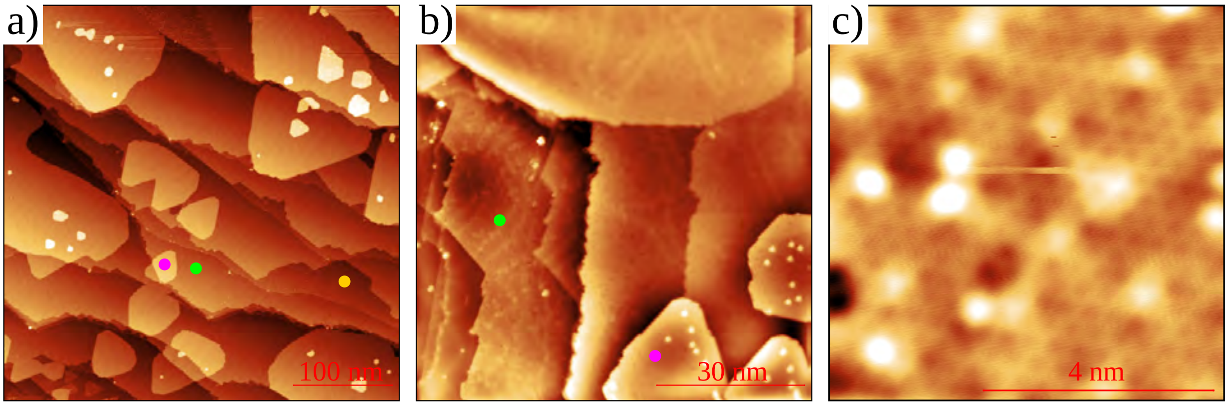

Figure 5.9: a) Topographic STM image of a sub-ML sample of $MnBr_2$ on Au(111). The surface contains areas with clean Au indicated by the yellow dot in a), first- (green dot), and second-layer (purple dot) of $MnBr_2$. In b) a region with first- and second-layer of $MnBr_2$ on Au(111) is shown. Here the herringbone shines through the $MnBr_2$ layer in the upper part of the image. c) Atomic-resolution image of the first layer. a) $U_{\mathrm{Bias}} = 1.8\,\mathrm{V}$ and $I_{\mathrm{TC}} = 0.05\,\mathrm{nA}$, b) $U_{\mathrm{Bias}} = 1.8\,\mathrm{V}$ and $I_{\mathrm{TC}} = 0.05\,\mathrm{nA}$, and c) $U_{\mathrm{Bias}} = 1.8\,\mathrm{V}$ and $I_{\mathrm{TC}} = 0.95\,\mathrm{nA}$. The measurements were performed at 4.5 K.

Here the topographic image shows that many different coverages are coexisting on the surface. The increased roughness of the surface is a consequence of the RT growth. However, even at RT big islands are growing (5.10 a)), which is important for the later spectroscopic analysis. In b) the zoomed-in region of a second-layer defect area is shown (indicated by the red dot). In c) and d) the atomic-resolution images of the second-layer and the layer underneath (marked in purple) are displayed. The second-layer has a lattice constant of 4.1 ± 0.3 Å, which is still close to the literature value. The reason that the atoms are visualized as triangles is the tip during the measurements. Since the tip is also probed by the surface, a visualization of the tip shape is present. Therefore, it seems that the tip had more a triangular shape, due to a functionalization. Additionally, the image shows also a creep motion of the positioning piezos, which caused the non-symmetric elongation. For the layer underneath a lattice constant of 4.08 ± 0.24 Å was extracted, which matches the previous value of the ML sample.

In Figs. 5.11 and 5.12, the first layer of $MnCl_2$ on Au(111), grown at RT and elevated temperatures ($\approx 100\,^\circ\mathrm{C}$), is shown. By comparing the different growth temperatures, it is visible that the surface grows smoother with less defects at elevated temperatures. In Fig. 5.11, STM images of the sample grown at RT are displayed. Here it was not possible to measure the atomic resolution of the first layer. However, in a)-c) topographic images of the first-layer growth are shown, and it is visible that besides an island growth also ribbon-like structures are grown on the surface. These ribbon structures are not following any preferential orientation, but they seem to consist of two different species. In e) and f) atomic-resolution images of the ribbon structure are shown and it seems that the $MnCl_2$ starts to align along the Cl rows, forming this ribbon structure. It has been observed that Cl is forming stripe structures on Au(111), which could act like centers for the $MnCl_2$ attachment. However, since the structures are all over the surface and are forming the ribbons, the possibility of a surface contamination with some other molecules can be excluded (Fig. 5.11 e)). The Cl rows have a separation distance of ≈ 5.6 Å.

The ribbon structure can be separated in two distances. The first is ≈ 4.20 Å, which is coming from the atomic resolution of the outer boundaries of the ribbon (Fig. 5.11 e) red oval shape).

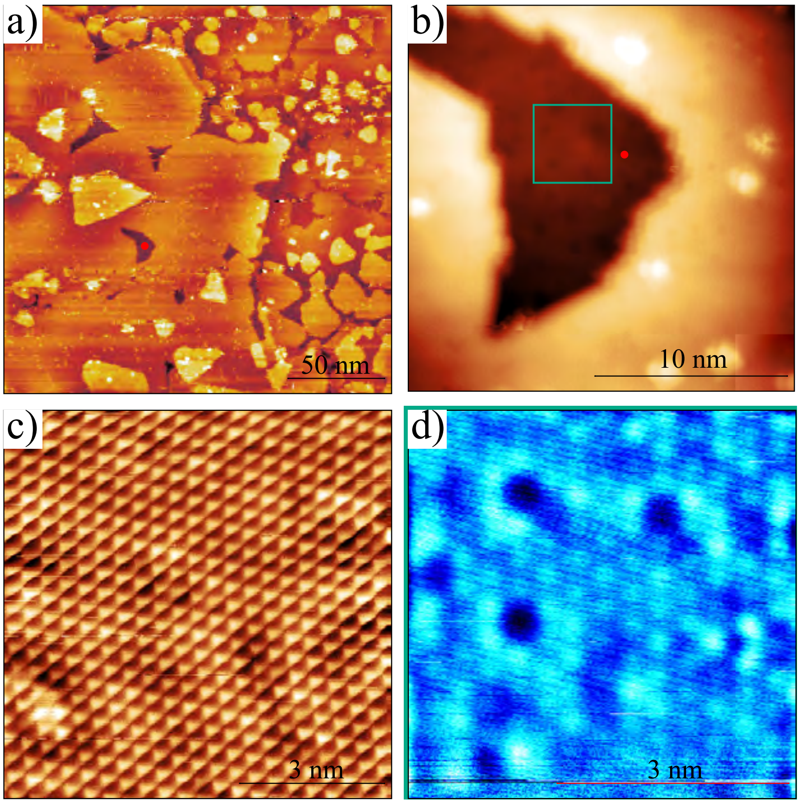

Figure 5.10: a) Topograpic overview of the BL to TL sample. The red circle in a) indicates the position of the surface area defect, which is shown in b). b) Zoomed in region to a defect area of the second layer, due to the RT growth. The purple rectangle indicates the area where the atomic-resolution image d) was measured. The hole of the second layer makes the first layer underneath accessible for STM measurements. c) Atomic-resolution measurement of the second layer of $MnBr_2$ on Au(111). d) Atomic-resolution image of the first layer of $MnBr_2$ on Au(111) inside the hole of the second layer. a) $U_{\mathrm{Bias}} = 1.8\,\mathrm{V}$ and $I_{\mathrm{TC}} = 0.01\,\mathrm{nA}$, b) $U_{\mathrm{Bias}} = 1.8\,\mathrm{V}$ and $I_{\mathrm{TC}} = 0.01\,\mathrm{nA}$, c) $U_{\mathrm{Bias}} = 1.8\,\mathrm{V}$ and $I_{\mathrm{TC}} = 0.02\,\mathrm{nA}$, and d) $U_{\mathrm{Bias}} = 1.8\,\mathrm{V}$ and $I_{\mathrm{TC}} = 0.53\,\mathrm{nA}$. The measurements were performed at 4.5 K.

The second distance is related to the inner ribbon part, indicated by the green oval shape, which has a lattice constant of ≈ 3.3 Å and a separation between the double atom structure (black oval shape) of ≈ 5.3 Å. Without the atomic-resolution image, the lattice distance between the ribbon dots is ≈ 8.5 Å in Fig. 5.11 c). In f) the Cl rows are atomically resolved. The row spacing is around 5.4 Å (dark blue oval shape) with an inner lattice periodicity parallel to the Cl rows of 2.57 Å (light blue oval shape). In Fig. 5.12, the sub-ML $MnCl_2$ on Au(111), which was grown at elevated temperatures is shown. In a) and e) the topographic overview of a ML patch is shown. The surface consists of bigger first-layer islands with small second-layer islands growing on top of it. In c) the atomic resolution of the first layer of $MnCl_2$ on Au(111) is shown. Here some defects are visible on the surface, but not periodically arranged. As observed for other Cl compounds, the herringbone reconstruction is visible through the first layer [132]. From c), a lattice constant of 3.84 ± 0.32 Å can be extracted, which is in good agreement with the literature value for $MnCl_2$ of 3.71 Å [124]. In d) the Cl row structure, which was more prominent on the RT sample, can

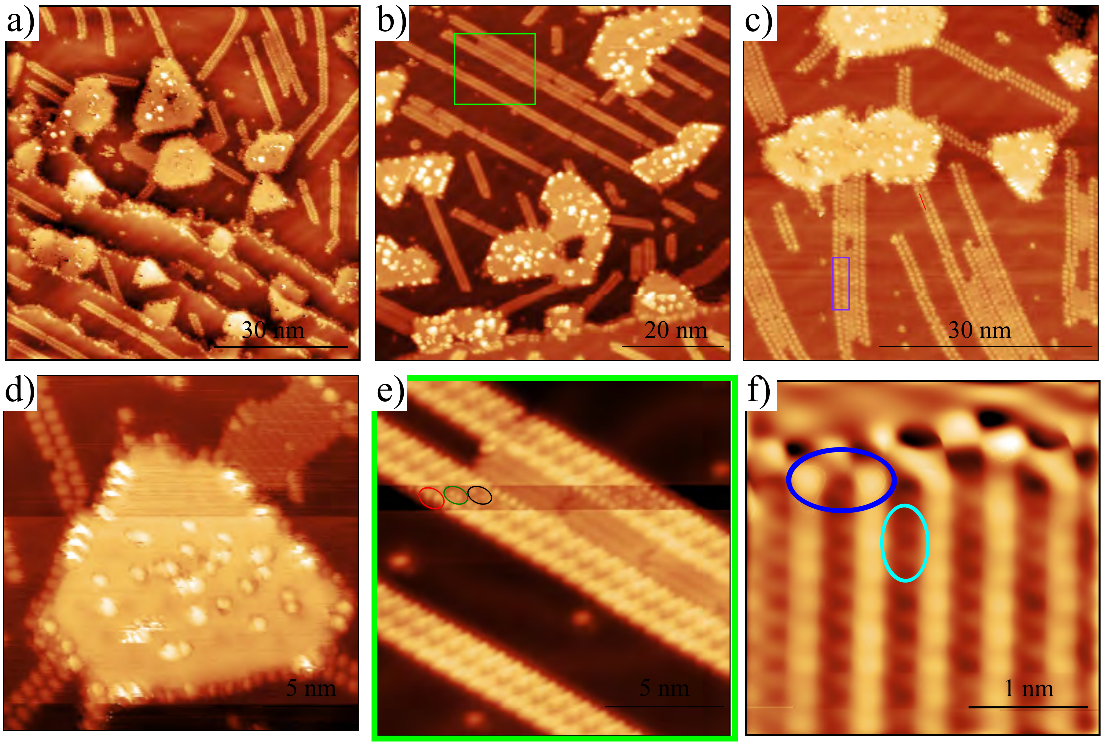

Figure 5.11: a) and b) Topographic overview images of a sub-ML of MnCl$_2$ on Au(111) grown at RT. In b) a green rectangle is used to indicate the position of the ribbon structure, which is shown in more detail in e). c) and d) Single Au terrace with islands of MnCl$_2$ connected to the ribbon structures and the Cl rows. e) and f) Atomic-resolution images of the ribbon structures. a) $U_{\text{Bias}} = 2.0$ V and $I_{\text{TC}} = 0.03$ nA, b) $U_{\text{Bias}} = 1.8$ V and $I_{\text{TC}} = 0.1$ nA, c) $U_{\text{Bias}} = 1.8$ V and $I_{\text{TC}} = 0.02$ nA, d) $U_{\text{Bias}} = 1.8$ V and $I_{\text{TC}} = 0.02$ nA, e) $U_{\text{Bias}} = 1.8$ V and $I_{\text{TC}} = 0.5$ nA, and f) $U_{\text{Bias}} = 0.2$ V and $I_{\text{TC}} = 1.5$ nA. The oval shapes in e) indicate the positions of the diffent lattice distances of the ribbon-like structures. In f) the oval shapes are used to indicate the lattice periodicity in vertical and horizontal direction for the possible Cl islands on Au(111). The measurements were performed at 4.5 K at the PEARL beamline at SLS.

be observed. Here the row distance is 5.4 ± 0.013 Å, which is in the same range as before on the sub-ML sample grown at RT. Due to the fact that some Cl rows are still visible, it means that the sample was not grown at temperatures high enough so that the Cl does not stick to the Au(111) surface anymore. However, the higher temperature caused a higher surface mobility, which results in a dense area of Cl rows at the Au terrace edge. In Fig. 5.13, the BL sample of MnCl$_2$ on Au(111) is shown. Here the surface contains a lot of defects and shows several different local coverages. This is completely related to the RT growth. In b) the atomic-resolution image of the second layer MnCl$_2$ on Au(111) is shown and the extracted lattice constant of 4.0 ± 0.26 Å is in good agreement with the literature value.

MnBr$_2$ and MnCl$_2$ grow epitaxially on Au(111). The extracted lattice constants are in good agreement with the literature values for both materials. The RT growth causes a shining though of the herringbone reconstruction for both materials. This is also visible in LEED where no superstructure is visible for both materials. Additionally, the STM measurements of MnCl$_2$ grown at ≈100 °C reveal a smoother growth with bigger islands and less defect areas. Therefore,

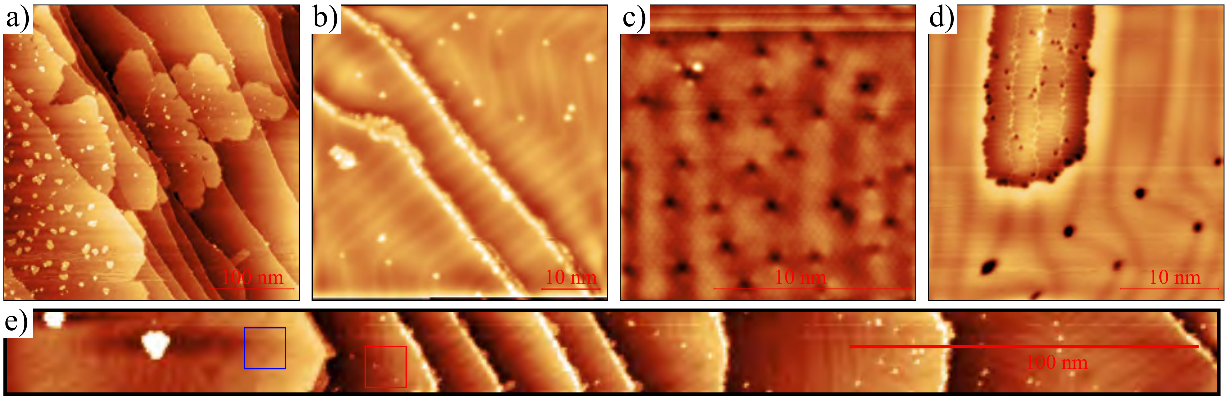

Figure 5.12: a) Topographic image of the first layer of $MnCl_2$ on Au(111) grown at elevated temperatures. b) Clean Au(111) surface area. c) Atomic-resolution of the first layer. d) Zoomed-in image on a Au terrace with some Cl rows attached to them, and e) topographic images over many terraces of Au(111), with some islands of $MnCl_2$. a) $U_{\text{Bias}} = 2.1$ V and $I_{\text{TC}} = 0.02$ nA, b) $U_{\text{Bias}} = 2.2$ V and $I_{\text{TC}} = 0.01$ nA, c) $U_{\text{Bias}} = 2.1$ V and $I_{\text{TC}} = 0.7$ nA, d) $U_{\text{Bias}} = 2.1$ V and $I_{\text{TC}} = 0.02$ nA, and e) $U_{\text{Bias}} = 2.2$ V and $I_{\text{TC}} = 0.01$ nA. The blue and red rectangle in e) indicate the position of the $MnCl_2$ island (blue) and the clean Au(111) surface (red). The clean Au surface can be identified by the nucleation zones at the elbow sites of the herringbone reconstruction. The measurements were performed at 4.5 K at the PEARL beamline at SLS.

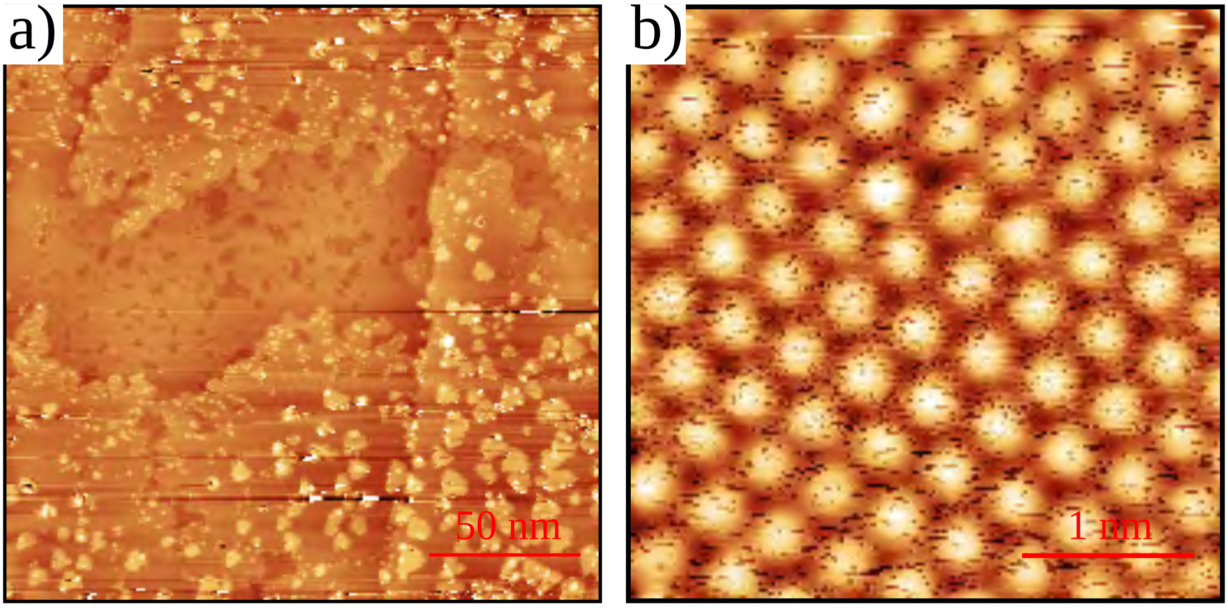

Figure 5.13: a) Topographic overview of the BL sample of $MnCl_2$ on Au(111) grown at RT. b) Atomic-resolution image of the second layer of $MnCl_2$. a) $U_{\text{Bias}} = 1.8$ V and $I_{\text{TC}} = 0.01$ nA and b) $U_{\text{Bias}} = 1.8$ V and $I_{\text{TC}} = 0.22$ nA. The measurements were performed at 4.5 K at the PEARL beamline at SLS.

the elevated temperature growth is preferred for $MnCl_2$ on Au(111) since it does not affect the structural properties by introducing any strain effects as also observed in LEED.

5.1.4 Chemical characterization

In the following part the chemical characterization via XPS of $MnBr_2$ and $MnCl_2$ on Au(111), including the coverage calculation, will be shown. All measurements were performed by using the Al anode of the x-ray gun. In Fig. 5.14, the XPS spectra for different coverages of $MnBr_2$ on Au(111) are shown. The Mn 2p and Br 3p spectra are normalized to the Au 4d peak. This normalization allows that the peak intensities and therefore the coverages can be set into relation. For both film peaks (Mn and Br) a shift to higher binding energies for increasing coverage can be observed. This phenomenon was also seen for $FeBr_2$ on Au(111) and indicates a possible property change in the material, since the superstructure pattern for the sub-ML sample is starting to disappear for higher coverages. Like for $FeBr_2$ on Au(111), the Au 4d spectra are not shifting. To estimate the coverage of the $MnBr_2$ compound, the peak intensity of the normalized Br peak is used. In the case of $FeBr_2$, the normalized Br peak has a peak height of 0.039 for a coverage of 0.6 ML, therefore the coverage of the $MnBr_2$ can be set into relation. This coverage estimation of $MnBr_2$ can be later used for estimating the $MnCl_2$ coverage, by comparing the normalized Mn peak heights. Since the Au $4p_{\frac{1}{2}}$ peak is sitting at the Mn $2p_{\frac{3}{2}}$ energy position, a perfect fit of the system is more difficult and includes a higher error. The intensity of the sum of the Mn $2p_{\frac{3}{2}}$ and Au $4p_{\frac{1}{2}}$ is around 0.0185 for 0.1 ML after normalization to the Au $4d_{\frac{5}{2}}$ peak. In Tab. 7.12 and Tab. 7.13, the Br, Cl and Mn normalized peak heights are mentioned, together with the corresponding coverage.

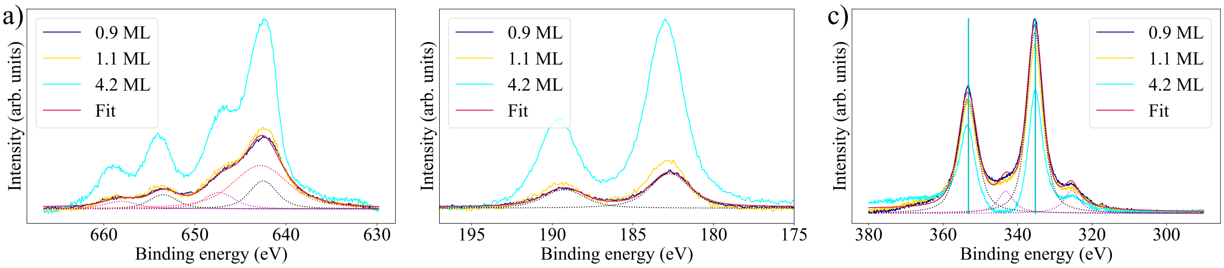

Figure 5.14: a)-c) Coverage-dependent XPS spectra of $MnBr_2$ on Au(111). a) Overlay of the Mn 2p spectra for different coverages. b) Overlay of the Br 3p spectra for different coverages, and c) overlay of the Au 4d spectra for different coverages. The Mn and Br spectra are normalized to the Au 4d main peak. All samples were grown in the temperature range between 117-128 °C as measured on the manipulator with a K-type thermocouple. The red dotted fit in panel a) shows the fit of the Au $4p_{\frac{1}{2}}$ peak, which overlays with the Mn $2p_{\frac{3}{2}}$ peak.

However, these coverage calculations are based on the normalization to the Shirley-background-corrected Au $4d_{\frac{5}{2}}$ peak, which, depending on the material coverage, was not always yielding to a perfect background subtraction. Therefore, the coverage error for samples with an increased coverage is higher. In Tab. 7.14 and Tab. 7.15, the fitting parameters which were used for $MnBr_2$ are displayed. The Shirley-background-corrected spectra of the Au 4d peak at highest coverage in Fig. 5.14 cause a higher coverage error, since it was not possible to perfectly subtract the background. In Fig. 5.15, the XPS spectra of $MnBr_2$ on Au(111) for different growth temperatures are shown. The growth temperature of a sub-ML $MnBr_2$ sample was varried from RT to 150 °C.

In Fig. 5.15, the spectra for 50 °C, 58 °C, 90 °C, and 120 °C growth temperature are displayed. Since the Br and Mn spectra are all normalized to the Au 4d spectra, the peak positions can be directly compared for the different growth temperatures, since the coverages are nearly the

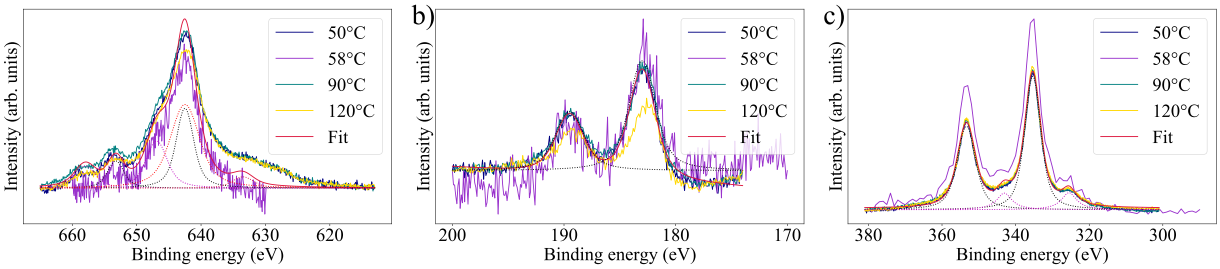

Figure 5.15: a)-c) Growth-temperature-dependent XPS spectra of $MnBr_2$ on Au(111). a) Overlay of the Mn 2p spectra, b) overlay of the Br 3p spectra, and c) overlay of the Au 4d spectra for different growth temperatures. The Mn and Br spectra are normalized to the Au 4d main peak. The coverage of the samples are 0.6, 0.9, 0.6, and 0.4 ML for increasing temperature.

same. For all growth temperatures the spectra are not shifting and the peak structure seems not to change, besides for the 120 °C sample. Therefore no property changes can be observed for the different growth temperatures, where the superstructure does not appear dominantly. At 120 °C growth temperature the Mn and Br peaks are shifted to lower binding energies, as seen for sub-ML $FeBr_2$ on Au(111). From the fits of the data, the material ratio of Mn:Br can be extracted by using the sensitivity factors of both materials. In the case of Br 3p, the same sensitivity factor as for $FeBr_2$ is used. The sensitivity factor for Mn 2p is thus $S_{Mn2p} = 2.659$ and for Br 3p $S_{Br3p} = 1.279$ [32], [206], [339]. The used sensitivity factor from the handbook [206] is for an emission angle of 54.7 °, which is same for Br and is the emission angle used in the XPS setup. By using these factors, a Mn:Br ratio of 0.68 for the 0.9 ML and 0.63 for the 4.2 ML sample can be extracted. For the other samples, especially the low-coverage sample in the range 0.5-0.6 ML, the XPS signal was weaker, and therefore the ratio calculation did not work. The peak position of the Mn 2p peaks and the Br 3p peaks are matching the literature value of a Mn^{2+} and a Br^{1-} state [206]. As previously observed for $FeBr_2$ on Au(111), the satellite peaks have a strong intensity, which also for $MnBr_2$ could be caused by the low electronegativity of Br.

In Fig. 5.16, the coverage-dependent XPS spectra of $MnCl_2$ on Au(111) are shown. In comparison

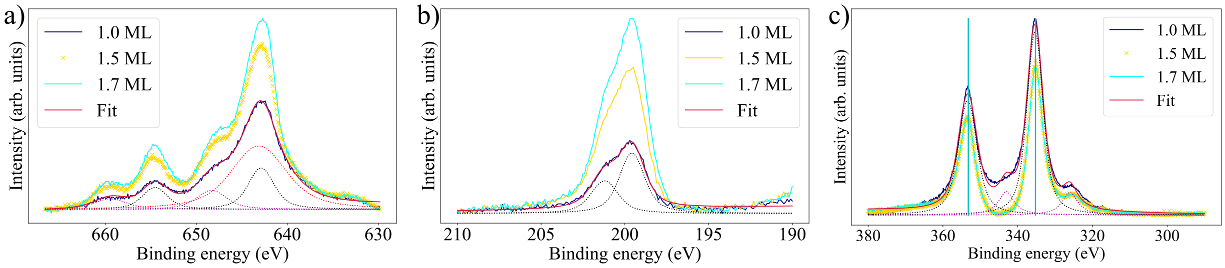

Figure 5.16: a)-c) Coverage-dependent XPS spectra of $MnCl_2$ on Au(111). a) Overlay of the Mn 2p spectra, b) overlay of the Cl 2p spectra, and c) overlay of the Au 4d spectra for different growth temperatures. The Mn and Cl spectra are normalized to the Au 4d main peak. All samples were grown in the temperature range 101-106 °C.

to $MnBr_2$ no shifts of the Mn 2p and Cl 2p peaks can be observed. Since the energy position is not changing, it indicates that, in contrast to the Br compounds the Cl compounds are not changing their properties depending on the coverage. This was kind of expected, since in comparison to the Br compounds, no strong structural changes or strain effects were observed for any coverage. As observed in the LEED measurements, the only structural change is a more dominant domain structure, but without changing the lattice constant.

In Figs. 5.17 and 5.18, the coverage of $MnCl_2$ was varied from sub-ML to BL and the growth temperature was varied for the same sub-ML coverage. By growing the sample at RT, for all coverages a typical ring structure, where the sample contains multiple domains with different orientations and intensities on the Au(111) substrate, appears in LEED images. Here, no change between the spectra, besides the intensity, can be observed, therefore the increasing $MnCl_2$ coverage for samples grown at RT or elevated temperatures does not change their chemical properties (no binding energy shift), compared to Br TMDH compounds on Au(111). In Fig. 5.18, the XPS spectra of a BL $MnCl_2$ on Au(111) grown at different temperatures varying from RT to 102 °C are shown. As already extracted from the results for RT growth and higher-temperature growth for varying coverages, the properties of $MnCl_2$ are also not changing by growing a BL sample at different temperatures. The only observed change was that in LEED preferential domains are growing and the ring structure starts to disappear. However, in XPS, the BL coverage was chosen for the temperature-dependent growth study, since for smaller coverages the Au $4p_{\frac{1}{2}}$ peak would interfere strongly with the Mn $2p_{\frac{3}{2}}$ peak and could hide changes in the peak structure. The coverage for these samples is around 1.5 ML. The fitting parameters for the different coverages

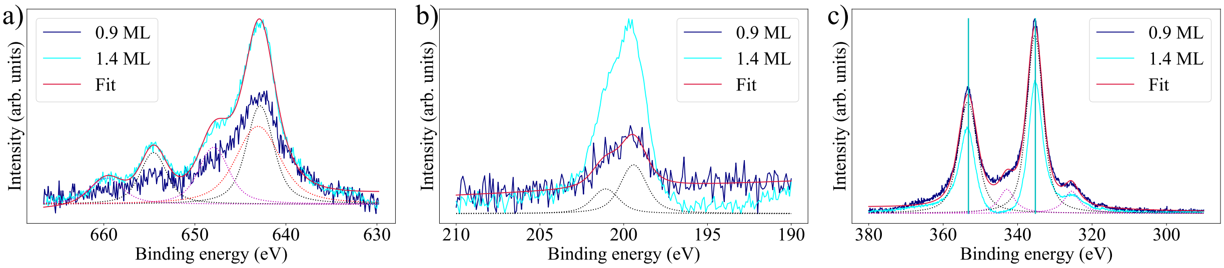

Figure 5.17: a)-c) XPS spectra for different coverages of $MnCl_2$ on Au(111). Both samples were grown at RT. a) Mn 2p spectra, b) Cl 2p spectra, and c) Au 4d spectra. The fit of the Mn spectra is for the 1.4 ML sample.

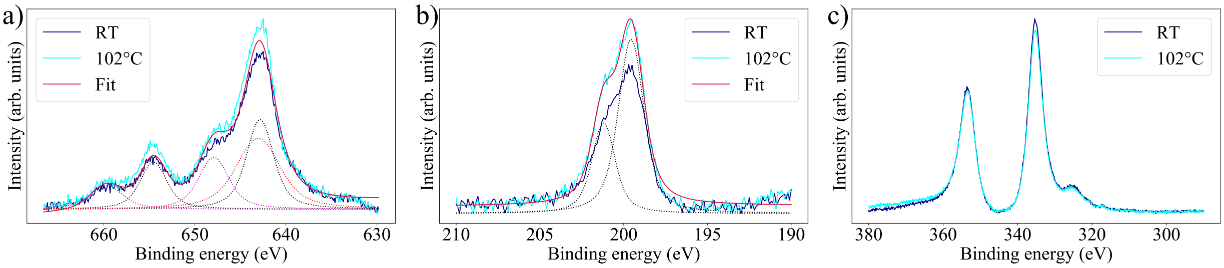

Figure 5.18: a)-c) XPS spectra for different coverages of $MnCl_2$ on Au(111). All samples were grown with nearly the same coverage at varying temperatures. a) Mn 2p spectra, b) Cl 2p spectra, and c) Au 4d spectra. The coverage extracted from the Mn spectra reveals a coverage of 1.4 ML for the sample grown at 102 °C and 1.7 ML for the sample grown at RT. The Au 4d spectra are not fitted, since due to the not optimal background subtraction the FWHM as well as the other fit parameters would not be perfect.

are shown in Tab. 7.16. As observed before for higher coverages of $MnBr_2$, the Mn peaks are matching with the positions for Mn^{2+}. In the case of $MnCl_2$, all coverages have matching peak positions for Mn^{2+} and the Cl peaks are matching with the positions of Cl^{1-} [206]. Because of the overlapping of the Au and Mn peaks, it was not possible to extract the ratio. The configuration can thus only be $MnCl_2$, since other configurations would lead to additional peaks and a different peak structure.

5.1.5 Magnetic characterization

In the following chapter the magnetic characterization of $MnBr_2$ and $MnCl_2$ on Au(111) will be shown. All samples were grown at RT and the corresponding LEED images are shown in Fig 7.44 and Fig. 7.45. As previously observed for $FeBr_2$ on Au(111) and on Bi_2Se_3, $MnBr_2$ and $MnCl_2$ do not show a strong magnetic anisotropy or in the case of $MnBr_2$ a preferential easy axis. In Fig. 5.19 and Fig. 5.20, the XAS and XMCD measurement of $MnBr_2$ and $MnCl_2$ on Au(111) at NI and GI are shown. In Fig. 5.19, no difference between the measurements at NI and GI can be observed, for both geometries the XAS and XMCD signals are not varying strongly. The minor variation in intensity can either be an effect of an easy axis, which is IP, as expected for this material, or just a result of the background correction. The magnetization curves in c) also show that between NI and GI no strong difference can be observed. However, it seems that the material shows a saturating behavior at higher field, but similar to the measurements on $FeBr_2$ on Au(111), a slope is still visible even at high fields for the Br compound. This phenomenon has been now observed for nearly all Br-based halides besides $NiBr_2$ [33]. However, for $CoBr_2$, $FeBr_2$, and $MnBr_2$, this slope behavior even at high fields has been observed, which indicates that the magnetic properties of the Br compounds are directly related to the Au(111) substrate, since this behavior has not been observed for $CoCl_2$ (paper in preparation, Samuel Kerschbaumer at CFM is the first author), $FeCl_2$ (paper in preparation, information received via internal communication) or $MnCl_2$.

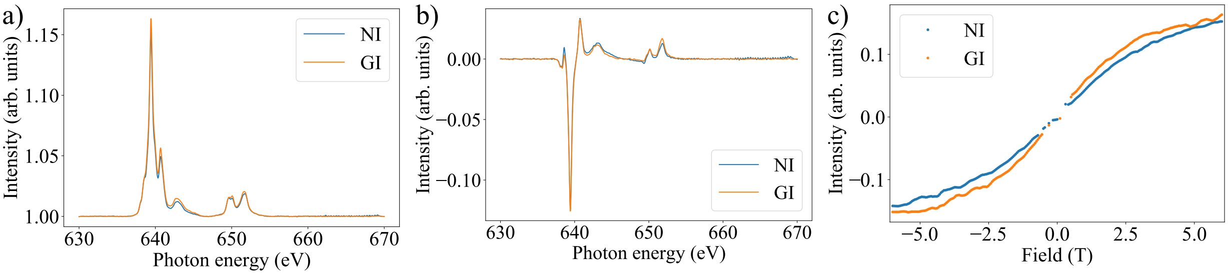

Figure 5.19: a) Isotropic XAS spectra performed at NI and GI of 1 ML $MnBr_2$ on Au(111). b) XMCD spectra for NI and GI measurements. c) XMCD magnetization curves of $MnBr_2$ at NI and GI. The sample was grown at RT and the measurements were performed at 1.7 K and 6 T. The magnetization curves are scaled to the peak height of the isotropic XAS.

In Fig. 5.20, the XAS, XMCD and magnetization curves for 1 ML of $MnCl_2$ on Au(111) are shown. By comparing the XAS and XMCD spectra for both materials and measurement geometries, no difference can be observed. Nevertheless, the magnetization curves of $MnCl_2$ on Au(111) for NI and GI are more different from each other than observed for $MnBr_2$ on Au(111). Here the magnetization curve starts saturating at 3.5 T and is stable at 6 T. The fact that the saturation occurs for the GI measurements shows that the easy axis of this material is IP. The

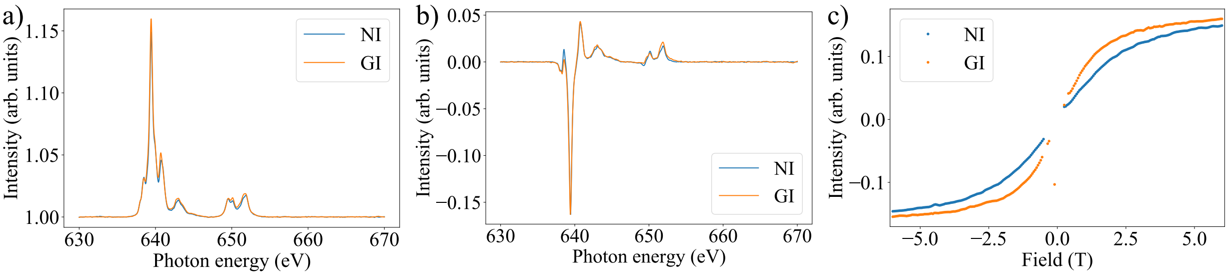

Figure 5.20: a) Isotropic XAS spectra performed at NI and GI of 1 ML $MnCl_2$ on Au(111). b) XMCD spectra for NI and GI measurements. c) XMCD magnetization curves of $MnCl_2$ at NI and GI. The sample was grown at RT and the measurements were performed at 1.7 K and 6 T. The magnetization curves are scaled to the peak height of the isotropic XAS.

coverage of $MnCl_2$ and $MnBr_2$ is estimated from the measured peak height of the isotropic XAS spectra. By using the Henke table [391], the Au substrate has a similar background with a different slope in the region of Mn and Fe. Additionally, Au has its N_2-edge peak at 642.7 eV, which overlaps with the Mn L_3 edge [392]. Therefore, the coverage was estimated by comparing the Mn peak height to the Fe peak height for a known sample coverage of $FeBr_2$ on Au(111). By using that a 0.6 ML $FeBr_2$ sample on Au(111) has a peak height of 12 %, the coverage for the peak height of 16.2 % of $MnCl_2$ on Au(111) would be 0.65 ML, due to the applied conversion factor considering the ratio of the number of holes for Mn and Fe (the conversion factor is 0.8). In the following, the 0.65-ML sample will be considered as 1.0-ML due to the coverage error, which was already present for $FeBr_2$ on Au(111). The coverage of 0.3 ML will be used in the follwoing as 0.5 ML. This coverage is identical to the one of $MnBr_2$ on Au(111) shown in Fig. 5.19 a). By comparing the 1.0 ML sample with a sub-ML one, the change in magnetic properties can be investigated, since the 1.0-ML sample contains also second-layer contributions. In Fig. 5.21 and Fig. 5.22, the coverage-dependent measurements for both Mn compounds are displayed. In Fig. 5.21, the spectra of the 0.5-ML and 1.0-ML samples of $MnBr_2$ on Au(111) are shown. By comparing the XAS and XMCD spectra for both coverages, no difference in the multiplet structure or XMCD spectra can be observed. This indicates that for RT growth no structural nor electronic property changes appear. The magnetization curves for both coverages are similar

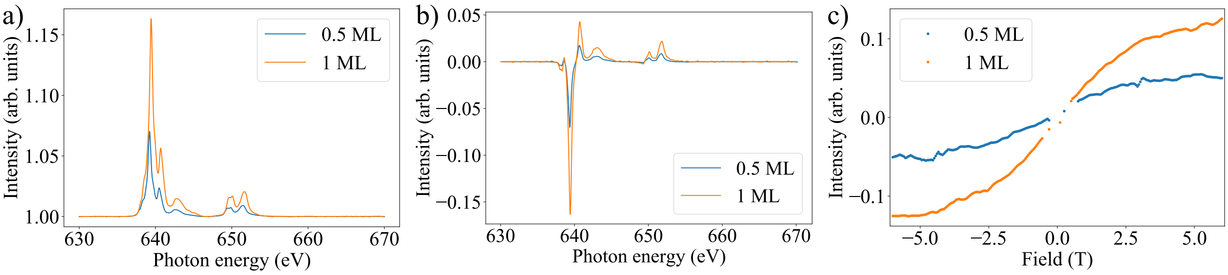

Figure 5.21: Comparison of XAS and XMCD measurements of 0.5 ML and 1.0 ML $MnBr_2$ on Au(111). a) Isotropic XAS, b) XMCD, and c) magnetization curves. Both samples were grown at RT and measured at 1.7 K and 6 T. The magnetization curves and XMCD spectra are scaled to the peak height of the isotropic XAS. The XMCD spectra are aligned by a small shift of 0.15 eV.

and even a possible saturating behavior for the 0.5 ML sample can be observed. However, since the spectra are more noisy than for the ML sample, the possible saturation for $MnBr_2$ could be an artifact, but since the saturation occurs for both field directions at the same field strength, it is probably real. In Fig. 5.22, the coverage-dependent measurements of $MnCl_2$ on Au(111) are displayed. As for $MnBr_2$, no change in the XAS or XMCD spectra can be observed. In c) the magnetization curves for both samples show the same trend and start to staurate around 3.5 T. Therefore, no coverage-dependent magnetic property changes are observed. However, for a more detailed understanding of possible property changes, a higher coverage than 1.0 ML would be needed, around 2.0-3.0 ML. For $MnBr_2$ and $MnCl_2$ the evaluation of the magnetic moments via sum-rule calculation was not useful, since the L_3 and L_2-edge peaks are so close that they overlap. Therefore, the extracted values would be strongly affected by this overlap and cause wrong moments.

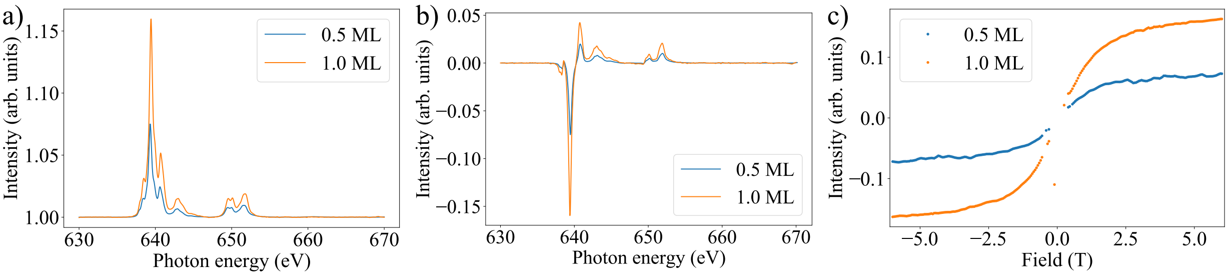

Figure 5.22: Comparison of XAS and XMCD measurements of 0.5 ML and 1.0 ML $MnCl_2$ on Au(111). a) Isotropic XAS, b) XMCD, and c) magnetization curves. Both samples were grown at RT and measured at 1.7 K and 6 T. The magnetization curves and XMCD spectra are scaled to the peak height of the isotropic XAS. The XMCD spectra are aligned by a small shift of 0.15 eV.

In Tab. 7.17 and Tab. 7.18 the extracted moments including the corresponding errors are displayed. Since the materials show a phase transition at low temperatures in the range of 2-2.5 K, these changes of the magnetic properties from the low-temperature AFM phase to the intermediate AFM phase, cannot be resolved by the XMCD measurements. However, the temperature-dependent measurements of $MnBr_2$ and $MnCl_2$ are displayed in Figs. 5.23 and 5.24, where the temperature-related decay of the XMCD signal as well as the temperature-dependent magnetization curves are shown.

In Fig. 5.23, the temperature-dependent XMCD and magnetization curve measurements for 0.5 ML and 1.0 ML $MnBr_2$ on Au(111) are shown. In both cases the saturation behavior of the magnetization curves completely disappears after reaching a temperature of 4 K and the intensity of the XMCD spectra is dropping continuously as expected for increasing temperatures. By comparing the $MnBr_2$ measurements with the ones on $MnCl_2$, the magnetization curves are still showing a saturation behavior up to 4 K for $MnCl_2$ on Au(111). Additionally, the magnetic moments are similar for 1.7 K and 4 K, which could mean that for $MnCl_2$ the saturation at 6 T survives at higher temperatures than for $MnBr_2$. This has also been observed for other previously mentioned Cl-based TMDH (papers in preparation, $CoCl_2$ on Au(111), $FeCl_2$ and $NiCl_2$ on Au(111), internal communication). Nevertheless, since the moment error for Mn is around 30 %, the stability of the effective spin moment at 4 K can be just an error-related artifact. The major difference to $FeBr_2$ on Au(111) is that in the case of $MnCl_2$ grown at RT on Au(111), no orbital magnetic moment was measured. This indicates a purely octahedral symmetry of the material. Therefore, the growth temperature seems to play a significant role not only in the

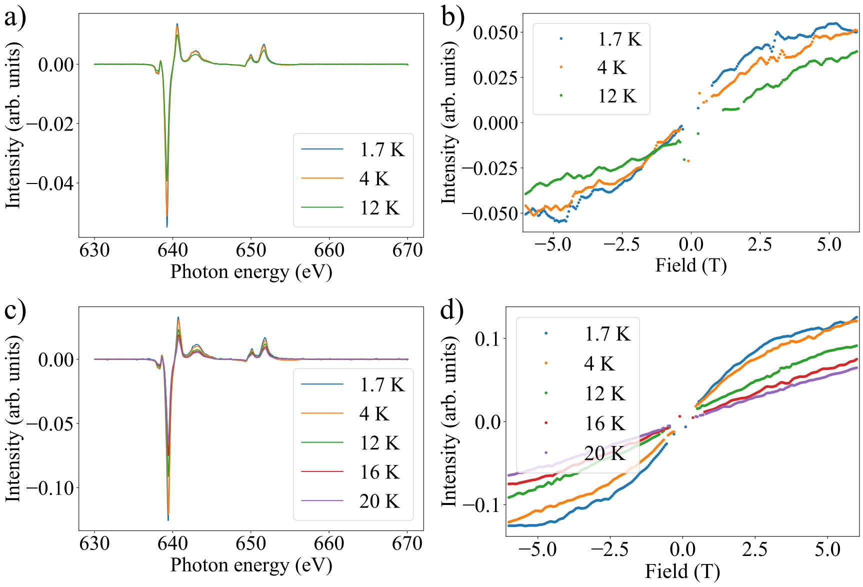

Figure 5.23: a)-b) 0.5 ML $MnBr_2$ on Au(111) and c)-d) 1.0 ML $MnBr_2$ on Au(111). a) and c) Temperature-dependent XMCD spectra. b) and d) Temperature-dependent magnetization curves. Both samples were grown at RT and the XMCD spectra were measured at 6 T. The magnetization curves are scaled to the temperature-dependent intensity of the XMCD signal.

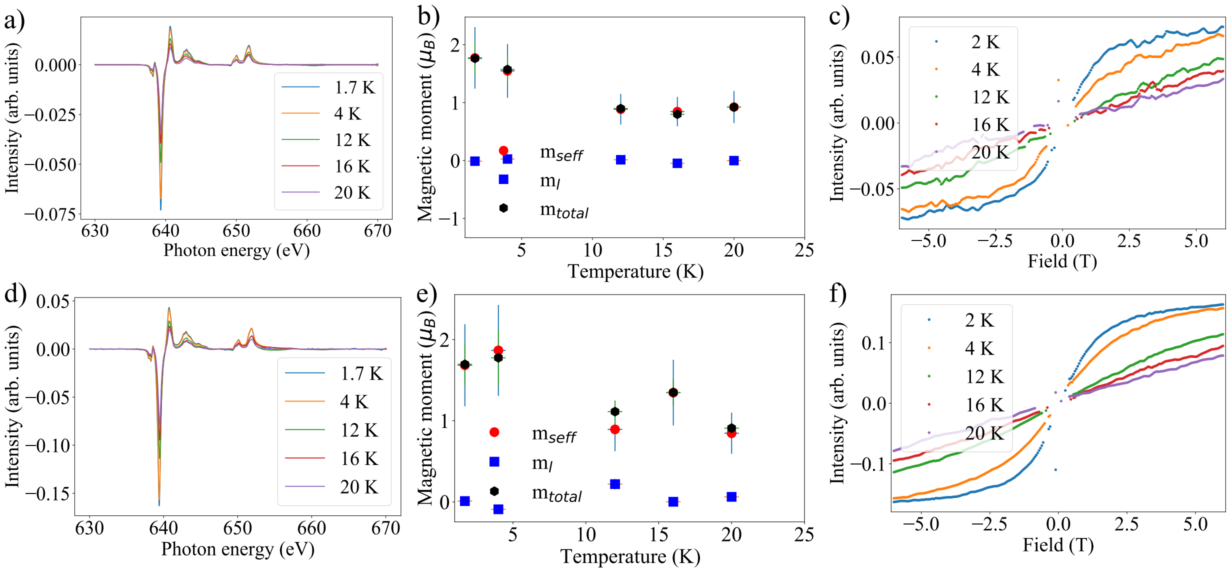

Figure 5.24: a)-c) 0.5 ML $MnCl_2$ on Au(111) and d)-f) 1.0 ML $MnCl_2$ on Au(111). For both coverages the temperature-dependent XMCD spectra as well as the magnetization curves are displayed in (a), d), and c), f)). In b) and e) the extracted magnetic moments for an external field of 6 T are shown. The magnetization curves are scaled to the temperature-dependent intensity of the XMCD signal.

surface structure, but also in the resulting symmetry changes of these materials. In the case of $MnBr_2$, the orbital moment is not zero and the system does not contain probably a purely octahedral symmetry. By comparing the measured XAS spectra in Fig. 5.25 for one ML of $MnBr_2$ and $MnCl_2$ on Au(111) with the simulated XAS multiplet spectra (Fig. 5.25 and Fig. 7.48), it can be observed that for both materials no difference in the multiplet structure exists, and that they are very similar to a Mn^{2+} spectrum with purely octahedral symmetry. The sub-ML and ML XAS measurements of $MnBr_2$ and $MnCl_2$ are matching with the measured XAS spectra in Ref. [393] were a difference of the multiplet structure (ratio between main peak and multiplet peak) at higher photon energies (below the L_3 peak) has been observed. The only difference is in the detailed multiplet splitting around the L_2 edge, which could possibly not be resolved. The magnetic properties of both Mn compounds could not fully be investigated, since the phase transition temperatures of $MnBr_2$ and $MnCl_2$ in bulk are in the regime of the lowest reachable temperature at the beamline. However, the measurements at 1.7 K revealed a saturating behavior for $MnCl_2$, which shows the possibility of aligning the moments along the easy axis at 6 T. The structure could potentially be antiferromagnetically ordered.

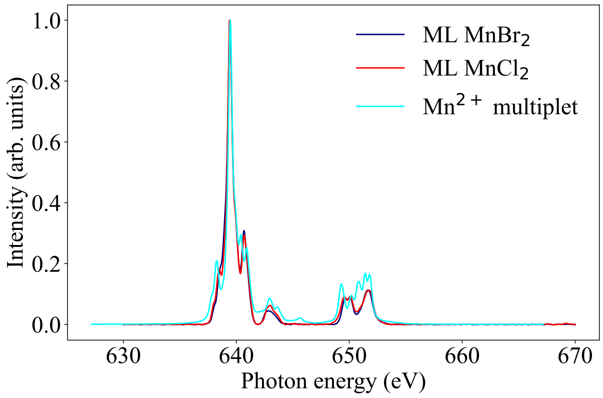

Figure 5.25: Comparison of the simulated multiplet structure for an isotropic Mn^{2+} system with octahedral symmetry and the Slater scaling factors $F_k = 0.8$, $G_k = 0.8$, and $\Gamma = 1.0$ for a Mn^{2+} oxidation state with octahedral symmetry at 2 K and 6 T. The simulations were performed by using a crystal electric field (10 Dq) of 1 eV. The final parameters are $F_2(3d, 3d) = 11.155$, $F_4(3d, 3d) = 6.943$, $\Gamma(3d) = 0.053$, and $\Gamma(2p) = 6.847$. The $MnBr_2$ and $MnCl_2$ spectra used for comparison are the ones of the ML samples measured at 1.7 K and 6 T. The signals are all normalized to 1 for better comparison. The multiplet simulation was performed by using Crispy [351].

However, due to the measurement temperature close to the transition temperature, a paramagnetic behavior can not be excluded. In the case of $MnBr_2$, the magnetization curves are not saturating even for high fields, which could indicate that the material does not behave paramagnetically. By comparing the L_3 edge for $MnBr_2$ and $MnCl_2$, a multiplet peak at low binding energies is more intense for $MnCl_2$ than for $MnBr_2$ on Au(111). Since the coverages in the case of $MnBr_2$ were all below a BL, it is not possible to judge if this peak, like in the case of $FeBr_2$ on Au(111), will regain strength for higher coverages. However, it can be concluded that the different interaction strength of Cl and Au compared to Br and Au is a driving factor for the peak suppression, since this multiplet peak is strongly visible for similar coverages on $MnCl_2$. The same effect has been observed for $FeCl_2$ on Au(111) (information through internal communication). This change in the electronic properties of the material is observable for RT growth of $MnBr_2$, even if no superstructure appears on the surface. Therefore, this peak suppression can be an indicator for the interaction of Au also with Br and not only with the transition metal.

5.1.6 Summary

Over the last sections, the structural, chemical, and magnetic properties of $MnBr_2$ and $MnCl_2$ on Au(111) have been analyzed, discussed, and compared. In the case of $MnBr_2$ grown at elevated temperatures (≈120 °C), a similar behavior as for $FeBr_2$ has been observed. If the $MnBr_2$ is grown at these elevated temperatures, a structural transition of the LEED pattern has been observed. This new structure showed a similar three-spot structure close to the first-order diffraction spots as observed for $FeBr_2$ on Au(111), with a strained lattice constant for the domain spots, which are under an angle to the main symmetry direction of Au(111). Additionally, a new type of superstructure around the (0,0)-spot has been observed. Here, the 12-spot structure as for $FeBr_2$ on Au(111) exists, however, the rotation of the layer to the substrate is higher, which causes a non-equal distribution of the 12 spots. This structure only appears for higher growth temperatures of $MnBr_2$ on Au(111), which was not the case for $FeBr_2$ on Au(111). If $MnBr_2$ is grown at RT on Au(111), then a ring structure appears close to the first-order diffraction spots, since many smaller islands are grown with many different rotations. Nevertheless, even by growing at RT, some dominant domain directions are still visible causing a three-spot pattern on top of the ring structure. Therefore, growing the material at elevated temperatures causes not only a structural change, but also introduces strain. This strain disappears for higher coverages, since the next layers can align to the $MnBr_2$ underneath.

From the chemical analysis of $MnBr_2$ on Au(111), a shift to higher binding energies for increasing coverages has been observed, but only if the sample was grown at elevated temperatures. In the case of RT growth, this shift has not been observed. This indicates that the structural transition which introduces strain also causes the electronic property changes that drive the binding energy shift. The STM measurements which were performed on samples grown at RT showed for $MnBr_2$ the herringbone shining through, which was previously only observed for Cl compounds. However, this can be expected, since the material shows also in the LEED measurement the typical ring structure with no lattice-constant strain effects. For $MnCl_2$, the LEED analysis revealed, similar to $MnBr_2$, a growth-temperature-dependent pattern change, but only for higher coverages. Nevertheless, this change only consists of a main symmetry direction growth, so that the ring structure disappears, but no lattice strain is introduced. The STM measurements revealed that the material grows more smoothly and nicely if the growth temperature is increased.

However, during the growth at RT, the low-coverage sample showed not only island growth of $MnCl_2$, but also ribbon-like structures. Some of these structures can be related to pure Cl on Au(111), which has been already observed for some other Cl-based TMDH compounds. The other ribbon-like structure can not be fully explained. From the extracted lattice constants it seems like a different structural phase of $MnCl_2$ on Au(111) and not like some molecules on the surface. Additionally, this kind of strip growth is not very common for molecules. The most similar structure are graphene nanoribbons. Therefore, a possible growth of $MnCl_2$ ribbons has been observed, but this would need to be investigated in more detail, for now it seems unlikely that a surface contamination, causes this structure. During the growth at elevated temperatures the $MnCl_2$ formed nice islands and still free Cl stayed on the surface (in minor amounts). In summary, the growth of $MnBr_2$ and $MnCl_2$ is smoother at elevated temperatures, but in the case of $MnBr_2$, this causes the growth of the superstructure phase. The chemical characterization for $MnCl_2$ did not show any shifts in binding energy for elevated-temperature or RT growth, which allows the conclusion that the material does not undergo any property changes related to the growth temperature.

In Fig. 7.46, the comparison of a high coverage of $MnBr_2$ and a high coverage of $MnCl_2$ is shown. In the case of $MnBr_2$, the satellite peaks are more pronounced, which could be related to the higher coverage, but could also be an effect of the lower electronegativity of Br. The high-coverage $MnBr_2$ layer is nearly at the same binding energy position, which indicates that higher coverages of $MnBr_2$ grown at elevated temperatures behave like $MnCl_2$. This behavior has been expected, since it was also observed for $FeBr_2$ on Au(111) in comparison to $FeBr_2$ on Bi_2Se_3. The magnetic characterization of $MnBr_2$ and $MnCl_2$ was performed on samples grown at RT. Therefore, no changes in the XAS spectra or XMCD have been observed. The main difference between both compounds is that $MnCl_2$ shows nearly no orbital moment and a distinct saturation of the magnetization curve at 1.7 K. However, the magnetic characterization would need to be performed at lower temperatures and with a more precise temperature control, since the transition temperatures are very close to each other and are in the range of the lowest possible temperature reachable at the beamline.

In summary, both materials show similar properties compared to the other Br and Cl TMDH compounds ($FeBr_2$, $FeCl_2$, $CoCl_2$, and $CoBr_2$), with some interesting structural phenomena and transitions. By increasing the mobility of $MnBr_2$ on the Au(111) surface, the superstructure is formed. At this moment the chemical and structural properties of $MnBr_2$ are changing, due to the introduced strain. For $MnCl_2$ and $MnBr_2$, the magnetic properties are very similar at low temperatures and high fields. Therefore, $MnBr_2$, unlike $FeBr_2$, does not show a change in the magnetic properties for sub-ML coverages compared to the corresponding Cl TMDH compounds. In the case of both Br compounds a less saturating magnetization curve has been observed with a slope even for high fields. This could indicate that by forming the superstructure, a stronger interaction between the Br atoms and the Au appears, due to the orientation on the surface.

6 Summary and outlook

In this thesis, materials from the family of TMDH were investigated. These materials had previously in bulk forms already shown promising magnetic properties and the ability to be exfoliated to the 2D limit, due to the vdW interlayer coupling. During this work, $FeBr_2$, $MnBr_2$, and $MnCl_2$ where grown on Au(111) and Bi_2Se_3 by using the corresponding stoichiometric powders. When sublimating the powder, it was possible to grow these materials epitaxially on Au(111) and Bi_2Se_3. The Br compounds on Au(111) show some property changes as a function of coverage. In the case of the first layer of $FeBr_2$ on Au(111), a dominant superstructure with a periodicity of $\approx$ 1 nm has been observed, which disappears for higher coverages. In addition to the different surface structure, a strong suppression of the magnetic properties, like the reduction of the expectation value of the spin magnetic moment at 6 T and 2 K and the magnetic spin ordering, was observed for the first-layer. This suppression of the saturation of the magnetization curve is indicative for a frustrated antiferromagnetic order in the first-layer or a spin-glass behavior. By Hund's rule, this material should have a magnetic spin moment of $4\,\mu_\mathrm{B}$, which was not observed for any coverage from ML to multilayer. In comparison to the first ML, the second-layer showed at 6 T and 2 K saturating magnetization curves and a higher expectation value of the magnetic spin moment. This change of the magnetic moment is related to a lower interaction of the second layer with the substrate. However, the observed moments are still $\approx$50 % weaker than predicted. Nevertheless, even if the magnetic properties and the surface structure are changing, no different oxidation state or composition of the material has been observed. The only change which was visible in XPS was a shift of the Fe and Br peaks to higher binding energies for increasing coverages with a saturating behavior around 5 ML.

These property changes are related to the Au(111) surface, which is strongly interacting with the Br atoms of $FeBr_2$. The fact that no moiré pattern for $FeBr_2$ on Au(111) was observed could be related to the herringbone reconstruction of Au. As a comparison, $FeBr_2$ was also evaporated on Bi_2Se_3, which is a vdW material. Here, no differences between the first and second-layer were observed, but a higher substrate temperature during growth was required to obtain bigger islands and the long-range moiré pattern. The higher coverages of $FeBr_2$ on Au(111) and any coverage on Bi_2Se_3 are only showing an effective spin moment of $\approx 2\,\mu_\mathrm{B}$ at 6 T and 2 K, which is far away from the expected value. This reduction seems to be an effect of the thin films, which exhibit different properties than the bulk. In Bi_2Se_3, a possible transition from thin film to bulk properties has been observed for higher coverages.

In the case of $MnBr_2$, similar phenomena as for $FeBr_2$ on Au(111) has been observed. The major difference between the observations of $FeBr_2$ and $MnBr_2$ on Au(111) are that $MnBr_2$ needed to be grown at elevated temperatures (120-150 °C) in order to create a dominant superstructure. Even if the superstructure is similar, it has a different lattice constant and rotation angle, so that the inner 12 additional spots of the LEED pattern around the (0,0)-spot are more compressed. This reconstruction is caused by a two rotational domains, which are rotated against the main symmetry direction of Au(111). If $MnBr_2$ is grown at low temperatures, only a ring structure appeared with three main rotational domains. In contrast to $MnBr_2$, $MnCl_2$ only shows a ring structure with one specific domain for low growth temperatures ($\approx$ RT) and only by heating the substrate to $\approx$ 120 °C, a pattern with three rotational domains appears. This indicates already that a weaker interaction between the Au(111) substrate and the Cl atoms of $MnCl_2$ is present, which causes a growth without a dominant superstructure and strain. For the magnetic characterization of both materials on Au(111), a difference in the magnetization curves has been observed, with a faster saturation for $MnCl_2$. However, due to the small energy separation between the L_3 and L_2 edges of Mn, a precise evaluation of the corresponding magnetic moments was not possible.

By comparing both compounds chemically via XPS and XAS, no difference in the oxidation state is visible. By comparing the different coverages of $MnBr_2$ on Au(111) grown at elevated temperatures a shift to higher binding energies for increasing coverages has been observed, which is not present in $MnCl_2$. A possible driving mechanism behind the superstructure and the corresponding strain can also be the growth speed in combination with the growth temperature. These two parameters are strongly influencing the kinetics of the deposited material on the Au(111) surface. In addition, the Au(111) surface consists normally of many terraces, which are working as accumulation zones, similar to the elbow site nucleation centers on Au(111). In comparison, Bi_2Se_3 and other vdW materials have a flatter surface, with less terraces if they are grown nicely or the exfoliation worked perfectly. However, in the case of Cl-based compounds, a possible explanation for the non-existing superstructure or the magnetic and chemical property changes compared to Br compounds can be the weaker interaction of Cl atoms with the Au(111) surface.

As a conclusion of the experimental work in this thesis, it was possible to epitaxially grow $FeBr_2$, $MnBr_2$, and $MnCl_2$ on different substrates in the 2D limit and to characterize the structural, chemical, and magnetic properties of these materials. This work can be used as a starting point for possible later device applications, since the materials are growing on vdW substrates like Bi_2Se_3, which may become the base for new device generations. The growth on Au(111) showed some changed properties for the first-layer. However, the materials properties stabilized for higher coverages therefore, the use of Au contacts is possible since the material will be grown with nm thickness and therefore the effect of the Au interaction is reduced.

As next steps, these materials should be grown under different conditions, by varying also the evaporation rate drastically to observe how the kinetics plays a role in the growth mechanism. To investigate the growth procedure, additional measurements like atomic force microscopy (AFM) and cryo transmission electron microscopy (Cryo-TEM) could be performed to get a more detailed understanding of the growth procedure and the structural symmetry of the materials. Since the XMCD measurements only show an average of the magnetic properties and therefore an average value of the spin magnetic moment, it would be helpful to perform the magnetic characterization more locally via spin-polarized STM measurements. These measurements would result in a nearly full understanding of the material and therefore would need to be performed on Bi_2Se_3 or graphene, which are the most common materials for devices. Therefore, a possible next substrate would be BLG, which can be grown easily on SiC as previously shown.

7 Appendix

7.1 Appendix

7.1.1 Intel Devices

Company	Model name	Year	Transistor Counts	Size [nm]	Source
Intel	Intel4004	1971	2300	10000	[2], [394], [395]
Intel	Intel8008	1972	3500	10000	[394], [396]
Intel	Intel8080	1974	6000	6000	[394], [397]
Intel	Intel8085	1977	6500	3000	[394], [398]
Intel	Intel8086	1978	29000	3000	[394], [399]
Intel	Intel8088	1979	29000	3000	[394], [400]
Intel	Intel80186	1982	55000	3000	[4], [394]
Intel	Intel80286	1982	134000	1500	[394], [401]
Intel	Intel80386	1985	275000	1500	[394], [402]
Intel	Inteli960	1988	250000	1500	[394], [403]
Intel	Inteli960CA	1989	600000	800	[394], [403]
Intel	Intel80486	1993	1180235	1000	[394], [404]
Intel	IntelPentiumPro	1995	5500000	500	[394], [405]
Intel	IntelPentiumII	1997	7500000	350	[394], [406]
Intel	IntelPentiumIII	1999	9500000	250	[394], [407]
Intel	IntelPentium4	2000	42000000	180	[394], [408]
Intel	IntelItanium2	2003	410000000	130	[394], [409]
Intel	Pentium 4 Prescott	2004	112000000	90	[394], [408]
Intel	IntelCore2 Duo	2006	291000000	65	[394], [410]
Intel	Six-core Xeon 7400	2008	1900000000	45	[394], [411]
Intel	Xeon Nehalem-EX	2010	230000000	45	[394], [411]
Intel	IntelItaniumPoulson	2012	3100000000	32	[394], [409]
Intel	Xeon Haswell-E5	2014	5560000000	22	[394], [412]
Intel	Core i7 Broadwell-U	2015	1900000000	14	[394], [413]
Intel	Core i7 Broadwell-E	2016	3200000000	14	[394], [413]
Intel	Xeon Broadwell-E5	2016	7200000000	14	[394], [413]
Intel	Xeon Platinum 8180	2017	8000000000	14	[394], [414]
Intel	Core 11th gen Rocket Lake	2021	6000000000	14	[394], [415]
Intel	Sapphire Rapids	2023	44000000000	10	[394], [416]

Table 7.1: Displayed is a selection of Intel chips, with the corresponding transistor counts and the size of the transistor. This table is graphically plotted in Fig. 1.1.

7.1.2 Used Equipment

Company	Equipment	Location
SPECS	EBE-4	FU-Berlin
Feinwerktechnik	Single Pocket	FU-Berlin
Prevac	EF 40C1	FU-Berlin
Prevac	HEAT3-PS	FU-Berlin
Prevac	QO 40A1	FU-Berlin
Prevac	TM14	FU-Berlin
Prevac	TMC-13	FU-Berlin
Scienta Omicron	PBN 5 A	FU-Berlin
Feinwerktechnik	Cryostage	FU-Berlin
Pfeiffer	HiScoll6	FU-Berlin
Pfeiffer	HiPace80	FU-Berlin
Pfeiffer	HiPace700	FU-Berlin
AML/Arunmicro	NGC2D	FU-Berlin
Statron	3252.3	FU-Berlin
Statron	3250	FU-Berlin
Heinzinger	LNC3000-20 pos.	FU-Berlin
Keysight	S3220A	FU-Berlin
SPECS	Phoibos 150	FU-Berlin
SPECS	2D CCD-Detector	FU-Berlin
SPECS	HSA3500	FU-Berlin
Fision Instruments	XR3E2	FU-Berlin
Fision Instruments	8025 X-ray Power Supply	FU-Berlin
AML/Arunmicro	NGC2	FU-Berlin
Heinzinger	LNG32-3.	FU-Berlin
Omicron	SPECTALEED CONTROL Unit	FU-Berlin
Creekside Technologies	Ion Bombardement Gun	FU-Berlin
Pfeiffer	HiPace300	FU-Berlin
Stanford Research Systems	SR830 DSP	FU-Berlin
STAIB Instruments	NESA2500	FU-Berlin
STAIB Instruments	NEK-310-IK	FU-Berlin
LEYBOLD	Netzgerät NV12	FU-Berlin
Dotecon	4x OMBE Source	CFM
MBE Komponenten	QCS	CFM
SPECS	IQE 11/35	CFM
SPECS	COSCON IS	CFM
Vacuum Micro Engeneering	MCP Power Supply	CFM
Vacuum Micro Engeneering	Digital LEED-AES Controller	CFM
SPECS	Phoibos 100 Analyzer	CFM
SPECS	HSA3500 plus	CFM
SPECS	CCX 60	CFM
SPECS	XRC 1000	CFM
SPECS	XR 50	CFM
SPECS	COSCON IS	CFM
SPECS	PCS-ECR-AO	CFM
Delta Elektronika	ES 030-10	CFM
Delta Elektronika	SM100-AR-75	CFM
Delta Elektronika	ES015-10 S108-10	CFM

Table 7.2: Equipment list of the different non-synchrotron labs. At CFM the measurements were performed in the XPS Nanophysics Lab and at FU-Berlin in the BESSY lab.

7.1.3 Preparation and measurement chamber at FU-Berlin

Detailed 3D image of the setup at FU-Berlin in room -1.2.03/BESSY lab (Fig. 7.1). Tab. 7.3 lists the mounted and used equipment parts. In Fig. 7.2, the new design of a direct current heating system is displayed. The previously shown direct current heater is a design by the company Scienta Omicron, which was used at the PEARL beamline for some first tests for the preparation of SiC.

Equipment Part PC	Equipment
1.)	PC Manipulator
2.)	QCM
3.)	Metal Evaporator
4.)	Powder Evaporator
5.)	Se Evaporator
6.)	Cryopump
7.)	Turbopump
8.)	Sample holder
9.)	Viewport

Equipment Part XC	Equipment
1.)	XC Manipulator
2.)	X-ray tube
3.)	Phoibos 150
4.)	2D-CCD
5.)	Sputter gun
6.)	Auger
7.)	LEED
8.)	Getter pump
9.)	Turbopump

Table 7.3: In both tables the important equipment parts of the preparation chamber (PC) and XPS chamber (XP) at FU Berlin are listed. The corresponding figure is Fig. 7.1. The table on the left lists the equipment of the preparation chamber and the one the right of the XPS chamber.

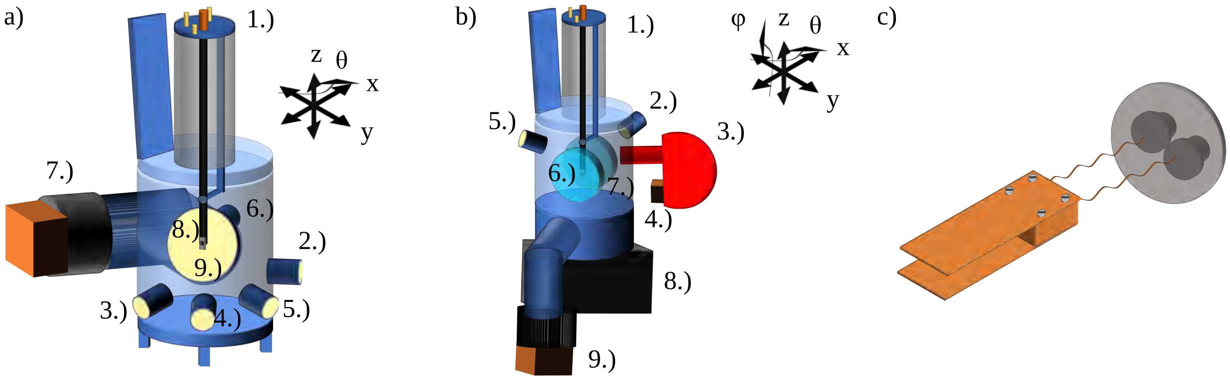

Figure 7.1: a) Setup of the preparation chamber and b) the one of the XPS chamber. The degrees of freedom of the manipulators are indicated in the right corner. The list of the mounted equipment is found in Tab. 7.3. In c) the cryopump in the preparation chamber for liquid-nitrogen cooling is displayed. The two Cu shields are creating a bigger area to attract the evaporated materials for faster pressure decrease due to the strong thermal gradient. The cryopump design was build and designed together with our engineer Uwe Lipowski. The displayed size differences are just schematic and do not represent the real ratio.

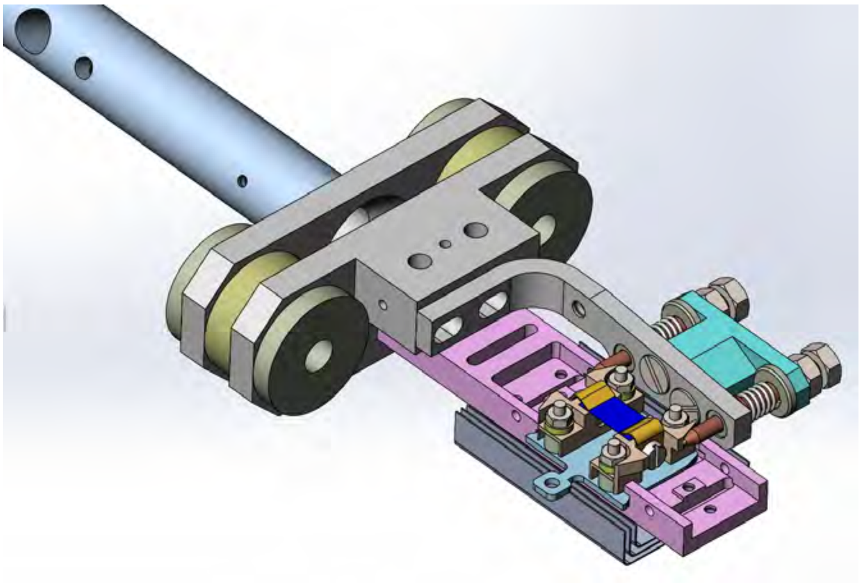

Figure 7.2: Direct current heater design. The current is guided through the Cu pins onto the sample plate. By moving in the direct current sample plate, the Cu pins slide along the connectors and are creating a contact area, where the current will flow through. The Cu pins are mounted with a spring mechanism, which allows that the sample plate can be easily moved in and out with an optimal contact of the Cu pins. The sample plate itself is of Mo and Ta. The mounting screws are decoupled from the current flow via Al_2O_3 connectors. The maximal dimensions of the used SiC crystals for optimal results is related to the used clamping mechanism size (yellow). The design was drawn by Uwe Lipowski the engineer of the AG Kuch and AG Weinelt at FU Berlin and the design iterations were performed by Marcel Walter, Uwe Lipowski, and me.

The design in Fig. 7.2 was successfully working in the preparation chamber at FU-Berlin. However, the design has again changed and was removed from the preparation chamber into a separate chamber, due to problems during the transfer from the preparation chamber to the analysis chamber (XPS chamber).

7.1.4 Preparation and measurement chamber at CFM

Detailed 3D image of the setup at CFM (Fig. 7.3). Tab. 7.4 lists the mounted equipment parts.

Equipment Part	Equipment	Equipment Part	Equipment
1.)	PC Manipulator	12.)	MCP LEED
2.)	LL	13.)	Getter pump
3.)	Transfer bar	14.)	Transfer bar
4.)	QCM	15.)	LC PC connection
5.)	Sputter Gun PC	16.)	LC XC connection
6.)	Evaporator 1	17.)	Sputter gun
7.)	Evaporator 2	18.)	Getter pump
8.)	QMS/Evaporator 3	19.)	Transfer bar
9.)	Turbopump	20.)	Phoibos 100
10.)	Ion Gauge	21.)	X-ray tube
11.)	Sample Garage PC	22.)	XC manipulator

Table 7.4: List of chamber parts of the Nanophysics lab at CFM in Donostia. The numbers are referring to the numbers in Fig. 7.3. The abbreviation LL stands for Load Lock, PC for preparation chamber, LC for LEED chamber, and XC for XPS chamber.

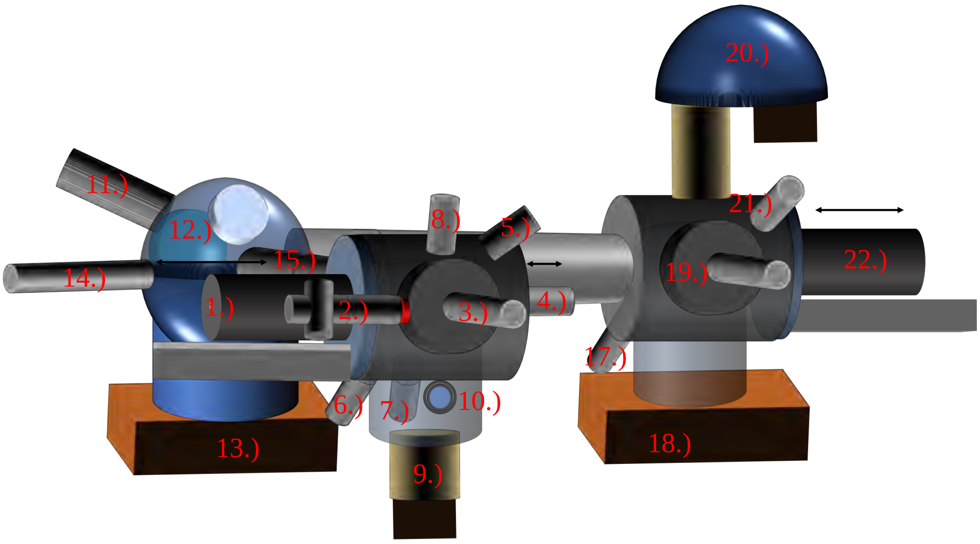

Figure 7.3: 3D view of the chamber used at CFM including a position-related description of each part. The red numbers indicate the position of the main equipment parts, which are listed in Tab. 7.4. The displayed size differences are just schematic and do not represent the real ratio.

For the majority of experiments, the Dodecon four-pocket evaporator is used in single-pocket operation mode. In Fig. 7.5, the temperature increase of a single-pocket is shown. The water cooling system is sufficient to keep the other pockets at RT [388] even for an crucible temperature of ≈700 °C of the heated pocket.

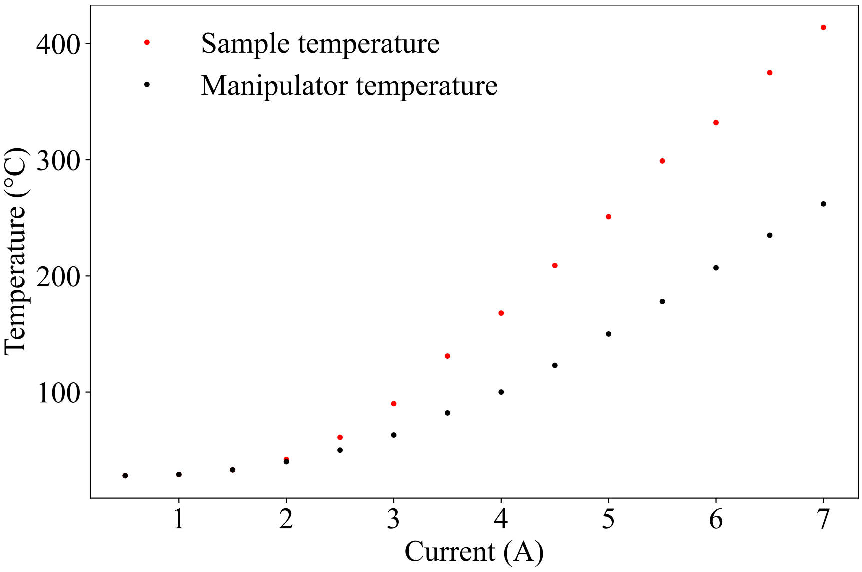

Figure 7.4: Temperature calibration of the preparation chamber at CFM. The measured temperature of the manipulator is compared to the temperature directly measured on top of a sample plate. The manipulator uses a filament heating system and has a liquid nitrogen cooling system, which is also used to cool the samples with compressed air, for a faster cooling after annealing. The temperature calibration of the preparation chamber heating system was performed at CFM in 2023 by Samuel Kerschbaumer.

In Fig. 7.4, the temperature calibration inside the preparation chamber is shown. The sample temperature was measured by a thermocouple, which was mounted directly onto an Omicron sample plate.

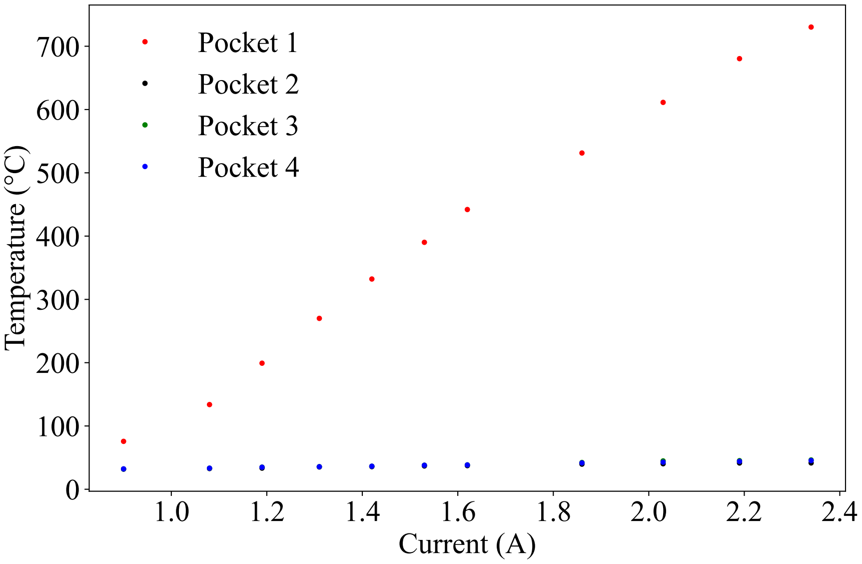

Figure 7.5: Temperature evolution of all four pockets of the Dodecon evaporator, during the heating process of pocket 1. The calibration informations are obtained from [388]. In the case of the used evaporator, the shutter is removed.

7.1.5 Beamline Sample shuttle

In Fig. 7.6, the different sample shuttle designs used at the different beamlines are shown.

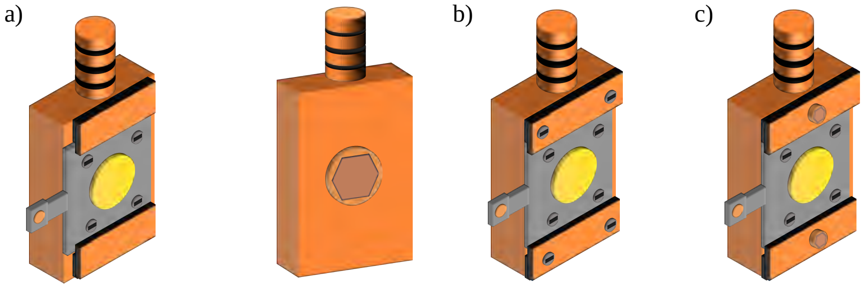

Figure 7.6: Different sample shuttle designs. a) Front and back view of the regular shuttle design for low-temperature and high-field measurements. This design is used at the DEIMOS and XTreme beamlines. On the back, a hexagonal screw is used to press the inserted sample plate against the front plates, so that it has an ideal thermal contact. b) Sample shuttle design of the VEKMAG beamline. Here the thermal contact is achieved by tightening the four small screws. c) BOREAS beamline shuttle design, which is a mixture of the VEKMAG and DEIMOS approach using a front tightening system with hexagonal screws. On top, all shuttles have a mounting system to screw it into the main-chamber manipulator. This needs to be tight for the ideal thermal contact and to avoid vibrations.

7.1.6 VEKMAG setup

In Fig. 7.7, the 3D image of the VEKMAG setup is shown. Tab. 7.5 shows the equipment list of the VEKMAG station (preparation chamber and endstation).

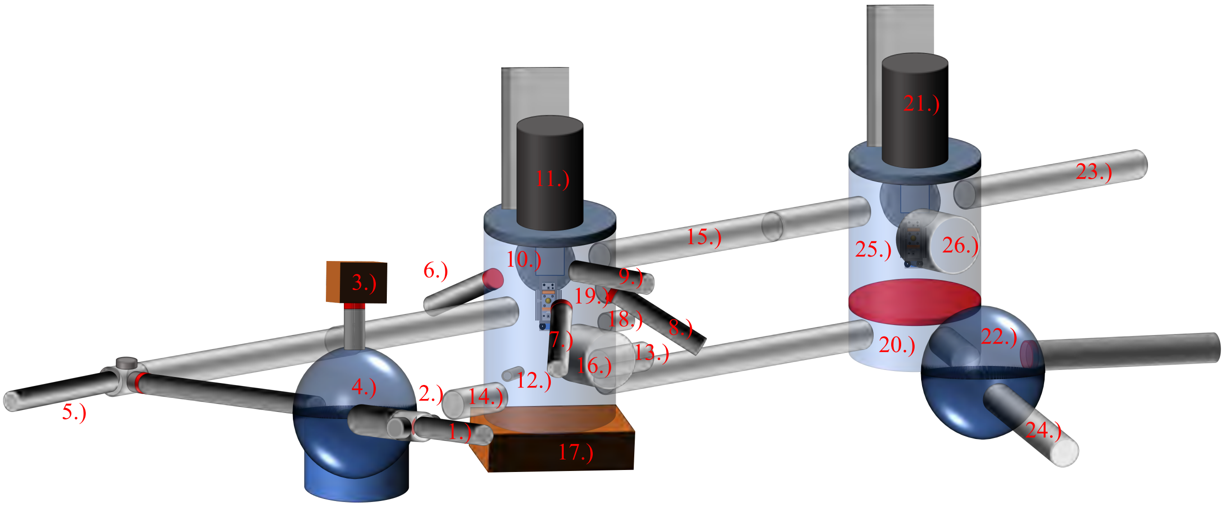

Figure 7.7: 3D view of the VEKMAG setup. In red, the gate valve positions are indicated. All important chamber parts are numbered and named in Tab. 7.5. The displayed sizes are not up to scale.

Equipment Part	Equipment	Equipment Part	Equipment
1.)	Transfer bar LL	14.)	Transfer bar MC
2.)	LL	15.)	X-ray beam port
3.)	ALI	16.)	Turbopump PC
4.)	ALI PC	17.)	Getter PC
5.)	Transfer bar PC	18.)	Ion gauge
6.)	Evaporator 1	19.)	Sputter gun
7.)	Evaporator 2	20.)	TC
8.)	Evaporator 3	21.)	Manipulator MC
9.)	QCM	22.)	MC LL
10.)	LEED	23.)	X-ray beam port
11.)	Manipulator PC	24.)	Transfer bar MC LL
12.)	Screw driver	25.)	MC
13.)	Flashing stage	26.)	View port

Table 7.5: List of chamber parts of the VEKMAG setup at BESSY II. The numbers are referring to the numbers in Fig. 7.7. The abbreviation LL stands for Load Lock, PC for preparation chamber, ALI for the atomic layer injection system chamber, TC for transfer chamber, and MC for magnet chamber.

7.1.7 DEIMOS setup

In Fig. 7.8, the 3D image of the DEIMOS setup is shown. Tab. 7.6 shows the equipment list of the DEIMOS station (preparation chambers and endstation).

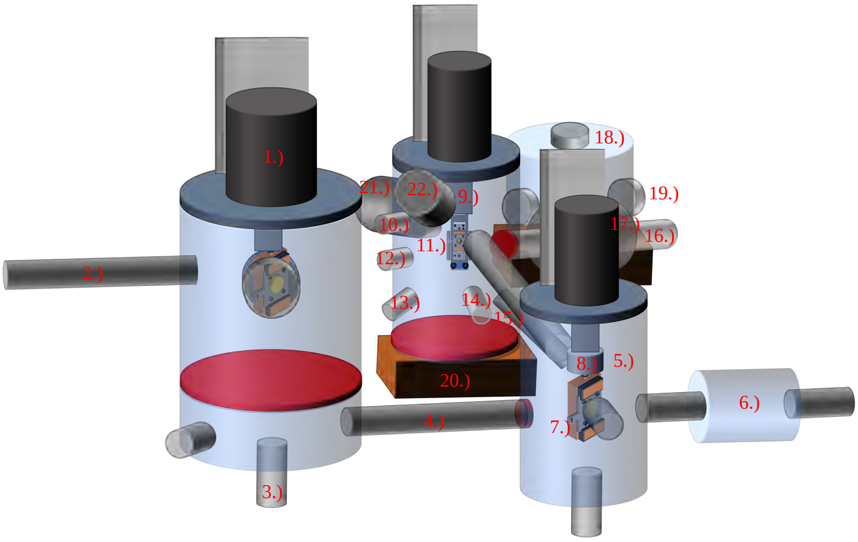

Figure 7.8: Detailed 3D image of the DEIMOS beamline including all connections and the main components. The positions of gate valves are indicated as red cylinders. The numbers refer to Tab. 7.6.

Equipment Part	Equipment	Equipment Part	Equipment
1.)	MC Manipulator	12.)	Needle Valve
2.)	Beam port	13.)	Ion Gauge
3.)	Shuttle mounting	14.)	QCM
4.)	Transfer connection	15.)	Evaporator
5.)	TC	16.)	Transfer bar
6.)	LL 1	17.)	Transfer STM PC
7.)	Shuttle holder 2	18.)	VT-STM
8.)	Sample garage 3	19.)	View Port
9.)	PC Manipulator	20.)	PC Getter
10.)	Needle Valve O_2	21.)	Auger
11.)	Needle Valve Ar	22.)	Sample Shutter

Table 7.6: List of chamber parts of the DEIMOS setup at SOLEIL. The numbers refer to the numbers in Fig. 7.8. The abbreviation LL stands for Load Lock, PC for preparation chamber, TC for transfer chamber, and MC for magnet chamber.

7.1.8 Crystals

In Fig. 7.9 a), a Au(111) single crystal and in b) a Bi_2Se_3 single crystal with spot-weld mounting are displayed. The mounting of the Au(111) crystal which was used for the majority of experiments is a screwed shield mounting. Therefore, the sample plate has a small groove inside, so that the crystal can be positioned nicely. The single-crystal shape which is needed for this mounting system is hat shape. In Fig. 7.10, the screw mounting mechanism is displayed on a VEKMAG sample shuttle.

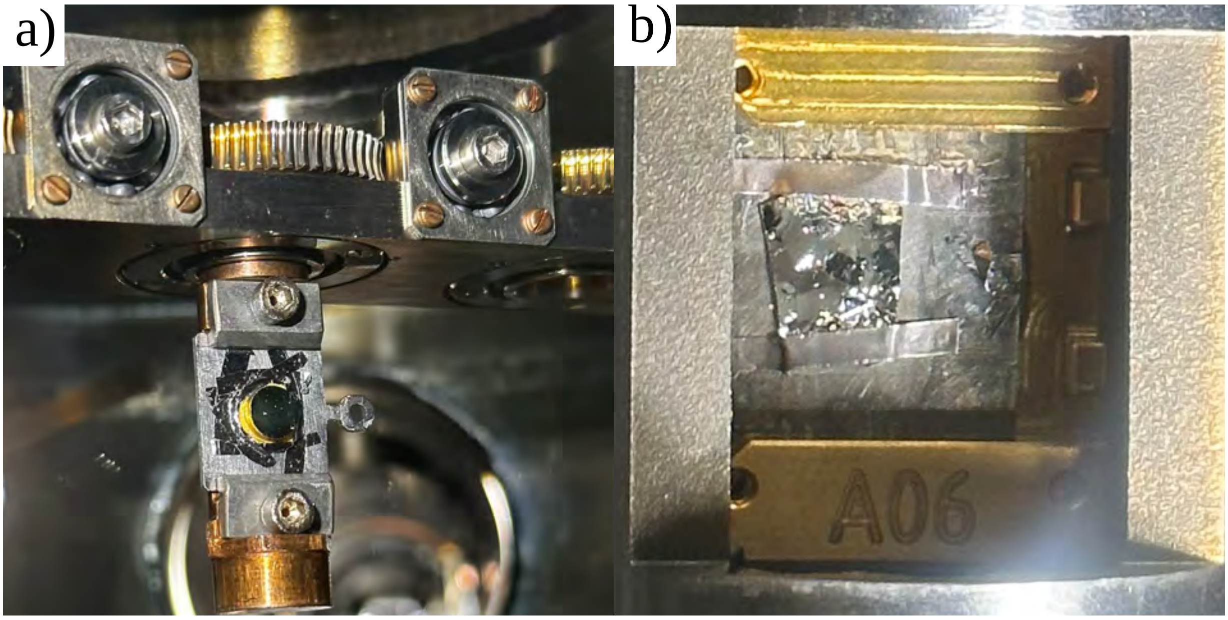

Figure 7.9: a) Au(111) single crystal mounted in a sample shuttle at the BOREAS beamline (the crystal belongs to CFM). b) Bi_2Se_3 single crystal from CFM mounted inside the sample shuttle at the XTreme beamline. The photos were taken by Samuel Kerschbaumer during our joint beamtime at BOREAS in 2023 and XTreme in 2023.

7.1.9 Material colors

In Fig. 7.11, the different powder colors are displayed. The numbers 2-4 are referring to the used pockets inside the Dodecon evaporator. In the case of $MnBr_2$ and $MnCl_2$, no difference in color can be observed. The powder stays in a white to light pinkish color. The $FeBr_2$ powder evolves depending on the environmental conditions. In a) the powder shows a red-orange color, which is related to a hydratization phase. After mounting the evaporator and pumping the chamber the powder color changes from orange to a mixture of yellow and gray. After the degassing process is finished the $FeBr_2$ powder is yellow. However, the powder color can also differ depending on the conditions and not always follows the same scheme (since the color also strongly depends on the hydratization state). If the powder stays in an environment with dry air, they can be used for a long time. The best conditions for these materials are a desiccator environment. For the used material in this thesis, the hydratization process is reversible. This was observed for $NiBr_2$, $NiCl_2$, $CoBr_2$, $CoCl_2$, $FeBr_2$, $FeCl_2$, $MnBr_2$, and $MnCl_2$ [32], [33], (information about $CoBr_2$, $CoCl_2$, $FeCl_2$, and $NiCl_2$ are from internal communications).

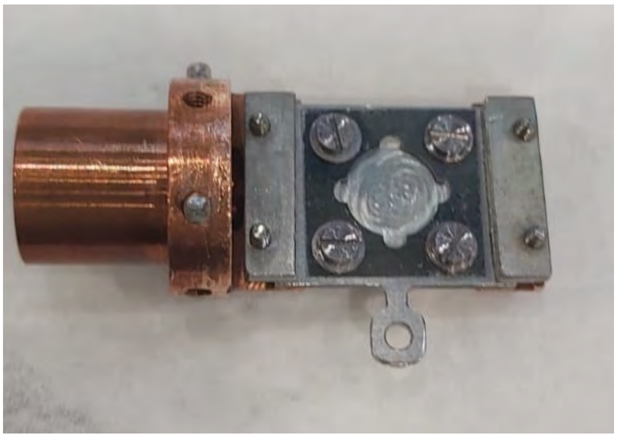

Figure 7.10: Screw mounting mechanism for single crystals mounted inside the VEKMAG sample shuttle. The photo was taken by Dr. Sangeeta Thakur in 2021 during the beamtime preparation of a joint beamtime to check if the new sample plate mounting fit into the VEKMAG sample shuttles.

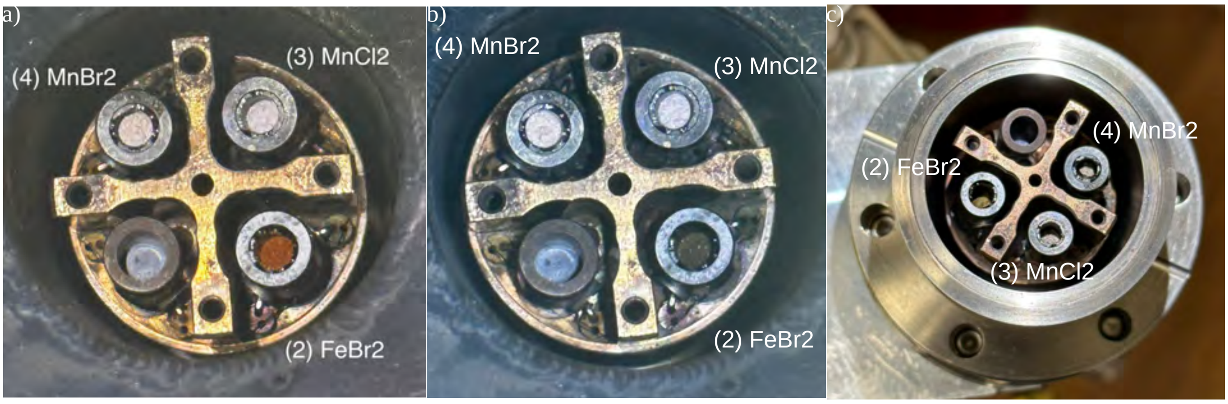

Figure 7.11: a)-c) Different stages of powder colors, depending on the environmental conditions. In a) the three loaded pockets are indicated by the numbering in front of the material name. The powder colors refer to a stage after hydratization. In b) the evaporator was mounted inside the pumped vacuum chamber, without degassing or baking the evaporator. In c) the evaporator was removed after finishing the experiment. The images a) and b) were taken at CFM and c) at the BOREAS beamline. The material loaded in c) is not the same powder as in a) and b). The photos were taken by Samuel Kerschbaumer during our joint beamtime at BOREAS in 2023 and the stays in Donostia at CFM during my experiments.

7.1.10 Coverage-dependent LEED pattern evolution of $FeBr_2$ on Au(111)

In Fig. 7.12, the coverage-dependent evolution of the LEED pattern of $FeBr_2$ on Au(111) is shown. All displayed images, were measured at 45 eV. It can be observed that with increasing coverage, the spot intensity of the sub-ML pattern is getting more intense. For this low-coverage regime the third set of spots around the main diffraction spot and around the (0,0)-spot is not visible. After overcoming a critical coverage around 0.6 ML to 1.6 ML, a mixed LEED pattern can be observed, which is caused by two competing material structures (sub-ML and the BL). For this coverage regime, the third set of spots appears. By further increasing the coverage, the regions with a sub-ML structure are vanishing and only the second layer pattern can be observed, which consists of a moiré pattern. The new structure shows a non rotated hexagonal pattern, which is aligned with the Au(111) structure. In Fig. 7.13, different LEED energies for the ML sample of $FeBr_2$ on Au(111) are displayed. The dominant structure type is related to the $FeBr_2$ sub-ML sample and the two different third-spot types (moiré pattern and second-layer spots) are related to the next-layer growth. At 25 eV, the third set of spots, inside the ring structure around the (0,0)-spot can be observed (indicated by the red circles). By increasing the energy further, a third spot around the (1,0)-spot can be observed. The calculated lattice constant based on the third set of spots has a smaller lattice constant than the one related to the two rotational domains. This indicates that the introduced strain of the first layer on Au(111) is not present for the second layer and that the material is growing with the expected lattice constant.

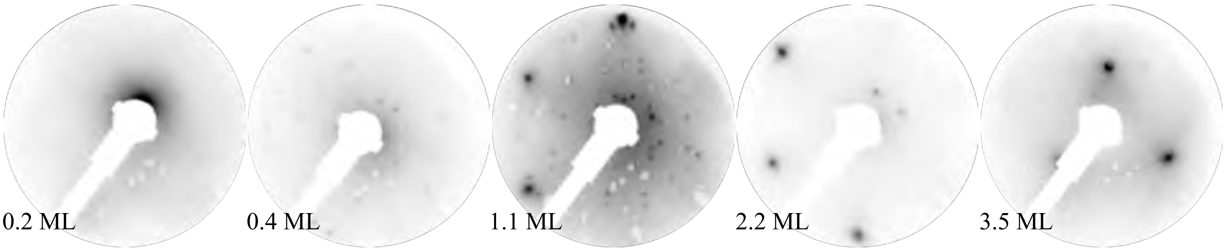

Figure 7.12: Different coverages ranging from 0.2 to 3.5 ML at 45 eV of $FeBr_2$ on Au(111). At coverages of around 1 ML, the third set of spots appears. The LEED images were measured at CFM in 2022 and 2023 in the Nanophysics XPS lab.

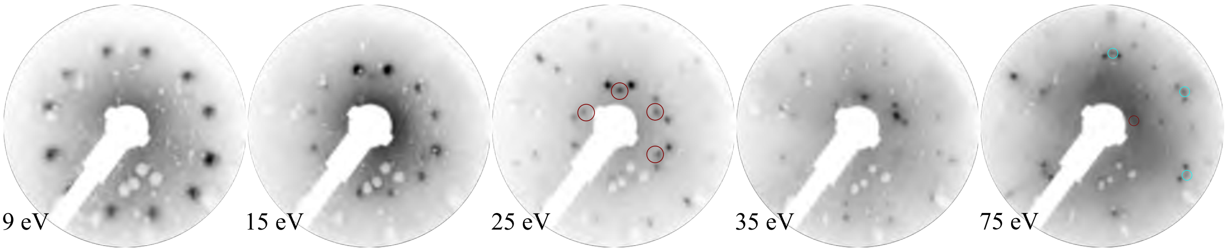

Figure 7.13: LEED patterns of the 1.1-ML sample of $FeBr_2$ on Au(111) measured at different energies ranging from 9 eV to 75 eV. The dark red circles indicate the third set of spots related to the observed moiré pattern and at 75 eV in turquoise the next-layer growth of $FeBr_2$ on Au(111) is indicated. Here the next-layer spots are aligned to the symmetry direction of the Au(111) surface layer. The LEED images were measured at CFM in 2022 and 2023 in the Nanophysics XPS lab.

7.1.11 Atomic-resolution images of $FeBr_2$ on Au(111)

In Fig. 7.14, the atomic-resolution STM image of $FeBr_2$ on Au(111) is displayed. In a) and b) the atomic structure as well as the superstructure and the two different defect types are shown. The inserts in both subfigures show the lattice-constant measurements for $FeBr_2$ (a)) and the superstructure (b)). In b) the two different defect types can be observed. The triangular defects are likely a result of a missing Br atom in the bottom layer, since the three surrounding Br atoms are visible. The second defect type are the bright hexagons, however, the origin of this type of defect is still not understood. In Fig. 7.15, the overlay of the $FeBr_2$ structure ontop of the measured STM image is displayed. Indicated in green and magenta are the defect/superstructure zones. The green circle corresponds to a Br atom directly sitting on top of a Au atom or in a 3-fold hollow site. The magenta circle is indicating the center of the triangular defects, where possibly a transition metal atom is missing.

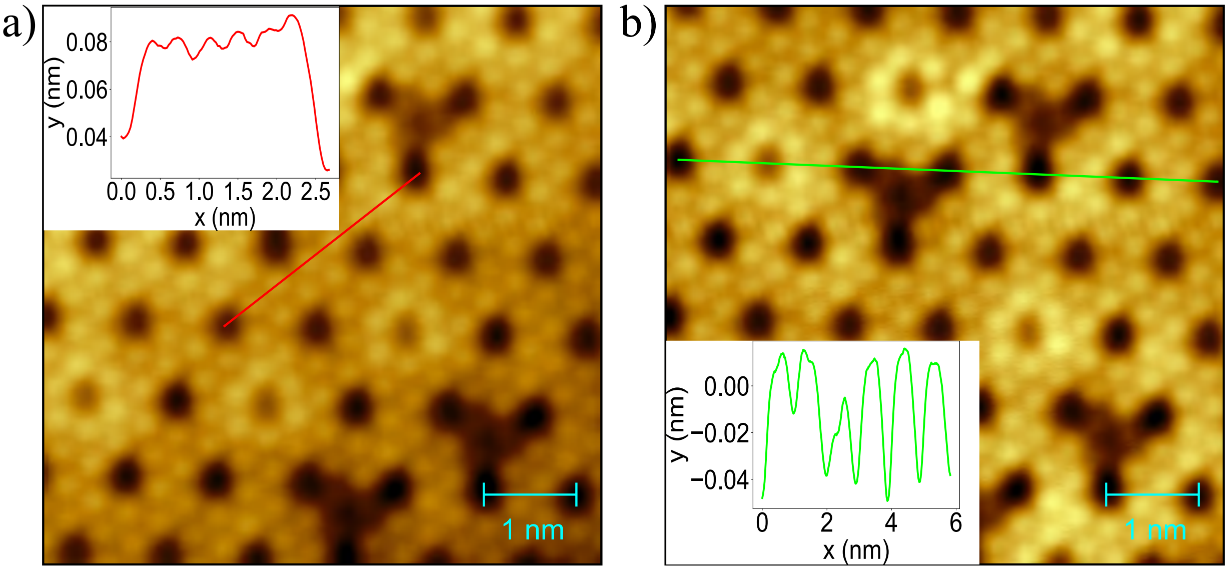

Figure 7.14: Exemplary lattice-constant measurements of the atomically resolved STM images of a sub-ML $FeBr_2$ on Au(111) sample. In a) the lattice constant of $FeBr_2$ is measured and in b) the superstructure lattice constant. The inserts in a) and b) are visualizing the line profiles. The measurement parameters are $U_{\mathrm{Bias}} = 2\,\mathrm{mV}$ and $I_{\mathrm{TC}} = 0.39\,\mathrm{nA}$. The STM measurements were performed in 2020 at CFM. The images is a modified version of the figure shown in Ref. [32].

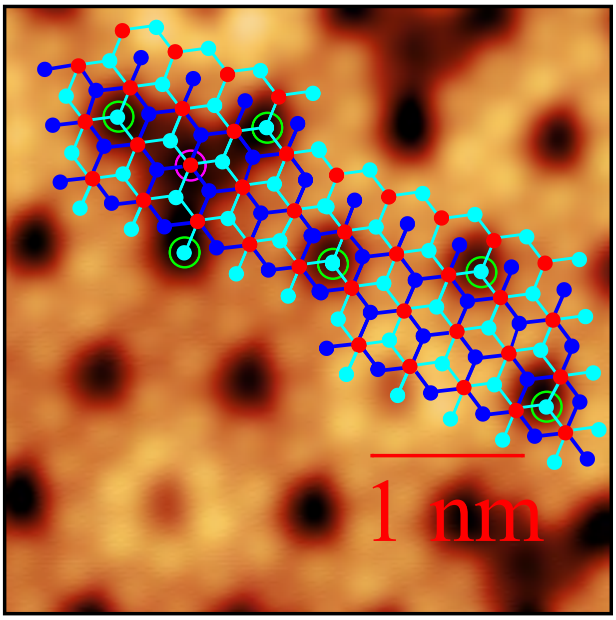

Figure 7.15: The measured STM structure is overlayed with the $FeBr_2$ structure. The green and magenta circle are indicating the atoms which are corresponding to the superstructure position and the center of the triangular defect, respectively. The measurement parameters are $U_{\text{Bias}} = 0.01\,\text{V}$ and $I_{\text{TC}} = 1\,\text{nA}$. The STM image was measured at CFM in 2020.

7.1.12 Real-space simulation of $FeBr_2$ on Au(111)

In Fig. 7.16, the stepwise simulation of the observed structure is displayed. The upper row shows in a) the real-space structure of only Au(111). At each crossing point of the grey grid, there is a Au atom. In b) and c) the $FeBr_2$ is simulated on top of the Au(111) structure. The two different images display the two rotational domains rotated by ±5 °. In this large-scale view the points where the Br atoms of $FeBr_2$ are sitting on top of Au(111) atoms are indicated by the red dots. This could be a possible explanation of the creation of the superstructure pattern, another possibility is, that the Br atom of the $FeBr_2$ is sitting in a 3-fold hollow site. In e) and f) the superstructure pattern for the case that the Br atom is sitting on top of a Au atom is displayed. Here the overlay matches the observed superstructure pattern. The pattern in real space is simulated by using the geometric matrices.

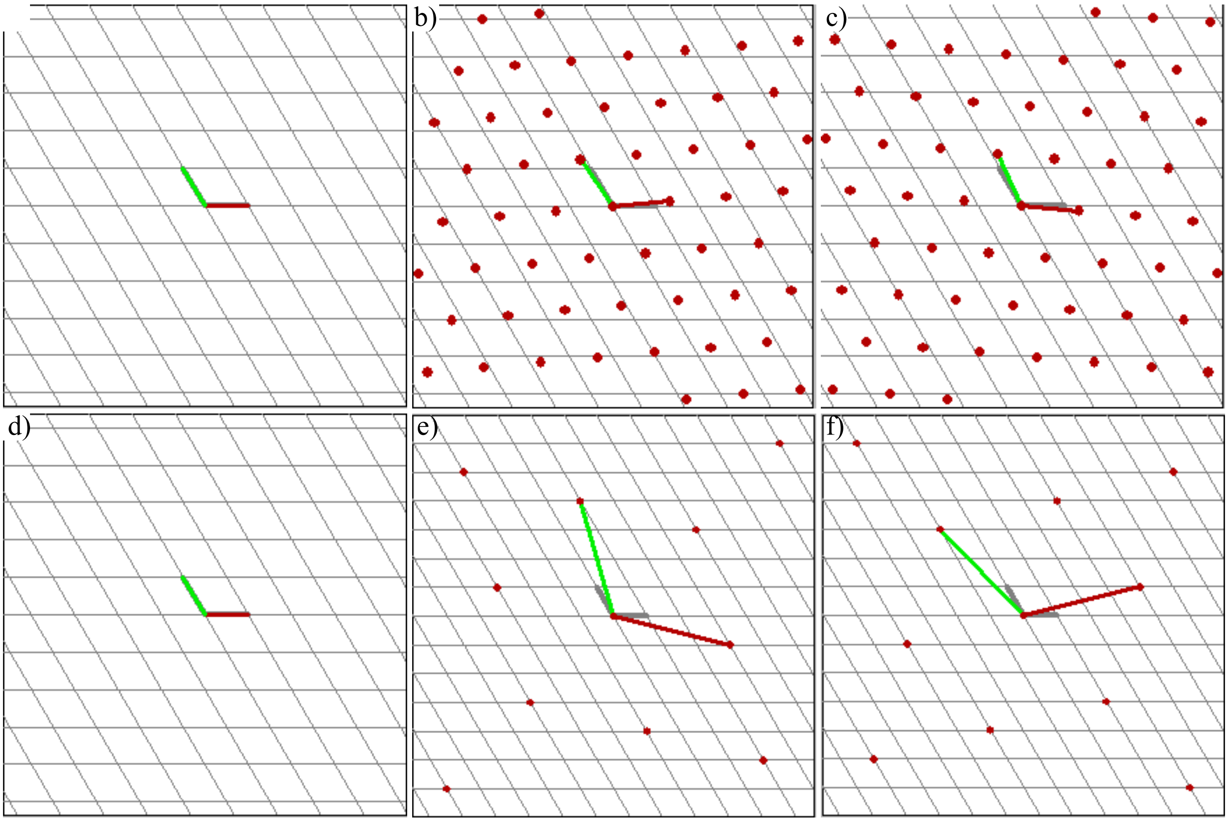

Figure 7.16: a) and d) Real-space grid of the Au(111) lattice. The atom positions are at the crossing points of the gray lines. In all figures the surface lattice vectors are displayed. Besides in a) and d), the Au(111) lattice vectors are marked in gray and the $FeBr_2$ and superstructure vectors are marked in red and green. In b) and c) the real-space image of the $FeBr_2$ lattice on top of Au(111) is displayed for both rotational domains (±5°) and in e) and f) for the superstructure on Au(111). The simulation was performed by using LEEDpat [332].

7.1.13 Coverage- and temperature-dependent growth of $FeBr_2$ on Au(111)

In Fig. 7.17, STM images of different coverages of $FeBr_2$ on Au(111) are displayed. The samples in a), b), and d) were all grown at RT and the one in c) was grown at slightly lower temperatures (around 275 K). The amount of $FeBr_2$ was calibrated during previous evaporations. In a) a nominally 0.1-0.2-ML sample was grown. The reason for the locally low-coverage is related to the high mobility of the material on the Au(111) surface. Therefore, the material only stops at terrace edges, so that the islands are relatively small for low coverages (not equal size over the whole sample) and not equally distributed over the whole surface. By increasing the amount of material, the islands are becoming bigger and more equally distributed over the whole sample surface. The bigger defect areas which are visible in b) can be related to a low growth temperature, as also visible in c). Since the growth temperature is measured via a thermocouple, a difference between the actual sample temperature and the displayed temperature is possible, also keeping in mind that the substrate was annealed before the growth (during the cleaning process).

Therefore, the growth temperature is probably in the region between 30-70 °C (called RT in this thesis). In c) the sample with close to one ML coverage is displayed. This sample shows as

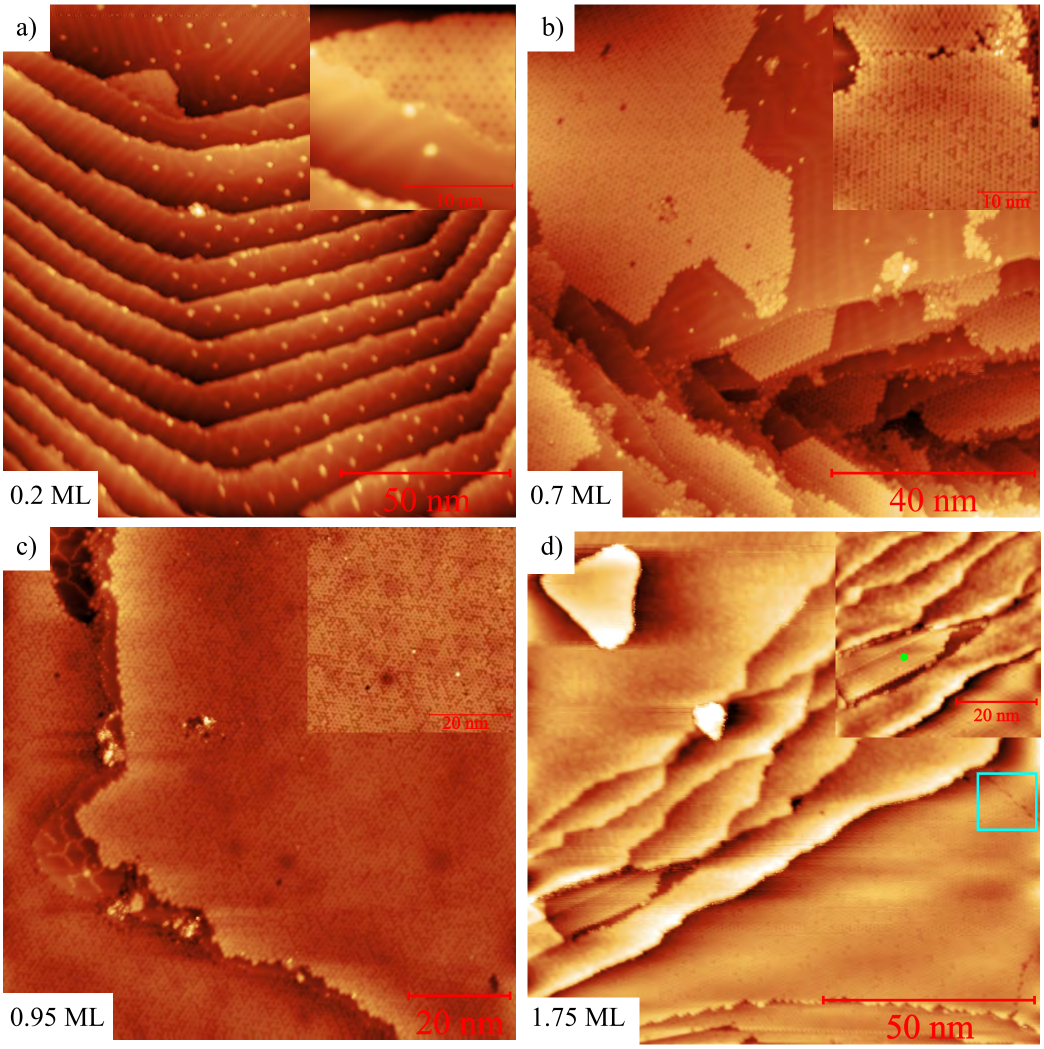

Figure 7.17: Different coverages of $FeBr_2$ on Au(111). The panels a), b), and d) were all measured at 77 K at CINN in 2023. The panel c) was measured at 4.3 K at the PEARL beamline at SLS in 2023. In the lower left corner, the nominal coverage of $FeBr_2$ on Au(111) is given and in the upper right corner a zoomed-in image with the first-layer reconstruction is displayed. The green circle in d) indicates the area of the first-layer growth and the turquoise rectangle indicates the position of a domain boundary between two first-layer regions with ±5 °. The samples a), b), and d) were grown at RT and the sample c) was grown in the temperature range between 270-290 K. The STM parameters are $U_{\text{Bias}} = 1.3$ V and $I_{\text{TC}} = 0.01$ nA ($U_{\text{Bias}} = 1.3$ V and $I_{\text{TC}} = 0.01$ nA for the insert) for a), for b) $U_{\text{Bias}} = 1.2$ V and $I_{\text{TC}} = 0.04$ nA ($U_{\text{Bias}} = 1.5$ V and $I_{\text{TC}} = 0.02$ nA for the insert), for c) $U_{\text{Bias}} = 1.3$ V and $I_{\text{TC}} = 0.05$ nA ($U_{\text{Bias}} = 1.8$ V and $I_{\text{TC}} = 0.1$ nA for the insert), and for d) $U_{\text{Bias}} = 1.2$ V and $I_{\text{TC}} = 0.1$ nA ($U_{\text{Bias}} = 1$ V and $I_{\text{TC}} = 0.03$ nA for the insert).

the only sample the Br-meshes previously observed for $NiBr_2$ on Au(111) observed. The reason for the appearance of these meshes can be various. The two major factors are the lower growth temperature (2 °C) as well as the high-coverage, which can push free Br atoms together. Another possible reason is the evaporation temperature of the material. During the evaporation, a different evaporator was used, which can reach higher temperatures. In d) the 1.75 ML sample is displayed. Here different important features can be observed. The first are the boundaries of the rotational domains in the bottom right corner. Here the two rotational domains of the sub-ML sample are visible. Second the ML structure growth along the terrace edges of Au(111). Third, it shows no second-layer growth directly on top of the first-layer structure and only third-layer growth on top of the second-layer. The reason for this phenomenon could be that the terrace with the first layer needs to be firstly fully filled before the next layer can grow on the surface. In the case of the second layer the properties have probably already changed, so that the material can easier accumulate on top of the second layer and create the next layer.

7.1.14 XPS core-level table

In Tab. 7.7, the important binding energies for the main core-level peaks are displayed. The binding energies are extracted from Ref. [206] and are sometimes related to the pure material like in the case of Fe (Fe^0 oxidation state).

Element	Core-level	Binding energy (eV)	Core-level	Binding energy (eV)
Au	4s	763	-	-
Au	$4p_{\frac{1}{2}}$	643	$4p_{\frac{3}{2}}$	547
Au	$4d_{\frac{3}{2}}$	353	$4d_{\frac{5}{2}}$	335
Au	$4f_{\frac{5}{2}}$	88	$4f_{\frac{7}{2}}$	84
Au	5s	110	-	-
Au	$5p_{\frac{1}{2}}$	74	$5p_{\frac{3}{2}}$	57
O	1s	531	-	-
C	1s	285	-	-
Fe	2s	845	-	-
Fe	$2p_{\frac{1}{2}}$	720	$2p_{\frac{3}{2}}$	707
Br	$3p_{\frac{1}{2}}$	189	$3p_{\frac{3}{2}}$	182
Br	$3d_{\frac{3}{2}}$	70	$3d_{\frac{5}{2}}$	69
Mo	$3p_{\frac{1}{2}}$	412	$3p_{\frac{3}{2}}$	394
Mo	$3d_{\frac{3}{2}}$	231	$3d_{\frac{5}{2}}$	228
Ta	$4p_{\frac{1}{2}}$	463	$4d_{\frac{3}{2}}$	401
Ta	$4d_{\frac{3}{2}}$	238	$4d_{\frac{5}{2}}$	226
Ta	5s	69	-	-

Table 7.7: The element-specific core-level peaks with the corresponding binding energies. The displayed values are extracted from Ref. [206].

7.1.15 XPS FWHM of FeBr$_2$ on Au(111)

Coverage	Element-Peaks	FWHM (eV)	Peak position (eV)	Amplitude (arb. units)
0.3 ML	Br 3p 3/2	2.99±0.11	182.36±0.06	206.15±11.14
	3p 1/2	3.03±0.19	188.8±0.10	131.99±11.51
0.3 ML	Au 4d 3/2	5.76±0.01	353.32±0.03	14078.1±193.0
	4d 5/2	5.87±0.04	335.40±0.02	22130.0±182.18
0.6 ML	Br 3p 3/2	3.00±0.05	182.35±0.03	1602.16±39.35
	3p 1/2	2.89±0.09	188.97±0.05	800.00± 33.59
0.6 ML	Au 4d 3/2	5.73±0.18	353.16±0.03	53228.12±704.15
	4d 5/2	5.66±0.03	335.25±0.02	80988.04±653.07
0.6 ML	Fe 2p 3/2	3.59±0.11	709.38±0.06	2121.41±173.07
	Fe 2p 1/2	3.78± 0.21	722.64±0.11	1147.94±104.84
	Fe Sat. 2p 3/2	7.10±0.31	714.57±0.16	3435.25±261.87
	Fe Sat. 2p 1/2	7.20± 0.40	728.87±0.26	1503.78±97.71
0.7 ML	Br 3p 3/2	3.28±0.08	182.62±0.05	631.60±22.83
	3p 1/2	3.03±0.19	189.09±0.08	305.89±22.22
0.7 ML	Au 4d 3/2	5.726±0.001	353.34±0.03	16239.19±237.06
	4d 5/2	5.76±0.04	335.43±0.02	25322.43±233.76
2.0 ML	Br 3p 3/2	2.78±0.02	182.69±0.01	3682.57±42.09
	3p 1/2	2.81±0.04	189.30±0.02	1800.00±40.48
2.0 ML	Au 4d 3/2	5.510±0.004	353.18±0.03	43264.20±570.11
	4d 5/2	5.48±0.03	335.27±0.02	63097±532.28
2.0 ML	Fe 2p 3/2	3.60±0.09	709.87±0.03	4651.17±159.05
	Fe 2p 1/2	3.82±0.09	723.18±0.05	2754.43±119.41
	Fe Sat. 2p 3/2	6.92±0.13	715.13±0.07	7149.08±242.87
	Fe Sat. 2p 1/2	6.61±0.18	729.38±0.08	3701.90±181.61
3.0 ML	Br 3p 3/2	2.87±0.01	182.870±0.007	1761.99±10.98
	3p 1/2	3.025±0.002	189.49±0.02	889.18±11.93
3.0 ML	Au 4d 3/2	4.71±0.05	353.70±0.03	12244.87±178.74
	4d 5/2	4.36±0.03	335.09±0.02	17404.09±160.83
3.0 ML	Fe 2p 3/2	3.59±0.03	710.02±0.02	2608.74±39.36
	Fe 2p 1/2	3.27±0.05	723.45±0.03	1100.31±26.38
	Fe Sat. 2p 3/2	6.00±0.07	715.22±0.04	2609.51±53.48
	Fe Sat. 2p 1/2	5.62±0.12	729.60±0.05	1182.90±53.83
5.0 ML	Br 3p 3/2	2.797±0.009	182.929±0.005	3228.98±14.44
	3p 1/2	2.85±0.02	189.58±0.01	1510.73±15.19
5.0 ML	Au 4d 3/2	4.69±0.06	353.76±0.03	9622.58±168.14
	4d 5/2	4.09±0.04	335.07±0.02	12546.92±145.95
5.0 ML	Fe 2p 3/2	3.28±0.03	710.12±0.01	3847.57±64.18
	Fe 2p 1/2	3.18±0.04	723.51±0.02	5010.99±99.16
	Fe Sat. 2p 3/2	6.00±0.07	715.22±0.04	1856.26±40.67
	Fe Sat. 2p 1/2	6.08±0.12	729.60±0.05	2529.62±108.33

Table 7.8: Fitting parameters of the Au 4d, Br 3p, and Fe 2p core-level peaks for different coverages of FeBr$_2$ on Au(111) ranging from 0.3-5.0 ML. The x-ray gun related peaks for the Au 4d spectra are not included. All profiles are fitted by using Voigt profiles. Therefore, the amplitude is not to the actual peak intensity of the fitted spectrum. For the coverages of above 2.0 ML the Shirley background routine did not worked perfectly for the Au 4d peaks. Therefore, the fit parameter for Au could change, as visible in the FWHM values.

During the fitting procedure the shirley background was removed from the XPS spectra. Afterwards the spectra were fitted with a specific amount of Voigt profiles. The amplitude, which is given in Tab. 7.8 is correlated to the peak height of the fit. In the following the equations for a Voigt profile are shown:

$$f(x; A, \mu, \sigma\gamma) = \frac{ARe[w(z)]}{\sigma\sqrt{2\pi}} \tag{7.1}$$

$$w(z) = e^{-z^2} erfc(-iz) \tag{7.2}$$

$$z = \frac{x - \mu + i\gamma}{\sigma\sqrt{2\pi}} \tag{7.3}$$

$$\mathrm{FWHM} = 3.6013 \cdot \sigma \tag{7.4}$$

Here $erfc()$ is the error function, A the amplitude, μ the center, σ the sigma value, and γ corresponds to the gamma parameter, which is as default identical to σ.

7.1.16 XPS Survey spectra of $FeBr_2$ on Au(111)

In Fig. 7.18, the survey spectra for a sub-ML and BL sample of $FeBr_2$ on Au(111) are shown. Both survey spectra are only showing the substrate related Au peaks as well as Fe and Br core-level peaks. No contamination of the surface with other materials is visible.

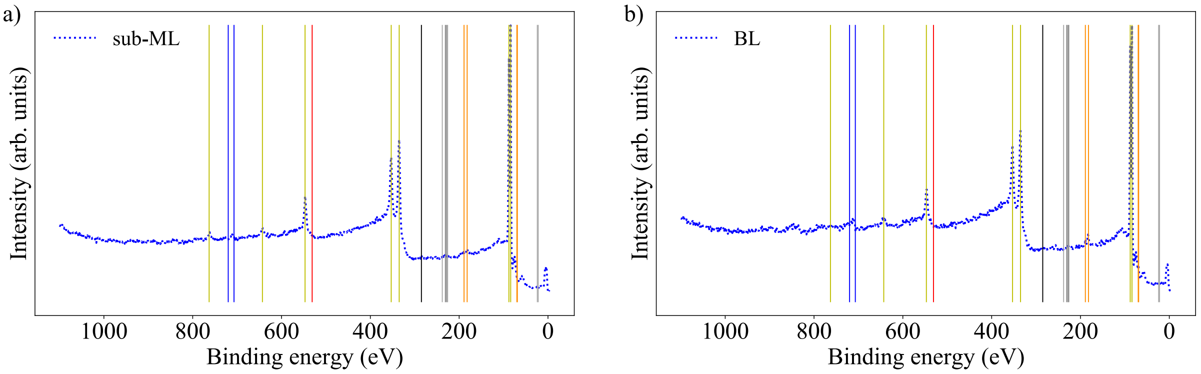

Figure 7.18: Measured survey spectra for the sub-ML (a)) and BL-sample of $FeBr_2$ on Au(111). For both spectra, an intensity increase at the Fe 2p and Br 3p position can be observed. In the BL case this is more pronounced. The vertical lines in a) and b) are guides to the eye and indicate the elemental core-level peaks. The yellow lines correspond to Au, the blue lines to Fe, the orange ones to Br, the black ones to C, red to O, and the grey lines to Mo and Ta. The measurements were performed at CFM in the Nanophysics XPS lab in 2020.

7.1.17 Temperature-dependent XPS of FeBr$_2$ on Au(111)

In Fig. 7.19, the XPS spectra for a ≈ 1.5 ML FeBr$_2$ sample on Au(111) are displayed. During the measurements, the temperature was continuously increased to observe the critical growth temperature for the first- and second-layer. At each temperature a total of four Br 3p, two Fe 2p and one Au 4d core-level spectra have been measured. The current was increased by 0.04 A every 18 min (in the beginning the current was stabilized to 0.5 A for 20 min without measuring XPS). Each 0.04 A are corresponding to around 8 °C (the temperature was extracted from the plot). The maximum reached current value was 2.18 A, which corresponded to a thermocouple temperature of 350 °C. By overcoming a temperature of around 200 °C, the material is reevaporated from the surface and only the clean Au(111) surface is left. The small remaining amount of intensity in the Fe 2p region is related to an Auger peak of Au while measuring with the Al anode, as later discussed in sec. 7.1.20. The current needed for reevaporate FeBr$_2$ on Au(111) is 1.4 A, which corresponds to ≈ 200 °C.

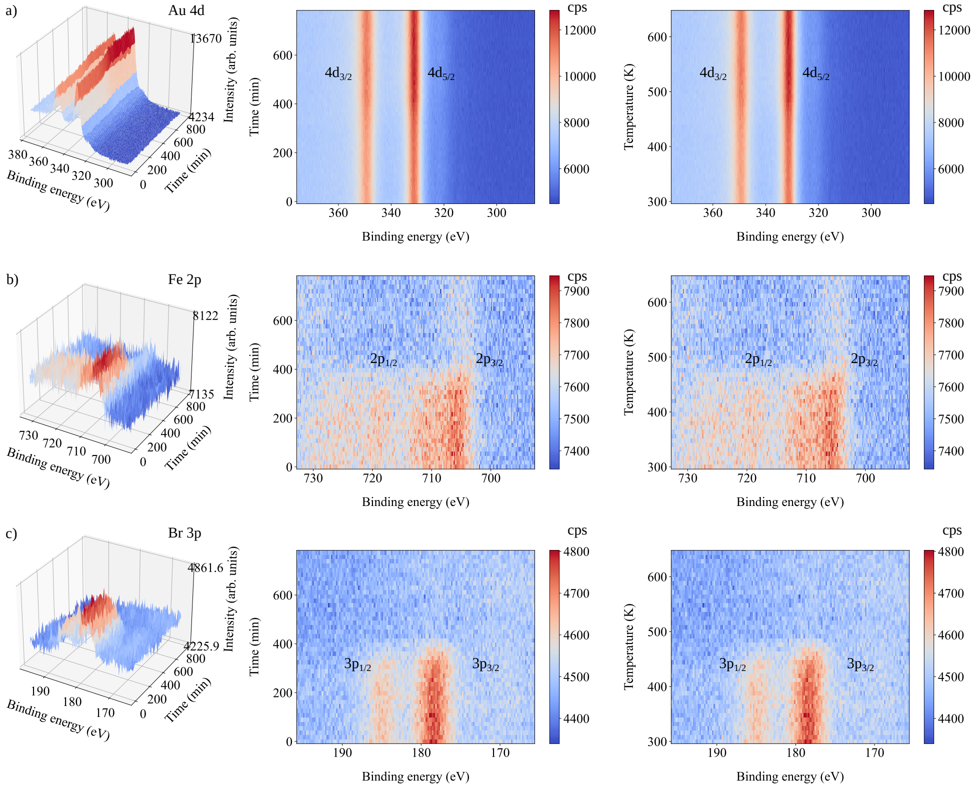

Figure 7.19: a), b), and c) 3D intensity plot as a function of the binding energy and the time. The data of Au 4d, Fe 2p and Br 3p are displayed from the side and top. The measurements were performed at CFM in the Nanophysics XPS lab in 2023. On the right side the temperature-dependent elemental XPS core-level spectra are shown.

7.1.18 Oxidation tests of $FeBr_2$ on Au(111)

In Fig. 7.21, the performed oxidation tests with a ≈ 0.7 ML $FeBr_2$ sample are displayed. The performed XPS measurements were only done with a low amount of scan repetitions. Therefore, some features are perhaps not fully observed. The ≈ 0.7 ML sample is subject to different amount of oxygen exposures.

In Fig. 7.21 a), the Fe 2p spectra for different oxygen concentrations and exposure times are displayed. In the case of ≈ 10 L, the sample was exposed for 12 s to a dry oxygen pressure of 10^{-6} mbar. For this exposure time, no additional oxygen has been observed as well as no change in peak intensity or shape of Br 3p, Fe 2p and O 1s. By exposing the sample to an atmosphere of $3 \cdot 10^{-3}$ mbar for 2 s, also no change has been observed. However, by keeping the oxygen condition the same as for the 1000 L case and starting the plasma source (3.8 kV with 50 mV at $4.3 \cdot 10^{-3}$ mbar for 2 min), the Br 3p peaks are disappearing and a strong oxygen peak can be observed. Additionally, the Fe spectrum shifts and changes the shape. The reason is that the $FeBr_2$ is oxidized and the Br has been removed.

In Fig. 7.21 b), the different shapes of $FeBr_2$ on Au(111) can be observed. The Fe $2p_{\frac{3}{2}}$ peak is shifted and changed shape, additionally the dominant satellite peaks of $FeBr_2$ disappear. The satellite peaks of $FeBr_2$ are visible in the red spectrum in b). This is caused by the effect of the increased electronegativity of oxygen compared to Br. Therefore, the Br was substituted with O and the Br coupled with H to HBr. The post-annealing process at 100 °C lowered the peak intensity and removed surface-coupled oxygen (Fig. 7.21 c), comparison between orange and black lines). The observed spectral shape and missing satellite peaks as well as vanished Br signal lead to the conclusion that the plasma procedure created an FeO film, which does not show any Fe 2p satellite peaks. The sample thickness is ≈ 0.7 ML and the LEED in Fig. 7.20 a) shows the third set of spots. The plasma source is ≈ 10-15 cm away from the sample position. The plasma source is a PS PCS-ECR H/I from SPECS [417] and used for 2 min at 3.8 kV and 50 mA at $\approx 4.2 \cdot 10^{-3}$ mbar.

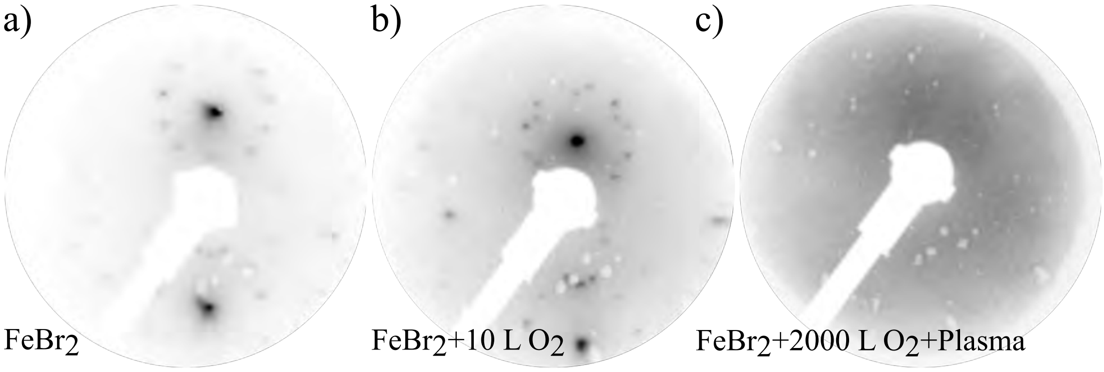

Figure 7.20: a)-c) LEED images measured at 45 eV. a) 0.7 ML of $FeBr_2$, b) 0.7 ML of $FeBr_2$ after exposure to 10 L (10 Langmuir) of dry oxygen and c) after the plasma procedure. The measurements were performed at CFM in the Nanophysics XPS lab in 2023.

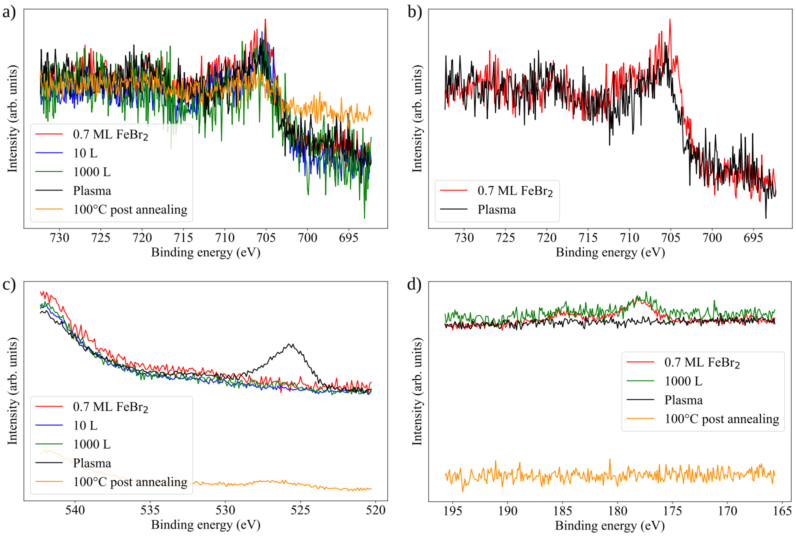

Figure 7.21: a) Overlay of the Fe 2p peaks of $FeBr_2$ on Au(111) for different oxygen concentration and plasma procedures. b) Comparison of the pure $FeBr_2$ Fe 2p spectra with the one after plasma exposure. Here the different shape as well as the disappearing satellite peaks can be observed. c) O 1s evolution for different exposure times. d) Br 3p peaks for different oxygen exposure times. After the plasma procedure, the Br peaks completely disappear. The measurements were performed at CFM in the Nanophysics XPS lab in 2023.

In Fig. 7.20, the LEED images of the ≈ 0.7 ML sample for different procedure steps are displayed. The superstructure LEED pattern stays visible for an exposure of 10 L, however, after the plasma procedure no pattern is visible anymore. Since the XPS measurements are still showing an Fe peak, it indicates that a new compound (FeO) was created with an amorphous pattern or just covered with oxygen from the surface, so that no superstructure is visible anymore.

7.1.19 Low-coverage XPS measurements of $FeBr_2$ on Au(111)

In Fig. 7.22, the different sub-ML and ML XPS measurements of $FeBr_2$ on Au(111) are shown. The measurements in 2020 were performed with an x-ray gun which had still the ability of approaching the sample. For later measurements the approaching of the x-ray gun was not possible and therefore the counts for later measurements were reduced. Additionally to the reduction in the counts per second (cps) due to the different x-ray gun distance, the aging of the channeltron also reduces the measured counts. The channeltron is checked every half year and the voltages are consequently adjusted. In a) the Fe 2p XPS spectra before background correction are shown. Due to the high intensity difference, only the Fe $2p_{\frac{3}{2}}$ and the corresponding satellite peak were used for later analysis. After the background was removed, the peaks are normalized to the main Au 4d intensity. It can be seen that the intensity is not strongly different for Fe 2p as well as Br 3p between the 0.5 and 1 ML sample after the normalization to the Au intensity. The Fe 2p signal for the measurements in 2020 has been removed from the normalized figure, since due the different backgrounds it seems that the signal intensity is lower than 0.5 ML, which does not fit the normalized Br 3p results as well as the corresponding LEED images. The strong different background between the 2020 sample and the other low coverage samples is causing the issue with the normalization. This is also visible in the previously performed comparison for higher coverages, since here the substrate background plays a lower role and the background gets flatter. This can be also obtained by higher count numbers for the signal, which decreases the noise faster as well as the background.

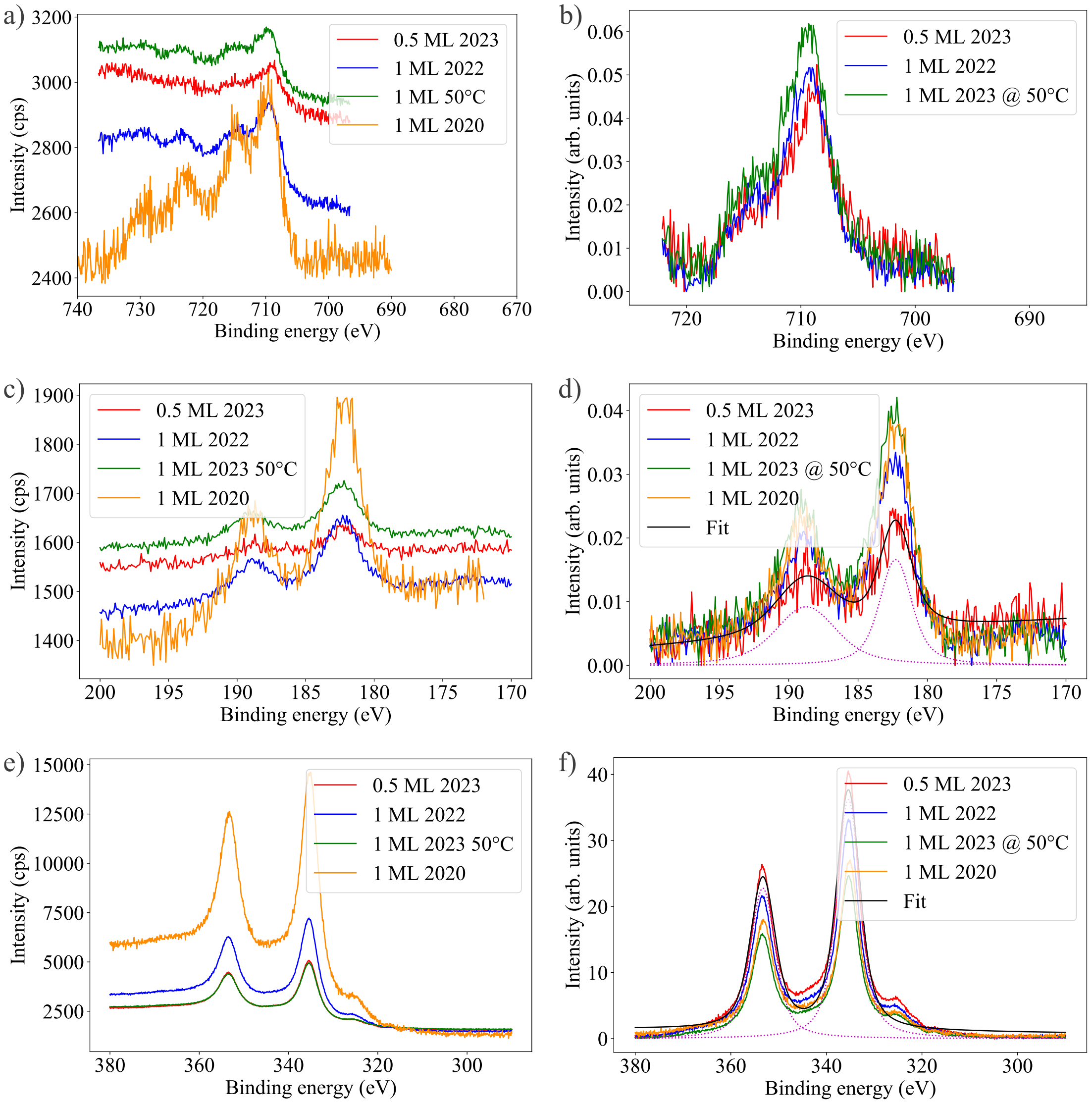

Figure 7.22: a), c), and e) Raw data of the different coverage- and growth-temperature core-level spectra. b), d), and f) Fe 2p, Br 3p, and Au 4d normalized core-level spectra. The Br and Fe spectra are normalized to the maximum intensity of the Au 4d spectra. Therefore the spectra are comparable even if they were measured in different years and for different coverage. The measurements were performed at CFM in the Nanophysics XPS lab in 2022 and 2023.

Therefore, even if the LEED (Fig. 7.23) shows that the third set of spots does not appear, the samples are nearly identical in coverage, which means that the transition to the third set of spots has a narrow starting window. Additionally, no difference between the ML $FeBr_2$ on Au(111) samples grown at RT and 50 °C can be observed. The 50 °C was measured via the thermocouple on the sample holder, which corresponds to a real sample temperature (from the calibration see

Fig. 7.4) of 60-70 °C on the sample plate. It is visible that even for a slightly elevated growth temperature, the growth of $FeBr_2$ on Au(111) is the same as for RT. The third set of spots is not visible for the sample with 0.5 ML coverage.

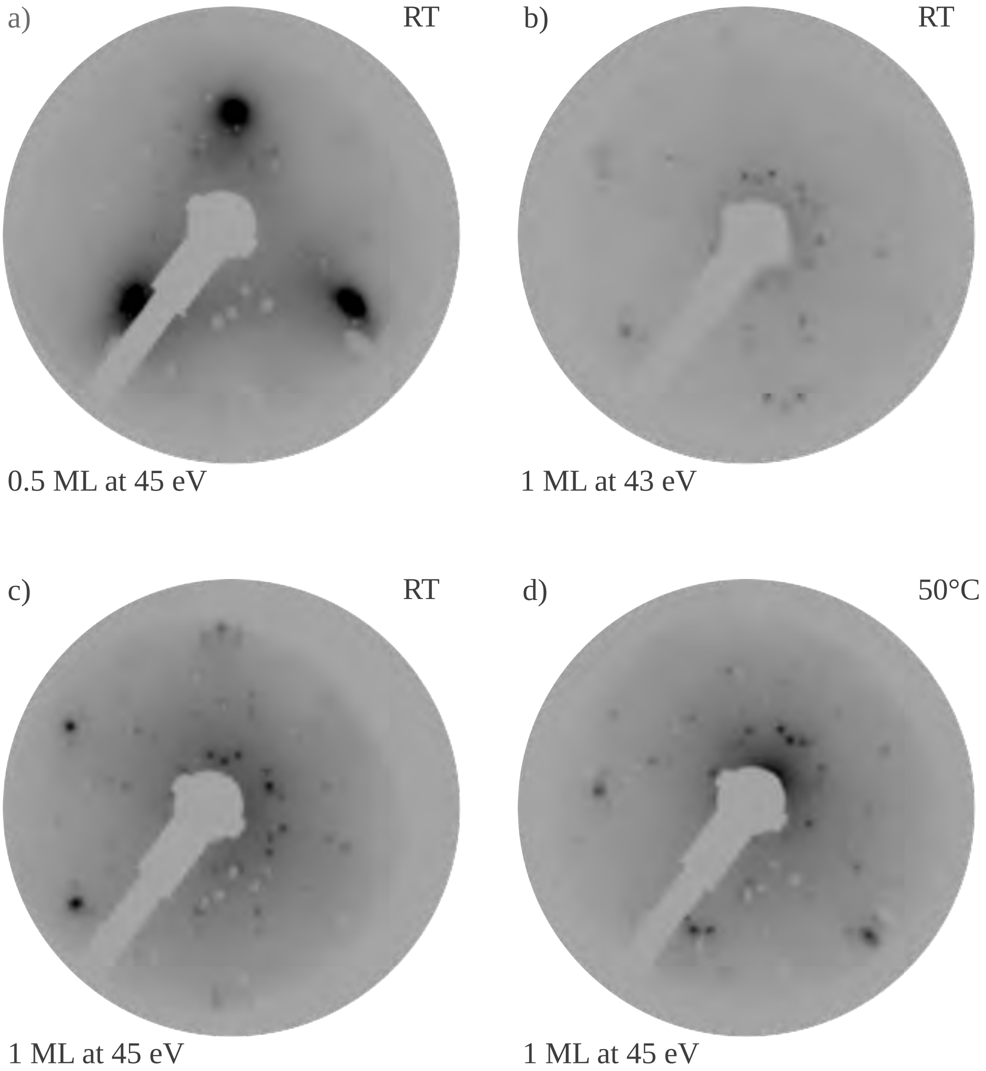

Figure 7.23: a)-d) LEED images for the different coverages and different growth temperatures. All images were measured at CFM in the Nanophysics XPS lab, by using an MCP LEED system. a) and d) were measured in 2023, b) in 2020 and c) in 2022.

7.1.20 Different anodes

In Fig. 7.24, the XPS spectra for clean Au(111) measured with two different anode materials (Mg, Al) are displayed. In a) the survey spectra for both anode materials are overlayed and it is visible that besides the Au peaks also peaks at around 220 eV are visible, which are related to the sample plate out of Mo and Ta (Ta shield for screw mounting mechanism). At higher binding energies (around 1000 eV), the Auger peak of Au can be observed. Since it is an Auger peak, it is not at the same position for both anode materials. In b) the clean Fe region is displayed. The small bump which is visible by using the Al anode is not visible for Mg, therefore it is related to an Auger peak.

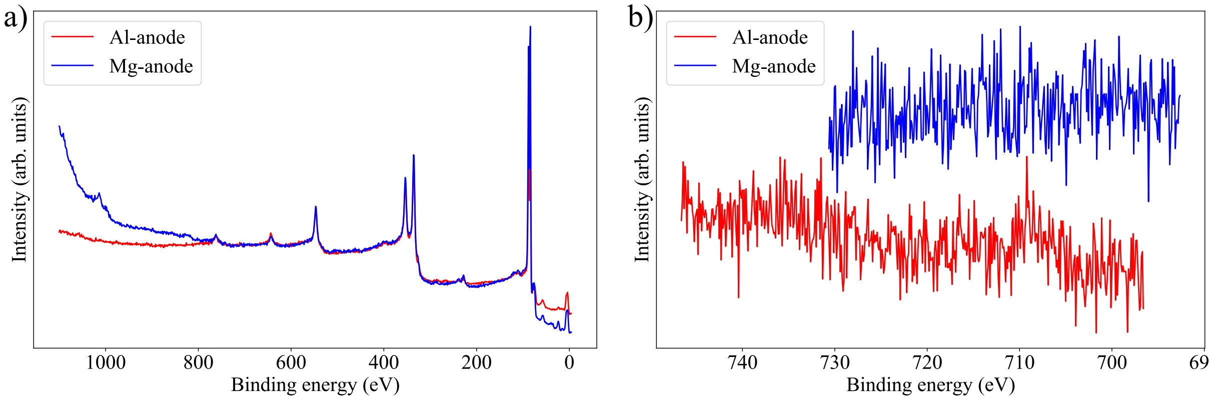

Figure 7.24: a) Survey spectra of clean Au(111) measured by using an Al and a Mg anode. b) Fe region measured with both anodes. By using the Al anode, a small bump is visible, which is probably related to an Auger peak of Au. The measurements were performed at CFM in the Nanophysics XPS lab in 2022.

7.1.21 XPS and LEED characterization of $FeBr_3$

In Fig. 7.25, the XPS and LEED measurements of $FeBr_3$ on Au(111) are displayed. The Dodecon evaporator was loaded with $FeBr_3$ powder with a purity of 98 % bought from Sigma Aldrich [418]. Already during the loading process, the powder started to react with the atmosphere and changed to a wet powder form. However, after loading and pumping the evaporator, the powder changed color into grey/yellow. The XPS and LEED measurements revealed that the powder changed from $FeBr_3$ to $FeBr_2$ probably already during the bakeout process. The same superstructure and XPS core-level peak positions have been observed, which means the material on Au(111) was in a Fe^{2+} oxidation state. The result was expected, since the powder strongly reacts to water and since the more stable form for these heavier TMDH based on transition metals from Mn-Ni is a $^{2+}$ oxidation state. The sample was grown under the same conditions as $FeBr_2$, which means that the Au(111) substrate was kept at RT. This behavior was also observed in Ref. [142]. Therefore, the TMDH is the more stable form of the halide compounds.

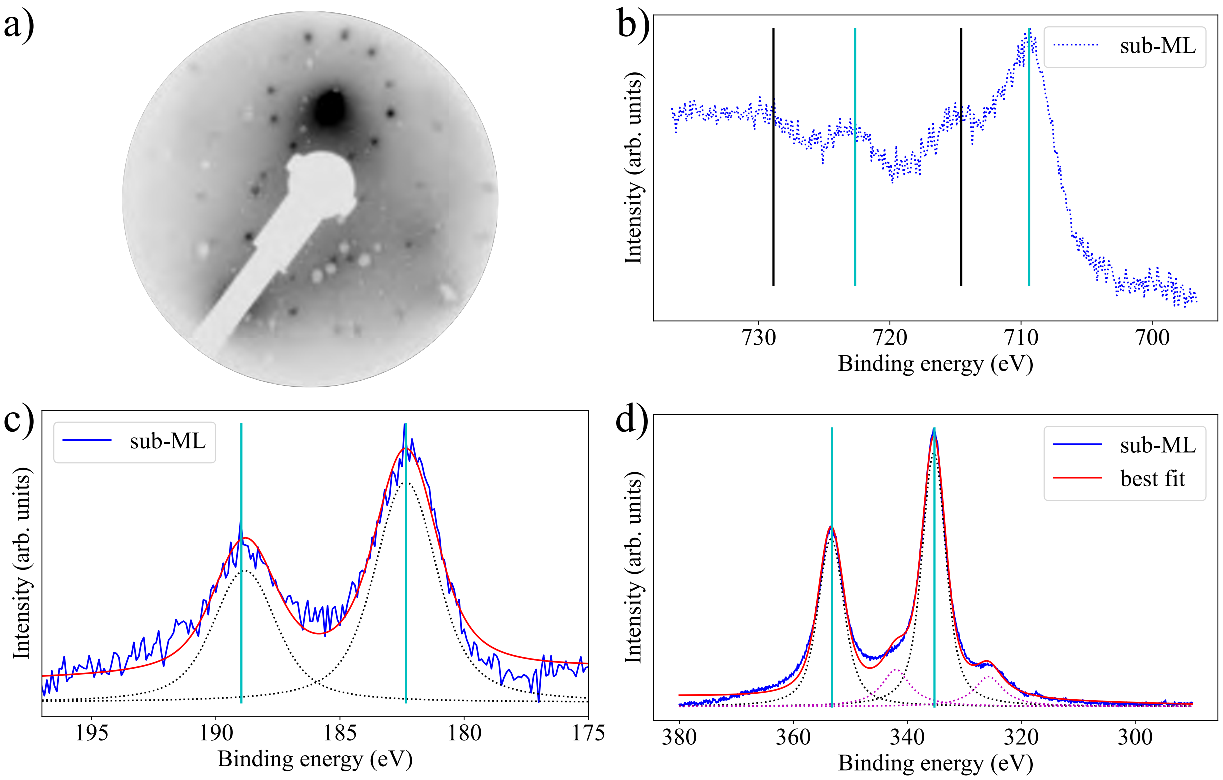

Figure 7.25: a) LEED image of a deposition of $FeBr_3$ on Au(111) measured at 42 eV. b)-d) XPS core-level peaks of Fe 2p, Br 3p, and Au 4d. The peaks are at the same position and show the same structure as the ones measured for $FeBr_2$ on Au(111). The XPS measurements were performed by using an Al anode. The measurements were performed at CFM in the Nanophysics XPS lab in 2022.

7.1.22 Thickness calibration of $FeBr_2$ on Au(111)

In Fig. 7.26, the isotropic XAS spectra of $FeBr_2$ on Au(111) are displayed. All measurements were performed at RT and with linear polarization in the absence of an external field. The three different coverages were measured at an angle of 55 °. In a) and c) the magic-angle measurements which where performed at the BOREAS beamline are shown and in b) the one which was performed at the VEKMAG beamline. To compare the consistence of the calibration via Ref. [345], the BOREAS sub-ML and BL samples were used. The VEKMAG sub-ML sample has a coverage of 0.7 ML with a peak height of 14 % at 10 K. Since the peak intensity increased at the VEKMAG station between the RT and 10- K measurements, due to a different measurement position, the measurements were repeated at the BOREAS beamline at ALBA. The BOREAS samples were cross checked with a new magic-angle measurement. In the case of the BOREAS sub-ML, a peak height of 5 % is related to 0.3 ML. Therefore, the peak height for the same coverage as the VEKMAG sample would be around 12 %, which means a 17 % error for the coverage needs to be assumed, which leads for the highest coverage to an error of 0.5 ML, and for 2.0 ML to an error of 0.34 ML. Together with all other potential error sources the coverage error can be assumed to be around 20-25 %. The sample in a) showed no third set of spots in the LEED pattern, which indicates that the material only consists of the first-layer. The LEED pattern for the sample in b) already showed the third set of spots, which is related to the start of the second-layer growth. Therefore, the varying peak intensity at different sample positions can be explained, with the contribution of the second layer in a different sample area. All coverage values extracted from the magic-angle measurements are matching the expected coverages via STM and LEED. In Fig. 7.27, the angle-dependent (NI (0 °), MA (55 °), and GI (70 °)) XAS spectra at RT and with linearly polarized light of the two sub-ML samples are displayed. As an insert, the peak intensity is plotted as a function of the incidence angle. The thickness was afterwards also compared to a sub-ML sample measured at the BOREAS beamline in 2021. In Fig. 7.28, the STM image of a sub-ML $FeBr_2$ on Au(111) sample measured in 2021 is displayed. Here the superstructure is visible with the characteristic ≈1 nm lattice constant. In panel b) the corresponding RT isotropic XAS is shown, which has a peak height of 4 %, and therefore corresponds to a coverage of 0.2 ML, the same the STM image shows.

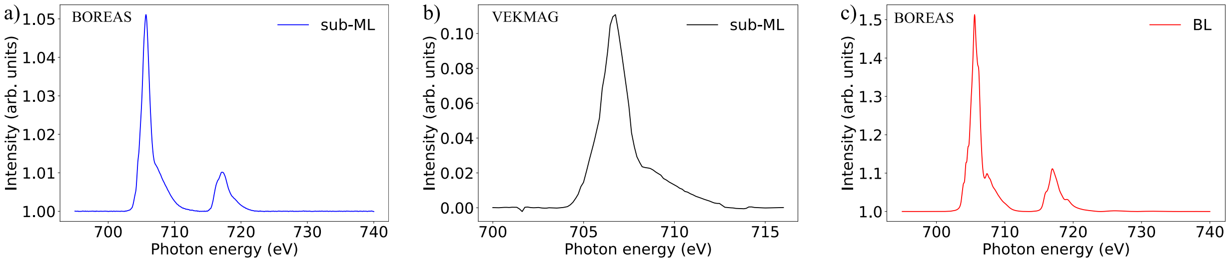

Figure 7.26: a), b), and c) XAS spectra measured with linear polarized light at RT without applying an external field under an angle of 55 °. a) and b) spectra of the sub-ML samples measured at BOREAS (performed in 2023) and VEKMAG (performed in 2021) and c) BL sample measured at BOREAS. The sub-ML sample measured at BOREAS showed no third set of LEED spots, therefore probably only consists of the first-layer.

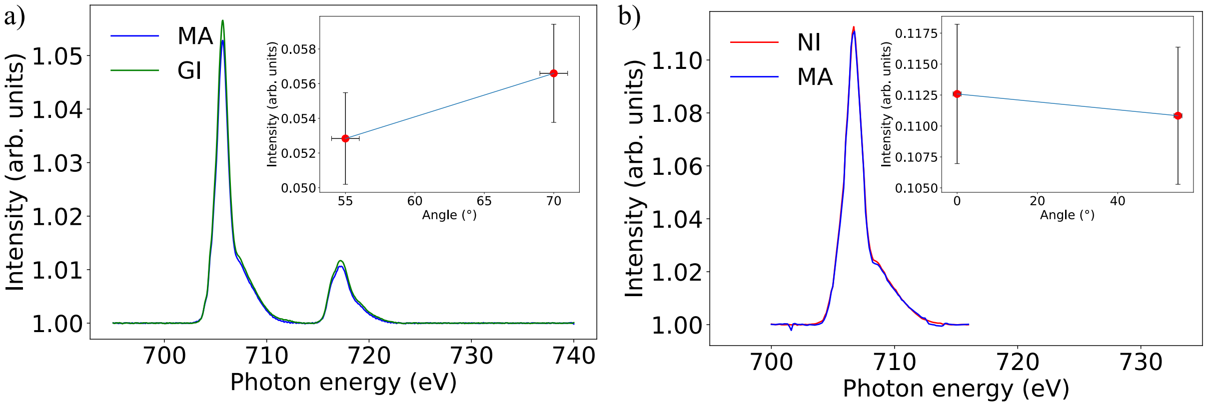

Figure 7.27: XLD measurements for different coverages at RT and 0 T. a) Sub-ML sample measured at the BOREAS beamline at ALBA (in 2023). The measurements were performed at two different incidence angles (MA and GI). The insert shows the angle-dependent intensity. b) sub-ML sample measured at the VEKMAG beamline at BESSY II (in 2021). The sample was measured in the preparation chamber at two different incidence angles (NI and MA). For both beamlines an angle error of 1 ° and an intensity error of 10 % is assumed.

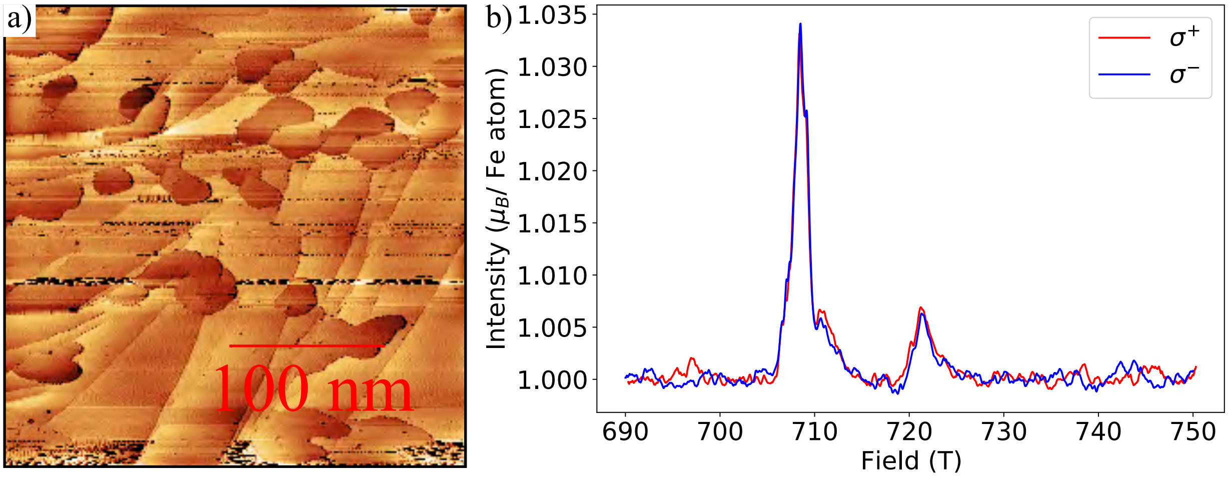

Figure 7.28: a) STM image of ≈ 0.2 ML $FeBr_2$ on Au(111) measured at 77 K. b) circular polarized XAS measurement measured at RT and NI. The STM parameters are $U_{Bias} = 1.39$ V and $I_{TC} = 0.35 \cdot 10^{-9}$ A. The measurements were performed at the BOREAS beamline in 2021 at the ALBA synchrotron radiation source.

7.1.23 Coverage dependent magnetic moments

C (ML)	T (K)	μ (μ_B/Fe at)					
		NI			GI		
		$m_{\text{s eff}}$	m_l	m_{total}	$m_{\text{s eff}}$	m_l	m_{total}
0.25	1.7	0.32	0.08	0.40	0.45	0.12	0.57
	2.5	0.55	0.07	0.62	-	-	-
	4.0	0.36	0.04	0.40	-	-	-
	12.0	0.50	0.19	0.69	-	-	-
	16.0	0.27	0.22	0.49	-	-	-
	20.0	0.54	0.07	0.61	-	-	-
0.3	2.5	0.57	0.10	0.67	0.53	0.18	0.71
0.5	1.7	0.65	0.16	0.81	0.52	0.15	0.67
	2.5	0.69	0.14	0.83	0.51	0.18	0.69
	4	0.49	0.16	0.65	0.54	0.16	0.70
	12	0.52	0.15	0.67	-	-	-
	16	0.44	0.10	0.54	-	-	-
	20	0.47	0.06	0.53	-	-	-
0.7	2.5	1.46	0.42	1.88	1.61	0.45	2.06
0.8	2.5	1.5	0.41	1.96	1.62	0.57	2.19
2.9	2.5	2.34	0.66	3.02	2.02	0.47	2.49
0.6	2	1.13	0.30	1.43	1.05	0.36	1.41
0.7	10	0.93	0.25	1.18	1.00	0.16	1.16
	12	-	-	-	1.25	0.23	1.48
	18	-	-	-	0.81	0.33	1.14
	25	-	-	-	0.54	0.18	0.72
	30	-	-	-	0.33	0.04	0.37
	35	-	-	-	0.52	0.11	0.63
1.5	2	1.814	0.60	2.414	2.03	0.45	2.48
2.0	2	2.15	0.70	2.85	1.91	0.47	2.38
	4	2.05	0.72	2.77	-	-	-
	7	1.97	0.66	2.63	-	-	-
	12	1.87	0.65	2.52	-	-	-
	17	1.69	0.47	2.16	-	-	-
	25	1.23	0.38	1.61	-	-	-
	40	0.88	0.23	1.11	-	-	-
	65	0.54	0.17	0.71	-	-	-
	100	0.39	0.14	0.53	-	-	-
2.9	10	2.12	0.79	2.91	1.21	0.40	1.61
	12	1.93	0.58	2.51	1.51	0.42	1.93
	16	-	-	-	1.05	0.33	1.38
	20	-	-	-	1.00	0.31	1.31

Table 7.9: Evaluated magnetic moment values at NI and GI for different temperatures. The degree of polarization is 77 % for the VEKMAG data (starting from 10 K) [294] and 100 % for the BOREAS data, C stands for the coverage in ML, T is the temperature and m_{total} is the expectation value of the total magnetic moment at 6 T. The error of $m_{\text{s eff}}$, m_l is ±10 %, and for m_{total} it is the calculated value via error propagation. The BOREAS measurements were performed in 2020, 2021, 2023 and VEKMAG in 2021.

7.1.24 LEED images of the $FeBr_2$ on Au(111) sample prepared at the BOREAS beamline

In Fig. 7.29, the measured LEED images of the $FeBr_2$ on Au(111) samples which were characterized by XAS and XMCD are shown. In the case of the low coverages (0.25 ML and 0.3 ML), the third-spot pattern is not visible. However, it could be that also these samples have small areas with second-layer contributions. This can happen, if the terrace sizes of the Au(111) crystal are not big enough and therefore can be quickly filled by the first layer which results in a possible second layer growth. The 0.8-ML and 0.7-ML samples, were grown during the same beamtime. The only difference between the two samples is the growth speed. This could be an indication that the structure which is observed depends on the growth rate and therefore can be influenced by kinematic effects. However, the previously discussed magnetic properties are not different. Therefore the different patterns can also be a consequence of other reasons like position during the LEED measurements. All other samples which were grown at the BOREAS beamline were evaporated under the similar conditions as the 0.8 ML, but they showed the expected pattern. Another possible explanation could be that two competing structures with and without superstructure are on the Au(111) surface. For the 2.9-ML sample, the regular hexagonal pattern is measured, but also a ring like structure. This structure is a consequence of the next-layer growth, which seems to grow with different domain rotations.

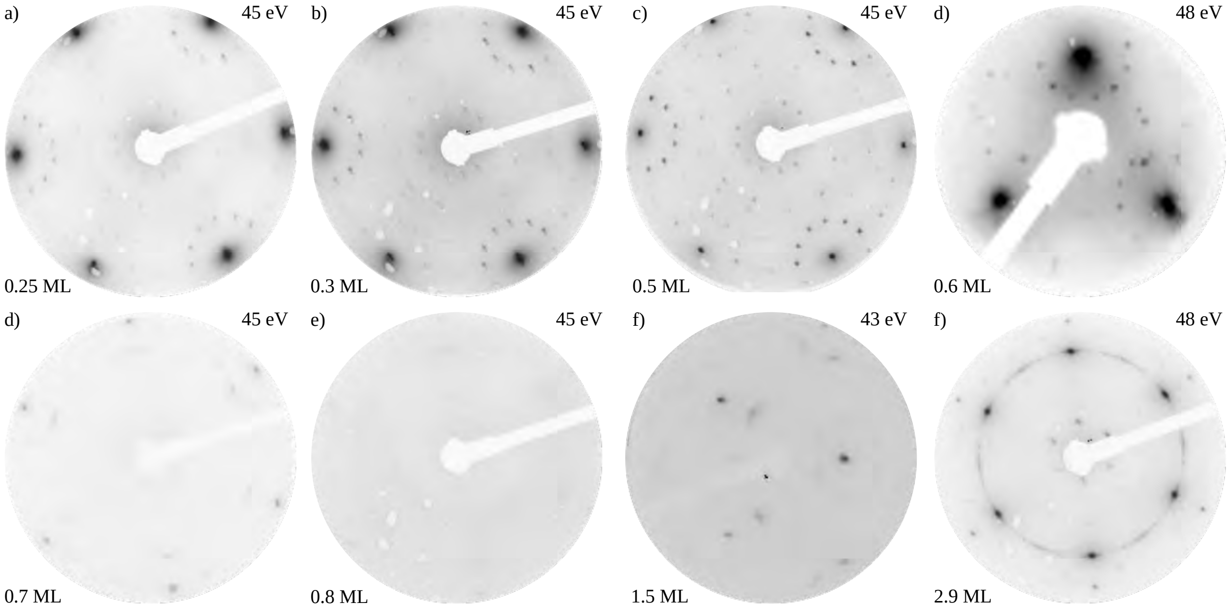

Figure 7.29: a)-f) LEED images at ≈45 eV for different coverages. All measurements were performed at the BOREAS beamline in 2021 (1.5 ML) and 2023, besides the 0.6 ML sample which was measured at CFM in the Nanophysics XPS Lab in 2020.

7.1.25 STM measurements of $FeBr_2$ on Au(111) at the BOREAS beamline

The STM measurements of the 1.5 and 2.0 ML $FeBr_2$ on Au(111) samples in Fig. 7.30 were performed at 77 K at the BOREAS beamline at ALBA before measuring XAS and XMCD. In a) the 1.5 ML sample shows triangular second and third layer islands on top of the ML. The blue rectangle indicates the area which is shown in the insert. Here some defect areas can be observed, which shows the substrate underneath the first layer. In b) the 2.0 ML sample is shown, here carpeting effects for the different heights can be observed.

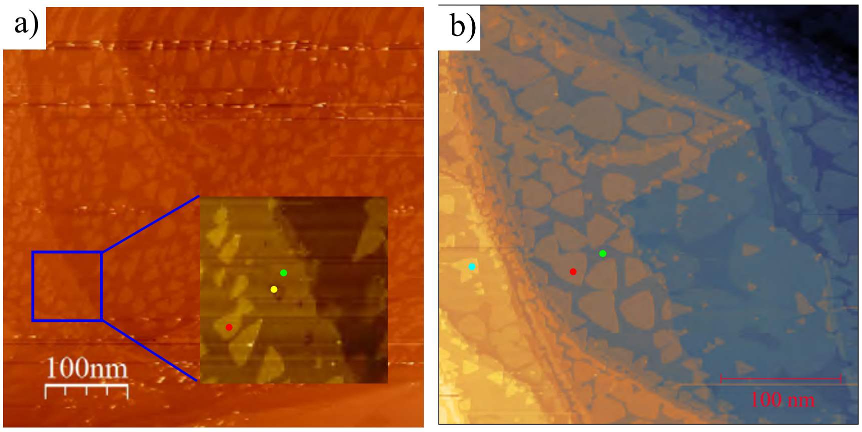

Figure 7.30: a) Topographic STM image of the 1.5 ML sample measured at 77 K at the BOREAS beamline at ALBA synchrotron. The dark blue rectangle indicate the position, which is shown in the insert as a zoomed-in sample region. b) Topographic STM image of the BL sample measured at the BOREAS beamline. In a) and b) the different dot colors (yellow, green, red, and light blue) are indicating the different observed coverages (Au surface, first-, second-, and third-layer). a) $U_{\mathrm{Bias}} = 1\,\mathrm{V}$ and $I_{\mathrm{TC}} = 0.3 \cdot 10^{-9}\,\mathrm{A}$, b) $U_{\mathrm{Bias}} = 1\,\mathrm{V}$ and $I_{\mathrm{TC}} = 0.3 \cdot 10^{-9}\,\mathrm{A}$. The measurements were performed at the BOREAS beamline in 2021. The image is a modified version of the figure shown in Ref. [32].

7.1.26 Field-dependent XMCD of $FeBr_2$ on Au(111) measured at the VEKMAG beamline

In Fig. 7.31, the XMCD measurements of a multilayer $FeBr_2$ on Au(111) for different field strengths are displayed. In a) and b) the isotropic XAS and XMCD measurements are displayed. It can be observed that for all different field strengths the isotropic XAS stays constant, which is expected, but also indicates that the sample has no x-ray damage. The measured XMCD signal continuously decreases with decreassing field strength. In d) the XMCD intensity is shown as a function of field and fitted by a $T = 10$ K Brillouin function. The result is a scaling factor of N=0.20 and J=2.

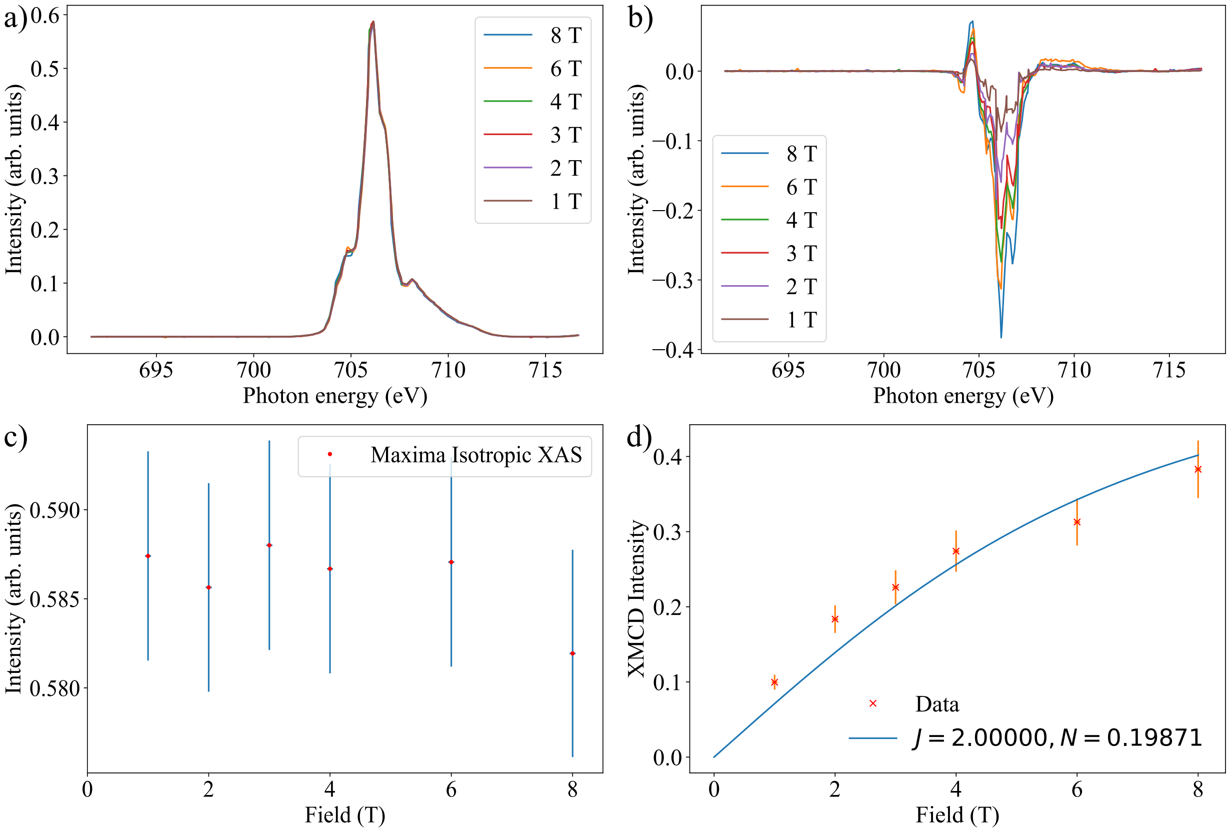

Figure 7.31: a) Isotropic XAS and b) XMCD measurements of a multilayer (2.9 ML) $FeBr_2$ on Au(111) sample for varying field strength. c) peak height of the isotropic XAS spectra for the different field strength and d) maximum intensity of the XMCD signal for decreasing maximal fields. The decreasing XMCD intensity is fitted by using a Brillouin function. The temperature at which the measurements were performed is 10 K at NI at the VEKMAG beamline in 2021.

7.1.27 XMCD measurements of $FeBr_2$ on Au(111) at the Br $L_{2,3}$ edge

In Fig. 7.32, the measured XAS and XMCD spectra for the Br $L_{2,3}$ edge are displayed. Here a different mirror setting needed to be used, since the Br $L_{2,3}$ edge is at higher photon energies. In a) the XAS spectra for Br are showing the expected step-like behavior due to the filled d orbitals. In b) the corresponding XMCD spectra is shown. Therefore, the decreased expectation value of the spin effective magnetic moment of Fe is not caused by the Br, since the measured Br XMCD signal is very weak.

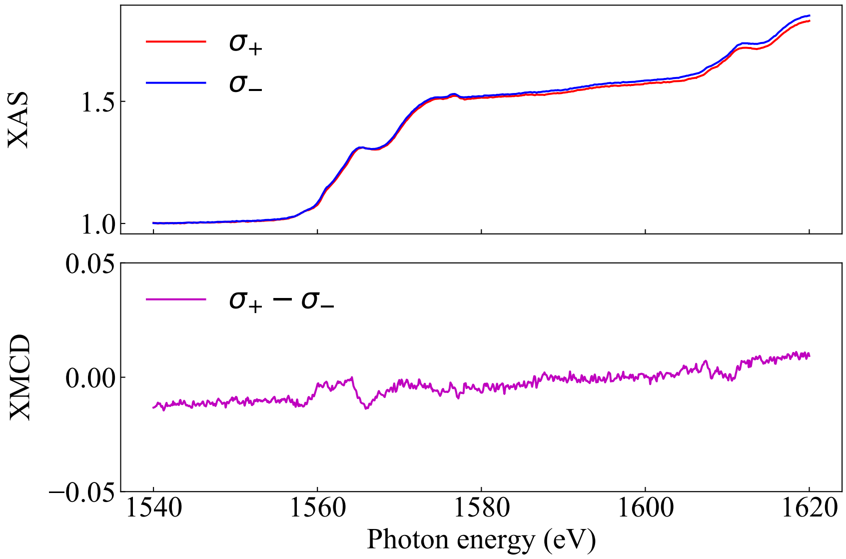

Figure 7.32: In the top, the Br $L_{2,3}$ edge for both circular polarization's is displayed. In the bottom figure, the corresponding XMCD is displayed, which only shows a weak magnetic contrast. The measurements were performed on the 1.5 ML sample at 2 K,6 T and NI at the BOREAS beamline in 2021. The image was taken from Ref. [32].

7.1.28 Temperature-dependent magnetization curves of $FeBr_2$ on Au(111)

In Fig. 7.33, the temperature-dependent magnetization curves for a sub-ML (a)) and a 2.0-ML sample (b)) of $FeBr_2$ on Au(111) are displayed. For the sub-ML, the magnetization curves nearly no curvature is visible, due to the complex magnetic properties of the material. With increasing temperature, a slight curvature that might be present at 2 K disappears. In the case of the 2.0-ML sample, the measured magnetization curves were acquired from the lowest temperature of 2 K up to 7 K (below the critical temperature). As previously observed for the expectation value of the magnetic moment in the temperature range between 2-7 K, are stable within the error, since the XMCD intensity at 6 T also does not vary strongly. Therefore, the magnetization curves are also not changing strongly.

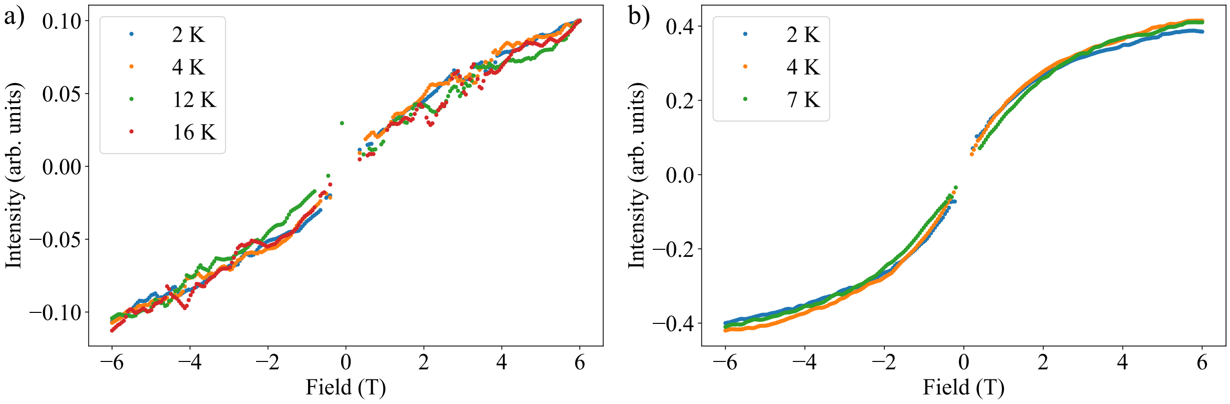

Figure 7.33: a) Magnetization curves of the 0.5 ML of $FeBr_2$ on Au(111) for different temperatures. In the low-temperature regime, the magnetization curve shows a slight curvature, which disappears above the critical temperature/antiferromagnetic ordering temperature. b) Magnetization curves of the 2.0-ML sample for different temperatures. All temperatures are below the critical temperature. The magnetization curves are scaled to the peak height of the corresponding isotropic XAS measurements. The measurements were performed at the BOREAS beamline in 2023 (a)) and 2021 (b)).

7.1.29 Comparison of XLD and XMLD measurements of $FeBr_2$ on Au(111)

In Fig. 7.34, the coverage-dependent XLD and XMLD spectra measured at 2 K are displayed. Both measurement types were performed by using horizontally and vertically linear polarized light. The difference between them is that an external magnetic field is applied. By comparing the spectra for the 0.3-ML and 0.5-ML samples it can be observed that the spectra do not show any peak-structure differences. Therefore, the first-layer samples are not showing coverage- or island-size-dependent properties. Even if the 0.5 ML shows in LEED a small indication of the second layer (third set of spots), the majority of signal is contributed by the first-layer. By comparing the sub-ML samples with the multilayer samples (c) and d)), it can be observed that the peak structure changes. These changes are a consequence of the second-layer growth, which has different magnetic properties. By comparing the two multilayer samples (1.5 ML and 2.9 ML) with each other, the change of the peak strength of the multiplet structure at the L_3 edge can be observed. Both samples show the same main peak structure, only the multiplet structure is weaker for the 1.5 ML sample, which can be a consequence of either the first-layer contribution or by interactions between the second layer and the first layer, which is coupled to the substrate.

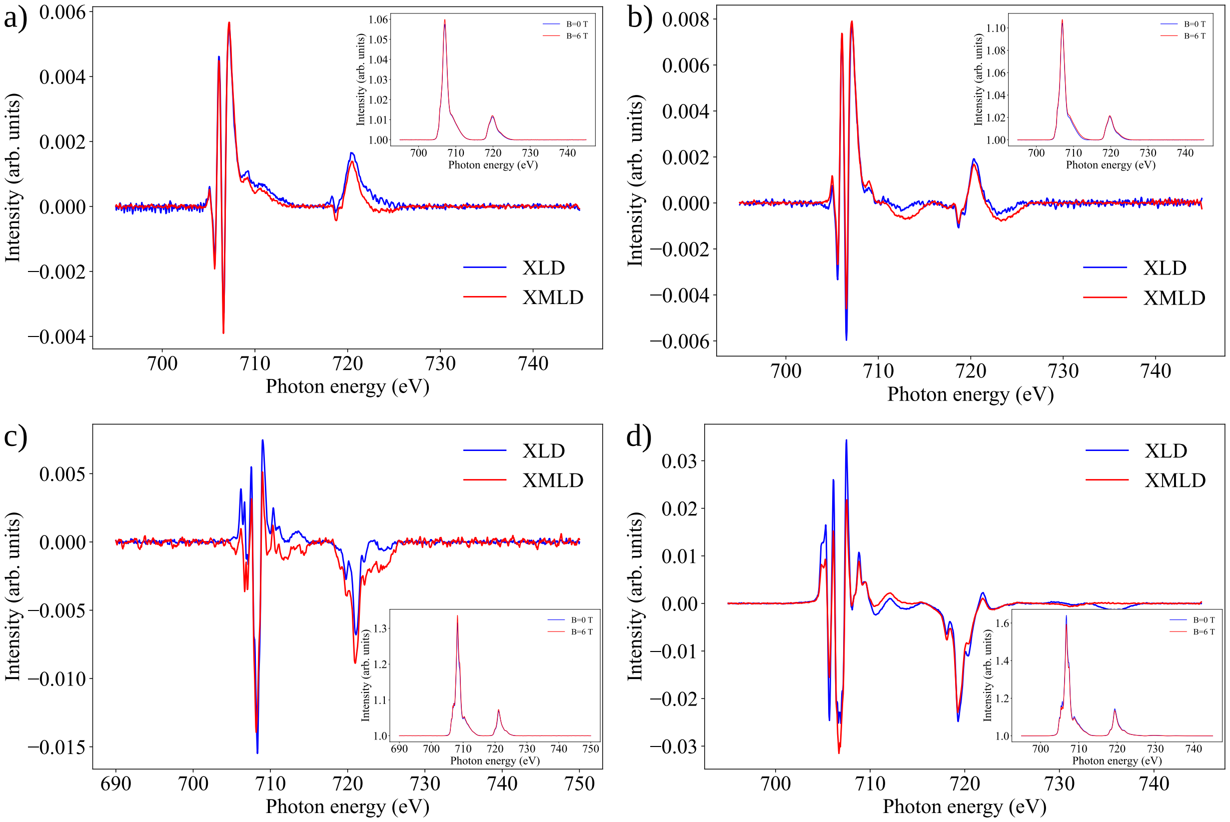

Figure 7.34: a)-d) Comparison of the measured XLD and XMLD spectra for different coverages (0.3 ML, 0.5 ML, 1.5 ML, and 2.9 ML). The measurements were performed at GI and 2 K at 0 T and 6 T. As an insert of each figure the related isotropic XAS spectra measured with linear polarization are displayed. The measurements were performed at the BOREAS beamline in 2023 (a), b), and d)) and 2021 (c)).

These interactions are weaker in the 2.9-ML sample, which already consists of the third and fourth layer. In Fig. 7.35, only the magnetic contribution of the XMLD measurements are shown. Here the XLD signal was removed from the XMLD signal, since the non-magnetic contribution is overlapped with the magnetic one. It is visible, that for lower coverages the magnetic contribution around the L_2-edge is mainly affected by the background, and only for higher coverages the L_2 edge signal can be extracted more precisely.

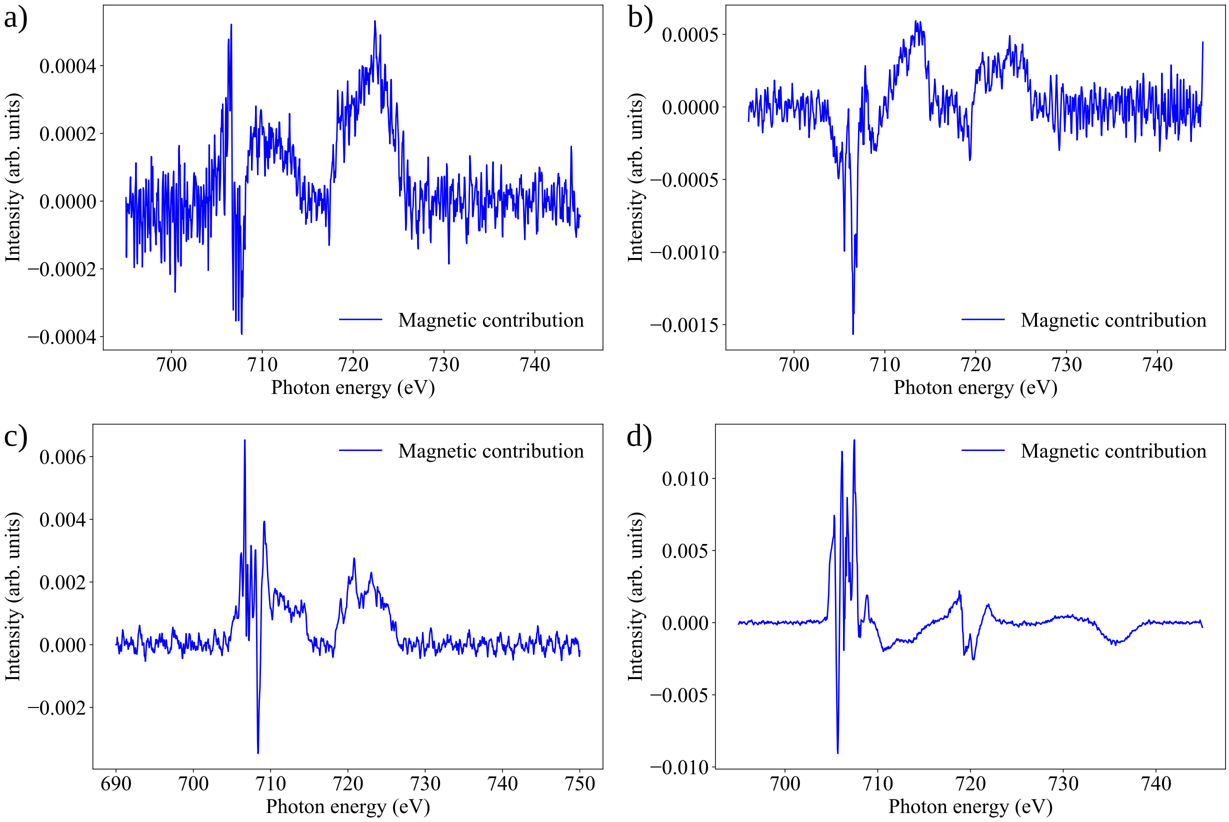

Figure 7.35: a)-d) Magnetic contribution of the coverage-dependent XMLD signal of $FeBr_2$ on Au(111).

7.1.30 Coverage-dependent magnetic moments of $FeBr_2$ on Bi_2Se_3

In Tab. 7.10, the expectation values of the effective spin, orbital and total magnetic moment at 6 T for all different coverages of $FeBr_2$ on Bi_2Se_3 are displayed, together with the temperature-dependence. All samples displayed in this table were grown at RT.

C (ML)	T (K)	μ (μ_B/Fe at)					
		NI			GI		
		$m_{\mathrm{s\ eff}}$	m_l	m_{total}	$m_{\mathrm{s\ eff}}$	m_l	m_{total}
0.7	2	1.58	0.49	2.07	1.65	0.22	1.87
	4	1.63	0.40	2.03	-	-	-
	10	1.10	0.29	1.39	-	-	-
	15	0.77	0.31	1.08	-	-	-
	20	0.85	0.22	1.07	-	-	-
2.8	2	2.34	0.68	3.02	2.02	0.48	2.50
	4	1.98	0.73	2.71	-	-	-
	10	1.86	0.70	2.56	-	-	-
	15	1.92	0.59	2.51	-	-	-
	20	1.47	0.54	2.01	-	-	-
	25	1.42	0.46	1.88	-	-	-
	35	1.00	0.32	1.32	-	-	-
	45	0.93	0.21	1.14	-	-	-
	55	0.64	0.21	0.85	-	-	-
	65	0.52	0.17	0.69	-	-	-
5.3	2	1.80	0.66	2.46	1.74	0.44	2.18

Table 7.10: Magnetic moment values for different coverages of $FeBr_2$ on Bi_2Se_3 at NI and GI. All moments were extracted via sum-rules from samples grown at RT. The expectation values of the spin effective moment and orbital moment at 6 T have an error of 10 % from the sum-rule evaluation. However, since the material has an easy axis OoP, the majority of measurements were performed at NI.

7.1.31 Coverage-dependent magnetic moments of $FeBr_2$ on Bi_2Se_3 grown at 100°C

In Tab. 7.11, the expectation values of the effective spin, orbital and total magnetic moment at 6 T for all different coverages of $FeBr_2$ on Bi_2Se_3 are displayed, together with the temperature dependence. All samples displayed in this table were grown at 100-150 °C.

C (ML)	T (K)	μ (μ_B/Fe at)					
		NI			GI		
		$m_{\mathrm{s\ eff}}$	m_l	m_{total}	$m_{\mathrm{s\ eff}}$	m_l	m_{total}
0.27	2	2.37	0.79	3.07	1.98	0.59	2.57
	4	2.24	0.71	2.95	-	-	-
	10	2.04	0.74	2.78	-	-	-
	15	1.86	0.70	2.56	-	-	-
	20	1.61	0.55	2.16	-	-	-
	25	1.41	0.47	1.88	-	-	-
0.53	2	2.26	0.82	3.08	2.04	0.62	2.66
	4	2.16	0.71	2.87	-	-	-
	10	1.60	0.23	1.83	-	-	-
	15	1.88	0.64	2.52	-	-	-
	20	1.66	0.51	2.17	-	-	-
	25	1.41	0.51	1.92	-	-	-
	35	1.00	0.41	1.41	-	-	-
	45	0.78	0.23	1.01	-	-	-
	55	0.66	0.29	0.95	-	-	-
	65	0.28	0.26	0.54	-	-	-
1.05	2	2.36	0.81	3.17	2.35	0.53	2.88
	4	2.34	0.83	3.17	-	-	-
	10	2.41	0.68	3.09	-	-	-
	15	2.16	0.63	2.79	-	-	-
	20	1.93	0.52	2.45	-	-	-
	25	1.69	0.42	2.11	-	-	-
	35	1.28	0.27	1.55	-	-	-
	45	0.78	0.27	1.05	-	-	-
	55	0.66	0.24	0.90	-	-	-
	65	0.52	0.20	0.72	-	-	-
5.3	2	2.00	0.78	2.78	1.94	0.42	2.36
	10	1.87	0.73	2.60	-	-	-

Table 7.11: Magnetic moment values for different coverages of $FeBr_2$ on Bi_2Se_3 at NI and GI. All moments were extracted via sum-rules from samples grown at temperatures around 100-150 °C. The expectation value of the spin effective moment and orbital moment at 6 T have an error of 10 % from the sum-rule evaluation. However, since the material has an easy axis OoP, the majority of measurements were performed at NI.

7.1.32 Comparison of the high-coverage magnetization loops of $FeBr_2$ on Bi_2Se_3 at different growth temperatures

In Fig. 7.36, XMCD magnetization loops of the two 5-ML samples grown at RT and at 100-150 °C are shown. For either peak-height scaling or moment scaling the loops are very similar. The only exception is the saturation field, but due to the noise level it could be identical as well. The small difference between the curvatures can be caused by the higher coverage at RT growth, therefore a slightly faster saturation can be caused by a higher amount of material (next-layer growth).

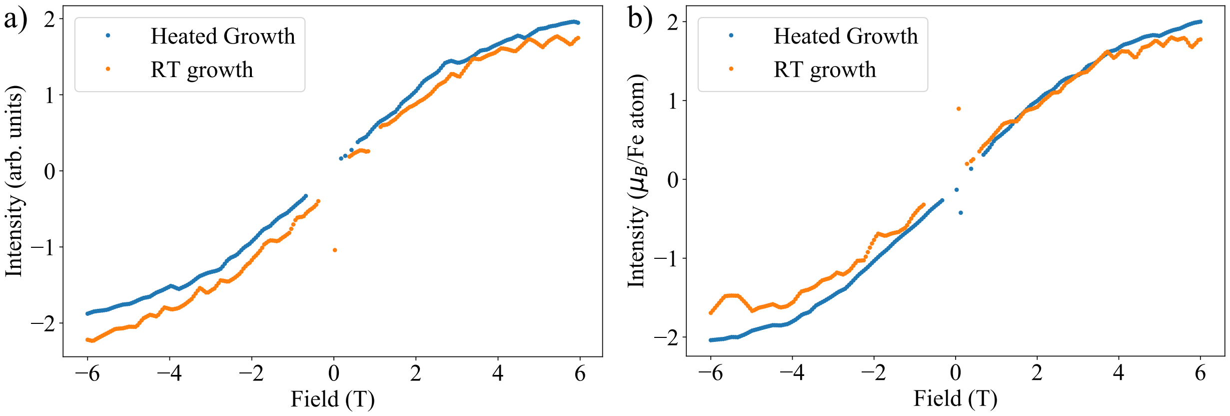

Figure 7.36: a) and b) Magnetization curves of two multilayer samples of $FeBr_2$ on Bi_2Se_3. In a) the magnetization curves are scaled to the maximum isotropic XAS peak height and in b) to the expectation value of the spin effective magnetic moment at 6 T. The measurements were performed at the BOREAS beamline in 2023.

7.1.33 Temperature-dependent magnetization curves for different coverages of $FeBr_2$ on Bi_2Se_3

In Fig. 7.37, the temperature-dependent magnetization curves of 0.7 ML and 2.8 ML $FeBr_2$ on Bi_2Se_3 are displayed. In the case of RT growth, the low-coverage sample does not show the normal magnetization curve behavior that was observed for the samples grown at elevated temperatures. Here, the magnetization curve does not saturate until 6 T. At 2 K, the curvature looks saturating in the negative field regime, but not for positive fields, which indicates that the behavior is measurement-related, not sample-related. After increasing the temperature to 4 K, no indication of any saturation is visible. However, in comparison to 0.7 ML, in the 2.8-ML sample the saturation behavior survives until 10 K. This could be related to the growth temperature, which would indicate that at RT only small islands are growing on the sample. In the case of higher coverages of $FeBr_2$ on Bi_2Se_3, the same magnetic properties as for smaller coverages on heated substrates are observed. This could be an indication, that the material starts to form larger islands only for heated growth or high coverages at RT. Therefore, the mobility of $FeBr_2$ on Bi_2Se_3 at RT seems to be lower than on Au(111), were at RT bigger islands are forming also for lower coverages. This possible explanation is also visible in the extracted magnetic moments, where the first layer grown at RT has a reduced moment by around 35 % compared to the multilayer samples or the sub-ML samples grown at elevated temperatures.

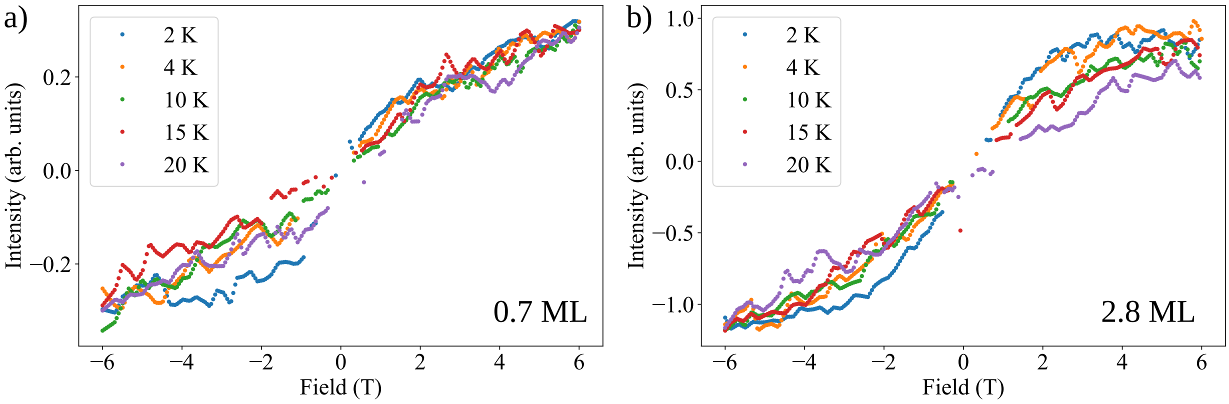

Figure 7.37: a)-b) Temperature-dependent magnetization curves for 0.7 and 2.8 ML of $FeBr_2$ on Bi_2Se_3. Both samples were grown at RT and measured at NI. The measurements were performed at the BOREAS beamline in 2023. The displayed magnetization curves are scaled to the isotropic XAS spectra of the corresponding coverage for a better comparability.

7.1.34 XLD and XMLD $FeBr_2$ on Bi_2Se_3

In Fig. 7.38 and 7.39, the measured XLD and XMLD spectra of different coverages of $FeBr_2$ on Bi_2Se_3 are shown. The performed XMLD measurements mainly consist of the structural dichroism from XLD, since the same parameters for XLD and XMLD were used, with the only difference of applying an external magnetic field of 6 T for XMLD. In Fig. 7.38, the comparison of the XLD and XMLD spectra for samples grown at RT is displayed. Here, a strong difference between the 0.7-ML and 2.8-ML samples can be observed at the L_3 and L_2 edge. For both samples the triple peak structure is visible at the L_3 edge only with a different background contribution. The main difference is the structure of the L_2 edge. Since the XAS and XMCD spectra are identical no structural or chemical change is expected. The change is most probably related to small island growth at RT for the sub-ML sample. For the multilayer grown at RT the same peak structure as for samples grown at elevated temperatures has been observed (Fig. 7.38 b)). In Fig. 7.39, the XLD and XMLD spectra for different coverages grown at 100-150 °C are shown. It is observed that for all samples ranging from very low to very high coverages the spectral shape and peak ratios are the same. The only strong difference occurs in the 5.3-ML sample, which also shows a different behavior of the magnetization curve. Here the L_3 edge shows a difference at ≈ 708 eV, where the peak intensities between the first and the second peak of the the triple-peak set are changing. This change could be an indication of the starting structural change. By comparing the two different growth temperatures with the samples on Au(111), it is observed that for BL

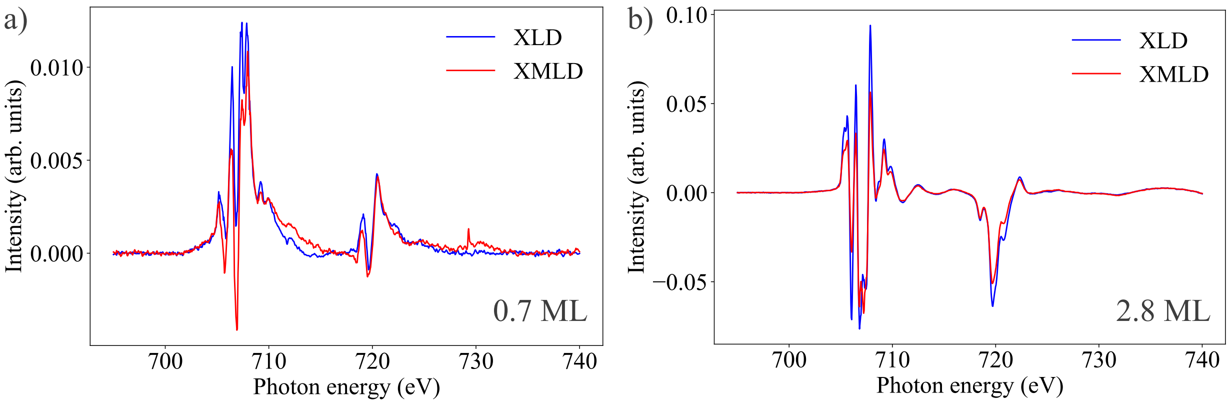

Figure 7.38: a) and b) Comparison of the XLD and XMLD spectra for different coverages of $FeBr_2$ grown on Bi_2Se_3 at RT. The spectra were all measured at 2 K and GI. The measurements were performed at the BOREAS beamline in 2023.

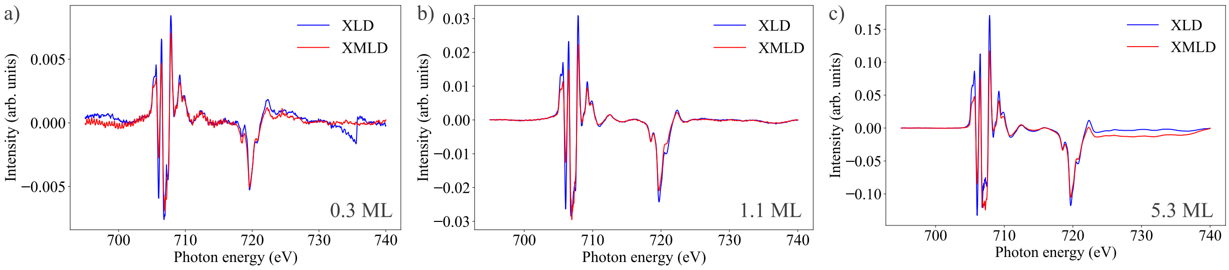

Figure 7.39: a) and b) comparison of the XLD and XMLD spectra for different coverages of $FeBr_2$ grown at 100-150 °C on Bi_2Se_3. The spectra were all measured at 2 K and GI. The measurements were performed at the BOREAS beamline in 2023.

coverages on Au(111), the spectral shape is identical to the one on heated Bi_2Se_3 or multilayer coverage on not-heated Bi_2Se_3. Therefore, a different first-layer structure on Au(111) is present compared to on other substrates. Also the island size could affect the peak structure of $FeBr_2$ grown at RT on Bi_2Se_3. In Fig. 7.40 a)-c), the magnetic signal for the three different coverages is displayed. The magnetic contribution spectra are showing the same peak structure, therefore also the magnetic properties are identical from sub-ML to multilayer. In d), the overlay of the XLD spectra for different coverages is displayed. The spectra are all normalized to 1, so that the peak structure can be easily compared. It is visible that for the different coverages grown at elevated temperature (100-150 °C), the XLD structure is not changing from sub-ML to multilayer samples. This shows that the properties and the structure of the layers for different coverages are identical.

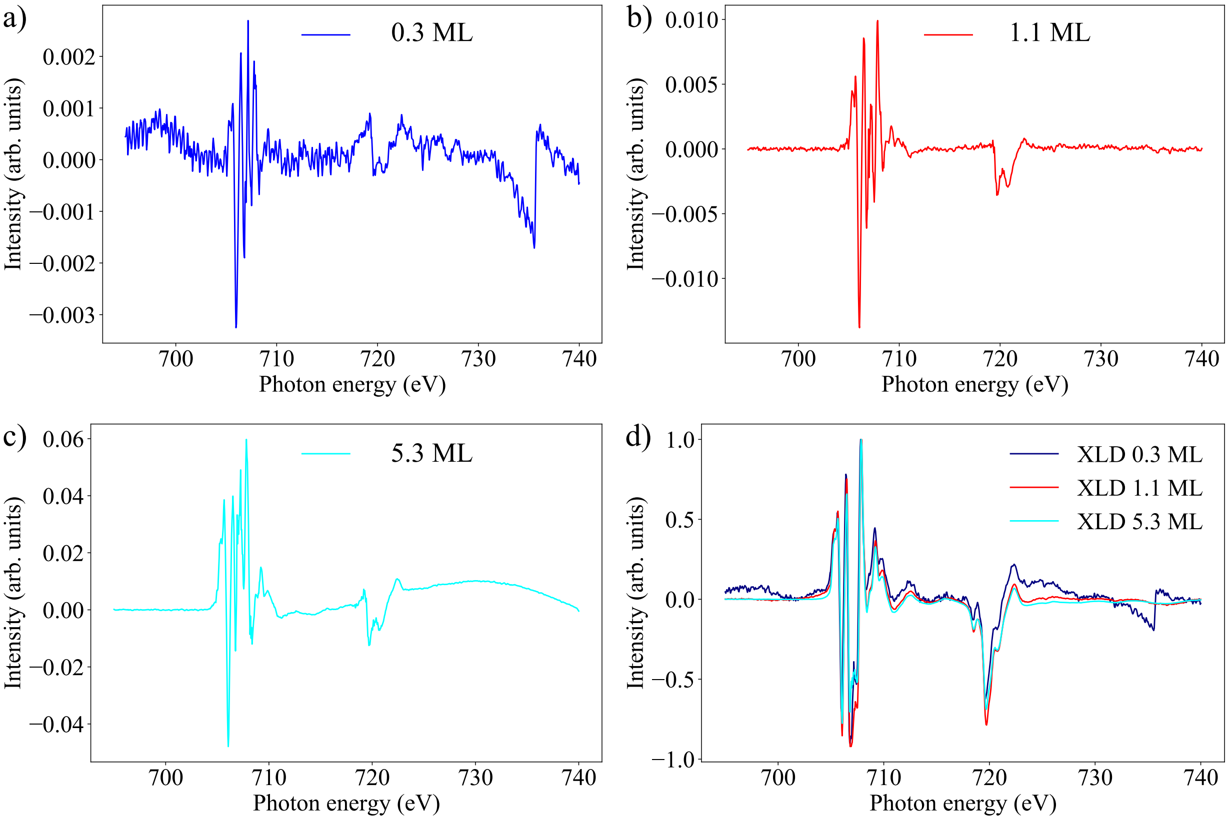

Figure 7.40: a)-c) Magnetic contribution of the XMLD spectra for different coverages of $FeBr_2$ on Bi_2Se_3. The magnetic contribution was extracted by subtracting the XLD spectra at 6 T and 2 K from the XLD spectra at 0 T. All spectra were measured at GI. In d), the comparison of the different XLD spectra for coverages ranging from sub-ML to multilayer is shown. The spectra are all normalized for a better comparison of the peak structure.

7.1.35 LEED images of $FeBr_2$ on Bi_2Se_3 measured at the BOREAS beamline

In Fig. 7.41 and 7.42, the LEED images of $FeBr_2$ on Bi_2Se_3 for the different coverages and growth temperatures are displayed. In the case of RT growth (Fig. 7.41), the first layer does not show the moiré pattern and for even higher coverages, the pattern is smeared out and more difficult to recognize. In the low-coverage regime, the moiré pattern is not visible, since the islands are probably too small, as previously discussed. With increasing coverage, the pattern appears, but still does not create sharp spots. In contrast, the samples which were grown at higher temperatures (Fig. 7.42), start already to show at around 0.5 ML the moiré pattern, which could be related to the growth of bigger islands. By comparing the LEED pattern in Fig. 7.41 and Fig. 7.42 it can be observed, that in the case of growing $FeBr_2$ on Bi_2Se_3 at RT a higher amount of material is needed to create the moiré pattern. For the heated samples this pattern starts to be weakly visible at around 0.5 ML with a strong visibility at 1.05 ML. For the growth at RT no moiré pattern has been observed for 0.7 ML. However, the pattern does probably not only appear at coverages above 2 ML, since besides a higher mobility the heated growth does not affect the material. The reason for the appearing of the moiré pattern for higher coverages at RT is, that $FeBr_2$ probably forms smaller islands at RT, which suppresses the creation of the moiré pattern until a specific lateral size is reached.

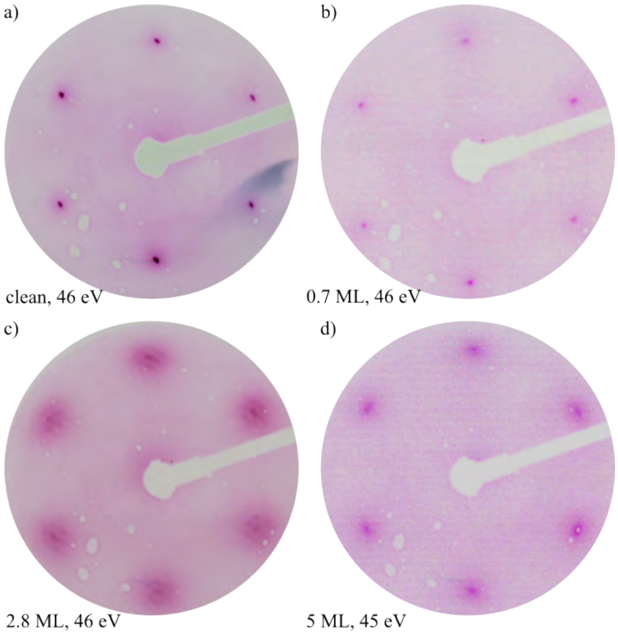

Figure 7.41: LEED images for different coverages of $FeBr_2$ grown on Bi_2Se_3 at RT compared to clean Bi_2Se_3 after in situ exfoliation. All images are measured at 46 eV. The measurements were performed at the BOREAS beamline in 2023.

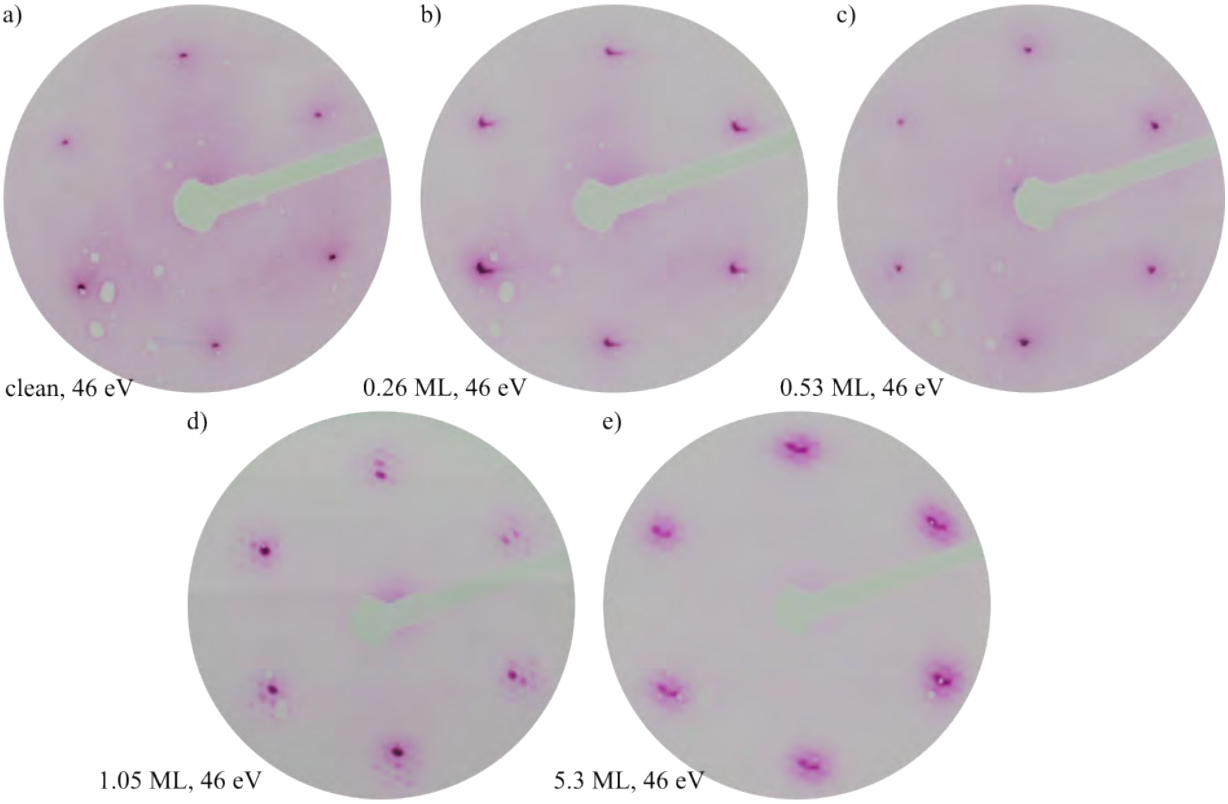

Figure 7.42: LEED images for different coverages of $FeBr_2$ grown on Bi_2Se_3 at 100-150 °C, compared to clean Bi_2Se_3 after in-situ exfoliation. All images are measured at 46 eV. The measurements were performed at the BOREAS beamline in 2023.

7.1.36 Brillouin function fit for $FeBr_2$ on Bi_2Se_3

In Fig. 7.43, the inverted expectation values of the total magnetic moment for 2.8 ML and 0.3 ML $FeBr_2$ on Bi_2Se_3 are displayed. As extracted from the magnetization loop, a critical temperature in the range of 10 K can be determined for both sample thicknesses (Fig. 7.43 a) and c)). In b) and d), the total magnetic moment values were fitted by using the Brillouin function, however, if the data from the full temperature range was used (starting from 2 K), the Brillouin function does not fit the experimental data. This is only achieved if the temperature range is reduced to temperatures above 10 K. Therefore, the magnetic behavior for low temperatures does not follow the paramagnetic behavior of the Brillouin function and therefore shows a magnetic ordering.

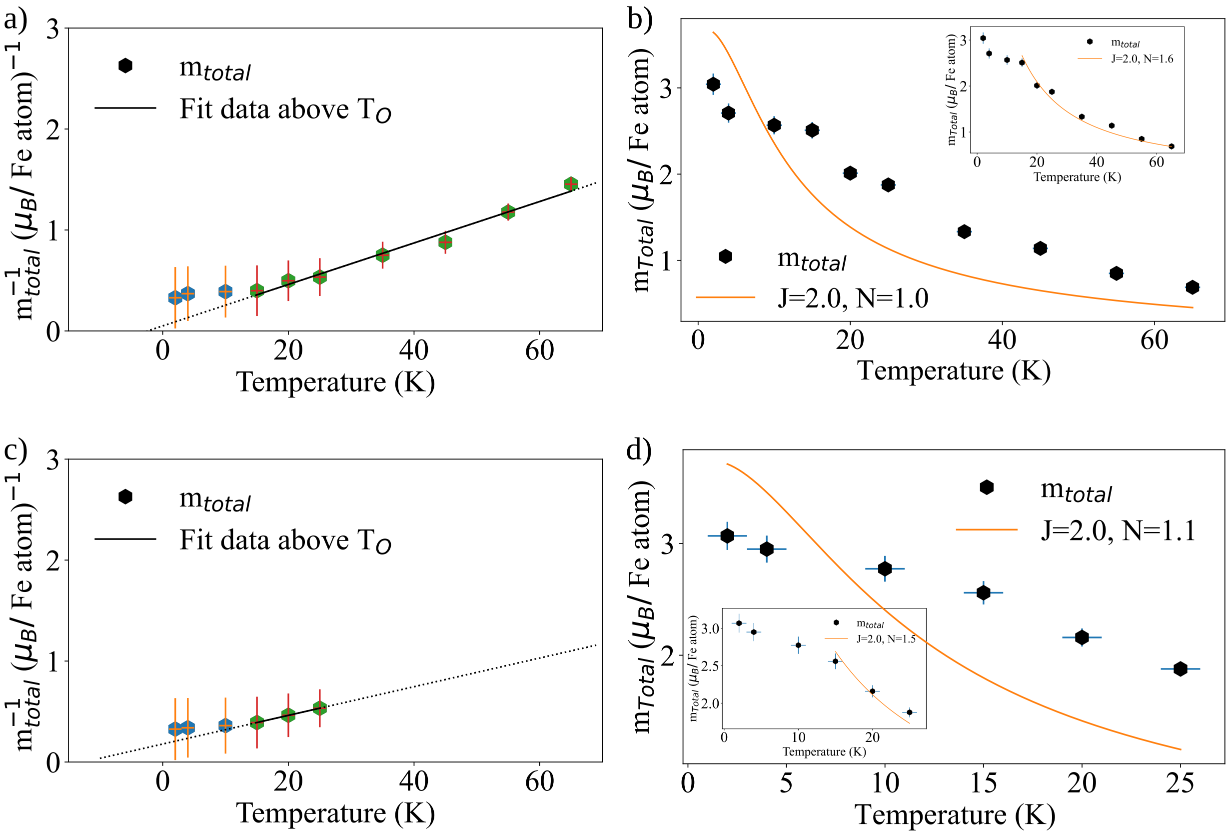

Figure 7.43: a) and c) Inverted expectation values of the total magnetic moment of 2.8 and 0.3 ML $FeBr_2$ on Bi_2Se_3. By using a linear fit, a critical/ordering temperature (T_O) is extracted. For both a) and c), the moment values for the temperatures ranging from 15-65 K and 15-25 K were used for the linear fit. For the 2.8-ML sample, the linear intercept value is $-0.0498 \pm 0.0541\ \mu_B/\mathrm{Fe\ atom}^{-1}$ and the slope is $0.0205 \pm 0.0013\ \mathrm{K} \cdot \mu_B/\mathrm{Fe\ atom}^{-1}$ with $\chi^2 = 0.018$. In the case of the 0.3-ML sample, the values for linear intercept are $-0.178 \pm 0.003\ \mu_B/\mathrm{Fe\ atom}^{-1}$ and for the slope $0.014 \pm 0.00002\ \mathrm{K} \cdot \mu_B/\mathrm{Fe\ atom}^{-1}$ with $\chi^2 = 1.4 \cdot 10^{-6}$. b) and d): total magnetic moment fitted with a Brillouin function. In the corresponding inserts, the Brillouin-function fit for a reduced temperature range is displayed (the same as for the linear fits). The 2.8-ML sample was grown at RT and the 0.3-ML one at 100-150 °C.

7.1.37 Coverage estimations by XPS

In Tab. 7.12 and 7.13, the estimated coverages of $MnBr_2$ and $MnCl_2$ are displayed. The calibration factor from the Br 3p peak of $FeBr_2$ on Au(111) is 0.0065 arb. units (XPS peak intensity of the Br $3p_{\frac{3}{2}}$ after normalization to Au $4d_{\frac{5}{2}}$) per 0.1 ML. By using the calibration for Br an estimated calibration for Mn would be 0.0167 arb. units per 0.1 ML (XPS peak intensity of the Mn $2p_{\frac{3}{2}}$ after normalization to Au $4d_{\frac{5}{2}}$). For the calibration, via XPS the 0.6-ML $FeBr_2$ on Au(111) sample has been used and for the Mn calibration the 0.8 ML $MnBr_2$ on Au(111) has been used.

I_{Br} (arb. units)	I_{Mn} (arb. units)	Coverage (ML)	T_{Growth} (°C)
0.03	-	0.5±0.36	120
0.04	-	0.6±0.24	50
0.04	-	0.6±0.24	90
0.055	0.15	0.85± 0.34	121
0.06	-	0.9±0.2	58
0.069	0.17	1.1± 0.44	117
0.27	0.4	4.2± 1.7	128

Table 7.12: Estimated coverages of the $MnBr_2$ samples on Au(111) by XPS. All given intensity values are normalized to the Au $4d_{\frac{5}{2}}$ peak. For the coverage estimation, the normalized Br $3p_{\frac{3}{2}}$ of 0.6 ML $FeBr_2$ is used, which had an intensity of 0.039 for 0.6 ML. Already this coverage had an error of 20 %, which causes even higher error for the Mn coverages.

The high coverage error for the 4.2 ML sample is also strongly visible by using the Mn calibration of the 0.8-ML sample for the 4.2 ML sample. Then, only a coverage of 2.1 ML would be calculated.

I_{Mn} (arb. units)	Coverage (ML)	T_{Growth} (°C)
0.16	1.0± 0.4	106
0.24	1.5± 0.6	101
0.28	1.7± 0.68	103

Table 7.13: Estimated coverages of the $MnCl_2$ samples on Au(111) by XPS. All given intensity values are normalized to the Au $4d_{\frac{5}{2}}$ peak. For the coverage estimation, the Mn intensities for $MnBr_2$ are compared to the ones of $MnCl_2$. The error from the calculation is mentioned in the table, but additionally, due to the problem with the Au background another ±0.5 ML needs to be taken into account.

7.1.38 Fitting parameters of XPS spectra of $MnBr_2$ on Au(111)

Coverage	T_{Growth}	Peaks	FWHM (eV)	Peak position (eV)	Amplitude (arb. units)
0.8 ML	121 °C	Br 3p 3/2	2.93	182.71	1066
		3p 1/2	3.03	189.28	590
0.8 ML	121 °C	Au 4d 3/2	6.05	353.37	26172
		4d 5/2	5.21	335.36	35637
0.8 ML	121 °C	Mn 2p 3/2	3.60	642.5	1550
		2p 1/2	3.66	653.47	800
		2p 3/2 sat	3.96	647.37	1000
		2p 1/2 sat	4.29	658.13	500
		Au 4p 1/2	7.20	642.80	4802
1.0 ML	117 °C	Br 3p 3/2	2.88	182.94	1273
		3p 1/2	3.03	189.51	706
1.0 ML	117 °C	Au 4d 3/2	6.10	353.40	22788
		4d 5/2	5.16	335.37	30176
1.0 ML	117 °C	Mn 2p 3/2	4.10	642.5	2850
		2p 1/2	4.24	653.85	1100
		2p 3/2 sat	4.01	647.21	1400
		2p 1/2 sat	3.90	658.89	544
		Au 4p 1/2	7.20	642.50	2643
4.2 ML	128 °C	Br 3p 3/2	2.81	183.01	3449
		3p 1/2	2.87	189.65	1639
4.2 ML	128 °C	Au 4d 3/2	4.87	353.72	14402
		4d 5/2	4.15	335.09	18327
4.2 ML	128 °C	Mn 2p 3/2	4.10	642.52	4500
		2p 1/2	3.36	654.00	2200
		2p 3/2 sat	3.96	647.21	3074
		2p 1/2 sat	3.96	659.05	1755
		Au 4p 1/2	6.12	642.80	2621

Table 7.14: Fitting parameters of the Au 4d, Br 3p, and Mn 2p core-level peaks for different coverages of $MnBr_2$ on Au(111) ranging from 0.8-4.2 ML. In this table only the fitting parameter related to the material peaks and not to the x-ray gun are shown. No error-bar is mentioned for the fits, since the Mn and Au core-level peaks are overlaping. As a maximum approximation a FWHM error of 10 %, an position error of 0.5 eV and an amplitude error of 10 % can be assumed.

7.1.39 Fitting parameters of XPS spectra of $MnBr_2$ on Au(111) grown at different temperatures

Coverage	T_{Growth}	Element-Peaks	FWHM (eV)	Peak position (eV)	
0.6 ML	50 °C	Br 3p 3/2	2.85	182.99	596
		3p 1/2	3.03	189.50	342
0.6 ML	50 °C	Au 4d 3/2	6.12	353.38	18365
		4d 5/2	5.10	335.33	23956
0.6 ML	50 °C	Mn 2p 3/2	3.24	642.5	900.
		2p 1/2	3.06	653.34	394
		2p 3/2 sat	3.96	647.17	950
		2p 1/2 sat	3.96	658.00	180
		Au 4p 1/2	5.40	642.50	3080
0.6 ML	90 °C	Br 3p 3/2	2.88	182.94	639
		3p 1/2	3.03	189.51	365
0.6 ML	90 °C	Au 4d 3/2	5.98	353.38	17962
		4d 5/2	5.19	335.35	24688
0.6 ML	90 °C	Mn 2p 3/2	3.24	642.5	900
		2p 1/2	3.06	653.08	550
		2p 3/2 sat	3.96	646.63	950
		2p 1/2 sat	3.96	658.00	450
		Au 4p 1/2	5.40	642.50	3427
0.5 ML	120 °C	Br 3p 3/2	2.72	182.71	410
		3p 1/2	3.03	189.24	273
0.5 ML	120 °C	Au 4d 3/2	6.07	353.38	18690
		4d 5/2	5.23	335.36	25593
0.5 ML	120 °C	Mn 2p 3/2	3.06	642.50	900
		2p 1/2	3.06	653.0	399
		2p 3/2 sat	3.96	647.11	950
		2p 1/2 sat	3.96	658.00	450
		Au 4p 1/2	5.40	642.50	2985

Table 7.15: Fitting parameters of the Au 4d, Br 3p, and Mn 2p core-level peaks for different growth temperatures of $MnBr_2$ on Au(111) ranging from 50-120 °C. No error-bar is mentioned for the fits, since the Mn and Au core-level peaks are overlapping. As a maximum approximation a FWHM error of 10 %, an position error of 0.5 eV and an amplitude error of 10 % can be assumed.

7.1.40 Fitting parameters of XPS spectra of $MnCl_2$ on Au(111)

Coverage	T_{Growth}	Element-Peaks	FWHM (eV)	Peak position (eV)	Amplitude (arb. units)
1.0 ML	106 °C	Cl 2p 3/2	1.81	199.57	517
		2p 1/2	1.94	201.21	300
1.0 ML	106 °C	Au 4d 3/2	6.04	353.386	26200
		4d 5/2	5.17	335.36	35951
1.0 ML	106 °C	Mn 2p 3/2	3.40	642.86	1550
		2p 1/2	3.32	654.53	800.0
		2p 3/2 sat	3.96	648.31	824
		2p 1/2 sat	4.32	659.42	500
		Au 4p 1/2	7.20	643.12	5026
1.5 ML	101 °C	Cl 2p 3/2	1.67	199.42	977
		2p 1/2	2.07	200.95	775
1.5 ML	101 °C	Au 4d 3/2	4.27	353.32	14895
		4d 5/2	4.31	335.16	22962
1.5 ML	101 °C	Mn 2p 3/2	3.24	642.97	2900
		2p 1/2	3.24	654.48	1450
		2p 3/2 sat	4.32	647.74	1900
		2p 1/2 sat	4.68	659.15	850
		Au 4p 1/2	6.12	642.7	4000
1.7 ML	103 °C	Cl 2p 3/2	1.70	199.50	754
		2p 1/2	2.07	201.01	607
1.7 ML	103 °C	Au 4d 3/2	4.95	353.70	16916
		4d 5/2	4.43	335.14	24578
1.7 ML	103 °C	Mn 2p 3/2	3.67	643.08	2700
		2p 1/2	3.96	654.50	1500
		2p 3/2 sat	4.28	647.50	1618
		2p 1/2 sat	4.14	659.59	765
		Au 4p 1/2	6.12	642.69	4000

Table 7.16: Fitting parameters of the Au 4d, Cl 2p, and Mn 2p core-level peaks for different coverages of $MnCl_2$ on Au(111) ranging from 0.8-1.5 ML. No error-bar is mentioned for the fits, since the Mn and Au core-level peaks are overlapping. As a maximum approximation a FWHM error of 10 %, an position error of 0.5 eV and an amplitude error of 10 % can be assumed.

7.1.41 LEED measurements of $MnBr_2$ and $MnCl_2$ on Au(111) measured at the BOREAS beamline

In Fig. 7.44 and Fig. 7.45, the two $MnBr_2$ and $MnCl_2$ samples grown at RT on Au(111) are shown. In the case of $MnBr_2$ a hexagonal pattern around the (0,0)-spot can be observed for a nominal coverage of one ML. In the case of $MnBr_2$ a ring structure as expected for the RT growth can be observed, with a sharp spot for the $MnBr_2$ aligned directly with the main symmetry direction of Au. As previously observed the samples grown at RT normally have three spots (3 rotational domains). However, the reason for not seeing these spots can be manifold starting from potential different growth rates to a LEED system, which does resolve the spots nicely. Nevertheless, the sharpness of these spots is a feature of $MnBr_2$, which does not exist on $MnCl_2$ at RT. For the 1.0 ML sample of $MnBr_2$ the hexagonal pattern around the (0,0)-spot can be observed, which was also visible for the other $MnBr_2$ samples with low coverages. In Fig. 7.45, the LEED images of the 0.5 and 1.0 ML $MnCl_2$ on Au(111) samples are shown. Here the dominant ring structure is visible, with a more smeared out main diffraction spot of $MnCl_2$.

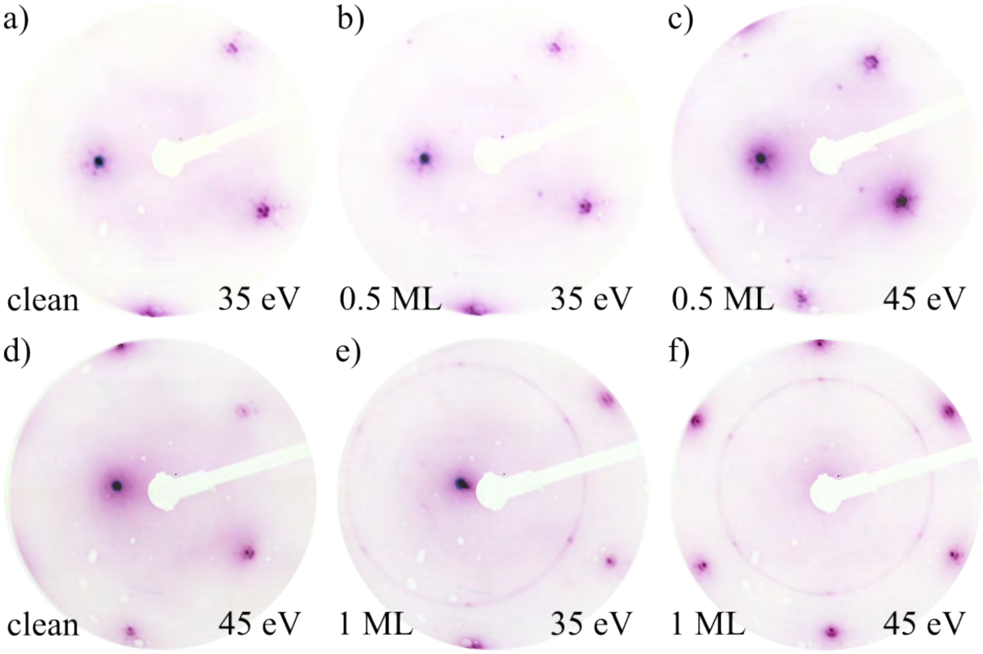

Figure 7.44: a)-c) Low energy LEED images of the 0.5 ML $MnBr_2$ on Au(111) sample. d)-f) Low energy LEED images of the 1.0 ML $MnBr_2$ on Au(111) sample. The LEED measurements were performed at the BOREAS beamline at ALBA in 2023. Both samples were grown at RT.

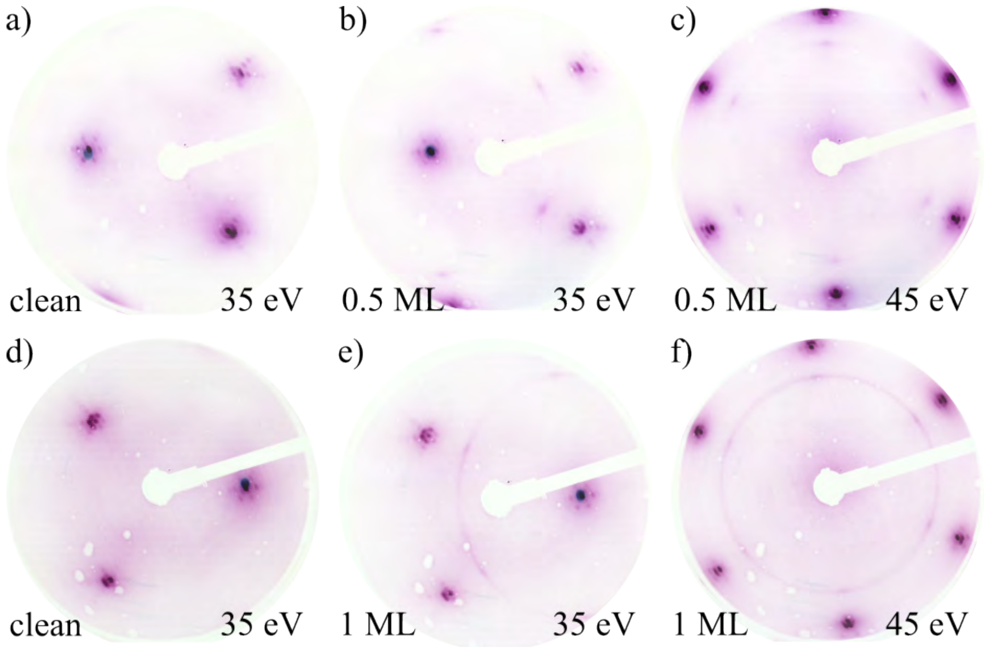

Figure 7.45: a)-c) Low energy LEED images of the 0.5 ML $MnCl_2$ on Au(111) sample. d)-f) Low energy LEED images of the 1.0 ML $MnCl_2$ on Au(111) sample. The LEED measurements were performed at the BOREAS beamline at ALBA in 2023. Both samples were grown at RT.

7.1.42 Magnetic moment values for different coverages of $MnBr_2$ on Au(111)

In Tab. 7.17, the expectation values of the magnetic moments from a sum-rule analysis of $MnBr_2$ on Au(111) are shown. They were calculated by using a Mn^{2+} system with $N_H = 5$ at 6 T.

C (ML)	T (K)	μ (μ_B/Mn at)					
		NI			GI		
		$m_{\text{s eff}}$	m_l	m_{total}	$m_{\text{s eff}}$	m_l	m_{total}
0.5	1.7	1.30	-	1.30	1.20	0.19	1.39
	4	-	-	-	1.05	0.19	1.24
	12	-	-	-	0.83	0.13	0.96
1.0	1.7	1.10	-	-	1.35	0.07	1.42
	4	-	-	-	1.11	0.21	1.32
	12	-	-	-	1.01	0.10	1.11
	16	-	-	-	0.85	0.07	0.92
	20	-	-	-	0.74	0.08	0.82

Table 7.17: Magnetic moment values for different coverages of $MnBr_2$ on Au(111). All moments were extracted via sum-rules from samples grown at RT. The expectation value of the spin effective moment and orbital moment at 6 T have an error of ≈30 % from the sum-rule evaluation [261]. For the orbital moment values at NI no value could be extracted.

7.1.43 Magnetic moment values for different coverages of $MnCl_2$ on Au(111)

In Tab. 7.18, the expectation values for the magnetic moments from sum-rule analysis of $MnCl_2$ on Au(111) are shown. They were calculated by using a Mn^{2+} system with $N_H = 5$ at 6 T.

C (ML)	T (K)	μ (μ_B/Mn at)					
		NI			GI		
		$m_{\text{s eff}}$	m_l	m_{total}	$m_{\text{s eff}}$	m_l	m_{total}
0.5	1.7	1.96	0.06	2.02	1.77	-0.01	1.76
	4	-	-	-	1.55	0.03	1.58
	12	-	-	-	0.88	0.01	0.89
	16	-	-	-	0.85	-0.05	0.80
	20	-	-	-	0.923	-0.001	0.922
1.0	1.7	1.60	0.1	1.7	1.68	0.01	1.69
	4	-	-	-	1.87	-0.09	1.78
	12	-	-	-	0.89	0.22	1.11
	16	-	-	-	1.346	0.002	1.348
	20	-	-	-	0.85	0.06	0.91

Table 7.18: Magnetic moment values for different coverages of $MnCl_2$ on Au(111). All moments were extracted via sum-rules from samples grown at RT. The expectation value of the spin effective moment and orbital moment at 6 T have an error of ≈30 % from the sum-rule evaluation [261].

7.1.44 Comparison of the XPS spectra of $MnBr_2$ and $MnCl_2$

In Fig. 7.46, the XPS spectra of 4.2 ML $MnBr_2$ and 1.7 ML $MnCl_2$ are compared. Both spectra are normalized to 1 for a better comparison. The peak positions for $MnBr_2$ and $MnCl_2$ are nearly identical, however this small shift can be still related to the substrate interaction. Since the estimated coverage of $MnBr_2$ has an error it is possible that for increasing amount of $MnBr_2$ the spectra would still continue to shift to higher binding energies till the spectra of $MnBr_2$ and $MnCl_2$ on Au(111) are overlapping. The major difference between the two spectra is the intensity of the satellite peaks, which could be related to the higher electronegativity of Cl, which causes therefore a reduction of the peak intensity.

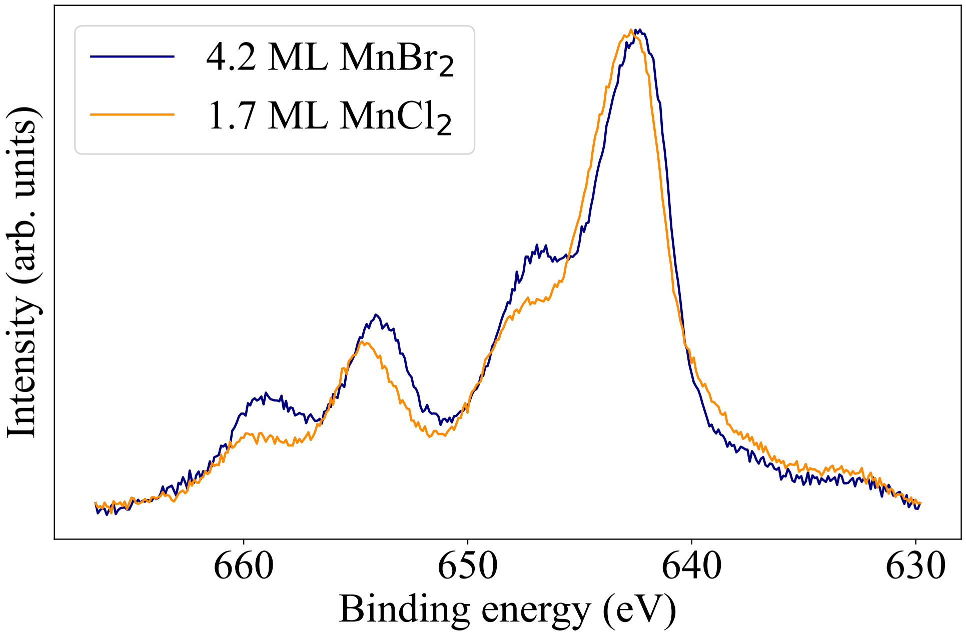

Figure 7.46: Comparison of the XPS spectra of 4.2 ML $MnBr_2$ and 1.7 ML $MnCl_2$. Both samples were grown at elevated temperatures (128 °C and 103 °C) and normalized to 1 for a better comparison of the peak structure. The XPS measurements were performed in 2022 at CFM in the Nanophysics XPS lab.

7.1.45 Comparison of the magnetic properties of $FeBr_2$ on Au(111) and on Bi_2Se_3

In Fig. 7.47, the XAS, XMCD and XLD spectra of $FeBr_2$ on Au(111) and on Bi_2Se_3 are shown. By comparing the high-coverage spectra of $FeBr_2$ on Au(111) with the ones on Bi_2Se_3, it can be observed that the peak structures for all spectroscopic techniques (XAS, XMCD and XLD) are identical, as well as the calculated expectation values of the magnetic moments. However, by comparing the XAS spectra of 0.6 ML and 1.5 ML $FeBr_2$ on Au(111) with the ones on Bi_2Se_3, a change of the peak structure at low photon energies (≈ 706 eV) is observed. Also the magnetic properties of the 0.6-ML sample are completely different compared to the ones on Bi_2Se_3. However, these changes can be related to the strong interaction with the Au(111) surface, which is also the reason for the different peak structure at around 706 eV. The comparison of the XLD spectra shows that for high coverages on Au(111), the spectral shape is identical to the ones on Bi_2Se_3 (ML to multilayer).

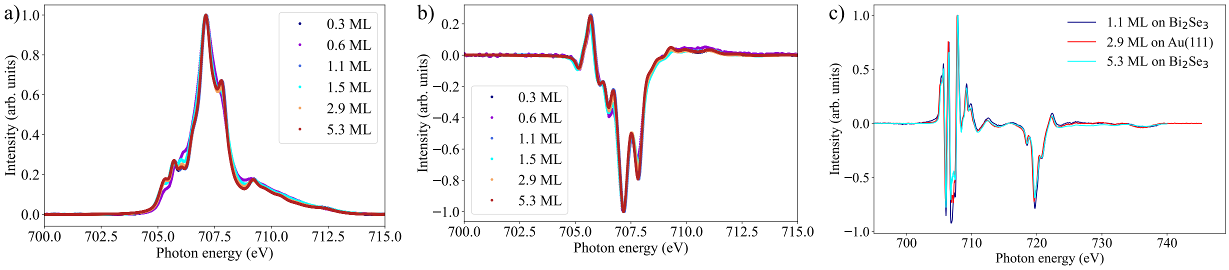

Figure 7.47: Comparison of the XAS a), XMCD b), and XLD c) spectra of $FeBr_2$ on Au(111) and Bi_2Se_3. The spectra are all normalized to 1, so that the spectral shape can be compared directly. All XAS and XMCD spectra were measured at 2 K and 6 T in NI. The XLD spectra in c) are measured in GI at 2 K and 0 T. The $FeBr_2$ samples with a coverage of 0.3, 1.1, and 5.3 ML were grown on Bi_2Se_3 at elevated temperatures (100-150 °C). The 0.6-, 1.5-, and 2.9-ML samples were grown at RT on Au(111).

7.1.46 Multiplet spectra comparison for Mn^{2+}

In Fig. 7.48, the isotropic XAS spectra of 1 ML of $MnCl_2$ and $MnBr_2$ on Au(111) are compared to the simulated multiplet spectra of Mn^{2+} with octahedral symmetry at 2 K and 6 T. The used crystal electric field values were obtained from Ref. [393]. The simulated spectra are in good agreement with the measured spectra on Au(111). The offset in the background of the L_3 edge can be related to the background correction routine.

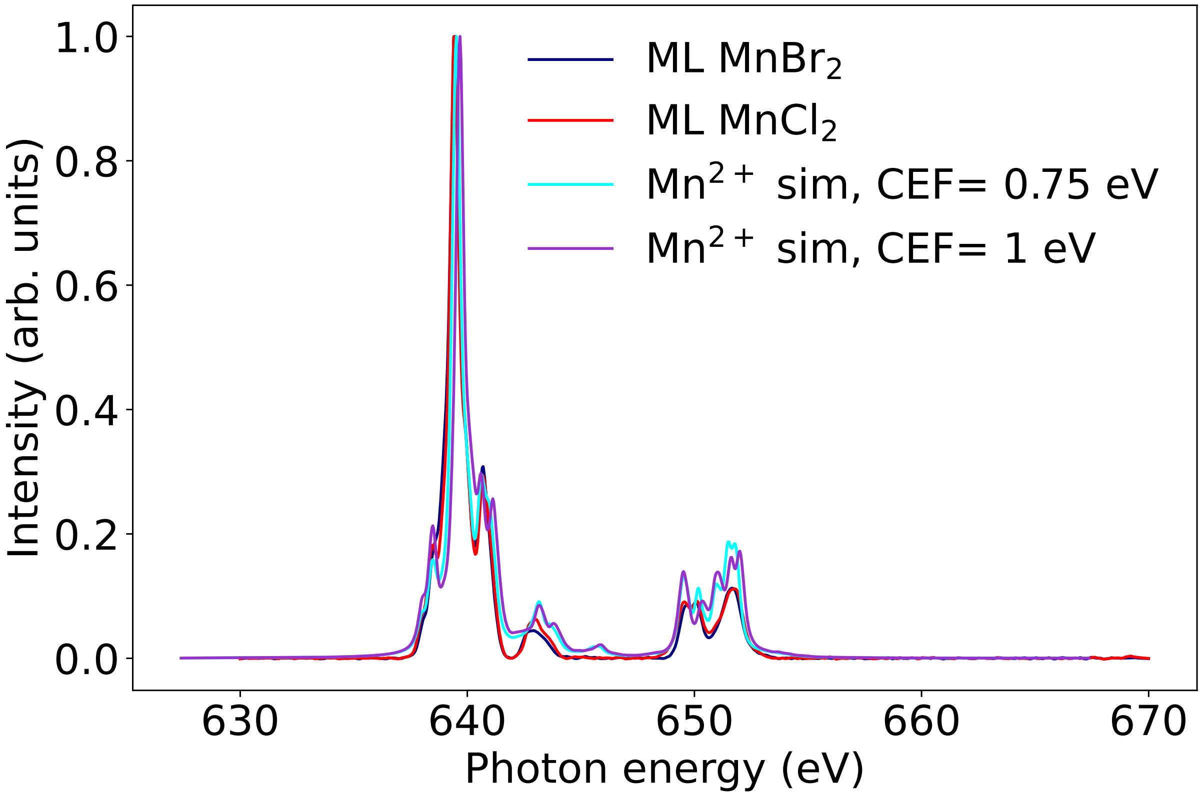

Figure 7.48: Comparison of the simulated Mn^{2+} spectra for different CEF values with the measured XAS spectra of $MnBr_2$ and $MnCl_2$ on Au(111). The simulations were calculated via Crispy [351].

7.1.47 Collaboration measurements

In Tab. 7.19 and Tab. 7.20, the measurements which were entirely performed by collaborators are listed. The mentioned data was measured by the collaboration partners. As part of the resulting publication (Ref. [32]), the data evaluation was discussed with all collaborators. All data in this thesis was evaluated and analyzed by me. The 1.5 ML XAS and XMCD data in this thesis has also been used by Dr. Carmen González-Orellana in her Ph.D. thesis. Additionally, the topographic STM image of 0.6 ML $FeBr_2$ on Au(111) (Fig. 4.14 b)) and the XPS data of the 0.6 and 2.0 ML $FeBr_2$ on Au(111) (only the Fe spectra) have been also used in the Ph.D. thesis of Dr. Carmen González-Orellana [419]. The data of $FeBr_2$ on Au(111) in Carmen's Ph.D. thesis are only used as a comparison to $FeBr_2$ on $NbSe_2$.

Measurement	Date	Sample	Location	Performed by
LT-STM	2020	0.6 ML of $FeBr_2$ on Au(111) (Figs. 4.14, 4.16, 4.17, 4.22), 7.14 and 7.15	CFM Apollo Lab (till Oct. 2022 at CFM)	Dr. James Lawrence and Prof. Dr. Dimas G. de Oteyza
LT-STM	2020	clean Au(111) (Figs. 4.14)	CFM Apollo Lab (till Oct. 2022 at CFM)	Dr. James Lawrence and Prof. Dr. Dimas G. de Oteyza
LEED	2020	0.6 ML of $FeBr_2$ on Au(111) (Figs. 4.5 and 7.23)	CFM Nanophysics Lab	Dr. Carmen González-Orellana and Dr. Djuro Bikaljević
XPS	2020	0.6 and 2.0 ML of $FeBr_2$ on Au(111) (Fig. 4.27)	CFM Nanophysics Lab	Dr. Carmen González-Orellana and Dr. Djuro Bikaljević
XMCD	2020 and 2021	0.6, 1.5 and 2.0 ML of $FeBr_2$ on Au(111) (Figs. 4.44, 7.32, 4.36, 4.35, and 4.34)	BOREAS beamline ALBA	Dr. Carmen González-Orellana and Dr. Maxim Ilyn
VT-STM	2021	0.6, 1.5 and 2.0 ML of $FeBr_2$ on Au(111) (Figs. 7.30 and 7.28)	BOREAS beamline ALBA	Dr. Carmen González-Orellana and Dr. Maxim Ilyn

Table 7.19: Data measured by collaboration partners. In the case of the XMCD measurements, it was not possible to join at the beamline due to Covid restrictions.

Measurement	Date	Sample	Location	Performed by
STM	2023	0.1, 0.75, and 1.75 ML of $FeBr_2$ on Au(111) (Figs. 4.24 and 7.17)	CINN Apollo Lab (since Oct. 2022 at CINN)	Andrea Aguirre Banos and Prof. Dr. Dimas G. de Oteyza
LEED	2023	0.0, 1.0 and 1.5 ML of $FeBr_2$ on Bi_2Se_3 (Fig. 4.31)	CFM Nanophysics Lab	Samuel Kerschbaumer and Dr. Maxim Ilyn
XPS	2023	0.0, 1.0 and 1.5 ML of $FeBr_2$ on Bi_2Se_3 (Fig. 4.31)	CFM Nanophysics Lab	Samuel Kerschbaumer and Dr. Maxim Ilyn
LEED	2023	0.6 ML of $MnBr_2$ on Au(111) (Fig. 5.3)	CFM Nanophysics Lab	Dr. Maxim Ilyn

Table 7.20: Data measured by collaboration partners. In the case of the XMCD measurements, it was not possible to join at the beamline due to Covid restrictions.

Bibliography

[1] D. A. Padua, Ed., *Encyclopedia of parallel computing* (Springer reference). New York, NY: Springer, (2011), OCLC: ocn751526277, ISBN: 978-0-387-09765-7 978-0-387-09766-4 978-0-387-09844-9.

[2] I. Company, *Intel's First Microprocessor*, Firmen Website, (2023). [Online]. Available: https://www.intel.com/content/www/us/en/history/museum-story-of-intel-4004.html.

[3] Intel, *Intel's first microprocessor*. [Online]. Available: https://www.intel.de/content/www/de/de/history/museum-story-of-intel-4004.html (visited on 01/18/2024).

[4] *Intel 80186*, (2023). [Online]. Available: https://de.wikipedia.org/wiki/Intel_80186 (visited on 06/28/2023).

[5] C. Lee, "Transistor degradations in very large-scale-integrated cmos technologies," in Feb. 2018, ISBN: 978-953-51-3863-1. DOI: 10.5772/intechopen.68825.

[6] C. NVIDIA, *NVIDIA H100 Tensor Core GPU*, (2023). [Online]. Available: https://resources.nvidia.com/en-us-tensor-core/nvidia-tensor-core-gpu-datasheet (visited on 05/04/2023).

[7] *Intel reveals plans for a trillion-transistor processor by 2030*, (2022). [Online]. Available: https://www.allaboutcircuits.com/news/intel-reveals-plans-for-a-trillion-transistor-processor-by-2030/ (visited on 01/16/2024).

[8] F. Streller, G. E. Wabiszewski, and R. W. Carpick, "Development and assessment of next-generation nanoelectromechanical switch contact materials," in *14th IEEE International Conference on Nanotechnology*, (2014). DOI: 10.1109/NANO.2014.6967966.

[9] J. R. Powell, "The quantum limit to moore's law," *IEEE*, 96, (2008). DOI: 10.1109/JPROC.2008.925411.

[10] C. IBM, *IBM Unveils World's First 2 Nanometer Chip Technology, Opening a New Frontier for Semiconductors*, (2023). [Online]. Available: https://newsroom.ibm.com/2021-05-06-IBM-Unveils-Worlds-First-2-Nanometer-Chip-Technology,-Opening-a-New-Frontier-for-Semiconductors (visited on 05/04/2023).

[11] F. Wu, H. Tian, Y. Shen, Z. Hou, J. Ren, G. Gou, Y. Sun, Y. Yang, and T.-L. Ren, "Vertical MoS_2 transistors with sub-1-nm gate lengths," *Nature*, 603, 259–264, (2022). DOI: 10.1038/s41586-021-04323-3.

[12] R. K. Cavin, P. Lugli, and V. V. Zhirnov, "Science and Engineering Beyond Moore's Law," *Proceedings of the IEEE*, 100, 1720–1749, (2012). DOI: 10.1109/JPROC.2012.2190155.

[13] M. Heyl and E. List-Kratochvil, "Only gold can pull this off: Mechanical exfoliations of transition metal dichalcogenides beyond scotch tape," *Applied Physics A*, 129, (2022). DOI: 10.1007/s00339-022-06297-z.

[14] C. Ma, J. Yan, Y. Huang, Z. Zheng, and G. Yang, "Direct–indirect bandgap transition in monolayer MoS $_2$ induced by an individual si nanoparticle," *Nanotechnology*, 31, DOI: 10.1088/1361-6528/ab50d2.

[15] S. B. Desai, S. R. Madhvapathy, A. B. Sachid, J. P. Llinas, Q. Wang, G. H. Ahn, G. Pitner, M. J. Kim, J. Bokor, C. Hu, H.-S. P. Wong, and A. Javey, "MoS_2 transistors with 1-nanometer gate lengths," *Science*, 354, 99–102, (2016). DOI: 10.1126/science.aah4698.

[16] N. D. Mermin and H. Wagner, "Absence of Ferromagnetism or Antiferromagnetism in One- or Two-Dimensional Isotropic Heisenberg Models," *Physical Review Letters*, 17, 1133–1136, (1966). DOI: 10.1103/PhysRevLett.17.1133.

[17] B. Huang, G. Clark, E. Navarro-Moratalla, D. R. Klein, R. Cheng, K. L. Seyler, D. Zhong, E. Schmidgall, M. A. McGuire, D. H. Cobden, W. Yao, D. Xiao, P. Jarillo-Herrero, and X. Xu, "Layer-dependent ferromagnetism in a van der Waals crystal down to the monolayer limit," *Nature*, 546, 270–273, (2017). DOI: 10.1038/nature22391.

[18] C. Gong, L. Li, Z. Li, H. Ji, A. Stern, Y. Xia, T. Cao, W. Bao, C. Wang, Y. Wang, Z. Q. Qiu, R. J. Cava, S. G. Louie, J. Xia, and X. Zhang, "Discovery of intrinsic ferromagnetism in two-dimensional van der Waals crystals," *Nature*, 546, 265–269, (2017). DOI: 10.1038/nature22060. [Online]. Available: http://www.nature.com/articles/nature22060.

[19] R. Roemer, C. Liu, and K. Zou, "Robust ferromagnetism in wafer-scale monolayer and multilayer Fe_3GeTe_2," *npj 2D Materials and Applications*, 4, 33, (2020). DOI: 10.1038/s41699-020-00167-z.

[20] Y. Deng, Y. Yu, Y. Song, J. Zhang, N. Z. Wang, Z. Sun, Y. Yi, Y. Z. Wu, S. Wu, J. Zhu, J. Wang, X. H. Chen, and Y. Zhang, "Gate-tunable room-temperature ferromagnetism in two-dimensional Fe_3GeTe_2," *Nature*, 563, 94–99, (2018). DOI: 10.1038/s41586-018-0626-9.

[21] S. Sarkar, S. Adhikary, and M. M. Rahman, "A novel model for analyzing current-voltage characterization of sic mosfet," 456–460, 2019. DOI: 10.1109/DEVIC.2019.8783905.

[22] P. Li, R. Z. Zeng, Y. B. Liao, Q. W. Zhang, and J. H. Zhou, "A Novel Graphene Metal Semi-Insulator Semiconductor Transistor and Its New Super-Low Power Mechanism," *Scientific Reports*, 9, 3642, (2019). DOI: 10.1038/s41598-019-40104-9.

[23] B. Radisavljevic, A. Radenovic, J. Brivio, V. Giacometti, and A. Kis, "Single-layer MoS_2 transistors," *Nature Nanotechnology*, 6, 147–150, (2011). DOI: 10.1038/nnano.2010.279.

[24] D. J. O'Hara, T. Zhu, A. H. Trout, A. S. Ahmed, Y. K. Luo, C. H. Lee, M. R. Brenner, S. Rajan, J. A. Gupta, D. W. McComb, and R. K. Kawakami, "Room Temperature Intrinsic Ferromagnetism in Epitaxial Manganese Selenide Films in the Monolayer Limit," *Nano Letters*, 18, 3125–3131, (2018). DOI: 10.1021/acs.nanolett.8b00683.

[25] M. Bonilla, S. Kolekar, Y. Ma, H. C. Diaz, V. Kalappattil, R. Das, T. Eggers, H. R. Gutierrez, M.-H. Phan, and M. Batzill, "Strong room-temperature ferromagnetism in VSe_2 monolayers on van der Waals substrates," *Nature Nanotechnology*, 13, 289–293, (2018). DOI: 10.1038/s41565-018-0063-9.

[26] B. Huang, G. Clark, D. R. Klein, D. MacNeill, E. Navarro-Moratalla, K. L. Seyler, N. Wilson, M. A. McGuire, D. H. Cobden, D. Xiao, W. Yao, P. Jarillo-Herrero, and X. Xu, "Electrical control of 2D magnetism in bilayer CrI3," *Nature Nanotechnology*, 13, 544–548, (2018). DOI: 10.1038/s41565-018-0121-3. (visited on 05/04/2023).

[27] A. Bedoya-Pinto, J.-R. Ji, A. K. Pandeya, P. Gargiani, M. Valvidares, P. Sessi, J. M. Taylor, F. Radu, K. Chang, and S. S. P. Parkin, "Intrinsic 2D-XY ferromagnetism in a van der Waals monolayer," *Science*, 374, 616–620, (2021). DOI: 10.1126/science.abd5146.

[28] K. S. Novoselov, A. K. Geim, S. V. Morozov, D. Jiang, Y. Zhang, S. V. Dubonos, I. V. Grigorieva, and A. A. Firsov, "Electric Field Effect in Atomically Thin Carbon Films," *Science*, 306, 666–669, (2004). DOI: 10.1126/science.1102896.

[29] J. Yue, J. Jian, P. Dong, L. Luo, and F. Chang, "Growth of Single-Layer MoS_2 by Chemical Vapor Deposition on sapphire substrate," *IOP Conference Series: Materials Science and Engineering*, 592, 012044, (2019). DOI: 10.1088/1757-899X/592/1/012044.

[30] J. Lei, Y. Xie, A. Kutana, K. V. Bets, and B. I. Yakobson, "Salt-Assisted MoS_2 Growth: Molecular Mechanisms from the First Principles," *Journal of the American Chemical Society*, 144, 7497–7503, (2022). DOI: 10.1021/jacs.2c02497.

[31] B. Liu, M. Fathi, L. Chen, A. Abbas, Y. Ma, and C. Zhou, "Chemical Vapor Deposition Growth of Monolayer WSe_2 with Tunable Device Characteristics and Growth Mechanism Study," *ACS Nano*, 9, 6119–6127, (2015). DOI: 10.1021/acsnano.5b01301.

[32] S. E. Hadjadj, C. González-Orellana, J. Lawrence, D. Bikaljević, M. Peña-Díaz, P. Gargiani, L. Aballe, J. Naumann, M. Á. Niño, M. Foerster, S. Ruiz-Gómez, S. Thakur, I. Kumberg, J. Taylor, J. Hayes, J. Torres, C. Luo, F. Radu, D. G. de Oteyza, W. Kuch, J. I. Pascual, C. Rogero, and M. Ilyn, "Epitaxial monolayers of magnetic 2D semiconductor $FeBr_2$ grown on Au(111)," (2023). DOI: 10.1021/acs.chemmater.3c00978.

[33] D. Bikaljević, C. González-Orellana, M. Peña-Díaz, D. Steiner, J. Dreiser, P. Gargiani, M. Foerster, M. Á. Niño, L. Aballe, S. Ruiz-Gomez, N. Friedrich, J. Hieulle, L. Jingcheng, M. Ilyn, C. Rogero, and J. I. Pascual, "Noncollinear Magnetic Order in Two-Dimensional $NiBr_2$ Films Grown on Au(111)," *ACS Nano*, 15, 14985–14995, (2021). DOI: 10.1021/acsnano.1c05221.

[34] J. Clark, C. Pak, H. Cao, and M. Shatruk, "Helimagnetism in MnBi2se4 driven by spin-frustrating interactions between antiferromagnetic chains," *Crystals*, 11, DOI: 10.3390/cryst11030242.

[35] S. Nakatsuji, Y. Nambu, H. Tonomura, O. Sakai, S. Jonas, C. Broholm, H. Tsunetsugu, Y. Qiu, and Y. Maeno, "Spin disorder on a triangular lattice," *Science*, 309, DOI: 10.1126/science.1114727. [Online]. Available: https://www.science.org/doi/10.1126/science.1114727.

[36] P. Mendels and F. Bert, "Quantum kagome frustrated antiferromagnets: One route to quantum spin liquids," *Comptes Rendus Physique*, 17, Dec. (2015). DOI: 10.1016/j.crhy.2015.12.001.

[37] H. Masuda, T. Seki, Y. Nii, H. Masuda, K. Takanashi, and Y. Onose, "Room-temperature chirality switching in a helimagnetic thin film," DOI: 10.48550/ARXIV.2205.13112.

[38] C. Zhang, J. Zhang, C. Liu, S. Zhang, Y. Yuan, P. Li, Y. Wen, Z. Jiang, B. Zhou, Y. Lei, D. Zheng, C. Song, Z. Hou, W. Mi, U. Schwingenschlögl, A. Manchon, Z. Q. Qiu, H. N. Alshareef, Y. Peng, and X.-X. Zhang, "Chiral helimagnetism and one-dimensional magnetic solitons in a cr-intercalated transition metal dichalcogenide," *Advanced Materials*, 33, DOI: 10.1002/adma.202101131.

[39] J. S. Miller, "Organic- and molecule-based magnets," *Materials Today*, 17, 2014. DOI: https://doi.org/10.1016/j.mattod.2014.04.023.

[40] T. Miyazaki and H. Jin, *The physics of ferromagnetism* (Springer series in materials science v. 158). Heidelberg ; New York: Springer, (2012), ISBN: 978-3-642-25582-3.

[41] M. Getzlaff, *Fundamentals of magnetism.* Berlin ; New York: Springer, (2008), ISBN: 978-3-540-31150-8.

[42] A. Ferrari, F. Körmann, M. Asta, and J. Neugebauer, "Simulating short-range order in compositionally complex materials," *Nat Comput Sci*, 3, Mar. 31, 2023, ISSN: 2662-8457. DOI: `10.1038/s43588-023-00407-4`. (visited on 01/16/2024).

[43] G. Delfino and G. Mussardo, "The spin-spin correlation function in the two-dimensional Ising model in a magnetic field at T = Tc," *Nuclear Physics B*, 455, 724–758, (1995). DOI: `10.1016/0550-3213(95)00464-4`.

[44] M. Naraschewski and R. J. Glauber, "Spatial coherence and density correlations of trapped Bose gases," *Physical Review A*, 59, 4595–4607, (1999). DOI: `10.1103/PhysRevA.59.4595`.

[45] S. Sachdev, "Topological order, emergent gauge fields, and Fermi surface reconstruction," *Reports on Progress in Physics*, 82, 014001, (2019). DOI: `10.1088/1361-6633/aae110`.

[46] E. Du Trémolet de Lacheisserie, D. Gignoux, and M. Schlenker, Eds., *Magnetism.* Norwell, Mass: Kluwer Academic Publishers, (2002), ISBN: 978-1-4020-7224-6 978-1-4020-7222-2 978-1-4020-7223-9.

[47] R. Skomski, *Simple models of magnetism.* Oxford ; New York: Oxford University Press, (2008), ISBN: 978-0-19-857075-2.

[48] M. Gibertini, M. Koperski, A. F. Morpurgo, and K. S. Novoselov, "Magnetic 2D materials and heterostructures," *Nature Nanotechnology*, 14, 408–419, (2019). DOI: `10.1038/s41565-019-0438-6`.

[49] J. Stöhr and H. C. Siegmann, *Magnetism: from fundamentals to nanoscale dynamics* (Springer series in solid-state sciences 152). Berlin ; New York: Springer, (2006), ISBN: 978-3-540-30282-7.

[50] S. J. Youn, B. R. Sahu, and K. S. Kim, "Large orbital magnetic moment and Coulomb correlation effects in $FeBr_2$," *Physical Review B*, 65, 052415, (2002). DOI: `10.1103/PhysRevB.65.052415`.

[51] W. Demtröder, *Experimentalphysik. 2: Elektrizität und Optik* (Springer-Lehrbuch), 7., korrigierte und erweiterte Auflage. Berlin: Springer, (2017), ISBN: 978-3-662-55789-1 978-3-662-55790-7.

[52] W. Heisenberg, "Zur Theorie des Ferromagnetismus," *Zeitschrift für Physik*, 49, 619–636, (1928). DOI: `10.1007/BF01328601`.

[53] L. Baraban, "Capped colloids as model systems for condensed matter," Ph. D. Thesis, Universität Konstanz Fachbereich Physik, (2008). [Online]. Available: `http://nbn-resolving.de/urn:nbn:de:bsz:352-opus-73032` (visited on 05/30/2023).

[54] C. Lacroix and E. Wissenschaftsstiftung, Eds., *Introduction to frustrated magnetism: materials, experiments, theory: [summer school which was held in Trieste in summer 2007 as an activity of the ESF network: within the context of the European Network on Highly Frustrated Magnetism]* (Springer series in solid-state sciences 164). Berlin Heidelberg: Springer, (2011), ISBN: 978-3-642-10589-0 978-3-642-10588-3.

[55] G. H. Wannier, "Antiferromagnetism. The Triangular Ising Net," *Physical Review*, 79, 357–364, (1950). DOI: `10.1103/PhysRev.79.357`.

[56] J. Struck, C. Ölschläger, R. Le Targat, P. Soltan-Panahi, A. Eckardt, M. Lewenstein, P. Windpassinger, and K. Sengstock, "Quantum simulation of frustrated classical magnetism in triangular optical lattices," *Science*, 333, DOI: `10.1126/science.1207239`.

[57] C. Gong and X. Zhang, "Two-dimensional magnetic crystals and emergent heterostructure devices," *Science*, 363, eaav4450, (2019). DOI: `10.1126/science.aav4450`. (visited on 04/26/2023).

[58] S. Hunklinger, *Festkörperphysik* (De Gruyter studium), 5. Auflage. Berlin ; Boston: De Gruyter, (2018), ISBN: 978-3-11-056774-8.

[59] N. W. Ashcroft and N. D. Mermin, *Solid state physics*, 12. Indian repr. Delhi: Cengage Learning, (2011), ISBN: 978-81-315-0052-1.

[60] K. S. Burch, D. Mandrus, and J.-G. Park, "Magnetism in two-dimensional van der Waals materials," *Nature*, 563, 47–52, (2018). DOI: `10.1038/s41586-018-0631-z`.

[61] E. Ising, "Beitrag zur theorie des ferromagnetismus," *Z. Physik*, 31, DOI: `10.1007/BF02980577`.

[62] L. Onsager, "Crystal Statistics. I. A Two-Dimensional Model with an Order-Disorder Transition," *Physical Review*, 65, 117–149, (1944). DOI: `10.1103/PhysRev.65.117`.

[63] J. M. Kosterlitz and D. J. Thouless, "Ordering, metastability and phase transitions in two-dimensional systems," *Journal of Physics C: Solid State Physics*, 6, 1181–1203, (1973). DOI: `10.1088/0022-3719/6/7/010`.

[64] Z. M. Dai, Y. Y. Dai, W. Liu, T. T. Wang, X. T. Zhao, X. G. Zhao, and Z. D. Zhang, "Magnetization reversal of vortex states driven by out-of-plane field in the nanocomposite Co/Pd/Ru/Py disks," *Applied Physics Letters*, 111, 022404, (2017). DOI: `10.1063/1.4992794`.

[65] M. E. Gouvea, F. G. Mertens, A. R. Bishop, and G. M. Wysin, "The classical two-dimensional XY model with in-plane magnetic field," *Journal of Physics: Condensed Matter*, 2, 1853–1868, (1990). DOI: `10.1088/0953-8984/2/7/016`.

[66] Z. Xiong, L. Zhong, H. Wang, and X. Li, "Structural Defects, Mechanical Behaviors, and Properties of Two-Dimensional Materials," *Materials*, 14, 1192, (2021). DOI: `10.3390/ma14051192`.

[67] M. Zeng, Y. Xiao, J. Liu, K. Yang, and L. Fu, "Exploring Two-Dimensional Materials toward the Next-Generation Circuits: From Monomer Design to Assembly Control," *Chemical Reviews*, 118, 6236–6296, (2018). DOI: `10.1021/acs.chemrev.7b00633`.

[68] "Graphene and beyond: Recent advances in two-dimensional materials synthesis, properties, and devices," *ACS Nanosci. Au*, 2, DOI: `10.1021/acsnanoscienceau.2c00017`.

[69] N. Mounet, M. Gibertini, P. Schwaller, D. Campi, A. Merkys, A. Marrazzo, T. Sohier, I. E. Castelli, A. Cepellotti, G. Pizzi, and N. Marzari, "Two-dimensional materials from high-throughput computational exfoliation of experimentally known compounds," *Nature Nanotechnology*, 13, 246–252, (2018). DOI: `10.1038/s41565-017-0035-5`.

[70] X.-L. Sheng, C. Chen, H. Liu, Z. Chen, Z.-M. Yu, Y. X. Zhao, and S. A. Yang, "Two-Dimensional Second-Order Topological Insulator in Graphdiyne," *Physical Review Letters*, 123, 256402, (2019). DOI: `10.1103/PhysRevLett.123.256402`.

[71] K. Zhang, Y. Feng, F. Wang, Z. Yang, and J. Wang, "Two dimensional hexagonal boron nitride (2D-hBN): Synthesis, properties and applications," *Journal of Materials Chemistry C*, 5, 11992–12022, (2017). DOI: `10.1039/C7TC04300G`.

[72] S. S. Lin, “Light-Emitting Two-Dimensional Ultrathin Silicon Carbide,” *The Journal of Physical Chemistry C*, 116, 3951–3955, (2012). DOI: 10.1021/jp210536m.

[73] S. Chabi and K. Kadel, “Two-Dimensional Silicon Carbide: Emerging Direct Band Gap Semiconductor,” *Nanomaterials*, 10, 2226, (2020). DOI: 10.3390/nano10112226.

[74] B. Zhao, D. Shen, Z. Zhang, P. Lu, M. Hossain, J. Li, B. Li, and X. Duan, “2D Metallic Transition-Metal Dichalcogenides: Structures, Synthesis, Properties, and Applications,” *Advanced Functional Materials*, 31, 2105132, (2021). DOI: 10.1002/adfm.202105132.

[75] D. Qiu, C. Gong, S. Wang, M. Zhang, C. Yang, X. Wang, and J. Xiong, “Recent Advances in 2D Superconductors,” *Advanced Materials*, 33, 2006124, (2021). DOI: 10.1002/adma.202006124.

[76] A. K. Geim and I. V. Grigorieva, “Van der Waals heterostructures,” *Nature*, 499, 419–425, (2013). DOI: 10.1038/nature12385.

[77] I. Boustani, “New quasi-planar surfaces of bare boron,” *Surface Science*, 370, 355–363, (1997). DOI: 10.1016/S0039-6028(96)00969-7.

[78] B. Feng, J. Zhang, Q. Zhong, W. Li, S. Li, H. Li, P. Cheng, S. Meng, L. Chen, and K. Wu, “Experimental realization of two-dimensional boron sheets,” *Nature Chemistry*, 8, 563–568, (2016). DOI: 10.1038/nchem.2491.

[79] A. J. Mannix, X.-F. Zhou, B. Kiraly, J. D. Wood, D. Alducin, B. D. Myers, X. Liu, B. L. Fisher, U. Santiago, J. R. Guest, M. J. Yacaman, A. Ponce, A. R. Oganov, M. C. Hersam, and N. P. Guisinger, “Synthesis of borophenes: Anisotropic, two-dimensional boron polymorphs,” *Science*, 350, 1513–1516, (2015). DOI: 10.1126/science.aad1080.

[80] M. Yi and Z. Shen, “A review on mechanical exfoliation for the scalable production of graphene,” *Journal of Materials Chemistry A*, 3, 11700–11715, (2015). DOI: 10.1039/C5TA00252D.

[81] H. Huang, W. Chen, S. Chen, and A. T. S. Wee, “Bottom-up Growth of Epitaxial Graphene on 6H-SiC(0001),” *ACS Nano*, 2, 2513–2518, (2008). DOI: 10.1021/nn800711v.

[82] Y. Xu, H. Cao, Y. Xue, B. Li, and W. Cai, “Liquid-Phase Exfoliation of Graphene: An Overview on Exfoliation Media, Techniques, and Challenges,” *Nanomaterials*, 8, 942, (2018). DOI: 10.3390/nano8110942.

[83] X. Chen, L. Zhang, and S. Chen, “Large area CVD growth of graphene,” *Synthetic Metals*, 210, 95–108, (2015). DOI: 10.1016/j.synthmet.2015.07.005.

[84] F. Presel, H. Tetlow, L. Bignardi, P. Lacovig, C. A. Tache, S. Lizzit, L. Kantorovich, and A. Baraldi, “Graphene growth by molecular beam epitaxy: An interplay between desorption, diffusion and intercalation of elemental C species on islands,” *Nanoscale*, 10, 7396–7406, (2018). DOI: 10.1039/C8NR00615F.

[85] J. Dong, L. Zhang, X. Dai, and F. Ding, “The epitaxy of 2D materials growth,” *Nature Communications*, 11, 5862, (2020). DOI: 10.1038/s41467-020-19752-3.

[86] S. V. Morozov, K. S. Novoselov, M. I. Katsnelson, F. Schedin, D. C. Elias, J. A. Jaszczak, and A. K. Geim, “Giant Intrinsic Carrier Mobilities in Graphene and Its Bilayer,” *Physical Review Letters*, 100, 016602, (2008). DOI: 10.1103/PhysRevLett.100.016602.

[87] Q. Liu, X. Zhang, L. B. Abdalla, A. Fazzio, and A. Zunger, “Switching a Normal Insulator into a Topological Insulator via Electric Field with Application to Phosphorene,” *Nano Letters*, 15, 1222–1228, (2015). DOI: 10.1021/nl5043769.

[88] Z. Wu, Y. Lyu, Y. Zhang, R. Ding, B. Zheng, Z. Yang, S. P. Lau, X. H. Chen, and J. Hao, "Large-scale growth of few-layer two-dimensional black phosphorus," *Nature Materials*, 20, 1203–1209, (2021). DOI: 10.1038/s41563-021-01001-7.

[89] M. Baksi, D. Toffoli, O. Gulseren, and H. Ustunel, "Nanotribological Properties of the h-BN/Au(111) Interface: A DFT Study," *The Journal of Physical Chemistry C*, 123, 28411–28418, (2019). DOI: 10.1021/acs.jpcc.9b06767.

[90] W.-H. Lin, V. W. Brar, D. Jariwala, M. C. Sherrott, W.-S. Tseng, C.-I. Wu, N.-C. Yeh, and H. A. Atwater, "Atomic-Scale Structural and Chemical Characterization of Hexagonal Boron Nitride Layers Synthesized at the Wafer-Scale with Monolayer Thickness Control," *Chemistry of Materials*, 29, 4700–4707, (2017). DOI: 10.1021/acs.chemmater.7b00183.

[91] A. Hemmi, H. Cun, S. Brems, C. Huyghebaert, and T. Greber, "Wafer-scale, epitaxial growth of single layer hexagonal boron nitride on Pt(111)," *Journal of Physics: Materials*, 4, 044012, (2021). DOI: 10.1088/2515-7639/ac0d9e.

[92] S. J. U. White, T. Yang, N. Dontschuk, C. Li, Z.-Q. Xu, M. Kianinia, A. Stacey, M. Toth, and I. Aharonovich, "Electrical control of quantum emitters in a Van der Waals heterostructure," *Light: Science & Applications*, 11, 186, (2022). DOI: 10.1038/s41377-022-00877-7.

[93] L. Cao, "Two-dimensional transition-metal dichalcogenide materials: Toward an age of atomic-scale photonics," *MRS Bulletin*, 40, 592–599, (2015). DOI: 10.1557/mrs.2015.144.

[94] K. Parvez, "Two-Dimensional Nanomaterials: Crystal Structure and Synthesis," in *Biomedical Applications of Graphene and 2D Nanomaterials*, Elsevier, (2019), pp. 1–25, ISBN: 978-0-12-815889-0. DOI: 10.1016/B978-0-12-815889-0.00001-5. (visited on 06/29/2023).

[95] L. Su, Y. Zhang, Y. Yu, and L. Cao, "Dependence of coupling of quasi 2-D MoS_2 with substrates on substrate types, probed by temperature dependent Raman scattering," *Nanoscale*, 6, 4920–4927, (2014). DOI: 10.1039/C3NR06462J.

[96] K. Dolui, I. Rungger, C. Das Pemmaraju, and S. Sanvito, "Possible doping strategies for MoS_2 monolayers: An *ab initio* study," *Physical Review B*, 88, 075420, (2013). DOI: 10.1103/PhysRevB.88.075420.

[97] R. Ganatra and Q. Zhang, "Few-Layer MoS_2: A Promising Layered Semiconductor," *ACS Nano*, 8, 4074–4099, (2014). DOI: 10.1021/nn405938z.

[98] R. Sankar, G. Narsinga Rao, I. P. Muthuselvam, C. Butler, N. Kumar, G. Senthil Murugan, C. Shekhar, T.-R. Chang, C.-Y. Wen, C.-W. Chen, W.-L. Lee, M.-T. Lin, H.-T. Jeng, C. Felser, and F. C. Chou, "Polymorphic Layered $MoTe_2$ from Semiconductor, Topological Insulator, to Weyl Semimetal," *Chemistry of Materials*, 29, 699–707, (2017). DOI: 10.1021/acs.chemmater.6b04363.

[99] A. Hamill, B. Heischmidt, E. Sohn, D. Shaffer, K.-T. Tsai, X. Zhang, X. Xi, A. Suslov, H. Berger, L. Forró, F. J. Burnell, J. Shan, K. F. Mak, R. M. Fernandes, K. Wang, and V. S. Pribiag, "Two-fold symmetric superconductivity in few-layer $NbSe_2$," *Nature Physics*, 17, 949–954, (2021). DOI: 10.1038/s41567-021-01219-x.

[100] P. Darancet, A. J. Millis, and C. A. Marianetti, "Three-dimensional metallic and two-dimensional insulating behavior in octahedral tantalum dichalcogenides," *Physical Review B*, 90, 045134, (2014). DOI: 10.1103/PhysRevB.90.045134.

[101] A. Kuc, T. Heine, and A. Kis, "Electronic properties of transition-metal dichalcogenides," *MRS Bulletin*, 40, 577–584, (2015). DOI: 10.1557/mrs.2015.143.

[102] R. Lv, J. A. Robinson, R. E. Schaak, D. Sun, Y. Sun, T. E. Mallouk, and M. Terrones, "Transition Metal Dichalcogenides and Beyond: Synthesis, Properties, and Applications of Single- and Few-Layer Nanosheets," *Accounts of Chemical Research*, 48, 56–64, (2015). DOI: 10.1021/ar5002846.

[103] Y. Nakata, K. Sugawara, R. Shimizu, Y. Okada, P. Han, T. Hitosugi, K. Ueno, T. Sato, and T. Takahashi, "Monolayer 1T-$NbSe_2$ as a Mott insulator," *NPG Asia Materials*, 8, e321–e321, (2016). DOI: 10.1038/am.2016.157.

[104] A. V. Kolobov and J. Tominaga, *Two-dimensional transition-metal dichalcogenides* (Springer series in material science volume 239). Cham: Springer, (2016), ISBN: 978-3-319-31450-1 978-3-319-31449-5.

[105] C. Zhang, S. Kc, Y. Nie, C. Liang, W. G. Vandenberghe, R. C. Longo, Y. Zheng, F. Kong, S. Hong, R. M. Wallace, and K. Cho, "Charge Mediated Reversible Metal–Insulator Transition in Monolayer $MoTe_2$ and $W_xMo_{1-x}Te_2$ Alloy," *ACS Nano*, 10, 7370–7375, (2016). DOI: 10.1021/acsnano.6b00148.

[106] K. Chen, J. Deng, Y. Yan, Q. Shi, T. Chang, X. Ding, J. Sun, S. Yang, and J. Z. Liu, "Diverse electronic and magnetic properties of CrS_2 enabling strain-controlled 2D lateral heterostructure spintronic devices," *npj Computational Materials*, 7, 79, (2021). DOI: 10.1038/s41524-021-00547-z.

[107] H. Li, X. Jia, Q. Zhang, and X. Wang, "Metallic Transition-Metal Dichalcogenide Nanocatalysts for Energy Conversion," *Chem*, 4, 1510–1537, (2018). DOI: 10.1016/j.chempr.2018.03.012.

[108] T. Rao, H. Wang, Y.-J. Zeng, Z. Guo, H. Zhang, and W. Liao, "Phase Transitions and Water Splitting Applications of 2D Transition Metal Dichalcogenides and Metal Phosphorous Trichalcogenides," *Advanced Science*, 8, 2002284, (2021). DOI: 10.1002/advs.202002284.

[109] R. J. Toh, Z. Sofer, J. Luxa, D. Sedmidubský, and M. Pumera, "3R phase of MoS_2 and WS_2 outperforms the corresponding 2H phase for hydrogen evolution," *Chemical Communications*, 53, 3054–3057, (2017). DOI: 10.1039/C6CC09952A.

[110] Z. Li, Y. Song, and S. Tang, "Quantum spin Hall state in monolayer 1T'-TMDCs," *Journal of Physics: Condensed Matter*, 32, 333001, (2020). DOI: 10.1088/1361-648X/ab8660.

[111] M. Irshad, M. H. U. R. Mahmood, and M. Fatima, "Carbon nanostructures and 2D transition metal dichalcogenides," in *Graphene, Nanotubes and Quantum Dots-Based Nanotechnology*, Elsevier, (2022), pp. 537–556, ISBN: 978-0-323-85457-3. DOI: 10.1016/B978-0-323-85457-3.00033-5. (visited on 06/29/2023).

[112] X. Cui, Y. L. Huang, and A. T. S. Wee, "Functionalized 2D materials," in *Graphene, Nanotubes and Quantum Dots-Based Nanotechnology*, Elsevier, (2022), pp. 127–155, ISBN: 978-0-323-85457-3. DOI: 10.1016/B978-0-323-85457-3.00001-3. (visited on 06/29/2023).

[113] K. M. Freedy and S. J. McDonnell, "Contacts for Molybdenum Disulfide: Interface Chemistry and Thermal Stability," *Materials*, 13, 693, (2020). DOI: 10.3390/ma13030693.

[114] J. Brivio, D. T. L. Alexander, and A. Kis, "Ripples and Layers in Ultrathin MoS_2 Membranes," *Nano Letters*, 11, 5148–5153, (2011). DOI: 10.1021/nl2022288.

[115] Y. Zhang, T.-R. Chang, B. Zhou, Y.-T. Cui, H. Yan, Z. Liu, F. Schmitt, J. Lee, R. Moore, Y. Chen, H. Lin, H.-T. Jeng, S.-K. Mo, Z. Hussain, A. Bansil, and Z.-X. Shen, "Direct observation of the transition from indirect to direct bandgap in atomically thin epitaxial $MoSe_2$," *Nature Nanotechnology*, 9, 111–115, (2014). DOI: 10.1038/nnano.2013.277.

[116] S. B. Desai, G. Seol, J. S. Kang, H. Fang, C. Battaglia, R. Kapadia, J. W. Ager, J. Guo, and A. Javey, “Strain-Induced Indirect to Direct Bandgap Transition in Multilayer WSe_2,” *Nano Letters*, 14, 4592–4597, (2014). DOI: `10.1021/nl501638a`.

[117] I. G. Lezama, A. Arora, A. Ubaldini, C. Barreteau, E. Giannini, M. Potemski, and A. F. Morpurgo, “Indirect-to-Direct Band Gap Crossover in Few-Layer $MoTe_2$,” *Nano Letters*, 15, 2336–2342, (2015). DOI: `10.1021/nl5045007`.

[118] X. Wang, D. Li, Z. Li, C. Wu, C.-M. Che, G. Chen, and X. Cui, “Ferromagnetism in 2D Vanadium Diselenide,” *ACS Nano*, 15, 16236–16241, (2021). DOI: `10.1021/acsnano.1c05232`.

[119] X. Sun, W. Li, X. Wang, Q. Sui, T. Zhang, Z. Wang, L. Liu, D. Li, S. Feng, S. Zhong, H. Wang, V. Bouchiat, M. Nunez Regueiro, N. Rougemaille, J. Coraux, A. Purbawati, A. Hadj-Azzem, Z. Wang, B. Dong, X. Wu, T. Yang, G. Yu, B. Wang, Z. Han, X. Han, and Z. Zhang, “Room temperature ferromagnetism in ultra-thin van der Waals crystals of 1T-$CrTe_2$,” *Nano Research*, 13, 3358–3363, (2020). DOI: `10.1007/s12274-020-3021-4`.

[120] T. Chattopadhyay, J. Rossat-Mignod, and H. Fjellvåg, “Magnetic ordering in $MnSe_2$,” *Solid State Communications*, 63, 65–67, (1987). DOI: `10.1016/0038-1098(87)90067-6`.

[121] M. Kan, S. Adhikari, and Q. Sun, “Ferromagnetism in MnX_2 (X = S, Se) monolayers,” *Physical Chemistry Chemical Physics*, 16, 4990, (2014). DOI: `10.1039/c3cp55146f`.

[122] A. O. Fumega, M. Gobbi, P. Dreher, W. Wan, C. González-Orellana, M. Peña-Díaz, C. Rogero, J. Herrero-Martín, P. Gargiani, M. Ilyn, M. M. Ugeda, V. Pardo, and S. Blanco-Canosa, “Absence of Ferromagnetism in VSe_2 Caused by Its Charge Density Wave Phase,” *The Journal of Physical Chemistry C*, 123, 27802–27810, (2019). DOI: `10.1021/acs.jpcc.9b08868`.

[123] W. Zhang, L. Zhang, P. K. J. Wong, J. Yuan, G. Vinai, P. Torelli, G. van der Laan, Y. P. Feng, and A. T. S. Wee, “Magnetic Transition in Monolayer VSe_2 *via* Interface Hybridization,” *ACS Nano*, 13, 8997–9004, (2019). DOI: `10.1021/acsnano.9b02996`.

[124] M. McGuire, “Crystal and Magnetic Structures in Layered, Transition Metal Dihalides and Trihalides,” *Crystals*, 7, 121, (2017). DOI: `10.3390/cryst7050121`.

[125] B. Shabbir, M. Nadeem, Z. Dai, M. S. Fuhrer, Q.-K. Xue, X. Wang, and Q. Bao, “Long range intrinsic ferromagnetism in two dimensional materials and dissipationless future technologies,” *Applied Physics Reviews*, 5, 041105, (2018). DOI: `10.1063/1.5040694`.

[126] D. Amoroso, P. Barone, and S. Picozzi, “Spontaneous skyrmionic lattice from anisotropic symmetric exchange in a Ni-halide monolayer,” *Nature Communications*, 11, 5784, (2020). DOI: `10.1038/s41467-020-19535-w`.

[127] H. Kadowaki, K. Ubukoshi, K. Hirakawa, J. L. Martínez, and G. Shirane, “Experimental Study of New Type Phase Transition in Triangular Lattice Antiferromagnet VCl_2,” *Journal of the Physical Society of Japan*, 56, 4027–4039, (1987). DOI: `10.1143/JPSJ.56.4027`.

[128] A. P. Ramirez, “Strongly Geometrically Frustrated Magnets,” *Annual Review of Materials Science*, 24, 453–480, (1994). DOI: `10.1146/annurev.ms.24.080194.002321`.

[129] M. F. Collins and O. A. Petrenko, “*Review / Synthèse* : Triangular antiferromagnets,” *Canadian Journal of Physics*, 75, 605–655, (1997). DOI: `10.1139/p97-007`.

[130] S. Yang, T. Zhang, and C. Jiang, “Van der Waals Magnets: Material Family, Detection and Modulation of Magnetism, and Perspective in Spintronics,” *Advanced Science*, 8, 2002488, (2021). DOI: `10.1002/advs.202002488`.

[131] A. S. Botana and M. R. Norman, "Electronic structure and magnetism of transition metal dihalides: Bulk to monolayer," *Physical Review Materials*, 3, 044001, (2019). DOI: 10.1103/PhysRevMaterials.3.044001.

[132] X. Zhou, B. Brzostowski, A. Durajski, M. Liu, J. Xiang, T. Jiang, Z. Wang, S. Chen, P. Li, Z. Zhong, A. Drzewiński, M. Jarosik, R. Szczęśniak, T. Lai, D. Guo, and D. Zhong, "Atomically Thin 1T-$FeCl_2$ Grown by Molecular-Beam Epitaxy," *The Journal of Physical Chemistry C*, 124, 9416–9423, (2020). DOI: 10.1021/acs.jpcc.0c03050.

[133] Z. Zhang, J. Shang, C. Jiang, A. Rasmita, W. Gao, and T. Yu, "Direct Photoluminescence Probing of Ferromagnetism in Monolayer Two-Dimensional $CrBr_3$," *Nano Letters*, 19, 3138–3142, (2019). DOI: 10.1021/acs.nanolett.9b00553.

[134] L. Liu, S. Ye, J. He, Q. Huang, H. Wang, and S. Chang, "Magnetic tunneling junctions based on 2D CrI_3 and $CrBr_3$: Spin-filtering effects and high tunnel magnetoresistance via energy band difference," *Semiconductor Science and Technology*, 37, 015006, (2022). DOI: 10.1088/1361-6641/ac3639.

[135] X. Cai, T. Song, N. P. Wilson, G. Clark, M. He, X. Zhang, T. Taniguchi, K. Watanabe, W. Yao, D. Xiao, M. A. McGuire, D. H. Cobden, and X. Xu, "Atomically Thin $CrCl_3$: An In-Plane Layered Antiferromagnetic Insulator," *Nano Letters*, 19, 3993–3998, (2019). DOI: 10.1021/acs.nanolett.9b01317. (visited on 06/30/2023).

[136] S. Mugiraneza and A. M. Hallas, "Tutorial: A beginner's guide to interpreting magnetic susceptibility data with the curie-weiss law," *Commun Phys*, 5, DOI: 10.1038/s42005-022-00853-y.

[137] A.-M. Haghiri-Gosnet and J.-P. Renard, "CMR manganites: Physics, thin films and devices," *J. Phys. D: Appl. Phys.*, 36, Apr. 21, 2003. DOI: 10.1088/0022-3727/36/8/201. (visited on 01/16/2024).

[138] F. Sayed and F. El Haj Hassan, "Hollow magnetic nanoparticles : Experimental and numerical study," (2016). DOI: 10.13140/RG.2.2.33777.94565.

[139] M.-C. Wang and C.-R. Chang, "Goodenough-Kanamori-Anderson Rules in $CrI_3/MoTe_2/CrI_3$ Van der Waals Heterostructure," *Journal of The Electrochemical Society*, 169, 053507, (2022). DOI: 10.1149/1945-7111/ac7006.

[140] V. V. Kulish and W. Huang, "Single-layer metal halides MX_2 (X = Cl, Br, I): Stability and tunable magnetism from first principles and Monte Carlo simulations," *Journal of Materials Chemistry C*, 5, 8734–8741, (2017). DOI: 10.1039/C7TC02664A.

[141] S. Jiang, G. Wang, H. Deng, K. Liu, Q. Yang, E. Zhao, L. Zhu, W. Guo, J. Yang, C. Zhang, H. Wang, X. Zhang, J.-F. Dai, G. Luo, Y. Zhao, and J. Lin, "General Synthesis of 2D Magnetic Transition Metal Dihalides via Trihalide Reduction," *ACS Nano*, 17, 363–371, (2023). DOI: 10.1021/acsnano.2c08693.

[142] F. Xiang, N. Bisht, B. Da, M. Mohammed, C. Neiß, A. Görling, and S. Maier, "Intrinsically patterned two-dimensional transition metal halides," (2023). DOI: arXiv:2305.06489.

[143] K. Katsumata, H. A. Katori, S. Kimura, Y. Narumi, M. Hagiwara, and K. Kindo, "Phase transition of a triangular lattice Ising antiferromagnet FeI_2," *Physical Review B*, 82, 104402, (2010). DOI: 10.1103/PhysRevB.82.104402.

[144] H. Liu, X. Wang, J. Wu, Y. Chen, J. Wan, R. Wen, J. Yang, Y. Liu, Z. Song, and L. Xie, "Vapor Deposition of Magnetic Van der Waals NiI_2 Crystals," *ACS Nano*, 14, 10544–10551, (2020). DOI: 10.1021/acsnano.0c04499.

[145] K. S. Novoselov, A. Mishchenko, A. Carvalho, and A. H. Castro Neto, “2D materials and van der Waals heterostructures,” *Science*, 353, aac9439, (2016). DOI: `10.1126/science.aac9439`.

[146] F. Pizzocchero, L. Gammelgaard, B. S. Jessen, J. M. Caridad, L. Wang, J. Hone, P. Bøggild, and T. J. Booth, “The hot pick-up technique for batch assembly of van der Waals heterostructures,” *Nature Communications*, 7, 11894, (2016). DOI: `10.1038/ncomms11894`.

[147] P. Wang, C. Jia, Y. Huang, and X. Duan, “Van der Waals Heterostructures by Design: From 1D and 2D to 3D,” *Matter*, 4, 552–581, (2021). DOI: `10.1016/j.matt.2020.12.015`.

[148] C. R. Dean, A. F. Young, I. Meric, C. Lee, L. Wang, S. Sorgenfrei, K. Watanabe, T. Taniguchi, P. Kim, K. L. Shepard, and J. Hone, “Boron nitride substrates for high-quality graphene electronics,” *Nature Nanotechnology*, 5, 722–726, (2010). DOI: `10.1038/nnano.2010.172`.

[149] R. Frisenda, E. Navarro-Moratalla, P. Gant, D. Pérez De Lara, P. Jarillo-Herrero, R. V. Gorbachev, and A. Castellanos-Gomez, “Recent progress in the assembly of nanodevices and van der Waals heterostructures by deterministic placement of 2D materials,” *Chemical Society Reviews*, 47, 53–68, (2018). DOI: `10.1039/C7CS00556C`.

[150] J. Qi, Z. Wu, W. Wang, K. Bao, L. Wang, J. Wu, C. Ke, Y. Xu, and Q. He, “Fabrication and applications of van der Waals heterostructures,” *International Journal of Extreme Manufacturing*, 5, 022007, (2023). DOI: `10.1088/2631-7990/acc8a1`.

[151] K. L. Haley, J. A. Cloninger, K. Cerminara, R. M. Sterbentz, T. Taniguchi, K. Watanabe, and J. O. Island, “Heated Assembly and Transfer of Van der Waals Heterostructures with Common Nail Polish,” *Nanomanufacturing*, 1, 49–56, (2021). DOI: `10.3390/nanomanufacturing1010005`.

[152] S. G. Martanov, N. K. Zhurbina, M. V. Pugachev, A. I. Duleba, M. A. Akmaev, V. V. Belykh, and A. Y. Kuntsevich, “Making van der Waals Heterostructures Assembly Accessible to Everyone,” *Nanomaterials*, 10, 2305, (2020). DOI: `10.3390/nano10112305`.

[153] A. R. Sandy, S. G. J. Mochrie, D. M. Zehner, K. G. Huang, and D. Gibbs, “Structure and phases of the au(111) surface: X-ray-scattering measurements,” *Phys. Rev. B*, 43, (1991). DOI: `10.1103/PhysRevB.43.4667`.

[154] L. A. Kibler, “Preparation and Characterization of Noble Metal Single Crystal Electrode Surfaces,” University of Ulm - Department of Electrochemistry, Summary of several Ph.D. thesis, (2003), p. 56. [Online]. Available: `https://www.uni-ulm.de/fileadmin/website_uni_ulm/nawi.inst.080/mitarbeiter/Kibler/KiblerSingleCrystals2003.pdf` (visited on 06/13/2023).

[155] R. K. Nagaosa, T. H. Takashi Hatae, and Y. M. Yasuhiko Miyamoto, “The crystal structure of solid c $_{70}$,” *Jpn. J. Appl. Phys.*, 36, ISSN: 0021-4922, 1347-4065. DOI: `10.1143/JJAP.36.5600`. [Online]. Available: `https://iopscience.iop.org/article/10.1143/JJAP.36.5600`.

[156] K. Schouteden, P. Lievens, and C. Van Haesendonck, “Fourier-transform scanning tunneling microscopy investigation of the energy versus wave vector dispersion of electrons at the Au(111) surface,” *Physical Review B*, 79, 195409, (2009). DOI: `10.1103/PhysRevB.79.195409`.

[157] P. Li and F. Ding, “Origin of the herringbone reconstruction of au(111) surface at the atomic scale,” *Sci. Adv.*, 8, eabq2900, DOI: `10.1126/sciadv.abq2900`.

[158] C. J. Murphy, X. Shi, A. D. Jewell, A. F. McGuire, D. O. Bellisario, A. E. Baber, H. L. Tierney, E. A. Lewis, D. S. Sholl, and E. C. H. Sykes, "Impact of branching on the supramolecular assembly of thioethers on au(111)," *The Journal of Chemical Physics*, 142, 101915, DOI: 10.1063/1.4907270.

[159] Y. Zheng, J. Gao, C. Han, and W. Chen, "Ohmic contact engineering for two-dimensional materials," *Cell Reports Physical Science*, 2, no. 1, 100298, Jan. 2021, ISSN: 26663864. DOI: 10.1016/j.xcrp.2020.100298. [Online]. Available: https://linkinghub.elsevier.com/retrieve/pii/S2666386420303246 (visited on 01/23/2024).

[160] N. A. Mahynski, A. Z. Panagiotopoulos, D. Meng, and S. K. Kumar, "Stabilizing colloidal crystals by leveraging void distributions," *Nature Communications*, 5, 4472, (2014). DOI: 10.1038/ncomms5472.

[161] Y. Wu, Z. Li, H. Feng, and S. He, "Atomic Interactions and Order–Disorder Transition in FCC-Type FeCoNiAl$_{1-x}$Ti$_x$ High-Entropy Alloys," *Materials*, 15, 3992, (2022). DOI: 10.3390/ma15113992.

[162] Y. Zhang, K. He, C.-Z. Chang, C.-L. Song, L.-L. Wang, X. Chen, J.-F. Jia, Z. Fang, X. Dai, W.-Y. Shan, S.-Q. Shen, Q. Niu, X.-L. Qi, S.-C. Zhang, X.-C. Ma, and Q.-K. Xue, "Crossover of the three-dimensional topological insulator bi2se3 to the two-dimensional limit," *Nature Phys*, 6, DOI: 10.1038/nphys1689.

[163] K. Mazumder and P. M. Shirage, "A brief review of bi$_2$se$_3$ based topological insulator: From fundamentals to applications," *Journal of Alloys and Compounds*, 888, 161492, (2021). DOI: https://doi.org/10.1016/j.jallcom.2021.161492.

[164] G. Offergeld and J. Van Cakenberghe, "Stoichiometry of bismuth telluride and related compounds," *Nature*, 184, 185–186, DOI: 10.1038/184185b0.

[165] V. Bhide, B. Patki, and A. Nigavekar, "X-ray spectroscopic investigation of bismuth selenide, bismuth telluride and their alloy," *Journal of Physics and Chemistry of Solids*, 32, 1565–1571, (1971). DOI: https://doi.org/10.1016/S0022-3697(71)80050-1.

[166] B.-T. Wang and P. Zhang, "Phonon spectrum and bonding properties of bi$_2$se$_3$: Role of strong spin-orbit interaction," *Applied Physics Letters*, 100, (2012). DOI: 10.1063/1.3689759.

[167] A. Ptok, K. Kapcia, and A. Ciechan, "Electronic properties of bi2se3dopped by 3d transition metal (mn, fe, co, or ni) ions," *Journal of physics. Condensed matter : an Institute of Physics journal*, 33, (2020). DOI: 10.1088/1361-648X/abba6a.

[168] A. Liebig, C. Setescak, A. Weindl, and F. Giessibl, "Structural characterization of defects in the topological insulator bi$_2$se$_3$ at the picometer scale," *The Journal of Physical Chemistry C*, 126, (2022). DOI: 10.1021/acs.jpcc.2c06084.

[169] G. Tuci, Y. Liu, A. Rossin, X. Guo, C. Pham, G. Giambastiani, and C. Pham-Huu, "Porous Silicon Carbide (SiC): A Chance for Improving Catalysts or Just Another Active-Phase Carrier?" *Chemical Reviews*, 121, 10559–10665, (2021). DOI: 10.1021/acs.chemrev.1c00269.

[170] C. Langpoklakpam, A.-C. Liu, K.-H. Chu, L.-H. Hsu, W.-C. Lee, S.-C. Chen, C.-W. Sun, M.-H. Shih, K.-Y. Lee, and H.-C. Kuo, "Review of Silicon Carbide Processing for Power MOSFET," *Crystals*, 12, 245, (2022). DOI: 10.3390/cryst12020245.

[171] F. Schwierz, "Graphene transistors," *Nature Nanotech*, 5, DOI: 10.1038/nnano.2010.89.

[172] A. T. S. Wee and W. Chen, "Molecular interactions on epitaxial graphene," *Physica Scripta*, T146, 014007, (2012). DOI: `10.1088/0031-8949/2012/T146/014007`.

[173] S. W. Poon, W. Chen, E. S. Tok, and A. T. S. Wee, "Probing epitaxial growth of graphene on silicon carbide by metal decoration," *Applied Physics Letters*, 92, 104102, (2008). DOI: `10.1063/1.2883941`.

[174] S. W. Poon, W. Chen, A. T. S. Wee, and E. S. Tok, "Growth dynamics and kinetics of monolayer and multilayer graphene on a 6H-SiC(0001) substrate," *Physical Chemistry Chemical Physics*, 12, 13522, (2010). DOI: `10.1039/b927452a`.

[175] I. Razado-Colambo, J. Avila, D. Vignaud, S. Godey, X. Wallart, D. P. Woodruff, and M. C. Asensio, "Structural determination of bilayer graphene on SiC(0001) using synchrotron radiation photoelectron diffraction," *Sci Rep*, 8, 10190, DOI: `10.1038/s41598-018-28402-0`.

[176] N. Srivastava, G. He, Luxmi, P. C. Mende, R. M. Feenstra, and Y. Sun, "Graphene formed on SiC under various environments: Comparison of si-face and c-face," *J. Phys. D: Appl. Phys.*, 45, 154001, DOI: `10.1088/0022-3727/45/15/154001`.

[177] W. Chen, D. Qi, X. Gao, and A. T. S. Wee, "Surface transfer doping of semiconductors," *Progress in Surface Science*, 84, 279–321, DOI: `10.1016/j.progsurf.2009.06.002`.

[178] H. Huang and A. T. Shen Wee, "Adsorption on epitaxial graphene on SiC(0001)," *J. Mater. Res.*, 29, 447–458, DOI: `10.1557/jmr.2013.236`.

[179] Q. Wei, K.-D. Li, J. Lian, and L. Wang, "Angular dependence of sputtering yield of amorphous and polycrystalline materials," *Journal of Physics D: Applied Physics*, 41, 172002, (2008). DOI: `10.1088/0022-3727/41/17/172002`.

[180] P. Sigmund, "Theory of Sputtering. I. Sputtering Yield of Amorphous and Polycrystalline Targets," *Physical Review*, 184, 383–416, (1969). DOI: `10.1103/PhysRev.184.383`.

[181] S. Omicron, *Theory of scanning tunneling microscopy.* [Online]. Available: `https://scientaomicron.com/spareparts/sparepart/Resistive-Sample-Heater-for-Secondary-Rotation/1065` (visited on 01/16/2024).

[182] E. I. Altman and R. J. Colton, "Nucleation, growth, and structure of fullerene films on Au(111)," *Surface Science*, 279, 49–67, (1992). DOI: `10.1016/0039-6028(92)90741-N`.

[183] K. Uosaki, Y. Shen, and T. Kondo, "Preparation of a Highly Ordered Au(111) Phase on a Polycrystalline Gold Substrate by Vacuum Deposition and Its Characterization by XRD, GISXRD, STM/AFM, and Electrochemical Measurements," *The Journal of Physical Chemistry*, 99, 14117–14122, (1995). DOI: `10.1021/j100038a051`.

[184] R. Musket, W. McLean, C. Colmenares, D. Makowiecki, and W. Siekhaus, "Preparation of atomically clean surfaces of selected elements: A review," *Applications of Surface Science*, 10, 143–207, (1982). DOI: `10.1016/0378-5963(82)90142-8`.

[185] D. Eberl, *MBE Komponenten Au*, (2023). [Online]. Available: `https://www.mbe-komponenten.de/selection-guide/element/au.php` (visited on 11/23/2023).

[186] H. Yang, Y. Wang, Z. C. Tiu, S. J. Tan, L. Yuan, and H. Zhang, "All-optical modulation technology based on 2d layered materials," *Micromachines*, 13, DOI: `10.3390/mi13010092`.

[187] Q. Hao, C. Wang, W. Liu, X. Liu, J. Liu, and H. Zhang, "Low-dimensional saturable absorbers for ultrafast photonics in solid-state bulk lasers: Status and prospects," *Nanophotonics*, 9, (2020). DOI: `10.1515/nanoph-2019-0544`.

[188] Z.-L. Lei and B. Guo, "2d material-based optical biosensor: Status and prospect," *Advanced Science*, 9, (2021). DOI: 10.1002/advs.202102924.

[189] X. Liu, X. Yang, W. Sang, H. Huang, W. Li, Y.-F. Lin, and J. Chu, "Thin-film electronics based on all-2D van der Waals heterostructures," *Journal of Information Display*, 22, 231–245, (2021). DOI: 10.1080/15980316.2021.1982782.

[190] Y. Huang, Y.-H. Pan, R. Yang, L.-H. Bao, L. Meng, H.-L. Luo, Y.-Q. Cai, G.-D. Liu, W.-J. Zhao, Z. Zhou, L.-M. Wu, Z.-L. Zhu, M. Huang, L.-W. Liu, L. Liu, P. Cheng, K.-H. Wu, S.-B. Tian, C.-Z. Gu, Y.-G. Shi, Y.-F. Guo, Z. G. Cheng, J.-P. Hu, L. Zhao, G.-H. Yang, E. Sutter, P. Sutter, Y.-L. Wang, W. Ji, X.-J. Zhou, and H.-J. Gao, "Universal mechanical exfoliation of large-area 2D crystals," *Nature Communications*, 11, 2453, (2020). DOI: 10.1038/s41467-020-16266-w.

[191] Z. Li, R. J. Young, C. Backes, W. Zhao, X. Zhang, A. A. Zhukov, E. Tillotson, A. P. Conlan, F. Ding, S. J. Haigh, K. S. Novoselov, and J. N. Coleman, "Mechanisms of Liquid-Phase Exfoliation for the Production of Graphene," *ACS Nano*, 14, 10976–10985, (2020). DOI: 10.1021/acsnano.0c03916.

[192] V. Nicolosi, M. Chhowalla, M. G. Kanatzidis, M. S. Strano, and J. N. Coleman, "Liquid Exfoliation of Layered Materials," *Science*, 340, 1226419, (2013). DOI: 10.1126/science.1226419.

[193] A. S. H. Makhlouf and I. Tiginyanu, Eds., *Nanocoatings and ultra-thin films: technologies and applications* (Woodhead Publishing in materials). Oxford: Woodhead Publishing, (2011), OCLC: ocn745978762, ISBN: 978-1-84569-812-6. DOI: https://doi.org/10.1533/9780857094902.1.3.

[194] Y. Liang, Y. Chen, Y. Sun, S. Xu, J. Wu, C. Tan, X. Xu, H. Yuan, L. Yang, Y. Chen, P. Gao, J. Guo, and H. Peng, "Molecular Beam Epitaxy and Electronic Structure of Atomically Thin Oxyselenide Films," *Advanced Materials*, 31, 1901964, (2019). DOI: 10.1002/adma.201901964.

[195] "Metal Deposition: Plasma-Based Processes," in *Encyclopedia of Plasma Technology*, J. L. Shohet, Ed., 0th ed., CRC Press, (2016), pp. 722–740, ISBN: 978-1-4822-1431-4. DOI: 10.1081/E-EPLT-120053919.

[196] A. Tiwari, Ed., *Handbook of antimicrobial coatings*. Amsterdam, Netherlands ; Cambridge, MA: Elsevier, (2018), ISBN: 978-0-12-811982-2.

[197] S. K. Padamata, A. Yasinskiy, V. Yanov, and G. Saevarsdottir, "Magnetron Sputtering High-Entropy Alloy Coatings: A Mini-Review," *Metals*, 12, 319, (2022). DOI: 10.3390/met12020319.

[198] L. Sun, G. Yuan, L. Gao, J. Yang, M. Chhowalla, M. H. Gharahcheshmeh, K. K. Gleason, Y. S. Choi, B. H. Hong, and Z. Liu, "Chemical vapour deposition," *Nature Reviews Methods Primers*, 1, 5, (2021). DOI: 10.1038/s43586-020-00005-y.

[199] Y. Zhang, L. Zhang, and C. Zhou, "Review of Chemical Vapor Deposition of Graphene and Related Applications," *Accounts of Chemical Research*, 46, 2329–2339, (2013). DOI: 10.1021/ar300203n.

[200] M. Sabzi, S. Mousavi Anijdan, M. Shamsodin, M. Farzam, A. Hojjati-Najafabadi, P. Feng, N. Park, and U. Lee, "A review on sustainable manufacturing of ceramic-based thin films by chemical vapor deposition (CVD): Reactions kinetics and the deposition mechanisms," *Coatings*, 13, DOI: 10.3390/coatings13010188.

[201] J. M. Blocher, M. F. Browning, and D. M. Barrett, "Chemical vapor deposition of ceramic materials," in *Emergent Process Methods for High-Technology Ceramics*, R. F. Davis, H. Palmour, and R. L. Porter, Eds., Boston, MA, pp. 299–316, ISBN: 978-1-4684-8207-2 978-1-4684-8205-8. DOI: 10.1007/978-1-4684-8205-8_23.

[202] C. Nordling, E. Sokolowski, and K. Siegbahn, "Precision Method for Obtaining Absolute Values of Atomic Binding Energies," *Physical Review*, 105, 1676–1677, (1957). DOI: 10.1103/PhysRev.105.1676.

[203] M. Hargittai, "Kai M. Siegbahn (1918–2007): A pioneer in high-resolution electron spectroscopy," *Structural Chemistry*, 33, 307–310, (2022). DOI: 10.1007/s11224-021-01865-0.

[204] M. El-Desawy, "Characterization and application of aromatic self-assembled monolayers," Ph. D. Thesis, Faculty of Physics University of Bielefeld, (2007). [Online]. Available: https://www.researchgate.net/publication/36449318_Characterization_and_application_of_aromatic_self-assembled_monolayers (visited on 05/30/2023).

[205] M. Linford, "Introduction to surface and material analysis and to various analytical techniques," *Vacuum Technology and Coating*, 27–33, Feb. (2014). [Online]. Available: https://www.researchgate.net/publication/260265755_Introduction_to_Surface_and_Material_Analysis_and_to_Various_Analytical_Techniques.

[206] J. F. Moulder and J. Chastain, Eds., *Handbook of X-ray photoelectron spectroscopy: a reference book of standard spectra for identification and interpretation of XPS data*, Update. Eden Prairie, Minn: Perkin-Elmer Corporation, (1992), ISBN: 978-0-9627026-2-4.

[207] P. Potts, "X-RAY FLUORESCENCE AND EMISSION | Wavelength Dispersive X-Ray Fluorescence," in *Encyclopedia of Analytical Science*, Elsevier, (2005), pp. 419–429, ISBN: 978-0-12-369397-6. DOI: 10.1016/B0-12-369397-7/00674-9. [Online]. Available: https://linkinghub.elsevier.com/retrieve/pii/B0123693977006749 (visited on 05/26/2023).

[208] T. F. S. Inc., "Xr3: Twin anode x-ray source," DOI: 10.3390/mi13010092. [Online]. Available: http://www.thermoscientific.com/content/dam/tfs/ATG/CAD/CAD.pdf.

[209] F. A. Stevie and C. L. Donley, "Introduction to x-ray photoelectron spectroscopy," *Journal of Vacuum Science & Technology A*, 38, 063204, (2020). DOI: 10.1116/6.0000412.

[210] J. F. Watts and J. Wolstenholme, *An introduction to surface analysis by XPS and AES*. Chichester, West Sussex, England ; New York: J. Wiley, (2003), ISBN: 978-0-470-84712-1 978-0-470-84713-8. DOI: 10.1002/0470867930.

[211] M. Anwar, M. A. Shaikh Abdul, U. M. Khan, M. Hassan, A. H. Khoja, and A. Muchtar, "A Review of X-ray Photoelectron Spectroscopy Technique to Analyze the Stability and Degradation Mechanism of Solid Oxide Fuel Cell Cathode Materials," *Materials*, 15, 2540, (2022). DOI: 10.3390/ma15072540.

[212] T. Zouros and E. Benis, "The hemispherical deflector analyser revisited. I. Motion in the ideal 1/r potential, generalized entry conditions, Kepler orbits and spectrometer basic equation," *Journal of Electron Spectroscopy and Related Phenomena*, 125, 221–248, (2002). DOI: 10.1016/S0368-2048(02)00137-8.

[213] I. Mills and I. U. of Pure and Applied Chemistry, Eds., *Quantities, units, and symbols in physical chemistry*, 3rd ed. Cambridge, UK: RSC Pub, (2007), ISBN: 978-0-85404-433-7.

[214] E. Al-Dmour, "Fundamentals of Vacuum Physics and Technology," (2020). DOI: 10.48550/ARXIV.2006.01464.

[215] O. PHYSICS, *Scientific overviews: What is uhv?* [Online]. Available: `https://www.orsayphysics.com/what-is-uhv` (visited on 01/26/2024).

[216] F. Bergaya and G. Lagaly, Eds., *Handbook of clay science* (Developments in clay science), Second edition. Amsterdam: Elsevier, (2013), OCLC: ocn827266692, ISBN: 978-0-08-099364-5 978-0-08-098259-5 978-0-08-098258-8.

[217] M. Hortigüela and G. Irurueta, *X-ray Photoelectron Spectroscopy A surface characterization technique*, 1. Auflage. (2019), ISBN: 978-972-789-602-8. [Online]. Available: `https://www.researchgate.net/publication/339140872_X-ray_Photoelectron_Spectroscopy_A_surface_characterization_technique`.

[218] E. Bolli, S. Kaciulis, and A. Mezzi, "ESCA as a tool for exploration of metals' surface," *Coatings*, 10, DOI: `10.3390/coatings10121182`.

[219] M. P. Seah and W. A. Dench, "Quantitative electron spectroscopy of surfaces: A standard data base for electron inelastic mean free paths in solids," *Surface and Interface Analysis*, 1, 2–11, (1979). DOI: `10.1002/sia.740010103`.

[220] D. R. Baer, K. Artyushkova, C. Richard Brundle, J. E. Castle, M. H. Engelhard, K. J. Gaskell, J. T. Grant, R. T. Haasch, M. R. Linford, C. J. Powell, A. G. Shard, P. M. A. Sherwood, and V. S. Smentkowski, "Practical guides for x-ray photoelectron spectroscopy: First steps in planning, conducting, and reporting XPS measurements," *Journal of Vacuum Science & Technology A*, 37, 031401, (2019). DOI: `10.1116/1.5065501`.

[221] G. Greczynski and L. Hultman, "A step-by-step guide to perform x-ray photoelectron spectroscopy," *Journal of Applied Physics*, 132, 011101, (2022). DOI: `10.1063/5.0086359`.

[222] D. A. Shirley, "High-Resolution X-Ray Photoemission Spectrum of the Valence Bands of Gold," *Physical Review B*, 5, 4709–4714, (1972). DOI: `10.1103/PhysRevB.5.4709`.

[223] S. Tougaard and A. Ignatiev, "Concentration depth profiles by XPS; A new approach," *Surface Science*, 129, 355–365, (1983). DOI: `10.1016/0039-6028(83)90186-3`.

[224] S. Tougaard, "Composition depth information from the inelastic background signal in XPS," *Surface Science*, 162, 875–885, (1985). DOI: `10.1016/0039-6028(85)90992-6`.

[225] S. Tougaard, "Non-destructive in-depth composition information from XPS," *Surface Science*, 172, L503–L506, (1986). DOI: `10.1016/0039-6028(86)90575-3`.

[226] S. Tougaard, "X-ray photoelectron spectroscopy peak shape analysis for the extraction of in-depth composition information," *Journal of Vacuum Science & Technology A: Vacuum, Surfaces, and Films*, 5, 1275–1278, (1987). DOI: `10.1116/1.574789`.

[227] E. Kleimenov, "High-pressure X-ray photoelectron spectroscopy applied to vanadium phosphorus oxide catalysts under reaction conditions," Ph. D. Thesis, Technischen Universität Berlin, Berlin, (2005). [Online]. Available: `https://pure.mpg.de/rest/items/item_738775_3/component/file_738774/content?download=true` (visited on 05/30/2023).

[228] F. Calavalle, P. Dreher, A. P. Surdendran, W. Wan, M. Timpel, R. Verucchi, C. Rogero, T. Bauch, F. Lombardi, F. Casanova, M. V. Nardi, M. M. Ugeda, L. E. Hueso, and M. Gobbi, "Tailoring Superconductivity in Large-Area Single - Layer $NbSe_2$ via Self-Assembled Molecular Adlayers," *Nano Letters*, 21, 136–143, (2021). DOI: `10.1021/acs.nanolett.0c03386`.

[229] P. Borghetti, A. El-Sayed, E. Goiri, C. Rogero, J. Lobo-Checa, L. Floreano, J. E. Ortega, and D. G. de Oteyza, "Spectroscopic Fingerprints of Work-Function-Controlled Phthalocyanine Charging on Metal Surfaces," *ACS Nano*, 8, 12786–12795, (2014). DOI: `10.1021/nn5060333`.

[230] Y.-K. Lin, R.-S. Chen, T.-C. Chou, Y.-H. Lee, Y.-F. Chen, K.-H. Chen, and L.-C. Chen, "Thickness-dependent binding energy shift in few-layer MoS_2 grown by chemical vapor deposition," *ACS Appl. Mater. Interfaces*, 8, 22637–22646, DOI: 10.1021/acsami.6b06615.

[231] P. Van Der Heide, "Multiplet splitting patterns exhibited by the first row transition metal oxides in x-ray photoelectron spectroscopy," *Journal of Electron Spectroscopy and Related Phenomena*, 164, DOI: 10.1016/j.elspec.2008.04.001.

[232] P. S. Bagus, C. J. Nelin, Y. Al-Salik, E. S. Ilton, and H. Idriss, "Multiplet splitting for the XPS of heavy elements: Dependence on oxidation state," *Surface Science*, 643, 142–149, (2016). DOI: 10.1016/j.susc.2015.06.002.

[233] F. Jimenez-Villacorta, C. Prieto, Y. Huttel, N. Telling, and G. Laan, "X-ray magnetic circular dichroism study of the blocking process in nanostructured iron-iron oxide core-shell systems," *Physical Review B*, 84, 2011. DOI: 10.1103/PhysRevB.84.172404.

[234] D. Liu, C. wu, M. Yan, and J. Wang, "Correlating the microstructure, growth mechanism and magnetic properties of fesial soft magnetic composites fabricated via hno 3 oxidation," *Acta Materialia*, 146, Mar. 2018. DOI: 10.1016/j.actamat.2018.01.001.

[235] W. Xu, Y. Liu, A. Marcelli, P. Shang, and W. Liu, "The complexity of thermoelectric materials: Why we need powerful and brilliant synchrotron radiation sources?" *Materials Today Physics*, 6, 68–82, (2018). DOI: 10.1016/j.mtphys.2018.09.002.

[236] F. Düll, "Metal Nanocluster Arrays as Model System for Catalysts," Ph. D. Thesis, Friedrich-Alexander-Universität Erlangen-Nürnberg, (2019). [Online]. Available: https://www.researchgate.net/publication/338147049_Metal_Nanocluster_Arrays_as_Model_System_for_Catalysts (visited on 06/02/2023).

[237] J. C. Lang, "X-ray Magnetic Circular Dichroism," in *Characterization of Materials*, E. N. Kaufmann, Ed., Hoboken, NJ, USA: John Wiley & Sons, Inc., (2012), com078.pub2, ISBN: 978-0-471-26696-9. DOI: 10.1002/0471266965.com078.pub2. [Online]. Available: https://onlinelibrary.wiley.com/doi/10.1002/0471266965.com078.pub2 (visited on 06/02/2023).

[238] A. Synchrotron, *ALBA Accelerators*, (2014). [Online]. Available: https://www.albasynchrotron.es/en/accelerators/linac (visited on 06/02/2023).

[239] M. Pont, U. Iriso, R. Munoz, and F. Perez, "Operation of the ALBA injector," (2011). [Online]. Available: https://www.researchgate.net/publication/268182659_Operation_of_the_ALBA_injector.

[240] E. Jaeschke, D. Kramer, B. Kuske, P. Kuske, M. Scheer, E. Weihreter, and G. Wustefeld, "Lattice design for the 1.7-GeV light source BESSY II," in *Proceedings of International Conference on Particle Accelerators*, Washington, DC, USA: IEEE, (1993), pp. 1474–1476, ISBN: 978-0-7803-1203-6. DOI: 10.1109/PAC.1993.309063. [Online]. Available: http://ieeexplore.ieee.org/document/309063/ (visited on 06/02/2023).

[241] S. Sabchevski, E. Di Palma, I. Spassovsky, and G. Dattoli, "Gyrotrons as High-Frequency Drivers for Undulators and High-Gradient Accelerators," *Applied Sciences*, 12, 6101, (2022). DOI: 10.3390/app12126101.

[242] C. Schmitz-Antoniak, "X-ray absorption spectroscopy on magnetic nanoscale systems for modern applications," *Reports on Progress in Physics*, 78, 062501, (2015). DOI: 10.1088/0034-4885/78/6/062501.

[243] A. Shabalin, “Coherent X-ray diffraction studies of mesoscopic materials,” Ph. D. Thesis, Department Physik der Universit "at Hamburg, Hamburg, (2015). [Online]. Available: https://bib-pubdb1.desy.de/record/291304 (visited on 06/02/2023).

[244] M. Räkers, “An x-ray spectroscopic study of novel materials for electronic applications,” Ph. D. Thesis, Osnabrück, Osnabrück, (2009). (visited on 06/27/2023).

[245] Y. Shokr, “Interaction Mechanisms and Magnetization Dynamics in Ultrathin Antiferromagnetic Films and their Correlation with Structure and Morphology,” Ph.D. dissertation, Freie Universität Berlin, Berlin, (2016). [Online]. Available: https://www.researchgate.net/publication/320443598_Interaction_Mechanisms_and_Magnetization_Dynamics_in_Ultrathin_Antiferromagnetic_Films_and_their_Correlation_with_Structure_and_Morphology (visited on 06/02/2023).

[246] H. Wende, “Recent advances in x-ray absorption spectroscopy,” *Reports on Progress in Physics*, 67, 2105–2181, (2004). DOI: 10.1088/0034-4885/67/12/R01.

[247] S. Sasaki, “Analyses for a planar variably-polarizing undulator,” *Nuclear Instruments and Methods in Physics Research Section A: Accelerators, Spectrometers, Detectors and Associated Equipment*, 347, 83–86, (1994). DOI: 10.1016/0168-9002(94)91859-7.

[248] M. Yamamoto, T. Kumasaka, T. Fujisawa, and T. Ueki, “Trichromatic Concept at Spring-8 RIKEN Beamline I,” *Journal of Synchrotron Radiation*, 5, 222–225, (1998). DOI: 10.1107/S0909049597014738.

[249] P. Ohresser, E. Otero, F. Choueikani, S. Stanescu, F. Deschamps, L. Ibis, T. Moreno, F. Polack, B. Lagarde, F. Marteau, F. Scheurer, L. Joly, J.-P. Kappler, B. Muller, and P. Sainctavit, “Polarization characterization on the DEIMOS beamline using dichroism measurements,” *Journal of Physics: Conference Series*, 425, 212007, (2013). DOI: 10.1088/1742-6596/425/21/212007.

[250] S. S. DEIMOS, *Deimos*, (2022). [Online]. Available: https://www.synchrotron-soleil.fr/en/beamlines/deimos (visited on 01/25/2024).

[251] M. Wang, L. Árnadóttir, Z. J. Xu, and Z. Feng, “In Situ X-ray Absorption Spectroscopy Studies of Nanoscale Electrocatalysts,” *Nano-Micro Letters*, 11, 47, (2019). DOI: 10.1007/s40820-019-0277-x.

[252] S. Tripathi, “XMCD investigation at $M_{4,5}$ edges of the rare earth elements in high-performance permanent magnet,” Ph.D. dissertation, Max-Planck-Institut für Intelligente Systeme, Stuttgart, Stuttgart, (2018). [Online]. Available: https://elib.uni-stuttgart.de/handle/11682/10209 (visited on 06/02/2023).

[253] A. Singha, “Magnetic properties of surface-adsorbed single rare earth atoms, molecules, and atomic scale clusters,” Ph.D. dissertation, École Polytechnique Fédérale de Lausanne, LAUSANNE, (2017). [Online]. Available: https://infoscience.epfl.ch/record/232433 (visited on 06/02/2023).

[254] J. Penner-Hahn, “X-ray Absorption Spectroscopy,” in *Comprehensive Coordination Chemistry II*, Elsevier, (2003), pp. 159–186, ISBN: 978-0-08-043748-4. DOI: 10.1016/B0-08-043748-6/01063-X. [Online]. Available: https://linkinghub.elsevier.com/retrieve/pii/B008043748601063X (visited on 06/28/2023).

[255] B. Watts, L. Thomsen, and P. Dastoor, “Methods in carbon K-edge NEXAFS: Experiment and analysis,” *Journal of Electron Spectroscopy and Related Phenomena*, 151, 105–120, (2006). DOI: 10.1016/j.elspec.2005.11.006. (visited on 06/02/2023).

[256] Z. Németh, É. G. Bajnóczi, B. Csilla, and G. Vankó, "Laboratory EXAFS determined structure of the stable complexes in the ternary Ni(II)–EDTA–CN^- system," *Physical Chemistry Chemical Physics*, 21, 9239–9245, (2019). DOI: 10.1039/C9CP00982E.

[257] C. Sorg, "Magnetic Properties of 3d and 4f Ferromagnets Studied by X-Ray Absorption Spectroscopy," Ph.D. dissertation, Freie Universität Berlin, Berlin, (2005). [Online]. Available: `http://users.physik.fu-berlin.de/~bab/start_frame2/diss/CSdiss.pdf` (visited on 06/02/2023).

[258] J. Stöhr, *NEXAFS Spectroscopy* (Springer Series in Surface Sciences), G. Ertl, R. Gomer, D. L. Mills, and H. K. V. Lotsch, Eds. Berlin, Heidelberg: Springer Berlin Heidelberg, (1992), vol. 25, ISBN: 978-3-642-08113-2 978-3-662-02853-7. DOI: 10.1007/978-3-662-02853-7. [Online]. Available: `http://link.springer.com/10.1007/978-3-662-02853-7` (visited on 06/02/2023).

[259] J. Stöhr, "Exploring the microscopic origin of magnetic anisotropies with X-ray magnetic circular dichroism (XMCD) spectroscopy," *Journal of Magnetism and Magnetic Materials*, 200, 470–497, (1999). DOI: 10.1016/S0304-8853(99)00407-2.

[260] C.-I. Lu, C.-H. Huang, K.-H. Ou Yang, K. B. Simbulan, K.-S. Li, F. Li, J. Qi, M. Jugovac, I. Cojocariu, V. Feyer, C. Tusche, M.-T. Lin, T.-H. Chuang, Y.-W. Lan, and D.-H. Wei, "Spontaneously induced magnetic anisotropy in an ultrathin Co/MoS_2 heterojunction," *Nanoscale Horizons*, 5, 1058–1064, (2020). DOI: 10.1039/D0NH00108B.

[261] C. Piamonteze, P. Miedema, and F. M. F. d. Groot, "The accuracy of the spin sum rule in XMCD," *Journal of Physics: Conference Series*, 190, 012015, (2009). DOI: 10.1088/1742-6596/190/1/012015.

[262] B. T. Thole, P. Carra, F. Sette, and G. van der Laan, "X-ray circular dichroism as a probe of orbital magnetization," *Physical Review Letters*, 68, 1943–1946, (1992). DOI: 10.1103/PhysRevLett.68.1943.

[263] P. Carra, B. T. Thole, M. Altarelli, and X. Wang, "X-ray circular dichroism and local magnetic fields," *Physical Review Letters*, 70, 694–697, (1993). DOI: 10.1103/PhysRevLett.70.694.

[264] W. Kuch, "X-ray Magnetic Circular Dichroism for Quantitative Element-Resolved Magnetic Microscopy," *Physica Scripta*, T109, 89, (2004). DOI: 10.1238/Physica.Topical.109a00089.

[265] S. R. A. Venkata, "The effects of interfaces on the magnetic properties of ultra-thin ferromagnetic films," Ph. D. Thesis, Basel, Basel, (2018). [Online]. Available: `https://edoc.unibas.ch/64587/` (visited on 06/15/2023).

[266] C. T. Chen, Y. U. Idzerda, H.-J. Lin, N. V. Smith, G. Meigs, E. Chaban, G. H. Ho, E. Pellegrin, and F. Sette, "Experimental Confirmation of the X-Ray Magnetic Circular Dichroism Sum Rules for Iron and Cobalt," *Physical Review Letters*, 75, 152–155, (1995). DOI: 10.1103/PhysRevLett.75.152.

[267] A. Zakharova, "Magnetic and electronic properties of oxides heterostructures probed with x-ray spectroscopy," Ph. D. Thesis, Universit¨at Basel, Basel, (2022). (visited on 06/27/2023).

[268] A. Scholl, "Thin-film Magnetism: PEEM Studies," in *Encyclopedia of Materials: Science and Technology*, Elsevier, (2002), pp. 1–5, ISBN: 978-0-08-043152-9. DOI: `10.1016/B0-08-043152-6/01823-4`. [Online]. Available: `https://linkinghub.elsevier.com/retrieve/pii/B0080431526018234` (visited on 06/27/2023).

[269] J. Stöhr, H. A. Padmore, S. Anders, T. Stammler, and M. R. Scheinfein, "Principles of X-Ray Magnetic Dichroism Spectromicroscopy," *Surface Review and Letters*, 05, 1297–1308, (1998). DOI: `10.1142/S0218625X98001638`.

[270] P. Wadley, K. W. Edmonds, M. R. Shahedkhah, R. P. Campion, B. L. Gallagher, J. Železný, J. Kuneš, V. Novák, T. Jungwirth, V. Saidl, P. Němec, F. Maccherozzi, and S. S. Dhesi, "Control of antiferromagnetic spin axis orientation in bilayer Fe/CuMnAs films," *Scientific Reports*, 7, 11147, (2017). DOI: `10.1038/s41598-017-11653-8`.

[271] M. Pilard, O. Ersen, S. Cherifi, B. Carvello, L. Roiban, B. Muller, F. Scheurer, L. Ranno, and C. Boeglin, "Magnetic properties of coupled ultrathin NiO/Fe_3O_4(001) films," *Physical Review B*, 76, 214436, (2007). DOI: `10.1103/PhysRevB.76.214436`.

[272] H. Ibach and H. Lüth, *Festkörperphysik: Einführung in die Grundlagen ; mit 18 Tafeln und 104 Übungen* (Springer-Lehrbuch), 7. Aufl. Berlin: Springer, (2009), ISBN: 978-3-540-85794-5 978-3-540-85795-2.

[273] F. Kubli, "Louis de broglie und die entdeckung der materiewellen," *Arch. Rational Mech.*, 7, DOI: `10.1007/BF00328784`.

[274] W. Demtröder, *Experimentalphysik. Bd. 3: Atome, Moleküle und Festkörper: mit 9 Farbtafeln, 48 Tabellen, zahlreichen durchgerechneten Beispielen und 151 Übungsaufgaben mit ausführlichen Lösungen* (Springer-Lehrbuch), 4., überarb. Aufl. Berlin: Springer, (2010), ISBN: 978-3-642-03910-2 978-3-642-03911-9.

[275] S. Speller, W. Heiland, and M. Schleberger, "SURFACE CHARACTERIZATION: COMPOSITION, STRUCTURE AND TOPOGRAPHY," in *Handbook of Surfaces and Interfaces of Materials*, Elsevier, (2001), pp. 1–53, ISBN: 978-0-12-513910-6. DOI: `10.1016/B978-012513910-6/50020-7`. [Online]. Available: `https://linkinghub.elsevier.com/retrieve/pii/B9780125139106500207` (visited on 05/26/2023).

[276] G. Binnig and H. Rohrer, "Scanning tunneling microscopy," *Surface Science*, 126, 236–244, (1983). DOI: `10.1016/0039-6028(83)90716-1`.

[277] *The Nobel Prize in Physics 1986*, (1986). [Online]. Available: `https://www.nobelprize.org/prizes/physics/1986/summary/` (visited on 11/22/2023).

[278] V. A. Valencia, A. A. Thaker, J. Derouin, D. N. Valencia, R. G. Farber, D. A. Gebel, and D. R. Killelea, "Preparation of scanning tunneling microscopy tips using pulsed alternating current etching," *Journal of Vacuum Science & Technology A: Vacuum, Surfaces, and Films*, 33, DOI: `10.1116/1.4904347`.

[279] F. Mohn, B. Schuler, L. Gross, and G. Meyer, "Different tips for high-resolution atomic force microscopy and scanning tunneling microscopy of single molecules," *Applied Physics Letters*, 102, DOI: `10.1063/1.4793200`.

[280] J. Morán Meza, C. Lubin, F. Thoyer, K. Villegas Rosales, A. Gutarra Espinoza, F. Martin, and J. Cousty, "Fabrication of ultra-sharp tips from carbon fiber for scanning tunneling microscopy investigations of epitaxial graphene on 6h-sic(0001) surface," *Carbon*, 86, 2015. DOI: `https://doi.org/10.1016/j.carbon.2015.01.050`.

[281] F. Trixler, "Quantum Tunnelling to the Origin and Evolution of Life," *Current Organic Chemistry*, 17, 1758–1770, (2013). DOI: 10.2174/13852728113179990083.

[282] C. D. S. Enriquez, "Scanning tunneling microscopy on low dimensional systems: Dinickel molecular complexes and iron nanostructures," Ph. D. Thesis, TU Dresden, Dresden, (2016). [Online]. Available: https://tud.qucosa.de/api/qucosa%3A29882/attachment/ATT-1/?L=1 (visited on 01/25/2024).

[283] M. A. Reed, "Inelastic electron tunneling spectroscopy," *Materials Today*, 11, 46–50, (2008). DOI: 10.1016/S1369-7021(08)70238-4.

[284] J. M. Jandke, "Elastic and Inelastic Scanning Tunneling Spectroscopy on Iron-Based Superconductors," Ph. D. Thesis, Karlsruher Instituts f ¨ ur Technologie, Karlsruhe, (2017). [Online]. Available: https://www.ksp.kit.edu/site/books/m/10.5445/KSP/1000078103/ (visited on 06/27/2023).

[285] P. Ngabonziza, Y. Wang, P. A. van Aken, J. Maier, and J. Mannhart, "Inelastic electron tunneling spectroscopy at high-temperatures," *Advanced Materials*, 33, 2007299, DOI: 10.1002/adma.202007299.

[286] S. Lounis, *Theory of scanning tunneling microscopy.* DOI: https://doi.org/10.48550/arXiv.1404.0961. arXiv: 1404.0961[cond-mat]. (visited on 09/24/2023).

[287] S. Kano, T. Tada, and Y. Majima, "Nanoparticle characterization based on STM and STS," *Chemical Society Reviews*, 44, 970–987, (2015). DOI: 10.1039/C4CS00204K.

[288] F. Besenbacher, E. Lægsgaard, and I. Stensgaard, "Fast-scanning STM studies," *Materials Today*, 8, 26–30, (2005). DOI: 10.1016/S1369-7021(05)00843-6. (visited on 05/22/2023).

[289] M. Ternes, "Scanning tunneling spectroscopy at the single atom scale," Ph. D. Thesis, École Polytechnique Fédérale de Lausanne, Lausanne, (2006). [Online]. Available: https://infoscience.epfl.ch/record/64356 (visited on 06/27/2023).

[290] G. Sauerbrey, "Verwendung von Schwingquarzen zur Wägung dünner Schichten und zur Mikrowägung," *Zeitschrift für Physik*, 155, 206–222, (1959). DOI: 10.1007/BF01337937.

[291] *Prevac*, (2022). [Online]. Available: https://prevac.eu/14798/ (visited on 11/22/2023).

[292] B. S.L., *Atomic Layer Injection ALI-100.* [Online]. Available: https://nanoscore.de/wp-content/uploads/2016/11/08_brochure_ALI_1000_atomic_layer_injection_depositon.pdf (visited on 06/27/2023).

[293] T. Noll and F. Radu, "The Mechanics of the Vekmag Experiment," *Proceedings of the 9th Edition of the Mechanical Engineering Design of Synchrotron Radiation Equipment and Instrumentation Conference*, MEDSI2016, (2017). DOI: 10.18429/JACOW-MEDSI2016-WEPE38.

[294] K. Prokeš, C. Luo, H. Ryll, E. Schierle, D. Marchenko, E. Weschke, F. Radu, R. Abrudan, V. V. Volobuev, G. Springholz, and O. Rader, "Search for enhanced magnetism at the interface between Bi_2Se_3 and EuSe," *Physical Review B*, 103, 115438, (2021). DOI: 10.1103/PhysRevB.103.115438.

[295] S. Ossinger, L. Kipgen, H. Naggert, M. Bernien, A. J. Britton, F. Nickel, L. M. Arruda, I. Kumberg, T. A. Engesser, E. Golias, C. Näther, F. Tuczek, and W. Kuch, "Effect of ligand methylation on the spin-switching properties of surface-supported spin-crossover molecules," *Journal of Physics: Condensed Matter*, 32, 114003, (2020). DOI: 10.1088/1361-648X/ab5c92.

[296] S. Thakur, E. Golias, I. Kumberg, K. Senthil Kumar, R. Hosseinifar, J. Torres-Rodríguez, L. Kipgen, C. Lotze, L. M. Arruda, C. Luo, F. Radu, M. Ruben, and W. Kuch, “Thermal- and light-induced spin-crossover characteristics of a functional iron(ii) complex at submonolayer coverage on hopg,” *The Journal of Physical Chemistry C*, 125, 13925–13932, (2021). DOI: 10.1021/acs.jpcc.1c02774.

[297] A. Barla, J. Nicolás, D. Cocco, S. M. Valvidares, J. Herrero-Martín, P. Gargiani, J. Moldes, C. Ruget, E. Pellegrin, and S. Ferrer, “Design and performance of BOREAS, the beamline for resonant X-ray absorption and scattering experiments at the ALBA synchrotron light source,” *Journal of Synchrotron Radiation*, 23, 1507–1517, (2016). DOI: 10.1107/S1600577516013461.

[298] A. Synchrotron, *BL29 - BOREAS*, (2014). [Online]. Available: https://www.cells.es/en/beamlines/bl29-boreas (visited on 06/27/2023).

[299] Y. He, G. H. Fecher, C. Fu, Y. Pan, K. Manna, J. Kroder, A. Jha, X. Wang, Z. Hu, S. Agrestini, J. Herrero-Martín, M. Valvidares, Y. Skourski, W. Schnelle, P. Stamenov, H. Borrmann, L. H. Tjeng, R. Schaefer, S. S. P. Parkin, J. M. D. Coey, and C. Felser, “A new highly anisotropic rh-based heusler compound for magnetic recording,” *Advanced Materials*, 32, DOI: 10.1002/adma.202004331.

[300] S. Synchrotron, *DEIMOS*, (2016). [Online]. Available: https://www.synchrotron-soleil.fr/en/beamlines/deimos (visited on 06/27/2023).

[301] L. Joly, B. Muller, E. Sternitzky, J.-G. Faullumel, A. Boulard, E. Otero, F. Choueikani, J.-P. Kappler, M. Studniarek, M. Bowen, and P. Ohresser, “Versatile variable temperature insert at the DEIMOS beamline for *in situ* electrical transport measurements,” *Journal of Synchrotron Radiation*, 23, 652–657, (2016). DOI: 10.1107/S1600577516002551.

[302] J.-P. Kappler, E. Otero, W. Li, L. Joly, G. Schmerber, B. Muller, F. Scheurer, F. Leduc, B. Gobaut, L. Poggini, G. Serrano, F. Choueikani, E. Lhotel, A. Cornia, R. Sessoli, M. Mannini, M.-A. Arrio, P. Sainctavit, and P. Ohresser, “Ultralow-temperature device dedicated to soft X-ray magnetic circular dichroism experiments,” *Journal of Synchrotron Radiation*, 25, 1727–1735, (2018). DOI: 10.1107/S1600577518012717. (visited on 06/27/2023).

[303] T. Moreno, E. Otero, and P. Ohresser, “*In situ* characterization of undulator magnetic fields,” *Journal of Synchrotron Radiation*, 19, 179–184, (2012). DOI: 10.1107/S0909049511052873.

[304] S. Synchrotron, *Experimental Station*. [Online]. Available: https://www.psi.ch/en/sls/pearl/endstation (visited on 06/27/2023).

[305] M. Muntwiler, J. Zhang, R. Stania, F. Matsui, P. Oberta, U. Flechsig, L. Patthey, C. Quitmann, T. Glatzel, R. Widmer, E. Meyer, T. A. Jung, P. Aebi, R. Fasel, and T. Greber, “Surface science at the PEARL beamline of the Swiss Light Source,” *Journal of Synchrotron Radiation*, 24, 354–366, (2017). DOI: 10.1107/S1600577516018646.

[306] S. Synchrotron, *PEARL - X03DA: Photoemission and Atomic Resolution Laboratory*. [Online]. Available: https://www.psi.ch/en/sls/pearl (visited on 06/27/2023).

[307] P. Oberta, U. Flechsig, M. Muntwiler, and C. Quitmann, “Optical design study of the PEARL beamline at SLS,” *Nuclear Instruments and Methods in Physics Research Section A: Accelerators, Spectrometers, Detectors and Associated Equipment*, 635, 116–120, (2011). DOI: 10.1016/j.nima.2011.01.076.

[308] W. B. Yelon, Oelete, and C. Vettier, "Neutron scattering study of the magnetic excitations in $FeBr_2$," *Journal of Physics C: Solid State Physics*, 8, 2760–2768, (1975). DOI: 10.1088/0022-3719/8/17/016.

[309] M. K. Wilkinson, J. W. Cable, E. O. Wollan, and W. C. Koehler, "Neutron Diffraction Investigations of the Magnetic Ordering in $FeBr_2$, $CoBr_2$, $FeCl_2$, and $CoCl_2$," *Physical Review*, 113, 497–507, (1959). DOI: 10.1103/PhysRev.113.497.

[310] "A POSSIBLE EXPLANATION OF THE FIELD DEPENDENCE OF THE SUSCEPTIBILITY AT LOW TEMPERATURES," in *Collected Papers of L.D. Landau*, Elsevier, (1965), pp. 73–76, ISBN: 978-0-08-010586-4. DOI: 10.1016/B978-0-08-010586-4.50017-1. (visited on 07/21/2023).

[311] C. Binek, T. Kato, W. Kleemann, O. Petracic, D. Bertrand, F. Bourdarot, P. Burlet, H. A. Katori, K. Katsumata, K. Prokes, and S. Welzel, "Neutron scattering study of transverse magnetism in the metamagnet," *The European Physical Journal B*, 15, 35–40, (2000). DOI: 10.1007/PL00011034.

[312] K. Momma and F. Izumi, "*VESTA 3* for three-dimensional visualization of crystal, volumetric and morphology data," *Journal of Applied Crystallography*, 44, 1272–1276, (2011). DOI: 10.1107/S0021889811038970.

[313] N. Available, *Materials Data on $FeBr_2$ by Materials Project*, (2020). DOI: 10.17188/1199047. (visited on 04/08/2022).

[314] K. Katsumata, H. A. Katori, S. M. Shapiro, and G. Shirane, "Neutron-scattering studies of a phase transition in the metamagnet FeBr 2 under external magnetic fields," *Physical Review B*, 55, 11466–11470, (1997). DOI: 10.1103/PhysRevB.55.11466. (visited on 07/21/2023).

[315] J. Haberecht, H. Borrmann, and R. Kniep, "Refinement of the crystal structure of iron dibromide, $FeBr_2$," *Zeitschrift für Kristallographie - New Crystal Structures*, 216, (2001). DOI: 10.1524/ncrs.2001.216.14.544.

[316] S. Terakawa, S. Hatta, H. Okuyama, and T. Aruga, "Epitaxial Growth and Electronic Properties of Single- and Few-Layer $FeBr_2$ on Bi(111)," *The Journal of Physical Chemistry C*, acs.jpcc.3c02188, (2023). DOI: 10.1021/acs.jpcc.3c02188.

[317] Z. Ropka, R. Michalski, and R. J. Radwanski, "Electronic and magnetic properties of $FeBr_2$," *Physical Review B*, 63, 172404, (2001). DOI: 10.1103/PhysRevB.63.172404.

[318] M. Pleimling and W. Selke, "Anomalies in the antiferromagnetic phase of the metamagnet $FeBr_2$," *Physical Review B*, 56, 8855–8862, (1997). DOI: 10.1103/PhysRevB.56.8855.

[319] M. de Azevedo, C. Binek, J. Kushauer, W. Kleemann, and D. Bertrand, "Transient spin structures at the antiferro-to-paramagnetic phase boundary of $FeBr_2$," *Journal of Magnetism and Magnetic Materials*, 140-144, 1557–1558, (1995). DOI: 10.1016/0304-8853(94)00909-0.

[320] J. Pelloth, R. A. Brand, S. Takele, M. M. Pereira de Azevedo, W. Kleemann, C. Binek, J. Kushauer, and D. Bertrand, "Local magnetic properties of antiferromagnetic $FeBr_2$," *Physical Review B*, 52, 15372–15386, (1995). DOI: 10.1103/PhysRevB.52.15372.

[321] S. Aldrich, *Eisen(ii)-bromid - 400831*, (2023). [Online]. Available: https://www.sigmaaldrich.com/DE/de/product/aldrich/400831 (visited on 11/23/2023).

[322] S. Aldrich, *Eisen(ii)-bromid - 434000*, (2023). [Online]. Available: https://www.sigmaaldrich.com/DE/de/product/aldrich/434000 (visited on 11/23/2023).

[323] S. Aldrich, *Eisen(ii)-bromid - Product Specifications*, (2023). [Online]. Available: https://www.sigmaaldrich.com/specification-sheets/745/522/400831-BULK_______ALDRICH__.pdf (visited on 11/23/2023).

[324] S. Aldrich, *Eisen(ii)-bromid - Product Specifications*, (2023). [Online]. Available: https://www.sigmaaldrich.com/specification-sheets/295/955/434000-BULK_______ALDRICH__.pdf (visited on 11/23/2023).

[325] R. J. Sime and N. W. Gregory, "Vapor pressures of $FeCl_2$, $FeBr_2$ and FeI_2 by the torsion effusion method," *The Journal of Physical Chemistry*, 64, 86–89, (1960). DOI: 10.1021/j100830a021.

[326] V. B. Parker and I. L. Khodakovskii, "Thermodynamic Properties of the Aqueous Ions ($^{2+}$ and $^{3+}$) of Iron and the Key Compounds of Iron," *Journal of Physical and Chemical Reference Data*, 24, 1699–1745, (1995). DOI: 10.1063/1.555964.

[327] K. Sun, T. Nishiuchi, K. Sahara, T. Kubo, A. Foster, and S. Kawai, "Low-temperature removal of dissociated bromine by silicon atoms for on-surface ullmann reaction," *The Journal of Physical Chemistry C*, 124, 19675–19680, (2020). DOI: 10.1021/acs.jpcc.0c06188.

[328] R. Zuzak, A. Jančařík, A. Gourdon, M. Szymonski, and S. Godlewski, "On-surface synthesis with atomic hydrogen," *ACS Nano*, 14, 13316–13323, (2020). DOI: 10.1021/acsnano.0c05160.

[329] N. Merino-Díez, A. Pérez Paz, J. Li, M. Vilas-Varela, J. Lawrence, M. S. G. Mohammed, A. Berdonces-Layunta, A. Barragán, J. I. Pascual, J. Lobo-Checa, D. Peña, and D. G. de Oteyza, "Hierarchy in the halogen activation during surface-promoted ullmann coupling," *ChemPhysChem*, 20, 2305–2310, (2019). DOI: 10.1002/cphc.201900633.

[330] K. Sun, T. Nishiuchi, K. Sahara, T. Kubo, A. S. Foster, and S. Kawai, "Low-temperature removal of dissociated bromine by silicon atoms for an on-surface ullmann reaction," *The Journal of Physical Chemistry C*, 124, 19675–19680, (2020). DOI: 10.1021/acs.jpcc.0c06188.

[331] D. Eberl, *QCS quad cluster source*, (2023). [Online]. Available: https://www.mbe-komponenten.de/products/mbe-components/source-clusters/qcs.php (visited on 12/05/2023).

[332] K. Hermann and M. Van Hove, *LEEDpat4*, (2016). [Online]. Available: https://www.fhi.mpg.de/958975/LEEDpat4 (visited on 09/28/2022).

[333] None Available, *Materials data on au by materials project*, in collab. with The Materials Project. DOI: 10.17188/1307925. [Online]. Available: https://www.osti.gov/servlets/purl/1307925/ (visited on 02/11/2024).

[334] M. Newville, T. Stensitzki, D. B. Allen, and A. Ingargiola, *LMFIT: Non-Linear Least-Square Minimization and Curve-Fitting for Python*, (2014). DOI: 10.5281/ZENODO.11813. (visited on 08/16/2021).

[335] L. Martín-García, I. Bernal-Villamil, M. Oujja, E. Carrasco, R. Gargallo-Caballero, M. Castillejo, J. F. Marco, S. Gallego, and J. de la Figuera, "Unconventional properties of nanometric FeO(111) films on Ru(0001): Stoichiometry and surface structure," *Journal of Materials Chemistry C*, 4, 1850–1859, (2016). DOI: 10.1039/C5TC03871E.

[336] A. P. Grosvenor, B. A. Kobe, M. C. Biesinger, and N. S. McIntyre, "Investigation of multiplet splitting of Fe 2p XPS spectra and bonding in iron compounds," *Surface and Interface Analysis*, 36, 1564–1574, (2004). DOI: 10.1002/sia.1984.

[337] T. Yamashita and P. Hayes, "Analysis of XPS spectra of Fe^{2+} and Fe^{3+} ions in oxide materials," *Applied Surface Science*, 254, 2441–2449, (2008). DOI: 10.1016/j.apsusc.2007.09.063.

[338] E. J. Little and M. M. Jones, "A complete table of electronegativities," *J. Chem. Educ.*, 37, DOI: 10.1021/ed037p231.

[339] M. Biesinger, *Relative Sensitivity Factors (R.S.F.)* (2009). [Online]. Available: http://www.xpsfitting.com/2009/04/relative-sensitivity-factors-rsf.html (visited on 09/12/2022).

[340] C. D. Wagner, L. E. Davis, M. V. Zeller, J. A. Taylor, R. H. Raymond, and L. H. Gale, "Empirical atomic sensitivity factors for quantitative analysis by electron spectroscopy for chemical analysis," *Surface and Interface Analysis*, 3, 211–225, (1981). DOI: 10.1002/sia.740030506.

[341] C. Wagner, "Sensitivity factors for XPS analysis of surface atoms," *Journal of Electron Spectroscopy and Related Phenomena*, 32, 99–102, (1983). DOI: 10.1016/0368-2048(83)85087-7.

[342] A. G. Shard, J. D. Counsell, D. J. H. Cant, E. F. Smith, P. Navabpour, X. Zhang, and C. J. Blomfield, "Intensity calibration and sensitivity factors for XPS instruments with monochromatic Ag L_α and Al K_α sources," *Surface and Interface Analysis*, 51, 763–773, (2019). DOI: 10.1002/sia.6647. (visited on 09/13/2022).

[343] A. J. Green, S. Dey, Y. Q. An, B. O'Brien, S. O'Mullane, B. Thiel, and A. C. Diebold, "Surface oxidation of the topological insulator Bi_2Se_3," *Journal of Vacuum Science and Technology A*, 34, 061403, (2016). DOI: 10.1116/1.4964637.

[344] S. Datta, A. Pramanik, R. Pandeya, A. Sakhya, A. Thamizhavel, and K. Maiti, "Preparation, characterization and electronic structure of ti-doped Bi_2Se_3," *AIP Conf. Proc.*, 030381, (2020). DOI: https://doi.org/10.1063/5.0017185.

[345] T. G. Gopakumar, M. Bernien, H. Naggert, F. Matino, C. F. Hermanns, A. Bannwarth, S. Mühlenberend, A. Krüger, D. Krüger, F. Nickel, W. Walter, R. Berndt, W. Kuch, and F. Tuczek, "Spin-crossover complex on Au(111): Structural and electronic differences between mono- and multilayers," *Chemistry - A European Journal*, 19, 15702–15709, (2013). DOI: 10.1002/chem.201302241.

[346] H. Herper, B. Brena, S. Bhandary, and B. Sanyal, "Deposited transition metal-centered porphyrin and phthalocyanine molecules: Influence of the substrates on the magnetic properties," in Jun. (2017), ISBN: 978-953-51-3255-4. DOI: 10.5772/intechopen.68224.

[347] S. Stepanow, P. S. Miedema, A. Mugarza, G. Ceballos, P. Moras, J. C. Cezar, C. Carbone, F. M. F. de Groot, and P. Gambardella, "Mixed-valence behavior and strong correlation effects of metal phthalocyanines adsorbed on metals," *Phys. Rev. B*, 83, 220401, (2011). DOI: 10.1103/PhysRevB.83.220401.

[348] J. Everett, E. Céspedes, L. R. Shelford, C. Exley, J. F. Collingwood, J. Dobson, G. van der Laan, C. A. Jenkins, E. Arenholz, and N. D. Telling, "Ferrous iron formation following the co-aggregation of ferric iron and the Alzheimer's disease peptide β-amyloid (1–42)," *Journal of The Royal Society Interface*, 11, 20140165, (2014). DOI: 10.1098/rsif.2014.0165.

[349] J. K. Kowalska, B. Nayyar, J. A. Rees, C. E. Schiewer, S. C. Lee, J. A. Kovacs, F. Meyer, T. Weyhermüller, E. Otero, and S. DeBeer, "Iron $L_{2,3}$ -edge x-ray absorption and x-ray magnetic circular dichroism studies of molecular iron complexes with relevance to the FeMoCo and FeVCo active sites of nitrogenase," *Inorganic Chemistry*, 56, 8147–8158, (2017). DOI: 10.1021/acs.inorgchem.7b00852.

[350] P. S. Miedema and F. M. de Groot, "The iron L edges: Fe 2p x-ray absorption and electron energy loss spectroscopy," *Journal of Electron Spectroscopy and Related Phenomena*, 187, 32–48, (2013). DOI: 10.1016/j.elspec.2013.03.005.

[351] M. W. H. et al., *Crispy — quanty*, [Online; accessed 6-October-2023], (2018). [Online]. Available: https://www.quanty.org/doku.php?id=crispy:start&rev=1528029815.

[352] A. Koehl, D. Kajewski, J. Kubacki, C. Lenser, R. Dittmann, P. Meuffels, K. Szot, R. Waser, and J. Szade, "Detection of Fe^{2+} valence states in Fe doped $SrTiO_3$ epitaxial thin films grown by pulsed laser deposition," *Physical Chemistry Chemical Physics*, 15, 8311, (2013). DOI: 10.1039/c3cp50272d.

[353] M. Giménez-Marqués, E. Bellido, T. Berthelot, T. Simón-Yarza, T. Hidalgo, R. Simon-Vazquez, A. Gonzalez-Fernandez, J. Avila, M. C. Asensio, R. Gref, P. Couvreur, C. Serre, and P. Horcajada, "GraftFast surface engineering to improve MOF nanoparticles furtiveness," *Small*, 14, 1801900, (2018). DOI: 10.1002/smll.201801900.

[354] S. Gota, F. Jollet, J. P. Crocomhette, Z. Y. Wu, M. Pollak, N. Thromat, M. Gautier-Soyer, and C. R. Natoli, "Characterization of iron oxides by XAS at the Fe $L_{2,3}$ and O K edges," *Le Journal de Physique IV*, 7, C2–507–C2–508, (1997). DOI: 10.1051/jp4/1997072.

[355] M. Sassi, C. I. Pearce, P. S. Bagus, E. Arenholz, and K. M. Rosso, "First-principles Fe $L_{2,3}$ -edge and O K-edge XANES and XMCD spectra for iron oxides," *The Journal of Physical Chemistry A*, 121, 7613–7618, (2017). DOI: 10.1021/acs.jpca.7b08392.

[356] L. Kipgen, "Evolution of cooperativity in the spin transition of an iron(ii) complex on a graphite surface," *Nature Communications*, 9, 2984, (2018). DOI: 10.1038/s41467-018-05399-8.

[357] S.-J. Baek, A. Park, Y.-J. Ahn, and J. Choo, "Baseline correction using asymmetrically reweighted penalized least squares smoothing," *Analyst*, 140, (2014). DOI: 10.1039/C4AN01061B.

[358] C. Piamonteze, P. Miedema, and F. M. F. de Groot, "Accuracy of the spin sum rule in xmcd for the transition-metal L edges from manganese to copper," *Phys. Rev. B*, 80, 184410, (2009). DOI: 10.1103/PhysRevB.80.184410.

[359] J. Hu, H. Jinping, Z.-D. Zhang, K. Shen, S. Leung, H. Zhang, Q. Tian, P. Wang, Z. Jiang, H. Huang, J. Wells, and F. Song, "Ullmann coupling of 2, 7-dibromopyrene on au(111) assisted by surface adatoms," *Applied Surface Science*, 513, 145797, (2020). DOI: 10.1016/j.apsusc.2020.145797.

[360] D. Oteyza, N. Merino-Díez, A. Paz, J. Li, M. Vilas-Varela, J. Lawrence, M. Mohammed, A. Berdonces-Layunta, A. Barragán, J. Pascual, J. Lobo-Checa, and D. Peña, "Hierarchy in the halogen activation during surface-promoted ullmann coupling," *ChemPhysChem*, 20, (2019). DOI: 10.1002/cphc.201900633.

[361] A. Leonov, "Multiply periodic states and isolated skyrmions in an anisotropic frustrated magnet," *Nature Communications*, 6, 8275, (2015). DOI: 10.1038/ncomms9275.

[362] G. Stamokostas and G. Fiete, “Mixing of t_{2g}-e_g orbitals in 4d and 5d transition metal oxides,” *Phys. Rev. B*, (2017). DOI: 10.1103/PhysRevB.97.085150.

[363] Y. Y. Zhang, S. X. Du, and H.-J. Gao, “Binding configuration, electronic structure, and magnetic properties of metal phthalocyanines on a au(111) surface studied with ab initio calculations,” *Phys. Rev. B*, 84, 125446, (2011). DOI: 10.1103/PhysRevB.84.125446.

[364] S. Yazdani, J. Phillips, T. K. Ekanayaka, R. Cheng, and P. A. Dowben, “The influence of the substrate on the functionality of spin crossover molecular materials,” *Molecules*, 28, (2023). DOI: 10.3390/molecules28093735.

[365] L. Kipgen, M. Bernien, F. Tuczek, and W. Kuch, “Spin-crossover molecules on surfaces: From isolated molecules to ultrathin films,” *Advanced Materials*, 33, (2021). DOI: 10.1002/adma.202105663.

[366] M. Gruber and R. Berndt, “Spin-crossover complexes in direct contact with surfaces,” *Magnetochemistry*, 6, (2020). DOI: 10.3390/magnetochemistry6030035.

[367] A. Turkiewicz, W. Tomlinson, M. I. Gonzalez, J. P. Hooper, and J. R. Long, “Templated growth of a spin-frustrated cluster fragment of $MnBr_2$ in a metal–organic framework,” *Inorganic Chemistry*, 60, 16103–16110, (2021). DOI: 10.1021/acs.inorgchem.1c01345.

[368] T. Sato, H. Kadowaki, and K. Iio, “Successive phase transitions in the hexagonal-layered heisenberg antiferromagnets MnX_2 (x = br, i),” *Physica B: Condensed Matter*, 213-214, 224–226, (1995). DOI: https://doi.org/10.1016/0921-4526(95)00112-M.

[369] J. W. Stout, “Absorption Spectra of $MnCl_2$ and $MnBr_2$,” *The Journal of Chemical Physics*, 33, 303–303, (2004), ISSN: 0021-9606. DOI: 10.1063/1.1731111.

[370] R. Pappalardo, “Ligand Field Theory and the Absorption Spectra of $MnCl_2$ and $MnBr_2$,” *The Journal of Chemical Physics*, 31, 1050–1061, (2004). DOI: 10.1063/1.1730502.

[371] R. Pappalardo, “Note on the Optical Absorption of $MnCl_2$ and $MnBr_2$,” *The Journal of Chemical Physics*, 33, 613–614, (1960). DOI: 10.1063/1.1731199.

[372] W. B. Hadley and J. W. Stout, “Heat Capacity of MnBr2 between 1.7 and 20°K. Magnetic Ordering in $MnBr_2$,” *The Journal of Chemical Physics*, 39, 2205–2210, (1963). DOI: 10.1063/1.1701418.

[373] H. Hoekstra, H. Folkersma, and C. Haas, “Optical absorption and magnetic circular dichroism of $MnBr_2$,” *Physica B+C*, 128, 133–143, (1985). DOI: https://doi.org/10.1016/0378-4363(85)90097-X.

[374] E. O. Wollan, W. C. Koehler, and M. K. Wilkinson, “Neutron diffraction study of the magnetic properties of $MnBr_2$,” *Phys. Rev.*, 110, 638–646, 3 (1958). DOI: 10.1103/PhysRev.110.638.

[375] M. Lubben, A. Meetsma, and B. L. Feringa, “Crystal and molecular structure of polymeric $[MnCl_2(bpy)]_n$,” *Inorganica Chimica Acta*, 230, 169–172, (1995). DOI: https://doi.org/10.1016/0020-1693(94)04182-U.

[376] J. D. Tornero and J. Fayos, “Single crystal structure refinement of $MnCl_2$,” *Zeitschrift für Kristallographie - Crystalline Materials*, 192, 147–148, (1990). DOI: 10.1524/zkri.1990.192.14.147.

[377] K. I. Pokhodnya, M. Bonner, A. G. DiPasquale, A. L. Rheingold, J.-H. Her, P. W. Stephens, J.-W. Park, B. S. Kennon, A. M. Arif, and J. S. Miller, “Structural and magnetic properties of MCl_2 (M = Fe, Mn, Co): Acetonitrile solvates,” *Inorganic Chemistry*, 46, 2471–2477, (2007). DOI: 10.1021/ic061877n.

[378] D. Wiesler, M. Suzuki, I. Suzuki, and N. Rosov, "Determination of anomalous superexchange in $MnCl_2$ and its graphite intercalation compound," *Phys Rev Lett.*, 5, 942–945, (1995). DOI: 10.1103/PhysRevLett.75.942.

[379] H. Ju, Y. Lee, K.-T. Kim, I. H. Choi, C. J. Roh, S. Son, P. Park, J. H. Kim, T. S. Jung, J. H. Kim, K. H. Kim, J.-G. Park, and J. S. Lee, "Possible Persistence of Multiferroic Order down to Bilayer Limit of van der Waals Material NiI_2," *Nano Letters*, 21, 5126–5132, (2021). DOI: 10.1021/acs.nanolett.1c01095.

[380] S. Son, Y. Lee, J. H. Kim, B. H. Kim, C. Kim, W. Na, H. Ju, S. Park, A. Nag, K.-J. Zhou, Y.-W. Son, H. Kim, W.-S. Noh, J.-H. Park, J. S. Lee, H. Cheong, J. H. Kim, and J.-G. Park, "Multiferroic-Enabled Magnetic-Excitons in 2D Quantum-Entangled Van der Waals Antiferromagnet NiI_2," *Advanced Materials*, 34, 2109144, (2022). DOI: 10.1002/adma.202109144.

[381] S. Cai, F. Yang, and C. Gao, "$FeCl_2$ monolayer on HOPG: Art of growth and momentum filtering effect," *Nanoscale*, 12, 16041–16045, 30 (2020). DOI: 10.1039/D0NR03128C.

[382] J. Luo, G. Xiang, Y. Tang, K. Ou, and X. Chen, "The electric and magnetic properties of novel two-dimensional $MnBr_2$ and MnI_2 from first-principles calculations," *Journal of Applied Physics*, 128, 113901, (2020). DOI: 10.1063/5.0015936.

[383] T. Sato, H. Kadowaki, H. Masuda, and K. Iio, "Neutron diffraction study of successive phase transitions in the heisenberg antiferromagnet MnBr $_2$," *J. Phys. Soc. Jpn.*, 63, DOI: 10.1143/JPSJ.63.4583.

[384] R. B. Murray, "Specific heat of single-crystal $MnCl_2$ in applied magnetic fields," *Phys. Rev.*, 128, 1570–1574, 4 (1962). DOI: 10.1103/PhysRev.128.1570.

[385] None Available, *Materials data on MnBr2 by materials project*, in collab. with The Materials Project. DOI: 10.17188/1202436.

[386] S. Aldrich, *Mangan(ii)-bromid - 223646*, (2023). [Online]. Available: https://www.sigmaaldrich.com/DE/de/product/aldrich/223646 (visited on 11/23/2023).

[387] S. Aldrich, *Mangan(ii)-chlorid - 244589*, (2023). [Online]. Available: https://www.sigmaaldrich.com/DE/de/product/aldrich/244589 (visited on 11/23/2023).

[388] D. Company, *4x ombe source*, Firmen Website, (2018). [Online]. Available: http://www.dodecon.de/4xOMBE.html (visited on 11/22/2023).

[389] S. Aldrich, *Mangan(ii)-chlorid - Product Specifications*, (2023). [Online]. Available: https://www.sigmaaldrich.com/specification-sheets/119/434/223646-BULK_______ALDRICH__.pdf (visited on 11/23/2023).

[390] S. Aldrich, *Mangan(ii)-chlorid - Product Specifications*, (2023). [Online]. Available: https://www.sigmaaldrich.com/specification-sheets/235/679/244589-BULK_______ALDRICH__.pdf (visited on 11/23/2023).

[391] *Gold transmission data*, (2024). [Online]. Available: https://henke.lbl.gov/cgi-bin/filter.pl (visited on 01/10/2024).

[392] E. Gullikson, *Gold (au) $z = 79$, energy $= 1000.00$ ev*, (2024). [Online]. Available: https://henke.lbl.gov/cgi-bin/pert_cgi.pl (visited on 01/10/2024).

[393] J. Ma, Q. Yao, J. A. McLeod, L.-Y. Chang, C.-W. Pao, J. Chen, T.-K. Sham, and L. Liu, "Investigating the luminescence mechanism of mn-doped CsPb(br/cl) $_3$ nanocrystals," *Nanoscale*, 11, DOI: 10.1039/C9NR00143C. [Online]. Available: http://xlink.rsc.org/?DOI=C9NR00143C.

[394] *Transistor count*, (2024). [Online]. Available: https://en.wikipedia.org/wiki/Transistor_count (visited on 02/11/2024).

[395] *Transistor count*, (2024). [Online]. Available: https://en.wikipedia.org/wiki/Intel_4004 (visited on 02/11/2024).

[396] C. Intel, *The Intel 8008*, (2023). [Online]. Available: https://www.intel.com/content/www/us/en/history/virtual-vault/articles/the-8008.html (visited on 06/15/2023).

[397] *Wikipedia - Intel 8080*, (2023). [Online]. Available: https://en.wikipedia.org/wiki/Intel_8080 (visited on 06/28/2023).

[398] *Wikipedia - Intel 8085*, (2023). [Online]. Available: https://en.wikipedia.org/wiki/Intel_8085 (visited on 06/28/2023).

[399] *Wikipedia - Intel 8086*, (2023). [Online]. Available: https://en.wikipedia.org/wiki/Intel_8086 (visited on 06/28/2023).

[400] *Wikipedia - Intel 8088*, (2023). [Online]. Available: https://en.wikipedia.org/wiki/Intel_8088 (visited on 06/28/2023).

[401] *Wikipedia - Intel 80286*, (2023). [Online]. Available: https://en.wikipedia.org/wiki/Intel_80286 (visited on 06/28/2023).

[402] *Wikipedia - i386*, (2023). [Online]. Available: https://en.wikipedia.org/wiki/I386 (visited on 06/28/2023).

[403] *Wikipedia - Intel i960*, (2023). [Online]. Available: https://en.wikipedia.org/wiki/Intel_i960 (visited on 06/28/2023).

[404] *Wikipedia - i486*, (2023). [Online]. Available: https://en.wikipedia.org/wiki/I486 (visited on 06/28/2023).

[405] *Wikipedia - Pentium Pro*, (2023). [Online]. Available: https://en.wikipedia.org/wiki/Pentium_Pro (visited on 06/28/2023).

[406] *Wikipedia - Pentium II*, (2023). [Online]. Available: https://en.wikipedia.org/wiki/Pentium_II (visited on 06/28/2023).

[407] *Wikipedia - Pentium III*, (2023). [Online]. Available: https://en.wikipedia.org/wiki/Pentium_III (visited on 06/28/2023).

[408] *Wikipedia - Pentium 4*, (2023). [Online]. Available: https://en.wikipedia.org/wiki/Pentium_4 (visited on 06/28/2023).

[409] *Wikipedia - Itanium*, (2023). [Online]. Available: https://en.wikipedia.org/wiki/Itanium#Itanium_2_(McKinley_and_Madison):_2002%E2%80%932005 (visited on 06/28/2023).

[410] *Wikipedia - Intel Core*, (2023). [Online]. Available: https://en.wikipedia.org/wiki/Intel_Core#Core_2_Duo (visited on 06/28/2023).

[411] *Wikipedia - Xeon*, (2023). [Online]. Available: https://en.wikipedia.org/wiki/Xeon (visited on 06/28/2023).

[412] *Wikipedia - Haswell (microarchitecture)*, (2023). [Online]. Available: https://en.wikipedia.org/wiki/Haswell_(microarchitecture) (visited on 06/28/2023).

[413] *Wikipedia - Broadwell (microarchitecture)*, (2023). [Online]. Available: https://en.wikipedia.org/wiki/Broadwell_(microarchitecture) (visited on 06/28/2023).

[414] *Wikipedia - Skylake (microarchitecture)*, (2023). [Online]. Available: `https://en.wikipedia.org/wiki/Skylake_(microarchitecture)` (visited on 06/28/2023).

[415] *Wikipedia - Rocket Lake*, (2023). [Online]. Available: `https://en.wikipedia.org/wiki/Rocket_Lake` (visited on 06/28/2023).

[416] *Wikipedia - Sapphire Rapids*, (2023). [Online]. Available: `https://en.wikipedia.org/wiki/Sapphire_Rapids` (visited on 06/28/2023).

[417] SPECS, *PCS-ECR-AO*, (2023). [Online]. Available: `https://www.specs-group.com/nc/specs/products/detail/pcs-ecr-ao/` (visited on 12/14/2023).

[418] S. Aldrich, *Eisen(iii)-bromid (217883)*, (2024). [Online]. Available: `https://www.sigmaaldrich.com/DE/de/product/aldrich/217883` (visited on 02/01/2024).

[419] C. González Orellana, "Exploring the frontiers of ferromagnetic insulator/superconductor-based devices: Surface science developments to explain mesoscopic properties," Ph. D. Thesis, UNIVERSIDAD DEL PAÍS VASCO EUSKAL HERRIKO UNIBERSITATEA, (May 2023). [Online]. Available: `https://cfm.ehu.es/view/files/PhD-Thesis-Carmen-GO.pdf` (visited on 01/12/2024).

[420] Hao Wang and M. R. Linford, *X-ray Photoelectron Spectroscopy and Auger Electron Spectroscopy: Comparison and Basic Principles*. Vacuum Technology and Coating, (2015). [Online]. Available: `https://www.researchgate.net/publication/272790716_X-ray_Photoelectron_Spectroscopy_and_Auger_Electron_Spectroscopy_Comparison_and_Basic_Principles`.

[421] S. Sachdev, "Topological order in XY models in D = 3," 11, (2018).

[422] G. Eda, T. Fujita, H. Yamaguchi, D. Voiry, M. Chen, and M. Chhowalla, "Coherent Atomic and Electronic Heterostructures of Single-Layer MoS_2," *ACS Nano*, 6, 7311–7317, (2012). DOI: `10.1021/nn302422x`.

[423] B. Van Waeyenberge, A. Puzic, H. Stoll, K. W. Chou, T. Tyliszczak, R. Hertel, M. Fähnle, H. Brückl, K. Rott, G. Reiss, I. Neudecker, D. Weiss, C. H. Back, and G. Schütz, "Magnetic vortex core reversal by excitation with short bursts of an alternating field," *Nature*, 444, 461–464, (2006). DOI: `10.1038/nature05240`.

[424] D. Akinwande, C. J. Brennan, J. S. Bunch, P. Egberts, J. R. Felts, H. Gao, R. Huang, J.-S. Kim, T. Li, Y. Li, K. M. Liechti, N. Lu, H. S. Park, E. J. Reed, P. Wang, B. I. Yakobson, T. Zhang, Y.-W. Zhang, Y. Zhou, and Y. Zhu, "A review on mechanics and mechanical properties of 2D materials—Graphene and beyond," *Extreme Mechanics Letters*, 13, 42–77, (2017). DOI: `10.1016/j.eml.2017.01.008`.

[425] Q. H. Wang, K. Kalantar-Zadeh, A. Kis, J. N. Coleman, and M. S. Strano, "Electronics and optoelectronics of two-dimensional transition metal dichalcogenides," *Nature Nanotechnology*, 7, 699–712, (2012). DOI: `10.1038/nnano.2012.193`.

[426] J. Gusakova, X. Wang, L. L. Shiau, A. Krivosheeva, V. Shaposhnikov, V. Borisenko, V. Gusakov, and B. K. Tay, "Electronic Properties of Bulk and Monolayer TMDs: Theoretical Study Within DFT Framework (GVJ-2e Method)," *Physica Status Solidi (a)*, 214, 1700218, (2017). DOI: `10.1002/pssa.201700218`.

[427] S. Joseph, J. Mohan, S. Lakshmy, S. Thomas, B. Chakraborty, S. Thomas, and N. Kalarikkal, "A review of the synthesis, properties, and applications of 2D transition metal dichalcogenides and their heterostructures," *Materials Chemistry and Physics*, 297, 127332, (2023). DOI: `10.1016/j.matchemphys.2023.127332`.

[428] A. Devi, A. Kumar, P. Ahluwalia, and A. Singh, “Novel properties of transition metal dichalcogenides monolayers and nanoribbons (MX_2, where M = Cr, Mo, W and X = S, Se): A spin resolved study,” *Materials Science and Engineering: B*, 271, 115237, (2021). DOI: 10.1016/j.mseb.2021.115237.

[429] I. Song, C. Park, and H. C. Choi, “Synthesis and properties of molybdenum disulphide: From bulk to atomic layers,” *RSC Advances*, 5, 7495–7514, (2015). DOI: 10.1039/C4RA11852A.

[430] J. D. van der Waals, “The thermodynamic theory of capillarity under the hypothesis of a continuous variation of density,” *Journal of Statistical Physics*, 20, 200–244, (1979). DOI: 10.1007/BF01011514.

[431] Y. Duan, C. D. Stinespring, and B. Chorpening, “Electronic Structures, Bonding Configurations, and Band-Gap-Opening Properties of Graphene Binding with Low-Concentration Fluorine,” *ChemistryOpen*, 4, 642–650, (2015). DOI: 10.1002/open.201500074.

[432] Y. Zhu, S. Murali, W. Cai, X. Li, J. W. Suk, J. R. Potts, and R. S. Ruoff, “Graphene and Graphene Oxide: Synthesis, Properties, and Applications,” *Advanced Materials*, 22, 3906–3924, (2010). DOI: 10.1002/adma.201001068.

[433] M. Long, L. Tang, D. Wang, Y. Li, and Z. Shuai, “Electronic Structure and Carrier Mobility in Graphdiyne Sheet and Nanoribbons: Theoretical Predictions,” *ACS Nano*, 5, 2593–2600, (2011). DOI: 10.1021/nn102472s.

[434] A. Hirsch, “The era of carbon allotropes,” *Nature Materials*, 9, 868–871, (2010). DOI: 10.1038/nmat2885.

[435] X. Huang, S. Tang, X. Mu, Y. Dai, G. Chen, Z. Zhou, F. Ruan, Z. Yang, and N. Zheng, “Freestanding palladium nanosheets with plasmonic and catalytic properties,” *Nature Nanotechnology*, 6, 28–32, (2011). DOI: 10.1038/nnano.2010.235.

[436] R. Chau, B. Doyle, S. Datta, J. Kavalieros, and K. Zhang, “Integrated nanoelectronics for the future,” *Nature Materials*, 6, 810–812, (2007). DOI: 10.1038/nmat2014.

[437] G. E. Moore, “Cramming more components onto integrated circuits, Reprinted from Electronics, volume 38, number 8, April 19, 1965, pp.114 ff.,” *IEEE Solid-State Circuits Society Newsletter*, 11, 33–35, (2006). DOI: 10.1109/N-SSC.2006.4785860.

[438] C. Samsung, *Samsung Begins Chip Production Using 3nm Process Technology With GAA Architecture*, (2022). [Online]. Available: https://news.samsung.com/global/samsung-begins-chip-production-using-3nm-process-technology-with-gaa-architecture (visited on 11/22/2023).

[439] C. J. Chen, “Role of Tip Material in Scanning Tunneling Microscopy,” *MRS Proceedings*, 159, 289, (1989). DOI: 10.1557/PROC-159-289.

[440] F. Fang and B. Ju, “Scanning Tunneling Microscope,” in *CIRP Encyclopedia of Production Engineering*, The International Academy for Produ, L. Laperrière, and G. Reinhart, Eds., Berlin, Heidelberg: Springer Berlin Heidelberg, (2016), pp. 1–4, ISBN: 978-3-642-35950-7. DOI: 10.1007/978-3-642-35950-7_6596-4. (visited on 05/22/2023).

[441] *Constant Height mode*, (2015-2023). [Online]. Available: https://www.ntmdt-si.com/resources/spm-principles/stm-techniques/constant-height-mode (visited on 11/22/2023).

[442] *Constant Current mode*, (2015-2023). [Online]. Available: https://www.ntmdt-si.com/resources/spm-principles/stm-techniques/constant-current-mode (visited on 11/22/2023).

[443] L. E. C. van de Leemput and H. van Kempen, “Scanning tunnelling microscopy,” 55, 1165, (1992). DOI: 10.1088/0034-4885/55/8/002.

[444] P. Borghetti, A. El-Sayed, E. Goiri, C. Rogero, J. Lobo-Checa, L. Floreano, J. E. Ortega, and D. G. de Oteyza, “Spectroscopic Fingerprints of Work-Function-Controlled Phthalocyanine Charging on Metal Surfaces,” *ACS Nano*, 8, 12786–12795, (2014). DOI: 10.1021/nn5060333. (visited on 05/30/2023).

[445] F. Calavalle, P. Dreher, A. P. Surdendran, W. Wan, M. Timpel, R. Verucchi, C. Rogero, T. Bauch, F. Lombardi, F. Casanova, M. V. Nardi, M. M. Ugeda, L. E. Hueso, and M. Gobbi, “Tailoring Superconductivity in Large-Area Single - Layer $NbSe_2$ via Self-Assembled Molecular Adlayers,” *Nano Letters*, 21, 136–143, (2021). DOI: 10.1021/acs.nanolett.0c03386.

[446] H. Wende, C. Litwinski, A. Scherz, T. Gleitsmann, Z. Li, C. Sorg, K. Baberschke, A. Ankudinov, J. J. Rehr, and C. Jung, “A systematic study of embedded atom EXAFS: The (2 1)O/Cu(110) reconstruction as an ideal prototype system,” *Journal of Physics: Condensed Matter*, 15, 5197–5206, (2003). DOI: 10.1088/0953-8984/15/30/302.

[447] J. R. Lee, M. Bagge-Hansen, T. M. Willey, R. W. Meulenberg, M. H. Nielsen, I. C. Tran, and T. van Buuren, “X-ray Absorption Spectroscopy for the Structural Investigation of Self-Assembled-Monolayer-Directed Mineralization,” in *Methods in Enzymology*, vol. 532, Elsevier, (2013), pp. 165–187, ISBN: 978-0-12-416617-2. DOI: 10.1016/B978-0-12-416617-2.00008-4. [Online]. Available: https://linkinghub.elsevier.com/retrieve/pii/B9780124166172000084 (visited on 06/02/2023).

[448] S. E. Hadjadj, “Growth and Characterization of van-der-Waals Magnetic Materials,” Freie Universität Berlin, Berlin, Master Thesis, (2020), p. 101.

[449] M. Yi and Z. Shen, “A review on mechanical exfoliation for the scalable production of graphene,” *Journal of Materials Chemistry A*, 3, 11700–11715, (2015). DOI: 10.1039/C5TA00252D.

[450] K. S. Novoselov, A. K. Geim, S. V. Morozov, D. Jiang, Y. Zhang, S. V. Dubonos, I. V. Grigorieva, and A. A. Firsov, “Electric Field Effect in Atomically Thin Carbon Films,” *Science*, 306, 666–669, (2004). DOI: 10.1126/science.1102896.

[451] C. Sorg, “Magnetic Properties of 3d and 4f Ferromagnets Studied by X-Ray Absorption Spectroscopy,” Ph.D. dissertation, Freie Universität Berlin, Berlin, (2005). [Online]. Available: http://users.physik.fu-berlin.de/~bab/start_frame2/diss/CSdiss.pdf (visited on 06/15/2023).

[452] A. Singha, “Magnetic properties of surface-adsorbed single rare earth atoms, molecules, and atomic scale clusters,” Ph. D. Thesis, École Polytechnique Fédérale de Lausanne, LAUSANNE, (2017). [Online]. Available: https://infoscience.epfl.ch/record/232433 (visited on 06/15/2023).

[453] E. Goering, A. Fuss, W. Weber, J. Will, and G. Schütz, “Element specific x-ray magnetic circular dichroism magnetization curves using total electron yield,” *Journal of Applied Physics*, 88, 5920–5923, (2000). DOI: 10.1063/1.1308095.

[454] P. Wadley, K. W. Edmonds, M. R. Shahedkhah, R. P. Campion, B. L. Gallagher, J. Železný, J. Kuneš, V. Novák, T. Jungwirth, V. Saidl, P. Němec, F. Maccherozzi, and S. S. Dhesi, “Control of antiferromagnetic spin axis orientation in bilayer Fe/CuMnAs films,” *Scientific Reports*, 7, 11147, (2017). DOI: 10.1038/s41598-017-11653-8.

[455] L. Aballe, M. Foerster, E. Pellegrin, J. Nicolas, and S. Ferrer, "The ALBA spectroscopic LEEM-PEEM experimental station: Layout and performance," *Journal of Synchrotron Radiation*, 22, 745–752, (2015). DOI: 10.1107/S1600577515003537.

[456] A. Synchrotron, *BL24 - CIRCE*, (2014). [Online]. Available: https://www.cells.es/en/beamlines/bl24-circe (visited on 06/27/2023).

[457] C. Piamonteze, U. Flechsig, S. Rusponi, J. Dreiser, J. Heidler, M. Schmidt, R. Wetter, M. Calvi, T. Schmidt, H. Pruchova, J. Krempasky, C. Quitmann, H. Brune, and F. Nolting, "X-Treme beamline at SLS: X-ray magnetic circular and linear dichroism at high field and low temperature," *Journal of Synchrotron Radiation*, 19, 661–674, (2012). DOI: 10.1107/S0909049512027847.

[458] S. Synchrotron, *X-Treme / X07MA: X-ray absorption spectroscopy at high magnetic field and low temperature*, (2023). [Online]. Available: https://www.psi.ch/en/sls/xtreme (visited on 06/27/2023).

[459] S. Synchrotron, *End-station*. [Online]. Available: https://www.psi.ch/en/sls/xtreme/endstations (visited on 06/27/2023).

[460] A. Shiotari, "Inelastic Electron Tunneling Spectroscopy," in *Compendium of Surface and Interface Analysis*, The Surface Science Society of Japa, Ed., Singapore: Springer Singapore, (2018), pp. 283–288, ISBN: 978-981-10-6155-4 978-981-10-6156-1. DOI: 10.1007/978-981-10-6156-1_46. [Online]. Available: http://link.springer.com/10.1007/978-981-10-6156-1_46 (visited on 06/27/2023).

[461] W. Moritz, "Atomic Structures of Surfaces and Interfaces," in *Encyclopedia of Interfacial Chemistry*, Elsevier, (2018), pp. 55–58, ISBN: 978-0-12-809894-3. DOI: 10.1016/B978-0-12-409547-2.05359-2. [Online]. Available: https://linkinghub.elsevier.com/retrieve/pii/B9780124095472053592.

[462] S. Group, *LEEM, PEEM*. [Online]. Available: https://www.specs-group.com/nc/specsgroup/knowledge/methods/detail/leem-peem/ (visited on 06/28/2023).

[463] E. Bauer, "Low energy electron microscopy," *Reports on Progress in Physics*, 57, 895–938, (1994). DOI: 10.1088/0034-4885/57/9/002.

[464] M. S. Altman, "Trends in low energy electron microscopy," *Journal of Physics: Condensed Matter*, 22, no. 8, 084017, (2010). DOI: 10.1088/0953-8984/22/8/084017.

[465] E. Bauer, "Surface microscopy with low energy electrons: LEEM," *Journal of Electron Spectroscopy and Related Phenomena*, 241, 146806, (2020). DOI: 10.1016/j.elspec.2018.11.005.

[466] T. d. Jong, "Superlattices in van der Waals materials: A low-energy electron microscopy study," Ph. D. Thesis, Universität Leiden, Leiden, (2022). [Online]. Available: https://scholarlypublications.universiteitleiden.nl/handle/1887/3485753 (visited on 06/28/2023).

[467] Z. DAI, "Atomic Structure Studies of 2D materials and Advancement of Dynamical LEEM/uLEED-IV Analysis," Ph. D. Thesis, University of New Hampshire, (2018). [Online]. Available: https://scholars.unh.edu/dissertation/2404/ (visited on 06/28/2023).

[468] L. Aballe and M. Foerster, *Working principles of LEEM-PEEM*, Vortrag Power Point, ALBA, (2015). [Online]. Available: https://indico.cells.es/event/24/contributions/532/attachments/387/520/PEEMworkshopFoerster.pdf (visited on 06/28/2023).

[469] H. S. Nalwa, Ed., *Handbook of surfaces and interfaces of materials*. San Diego: Academic Press, (2001), ISBN: 978-0-12-513910-6 978-0-12-513911-3 978-0-12-513912-0 978-0-12-513913-7 978-0-12-513914-4 978-0-12-513915-1.

[470] L. Wittenbecher, "Time-Resolved Photoemission Electron Microscopy: Development and Applications," Ph. D. Thesis, Lund University, Lund, (2021). [Online]. Available: https://lucris.lub.lu.se/ws/portalfiles/portal/102264694/Lukas_Wittenbecher_web.pdf (visited on 06/28/2023).

[471] M. Mirolo, "Multiple scales post mortem and operando XPS, XAS and XPEEM investigations of reactivity at interfaces in Li-ion batteries," Ph. D. Thesis, ETH Zürich, Zürich, (2020). [Online]. Available: https://www.research-collection.ethz.ch/bitstream/handle/20.500.11850/479623/1/202104-Thesis_VF_organized.pdf (visited on 06/28/2023).

[472] E. Brueche, "Elektronenmikroskopische Abbildung mit lichtelektrischen Elektronen," *Zeitschrift f r Physik*, 86, 448–450, (1933). DOI: 10.1007/BF01341360.

[473] S. H. Chew, "Photoemission Electron Microscopy for Nanoscale Imaging and Attosecond Control of Light-Matter Interaction at Metal Surfaces," Ph. D. Thesis, LMU München, München, (2017). [Online]. Available: https://edoc.ub.uni-muenchen.de/22169/ (visited on 06/28/2023).

[474] M. Baksi, D. Toffoli, O. Gulseren, and H. Ustunel, "Nanotribological Properties of the h-BN/Au(111) Interface: A DFT Study," *The Journal of Physical Chemistry C*, 123, 28411–28418, (2019). DOI: 10.1021/acs.jpcc.9b06767.

[475] W.-H. Lin, V. W. Brar, D. Jariwala, M. C. Sherrott, W.-S. Tseng, C.-I. Wu, N.-C. Yeh, and H. A. Atwater, "Atomic-Scale Structural and Chemical Characterization of Hexagonal Boron Nitride Layers Synthesized at the Wafer-Scale with Monolayer Thickness Control," *Chemistry of Materials*, 29, 4700–4707, (2017). DOI: 10.1021/acs.chemmater.7b00183. (visited on 06/28/2023).

[476] M. Bonilla, S. Kolekar, Y. Ma, H. C. Diaz, V. Kalappattil, R. Das, T. Eggers, H. R. Gutierrez, M.-H. Phan, and M. Batzill, "Strong room-temperature ferromagnetism in VSe_2 monolayers on van der Waals substrates," *Nature Nanotechnology*, 13, 289–293, (2018). DOI: 10.1038/s41565-018-0063-9.

[477] J. Xiao and B. Yan, "An electron-counting rule to determine the interlayer magnetic coupling of the van der waals materials," *2D Materials*, 7, 045010, (2020). DOI: 10.1088/2053-1583/ab9ea4.

[478] I. Horcas, R. Fernández, J. M. Gómez-Rodríguez, J. Colchero, J. Gómez-Herrero, and A. M. Baro, "Wsxm: A software for scanning probe microscopy and a tool for nanotechnology," *Review of Scientific Instruments*, 78, 013705, (2007). DOI: 10.1063/1.2432410.

List of Figures

List of Tables

List of Publications

- "Ivar Kumberg, Evangelos Golias, Sebastien E. Hadjadj, Rahil Hosseinifar, Sangeeta Thakur, Tauqir Shinwari, Ismet Gelen, Niko Pontius, Christian Schüßler-Langeheine, Clemens von Korff Schmising, Sangeeta Sharma, and Wolfgang Kuch - Ultrafast laser-induced magneto-optical changes in resonant magnetic x-ray reflectivity, Phys. Rev. B 108, (2023) "

- "Sebastien E. Hadjadj, Carmen González-Orellana, James Lawrence, Djuro Bikaljević, Marina Peña-Díaz, Pierluigi Gargiani, Lucia Aballe, Jan Naumann, Miguel Ángel Niño, Michael Foerster, Sandra Ruiz-Gómez, Sangeeta Thakur, Ivar Kumberg, James M. Taylor, Jack Hayes, Jorge Torres, Chen Luo, Florin Radu, Dimas G. de Oteyza, Wolfgang Kuch, José Ignacio Pascual, Celia Rogero, and Maxim Ilyn - Epitaxial Monolayers of the Magnetic 2D Semiconductor $FeBr_2$ Grown on Au(111), ACS Chem. Mater., (2023)".

- "Ismet Gelen, Tauqir Shinwari, Ivar Kumberg, Sebastien Elie Hadjadj, Yasser A. Shokr, Evangelos Golias and Wolfgang Kuch - Growth of Mn_xAu_{1-x} films on Cu(001) and Ag(001) single-crystal substrates, PSS B (2024)"

- "Marcel Walter, Clara Tromer, Sebastien E. Hadjadj, Jorge Torres, David Swerev, Chen Luo, Florin Radu, Felix Tucek, Wolfgang Kuch, Sangeeta Thaku- Spin crossover properties of binuclear Fe^{2+} on HOPG (Paper is in preparation)"

- "Samuel Kerschbaumer, Sebastien E. Hadjadj, Andrea Aguirre Baños, Danilo Longo, Fadi Choueikani, Matthias Muntwiler, Wolfgang Kuch, José Ignacio Pascual, Martina Corso, Celia Rogero, Maxim Ilyn - Strong in plane anisotropy of magnetic 2D semiconductors $CoBr_2$ and $CoCl_2$ on Au(111) (Paper is in preparation)"

- "Jorge Torres, Sangeeta Thakur, Sascha Ossinger, Ivar Kumberg, Evangelos Golias, Clara W.A. Trommer, Sebastien E. Hadjadj, Marcel Walter, Jendrik Gördes, Rahil Hosseinifar, Pin-Chi Liu, Chen Luo, Lalminthang Kipgen, Florin Radu, Felix Tuczek, and Wolfgang Kuch - Relation between polymorphic phases and LIESST temperatures as a function of thickness of mono- and sub-monolayer films of a high $T_{\frac{1}{2}}$ spin-crossover molecule consisting of a tridentate organo-borate ligand deposited on HOPG (Paper is in preparation)"

- "Rahil Hosseinifar, Ivar Kumberg, Felix Steinbach, Sangeeta Thakur, Sebastien E. Hadjadj, Jendrik Gördes, Mario Fix, José Miguel Lendínez, Chowdhury Awsaf, Manfred Albrecht, Florian Kronast, Unai Atxitia, Clemens von Korff Schmising, and Wolfgang Kuch- Studying all-optical magnetization switching of GdFe by double-pulse excitation (Paper is in preparation)"

- "Sebastien E. Hadjadj, Samuel Kerschbaumer, Andrea Aguirre-Baños, Amitayush J. Thakur, Danilo Longo, David Caldevilla-Asenjo, Carmen González-Orellana, Pierluigi Gargiani, Matthias Muntwiler, Martina Corso, José Ignacio Pascual, Wolfgang Kuch, Celia Rogero, and Maxim Ilyn - Epitaxial growth of 2D semiconductor $FeBr_2$ monolayers on Bi_2Se_3 (Paper is in preparation)"

- "Sebastien E. Hadjadj, Samuel Kerschbaumer, Andrea Aguirre-Baños, Amitayush J. Thakur, Danilo Longo, David Caldevilla-Asenjo, Pierluigi Gargiani, Matthias Muntwiler, Martina Corso, José Ignacio Pascual, Wolfgang Kuch, Celia Rogero, and Maxim Ilyn - Epitaxial monolayers at the 2D limit of $MnBr_2$ and $MnCl_2$ grown on Au(111) (Paper is in preparation)"

List of Talks and Posters

- "Sebastien Elie Hadjadj, Evangelos Golias, Jack Hayes, Marcel Walter, Christian Lotze, Sangeeta Thakur, Ivar Kumberg, Ismet Gelen, Jorge Torres, and Wolfgang Kuch - Growth and characterization of monolayer $MnSe_2$ on Au(111), Poster, DPG, Regensburg 2022"
- "Sebastien E. Hadjadj, Samuel Kerschbaumer, Andrea Aguirre Baños, Danilo Longo, Fadi Choueikani, Celia Rogero, José Ignacio Pascual, Wolfgang Kuch, Maxim Ilyn - Magnetic properties of transition metal dihalides measured by x-ray magnetic circular dichrosim (XMCD), Poster, Quanty Workshop, Heidelberg 2022"
- "Sebastien E. Hadjadj, Samuel Kerschbaumer, Andrea Aguirre Baños, Danilo Longo, Fadi Choueikani, Celia Rogero, José Ignacio Pascual, Wolfgang Kuch, Maxim Ilyn - Magnetic properties of transition metal dihalides measured by x-ray magnetic circular dichroism (XMCD), Poster, DPG, Dresden 2023"
- "Sebastien E. Hadjadj, Carmen González-Orellana, James Lawrence, Djuro Bikaljević, Marina Peña-Díaz, Pierluigi Gargiani, Lucia Aballe, Jan Naumann, Miguel Ángel Niño, Michael Foerster, Sandra Ruiz-Gómez, Sangeeta Thakur, Ivar Kumberg, James M. Taylor, Jack Hayes, Jorge Torres, Chen Luo, Florin Radu, Dimas G. de Oteyza, Wolfgang Kuch, José Ignacio Pascual, Celia Rogero, and Maxim Ilyn - Structural and chemical characterization of epitaxially grown $FeBr_2$ on Au(111), Talk, DPG, Dresden 2023"
- "Sebastien E. Hadjadj, Carmen González-Orellana, James Lawrence, Djuro Bikaljević, Marina Peña-Díaz, Pierluigi Gargiani, Lucia Aballe, Jan Naumann, Miguel Ángel Niño, Michael Foerster, Sandra Ruiz-Gómez, Sangeeta Thakur, Ivar Kumberg, James M. Taylor, Jack Hayes, Jorge Torres, Chen Luo, Florin Radu, Dimas G. de Oteyza, Wolfgang Kuch, José Ignacio Pascual, Celia Rogero, and Maxim Ilyn - Epitaxial growth and properties of sub-monolayer to multilayer $FeBr_2$ on Au(111), Poster, DPG, Berlin 2024"

Acknowledgement

I would like to thank Prof. Dr. Wolfgang Kuch and Prof. Dr. Katharina Franke for the opportunity, interest and support during my Ph.D. thesis. I would also like to thank the whole AG Kuch in particular Dr. Ivar Kumberg, Dr. Sangeeta Thakur and Marcel Walter for the friendly conversations and constructive discussions. I would like to thank Uwe Lipowski for his active support in the design of new components and the constructive discussions that expanded my knowledge of possible solutions and new constructions of UHV components. My thanks also go to the IT, Electronics and Feinwerktechnik of the physics department for the perfect realization of the new ideas we discussed and the quick help with the many repairs. My special thanks go to Dr. Maxim Ilyn, Dr. Celia Rogero and Prof. Dr. Dimas G. de Oteyza for the opportunities, the constant support to increase my knowledge, as well as for all constructive ideas and goal-oriented discussions. I also want to thank all other collaborators, colleagues and friends at CFM and Nanogune in Donostia and all beamlines. I would also like to thank all my friends who has supported me during my studies. Last but not least, I would like to thank my family from the bottom of my heart for their constant and never-ending support.

Selbstständigkeitserklärung

Nachname	Hadjadj
Vorname	Sebastien Elie

Ich erkläre gegenüber der Freien Universität Berlin, dass ich die vorliegende Dissertation selbstständig und ohne Benutzung anderer als der angegebenen Quellen und Hilfsmittel angefertigt habe. Die vorliegende Arbeit ist frei von Plagiaten. Alle Ausführungen, die wörtlich oder inhaltlich aus anderen Schriften entnommen sind, habe ich als solche kenntlich gemacht. Diese Dissertation wurde in gleicher oder ähnlicher Form noch in keinem früheren Promotionsverfahren eingereicht. Mit einer Prüfung meiner Arbeit durch ein Plagiatsprüfungsprogramm erkläre ich mich einverstanden.

Ort, Datum

Unterschrift

Decleration of authorship

Name	Hadjadj
First name	Sebastien Elie

I declare to the Freie Universität Berlin that I have completed the submitted dissertation independently and without the use of sources and aids other than those indicated. The present thesis is free of plagiarism. I have marked as such all statements that are taken literally or in content from other writings. This dissertation has not been submitted in the same or similar form in any previous doctoral procedure. I agree to have my thesis examined by a plagiarism examination software.

Ort, Datum

Unterschrift